Design and Synthesis of Fluorescent and Antibiotic Conjugates of Vitamin B_{12} and Cobinamide

Jessica Fredericksen

A thesis submitted to

Auckland University of Technology

in fulfilment of the requirements for the degree of

Doctor of Philosophy (PhD)

2025

School of Science

Abstract

The essential micronutrient vitamin B_{12} has shown considerable promise as a delivery vehicle for antibiotics into bacteria. Novel antibiotic therapies using this 'Trojan horse' approach have considerable potential in the battle against antibiotic resistance. The goals of this research were 1) to synthesise highly fluorescent derivatives of vitamin B_{12} and its naturally occurring analogue cobinamide, and 2) to synthesise vitamin B_{12} conjugates of the widely used antibiotics gentamycin and ciprofloxacin. Vitamin B_{12} has its own specific and active uptake pathway within bacterial cells.

Fluorescent conjugates were designed to function as tools to follow the uptake, transport and cellular localisation of vitamin B_{12} and cobinamide in bacteria. Although the synthesis of fluorescent CNCbl derivatives is well-documented, no fluorescent derivatives of CNCbi have been reported to the best of our knowledge. Furthermore, practically all existing vitamin B_{12} derivatives of fluorophores exhibit significant fluorescence quenching. The key focus of this work was to synthesise vitamin B_{12} and cobinamide conjugates with high fluorescent quantum yields.

A range of fluorescent derivatives of CNCbl and CNCbi incorporating NBD-X, sulfo-Cyanine5 and Cyanine7 have been successfully synthesised in high purities (≥90%) and very good to reasonable yields. These conjugates were designed to retain their binding capacity to the Btu uptake system (including BtuB, BtuF and BtuCD transport proteins) for CNCbl/CNCbi uptake in the gram-negative bacterium *Escherichia coli*. Fluorescence analysis established high quantum yields (>0.20) for CNCbl/CNCbi conjugates incorporating sulfo-Cyanine5 and Cyanine7 fluorophores. An exciting finding from this research was that the conjugation of the near infrared emitting Cyanine7 to CNCbl and CNCbi resulted in no observable fluorescence quenching. Significant fluorescence quenching was observed for the conjugates that incorporated the NBD-X fluorophore. Solution studies between the free components suggested a dynamic quenching mechanism. For the conjugates, where the donor-acceptor distance is constrained, the significant spectral overlap between NBD-X emission and the CNCbl absorbance suggests Förster Resonance Energy Transfer (FRET) is a likely contributor, though other mechanisms such as Photoinduced Electron Transfer (PeT) cannot be excluded.

Recently a vitamin B_{12} conjugate of the antibiotic ampicillin was shown to be 500 times more effective than ampicillin itself in killing *E coli*. Once robust synthetic approaches were developed for synthesising the fluorescent CNCbl conjugates, these procedures were used to inform the synthesis of two antibiotic conjugates of CNCbl. Novel CNCbl-linker-antibiotic conjugates were synthesised incorporating the antibiotics gentamicin and ciprofloxacin. The conjugation of ciprofloxacin to CNCbl was achieved at two sites – the carboxylic acid and the secondary amine functionalities of ciprofloxacin. Site-selective conjugation of gentamicin via an amine is challenging, as multiple reactive amines are available for conjugation. However, conjugation of gentamicin to CNCbl was determined to occur selectively at one amine site using both LC-MS and ^{1}H NMR spectroscopy. The purification of CNCbl-linker-antibiotic conjugates was achieved by reversed-phase C18 chromatography and required isocratic conditions and the collection of small fractions to achieve purities of >95%. This was reflected in lower product yields (9-40%); however, conjugates were isolated for analysis and are suitable for biological testing. These conjugates will allow others to investigate the uptake and efficiency of CNCbl/CNCbi delivery system as a Trojan horse strategy to deliver antibiotics into bacteria – a relatively unexplored and promising area of medicinal chemistry.

Table of Contents

Table of Figures

Table of Schemes

Table of Tables

List of Abbreviations

calcd.	Calculated
COSY	Correlation spectrum
D_2O	Deuterated water
d	Doublet
DAD	Diode array detector
DMF	Dimethyformamide
DMSO	Dimethylsulfoxide
DMSO-d_6	Deuterated dimethylsulfoxide
EIC	Extracted ion count
ESI	Electrospray ionisation
EtOH	Ethanol
eq.	Equivalents
h	Hours
HPLC	High-pressure liquid chromatography
HRMS	High-resolution mass spectrometry
HSQC	Heteronuclear single quantum coherence
LCMS	Liquid chromatography-mass spectrometry
m/z	Mass to charge ratio
m	Multiplet
min	Minute
MeOH-d_4	Deuterated methanol
PeT	Photoinduced electron transfer
pH	$-\log[H_3O^+]$
ppm	Parts per million
RP-18	Reversed-phase C18

TIC	Total ion count
TLC	Thin-layer chromatography
r.t	Room temperature
UV/Vis	Ultraviolet-visible
Φ	Fluorescence quantum yield
μ	micro
η	refractive index

Attestation of Authorship

I hereby declare that this submission is my own work and that, to the best of my knowledge and belief, it contains no material previously published or written by another person (except where explicitly defined in the acknowledgements), nor used artificial intelligence tools or generative artificial intelligence tools (unless it is clearly stated, and referenced, along with the purpose of use), nor material which to a substantial extent has been submitted for the award of any other degree or diploma of a university or other institution of higher learning.

29/04/2025

Signature Date

Acknowledgements

Completing this PhD has been a journey of both intellectual and personal growth, and I would not have reached this point without the support, guidance, and encouragement of many people.

First and foremost, I would like to express my deepest gratitude to my supervisor, Professor Nicola E. Brasch for her invaluable mentorship, support, and feedback throughout the course of my research. I am also deeply thankful to the wider AUT team, particularly the technical team for their thoughtful input and encouragement at every stage. This body of work would not have been possible without you.

To my friends in the lab, thank you for the unwavering support and kindness. I would especially like to acknowledge Bronte, whose friendship has been a constant source of strength and joy throughout this journey. Your support, late-night debriefs, and shared sense of humour made the toughest moments easier to bear—and the good ones even better. I couldn't have asked for a better friend to walk alongside through the highs and lows of PhD life. A heartfelt thanks also goes to Ben, my brilliant B_{12} research buddy, whose enthusiasm, curiosity, and dedication helped shape not only the science in this thesis but my own thinking and approach as a researcher. Our countless conversations—equal parts rigorous and ridiculous—pushed me to be better and made the research process feel like a true collaboration.

I extend my heartfelt thanks to my family for their endless patience and belief in me, especially Mitchell, whose love and support kept me grounded, and Lilith and Jade for being my inspiration and constant reminders of what truly matters. To my mum and stepdad, thank you for being my unwavering pillars of strength and perspective. Your steady presence, wisdom, and unconditional support have grounded me through the many ups and downs of this journey. Mum, your belief in me—especially during moments when I doubted myself—meant more than words can express. And to Jimbo, thank you for always offering a calm, thoughtful perspective and for reminding me to keep my feet on the ground even when my head is in the cloud. This achievement is as much yours as it is mine.

To my friends outside of AUT and academia—thank you for reminding me to take breaks, laugh often, and keep life in perspective.

Chapter 1 Literature review

1.1 Chapter overview

This chapter provides an overview of the key concepts underpinning this thesis. It begins with a discussion of the structure and biological significance of vitamin B_{12} and its precursor, cobinamide. The use of vitamin B_{12} as a delivery molecule is then introduced, together with an outline of the protein-mediated uptake pathway in the gram-negative bacterium *Escherichia coli*. This is followed by a review of the synthesis of fluorescent vitamin B_{12} derivatives and their application in studies of uptake, transport, and cellular localisation. Given the central role of fluorescence in this research, the principles of fluorescence and methods for determining quantum yield are also described. The chapter then examines the development of antibiotic resistance in gram-negative bacteria, with particular attention to trojan horse therapies that exploit vitamin B_{12} as a carrier. Finally, the mechanisms of action of ciprofloxacin and gentamicin are considered, with emphasis on synthetic strategies used to modify these antibiotics.

1.2 Chemistry and biological importance of vitamin B_{12}

Corrinoids are a group of chemically distinct molecules built upon the corrin ring skeleton[1]. The corrin ring, similar to a porphyrin, is a macrocycle containing four pyrrole rings. Vitamin B_{12}, termed a complete corrinoid, is an essential micronutrient required by most forms of life. B_{12} belongs to the biologically important class of cobalt-containing enzymes. Except for higher plants, organisms from all kingdoms of life are known to utilisee B_{12}-dependant enzymes.[2] B_{12}-dependent enzymes are most well known for their roles in the production of red blood cells, synthesis and regulation of DNA and nervous system function.[3] The following section will discuss the structure and biological relevance of both complete and incomplete corrinoids, with a particular focus on vitamin B_{12} and its naturally occurring precursor, cobinamide (Cbi).

1.2.1 Complete corrinoids

Complete corrinoids refer to the nucleotide-containing vitamin B_{12} family.[4] Beginning with the central macrocycle, the structure consists of four five-membered pyrrole rings coordinated to a central cobalt atom (Figure 1). Surrounding the macrocycle periphery are three acetamide and four propionamide substituents. In the case of ‘complete’

corrinoids, one of the propionamide residues is further functionalised as a pseudo peptide backbone. This comprises a phosphate moiety attached to a ribose ring followed by a 5,6-dimethylbenzimidazole group. The nitrogen residue of the 5,6-dimethylbenzimidazole typically coordinates to the lower axial site of the macrocycle-bound cobalt. The coordination of this lower ligand occurs in a 'base-on' or 'base-off' state. The 'base-off' state occurs upon protonation of the dimethylbenzimidizole nitrogen where the lower axial site is occupied by an exogenous ligand (often solvent or protein residue). The upper axial ligand coordinated to the Co centre can vary and is most often occupied by a cyano, hydroxo, methyl or adenosyl ligand (Figure 1). The two co-enzyme forms of vitamin B_{12} contain the methyl and adenosyl ligands, termed adenosylcobalamin and methylcobalamin, respectively. Adenosylcobalamin is known for its role in enzymatic catalysis by homolytic cleavage of the Co(III)-C bond, with the resulting adenosyl radical initiating rearrangement reactions. Methylcobalamin, however, converts between the Co(III) to Co(I) state with methylation of the substrates via heterolytic bond cleavage upon nucleophilic attack of MeCbl by the substrate.[3–6] The work discussed here uses the commercially available cyanocobalamin (CNCbl) complex, also known as vitamin B_{12}.

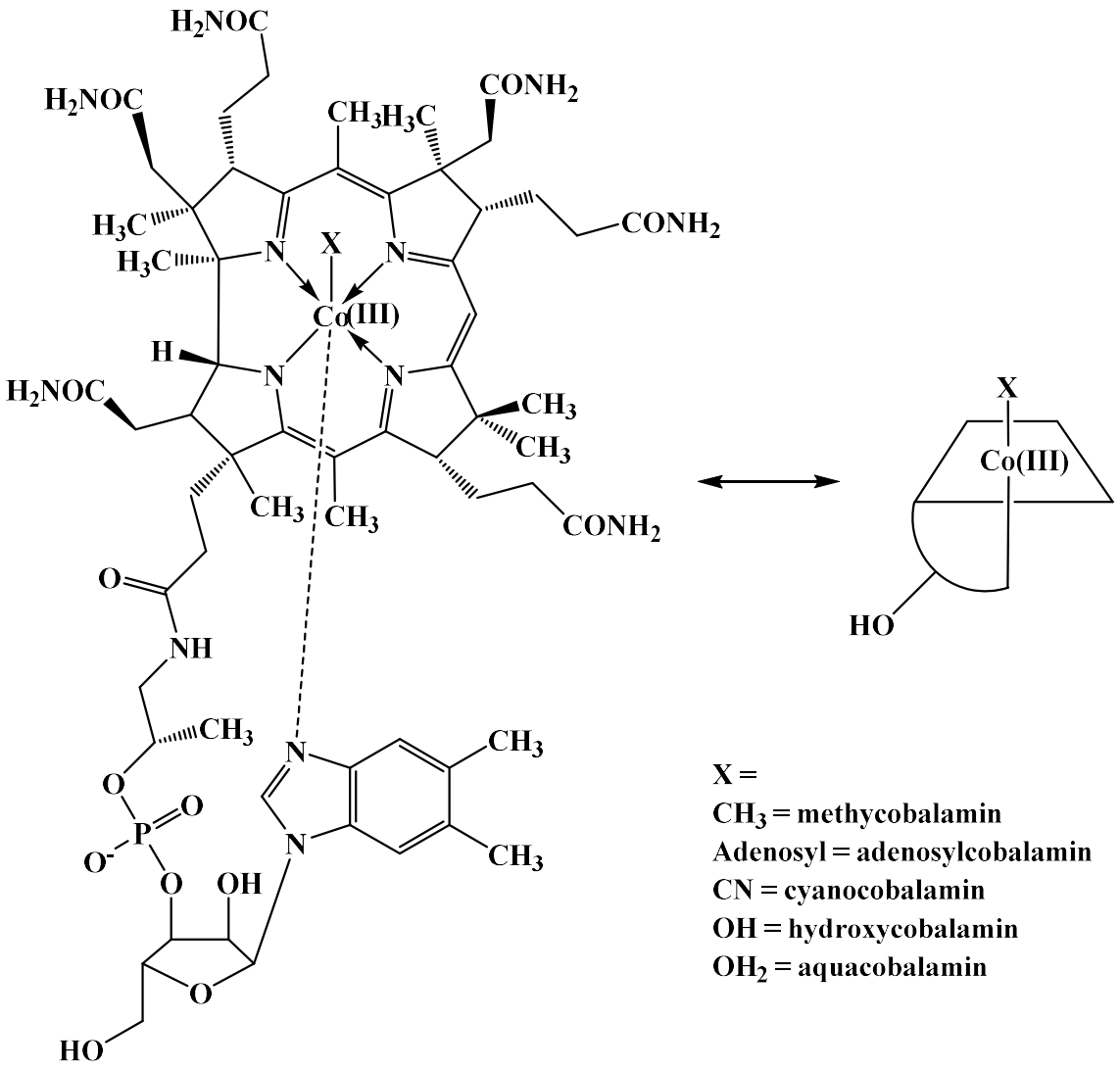

Figure 1: Full and simplified structure of 'complete' corrinoid of vitamin B_{12} and its derivatives.

1.2.2 Incomplete corrinoids

Incomplete corrinoids refer to the truncated analogues of complete corrinoids where part or all of the entire lower nucleotide is absent.[7–9] Incomplete corrinoids are often referred to as vitamin B_{12} precursors, as these molecules are typically intermediates in the biosynthetic pathways for the complete vitamin B_{12} complex. Cobinamide (Cbi) and cobyric acid (Cby) are two notable examples of incomplete corrinoids. Cbi contains the complete central macrocycle but lacks the lower co-ordinated nucleotide moiety. This means Cbi has two available axial ligand sites, providing a greater ligand-binding capacity than vitamin B_{12}. Cby in comparison is similar in structure to Cbi but is

hydrolysed at the f sidechain of the corrin (Figure 2, see Figure 3 for assignment of the sidechains).

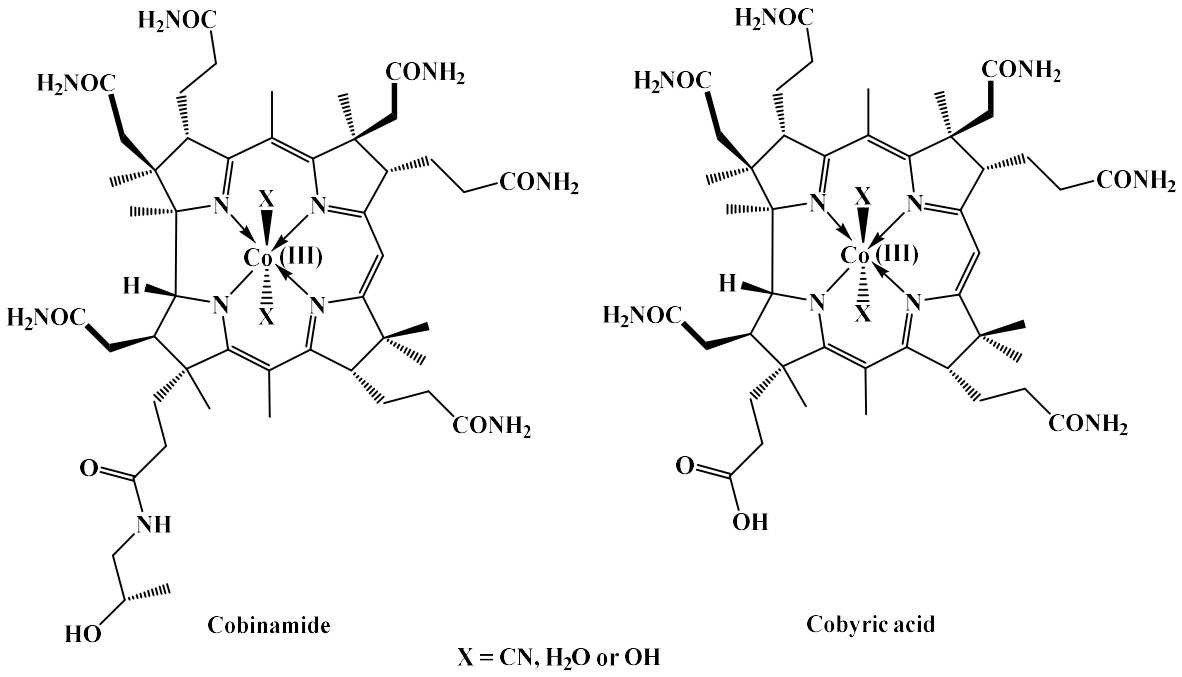

Figure 2: Structures of vitamin B_{12} analogues cobinamide (Cbi) and cobyric acid (Cby).

Cbi and Cby were first synthesised and characterised as part of attempts to synthesise the complete vitamin B_{12} complex.[9,10] Synthesis of Cbi and Cby are now achieved by acid hydrolysis of vitamin B_{12} or exposure to high quantities of cyanide salts (NaCN).[9,11] The Cbi precursor is used in this research for the development of novel Cbi-fluorophore conjugates.

1.3 CNCbl as a delivery molecule

CNCbl can be exploited as a natural carrier molecule for delivering many types of cargo into different cell types.[12] Many CNCbl-cargo derivatives have been synthesised, focusing on therapeutics and imaging agents as cargo.[5,13,14] The complex structure of CNCbl offers many locations for chemical modification, i.e. the β-axial site, amide residues of the side chains (a-g, typically by partial hydrolysis to monocarboxylic acids),

alteration of the peptide side chain (f) and the 5'-OH of the lower ribose ring (Figure 3).[13]

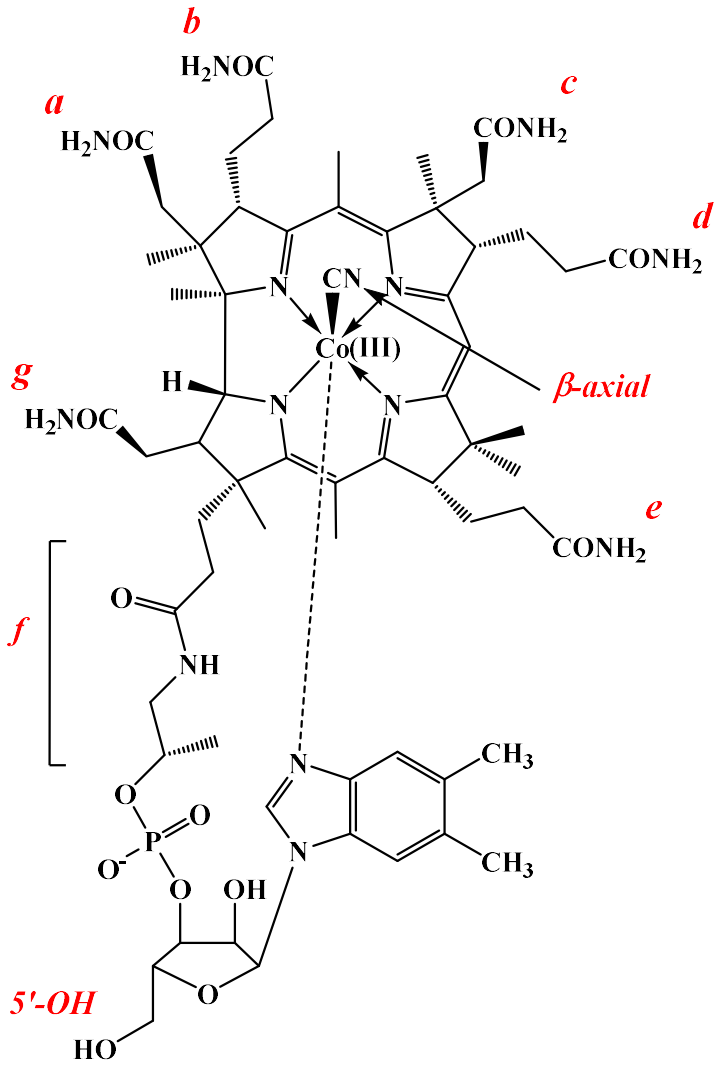

Figure 3: Structure of CNCbl with common modification sites highlighted.

Vitamin B_{12} derivatives have been developed as anti-cancer agents, where chemotherapeutics such as cisplatin and other pro-drugs have been conjugated to enhance tumour targeting capacity.[15,16] The use of vitamin B_{12} as an imaging agent for tumours and inflammatory lesions has been demonstrated using gadolinium or radioactive ^{99m}Tc derivatives.[17,18] These derivatives exploit the increased uptake and sequestering of vitamin B_{12} in rapidly growing cancer cell lines.[18] Other derivatives of vitamin B_{12} have been developed to target specific diseases. The most notable example is vitamin B_{12} as a carrier for insulin and other related drugs to prevent off-target side effects.[19–21] More recent research has shifted to nanoparticles functionalised with vitamin B_{12}. These

nanoparticle derivatives have enabled targeted drug delivery for small interfering RNAs and hydrophobic drugs within cancer cells.[22,23] The use of vitamin B_{12} as a carrier for many types of cargo provides key advantages such as improved solubility of hydrophobic drugs, reduced off-target toxicity, lower required therapeutic doses and targeted delivery.[12,24] Vitamin B_{12} derivatives of antibiotics, peptide nucleic acids and fluorophores have been discussed in Section 1.8.2

To ensure the binding of the CNCbl conjugate to B_{12} uptake and transport proteins, it is important to choose the modification site carefully. CNCbl is delivered intracellularly within bacterial systems via the CNCbl uptake pathway, known as Btu.[25,26] In mammalian cells, transport and uptake are achieved by a multi-protein mediated pathway including intrinsic factor (IF), haptocorrin (HC) and transcobalamin (TC).[27] Modifications at the 5'-OH position are well tolerated by these uptake proteins in both bacterial and mammalian cells (Figure 3).[19,21,28–33] Chemical modification at this site is well-documented, with multiple synthetic pathways available.[13]

The research described herein utilises a carbamate bond between the 5'-OH alcohol residue of CNCbl and a primary amine-containing linker. The employment of a linker has been carried out for two key reasons. The first is to provide a suitable synthetic handle for the attachment of the cargo (an amine or carboxylic acid residue). Secondly, others have shown that the inclusion of a linker of less than two or greater than 12 atoms between the B_{12} and the cargo is best for the delivery and subsequent activity of the attached cargo.[24] Two closely related methods for functionalisation of CNCbl at the 5'-OH site utilise either carbonyldiimidazole (CDI) or carbonylditriazole (CDT) as the alcohol-activating reagent. Upon nucleophilic attack by the primary amine of the linker, the imidazole/triazole moiety is substituted resulting in a carbamate bond between the CNCbl and linker molecule (Scheme 1). Although both CDI and CDT result in the formation of

the desired linkage, it has been shown in the literature that the use of CDT results in a better yield (50-90%).[28,29,32,34–37]

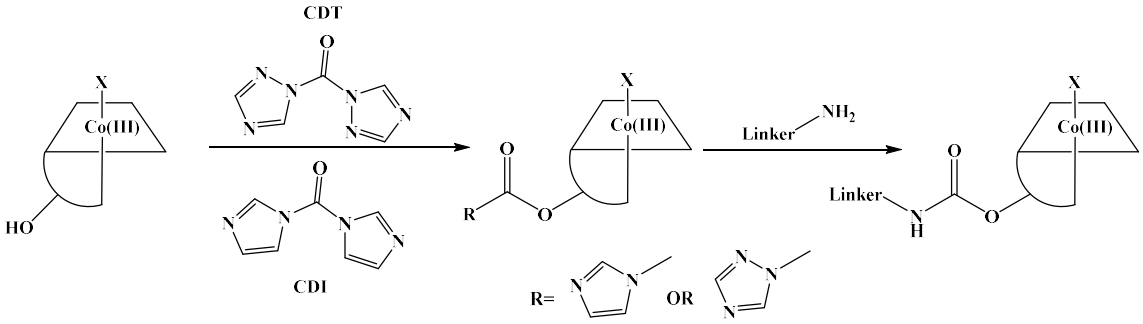

Scheme 1: Activation of the 5'-OH residue of B_{12} with CDI or CDT followed by the formation of a carbamate bond between the B_{12} and the linker.

The linkers selected in this work are based on the polyethylene glycol scaffold or the short disulphide-containing cystamine molecule (Figure 4). Polyethylene glycol linkers have been used by others in CNCbl-therapeutics within the literature. Równicki et al. (2017) reported a polyethylene glycol (PEG) linked CNCbl conjugate, where peptide nucleic acids (PNAs) were covalently bound to CNCbl via a short two-unit PEG linker.[24] This study showed that attachment to CNCbl increased the transport of PNAs into the cytoplasm of gram-negative *Escherichia Coli* cells where traditional PNAs suffer from low uptake. The PEG linker between CNCbl and the bioactive PNA was found to be stable in bacterial media and serum. Since this publication, numerous CNCbl conjugates have been synthesised where PEG has been used as a linker, including nanoparticle/nanocapsule systems[22,38] and in the targeted drug delivery of insulin.[20,39] The use of cystamine-based linkers for CNCbl-therapeutics is novel. Using a disulfide-containing moiety for targeting drug delivery and release, however, is not.[24,40] A disulfide moiety will result in the release of the therapeutic in reductive cytosolic compartments.[41,42] This may result in greater therapeutic activity of the cargo.

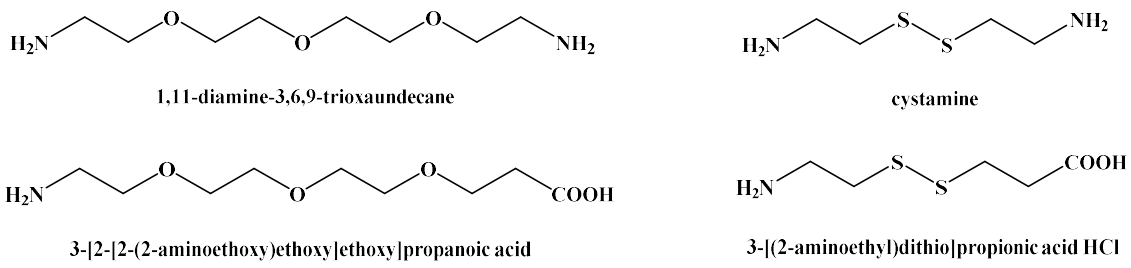

Figure 4: Structures of linkers employed in the CNCbl-fluorophore and CNCbl-antibiotic conjugates synthesised in this research.

1.4 Protein-mediated CNCbl uptake in gram-negative bacteria, *Escherichia coli*

Bacterial uptake of vitamin B_{12} is achieved by the Btu (B twelve uptake) system.[31] This system has been well characterised in the gram-negative bacterium, *E Coli*. The Btu uptake system is composed of an orchestra of transmembrane and periplasmic proteins (Figure 5).

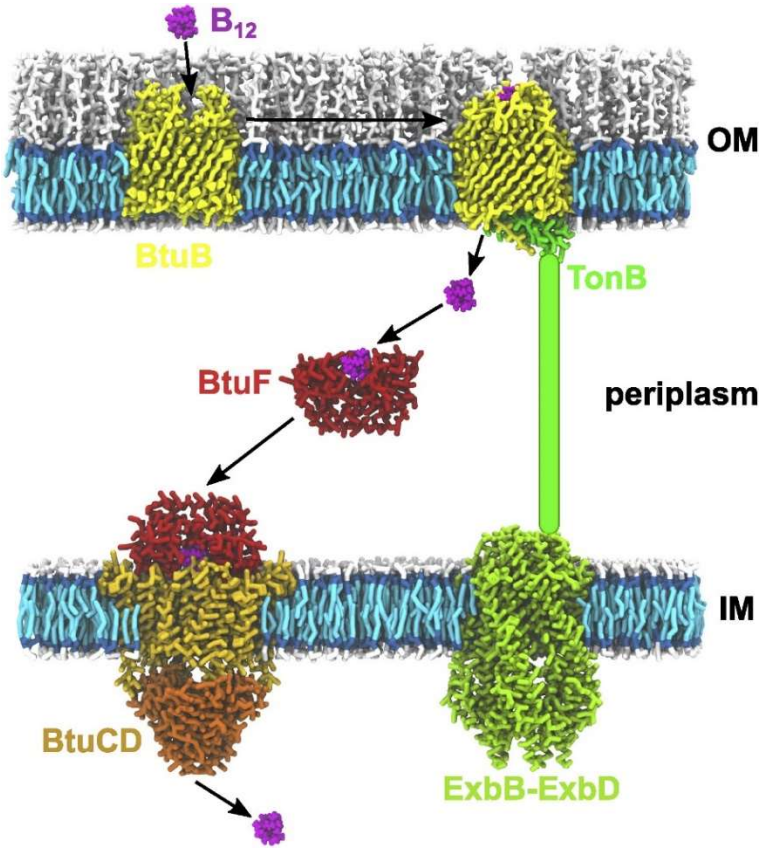

Figure 5: Schematic representation of the Btu system of Escherichia Coli.[30]

Transport of B_{12} across the outer membrane is achieved by the BtuB protein, supported by the inner membrane protein, TonB. BtuB is composed of two key domains, an *N*-terminal globular-like domain (often referred to as the 'hatch' domain) and a 22-stranded β-barrel domain (Figure 6). The loop domains connecting select β-barrel regions located on the extracellular side of the outer membrane play a key role in B_{12} binding and recognition, with the help of Ca^{2+} ions. Electron density mapping has identified two Ca^{2+} ions trapped by these loop domains, serving to prise the loop domains open and exposing the extracellular binding site, which has a high affinity for B_{12}. In the absence of Ca^{2+} ions, the loop domains are likely mobile and prevent B_{12} from reaching this recognition site. Initial binding of B_{12} to this recognition site is energy independent, with the β-axial site exposed to the extracellular environment. Several conformational changes take place upon B_{12} binding, the most notable of which is the conformational change of the Ton box located on the periplasmic side of BtuB. This conformational change is energy-independent and acts to increase the affinity of the inner membrane-bound TonB protein to BtuB, promoting coupling between the TonB protein and BtuB.[43] TonB-dependent transporters are well known to assist in the uptake of essential nutrients within gram-negative bacteria. In addition to ExbB-ExbD, TonB provides the necessary energy for B_{12} transport across the outer membrane in the form of a proton-motive force.[44] Upon coupling and energy transfer by TonB, a rearrangement (or 'unfolding') of the hatch domain of BtuB occurs, allowing B_{12} to permeate through the BtuB. Although B_{12} binds to BtuB in an 'axial-up' conformation, molecular docking studies have identified that the

molecule rotates during its pathway through BtuB, such that the corrin ring is perpendicular to the surface of the membrane.[45]

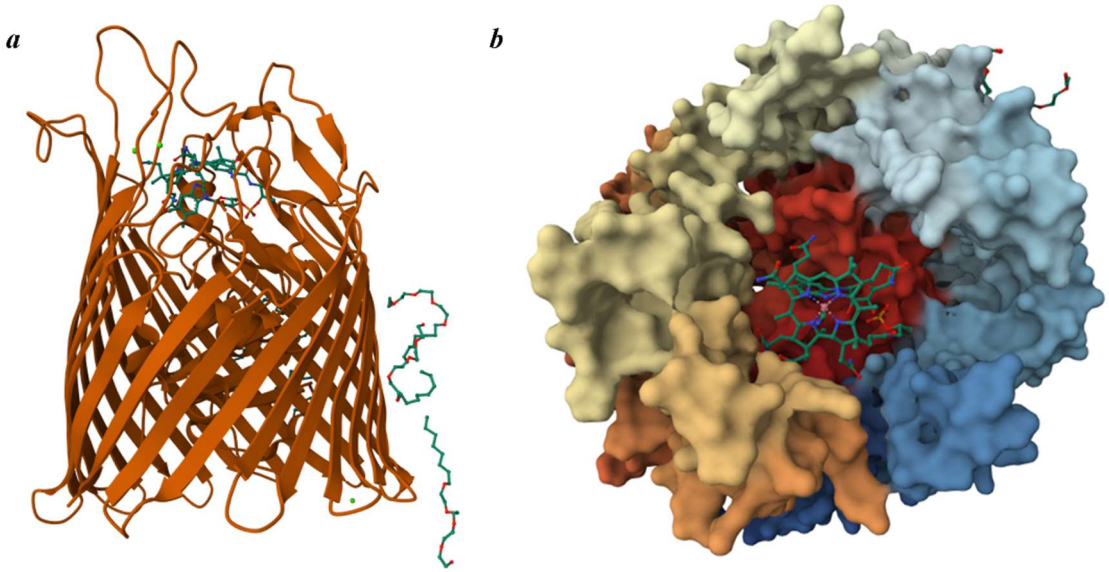

Figure 6: Structures of B_{12} bound BtuB protein of Escherichia Coli (PDB code 1NQH). a) Cartoon representation of the β-barrel domain in orange in a side on view, bound B_{12} shown as a ball and stick model. b) Top-down space-filling model of the BtuB protein with hatch residue shown in red and B_{12} shown in a ball and stick representation.[46]

Crystal structures have confirmed that B_{12} binds to BtuB in an 'axial-up' conformation, with the β-axial CN ligand exposed.[46] This indicates that the 5'-OH residues of the ribose ring (used in this research as a site of functionalisation) would therefore be constrained for space as it is protein-embedded. However, a notable publication on which much of the work discussed here is founded, delivered a large peptide nucleic acid (PNA) conjugate tethered to the 5'-OH residue of B_{12} via this Btu system.[24] Molecular dynamic (MD) simulations were utilised to elucidate the mechanism of transport for the B_{12}-PNA conjugates. Transport via BtuB was confirmed using genetically engineered BtuB mutants of *E. Coli*, showing no conjugate uptake. MD simulations showed that the B_{12}-PNA conjugates bound to BtuB in an upside-down conformation, with the β-axial CN ligand now facing into the lumen of the BtuB protein. Predictions determined that the binding of the conjugate and unfolding of the BtuB lumen were energetically favourable. Once internalised, the large PNA residue unfolded, allowing transport of the conjugate through the BtuB barrel.[30] Therefore, it seems that BtuB tolerates conjugation at the 5'-OH residue of B_{12}.

Following transport through the outer membrane, B_{12} is sequestered by the periplasmic BtuF protein. BtuF comprises a rigid α-helix linking two globular domains.[47] Commonly, the globular N-terminal domain and C-terminal domain are referred to as domain I and II, respectively.[47] Domain I has key interactions with the DMB and propionamide residues of B_{12}. Domain II, however, has interactions with the catalytic surface of B_{12}, namely the β face of the corrin ring. There is a relatively small number of direct interactions between B_{12} and BtuF (89 in total) when compared to B_{12}-dependent enzymes.[47] This is likely due to the requirement of BtuF to sequester B_{12} from BtuB in the periplasmic space and transfer it to the inner membrane protein complex BtuCD.[47] Analogous to the BtuB binding, B_{12} interacts with BtuF in a 'base-on' configuration to maintain B_{12} stability during transport.[48] Figure 7 (b) highlights the 5'-OH residue of the ribose ring of B_{12} that has been widely utilised for the conjugation of cargo. The residue sits in a large open pocket between domains I and II of the BtuF protein. This pocket is well-sized to accommodate the cargo with minimal impact on the binding interactions between B_{12} and BtuF.

Cbi differs from B_{12} as it lacks the lower dimethylbenzimidizole (DMB) ligand, Figure 2. The binding of BtuF with Cbi is analogous to that identified for B_{12} with the absence of DMB compensated for by a tryptophan residue (W66) of BtuF. It was also noted that there is significant flexibility in the binding pocket for BtuF, further supporting the ability of this protein to recognise B_{12} analogues.[49]

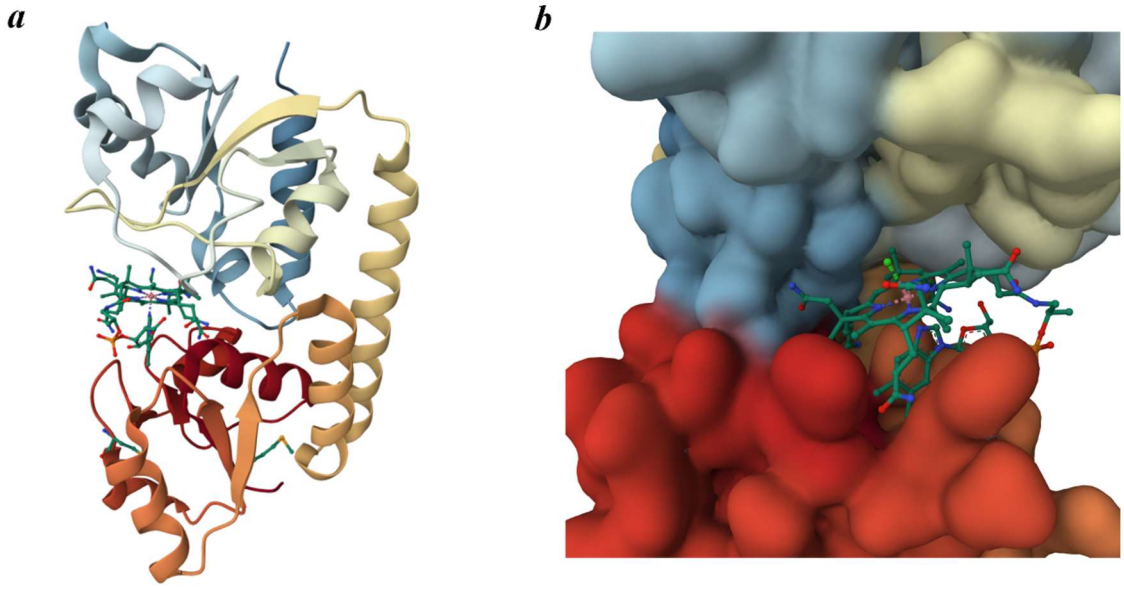

Figure 7: Structures of B_{12} bound BtuF protein of Escherichia Coli (PBD code 1N4A), a) Cartoon representation of BtuF the domains in a side on view, bound B_{12} shown as a ball and stick model, b) Side on space-filling model of the BtuF protein, B_{12} shown in a ball and stick model.[50]

The final step in the uptake pathway of B_{12} to the cytoplasm of *E. coli* is through the ABC transporter BtuCD. To date, no crystal structures have been obtained where B_{12} is bound to this complex due to the dynamic nature of ABC transporters in detergent solutions.[51] There is, however, a large number of studies on the protein-to-protein interactions between BtuF and BtuCD. Protein-to-protein interactions are essential for the transfer of B_{12} through the periplasmic space and the inner cell membrane. The BtuCD transporter is a transmembrane protein complex comprising two BtuC subunits embedded in the inner membrane, with two BtuD subunits in the cytoplasm. The binding of BtuF to BtuCD is achieved by salt bridges. These arise between the negatively charged glutamic acid residues (72 and 202) of BtuF and the positively charged arginine 'pockets' (56, 59 and 295) at the BtuC surface.[48] The B_{12} binding pocket for both BtuF and BtuCD is located in the centre of these salt bridge contacts (Figure 8).[48] Translocation through the BtuCD complex has not been elucidated to date, but structural components of the BtuCD transporter have been identified in other well characterised ABC transporters, such as the DNA repair enzyme, Rad50.[48] These common characteristics have provided some insight into the probable transport mechanism of this complex. ABC transporters are known to undergo many complex energy-requiring rearrangements. In the case of BtuCD it is likely that the two BtuC units swing together once activated (either by B_{12} binding or ATP

activation).[48] This expands the membrane-spanning subunits, opening a translocation pathway for B_{12} to permeate (Figure 8). The role of the BtuD subunits during this process is to bind and hydrolyse ATP to facilitate transport. Once the BtuC subunits adopt this pinched conformation, B_{12} can be released into the cytoplasm by several mechanisms, such as passive diffusion or peristaltic forces of the BtuC subunits.[51] Due to the proposed mechanism of uptake and the considerable space identified in the BtuF binding pocket for B_{12}, the modifications at the 5'-OH site of B_{12} will likely be well tolerated by the BtuCD-F uptake system.[51]

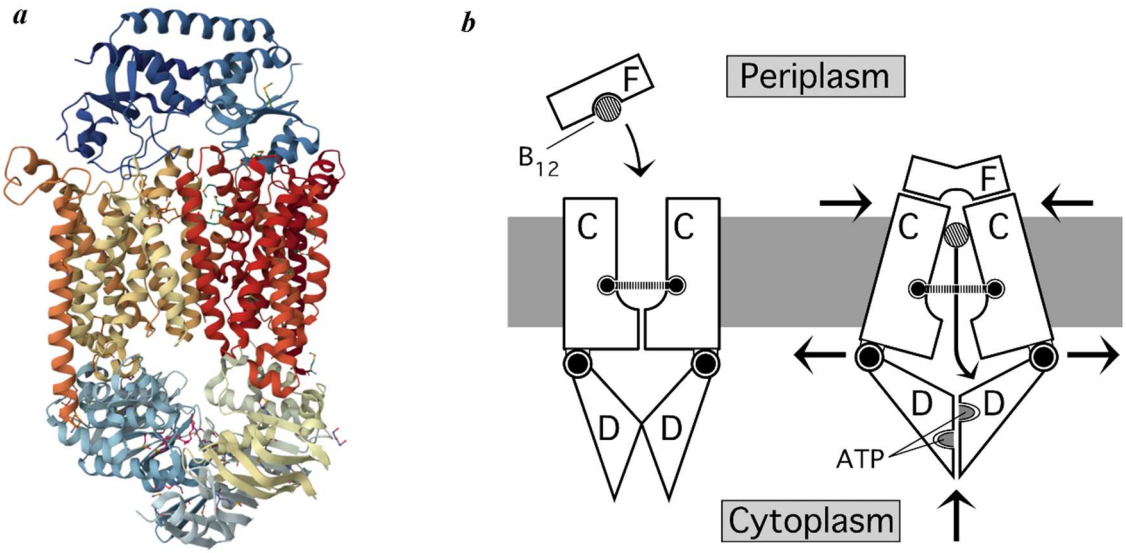

Figure 8: Structures of the BtuCD-F protein complex of Escherichia Coli (PDB code 1NQH), a) Cartoon representation of BtuCD-F, the two BtuC subunits are shown in orange and red, the two BtuD subunits in blue and yellow with BtuF shown in blue b) Simplified proposed uptake mechanism of B_{12} through the BtuCD-F ABC transporter.[51]

1.5 Synthesis and fluorescent properties of vitamin B_{12} conjugates incorporating fluorophores

1.5.1 β-axial bound conjugates

The synthesis of β-axial fluorescent conjugates of vitamin B_{12} use two different methods - reduction of the Co(III) centre to Co(I) followed by addition of an alkyl halide of the fluorophore to form an alkycobalamin or coordination of the fluorophore to the axial bound cyanido ligand (Table 1).[52,53]

The earliest reported synthesis of a β-axial bound fluorescent conjugate utilised Zn dust in the presence of NH_4Cl as the reducing agent for the reduction of CNCbl.[52] This resulted in the formation of the supernucleophilic co(I)balamin. Reactions proceeding via the Co(I) intermediate require strict anaerobic conditions. The addition of a 5'-halonucleoside or an alkyl halide resulted in formation of a Co-C bond between the fluorophore and Cbl. Several fluorescent adenosine analogues were ligated to Cbl with yields obtained between 50-80%.[52] Purification was achieved by multiple phenol-chloroform extractions, SP-Sephadex, phosphocellulose and preparative paper chromatography methods. Cbl derivatives that contain a Co-C bond require strict low/red light conditions to prevent light-induced Co-C bond cleavage.[52]

A minor modification of this synthetic method utilised aquacobalamin (H_2OCbl), rather than CNCbl.[54] The reducing agents used were $NaBH_4$ in the presence of a $CoCl_2$ catalyst to form Co(I). Formation of a Co-C bond was achieved upon the addition of the 5'-chloro-5'-deoxybenzoadenosine. Despite these modifications, the yield obtained was only 54%. Purification was achieved via phenol/CH_2Cl_2 extraction and ion exchange chromatography on Dowex.[54]

Linkers were subsequently attached at the β-axial site with a terminal carboxylate or amine and fluorescent moieties were conjugated to the linker via peptide coupling. To form the linker-Cbl intermediates, reduction of the Co(III) centre was achieved using either $NaBH_4$[55] or Zn[56–59] dust, with chloropropylamine or chlorobutyric acid as linkers. Yields for the butyric acid derivatives ranged between 82-96%[55] and aminopropyl derivatives between 73-99%.[56-59] Lower yields can be possibly linked to purification by reversed-phase C18 high-pressure liquid chromatography (RP-HPLC). Higher yields were typically found upon purification by ion exchange or reversed-phase C18 flash chromatography. For the efficient conjugation of the fluorescent groups to the terminal functional group of the linker at the β-axial site, multiple reagents have been used. Peptide coupling procedures have been used, either using activated *N*-hydroxysuccinamide (NHS) ester or *N,N,N′N′*-tetramethyl-O-(N-succinimidyl)uronium tetrafluoroborate (TSTU), 1-ethyl-3-(3-dimethylaminopropyl)carbodiimide (EDC) and *N,N,N′,N′*-tetramethyl-O-(1H-benzotriazol-1-yl)uronium hexafluorophosphate (HBTU) coupling reagents.[55-59] Yields ranged from 64-92% with higher yields often afforded using the NHS ester of the fluorophore.[55-59] Purification of the β-axial bound fluorescent conjugates was

typically achieved by semi-preparative reversed-phase HPLC chromatography on a ≤5 mg scale.

Fluorescence quantum yields were established for three of the β-axial conjugates with the Oregon green, fluorescein and the 5,6-carboxynapthofluorescein fluorophores. The quantum yields were 0.16, 0.14 and 0.013, respectively, where the free fluorescein molecule has a quantum yield of 0.93. The fluorescence quantum yields of Oregon green and 5,6-carboxynapthofluorescein have not been published. This demonstrates that the fluorophore appended to the β-axial of vitamin B_{12} experiences quenching by the coring macrocycle.

Table 1: List of β-axial fluorescent conjugates of vitamin B_{12}, highlighting the Cbl reactant, reducing agent, linker (if used), fluorophore, yield (if given) and Φ_f when available.

Cbl	**Reducing agent**	**Linker**	**Fluorophore**	**% Yield**	**Φ_f**
CNCbl	Zn,	-	ε-Adenosine	-[60]	-
CNCbl	Zn,	-	Formycin	-[60]	-
CNCbl	Zn,	-	2-Aminoebularine	-[60]	-
CNCbl	Zn,	-	2,6-Diaminonebularine	-[60]	-
CNCbl	Zn,	-	Dansylamidopropylchrloride	80[60]	-
OHCbl	$NaBH_4$	-	5'-Chloro-5'-deoxy-lin-denzoadenosine	54[54]	-
OHCbl	$NaBH_4$	Chlorobutyric acid	6,7-Dimethoxy-1-methyl-2(1H)-quinoxaline-3-propionylcarboxylic acid	-[55]	-
OHCbl	Zn	3-Aminopropylchloride	Oregon green	73[56]	0.16
OHCbl	Zn	3-Aminopropylchloride	Fluorescein	60[56]	0.14
OHCbl	Zn	3-Aminopropylchloride	5-6-Carboxynapthofluorescein	64[56]	0.013
OHCbl	Zn	3-Aminopropylchloride	Fluorescein-5-thiourea	76[56]	-
CNCbl	N/A	-	Dansyl-imidazole	45[53]	

OHCbl	Zn	3-Aminopropylchloride	6-Carboxytetramethylrhodamin	68[57]	-
OHCbl	Zn	3-Aminopropylchloride	6-Carboxytetramethylrhodamin	89[58]	-
OHCbl	Zn	3-Aminopropylchloride	Sulfo-Cyanine5	66[58]	-
OHCbl	Zn	3-Aminopropylchloride	Atto725	92[58]	-
OHCbl	Zn	3-Aminopropylchloride	DyLight800	72[58]	-
OHCbl	Zn	3-Aminopropylchloride	Alexa700	88[58]	-
OHCbl	Zn	3-Aminopropylchloride	Bodipy650	73[58]	
OHCbl	Zn	3-Aminopropylchloride	6-Carboxytetramethylrhodamin	75[59]	-
OHCbl	Zn	3-Aminopropylchloride	5/6-Carboxyfuorescein	90[59]	-

1.5.2 5'-OH bound conjugates

Fluorescent vitamin B_{12} conjugates have been synthesised via conjugation at the 5'-OH site of the ribose ring (Figure 3), typically through alcohol activation followed by peptide coupling to form carbamate bonds. Between 2003-2008, derivatives of sulfo-Cyanine5[61–63], 5/6-carboxyrhodamine[64] and 6-carboxyfluorescein[65] were synthesised using CDI or CDT as coupling agents with 1,6-diaminohexane or 4,7,10-trioxa-1,13-tridecanediamine linkers (40-50% yield, purified by reversed-phase HPLC).[65,61–63] Fluorophore-NHS esters were attached via peptide coupling (40-60% yield, ≤5 mg scale). The fluorescence quantum yield of the sulfo-Cyanine5 conjugate was 0.011 (free sulfo-Cyanine5 has a fluorescence quantum yield of 0.30), demonstrating fluorescence quenching. Fluorescence quantum yields were not determined for the other conjugates but a reduction in fluorescence was noted upon conjugation of the fluorophore to B_{12} (Table 2).

To mitigate quenching, Grissom and Lee (2003) introduced a 'rigid' cyclohexane linker between CNCbl and the fluorophores 5(6)-carboxyfluorescein and rhodamine 6G. Linker attachment was achieved via CDT-mediated coupling with yields of 22-24%. Unlike previous methods, 1-ethyl-3-(3-dimethylaminopropyl)carbodiimide (EDAC) was used as

a peptide coupling reagent instead of NHS esters of the fluorophore. Fluorescence quantum yields of the 5(6)-carboxyfluorescein and rhodamine 6G conjugates were 0.1 and 0.2, respectively. An increase in fluorescence was noted for the conjugates containing the 'rigid' linker, but no fluorescence quantum yield were reported for conjugates of these fluorophores with flexible linkers 4,7,10-trioxa-1,13-tridecanediamine.[66]

Welfare et al. (2022) used the 1,4-diaminohexane linker for BODIPY, Cyanine-3, and carboxytetramethylrhodamine conjugates of CNCbl in addition to flexible ethylenediamine linkers.[67] CDI-mediated amide coupling followed by Fmoc protection yielded CNCbl-linker-Fmoc (60-65%). Subsequent reduction with $NaBH_4$ in the presence of iodoethane resulted in the coordination of an ethyl group as the β-axial ligand. The Fmoc group was removed from the linker and the fluorophores were attached via HATU-mediated peptide coupling (26-78% yield, lowest for Cyanine3).[67] CNCbl-linker-BODIPY exhibited significantly faster Co-C bond cleavage with the flexible ethylenediamine linker in comparison to the ethyl-Cbl derivative with no appended fluorophore.[67] This work demonstrated the electronic interaction between the fluorophore and the corrin ring, enhancing Co-C bond cleavage. However, the nature of this interaction was not investigated in this work.

Subsequent research by Viola-Villegas et al. (2009), Santoro et al. (2015) and Vortherms et al. (2011) focused on fluorescent Re probes conjugated to CNCbl via CDT-mediated carbamate coupling at the 5'-OH site.[68–70] A β-axial Co(III)-CN-Re conjugation route was also explored were the Re atom coordinated to the N of the β-axial CN ligand. Fluorescence of the 5'-OH bound $[BBQA\text{-}Re(CO)_3]^+$ conjugate was restored when bound to the human IF protein. It was indicated that the CNCbl molecule was encased in the IF binding pocket and the $[BBQA\text{-}Re(CO)_3]^+$ remained outside of the binding pocket, preventing the electronic interaction between the two moieties.

Rodgers et al. (2016) synthesised cobalamin conjugates of Alexa350, DECA, and TAMRA by CDT-mediated ethylenediamine coupling at 5'-OH, followed by peptide coupling between the linker and the NHS-ester of the fluorophore. The β-axial aqua ligand of aquacobalamin was substituted with *N*-acetylcysteine (forming a β-axial Co-S B_{12} derivative). Fluorescence quantum yields were not reported for the conjugates, but photolysis studies indicated enhanced Co-S bond cleavage of the fluorophore-appended

conjugates. β-axial Co-S bond cleavage was one order of magnitude faster for the fluorescent conjugates compared to the analogous conjugates without a fluorophore.[71]

Cyanine5 and FL800 fluorophores were conjugated to β-axial drug-Cbl conjugates (methotrexate, colchicine, paclitaxel). The fluorophores were attached to a Cbl-ethylenediamine derivative using either HBTU or NHS-ester peptide coupling procedures, providing synthetic yields of 32-68%.[72] Photolysis experiments of the conjugates demonstrated that excitation of the fluorophore (at wavelengths where cobalamin has no absorbance, i.e. beyond 600 nm) induced β-axial Co-C bond cleavage, releasing the β-axial bound drug.[72] This demonstrated that energy and/or electron transfer occurs between the appended fluorophore and the coring ring. A subsequent study used the same methodology to produce a docetaxel-Cbl-Cyanine5 conjugate, yielding 41% after reversed-phase C18 purification.[73] This study also demonstrated that excitation of the Cyanine5 fluorophore at wavelengths above 600 nm resulted in β-axial Co-C bond cleavage.

A fluorescent derivative of a B_{12} analogue (cobyric acid) was reported by Lawrence et al. (2018), conjugating Oregon green (514) or BODIPY TR-X via NHS-mediated peptide coupling. The synthesis of these conjugates was carried out by enzymatic bioengineering. No yields or fluorescence data were published, but fluorescence microscopy studies were conducted showing uptake of both conjugates into *E. coli*.[32]

A novel Cu-catalyzed azide-alkyne cycloaddition (CuAAC) method was introduced by Chrominski and Gryko (2013), linking BODIPY to CNCbl via a mesylate-azide intermediate (31% yield).[74] CuAAC was also used to attach a photolabile *O*-nitrobenzyl moiety to B_{12} via PEG linkers with ATTO 590 (82% yield).[75] A fluorescent quantum yield was not obtained for the CNCbl-BODIPY conjugate.

Although few of these conjugates have published fluorescent quantum yields, the reduced fluorescence emission noted for a large number of these conjugates indicated that fluorescence quenching occurs when fluorophores are appended to Cbl at either the β-axial or 5'-OH location. This indicates that there is an electronic interaction between the corrin ring of Cbl and the fluorophores. Jacobsen et al. (1979) reported that a nonradiative transfer of energy between the fluorophore and Cbl and referred to this process as 'cryptofluorescence'.[60] Grissom and Lee (2003) noted an increase in the fluorescence quantum yield when a 'rigid' linker was employed between the B_{12} and fluorophore,

indicating a distance-dependent energy transfer mechanism.[66] Studies by Welfare et al. (2022), Rodgers et al. (2016) and Hughes et al. (2016) demonstrated that excitation of fluorophores appended to Cbl resulted in increased rates of Co-C and Co-S bond cleavage, likely due to photoinduced electron transfer between the excited state fluorophore and Cbl.[67,72,72]

Table 2: List of 5'-OH fluorescent conjugates of vitamin B_{12}, including starting material, reductive agent, linker (if used), fluorophore, yield (if given) and fluorescence quantum yield when available.

Activating agent	Linker	Fluorophore	% Yield	Excitation/ emission maximum	Conjugate Φ_f	Fluorophore Φ_f
CDI	1,6-Diaminohexane	Sulfo-Cyanine5	59[61–63]	649/ 666[76,77]	0.011[61–63]	0.30 (EtOH)[77]
CDT	4,7,10-Trioxa-1,13-tridecanediamine	5-6-Carboxyrhodamine	-[64]	~525/550[64]	-	0.95 (EtOH)[65,78]
CDI	4,7,10-Trioxa-1,13-tridecanediamine	6-Carboxyfluorescein	~50%[65]	492/518[65]	-	0.93 (0.1 M NaOH)[65]
CDT	1,4-Diaminohexane	5(6)-Carboxyfluorescein	22%[66]	492/518[65]	0.1	0.93 (0.1 M NaOH)[65]
CDT	1,4-Diaminohexane	Rhodamine 6G	24%[66]	~525/550[64]	0.2	0.95(EtOH)[65,78]
CDI	1,4-Diaminohexane	BODIPY	59%[67]	501/510[79]	-	0.76[79] (CH_2Cl_2)
CDI	1,4-Diaminohexane	Cyanine-3	27% [67]	554/566[80]	-	-

CDI	1,4-Diaminohexane	Carboxytetramethylrhodamine	73% [67]	548/572[81]	-	0.41 [81] (H_2O)
CDI	Ethylenediamine	BODIPY	70%[67]	501/510[79]	-	0.76[79] (CH_2Cl_2)
CDI	Ethylenediamine	Cyanine-3	55%[67]	554/566[80]	-	-
CDI	Ethylenediamine	Carboxytetramethylrhodamine	77%[67]	548/572[81]	-	0.41 [81] (H_2O)
CDT	-	B_{12}-BQBA-$[Re(CO)_3]^+$	15%[68]	488/560[68]	-	-
CDT	-	[dithiazolate-$Re(I)(CO)_3$]	13%[70]	466/555[70]	-	-
CDT	4-Picolylamine	$[Re(CO)_3(Me_2\text{-phen})]^+$	18%[69]	369/567[69]	-<0.01[69]	
CDT	Ethylenediamine	Alexa350	78%[71]	346/442[82]	-	
CDT	Ethylenediamine	DEAC	79%[71]	380/443[83]	-	0.39 (EtOH)[83]
CDT	Ethylenediamine	TAMRA	77%[71]	548/572[81]	-	0.41 [81] (H_2O)
CDT	Ethylenediamine	Cyanine5	68%[72]	649/ 666 nm[76,77]	-	0.30 (EtOH)[77]
CDT	Ethylenediamine	Cyanine5	32%[72]	649/ 666 nm[76,77]	-	0.30 (EtOH)[77]
CDT	Ethylenediamine	FL800	68%[72]	788/835[84]	-	-
CDT	Ethylenediamine	Cyanine5	41%[73]	649/ 666 nm[76,77]	-	0.30 (EtOH)[77]

CDI	Ethylenediamine	Oregon Green 514	-[32]	489/526[85]	-	-
CDI	Ethylenediamine	BODIPY TR-X	-[32]	589/616[86]	-	-
Cobyric acid-linker	-	Oregon Green 514	-[32]	489/526[85]	-	-
Cobyric acid-linker	-	BODIPY TR-X	-[32]	589/616[86]	-	-
-	Triazole	BODIPY	31%[74]	501/510[79]	-	0.76[79] (CH_2Cl_2)
CDT	PEG	ATTO590	82%[75]	592/622[87]	-	-

1.6 Uptake, transport and cellular localisation studies using fluorescent vitamin B_{12} conjugates.

Fluorescent derivatives of vitamin B_{12} have been widely employed as probes to study cellular uptake pathways, intracellular transport, and subcellular localisation.[35] These conjugates provided insight into how B_{12} and its analogues interact with transport proteins, traverse biological membranes, and accumulate within tissues.

Early investigations with β-axial fluorescent adenosyl-B_{12} analogues demonstrated that these conjugates could act as competitive inhibitors of transcobalamin II-mediated B_{12} transport into mammalian L1210 cells.[52] This study confirmed that modified vitamin B_{12} derivatives were still taken up by protein-mediated uptake systems. Subsequent studies extended these observations to show that vitamin B_{12} conjugates can interact with coenzyme-dependent enzymes such as ribonucleotide reductase, although enzymatic activity was slightly impaired.[52] Later fluorescent vitamin B_{12} conjugates were explicitly developed as cellular imaging agents. McGreevy et al. (2003) reported a 5′-OH-linked vitamin B_{12}–Cyanine5 conjugate (commercialised as "CobalaFluor"), which was successfully used to visualise lymphatic drainage and sentinel nodes in pigs, highlighting the utility of red-shifted probes for deep-tissue imaging.[61] This approach was further refined by Kinoshita et al. (2018), who demonstrated that the vitamin B_{12}–Cyanine5

conjugate crosses the inner blood–retinal barrier in vitro and in vivo, with transport shown to depend on transcobalamin-mediated uptake and subsequent delivery across the retinal membranes.[88]

Other studies showed that fluorescent B_{12} conjugates replicate native vitamin B_{12} protein-binding interactions. For example, the vitamin B_{12} 5′-OH rhodamine-labelled derivative CBC-244, bound to both intrinsic factor (IF) and transcobalamin with similar affinities to native B_{12}, and exhibited increased fluorescence upon binding due to reduced quenching in the protein-bound state.[64,89] Importantly, CBC-244–protein complexes were recognised by cell-surface receptor proteins involved in B_{12} uptake. This supported the suitability of such conjugates for tracing receptor-mediated uptake into mammalian cells. Parallel studies using vitamin B_{12}–Re complexes also highlighted the importance of IF/cubilin pathways in the uptake of vitamin B_{12}.[68,70] Using confocal microscopy, the cytoplasmic localisation of the vitamin B_{12}-Re complex was identified following receptor-mediated uptake.

In bacteria, Lawrence et al. (2018) demonstrated that both fluorescent vitamin B_{12} and cobyric acid conjugates could be internalised by *E. coli*, although cobyric acid conjugates were detected at lower concentrations, suggesting greater uptake efficiency for vitamin B_{12}.[90] Interestingly, subsequent feeding of labelled *E. coli* to *Caenorhabditis elegans* led to the accumulation of vitamin B_{12} conjugates in distinct anatomical regions, confirming organism-level transport and selective subcellular localisation of intact vitamin B_{12} derivatives. Plant studies further showed unspecific uptake of fluorescent vitamin B_{12} into vacuoles, likely via diffusion-driven mechanisms. [90]

Mammalian cell culture models have provided detailed insights into the endocytic sequestering of vitamin B_{12} conjugates. A B_{12}–BODIPY derivative was shown to colocalise with LysoTracker (a fluorescent probe), confirming endosomal and lysosomal trafficking consistent with established transcobalamin II-mediated uptake.[91] Blocking experiments with transcobalamin antibodies abolished internalisation, further supporting transcobalamin-dependent endocytosis as the uptake route. Other red blood cell (RBC)-loading studies utilised fluorescent vitamin B_{12} conjugates as carriers for controlled intracellular release, demonstrating orthogonal light-triggered drug and fluorophore release from RBC carriers and successful delivery to co-cultured HeLa cells.[92] In vivo experiments in mice confirmed prolonged circulation of RBC-encapsulated vitamin B_{12}-

fluorophore conjugates compared to free analogues, validating this approach as a delivery and imaging platform.

Collectively, these studies establish that fluorescent vitamin B_{12} derivatives not only follow the uptake mechanisms of native B_{12} but also enable direct visualisation of cellular trafficking and localisation. Key findings include the dependence on transcobalamin and intrinsic factor for transport across physiological barriers, the potential for targeted delivery in cancer and ocular systems, and the use of vitamin B_{12} as a vector in bacterial, nematode, plant, and mammalian models. These results underpin the use of vitamin B_{12}-fluorophore conjugates as powerful tools to probe vitamin B_{12} biology and as promising vectors for imaging and therapeutic applications.

1.7 Fluorescence quenching and methods for determining fluorescence quantum yields

The synthesis of CNCbl derivatives incorporating fluorophores has been well-studied in the literature. [1–5] Fluorescence is one mechanism by which excited molecules release their energy and return to the ground state. Fluorescent molecules absorb light, which excites electrons to a singlet excited state. When the molecule returns to the ground state, it emits light (fluorescence).

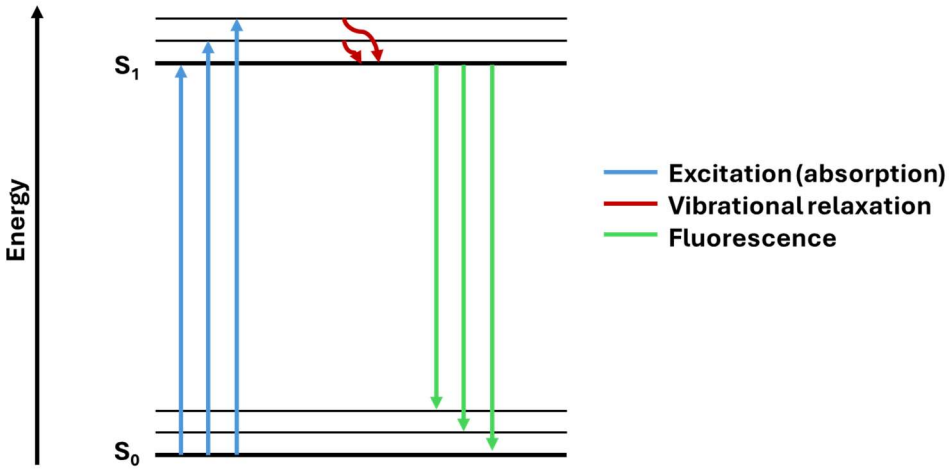

Figure 9: Simplified Jablonski diagram showing electronic transitions resulting in fluorescence.

1.7.1 Fluorescence quenching mechanisms

The fluorescence properties of vitamin B_{12}–B_{12}-fluorophore conjugates are of particular interest in this thesis. To interpret these observations, it is necessary to understand the mechanisms by which fluorescence can be quenched.

Fluorescence quenching refers to any process that decreases the intensity of emitted light from a fluorophore. Broadly, quenching can occur through dynamic (collisional) quenching or static quenching.[93] Dynamic quenching arises when an excited-state donor (fluorophore) interacts with a quencher (vitamin B_{12}) molecule through collisions in solution, leading to non-radiative relaxation. Static quenching, in contrast, occurs when the fluorophore forms a non-fluorescent ground-state complex with the quencher prior to excitation.[93]

These processes can often be distinguished using Stern–Volmer analysis, which relates the fluorescence intensity (or lifetime) to quencher concentration.[94] One method of employing Stern-Volmer analysis is to plot I_0/I against the concentration of the quencher (where I_0 is the fluorescence of the donor in the absence of the quencher and I is the fluorescence of the donor in the presence of increasing concentrations of the quencher).[95] A second method is to plot τ_0/τ against the concentration of the quencher (where τ_0 is the fluorescence of the donor in the absence of the quencher and τ is the fluorescence of the donor in the presence of increasing concentrations of the quencher).[94] With dynamic quenching, both fluorescence intensity and lifetime decrease with quencher concentration. For static quenching, non-fluorescent complexes form in the ground state; only fluorescence intensity is affected, while the fluorescence lifetime remains unchanged.[93] Deviations from linear Stern–Volmer plots often indicate mixed static/dynamic contributions or intramolecular quenching pathways.

The Stern-Volmer plot is useful in understanding quenching in a bimolecular system. However, with fluorescent vitamin B_{12} systems, the quenching mechanisms are likely intramolecular as the donor and acceptor are directly bonded to one another. Therefore, quenching by specialised intramolecular mechanisms need to be understood.

Förster Resonance Energy Transfer (FRET) is a non-radiative dipole–dipole coupling process in which energy is transferred from an excited donor fluorophore to an acceptor.

FRET efficiency (EEE) depends strongly on the donor–acceptor distance (between 1–10 nm).[96] Photoinduced Electron Transfer (PeT) occurs when an excited fluorophore undergoes electron transfer to or from a nearby quencher.[97] PeT occurs over short distances, often ~1 nm. Solvent polarity, redox properties, and linker distance/rigidity all play crucial roles in determining PeT efficiency.[98] Dexter Energy Transfer is a simultaneous electron exchange process requiring orbital overlap between donor and acceptor. Dexter transfer is effective only over very short distances (<1 nm), requiring strong orbital overlap and spin conservation.[99]

1.7.2 Determining fluorescence quantum yields

The fluorescence efficiency of a molecule is expressed as a fluorescence quantum yield (Φ). The fluorescence quantum yield is the ratio of the photons absorbed and the photons emitted through fluorescence.[6] There are two main methods of fluorescence quantum yield determination, absolute and relative. The absolute fluorescence quantum yield is determined in a single measurement with an integrating sphere set up, allowing each emitted photon to be counted over all available wavelengths.[7] This method is typically utilised when there is no suitable fluorescent reference is available and is considered the gold standard for fluorescence quantum yield determination. Relative fluorescence quantum yield determination, however, is more common. This requires a reference dye with a known fluorescence quantum yield. The selection of reference dye is important to ensure reliable results. Key components of a suitable reference are good spectral overlap between the reference and samples absorbance and emission spectra, a higher quantum yield than that expected for the sample and a sufficient Stokes shift to ensure the complete emission peak can be obtained from a fluorimeter upon excitation.[65,78,100,101] When a suitable fluorescent dye has been identified, either a single measurement or a calibration curve can be determined to calculate the sample's relative fluorescence quantum yield. Calibration curves are more precise and are ideally achieved by the use of five solutions of the reference dye. UV/Vis spectra are obtained where the absorbance value at the chosen excitation peak ranges between 0.01 and 0.1.[65,78,100,101] The fluorescence intensity is measured for each sample as a function of wavelength, ensuring the entire emission peak is obtained. This can be optimised by modifying the excitation peak as required. Using this data, a plot of integrated fluorescent intensity versus absorbance at the excitation wavelength is constructed. The same experiment is carried out with the sample compound to obtain a plot of integrated fluorescence emission versus absorbance. The

equation below illustrates how relative fluorescence quantum yield is calculated using this data.[8] Where necessary, different solvents for the reference and sample solutions can be corrected for in the calculation by obtaining refractive index values of the solvents.

$$\phi_s = \phi_r \left(\frac{m_s}{m_r}\right)\left(\frac{\eta_s^2}{\eta_r^2}\right)$$

Φ represents the fluorescence quantum yield, m is the slope of integrated fluorescence emission against absorbance at the excitation wavelength, η is the solution refractive index, r denotes the reference and s denotes the sample.

The fluorescence quantum yields of CNCbl and Cbi fluorescent conjugates synthesis in this thesis have been determined using the relative quantum yield methodology outlined above.

1.8 Development of antibiotic resistance by gram-negative bacteria.

Antimicrobial resistance among bacterial populations is emerging as a significant global threat, contributing to over 1 million deaths annually.[102] Carbapenems, a last-resort class of antibiotics for treating multidrug-resistant bacterial infections, are becoming increasingly ineffective as resistance to these drugs rises worldwide.[103] The World Health Organisation has identified carbapenem-resistant gram-negative *Enterobacteriaceae* as a top priority for new antibiotic development. A major factor driving multidrug resistance is the overuse of antibiotics, particularly in agriculture, where they are frequently administered to promote growth and prevent disease in livestock. Additionally, antibiotic misuse in human medicine is widespread, with an estimated 50% of prescriptions deemed unnecessary. This excessive use results in the accumulation of antibiotics in both the human body and the environment, encouraging bacterial populations to develop resistance mechanisms.[102]

Many of the antibiotics in use today are derived from natural compounds and have been modified by synthetic chemists to enhance their efficacy.[104] Some fungi and saprophytic bacteria naturally produce antimicrobial substances, such as *Penicillium chrysogenum*, which produces penicillin.[105] Initially, it was believed that these compounds were synthesised to inhibit competing microbial species, but more recent research suggests a

more complex role, including potential involvement in bacterial communication and biofilm formation.[103] While antimicrobial resistance can occur naturally in bacteria, usually through genetic mutations, it can also be acquired through horizontal gene transfer.[106] Natural resistance encompasses both intrinsic and induced resistance mechanisms. Intrinsic resistance occurs when bacteria possess inherent traits that confer protection, such as variations in efflux pump expression, while induced resistance arises when resistance genes become activated following antibiotic exposure.[107,108] One example of intrinsic resistance is the *Pseudomonas* species' resistance to triclosan due to an enoyl-ACP-reductase enzyme that is unaffected by the antibiotic.[109] Acquired resistance, on the other hand, emerges when bacteria gain new resistance traits through genetic mutations or horizontal gene transfer. Conjugation is a primary mechanism by which bacteria acquire resistance, as resistance genes are often located on self-replicating plasmids that can be transferred between bacterial cells.[107,108]

Resistance mechanisms vary in specificity and typically fall into four main categories: enzymatic modification or inactivation of the antibiotic, alteration of the antibiotic's target site, reduced uptake of the antibiotic, or active efflux of the drug from the cell.[107,108] Some bacterial species of *Pseudomonas* and *Actinobacter* have developed resistance to newer antibiotics like cephalosporins by downregulating general porins in favour of more selective porins that limit antibiotic entry.[106,109,110] Efflux pumps, which expel toxic substances from bacterial cells, also play a crucial role in resistance. These pumps are classified into five major families: the multidrug and toxic compound extrusion (MATE) family, the ATP-binding cassette (ABC) family, the small multidrug resistance (SMR) family, the resistance-nodulation-division (RND) family, and the major facilitator superfamily (MFS).[111–113] Each of these efflux systems has distinct functions, with some, such as the RND family, contributing significantly to multidrug resistance by expelling a broad range of antibiotics. For instance, the MexAB-OprM efflux pump in Pseudomonas aeruginosa provides resistance against β-lactams and sulfamethoxazole.[114,115]

Efflux pump inhibitors (EPIs) have been developed to counteract antibiotic resistance, with initial efforts focusing on modifying naturally occurring molecules like quinoline and indole.[113,114,116] While some EPIs showed promise, most failed in clinical trials due to toxicity issues at effective doses.[113,114,116] One exception, *bis*(pyrimidine)sulfonamide, demonstrated potential in treating multidrug-resistant *Pseudomonas aeruginosa* but was discontinued due to tolerability concerns.[117]

1.8.1 'Trojan horse' antibiotic therapies

The development of 'Trojan horse' therapies has emerged as a way to overcome antibiotic resistance by using essential bacterial uptake mechanisms for drug delivery.[118] This approach involves conjugating established antibiotics to molecules that bacteria recognise and transport under normal growth conditions. This potentially allows for an increase in intracellular drug accumulation and improved efficacy against resistant strains compared with unmodified antibiotics.[119] One of the most notable mechanisms uses the bacterial iron transport system, where siderophore-antibiotic conjugates such as cefiderocol utilise bacterial iron acquisition pathways to enter and kill resistant pathogens.[120,121] Similarly, vitamin B_{12}-based conjugates exploit bacterial Btu transport systems to facilitate the delivery of antibiotics and other materials.[45,47,48,51] One study demonstrated that a vitamin B_{12}-antibiotic conjugate significantly enhanced drug potency, where a B_{12}-ampicillin construct exhibited a 500-fold increase in activity against *E. coli*.[122] Other B_{12} based Trojan horse strategies involve peptide-nucleic acid conjugates, which bind to cytoplasmic targets.[24] These approaches enhance drug effectiveness; they can also minimise off-target effects and reduce the likelihood of resistance development. The continued refinement of Trojan horse therapies, particularly in the design of novel conjugates and their optimisation for clinical use, represents a crucial avenue in the fight against multidrug-resistant bacterial infections.

1.8.2 Derivatives of vitamin B_{12} for therapeutic applications

Vitamin B_{12} has been extensively investigated as a carrier for therapeutic cargo, demonstrating significant potential in enhancing drug delivery across multiple applications. The use of vitamin B_{12} conjugates for bacterial treatments has been particularly notable, with studies highlighting improved oligonucleotide transport and enhanced antibiotic efficacy.[24,29,30] Vitamin B_{12} derivatives have been produced by conjugation, enabling their use in the transport of chemotherapeutics, peptides, proteins, and nucleic acids.[15,16,20,22] These modifications can enhance the specificity, efficiency, and cellular uptake of therapeutic agents.

Vitamin B_{12} drug conjugates have shown efficacy in bacterial treatment, particularly in *E. coli* and *Salmonella Typhimurium*. The following conjugate designs exemplify its potential. Giedyk et al. (2019) successfully transported oligonucleotides into *E. coli* and *S. Typhimurium* cells.[29] Pereira et al. (2021) attempted to deliver antisense

oligonucleotides to *E. coli*, but with limited efficiency.[123] Pieńko et al. (2021) demonstrated the successful transport of peptide nucleic acids through the BtuB receptor in *E. coli*.[30] Równicki et al. (2017 & 2019) showed efficient transport of antisense PNA into *E. coli* cells followed the inhibition of *E. coli* growth.[24,28] Wierzba et al. (2018) investigated the efficiency of PNA transport into bacterial cells based on conjugation site and demonstrated efficient delivery to *E. coli* and S. *Typhimurium*.[36] Zhao et al. (2020) developed vitamin B_{12}-ampicillin conjugates with significantly improved activity against *E. coli*.[122] Brenig et al. (2022) and Mesitzo et al. (2024) synthesised vitamin B_{12} antimetabolites (B_{12} analogues which are not metabolically active) and evaluated their antibiotic properties in several bacteria.[124,125] Furthermore, Zelenka et al. (2011) developed B_{12} derivatives containing quinoline directly at the 5'-OH location of vitamin B_{12} and investigated their antimicrobial properties on the growth of *Lactobacillus delbrueckii*.[126] These studies highlight the ability of vitamin B_{12} derivatives to facilitate drug entry into bacterial cells, enhancing therapeutic efficacy and potentially improving treatment outcomes for antibiotic-resistant infections.

Research strongly supports the utility of vitamin B_{12} derivatives in therapeutic cargo delivery. Conjugation-based modifications enable the efficient transport of diverse therapeutic agents, with particularly promising applications in bacterial treatment, cancer therapy, and targeted drug administration. While the effectiveness of these carriers is well-documented, further research is needed to optimise delivery mechanisms within bacterial cell lines. Studies here focus on the development of highly fluorescent vitamin B_{12} and cyanocobinamide derivatives as tools to follow the uptake of vitamin B_{12} derivatives into *E. coli* and other bacteria.

Ciprofloxacin

Ciprofloxacin is a second-generation fluoroquinolone antibiotic. It is widely used in the treatment of bacterial infections due to its ability to inhibit essential enzymes involved in DNA replication and transcription (bacterial DNA gyrase and topoisomerase IV).[127] Despite its broad-spectrum activity and high efficacy, the therapeutic potential of ciprofloxacin is limited by low tissue penetration and the inability to permeate the dual membranes of gram-negative bacteria.[128] To overcome these limitations, conjugation of ciprofloxacin to carrier molecules, including peptides, polymers, and nanoparticles, has been explored as a strategy to enhance its therapeutic profile.[129–133] These conjugates aim to improve bioavailability, target bacterial infections and modulate drug release.

Ciprofloxacin contains two main functional groups that are suitable for chemical modification: the carboxylic acid (-COOH) at position 3 of the quinolone core and the secondary amine (-NH) of the piperazine moiety at position 7 (Figure 10). These sites have been utilised previously as conjugation sites.[131,132,134] The carboxylic acid group is often targeted for amide or ester bond formation, allowing for conjugation to amine-containing biomolecules such as peptides or polymeric carriers.[130,131] Activation of the carboxyl is commonly achieved using carbodiimide-based chemistry, wherein 1-ethyl-3-(3-dimethylaminopropyl)carbodiimide (EDC), often in combination with *N*-hydroxysuccinimide (NHS), facilitates the formation of a stable amide linkage.[131] Esterification using alcohol-functionalized molecules in the presence of dicyclohexylcarbodiimide (DCC) or enzymatic catalysts has enabled the synthesis of prodrugs with an aim to enhance ciprofloxacin's bioavailability.[133]

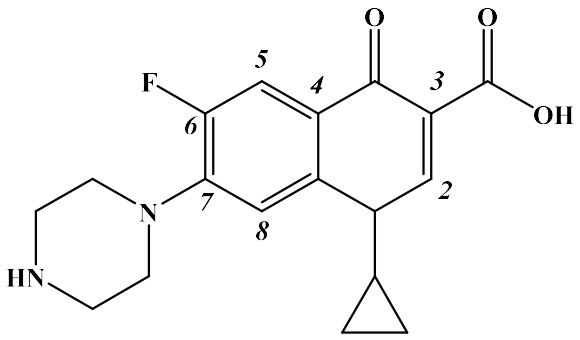

Figure 10: Structure of ciprofloxacin where the fluoroquinolone core has been numbered 2-8.

In addition to conjugation at the carboxylic acid, the secondary amine of the piperazine ring provides another site for modification. This site has been used more frequently for ciprofloxacin derivatisation or conjugation.[134] The secondary amine is amenable to acylation or alkylation reactions, which can introduce functional groups that alter the drug's physicochemical properties, including solubility and membrane permeability.[104,127,135] Acylation of the piperazine nitrogen is achieved with acyl chlorides or activated esters. Alkylation uses alkyl halides in the presence of a base such as sodium hydride or potassium carbonate.[132] These modifications have been employed to attach targeting ligands to improve drug localisation at infection sites and/or enhance intracellular uptake.

An interesting delivery strategy for improving the efficacy of ciprofloxacin incorporates ciprofloxacin into nanoparticle-based drug delivery systems. This has been achieved by either encapsulating ciprofloxacin or by chemical conjugation of ciprofloxacin to the nanoparticle surface.[131] Functionalization of nanoparticles with ciprofloxacin has utilised ionic interactions, amide bond formation, or esterification. Polymer-based carriers such as poly(lactic-co-glycolic acid) (PLGA) and chitosan have been extensively studied for their ability to encapsulate ciprofloxacin and control its release.[130] Additionally, conjugation to hydrophilic polymers such as polyethylene glycol (PEG) has been used to enhance drug solubility and prolong systemic circulation, reducing the frequency og administration and potentially minimising the development of antibiotic resistance.[136]

The conjugates discussed in this thesis herein have focused on the conjugation of ciprofloxacin to the essential micronutrient, vitamin B_{12}. Both the carboxyl and secondary amine have been utilised as conjugation sites for attachment to vitamin B_{12}. It is proposed that vitamin B_{12}-ciprofloxacin conjugates will overcome limited permeability in gram-negative bacteria.

Gentamicin

Gentamicin is an aminoglycoside antibiotic widely used for the treatment of gram-negative bacterial infections due to its potent bactericidal activity.[137–139] It exerts its antimicrobial effect by binding to the 30S ribosomal subunit, leading to inhibition of protein synthesis and the production of aberrant proteins that compromise bacterial viability.[137] Despite its broad-spectrum activity, the therapeutic application of gentamicin is often limited by nephrotoxicity, ototoxicity, and poor membrane permeability.[137,139,140] Consequently, the conjugation of gentamicin to carrier molecules such as polymers, nanoparticles, and targeting ligands has been explored as a strategy to improve its pharmacokinetics and therapeutic selectivity while minimising off-target toxicity.[141–144]

Gentamicin is a complex mixture of structurally related aminoglycosides, primarily consisting of gentamicin C1, C1a, C2, C2a, and C2b, with gentamicin C1a often chosen for chemical modifications due to its well-defined structure and relative abundance (Figure 11).[138] The molecular structure of gentamicin includes multiple amine and hydroxyl functional groups, presenting both an opportunity and a challenge for selective chemical conjugation. The primary and secondary amines distributed across different ring

systems makes it difficult to achieve regioselective modification without using extensive protection-deprotection chemistry[145]

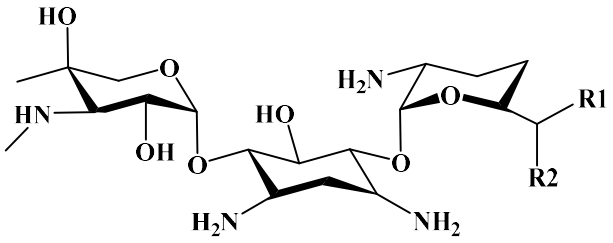

Gentamicin C1: R1 = NHMe, R2 = Me;
Gentamicin C1a: R1 = NH_2, R2 = H;
Gentamicin C2: R1 = NH_2, R2 = Me;
Gentamicin C2a: R1 = Me, R2 = NH_2;
Gentamicin C2b: R1 = NHMe, R2 = H

Figure 11: Structures of the five main sub-types of gentamicin.

Efforts to functionalize gentamicin have primarily focused on the selective derivatisation of the amine groups, which can be exploited for conjugation via acylation, carbamate formation, or Schiff base chemistry.[146–148] Acylation is one of the most commonly employed strategies, wherein carboxyl-activated agents such as *N*-hydroxysuccinimide (NHS) esters or acyl chlorides react with primary amines to form amide linkages. However, due to the presence of multiple reactive sites, achieving selective acylation without extensive side reactions remains a significant challenge.[144,145,149] The selective modification of gentamicin C1a has garnered particular interest due to its relatively simpler structure compared to other isomers. However, recent advancements in regioselective chemistry have employed enzymatic approaches as classic chemical approaches have not been successful.[150]

Nanoparticle and polymer conjugation strategies have been extensively explored to enhance the delivery and controlled release of gentamicin. Functionalization of polymeric carriers such as chitosan or poly(lactic-co-glycolic acid) (PLGA) can improve systemic circulation and reduce nephrotoxicity by altering drug biodistribution.[22,143] Moreover, the conjugation of gentamicin to targeting ligands, such as antibodies or peptides, has been investigated to enable site-specific drug delivery, particularly for intracellular infections or biofilm-associated bacterial populations.[139,140,145,149]

Despite the therapeutic potential of gentamicin conjugates, challenges remain in achieving high selectivity in chemical modification. This thesis presents the synthesis of vitamin B_{12}-linker-gentamicin conjugates where conjugation of gentamicin C1a fortuitously occurs selectively at one location.

1.9 References

(1) IUPAC-IUB Comm. on Biochem. Nomenclature. Nomenclature of Corrinoids (1973 Recommendations). IUPAC-IUB Commission on Biochemical Nomenclature. *Biochemistry* **1974**, *13* (7), 1555–1560. https://doi.org/10.1021/bi00704a036.
(2) Kräutler, B. Cobalt Enzymes. In *Comprehensive Inorganic Chemistry III*; Elsevier, 2023; pp 268–301. https://doi.org/10.1016/B978-0-12-823144-9.00146-1.
(3) Giedyk, M.; Goliszewska, K.; Gryko, D. Vitamin B_{12} Catalysed Reactions. *Chem. Soc. Rev.* **2015**, *44* (11), 3391–3404. https://doi.org/10.1039/C5CS00165J.
(4) Kräutler, B. Vitamin B_{12} and B_{12}-Proteins. In *Encyclopedia of Biological Chemistry*; Lennarz, W. J., Lane, M. D., Eds.; Elsevier: New York, 2004; pp 360–366. https://doi.org/10.1016/B0-12-443710-9/00740-7.
(5) Gruber, K.; Puffer, B.; Kräutler, B. Vitamin B_{12}-Derivatives—Enzyme Cofactors and Ligands of Proteins and Nucleic Acids. *Chem. Soc. Rev.* **2011**, *40* (8), 4346–4363. https://doi.org/10.1039/c1cs15118e.
(6) Kräutler, B. *Chemistry and Biochemistry of B_{12}*; Banerjee, R., Ed.; Wiley: New York, 1999.
(7) Green, R. Vitamin B_{12}: Physiology, Dietary Sources, and Requirements. In *Encyclopedia of Human Nutrition (Fourth Edition)*; Caballero, B., Ed.; Academic Press: Oxford, 2023; pp 482–488. https://doi.org/10.1016/B978-0-12-821848-8.00188-8.
(8) Villa, E. A.; Escalante-Semerena, J. C. Corrinoid Salvaging and Cobamide Remodeling in Bacteria and Archaea. *J. Bacteriol.* **2024**, *206* (11), e00286-24. https://doi.org/10.1128/jb.00286-24.
(9) Ford, S. H.; Nichols, A.; Shambee, M. The Preparation and Characterization of the Diaquo- Forms of Several Incomplete Corrinoids: Cobyric Acid, Cobinamide, and Three Isomeric Cobinic Acid Pentaamides. *J. Inorg. Biochem.* **1991**, *41* (4), 235–244. https://doi.org/10.1016/0162-0134(91)80015-A.
(10) Bonnett, R.; Godfrey, J. M.; Redman, D. G. Cobyric Acid and Related Compounds from Vitamin B_{12}. *J. Chem. Soc. C Org.* **1969**, No. 8, 1163–1166. https://doi.org/10.1039/J39690001163.
(11) Proinsias, K. ó; Karczewski, M.; Zieleniewska, A.; Gryko, D. Microwave-Assisted Cobinamide Synthesis. *J. Org. Chem.* **2014**, *79* (16), 7752–7757. https://doi.org/10.1021/JO501364B.
(12) Rutkowska-Zbik, D.; Mazur, G.; Drzewiecka-Matuszek, A.; Orzeł, Ł.; Stochel, G. Exploring Novel Modified Vitamin B_{12} as a Drug Carrier: Forecast from Density Functional Theory Modeling. *J. Phys. Chem. B* **2013**, *117* (33), 9655–9661. https://doi.org/10.1021/JP405821K/ASSET/IMAGES/JP-2013-05821K_M004.GIF.
(13) Proinsias, K.; Giedyk, M.; Gryko, D. Vitamin B_{12}: Chemical Modifications. *Chem. Soc. Rev.* **2013**, *42* (16), 6605–6619. https://doi.org/10.1039/c3cs60062a.
(14) Bridwell-Rabb, J.; Drennan, C. L. Vitamin B_{12} in the Spotlight Again. *Curr. Opin. Chem. Biol.* **2017**, *37*, 63–70. https://doi.org/10.1016/j.cbpa.2017.01.013.
(15) Mundwiler, S.; Spingler, B.; Kurz, P.; Kunze, S.; Alberto, R. Cyanide-Bridged Vitamin B_{12}-Cisplatin Conjugates. *Chem. - Eur. J.* **2005**, *11* (14), 4089–4095. https://doi.org/10.1002/CHEM.200500117.
(16) Rossier, J.; Hauser, D.; Kottelat, E.; Rothen-Rutishauser, B.; Zobi, F. Organometallic Cobalamin Anticancer Derivatives for Targeted Prodrug Delivery via Transcobalamin-Mediated Uptake. *Dalton Trans.* **2017**, *46* (7), 2159–2164. https://doi.org/10.1039/C6DT04443C.
(17) Siega, P.; Wuerges, J.; Arena, F.; Gianolio, E.; Fedosov, S. N.; Dreos, R.; Geremia, S.; Aime, S.; Randaccio, L. Release of Toxic Gd3+ Ions to Tumour Cells by

Vitamin B_{12} Bioconjugates. *Chem. – Eur. J.* **2009**, *15* (32), 7980–7989. https://doi.org/10.1002/chem.200802680.
(18) Waibel, R.; Treichler, H.; Schaefer, N. G.; Staveren, D. R. van; Mundwiler, S.; Kunze, S.; Küenzi, M.; Alberto, R.; Nüesch, J.; Knuth, A.; Moch, H.; Schibli, R.; Schubiger, P. A. New Derivatives of Vitamin B_{12} Show Preferential Targeting of Tumors. *Cancer Res.* **2008**, *68* (8), 2904–2911. https://doi.org/10.1158/0008-5472.CAN-07-6771.
(19) Petrus, A. K.; Vortherms, A. R.; Fairchild, T. J.; Doyle, R. P. Vitamin B_{12} as a Carrier for the Oral Delivery of Insulin. *ChemMedChem* **2007**, *2* (12), 1717–1721. https://doi.org/10.1002/cmdc.200700239.
(20) Sarhadi, S.; Moosavian, S. A.; Mashreghi, M.; Rahiman, N.; Golmohamadzadeh, S.; Tafaghodi, M.; Sadri, K.; Chamani, J.; Jaafari, M. R. B_{12}-Functionalized PEGylated Liposomes for the Oral Delivery of Insulin: In Vitro and in Vivo Studies. *J. Drug Deliv. Sci. Technol.* **2022**, *69*, 103141. https://doi.org/10.1016/j.jddst.2022.103141.
(21) Clardy-James, S.; Allis, D. G.; Fairchild, T. J.; Doyle, R. P. Examining the Effects of Vitamin B_{12} Conjugation on the Biological Activity of Insulin: A Molecular Dynamic and in Vivo Oral Uptake Investigation. *MedChemComm* **2012**, *3* (9), 1054–1058. https://doi.org/10.1039/C2MD20040F.
(22) Chen, Z.; Liang, Y.; Feng, X.; Liang, Y.; Shen, G.; Huang, H.; Chen, Z.; Yu, J.; Liu, H.; Lin, T.; Chen, H.; Wu, D.; Li, G.; Zhao, B.; Guo, W.; Hu, Y. Vitamin-B_{12}-Conjugated PLGA-PEG Nanoparticles Incorporating miR-532-3p Induce Mitochondrial Damage by Targeting Apoptosis Repressor with Caspase Recruitment Domain (ARC) on CD320-Overexpressed Gastric Cancer. *Mater. Sci. Eng. C* **2021**, *120*, 111722. https://doi.org/10.1016/j.msec.2020.111722.
(23) Zendegani, E.; Dolatabadi, S. The Efficacy of Imipenem Conjugated with Synthesized Silver Nanoparticles Against Acinetobacter Baumannii Clinical Isolates, Iran. *Biol. Trace Elem. Res.* **2020**, *197* (1), 330–340. https://doi.org/10.1007/S12011-019-01962-6.
(24) Równicki, M.; Wojciechowska, M.; Wierzba, A. J.; Czarnecki, J.; Bartosik, D.; Gryko, D.; Trylska, J. Vitamin B_{12} as a Carrier of Peptide Nucleic Acid (PNA) into Bacterial Cells. *Sci. Rep.* **2017**, *7* (1). https://doi.org/10.1038/s41598-017-08032-8.
(25) Köster, W. ABC Transporter-Mediated Uptake of Iron, Siderophores, Heme and Vitamin B12. *Res. Microbiol.* **2001**, *152* (3–4), 291–301. https://doi.org/10.1016/S0923-2508(01)01200-1.
(26) Giannella, R. A.; Broitman, S. A.; Zamcheck, N. Vitamin B_{12} Uptake by Intestinal Microorganisms: Mechanism and Relevance to Syndromes of Intestinal Bacterial Overgrowth. *J. Clin. Invest.* **1971**, *50* (5), 1100–1107. https://doi.org/10.1172/JCI106581.
(27) Froese, D. S.; Fowler, B.; Baumgartner, M. R. Vitamin B_{12}, Folate, and the Methionine Remethylation Cycle—Biochemistry, Pathways, and Regulation. *J. Inherit. Metab. Dis.* **2019**, *42* (4), 673–685. https://doi.org/10.1002/JIMD.12009.
(28) Równicki, M.; Dąbrowska, Z.; Wojciechowska, M.; Wierzba, A. J.; Maximova, K.; Gryko, D.; Trylska, J. Inhibition of Escherichia Coli Growth by Vitamin B_{12}–Peptide Nucleic Acid Conjugates. *ACS Omega* **2019**, *4* (1), 819–824. https://doi.org/10.1021/acsomega.8b03139.
(29) Giedyk, M.; Jackowska, A.; Równicki, M.; Kolanowska, M.; Trylska, J.; Gryko, D. Vitamin B_{12} Transports Modified RNA into E. Coli and S. Typhimurium Cells. *Chem. Commun.* **2019**, *55* (6), 763–766. https://doi.org/10.1039/c8cc05064c.
(30) Pieńko, T.; Czarnecki, J.; Równicki, M.; Wojciechowska, M.; Wierzba, A. J.; Gryko, D.; Bartosik, D.; Trylska, J. Vitamin B_{12}-Peptide Nucleic Acids Use the BtuB

Receptor to Pass through the Escherichia Coli Outer Membrane. *Biophys. J.* **2021**, *120* (4), 725–737. https://doi.org/10.1016/J.BPJ.2021.01.004.
(31) Bradbeer, C.; Woodrow, M. L.; Khalifah, L. I. Transport of Vitamin B12 in Escherichia Coli: Common Receptor System for Vitamin B_{12} and Bacteriophage BF23 on the Outer Membrane of the Cell Envelope. *J. Bacteriol.* **1976**, *125* (3), 1032–1039.
(32) Lawrence, A. D.; Nemoto-Smith, E.; Deery, E.; Baker, J. A.; Schroeder, S.; Brown, D. G.; Tullet, J. M. A.; Howard, M. J.; Brown, I. R.; Smith, A. G.; Boshoff, H. I.; Barry, C. E.; Warren, M. J. *Construction of Fluorescent Analogs to Follow the Uptake and Distribution of Cobalamin (Vitamin B_{12}) in Bacteria, Worms, and Plants*. Cell Chemical Biology. https://doi.org/10.1016/j.chembiol.2018.04.012.
(33) Chalasani, K. B.; Russell-Jones, G. J.; Yandrapu, S. K.; Diwan, P. V.; Jain, S. K. A Novel Vitamin B_{12}-Nanosphere Conjugate Carrier System for Peroral Delivery of Insulin. *J. Controlled Release* **2007**, *117* (3), 421–429. https://doi.org/10.1016/j.jconrel.2006.12.003.
(34) Wierzba, A. J.; Maximova, K.; Wincenciuk, A.; Równicki, M.; Wojciechowska, M.; Nexø, E.; Trylska, J.; Gryko, D. Does a Conjugation Site Affect Transport of Vitamin B_{12}–Peptide Nucleic Acid Conjugates into Bacterial Cells? *Chem. – Eur. J.* **2018**, *24* (70), 18772–18778. https://doi.org/10.1002/chem.201804304.
(35) Zelder, F. Recent Trends in the Development of Vitamin B_{12} Derivatives for Medicinal Applications. *Chem. Commun.* **2015**, *51* (74), 14004–14017. https://doi.org/10.1039/C5CC04843E.
(36) Wierzba, A. J.; Hassan, S.; Gryko, D. Synthetic Approaches toward Vitamin B_{12} Conjugates. *Asian J. Org. Chem.* **2019**, *8* (1), 6–24. https://doi.org/10.1002/ajoc.201800579.
(37) McEwan, J. F.; Veitch, H. S.; Russell-Jones, G. J. Synthesis and Biological Activity of Ribose-5'-Carbamate Derivatives of Vitamin B_{12}. *Bioconjug. Chem.* **1999**, *10* (6), 1131–1136. https://doi.org/10.1021/BC990086P/ASSET/IMAGES/LARGE/BC990086PF00004.JPEG.
(38) Zhang, L.; Zhang, M.; Lu, J.; Tang, A.; Zhu, L. Highly Permeable Thin-Film Nanocomposite Membranes Embedded with PDA/PEG Nanocapsules as Water Transport Channels. *J. Membr. Sci.* **2019**, *586*, 115–121. https://doi.org/10.1016/j.memsci.2019.05.065.
(39) Nieto-Orellana, A.; Li, H.; Rosiere, R.; Wauthoz, N.; Williams, H.; Monteiro, C. J.; Bosquillon, C.; Childerhouse, N.; Keegan, G.; Coghlan, D.; Mantovani, G.; Stolnik, S. Targeted PEG-Poly(Glutamic Acid) Complexes for Inhalation Protein Delivery to the Lung. *J. Controlled Release* **2019**, *316*, 250–262. https://doi.org/10.1016/j.jconrel.2019.10.012.
(40) Wierzba, A.; Wojciechowska, M.; Trylska, J.; Gryko, D. Vitamin B_{12} Suitably Tailored for Disulfide-Based Conjugation. *Bioconjug. Chem.* **2016**, *27* (1), 189–197. https://doi.org/10.1021/acs.bioconjchem.5b00599.
(41) Vázquez-Meza, H.; Vilchis-Landeros, M. M.; Vázquez-Carrada, M.; Uribe-Ramírez, D.; Matuz-Mares, D. Cellular Compartmentalization, Glutathione Transport and Its Relevance in Some Pathologies. *Antioxidants* **2023**, *12* (4), 834. https://doi.org/10.3390/antiox12040834.
(42) Montero, D.; Tachibana, C.; Rahr Winther, J.; Appenzeller-Herzog, C. Intracellular Glutathione Pools Are Heterogeneously Concentrated. *Redox Biol.* **2013**, *1* (1), 508–513. https://doi.org/10.1016/j.redox.2013.10.005.
(43) Chimento, D. P.; Mohanty, A. K.; Kadner, R. J.; Wiener, M. C. Substrate-Induced Transmembrane Signaling in the Cobalamin Transporter BtuB. *Nat. Struct. Mol. Biol.* **2003**, *10* (5), 394–401. https://doi.org/10.1038/nsb914.

(44) Noinaj, N.; Guillier, M.; Barnard, T. J.; Buchanan, S. K. TonB-Dependent Transporters: Regulation, Structure, and Function. *Annu. Rev. Microbiol.* **2010**, *64*, 43–60. https://doi.org/10.1146/annurev.micro.112408.134247.
(45) Pieńko, T.; Trylska, J. Extracellular Loops of BtuB Facilitate Transport of Vitamin B_{12} through the Outer Membrane of E. Coli. *Comput. Biol.* **2021**, *17* (12). https://doi.org/10.1371/journal.pcbi.1008024.
(46) Bank, R. P. D. *RCSB PDB - 1NQH: OUTER MEMBRANE COBALAMIN TRANSPORTER (BTUB) FROM E. COLI, WITH BOUND CALCIUM AND CYANOCOBALAMIN (VITAMIN B_{12}) SUBSTRATE*. https://www.rcsb.org/structure/1nqh (accessed 2024-09-13).
(47) Karpowich, N. K.; Huang, H. H.; Smith, P. C.; Hunt, J. F. Crystal Structures of the BtuF Periplasmic-Binding Protein for Vitamin B_{12} Suggest a Functionally Important Reduction in Protein Mobility upon Ligand Binding*. *J. Biol. Chem.* **2003**, *278* (10), 8429–8434. https://doi.org/10.1074/jbc.M212239200.
(48) Borths, E. L.; Poolman, B.; Hvorup, R. N.; Locher, K. P.; Rees, D. C. In Vitro Functional Characterization of BtuCD-F, the Escherichia Coli ABC Transporter for Vitamin B_{12} Uptake. *Biochemistry* **2005**, *44* (49), 16301–16309. https://doi.org/10.1021/bi0513103.
(49) Mireku, S. A.; Ruetz, M.; Zhou, T.; Korkhov, V. M.; Kräutler, B.; Locher, K. P. Conformational Change of a Tryptophan Residue in BtuF Facilitates Binding and Transport of Cobinamide by the Vitamin B_{12} Transporter BtuCD-F. *Sci. Rep.* **2017**, *7*. https://doi.org/10.1038/srep41575.
(50) Bank, R. P. D. *RCSB PDB - 1N4A: The Ligand Bound Structure of E.coli BtuF, the Periplasmic Binding Protein for Vitamin B_{12}*. https://www.rcsb.org/structure/1N4A (accessed 2024-09-13).
(51) Locher, K. P.; Lee, A. T.; Rees, D. C. The E. Coli BtuCD Structure: A Framework for ABC Transporter Architecture and Mechanism. *Science* **2002**, *296* (5570), 1091–1098. https://doi.org/10.1126/science.1071142.
(52) Jacobsen, D. W.; Digir, P. M.; M Huennekens, A. F. Adenosylcobalamin Analogues as Inhibitors of Ribonucleotide Reductase and Vitamin B_{12} Transport. *Mol. Pharmacol.* **1974**, *11*, 174–184.
(53) Ruiz-Sánchez, P.; Mundwiler, S.; Alberto, R. Syntheses of Fluorescent Vitamin B_{12}-Pt(II) Conjugates and Their Pt(II) Release in a Spectroelectrochemical Assay. *CHIMIA* **2007**, *61* (4), 190. https://doi.org/10.2533/chimia.2007.190.
(54) Rosendahl, M. S.; Omann, G. M.; Leonard, N. J. Synthesis and Biological Activity of a Profluorescent Analogue of Coenzyme B_{12}. *Proc. Natl. Acad. Sci. U. S. A.* **1982**, *79* (11 I), 3480–3484. https://doi.org/10.1073/PNAS.79.11.3480.
(55) Watanabe, F.; Abe, K.; Takenaka, S.; Fujita, T.; Nakano, Y. Method for Quantitation of Total Vitamin B $_{12}$ in Foods Using a Highly Fluorescent Vitamin B $_{12}$ Derivative. *J. Agric. Food Chem.* **1997**, *45* (12), 4661–4663. https://doi.org/10.1021/jf970313m.
(56) Smeltzer, C. C.; Cannon, M. J.; Pinson, P. R.; Munger, J. D.; West, F. G.; Grissom, C. B. Synthesis and Characterization of Fluorescent Cobalamin (CobalaFluor) Derivatives for Imaging. *Org. Lett.* **2001**, *3* (6), 799–801. https://doi.org/10.1021/ol006825v.
(57) Priestman, M. A.; Shell, T. A.; Sun, L.; Lee, H.; Lawrence, D. S. Merging of Confocal and Caging Technologies: Selective Three-Color Communication with Profluorescent Reporters. *Angew. Chem. Int. Ed.* **2012**, *51* (31), 7684–7687. https://doi.org/10.1002/anie.201202820.
(58) Shell, T. A.; Shell, J. R.; Rodgers, Z. L.; Lawrence, D. S. Tunable Visible and Near-IR Photoactivation of Light-Responsive Compounds by Using Fluorophores as

Light-Capturing Antennas. *Angew. Chem. Int. Ed.* **2014**, *53* (3), 875–878. https://doi.org/10.1002/anie.201308816.
(59) Smith, W. J.; Oien, N. P.; Hughes, R. M.; Marvin, C. M.; Rodgers, Z. L.; Lee, J.; Lawrence, D. S. Cell-Mediated Assembly of Phototherapeutics. *Angew. Chem. Int. Ed.* **2014**, *53* (41), 10945–10948. https://doi.org/10.1002/anie.201406216.
(60) Jacobsen, D. W.; Holland, R. J.; Montejano, Y.; Huennekens, F. M. Cryptofluorescent Analogs of Cobalamin Coenzymes: Synthesis and Characterization. *J. Inorg. Biochem.* **1979**, *10* (1), 53–65. https://doi.org/10.1016/S0162-0134(00)81005-3.
(61) McGreevy, J. M.; Cannon, M. J.; Grissom, C. B. Minimally Invasive Lymphatic Mapping Using Fluorescently Labeled Vitamin B_{12}. *J. Surg. Res.* **2003**, *111* (1), 38–44. https://doi.org/10.1016/S0022-4804(03)00093-3.
(62) Cannon, M. J. Protein Binding, Cellular Localization, and Tissue Uptake of Breast Cancer Targeted Fluorescent Cobalamin Analogs. Ph.D., The University of Utah, United States -- Utah, 2001. https://www.proquest.com/docview/251795341/abstract/E9C89B3A9644C46PQ/1 (accessed 2024-04-10).
(63) Charles B. Grissom; Frederick G. West; James McGreevy; Joel S. Bentz; Michelle J. Cannon. Fluorescent Cobalamins and Uses Thereof, November 11, 2004. https://patents.google.com/patent/US20040224921 (accessed 2024-01-31).
(64) Fedosov, S. N.; Grissom, C. B.; Fedosova, N. U.; Moestrup, S. K.; Nexø, E.; Petersen, T. E. Application of a Fluorescent Cobalamin Analogue for Analysis of the Binding Kinetics: A Study Employing Recombinant Human Transcobalamin and Intrinsic Factor. *FEBS J.* **2006**, *273* (20), 4742–4753. https://doi.org/10.1111/J.1742-4658.2006.05478.X.
(65) Magde, D.; Wong, R.; Seybold, P. G. Fluorescence Quantum Yields and Their Relation to Lifetimes of Rhodamine 6G and Fluorescein in Nine Solvents: Improved Absolute Standards for Quantum Yields¶. *Photochem. Photobiol.* **2007**, *75* (4), 327–334. https://doi.org/10.1562/0031-8655(2002)0750327FQYATR2.0.CO2.
(66) Lee, M.; Grissom, C. B. Design, Synthesis, and Characterization of Fluorescent Cobalamin Analogues with High Quantum Efficiencies. *C J Lab Clin Med* **2004**, *43* (1), 799. https://doi.org/10.1021/ol900401z.
(67) Welfare, J. G.; Mortelliti, M. J.; McGlade, C. A.; Hartman, T. W.; Dempsey, J. L.; Lawrence, D. S. Assessment of Photoreleasable Linkers and Light-Capturing Antennas on a Photoresponsive Cobalamin Scaffold. *J. Org. Chem.* **2022**, *87* (8), 5076–5084. https://doi.org/10.1021/acs.joc.1c02931.
(68) Viola-Villegas, N.; Rabideau, A. E.; Bartholoma, M.; Zubieta, J.; Doyle, R. P. Targeting the Cubilin Receptor through the Vitamin B_{12} Uptake Pathway: Cytotoxicity and Mechanistic Insight through Fluorescent Re(I) Delivery. *J. Med. Chem.* **2009**, *52* (16), 5253–5261. https://doi.org/10.1021/JM900777V.
(69) Santoro, G.; Zlateva, T.; Ruggi, A.; Quaroni, L.; Zobi, F. Synthesis, Characterization and Cellular Location of Cytotoxic Constitutional Organometallic Isomers of Rhenium Delivered on a Cyanocobalmin Scaffold. *Dalton Trans.* **2015**, *44* (15), 6999–7008. https://doi.org/10.1039/C4DT03598D.
(70) Vortherms, A. R.; Kahkoska, A. R.; Rabideau, A. E.; Zubieta, J.; Andersen, L. L.; Madsen, M.; Doyle, R. P. A Water Soluble Vitamin B_{12}-Re(i) Fluorescent Conjugate for Cell Uptake Screens: Use in the Confirmation of Cubilin in the Lung Cancer Line A549. *Chem. Commun.* **2011**, *47* (35), 9792. https://doi.org/10.1039/c1cc13615a.
(71) Rodgers, Z. L.; Shell, T. A.; Brugh, A. M.; Nowotarski, H. L.; Forbes, M. D. E.; Lawrence, D. S. Fluorophore Assisted Photolysis of Thiolato-Cob(III)Alamins. *Inorg. Chem.* **2016**, *55* (5), 1962–1969. https://doi.org/10.1021/acs.inorgchem.5b02036.

(72) Hughes, R. M.; Marvin, C. M.; Rodgers, Z. L.; Ding, S.; Oien, N. P.; Smith, W. J.; Lawrence, D. S. Phototriggered Secretion of Membrane Compartmentalized Bioactive Agents. *Angew. Chem.* **2016**, *128* (52), 16314–16317. https://doi.org/10.1002/ange.201609731.
(73) Marvin, C. M.; Ding, S.; White, R. E.; Orlova, N.; Wang, Q.; Zywot, E. M.; Vickerman, B. M.; Harr, L.; Tarrant, T. K.; Dayton, P. A.; Lawrence, D. S. On Command Drug Delivery via Cell-Conveyed Phototherapeutics. *Small* **2019**, *15* (37), e1901442. https://doi.org/10.1002/smll.201901442.
(74) Chromiński, M.; Gryko, D. "Clickable" Vitamin B_{12} Derivative. *Chem. – Eur. J.* **2013**, *19* (16), 5141–5148. https://doi.org/10.1002/chem.201203899.
(75) Jackowska, A.; Gryko, D. Vitamin B_{12} Derivatives Suitably Tailored for the Synthesis of Photolabile Conjugates. *Org Lett* **2021**, *23*, 41. https://doi.org/10.1021/acs.orglett.1c00839.
(76) Martins, C. D. F.; Raposo, M. M. M.; Costa, S. P. G. A Sulfo-Cyanine Dye as a Colorimetric Chemosensor for Metal Cation Recognition. *Eng. Proc.* **2022**, *27* (1), 12. https://doi.org/10.3390/ecsa-9-13219.
(77) Mujumdar, S. R.; Mujumdar, R. B.; Grant, C. M.; Waggoner, A. S. Cyanine-Labeling Reagents: Sulfobenzindocyanine Succinimidyl Esters. *Bioconjug. Chem.* **1996**, *7* (3), 356–362. https://doi.org/10.1021/bc960021b.
(78) Kubin, R. F.; Fletcher, A. N. Fluorescence Quantum Yields of Some Rhodamine Dyes. *J. Lumin.* **1982**, *27* (4), 455–462. https://doi.org/10.1016/0022-2313(82)90045-X.
(79) Donuru, V. R.; Vegesna, G. K.; Velayudham, S.; Green, S.; Liu, H. Synthesis and Optical Properties of Red and Deep-Red Emissive Polymeric and Copolymeric BODIPY Dyes. *Chem. Mater.* **2009**, *21* (10), 2130–2138. https://doi.org/10.1021/cm900276r.
(80) *Cy3 Dye - NZ*. https://www.thermofisher.com/au/en/home/life-science/cell-analysis/fluorophores/cy3-dye.html (accessed 2025-03-04).
(81) Grimm, J. B.; English, B. P.; Chen, J.; Slaughter, J. P.; Zhang, Z.; Revyakin, A.; Patel, R.; Macklin, J. J.; Normanno, D.; Singer, R. H.; Lionnet, T.; Lavis, L. D. A General Method to Improve Fluorophores for Live-Cell and Single-Molecule Microscopy. *Nat. Methods* **2015**, *12* (3), 244–250. https://doi.org/10.1038/nmeth.3256.
(82) Panchuk-Voloshina, N.; Haugland, R. P.; Bishop-Stewart, J.; Bhalgat, M. K.; Millard, P. J.; Mao, F.; Leung, W.-Y.; Haugland, R. P. Alexa Dyes, a Series of New Fluorescent Dyes That Yield Exceptionally Bright, Photostable Conjugates. *J. Histochem. Cytochem.* **1999**, *47* (9), 1179–1188. https://doi.org/10.1177/002215549904700910.
(83) El-Daly, S. A.; El-Hallag, I. S. Photophysical Parameters, Photodecomposition, Fluorescence Quenching and Convolutive Voltammetry of 7-Diethylaminocoumarin (DEAC) Laser Dye -Journal of the Korean Chemical Society | Korea Science. *J. Korean Chem. Soc.* **2010**, *54* (1), 13–22.
(84) Malgorzata Lipowska; Gabor Patonay; Lucjan Strekowski. A NOVEL NEAR-INFRARED CYANINE DYE FOR BIO ANALYTICAL APPLICATIONS. **1995**. https://doi.org/10.1515/HC.1995.1.5-6.427.
(85) *Molecular Probes Oregon Green 514 Carboxylic Acid, Succinimidyl Ester, Quantity: Each of 1 | Fisher Scientific*. https://www.fishersci.com/shop/products/oregon-green-514-carboxylic-acid-succinimidyl-ester/O6139 (accessed 2025-03-04).
(86) *BDP® TR-X-NHS ester | CAS#:197306-80-2*. https://www.lumiprobe.com/p/bdp-tr-x-nhs-ester (accessed 2025-03-04).
(87) Meyer, S. A.; Ozbay, B. N.; Potcoava, M.; Salcedo, E.; Restrepo, D.; Gibson, E. A. Super-Resolution Imaging of Ciliary Microdomains in Isolated Olfactory Sensory Neurons Using a Custom Two-Color Stimulated Emission Depletion Microscope. *J. Biomed. Opt.* **2016**, *21* (6), 066017. https://doi.org/10.1117/1.JBO.21.6.066017.

(88) Kinoshita, Y.; Nogami, K.; Jomura, R.; Akanuma, S.; Abe, H.; Inouye, M.; Kubo, Y.; Hosoya, K. Investigation of Receptor-Mediated Cyanocobalamin (Vitamin B_{12}) Transport across the Inner Blood–Retinal Barrier Using Fluorescence-Labeled Cyanocobalamin. *Mol. Pharm.* **2018**, *15* (8), 3583–3594. https://doi.org/10.1021/acs.molpharmaceut.8b00617.
(89) Fedosov, S. N.; Berglund, L.; Fedosova, N. U.; Nexø, E.; Petersen, T. E. Comparative Analysis of Cobalamin Binding Kinetics and Ligand Protection for Intrinsic Factor, Transcobalamin, and Haptocorrin. *J. Biol. Chem.* **2002**, *277* (12), 9989–9996. https://doi.org/10.1074/JBC.M111399200.
(90) Lawrence, A. D.; Nemoto-Smith, E.; Deery, E.; Baker, J. A.; Schroeder, S.; Brown, D. G.; Tullet, J. M. A.; Howard, M. J.; Brown, I. R.; Smith, A. G.; Boshoff, H. I.; Barry, C. E.; Warren, M. J. Construction of Fluorescent Analogs to Follow the Uptake and Distribution of Cobalamin (Vitamin B_{12}) in Bacteria, Worms, and Plants. *Cell Chem. Biol.* **2018**, *25* (8), 941-951.e6. https://doi.org/10.1016/j.chembiol.2018.04.012.
(91) Giovengo, A. S. B12 Conjugates for Intracellular Tracking and Drug Delivery, Kent State University, 2019. https://etd.ohiolink.edu/acprod/odb_etd/etd/r/1501/10?clear=10&p10_accession_num=kent156639798539302 (accessed 2025-01-23).
(92) Chromiński, M.; Lewalska, A.; Karczewski, M.; Gryko, D. Vitamin B_{12} Derivatives for Orthogonal Functionalization. *J. Org. Chem.* **2014**, *79* (16), 7532–7542. https://doi.org/10.1021/jo501271g.
(93) Lakowicz, J. R. *Principles of Fluorescence Spectroscopy*; Springer: New York, NY, UNITED STATES, 2011.
(94) Gryczynski, Z. (Karol); Gryczynski, I. *Practical Fluorescence Spectroscopy*; Taylor & Francis Group: Milton, UNITED KINGDOM, 2019.
(95) Hassanin, H. A. Investigation on the Interaction of Riboflavin with Aquacobalamin (Vitamin B_{12}): A Fluorescence Quenching Study. *J. Photochem. Photobiol. Chem.* **2022**, *430*, 113968. https://doi.org/10.1016/j.jphotochem.2022.113968.
(96) Clegg, R. M. Chapter 1 Förster Resonance Energy Transfer—FRET What Is It, Why Do It, and How It's Done. In *Laboratory Techniques in Biochemistry and Molecular Biology*; Fret and Flim Techniques; Elsevier, 2009; Vol. 33, pp 1–57. https://doi.org/10.1016/S0075-7535(08)00001-6.
(97) Niu, H.; Liu, J.; M. O'Connor, H.; Gunnlaugsson, T.; D. James, T.; Zhang, H. Photoinduced Electron Transfer (PeT) Based Fluorescent Probes for Cellular Imaging and Disease Therapy. **2023**. https://doi.org/10.1039/D1CS01097B.
(98) Weller, A. Photoinduced Electron Transfer in Solution: Exciplex and Radical Ion Pair Formation Free Enthalpies and Their Solvent Dependence. **1982**.
(99) Murphy, C. B.; Zhang, Y.; Troxler, T.; Ferry, V.; Martin, J. J.; Jones, W. E. Probing Förster and Dexter Energy-Transfer Mechanisms in Fluorescent Conjugated Polymer Chemosensors. *J. Phys. Chem. B* **2004**, *108* (5), 1537–1543. https://doi.org/10.1021/jp0301406.
(100) Würth, C.; Grabolle, M.; Pauli, J.; Spieles, M.; Resch-Genger, U. Relative and Absolute Determination of Fluorescence Quantum Yields of Transparent Samples. *Nat. Protoc.* **2013**, *8* (8), 1535–1550. https://doi.org/10.1038/nprot.2013.087.
(101) Rurack, K.; Spieles, M. Fluorescence Quantum Yields of a Series of Red and Near-Infrared Dyes Emitting at 600−1000 Nm. *Anal. Chem.* **2011**, *83* (4), 1232–1242. https://doi.org/10.1021/ac101329h.
(102) Levy, S. B.; Bonnie, M. Antibacterial Resistance Worldwide: Causes, Challenges and Responses. *Nat. Med.* **2004**, *10* (12), S122–S129. https://doi.org/10.1038/nm1145.

(103) El-Gamal, M.; Brahim, I.; Hisham, N.; Aladdin, R.; Mohammed, H.; Bahaaeldin, A. Recent Updates of Carbapenem Antibiotics. *Eur. J. Med. Chem.* **2017**, *131*, 185–195. https://doi.org/doi.org/10.1016/j.ejmech.2017.03.022.
(104) Alsughayer, A.; Elassar, A.-Z. A.; Hasan, A. A.; Al Sagheer, F. Antibiotic Resistance and Drug Modification: Synthesis, Characterization and Bioactivity of Newly Modified Potent Ciprofloxacin Derivatives. *Bioorganic Chem.* **2021**, *108*, 104658. https://doi.org/10.1016/j.bioorg.2021.104658.
(105) Fleming, A. Penicillin. In *Nobel Lecture*; 1945.
(106) Blair, J. M. A.; Webber, M. A.; Baylay, A. J.; Ogbolu, D. O.; Piddock, L. J. V. Molecular Mechanisms of Antibiotic Resistance. *Nat. Rev. Microbiol.* **2015**, *13* (1), 42–51. https://doi.org/10.1038/nrmicro3380.
(107) Holmes, A. H.; Moore, L. S. P.; Sundsfjord, A.; Steinbakk, M.; Regmi, S.; Karkey, A.; Guerin, P. J.; Piddock, L. J. V. Understanding the Mechanisms and Drivers of Antimicrobial Resistance. *The Lancet* **2016**, *387* (10014), 176–187. https://doi.org/10.1016/S0140-6736(15)00473-0.
(108) Munita, J. M.; Arias, C. A. Mechanisms of Antibiotic Resistance. *Microbiol. Spectr.* **2016**, *4* (2), 464–472. https://doi.org/10.1128/MICROBIOLSPEC.VMBF-0016-2015.
(109) Hancock, R. E. W.; Brinkman, F. S. L. Function of Pseudomonas Porins in Uptake and Efflux. *Annu. Rev. Microbiol.* **2002**, *56*, 17–38. https://doi.org/10.1146/ANNUREV.MICRO.56.012302.160310.
(110) Reygaert, W. C. An Overview of the Antimicrobial Resistance Mechanisms of Bacteria. *AIMS Microbiol.* **2018**, *4* (3), 482–501. https://doi.org/10.3934/microbiol.2018.3.482.
(111) Poole, K. Efflux Pumps as Antimicrobial Resistance Mechanisms. *Ann. Med.* **2007**, *39* (3), 162–176. https://doi.org/10.1080/07853890701195262.
(112) Webber, M. A.; Piddock, L. J. V. The Importance of Efflux Pumps in Bacterial Antibiotic Resistance. *J. Antimicrob. Chemother.* **2003**, *51* (1), 9–11. https://doi.org/10.1093/JAC/DKG050.
(113) Lamut, A.; Mašič, L. P.; Kikelj, D.; Tomašič, T. Efflux Pump Inhibitors of Clinically Relevant Multidrug Resistant Bacteria. *Med. Res. Rev.* **2019**, *39* (6), 2460–2504. https://doi.org/10.1002/med.21591.
(114) Lorusso, A. B.; Carrara, J. A.; Barroso, C. D. N.; Tuon, F. F.; Faoro, H. Role of Efflux Pumps on Antimicrobial Resistance in Pseudomonas Aeruginosa. *Int. J. Mol. Sci.* **2022**, *23* (24), 15779. https://doi.org/10.3390/ijms232415779.
(115) Pesingi, P. V.; Singh, B. R.; Pesingi, P. K.; Bhardwaj, M.; Singh, S. V.; Kumawat, M.; Sinha, D. K.; Gandham, R. K. Frontiers | MexAB-OprM Efflux Pump of Pseudomonas Aeruginosa Offers Resistance to Carvacrol: A Herbal Antimicrobial Agent. *Front. Microbiol.* **2019**, *10*. https://doi.org/10.3389/fmicb.2019.02664.
(116) Ghosh, P.; Das, S. Synthesis and Functionalization of 4-Quinolones – A Progressing Story. *Eur. J. Org. Chem.* **2019**, *2019* (28), 4466–4516. https://doi.org/10.1002/EJOC.201900452.
(117) Avakh, A.; Grant, G. D.; Cheesman, M. J.; Kalkundri, T.; Hall, S. The Art of War with Pseudomonas Aeruginosa: Targeting Mex Efflux Pumps Directly to Strategically Enhance Antipseudomonal Drug Efficacy. *Antibiotics* **2023**, *12* (8), 1304. https://doi.org/10.3390/antibiotics12081304.
(118) Tillotson, G. S. Trojan Horse Antibiotics—A Novel Way to Circumvent Gram-Negative Bacterial Resistance? *Infect. Dis.* **2016**, *9*, 45–52. https://doi.org/10.4137/IDRT.S31567.

(119) Ij, S. A Trojan-Horse Strategy Including a Bacterial Suicide Action for the Efficient Use of a Specific Gram-Positive Antibiotic on Gram-Negative Bacteria. *PubMed* **2018**.
(120) Górska, A.; Sloderbach, A.; Marszałł, M. P. Siderophore–Drug Complexes: Potential Medicinal Applications of the 'Trojan Horse' Strategy. *Trends Pharmacol. Sci.* **2014**, *35* (9), 442–449. https://doi.org/10.1016/j.tips.2014.06.007.
(121) *Fetroja® (cefiderocol) | Overcoming carbapenem-resistance*. https://www.fetroja.com/overcoming-carbapenem-resistance (accessed 2022-02-22).
(122) Zhao, S.; Wang, Z.-P.; Wen, X.; Li, S.; Wei, G.; Guo, J.; He, Y. Synthesis of Vitamin B_{12}-Antibiotic Conjugates with Greatly Improved Activity against Gram-Negative Bacteria. *Org. Lett.* **2020**, *22* (16), 6632–6636. https://doi.org/10.1021/acs.orglett.0c02403.
(123) Pereira, S.; Yao, R.; Gomes, M.; Jørgensen, P. T.; Wengel, J.; Azevedo, N. F.; Sobral Santos, R. Can Vitamin B_{12} Assist the Internalization of Antisense LNA Oligonucleotides into Bacteria? *Antibiotics* **2021**, *10* (4), 379. https://doi.org/10.3390/antibiotics10040379.
(124) Mestizo, P. D.; Brenig, C.; Stephan, R.; Zelder, F.; Muchaamba, F. Assessing the Antimetabolite Activity of Modified Vitamin B_{12} Analogues against *Lactobacillus Delbrueckii* and *Listeria Monocytogenes*. *LWT* **2024**, *191*, 115641. https://doi.org/10.1016/j.lwt.2023.115641.
(125) Brenig, C.; Mestizo, P. D.; Zelder, F. Functionalisation of Vitamin B12 Derivatives with a Cobalt β-Phenyl Ligand Boosters Antimetabolite Activity in Bacteria. https://doi.org/10.1039/D2RA05748D.
(126) Zelenka, K.; Brandl, H.; Spingler, B.; Zelder, F. Coordination Chemistry and Biological Activity of 5′-OH Modified Quinoline–B_{12} Derivatives. *Dalton Trans.* **2011**, *40* (38), 9665. https://doi.org/10.1039/c1dt11161b.
(127) Zhang, G.-F.; Liu, X.; Zhang, S.; Pan, B.; Liu, M.-L. Ciprofloxacin Derivatives and Their Antibacterial Activities. *Eur. J. Med. Chem.* **2018**, *146*, 599–612. https://doi.org/10.1016/j.ejmech.2018.01.078.
(128) Thai, T.; Salisbury, B. H.; Zito, P. M. *Ciprofloxacin*. StatPearls. https://www.ncbi.nlm.nih.gov/books/NBK535454/ (accessed 2021-10-07).
(129) Dahiya, S.; Chuttani, K.; K. Khar, R.; Saluja, D.; K. Mishra, A.; Chopra, M. Synthesis and Evaluation of Ciprofloxacin Derivatives as Diagnostic Tools for Bacterial Infection by Staphylococcus Aureus. **2009**. https://doi.org/10.1039/B908474F.
(130) Egorov, A. R.; Kurliuk, A. V.; Rubanik, V. V.; Kirichuk, A. A.; Khubiev, O.; Golubev, R.; Lobanov, N. N.; Tskhovrebov, A. G.; Kritchenkov, A. S. Chitosan-Based Ciprofloxacin Extended Release Systems: Combined Synthetic and Pharmacological (In Vitro and In Vivo) Studies. *Molecules* **2022**, *27* (24), 8865. https://doi.org/10.3390/molecules27248865.
(131) Patra, P.; Mitra, S.; Debnath, N.; Pramanik, P.; Goswami, A. Ciprofloxacin Conjugated Zinc Oxide Nanoparticle: A Camouflage towards Multidrug Resistant Bacteria. *Bull. Mater. Sci.* **2014**, *37* (2), 199–206. https://doi.org/10.1007/s12034-014-0637-6.
(132) Patel, U. K.; Tiwari, P.; Tilak, R.; Joshi, G.; Kumar, R.; Agarwal, A. Synthesis of Ciprofloxacin-Linked 1,2,3-Triazole Conjugates as Potent Antibacterial Agents Using Click Chemistry: Exploring Their Function as DNA Gyrase Inhibitors via in Silico- and in Vitro-Based Studies. *RSC Adv.* **2024**, *14* (24), 17051–17070. https://doi.org/10.1039/D4RA01332H.
(133) Assali, M.; Joulani, M.; Awwad, R.; Assad, M.; Almasri, M.; Kittana, N.; Zaid, A. N. Facile Synthesis of Ciprofloxacin Prodrug Analogues to Improve Its Water

Solubility and Antibacterial Activity. *ChemistrySelect* **2016**, *1* (6), 1132–1135. https://doi.org/10.1002/slct.201600091.
(134) Khwaza, V.; Mlala, S.; Aderibigbe, B. A. Advancements in Synthetic Strategies and Biological Effects of Ciprofloxacin Derivatives: A Review. *Int. J. Mol. Sci.* **2024**, *25* (9), 4919. https://doi.org/10.3390/ijms25094919.
(135) Szulczyk, D.; Woziński, M.; Koliński, M.; Kmiecik, S.; Głogowska, A.; Augustynowicz-Kopeć, E.; Dobrowolski, M. A.; Roszkowski, P.; Struga, M.; Ciura, K. Menthol- and Thymol-Based Ciprofloxacin Derivatives against Mycobacterium Tuberculosis: In Vitro Activity, Lipophilicity, and Computational Studies. *Sci. Rep.* **2023**, *13* (1), 16328. https://doi.org/10.1038/s41598-023-43708-4.
(136) Mustaev, A.; Malik, M.; Zhao, X.; Kurepina, N.; Luan, G.; Oppegard, L. M.; Hiasa, H.; Marks, K. R.; Kerns, R. J.; Berger, J. M.; Drlica, K. Fluoroquinolone-Gyrase-DNA Complexes TWO MODES OF DRUG BINDING *. **2014**. https://doi.org/10.1074/jbc.M113.529164.
(137) Chaves, B. J.; Tadi, P. Gentamicin. In *StatPearls*; StatPearls Publishing: Treasure Island (FL), 2024.
(138) Deubner, R.; Schollmayer, C.; Wienen, F.; Holzgrabe, U. Assignment of the Major and Minor Components of Gentamicin for Evaluation of Batches. *Magn. Reson. Chem.* **2003**, *41* (8), 589–598. https://doi.org/10.1002/mrc.1222.
(139) Dagil, R.; O'Shea, C.; Nykjær, A.; Bonvin, A. M. J. J.; Kragelund, B. B. Gentamicin Binds to the Megalin Receptor as a Competitive Inhibitor Using the Common Ligand Binding Motif of Complement Type Repeats. *J. Biol. Chem.* **2013**, *288* (6), 4424–4435.
(140) Perni, S.; Martini-Gilching, K.; Prokopovich, P. Controlling Release Kinetics of Gentamicin from Silica Nano-Carriers. *Colloids Surf. Physicochem. Eng. Asp.* **2018**, *541*, 212–221. https://doi.org/10.1016/J.COLSURFA.2017.04.063.
(141) Ahangari, A.; Mojtaba, S.; Saghatchi, F. Gentamicin-Gold Nanoparticles Conjugate: A Contrast Agent for X-Ray Imaging of Infectious Foci Due to Staphylococcus Aureus. *IET Nanobiotechnol.* **2016**, *10* (4), 190–194. https://doi.org/10.1049/IET-NBT.2015.0034.
(142) Gomarasca, M.; Martins, T. F. C.; Greune, L.; Hardwidge, P. R.; Schmidt, M. A.; Rüter, C. Bacterium-Derived Cell-Penetrating Peptides Deliver Gentamicin to Kill Intracellular Pathogens. *Antimicrob. Agents Chemother.* **2017**, *61* (4). https://doi.org/10.1128/AAC.02545-16/SUPPL_FILE/ZAC004176004S1.PDF.
(143) Yan, T.; Kong, S.; Ouyang, Q.; Li, C.; Hou, T.; Chen, Y.; Li, S. Chitosan-Gentamicin Conjugate Hydrogel Promoting Skin Scald Repair. *Mar. Drugs* **2020**, *18* (233), 2–17. https://doi.org/10.3390/MD18050233.
(144) Sharma, D.; Chaudhary, A. One Pot Synthesis of Gentamicin Conjugated Gold Nanoparticles as an Efficient Antibacterial Agent. *J. Clust. Sci. 2020 324* **2020**, *32* (4), 995–1002. https://doi.org/10.1007/S10876-020-01864-X.
(145) Woiwode, U.; Sievers-Engler, A.; Lammerhofer, M. Preparation of Fluorescent Labeled Gentamicin as Biological Tracer and Its Characterization by Liquid Chromatography and High Resolution Mass Spectrometry. *J. Pharm. Biomed. Anal.* **2016**, *121*, 307–315. https://doi.org/doi.org/10.1016/j.jpba.2015.12.053.
(146) Jj, W.; A, C.; Pj, D.; Tl, N.; D, R.; Wn, T.; J, W. Selective N-Actylation of Gentamicin Antibiotics-Synthesis of 1-N-Acyl Derivatives. *PubMed* **1976**, *29* (7), 714–719.
(147) Umemura, E.; Sakamoto, Y.; Takahashi, Y.; Miyake, T. Synthesis and Antibacterial Activity of 1-N-[(S)-ω-Amino-2-Hydroxyalkyl] Derivatives of Dibekacin, 5-Deoxydibekacin, 3′-Deoxykanamycin A and Gentamicin B. *J. Antibiot. (Tokyo)* **2015**, *68* (6), 421–423. https://doi.org/10.1038/ja.2015.6.

(148) Boxler, D. L.; Brambilla, R.; Davies, D. H.; Mallams, A. K.; McCombie, S. W.; Morton, J. B.; Reichert, P.; Vernay, H. F. Semisynthetic Aminoglycoside Antibacterials. Part 9. Synthesis of Novel 1- and 3-Substituted and 1- and 3-Epi-Substituted Derivatives of Sisomicin and Gentamicin from the 1- and 3-Oxo-Derivatives. *J. Chem. Soc. Perkin 1* **1981**, 2168–2185. https://doi.org/10.1039/P19810002168.
(149) Nieves, I.; Hally, C.; Viappiani, C.; Agut, M.; Nonell, S. A Porphycene-Gentamicin Conjugate for Enhanced Photodynamic Inactivation of Bacteria. *Bioorganic Chem.* **2020**, *97*. https://doi.org/10.1016/J.BIOORG.2020.103661.
(150) Stojanovski, G.; Hailes, H. C.; Ward, J. M. Facile and Selective N-Alkylation of Gentamicin Antibiotics via Chemoenzymatic Synthesis. *Green Chem* **2022**, *24* (24), 9542–9551. https://doi.org/10.1039/D2GC03600B.

Chapter 2 Synthesis and characterisation of fluorescent CNCbl conjugates of NBD-X, sulfo-Cyanine5 and Cyanine7

2.1 Introduction

This chapter covers the synthesis and characterisation of CNCbl-linker complexes containing cystamine and polyethylene glycol linkers. The synthesis and characterisation of CNCbl-linker-fluorophore complexes of NBD-X, sulfo-Cyanine5 and Cyanine7 are also presented.

Modifications to CNCbl have been well documented, with a focus the development of CNCbl derivatives as therapeutics and imaging agents.[1–3] A primary goal of this work is to develop fluorescent CNCbl complexes that can be tracked through cellular uptake and transport by fluorescence microscopy, with an interest in uptake by the gram-negative bacterium, *E. Coli*.

2.1.1 Synthesis of CNCbl-linker complexes

Modification of CNCbl has been achieved in this work by functionalisation at the 5'-OH site of the ribose ring. The formation of the CNCbl-linker complexes was produced by carbamate formation between CNCbl and the attached linkers. Two linkers were employed in this study (Figure 12). The first linker utilised was the disulfide-containing cystamine linker. The second linker utilised is a short polyethylene glycol (PEG) moiety.

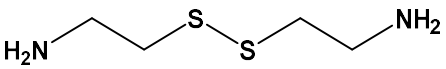

cystamine

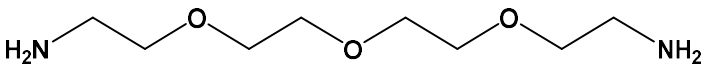

1,11-diamino-3,6,9-trioxaundecane

Figure 12: Structure of linkers cystamine and 1,11-diamine-3,6,9-trioxaundecane (PEG).

2.1.2 Synthesis of CNCbl-linker-fluorophore conjugates

Conjugation of a fluorescent molecule to CNCbl is well documented, with a particular emphasis on the attachment at either the β-axial or 5'-OH sites, with or without the inclusion of a linker, typically achieved via peptide coupling.[4–13] In this research, the 5'-OH functionalised CNCbl-linker molecules have been designed to contain a terminal amine. This provides a suitable site for the coupling of a fluorophore via peptide bond formation. The fluorophores selected contain a terminal carboxylic acid or *N*-hydroxysuccinimide ester, suitable for peptide coupling (Figure 13). The fluorophores used are 6-(*N*-(7-nitrobenz-2-oxa-1,3-diazol-4-yl)amino)hexanoic acid (NBD-X), sulfo-Cyanine5 NHS and Cyanine7 NHS.

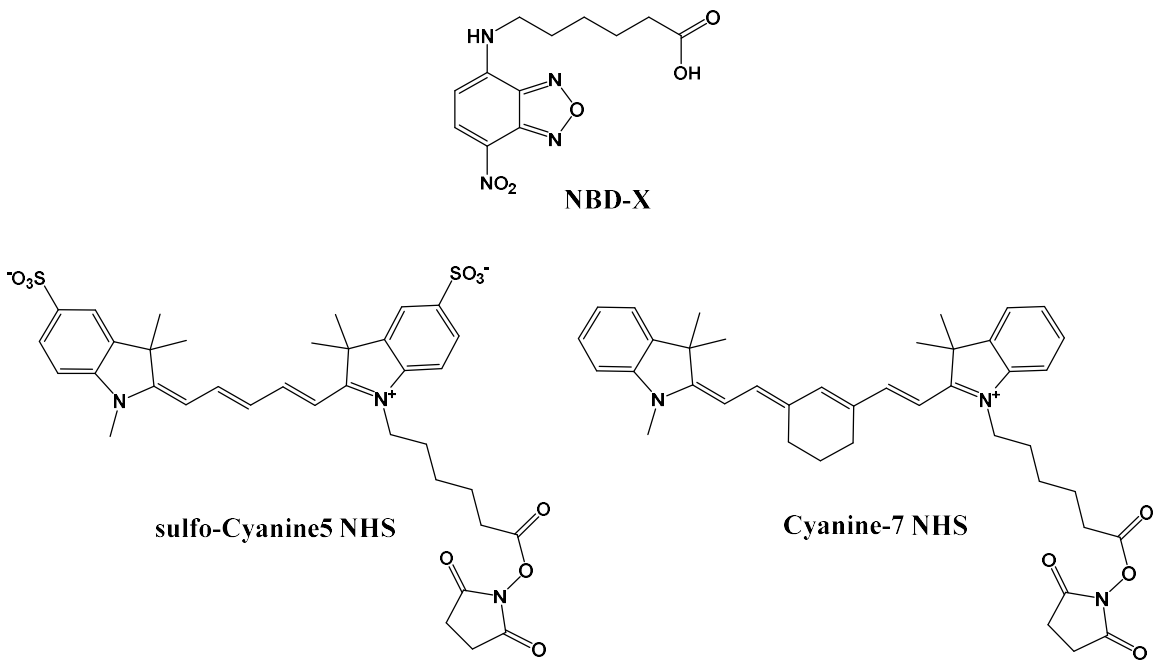

Figure 13: Structures of 6-(N-(7-Nitrobenz-2-oxa-1,3-diazol-4-yl)amino)hexanoic acid (NBD-X), sulfo-Cyanine5 NHS and Cyanine7 NHS esters.

2.2 Experimental

2.2.1 Chemicals

All chemicals were purchased from Merek NZ, AK Scientific or Lumiprobe. Solvents were purchased from ECP, ThermoFisher or Scharlau. Anhydrous solvents were stored under N_2 in a glove box. Ultra-pure water was obtained from a Purite Purewater 200 system. NMR solvents (MeOH-d_4, DMSO-d_6 and D_2O) were purchased from Eurisotop

and stored at 4°C. Reversed-phase silica (LiChroprep RP-C18 40-63 μm) was purchased from Merek.

2.2.2 Instrumentation

An MBraun LabMaster 130 nitrogen glove box was used for storing anhydrous solvents with O_2 and H_2O levels less than 5 ppm. NMR spectroscopy was carried out using a Bruker Ascend 400 NMR spectrometer and data analysed using MestReNova v12.0.0-20080. All spectra were obtained at 40°C and referenced to the relevant solvent peak (i.e. MeOH-d_4 quintuplet at 3.31 ppm or DMSO-d_6 quintuplet at 2.50 ppm) unless otherwise specified. NMR spectra obtained in D_2O were referenced to TSP. ^1H and ^{13}C NMR peaks listed in the experimental sections are listed, errors are possible due to overlapping peaks and/or overlapping solvent signals.

LC-MS analyses were carried out using an Agilent 1260 Infinity Quaternary LC System (Santa Clara, CA 95051 USA). The components of the instrument were as follows: 1260 quaternary pump (model number: G1311B), 1260 infinity ALS sampler (model number: G1329B), 1200 series autosampler thermostat FC/ALS/Therm (model number: G1330B), 1260 infinity TCC column component (model number: G1316A), 1260 infinity diode array detector (DAD) (model number: G4212B), connected to a 6420 triple quadrupole LC/MS system with multimode ionisation source (model number: G1948B) operating in positive electrospray ionisation mode. The autosampler was maintained at 4°C. Mass to charge data was analysed between 500 to 1800 *m/z*. Gas was maintained at a temperature of 300°C, with a flow of 6 L/min, nebuliser pressure at 15 psi and capillary voltage at 4000 V. Solvent flow was 0.3 mL/min. An Agilent Eclipse Plus C18 column (4.6 × 100 mm, 3.5 μm) was used for the analysis. The LC-MS system used Mass Hunter Workstation software (Agilent Technologies Inc. 2012, CA 95051, United States). Post-run analyses were carried out using Qualitative Analysis B.07.00 software.

HPLC analyses were conducted using an analytical HPLC instrument; a Shimadzu HPLC system consisting of a Prominence degassing unit (model number: DGU-20A5), Prominence pump (model number: LC-20AT), Prominence autosampler (model number: SIL-20AC HT), connected to a UV-visible detector (model number: SPD-20A). The column was maintained at 35°C. Peaks were detected at 350 nm unless stated otherwise. A Luna 5 μm C18(2) 100 A column (model number: 00G-4252-E0) analytical HPLC column was used.

2.2.3 General methods

Reactions were carried out under inert gas (N_2) and at room temperature unless otherwise stated. Samples were desalted by preparing a reversed-phase C18 silica plug (LiChroprep RP-18 40-63 μm) in CH_3CN in a fritted sinter filter and the reversed-phase C18 silica slurry was rinsed with two filter volumes of H_2O. The sample was dissolved in minimal H_2O and loaded onto the silica surface dropwise. The silica-bound sample was washed with H_2O (~100 mL per 25 mg solid) under a slight vacuum. The sample was eluted using CH_3OH and taken to dryness by rotary evaporation. Crude products were analysed by LC-MS. Purification of the compounds was achieved by reversed-phase chromatography using LiChroprep RP-C18 (40-63 μm) silica. The elutants used were CH_3CN and H_2O (with or without 0.1% formic acid). Columns were prepared by suspending silica in CH_3CN and loading it into a glass fritted column fitted with a tap (gel dimensions of 2.5 cm wide, 12.5 cm long). The column was washed with a mobile phase containing an increasing aqueous component (25, 50, 70% v/v H_2O in CH_3CN) and finally washed with 100% H_2O. Each solvent solution was degassed under a vacuum before addition to the column to prevent air bubbles from becoming trapped in the stationary phase, resulting in the cracking of the gel. Solid samples were dissolved in minimal H_2O and loaded onto the silica gel then washed with one column volume (equal to the volume of silica gel) of 5% v/v CH_3CN in H_2O. The organic component of the mobile phase was increased incrementally (i.e. 10% increase in the aqueous component) until the compounds began to elute. Crude LC-MS analysis was utilised to indicate the likely elution conditions. This was achieved by calculating the CH_3CN concentration where the product eluted by LC-MS and increasing the aqueous component of the solvent by 15%. Fractions were collected and analysed by direct injection MS. Fractions containing the product were combined and taken to dryness by rotary evaporation and the purity was determined by LC-MS.

2.2.4 LC-MS methods

Four LC-MS programs were used for the analysis of both crude and pure products. The mobile phase consisted of milliQ water + 0.1% formic acid (solvent A) and CH_3CN + 0.1% formic acid (solvent B). The mobile phase programs used are as below.

Method 1: 0-2 min isocratic elution 95:5 A:B, 2-30 min from 95:5 to 65:35 A:B and 30-31 from 65:35 to 10:90 A:B.

Method 2: 0-2 min isocratic elution 95:5 A:B, 2-30 min from 95:5 to 80:20 A:B, 30-35 min isocratic elution of 80:20 A:B.

Method 3: 0-5 min isocratic elution 95:5 A:B, 2-25 min from 95:5 to 65:35 A:B, 25-35 min from 65:35 to 10:90 A:B, 35-43 min of isocratic elution at 10:90 A:B.

2.2.5 Synthetic methods

CNCbl- (2-(2-aminoethyldisulfanyl)ethanamine) (CNCbl-cys-NH_2, 1)

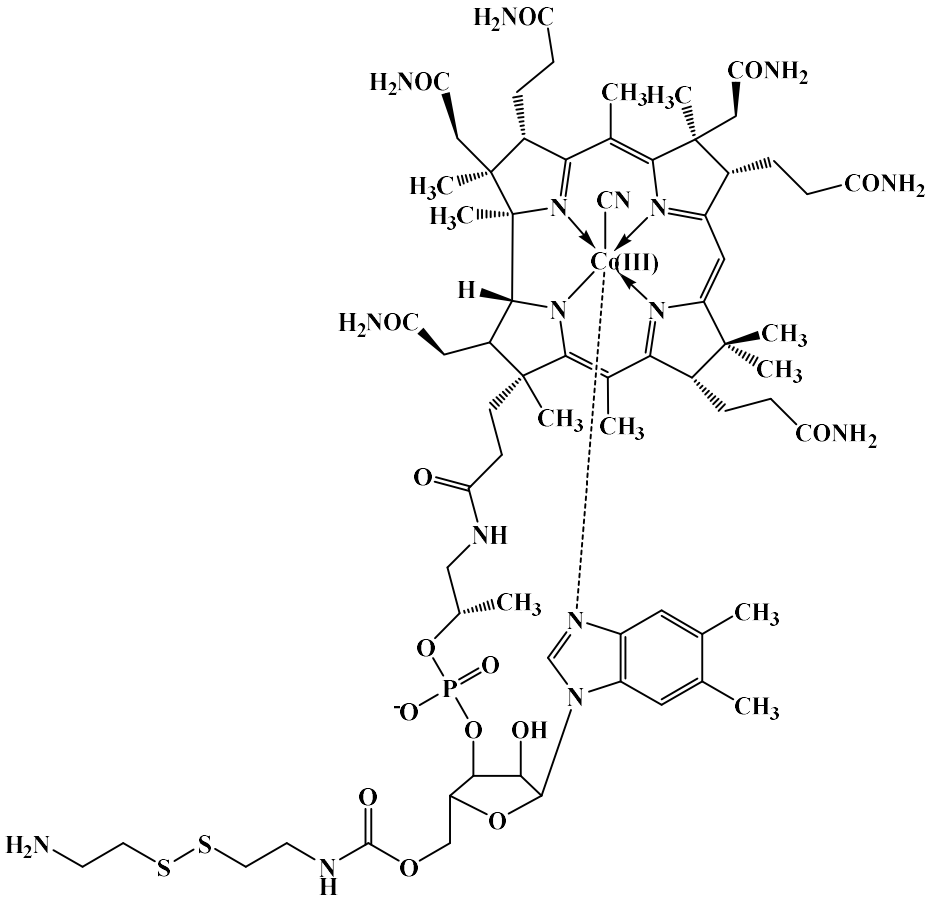

*Figure 14: Structure of **1**.*

Cyanocobalamin (CNCbl, 49.7 mg, 36.0 µmol) and 1,1-carbonyl-di(1,2,4-triazole) (CDT, 18.2 mg, 11.1 mmol) were dissolved in anhydrous DMSO (2 mL) and stirred for 30 min at 40 °C under N_2. Cystamine dihydrochloride (23.6 mg, 11.1 mmol) and Et_3N (37 µL, 7 mol eq.) were dissolved in anhydrous DMSO (1 mL) before adding to the CNCbl solution. The solution was stirred for 6 h at 40°C. The crude product was precipitated by dropwise addition to a solution of Et_2O and CH_2Cl_2 (1:1, 200 mL). The precipitate was washed with Et_2O (2 x 10 mL), released from the filter with CH_3OH and taken to dryness by rotary evaporation. Once dry, the crude was analysed by LC-MS. Purification was achieved by reversed-phase C18 chromatography. The product eluted as a red band at 12.5% CH_3CN in H_2O. 45.0 mg of the pure compound was obtained, representing an 80% yield, ≥ 95% purity established by LC-MS and ^{1}H NMR spectroscopy.

^{1}H NMR (400 MHz, MeOD) δ = 7.25 (s, 1H), 7.16 (s, 1H), 6.58 (s, 1H), 6.24 (d,*J*=3.0, 1H), 6.05 (s, 1H), 4.61 – 4.49 (m, 1H), 4.42 – 4.11 (m, 5H), 3.72 – 3.60 (m, 2H), 3.60 – 3.48 (m, 1H), 3.42 – 3.32 (m, 2H), 3.31 – 3.24 (m, 5H), 3.07 – 2.90 (m, 4H), 2.90 – 2.82 (m, 2H), 2.71 – 2.61 (m, 3H), 2.59 (s, 7H), 2.58 – 2.41 (m, 6H), 2.41 – 2.35 (m, 2H), 2.35 – 2.25 (m, 6H), 2.24 – 2.11 (m, 2H), 2.11 – 1.98 (m, 4H), 1.89 (s, 3H), 1.88 – 1.82 (m, 2H), 1.82 – 1.70 (m, 1H), 1.47 (s, 3H), 1.41 – 1.36 (m, 6H), 1.35 – 1.26 (m, 2H), 1.26 – 1.21 (m, 3H), 1.19 (s, 3H), 1.18 – 1.08 (m, 1H), 0.47 (s, 2H) ppm.

^{13}C NMR (101 MHz, DMSO) δ 179.60, 178.26, 175.17, 174.22, 173.70, 173.37, 172.93, 172.60, 171.69, 171.55, 171.23, 165.40, 164.72, 156.34, 142.19, 136.29, 132.80, 131.41, 129.66, 124.26, 116.43, 111.33, 105.94, 103.05, 93.65, 86.02, 84.43, 79.58, 74.82, 72.91, 71.01, 70.67, 68.87, 58.67, 55.05, 54.07, 53.06, 50.40, 48.67, 47.43, 46.61, 44.03, 42.17, 41.85, 40.43, 40.15, 39.94, 39.73, 39.52, 39.31, 39.10, 38.89, 38.31, 38.13, 35.17, 34.11, 32.18, 31.69, 30.94, 30.76, 30.54, 30.01, 29.05, 27.15, 25.64, 19.97, 19.64, 18.76, 16.56, 15.69, 15.08, 14.00 ppm.

CNCbl-(1,11-diamine-3,6,9-trioxaundecane) (CNCbl-PEG-$_{NH2}$, 2)

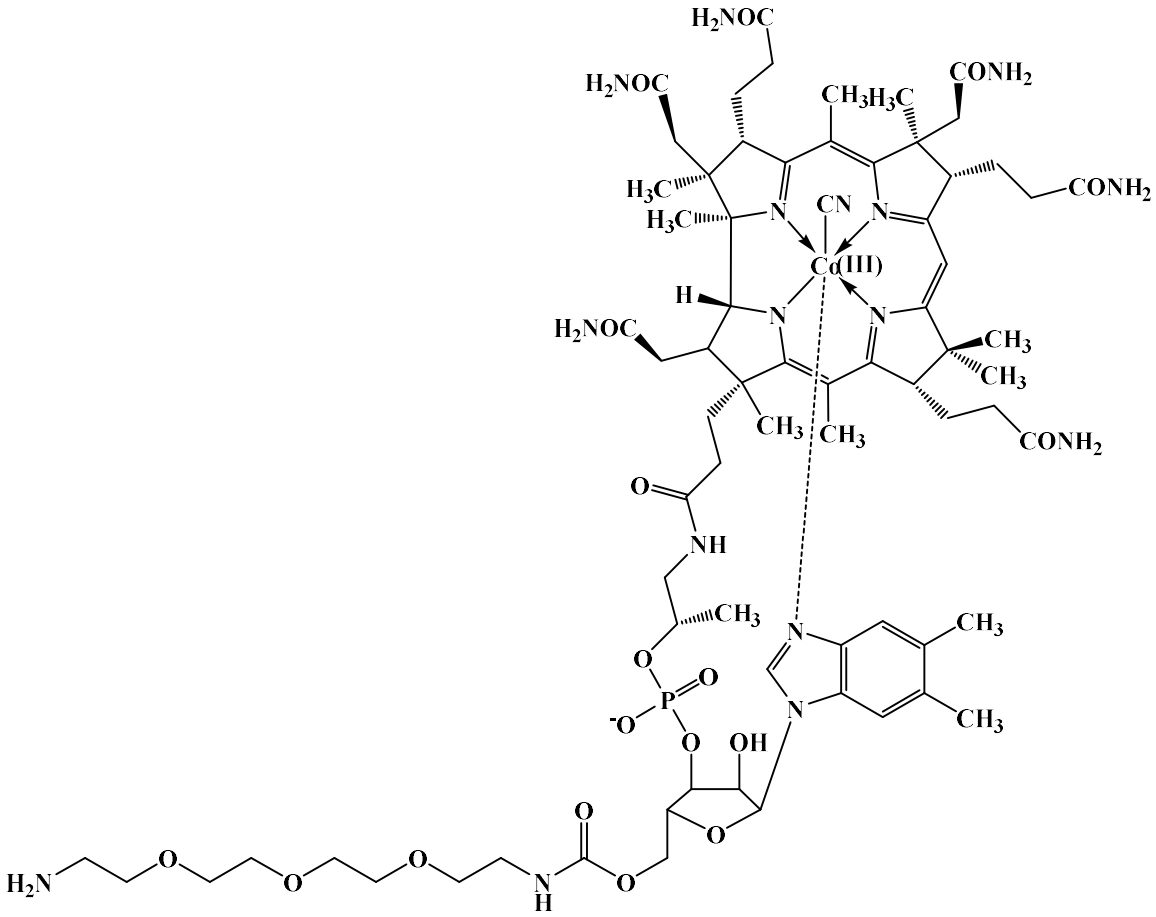

*Figure 15: Structure of **2**.*

CNCbl (102.2 mg, 73.8 µmol) and CDT (38.1 mg, 22.1 mmol) were dissolved in anhydrous DMSO (2 mL) and stirred for 30 min at 40°C. 1,11-Diamine-3,6,9-trioxaundecane (diamine-PEG-3, 41.4 µL, 22.1 mmol) and Et_3N (15.4 µL, 3 mol eq.) were dissolved in anhydrous DMSO (1 mL) before addition to the CNCbl solution. The solution was stirred for 6 h at 40 °C. The crude product was precipitated by dropwise addition to a solution of Et_2O and CH_2Cl_2 (1:1, 200 mL). The precipitate was washed with Et_2O (2 x 10 mL), released from the filter with CH_3OH and taken to dryness by rotary evaporation. Once dry, the sample was analysed by LC-MS. Purification was achieved by reversed-phase C18 chromatography. The product eluted as a red band at 15% CN_3CN in H_2O. 93.8 mg of pure product was obtained, representing a 78% yield, ≥95% purity established by LC-MS.

^{1}H NMR (400 MHz, MeOD) δ = 7.24 (s, 1H), 7.15 (s, 1H), 6.58 (s, 1H), 6.21 (d, *J*=3.0, 1H), 6.04 (s, 1H), 4.54 – 4.48 (m, 1H), 4.39 – 4.32 (m, 1H), 4.25 – 4.10 (m, 4H), 3.72 –

3.59 (m, 13H), 3.58 – 3.50 (m, 3H), 3.02 – 2.95 (m, 2H), 2.95 – 2.85 (m, 2H), 2.70 – 2.60 (m, 4H), 2.59 (s, 7H), 2.56 (s, 2H), 2.53 – 2.49 (m, 2H), 2.49 – 2.40 (m, 3H), 2.40 – 2.34 (m, 3H), 2.31 – 2.26 (m, 6H), 2.23 – 2.15 (m, 2H), 2.15 – 2.03 (m, 4H), 2.03 – 2.00 (m, 1H), 1.89 (s, 4H), 1.85 (s, 1H), 1.78 – 1.68 (m, 2H), 1.47 (s, 3H), 1.41 – 1.35 (m, 6H), 1.35 – 1.27 (m, 5H), 1.27 – 1.20 (m, 5H), 1.19 (s, 3H), 1.15 – 1.08 (m, 1H), 0.94 – 0.86 (m, 1H), 0.47 (s, 2H) ppm.

^{13}C NMR (101 MHz, DMSO) δ 179.60, 178.27, 175.15, 173.93, 173.34, 172.89, 171.64, 171.20, 171.12, 165.41, 164.70, 156.25, 145.98, 142.25, 141.30, 136.31, 132.75, 131.39, 129.92, 127.47, 126.70, 125.55, 116.45, 113.92, 111.31, 105.92, 103.08, 93.62, 86.00, 84.42, 79.42, 74.83, 72.61, 70.35, 69.20, 68.86, 63.12, 62.83, 60.26, 58.66, 54.97, 53.12, 50.37, 47.45, 46.79, 44.53, 42.09, 41.83, 40.15, 39.94, 39.10, 38.89, 35.16, 34.49, 33.9, 31.34, 30.44, 29.23, 28.74, 27.22, 25.86, 22.54, 20.18, 19.98, 18.75, 17.37, 16.56, 16.42, 15.69, 15.05, 14.01 ppm.

CNCbl-cys-NBD-X (3)

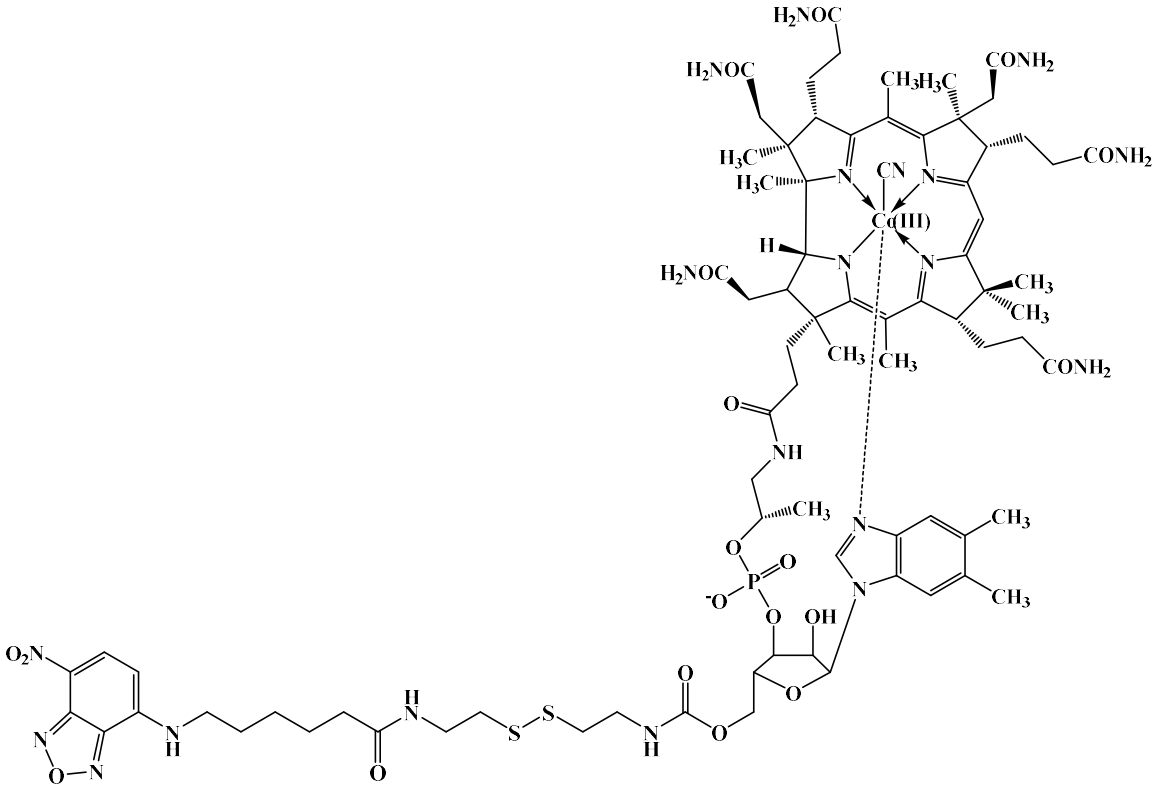

*Figure 16: Structure of **3**.*

Compound **1** (50.3 mg, 32.8 µmol), 1-hydroxybenzotriazole hydrate (HOBt, 14.6 mg, 108 µmol), 1-ethyl-3-(3-dimethylaminopropyl)carbodiimide (EDC, 12.1 mg, 78.3 µmol), 6-(*N*-(7-nitrobenz-2-oxa-1,3-diazol-4-yl)amino)hexanoic acid (NBD-X, 9.63 mg, 32.4 µmol) and Et_3N (11.0 µL, 2 mol eq.) were dissolved in anhydrous DMSO (2 mL) and stirred at 40 °C for 24 h. A further 1.0 equivalent (4.87 mg) of HOBt was added and the product mixture was stirred at 40°C for a further 24 h. The crude product was precipitated by dropwise addition to a solution of Et_2O and CH_2Cl_2 (1:1, 150 mL). The precipitate was washed with Et_2O (2 x 10 mL), released from the filter with CH_3OH and taken to dryness by rotary evaporation. The sample was purified by reversed-phase C18 chromatography. The product eluted as an orange band at 50% CH_3CN in H_2O. 31.9 mg of pure product was obtained, representing a 54% yield, ≥98% purity was established by LC-MS and ^1H NMR spectroscopy. HRMS ESI *m/z* $[M+2Na]^{2+}$ calculated for $C_{80}H_{110}CoN_{20}O_{19}PS_2Na_2$ 927.3280, found 927.3273.

^1H NMR (400 MHz, MeOD) δ = 8.52 (d, *J*=8.8, 1H), 7.24 (s, 1H), 7.15 (s, 1H), 6.58 (s, 1H), 6.36 (d, *J*=8.9, 1H), 6.27 – 6.20 (m, 1H), 6.04 (s, 1H), 4.56 – 4.49 (m, 1H), 4.41 –

4.31 (m, 1H), 4.26 – 4.10 (m, 3H), 3.70 – 3.49 (m, 6H), 3.49 – 3.36 (m, 4H), 3.31 – 3.27 (m, 5H), 2.95 – 2.74 (m, 6H), 2.71 – 2.61 (m, 3H), 2.61 – 2.52 (m, 9H), 2.52 – 2.31 (m, 6H), 2.31 – 2.10 (m, 10H), 2.10 – 1.98 (m, 4H), 1.89 (s, 3H), 1.87 – 1.83 (m, 1H), 1.83 – 1.75 (m, 3H), 1.75 – 1.63 (m, 3H), 1.54 – 1.41 (m, 5H), 1.41 – 1.21 (m, 13H), 1.21 – 1.09 (m, 4H), 0.47 (s, 2H) ppm.

^{13}C NMR (101 MHz, DMSO) δ 179.58, 178.23, 175.13, 173.99, 173.67, 173.27, 172.83, 172.53, 172.33, 171.15, 171.04, 165.38, 164.66, 156.16, 145.36, 144.55, 144.26, 142.21, 137.92, 136.26, 132.66, 131.28, 129.75, 120.23, 116.38, 105.88, 103.04, 99.22, 93.59, 85.98, 84.38, 74.82, 70.13, 69.80, 69.60, 68.90, 60.75, 58.61, 54.86, 53.99, 53.05, 50.33, 48.61, 47.36, 46.61, 44.50, 43.40, 42.06, 41.81, 40.15, 39.94, 39.73, 39.52, 39.31, 39.10, 38.89, 38.00, 37.35, 35.18, 34.04, 31.67, 31.31, 31.00, 29.86, 29.21, 29.02, 27.47, 27.17, 26.04, 25.57, 24.90, 20.02, 19.93, 19.84, 18.72, 16.51, 16.40, 15.68, 15.08, 13.98 ppm.

CNCbl-PEG-NBD-X (4)

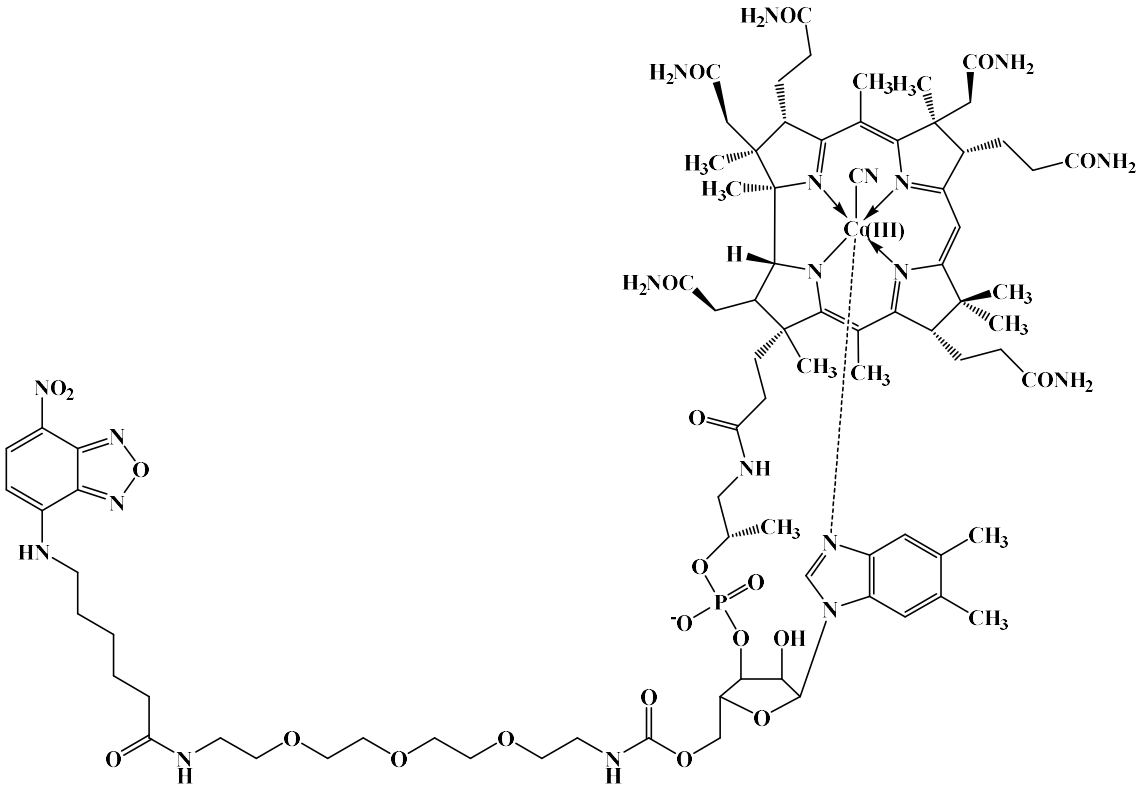

*Figure 17: Structure of **4**.*

Compound **2** (55.3 mg, 31.8 µmol), HOBt (11.1 mg, 63.6 µmol), EDC (6.11 mg, 31.8 µmol), NBD-X (4.68 mg, 15.9 µmol) and Et_3N (8.9 µL) were dissolved in anhydrous DMSO (2 mL) and stirred at 40 °C for 24 h. Excess of compound **2** was found to increase reaction yields. A further 1.0 equivalent (2.20 mg) of HOBt was added and the mixture was stirred at 40°C for a further 24 h. The crude product was precipitated by dropwise addition to a solution of Et_2O and CH_2Cl_2 (1:1, 100 mL). The precipitate was washed with Et_2O (2 x 10 mL), released from the filter with CH_3OH and taken to dryness by rotary evaporation. The compound was purified by reversed-phase C18 chromatography. The product eluted at 50% CH_3CN in H_2O. 26.1 mg of pure product was obtained, representing an 89% yield, ≥95% purity was established by LC-MS and ^{1}H NMR spectroscopy. HRMS ESI *m/z* $[M+2Na]^{2+}$ calculated for $C_{84}H_{118}CoN_{20}O_{22}PNa_2$ 947.3790, found 927.3781.

^{1}H NMR (400 MHz, MeOD) δ = 8.52 (d, *J*=8.9, 1H), 7.24 (s, 1H), 7.15 (s, 1H), 6.58 (s, 1H), 6.36 (d, *J*=8.9, 1H), 6.23 (d, *J*=3.0, 1H), 6.04 (s, 1H), 4.56 – 4.48 (m, 1H), 4.41 – 4.30 (m, 1H), 4.26 – 4.10 (m, 3H), 3.71 – 3.56 (m, 10H), 3.56 – 3.50 (m, 4H), 3.50 – 3.47

(m, 1H), 3.37 – 3.31 (m, 5H), 3.31 – 3.22 (m, 4H), 2.96 – 2.82 (m, 2H), 2.70 – 2.56 (m, 10H), 2.56 – 2.50 (m, 3H), 2.50 – 2.31 (m, 5H), 2.31 – 2.28 (m, 3H), 2.28 – 2.15 (m, 6H), 2.08 (s, 1H), 2.06 – 1.98 (m, 3H), 1.89 (s, 3H), 1.86 – 1.63 (m, 7H), 1.53 – 1.41 (m, 5H), 1.41 – 1.32 (m, 6H), 1.32 – 1.21 (m, 5H), 1.19 (s, 3H), 1.13 – 1.09 (m, 1H), 0.47 (s, 2H) ppm.

^{13}C NMR (101 MHz, DMSO) δ 179.68, 178.36, 175.29, 174.19, 173.80, 173.52, 173.08, 172.71, 172.49, 171.36, 171.22, 165.47, 164.82, 156.32, 145.39, 142.32, 138.16, 136.42, 132.91, 131.52, 129.79, 120.53, 116.54, 106.05, 103.19, 99.31, 93.73, 86.12, 84.51, 74.86, 69.82, 69.65, 69.28, 69.20, 68.88, 58.75, 55.13, 54.15, 53.17, 50.49, 48.74, 47.52, 46.69, 44.68, 43.41, 42.21, 40.43, 40.15, 39.94, 39.73, 39.52, 39.31, 39.10, 38.89, 38.58, 38.20, 35.29, 34.06, 31.76, 31.40, 31.28, 30.11, 29.15, 28.94, 28.80, 28.69, 27.52, 26.14, 25.91, 25.71, 25.24, 25.03, 22.22, 20.04, 19.95, 18.83, 16.61, 16.53, 15.74, 15.16, 14.08 ppm.

CNCbl-cys-sulfo-Cyanine5 (5)

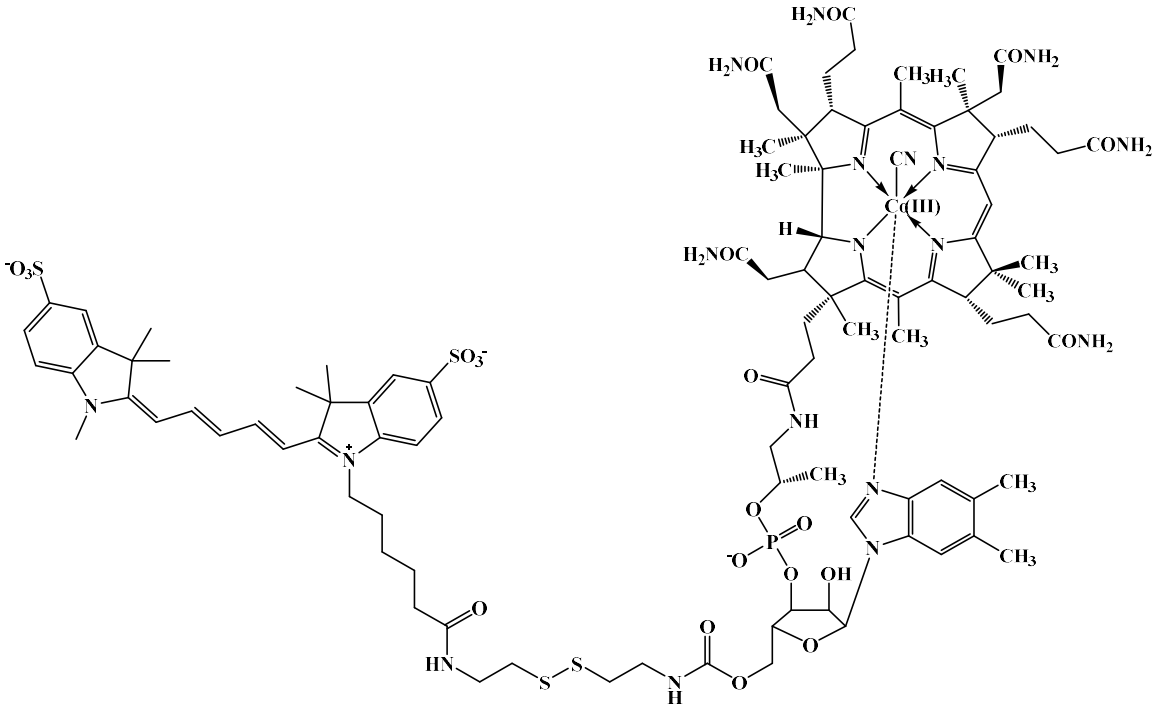

*Figure 18: Structure of **5**.*

Compound **1** (40.7 mg, 26.5 µmol), sulfo-Cyanine5-NHS ester (purchased from Lumiprobe, Cat #43320, 15.6 mg, 20.4 µmol) and Et_2N (5.7 µL) were dissolved in anhydrous DMSO (2 mL) and stirred at 40°C for 24 h. The crude product was precipitated by dropwise addition to a solution of Et_2O and CH_2Cl_2 (1:1, 100 mL). The precipitate was washed with Et_2O (2 x 10 mL), released from the filter with CH_3OH and H_2O (1:1, ~20 mL) and taken to dryness by rotary evaporation. The compound was purified by reversed-phase C18 chromatography. The product eluted as a blue band at 50% CH_3CN in H_2O. 39.8 mg of pure product was obtained, representing a 92% yield, ≥92% purity was established by LC-MS and ^{1}H NMR spectroscopy. HRMS ESI *m/z* $[M+3Na]^{2+}$ calculated for $C_{100}H_{133}CoN_{18}O_{22}PS_4Na_3$ 1112.3740, found 1112.3748.

^{1}H NMR (400 MHz, MeOD) δ = 8.33 – 8.15 (m, 2H), 7.89 (s, 3H), 7.38 – 7.29 (m, 2H), 7.26 (s, 1H), 7.17 – 7.10 (m, 1H), 6.76 – 6.64 (m, 1H), 6.56 (s, 1H), 6.38 – 6.29 (m, 2H), 6.25 (s, 1H), 6.02 (s, 1H), 4.51 – 4.44 (m, 1H), 4.21 (s, 1H), 4.16 – 4.08 (m, 2H), 3.70 – 3.64 (m, 3H), 3.62 – 3.50 (m, 2H), 3.48 – 3.37 (m, 3H), 3.37 – 3.33 (m, 1H), 3.30 (s, 3H), 2.89 – 2.76 (m, 5H), 2.67 (s, 1H), 2.63 – 2.59 (m, 3H), 2.57 (s, 5H), 2.56 – 2.43 (m, 5H), 2.40 – 2.31 (m, 2H), 2.31 – 2.24 (m, 5H), 2.24 – 2.16 (m, 2H), 2.14 – 2.06 (m, 2H), 2.06

– 1.93 (m, 3H), 1.91 – 1.78 (m, 6H), 1.77 – 1.71 (m, 10H), 1.51 – 1.42 (m, 4H), 1.40 – 1.36 (m, 3H), 1.36 – 1.10 (m, 12H), 0.45 (s, 2H) ppm.

^{13}C NMR (101 MHz, DMSO) δ 179.67, 178.30, 175.28, 174.22, 173.85, 173.49, 173.08, 172.95, 172.68, 172.44, 171.33, 171.23, 165.47, 164.80, 156.27, 154.34, 145.06, 144.80, 142.94, 142.30, 140.60, 140.56, 136.37, 132.90, 131.50, 129.78, 126.17, 125.88, 119.91, 116.50, 111.41, 110.29, 106.01, 103.80, 103.50, 103.12, 93.73, 86.12, 84.47, 74.85, 69.89, 69.79, 69.62, 68.87, 63.58, 62.87, 58.71, 55.08, 54.09, 53.16, 50.45, 48.97, 48.93, 48.72, 47.47, 46.65, 44.41, 43.52, 42.16, 41.89, 40.43, 40.15, 39.94, 39.73, 39.52, 39.31, 39.10, 38.89, 38.07, 37.41, 37.29, 35.13, 34.07, 31.76, 31.35, 30.08, 27.23, 27.04, 26.76, 25.96, 25.74, 24.95, 20.03, 19.91, 18.81, 16.58, 16.49, 15.74, 15.15 ppm.

CNCbl-PEG-sulfo-Cyanine5 (6)

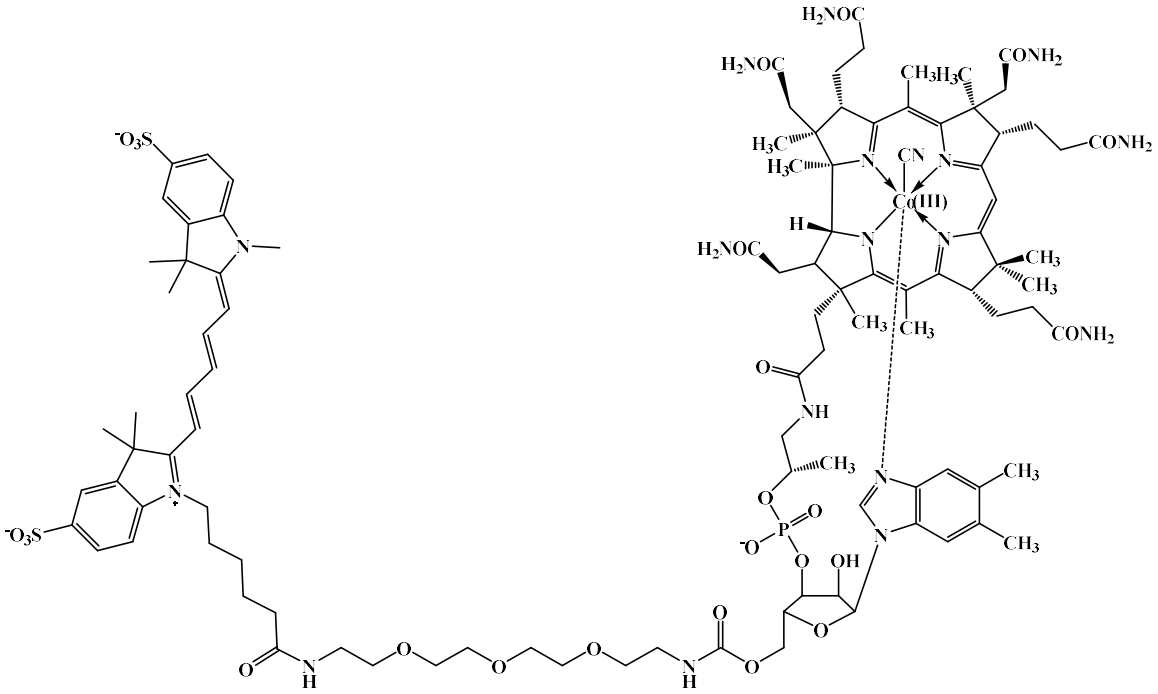

*Figure 19: Structure of **6**.*

Compound **2** (29.1 mg, 18.5 µmol), sulfo-Cyanine5-NHS ester (7.20 mg, 9.26 µmol) and Et_3N (3.0 µL) were dissolved in anhydrous DMSO (1.5 mL) and stirred at 40°C for 24 h. The crude product was precipitated by dropwise addition to a solution of Et_2O and CH_2Cl_2 (1:1, 100 mL). The precipitate was washed with Et_2O (2 x 10 mL), released from the filter with CH_3OH and H_2O (1:1, ~20 mL) and taken to dryness by rotary evaporation. The compound was purified by reversed-phase C18 chromatography. The product eluted as a blue band at 50% CH_3CN in H_2O. 18.1 mg of pure product was obtained, representing an 89% yield, ≥94% purity was established by LC-MS and ^1H NMR spectroscopy. HRMS ESI *m/z* $[M+3Na]^{2+}$ calculated for $C_{104}H_{141}CoN_{18}O_{25}PS_2Na_3$ 1132.4250, found 1132.4265.

^1H NMR (400 MHz, MeOD) δ = 8.35 – 8.17 (m, 2H), 7.93 – 7.80 (m, 3H), 7.36 – 7.29 (m, 2H), 7.24 (s, 1H), 7.14 (s, 1H), 6.75 – 6.62 (m, 1H), 6.58 (s, 1H), 6.39 – 6.27 (m, 2H), 6.23 (s, 1H), 6.03 (s, 1H), 4.26 – 4.15 (m, 2H), 4.15 – 4.08 (m, 2H), 3.65 (s, 3H), 3.61 – 3.52 (m, 8H), 3.52 – 3.48 (m, 2H), 3.37 – 3.31 (m, 5H), 3.31 – 3.27 (m, 7H), 2.93 – 2.83 (m, 2H), 2.66 – 2.59 (m, 2H), 2.59 – 2.50 (m, 9H), 2.50 – 2.35 (m, 3H), 2.31 – 2.18 (m, 7H), 2.18 – 2.05 (m, 3H), 2.05 – 1.93 (m, 3H), 1.78 – 1.72 (m, 10H), 1.53 – 1.41 (m, 4H),

1.37 (s, 2H), 1.36 – 1.30 (m, 2H), 1.29 (s, 3H), 1.27 – 1.21 (m, 3H), 1.18 (s, 2H), 0.46 (s, 2H) ppm.

^{13}C NMR (101 MHz, DMSO) δ 179.57, 178.23, 173.99, 173.70, 173.27, 172.91, 172.84, 172.53, 172.11, 171.15, 165.40, 156.12, 154.24, 145.27, 145.10, 142.77, 142.07, 140.51, 140.44, 136.28, 132.75, 131.38, 129.68, 126.10, 119.85, 110.11, 105.89, 103.05, 84.38, 74.83, 69.72, 69.56, 69.13, 58.67, 50.36, 48.88, 48.63, 47.41, 46.57, 40.15, 39.94, 39.73, 39.52, 39.31, 39.10, 38.89, 38.44, 35.04, 31.66, 31.24, 29.06, 28.75, 28.60, 27.13, 26.95, 26.59, 25.71, 25.13, 24.90, 22.12, 19.95, 19.86, 18.73, 16.55, 16.41, 15.66, 15.01, 13.99 ppm.

CNCbl-cys-Cyanine7 (7)

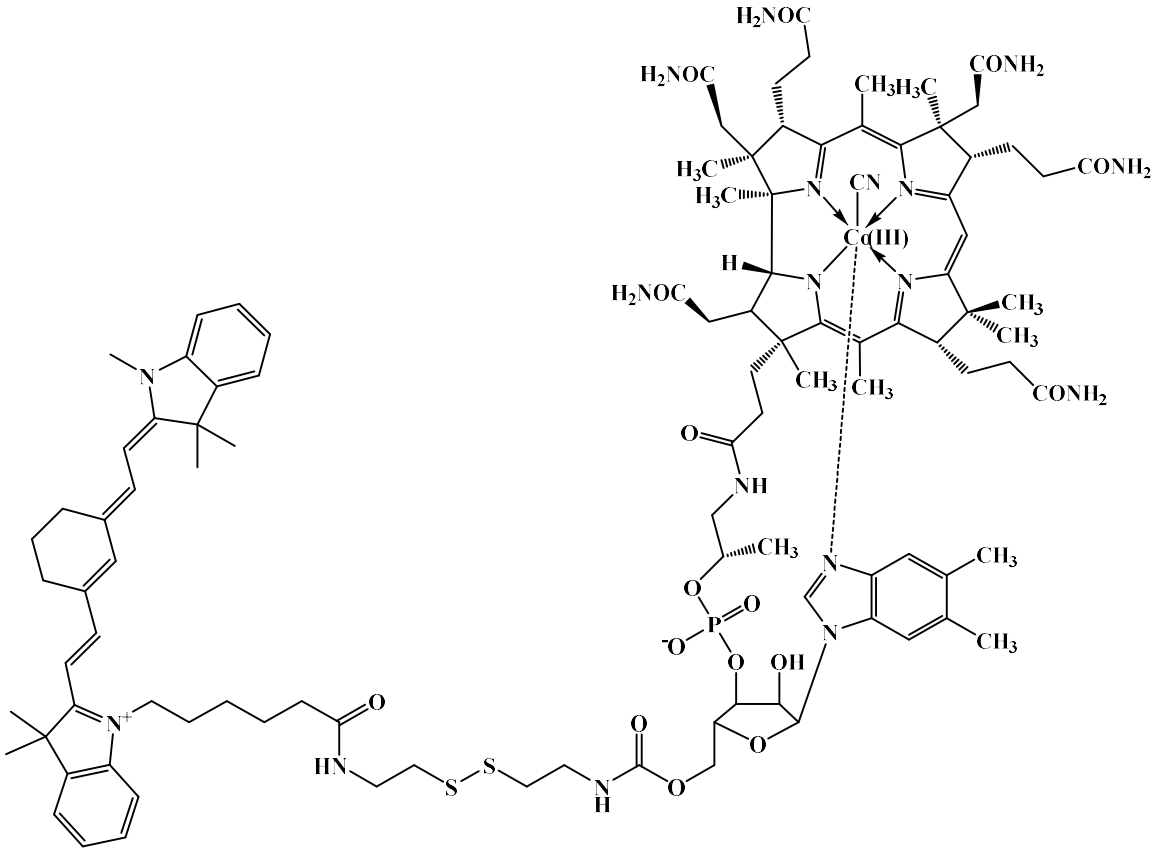

Figure 20: Structure of 7.

Compound **1** (40.7 mg, 26.5 µmol), Cyanine7-NHS ester (purchased from Lumiprobe, Cat #45020, 15.5 mg, 20.4 µmol) and Et_3N (5.7 µL) were dissolved in anhydrous DMSO (1.5 mL) and stirred at 40°C for 24 h. The crude product was precipitated by dropwise addition to a solution of Et_2O and CH_2Cl_2 (1:1, 100 mL). The precipitate was washed with Et_2O (2 x 10 mL), released from the filter with CH_3OH and taken to dryness by rotary evaporation. The compound was purified by reversed-phase C18 chromatography. The product eluted as an indigo band at 60% CH_3CN in (H_2O with 0.1% HCOOH). 26.2 mg of pure product was obtained, representing a 60% yield, ≥95% purity was established by LC-MS and ^1H NMR spectroscopy. HRMS ESI *m/z* $[M+Na]^{2+}$ calculated for $C_{105}H_{141}CoN_{18}O_{16}PS_2Na$ 1043.4590, found 1043.4623.

^1H NMR (400 MHz, MeOD) δ = 7.81 – 7.70 (m, 2H), 7.49 – 7.44 (m, 2H), 7.44 – 7.35 (m, 2H), 7.30 – 7.19 (m, 3H), 7.14 (s, 1H), 6.57 (s, 1H), 6.24 – 6.13 (m, 2H), 6.03 (s, 1H), 4.54 – 4.47 (m, 1H), 4.22 – 4.18 (m, 1H), 4.17 – 4.07 (m, 3H), 3.66 – 3.62 (m, 1H), 3.62 – 3.59 (m, 3H), 3.47 – 3.39 (m, 3H), 2.90 – 2.86 (m, 1H), 2.84 – 2.72 (m, 4H), 2.60 –

2.56 (m, 9H), 2.55 – 2.43 (m, 5H), 2.40 – 2.34 (m, 2H), 2.31 – 2.26 (m, 5H), 2.26 – 2.15 (m, 4H), 2.10 – 2.02 (m, 3H), 1.90 – 1.82 (m, 6H), 1.73 – 1.68 (m, 9H), 1.46 (s, 4H), 1.42 – 1.21 (m, 17H), 1.20 – 1.16 (m, 3H), 1.15 – 1.10 (m, 1H), 0.47 (s, 2H) ppm.

^{13}C NMR (101 MHz, DMSO) δ 179.55, 178.23, 175.11, 173.95, 173.67, 173.24, 172.81, 172.52, 172.15, 171.13, 171.00, 165.37, 164.64, 156.16, 142.95, 142.24, 140.85, 136.25, 132.65, 131.82, 131.28, 129.75, 128.39, 127.67, 124.39, 122.37, 122.27, 122.00, 110.85, 105.87, 103.03, 85.98, 84.37, 74.80, 69.80, 58.61, 54.89, 53.01, 50.32, 48.56, 47.35, 46.58, 43.32, 40.15, 39.94, 39.73, 39.52, 39.31, 39.10, 38.89, 38.02, 37.23, 35.11, 35.03, 34.04, 31.65, 31.08, 29.87, 29.04, 27.21, 27.04, 26.58, 25.77, 25.56, 24.87, 24.18, 23.40, 22.11, 21.13, 20.02, 19.93, 19.84, 18.71, 16.51, 16.39, 15.66, 15.06 ppm.

CNCbl-PEG-Cyanine7 (8)

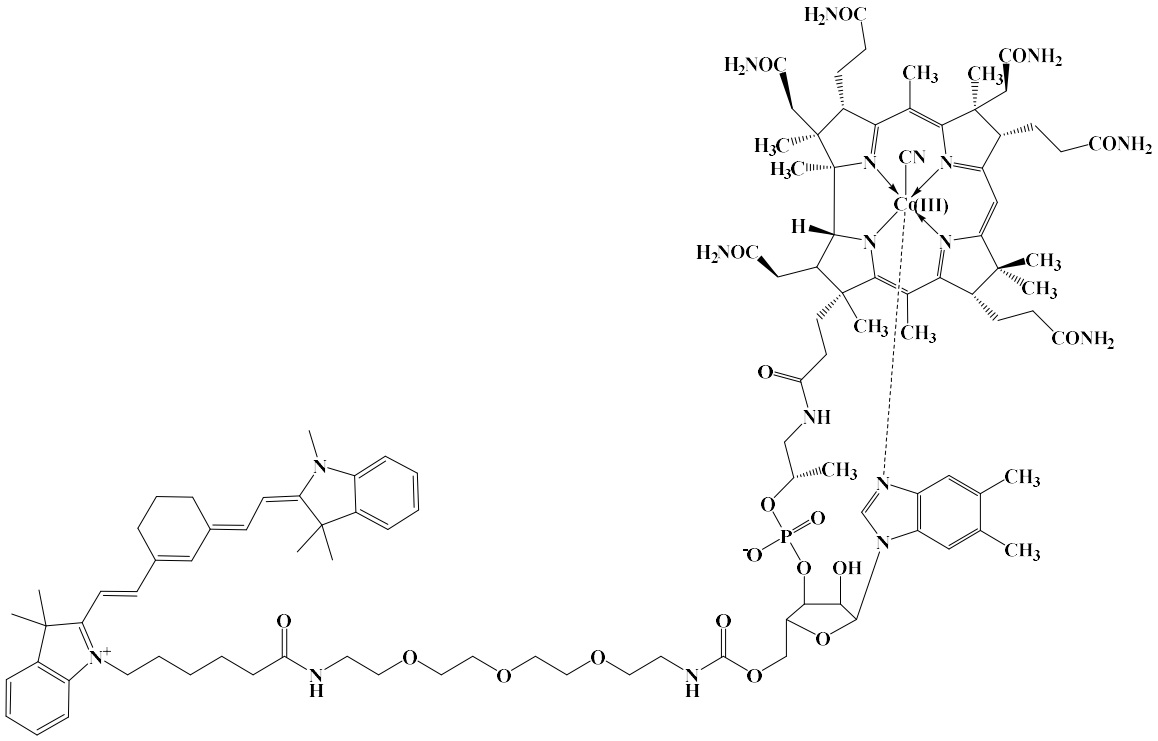

*Figure 21: Structure of **8**.*

Compound **2** (24.3 mg, 15.5 µmol), Cyanine7-NHS ester (5.01 mg, 6.82 µmol) and Et_3N (2.0 µL) were dissolved in anhydrous DMSO (1.5 mL) and stirred at 40°C for 24 h. The crude product was precipitated by dropwise addition to a solution of Et_2O and CH_2Cl_2 (1:1, 100 mL). The precipitate was washed with Et_2O (2 x 10 mL), released from the filter with CH_3OH and taken to dryness by rotary evaporation. The compound was purified by reversed-phase C18 chromatography. The product eluted as an indigo band at 60% CH_3CN in (H_2O + 0.1% HCOOH). 12.3 mg of pure product was obtained, representing an 86% yield, ≥91% purity was established by LC-MS and ^1H NMR spectroscopy. HRMS ESI *m/z* $[M+Na]^{2+}$ calculated for $C_{109}H_{149}CoN_{18}O_{19}PNa$ 1063.5100, found 1063.5149.

^1H NMR (400 MHz, MeOD) δ = 7.80 – 7.68 (m, 2H), 7.50 – 7.45 (m, 2H), 7.45 – 7.35 (m, 2H), 7.30 – 7.18 (m, 4H), 6.24 – 6.13 (m, 2H), 6.03 (s, 1H), 4.74 – 4.44 (m, 1H), 4.41 – 4.31 (m, 1H), 4.32 – 4.07 (m, 6H), 4.04 – 3.89 (m, 1H), 3.65 – 3.57 (m, 10H), 3.57 – 3.46 (m, 4H), 3.35 (s, 3H), 3.32 – 3.23 (m, 8H), 2.95 – 2.84 (m, 2H), 2.64 – 2.61 (m, 2H), 2.61 – 2.46 (m, 12H), 2.46 – 2.33 (m, 3H), 2.33 – 2.10 (m, 10H), 2.10 – 2.00 (m, 4H), 2.00 – 1.90 (m, 3H), 1.88 (s, 3H), 1.87 – 1.78 (m, 3H), 1.78 – 1.64 (m, 13H), 1.64 – 1.55

(m, 3H), 1.48 – 1.44 (m, 4H), 1.43 – 1.35 (m, 10H), 1.35 – 1.31 (m, 8H), 1.31 – 1.27 (m, 13H), 1.27 – 1.20 (m, 6H), 1.20 – 1.10 (m, 5H), 1.02 – 0.94 (m, 2H), 0.94 – 0.83 (m, 6H), 0.47 (s, 2H) ppm.

^{13}C NMR (101 MHz, DMSO) δ 179.58, 178.26, 175.15, 173.99, 173.69, 173.28, 172.84, 172.55, 172.09, 171.44, 171.16, 171.01, 170.52, 165.39, 164.66, 156.21, 147.78, 144.59, 142.96, 142.26, 140.86, 137.15, 136.28, 132.69, 131.95, 131.31, 129.77, 129.53, 128.41, 127.69, 127.03, 126.70, 124.54, 124.40, 122.29, 116.44, 110.86, 105.88, 103.08, 100.15, 99.68, 93.60, 85.96, 84.39, 74.79, 72.86, 69.81, 69.73, 69.57, 69.14, 63.36, 58.62, 54.92, 54.02, 53.04, 50.34, 48.58, 48.15, 47.39, 46.58, 44.85, 44.60, 43.19, 40.15, 39.94, 39.73, 39.52, 39.31, 39.10, 38.89, 38.44, 35.14, 35.03, 34.04, 31.68, 31.32, 31.10, 30.73, 29.94, 29.05, 28.85, 28.72, 27.79, 27.22, 27.05, 26.58, 25.80, 24.91, 24.19, 24.12, 23.43, 22.42, 22.12, 21.13, 19.94, 19.88, 18.73, 16.51, 16.42, 15.67, 15.07, 13.99, 10.94 ppm.

2.3 Results and Discussion

2.3.1 Synthesis of 1 and 2

The synthesis of CNCbl linker molecules in this research was optimised in previous unpublished work in which an adipic acid dihydrazide linker was attached at the 5'-OH location. The optimal conditions were found to be 1:3:3 mol ratios of CNCbl: CDT: linker, initially reacting CNCbl and CDT for 30 min followed by linker addition, anhydrous reaction conditions (anhydrous DMSO under N_2) and allowing the reaction to proceed at 40°C for 6 h with stirring.[14,15]

Compound 1

The use of cystamine as a linker, primarily for selective drug delivery[16–18], is not novel but not yet widely used. The rationale for the inclusion of a disulfide-containing linker that has been used here is that the disulfide would be cleaved in the reductive cytosolic compartments to release the cargo.[19] This may be a desirable aspect of the CNCbl conjugates if the concept was extended to deliver bioactive agents where the bioactive is inactive when bound to CNCbl. Subsequent delivery of the CNCbl conjugate into the cytoplasm of the cell would result in reductive S-S bond cleavage, freeing the attached cargo [drug/molecule] and promoting activity. This concept has been used in the literature with a focus on CNCbl-based delivery of bioactives.[20,21]

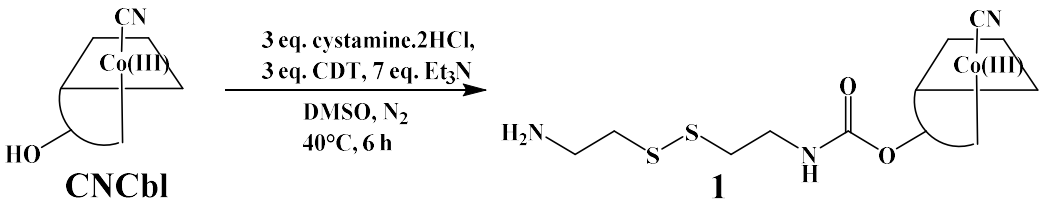

*Scheme 2: Synthetic scheme for the synthesis of **1**.*

The synthetic procedure for **1** maintained the 1:3:3 mol ratios of CNCbl: CDT: linker, with the inclusion of the sterically hindered base triethylamine (Et_3N) (Scheme 2). The 5'-OH residue of CNCbl was activated by 1,1-carbonylditriazole (CDT) in excess (3 mol equivalents) for 30 min. This was then followed by the addition of cystamine and Et_3N and the reaction mixture was left to stir at 40°C for 6 h. Et_3N was used to neutralise the dihydrochloride salt form of cystamine *in situ*. The crude product mixture was analysed by LC-MS and three peaks were observed (Figure 22). Two overlapping peaks eluting at

14.3 and 14.5 min were from the desired product ($C_{68}H_{98}CoN_{16}O_{15}PS_2$, calcd. *m/z* $[M+H]^+$ =1533.7 and $[M+2H]^{2+}$ = 767.3; found 1534.3 and 767.4). The final peak eluting at 16.0 min was the CNCbl starting material ($C_{63}H_{88}CoN_{14}O_{14}P$, calcd. *m/z* $[M+H]^+$ =1355.6 and $[M+2H]^{2+}$ = 678.3; found 1355.5 and 678.4). One small peak was also observed at 20.1 min with *m/z* values of 729.7, 972.4 and 1457.9. Further investigation identified this to be a CNCbl-cystamine-CNCbl dimer ($C_{132}H_{184}Co_2N_{30}O_{30}P_2S_2$, calcd. *m/z* $[M+H]^+$ = 2915.1, $[M+2H]^{2+}$ = 1458.1, $[M+3H]^{3+}$ = 972.4 and $[M+4H]^{4+}$ = 729.5, Figure 23). A CNCbl-linker-CNCbl dimer has been observed in the literature where the linker employed contained two terminal amines.[22] Conjugation at the ribose ring of CNCbl using CDT can occur at two possible locations, the 5'-OH or 2'-OH sites.[23] Formation of a carbamate bond to the ribose ring occurs more readily at the 5'-OH site due to reduced steric hindrance of the primary 5'-OH versus the secondary 2'-OH. The observation of the two overlapping peaks at 14 min suggests two possibilities; the formation of two CNCbl-linker isomers (5' and 2') or peak fronting during LC-MS analysis. This is a rare occurrence in chromatography and can be difficult to diagnose but is often related to sample overloading, uneven silica bed packing within the column itself and/or dead volume post-injection.[24,25]

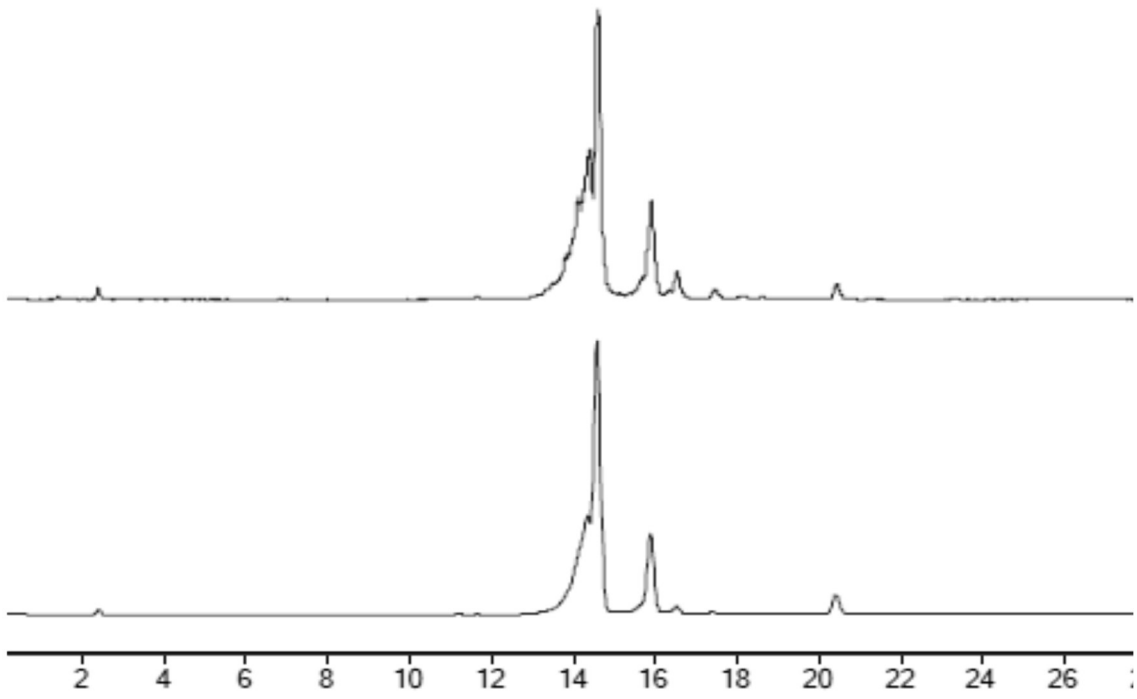

*Figure 22: LC-MS total ion count (TIC, top) and diode array detector (DAD, 361 nm, bottom) chromatograms of crude **1** (LC-MS method 1). Peaks at 14.3 and 14.5 min can be assigned to **1** (*$C_{68}H_{98}CoN_{16}O_{15}PS_2$*, m/z* $[M+H]^+$ *=1534.3 and* $[M+2H]^{2+}$*). Peaks at 22.2 and 32.3 min can be assigned to unreacted CNCbl and CNCbl-cys-CNCbl dimer, respectively.*

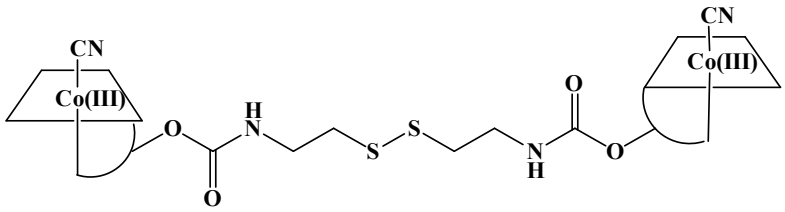

*Figure 23: Structure of the CNCbl-cystamine-CNCbl dimer formed during the synthesis of **1**.*

The crude solid obtained from this reaction was typically used as is without purification for the next step of the synthesis. Desalting, however, was carried out to remove any remaining CDT and free cystamine to prevent interference with subsequent reactions. Full purification of **1** was also carried out by reversed-phase C18 column chromatography and a final yield of 80% was obtained. The purity was confirmed by LC-MS where one peak was identified with the expected mass values ($C_{68}H_{98}CoN_{16}O_{15}PS_2$, calcd. *m/z* $[M+H]^+$ =1533.7 and $[M+2H]^{2+}$ =767.3; found 1534.3 and 767.4, Figure 24). Both the total ion count (TIC) and diode array detector (DAD, 361 nm) chromatograms were used

for the analysis of the purity of all conjugates. It was often observed that the two chromatograms showed slight differences. The DAD chromatogram at 361 nm is commonly used for the detection of CNCbl and CNCbl analogues by LC-MS owing to the large absorbance bands of the corrin ring at this wavelength.[1,26] The percent conversion of CNCbl to CNCbl derivatives in this work is determined on the assumption that the products and CNCbl retain the same molar absorptivity at 361 nm. In Figure 24, the DAD chromatogram shows one large peak eluting at 14.5 min representing **1**. The peak areas were used to establish the purity of the final product as ≥95%.

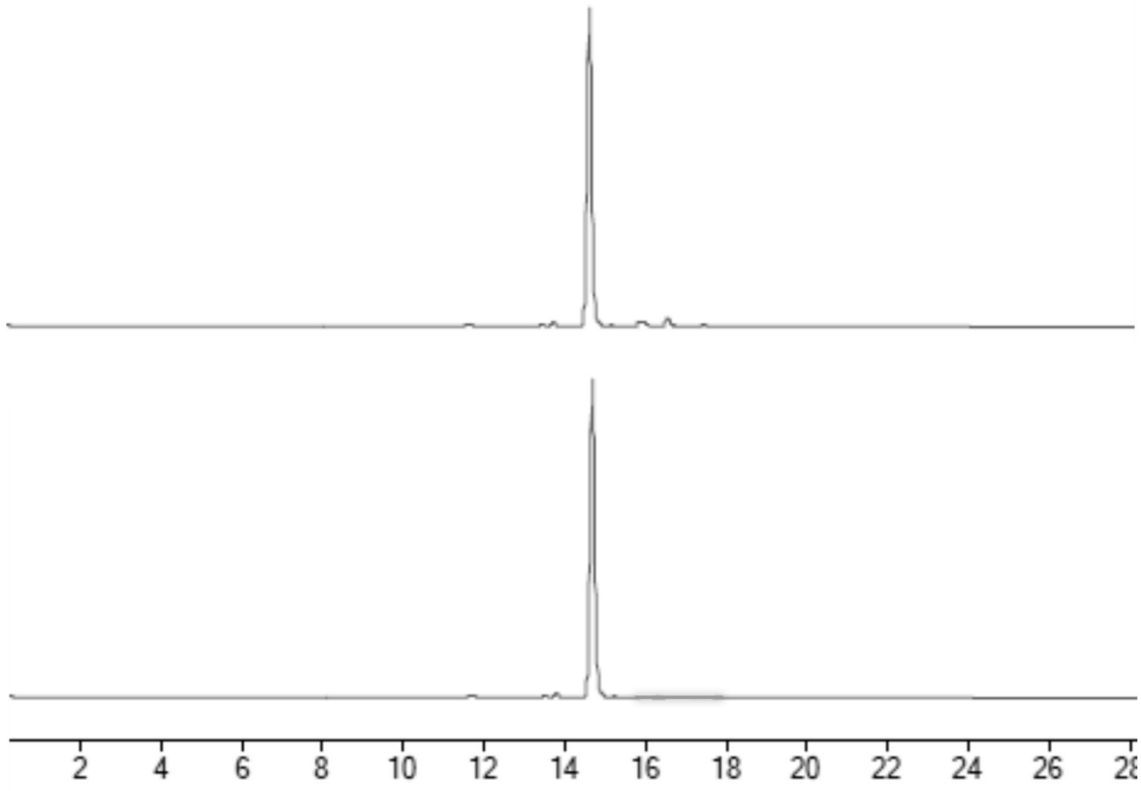

*Figure 24: LC-MS TIC (top) and DAD (361 nm, bottom) chromatograms of **1** after purification (LC-MS method 1). The peak at 14.5 min can be assigned to **1** (*$C_{68}H_{98}CoN_{16}O_{15}PS_2$*, m/z $[M+H]^+$ =1534.3 and $[M+2H]^{2+}$=767.3; found 1534.3 and 767.4).*

^{1}H NMR spectroscopic analysis was undertaken to characterise the five diagnostic peaks resonating in the aromatic region for CNCbl derivatives, namely the C10, R1, B4, B2 and B7 protons (Figure 25).[27,28] These residues have chemical shifts at 5.91, 6.28, 6.45, 7.01 and 7.32 ppm, respectively, in DMSO-d_6 with the corresponding carbon resonances observed at 85.39, 93.40, 116.23, 142.34 and 111.35 ppm, respectively.[23]

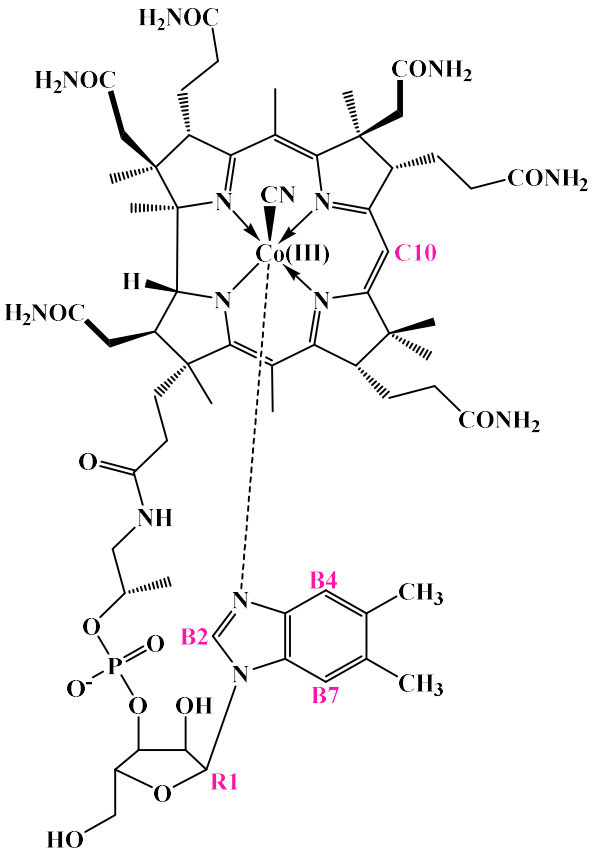

Figure 25: Structure of CNCbl with the protons resonating in the aromatic region highlighted (C10, R1, B4, B2 and B7).

Upon conjugation of a linker to form **1**, the proton and corresponding carbon resonances (determined by HSQC analysis obtained in DMSO-d_6) remain largely unchanged (C10, 5.89, 84.43; R1, 6.24, 93.65; B4, 6.43, 116.40; B2, 7.18, 142.19 and B7, 7.37 ppm, 111.33 ppm). There is, however, one key change that supports the formation of **1** – a new carbon signal is present in **1** at 156.62 ppm, consistent with literature values for the carbon atom of a carbamate bond formed at the 5'-OH location of CNCbl (CNCbl-$(CH_2)_6$-N_3[23] (Figure 26). Furthermore, HSQC NMR analysis confirmed that the carbon at 156.34 ppm was not directly bonded to a proton, as is expected for the carbamate residue.

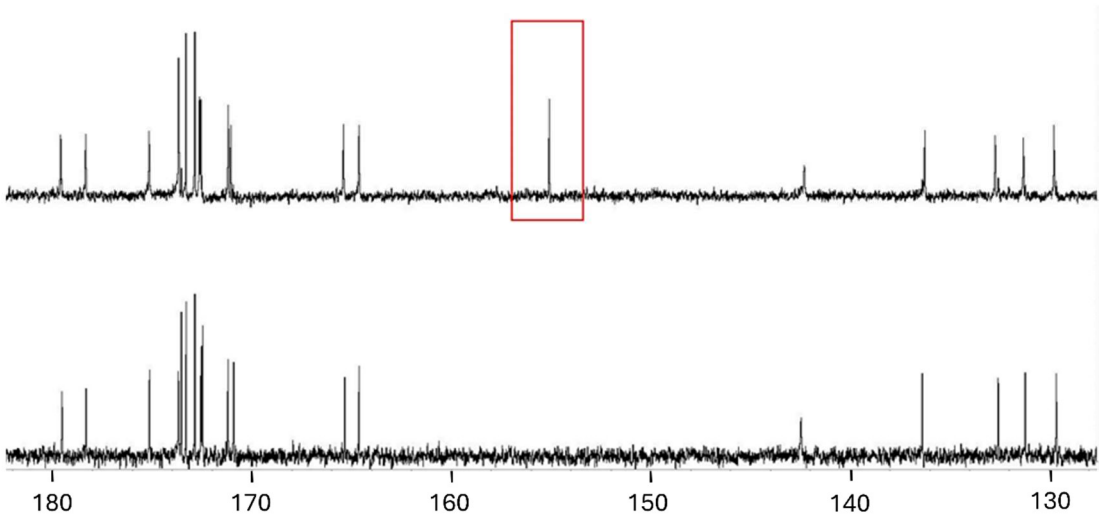

*Figure 26: ^{13}C NMR spectra of CNCbl (bottom) and **1** (top), highlighting the newly formed carbamate resonating at 156.34 ppm in DMSO-d_6.*

Further NMR analysis was carried out in MeOH-d_4. Obtaining an NMR in MeOH-d_4 is particularly useful to determine the purity of CNCbl complexes.[23,29–31] This is because of the extreme complexity of the low-field region in the ^{1}H NMR spectra of CNCbl and the corresponding CNCbl conjugates. CNCbl itself has 19 protons that resonate in the aromatic region of the ^{1}H NMR spectrum in aprotic DMSO-d_6 and five protons in protic solvents (i.e. MeOH-d_4). This is due to the amide protons of the corrin ring exchanging with deuterium in protic NMR solvents. In total, CNCbl has 88 protons and some of the CNCbl conjugates synthesised in this thesis have greater than 100 individual proton peaks in the low-field region of the ^{1}H NMR spectrum. To provide meaningful insight into the chemical structure of the conjugates, the resonances in the aromatic region are a more helpful diagnostic probe. However, the use of MeOH-d_4 as a solvent is only suitable for ^{1}H and COSY spectra due to limited solubility (~6 mg per 500 µL). CNCbl and the synthesised conjugates have a higher solubility in DMSO (~20 mg in 500 µL), which is necessary to obtain a ^{13}C NMR spectrum with a good signal-to-noise ratio.

The ^{1}H NMR spectrum in MeOH-d_4 shows five resonances for **1** in the aromatic region, at 6.05 (1H, C10), 6.23 (1H, R1), 6.58 (1H, B4), 7.16 (1H, B2) and 7.25 (1H, B7) ppm. When compared to the ^{1}H NMR spectrum of the CNCbl starting material, shifts in the proton resonances are observed, particularly for the R1 proton (6.27 in CNCbl and 6.23 ppm in **1**), which is located close to the conjugation site (Figure 27). Additionally, new

peaks are present at 2.96 and 3.27 ppm, likely due to the CH_2 residues of the cystamine linker. Cystamine.2HCl has two multiplets in the ^{1}H NMR spectrum at 3.04-3.01 and 3.29-3.32 ppm.

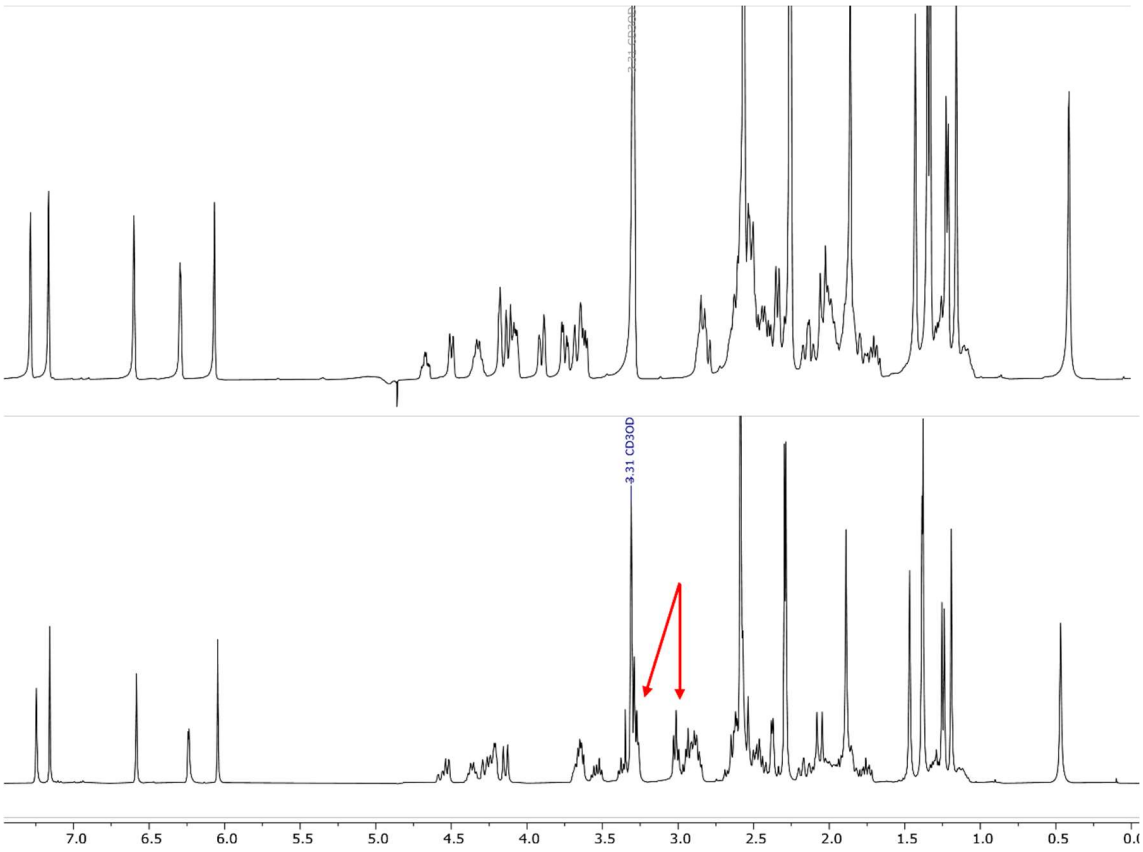

*Figure 27: ^{1}H NMR spectra of CNCbl (top) and **1** (bottom) obtained in MeOH-d_4. The peaks of **1** at 6.05 (1H), 6.23 (1H), 6.58 (1H), 7.16 (1H) and 7.25 (1H) ppm can be assigned to protons C10, R1, B4, B4, and B7. Peaks for **1** at 2.99 and 3.27 ppm corresponding to the CH_2 peaks of cystamine linker are highlighted.*

The synthesis of **1** was achieved in high yields (80%) following purification. Analysis by ^{1}H NMR spectroscopy and LC-MS indicate a purity of **1** of ≥95%.

Compound 2.

The second linker molecule utilised in this research was a short polyethylene glycol (PEG) chain, namely 1,11-diamine-3,6,9-trioxaundecane. This linker is commonly employed in biological applications, providing suitable functionalisation sites and/or improving water solubility.[32] Most commonly, PEG is utilised in polymer-based drug delivery where a prodrug-linker-PEG model is employed. Attachment of PEG, referred to as PEGylation, was first used by Davies and Abuchowski (1977) where PEG units of

varying lengths (1900-5000 daltons) were covalently linked to bovine serum albumin.[33] Specific to this study, PEG is known to be stable under biological conditions.[19,19,34] The successful use of polyethylene glycol as a linker for CNCbl functionalisation has been demonstrated previously.[19] The synthesis of **2** was achieved as shown in Scheme 3. The 5'-OH residue of CNCbl was activated with 3 mol equivalents of CDT for 30 min at 40°C followed by the addition of 3 mol equivalents of 1,11-diamine-3,6,9-trioxaundecane.

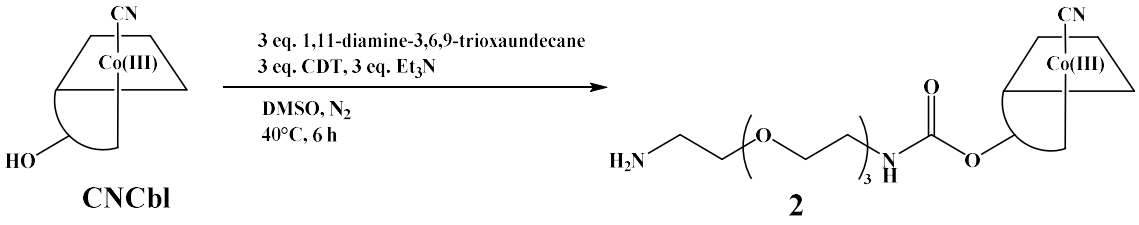

*Scheme 3: Synthetic scheme for the synthesis of **2**.*

Formation of the desired product was shown by LC-MS where two peaks were observed (Figure 28). The major peak eluting at 14.5 min represents the desired product ($C_{72}H_{106}CoN_{16}O_{18}P$, calcd. *m/z* $[M+H]^+$ = 1573.7 and $[M+2H]^{2+}$ = 787.4; found 1573.6 and 787.5 at 14.4 min). The peak at 14.3 min also represents **2**. The appearance of two peaks for the CNCbl-linker complex was observed previously during the synthesis of **1**. The two peaks may represent the formation of two isomers (functionalisation at either the 5'-OH or 2'-OH) or peak fronting during LC-MS analysis. The peaks retained at 15.9 and 18.2 min are from the CNCbl starting material ($C_{63}H_{88}CoN_{14}O_{14}P$, calcd. *m/z* $[M+H]^+$ =1355.6 and $[M+2H]^{2+}$ = 678.3; found 1355.5 and 678.4) and a CNCbl-PEG-CNCbl dimer ($C_{136}H_{192}Co_2N_{30}O_{33}P_2$, calcd. *m/z* = $[M+H]^+$ = 2955.3, $[M+2H]^{2+}$ = 1478.1, $[M+3H]^{3+}$ = 985.8 and $[M+4H]^{4+}$ = 739.6; found 1478.7, 985.8, 739.9). To ensure peak overloading was not the cause of split peaks observed for **1** and **2**, the injection volume of each sample into the LC-MS was reduced from 10 µL to 5 µL for all further analysis.

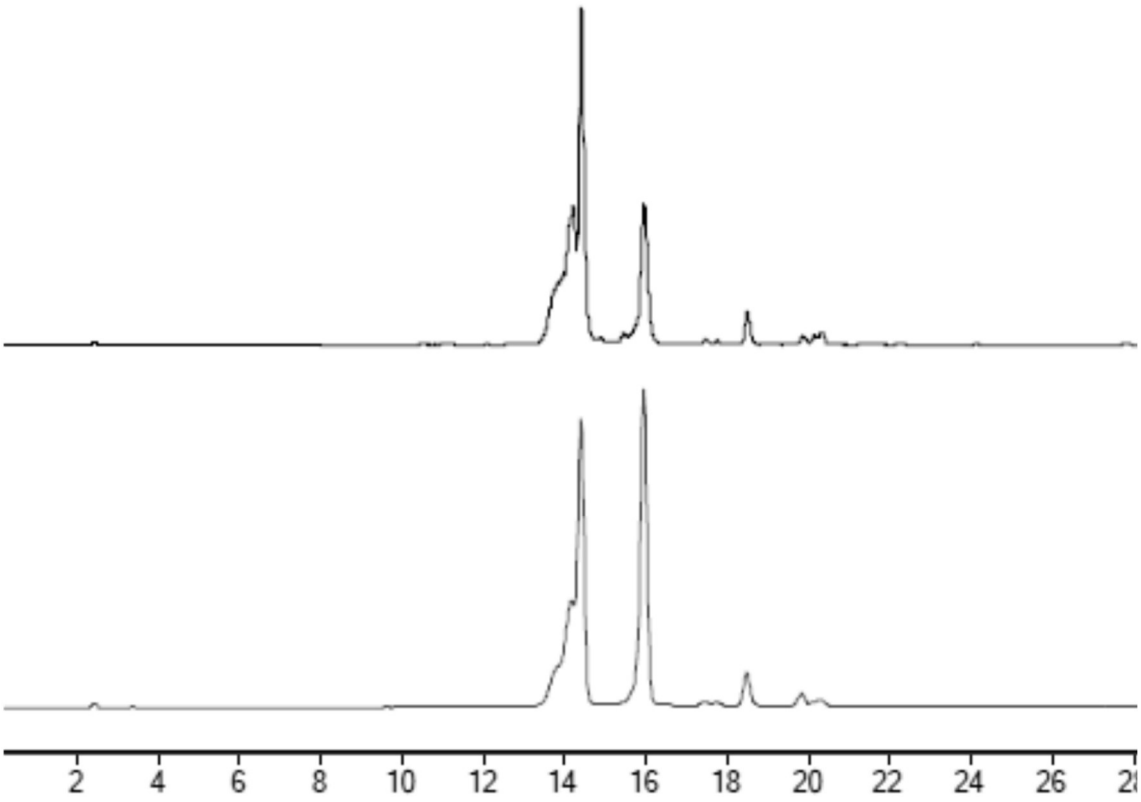

*Figure 28: LC-MS TIC (top) and DAD (361 nm, bottom) chromatograms of crude **2** (LC-MS method 1). The peaks at 14.1 and 14.4 min can be assigned to **2** ($C_{72}H_{106}CoN_{16}O_{18}P$, calcd. m/z $[M+H]^+$ = 1573.7 and $[M+2H]^{2+}$ = 787.4; found 1573.6 and 787.5). The peaks at 21.6 and 22.3 min can be assigned to CNCbl ($C_{63}H_{88}CoN_{14}O_{14}P$, calcd. m/z $[M+H]^+$ = 1355.6 and $[M+2H]^{2+}$ = 678.3; found 1355.5 and 678.4).*

The crude solid obtained after this reaction was further functionalised without purification. Desalting was carried out to remove any remaining CDT and linker. Purification of **2** was also carried out by reversed-phase C18 column chromatography where a final yield of 79% was obtained. The purity was confirmed by LC-MS where a single peak was observed ($C_{72}H_{106}CoN_{16}O_{18}P$, calcd. *m/z* $[M+H]^+$ = 1573.7 and $[M+2H]^{2+}$ = 787.4; found 1575.7 and 787.5 at 14.3 min, Figure 29). A small impurity peak in addition to the product was identified in the LC-MS of one collected fraction, eluting at 19.8 min (Figure 28). Analysis of the associated *m/z* values for this peak are consistent with a CNCbl-PEG-CNCbl dimer ($C_{136}H_{192}Co_2N_{30}O_{33}P_2$, calcd. *m/z* = $[M+H]^+$ = 2955.3, $[M+2H]^{2+}$ = 1478.1, $[M+3H]^{3+}$ = 985.8 and $[M+4H]^{4+}$ = 739.6; found 1478.7, 985.8, 739.9, Figure 30). As this dimer formed to such a small extent, no attempt was made to prevent this from occurring, such as protecting one amine of the linker.

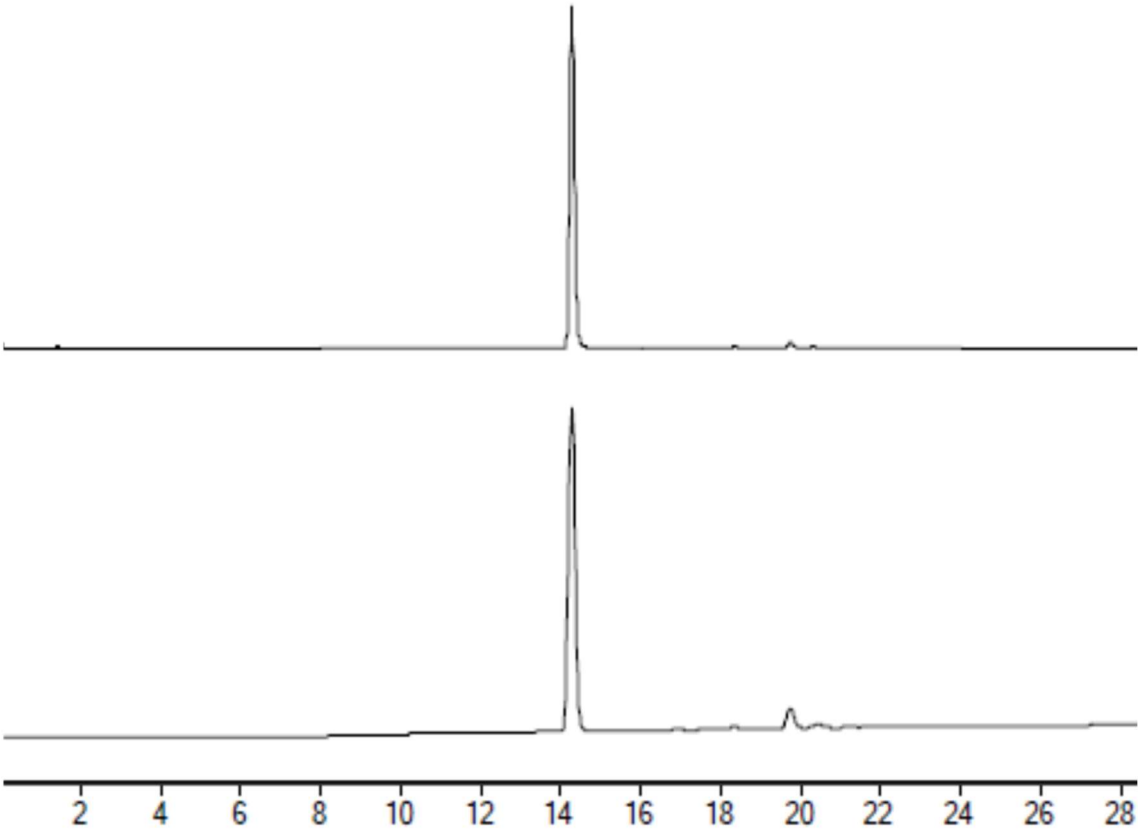

*Figure 29: LC-MS TIC (top) and DAD (361 nm, bottom) chromatogram of **2** after purification. The peak at 14.4 min can be assigned to **2** ($C_{72}H_{106}CoN_{16}O_{18}P$, calcd. m/z $[M+H]^+$ = 1573.7 and $[M+2H]^{2+}$ = 787.4; found 1573.6 and 787.5).*

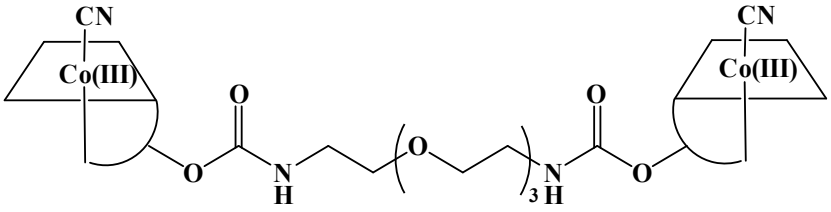

*Figure 30: Structure of the CNCbl-PEG-CNCbl dimer formed during the synthesis of **2**.*

^{1}H and ^{13}C NMR spectroscopic analysis were carried out in DMSO-d_6. The proton and corresponding carbon resonances of **2** remain largely unchanged (5.90 (86.01), C10; 6.23 (93.63), R1; 6.43 (116.45), B4; 7.07 (142.2), B2 and 7.30 ppm (111.31 ppm), B7) upon conjugation of the linker when compared to CNCbl (5.89 (84.43), C10; 6.24 (93.65), R1; 6.43 (116.40) B4; 7.18 (142.19) B2 and 7.37 ppm (111.33 ppm), B7). The presence of a new carbon signal at 156.62 ppm is consistent with literature values for the carbon atom of a carbamate bond formed at the 5'-OH location of CNCbl (Figure 31).[23] Furthermore,

HSQC NMR analysis confirmed that the carbon resonance at 156.25 ppm had no corresponding proton signals, as is expected for a carbamate.

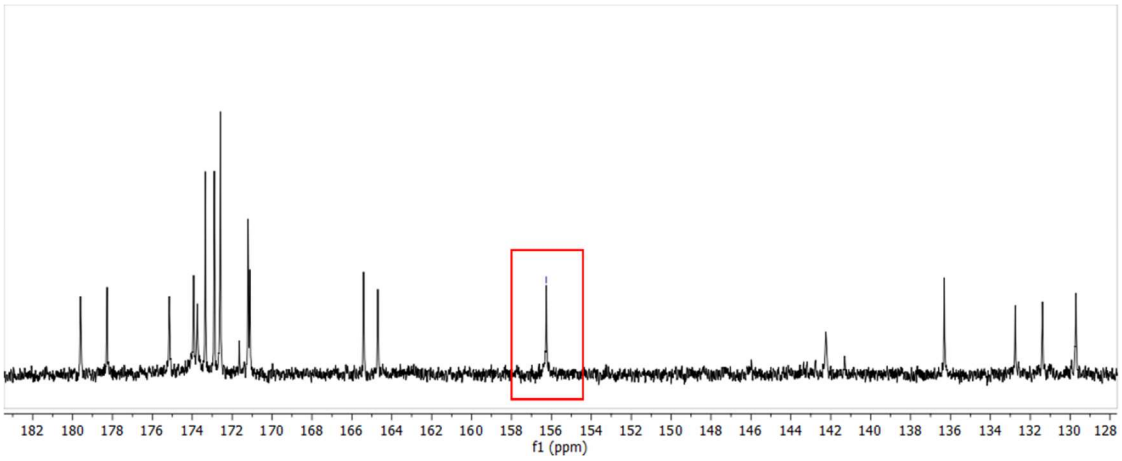

*Figure 31: ^{13}C NMR spectrum of **2** obtained in DMSO-d_6 highlighting the carbamate residue at 156.25 ppm.*

To further probe the purity of **2**, NMR spectroscopic analysis was also carried out in MeOH-d_4. Five peaks were observed in the aromatic region, 6.04 (1H, C10), 6.21 (1H, R1), 6.58 (1H, B4), 7.15 (1H, B2) and 7.24 (1H, B7) ppm (Figure 32). A smaller shift in the R1 resonance was observed upon the formation of **2** when compared to **1** and CNCbl (**1** = 6.23, CNCbl = 6.27 ppm). Furthermore, a new multiplet peak is observed for **2** at 3.66 ppm which integrates for 12 protons. This resonance is assigned to the six *O*-CH_2 protons of the PEG linker.

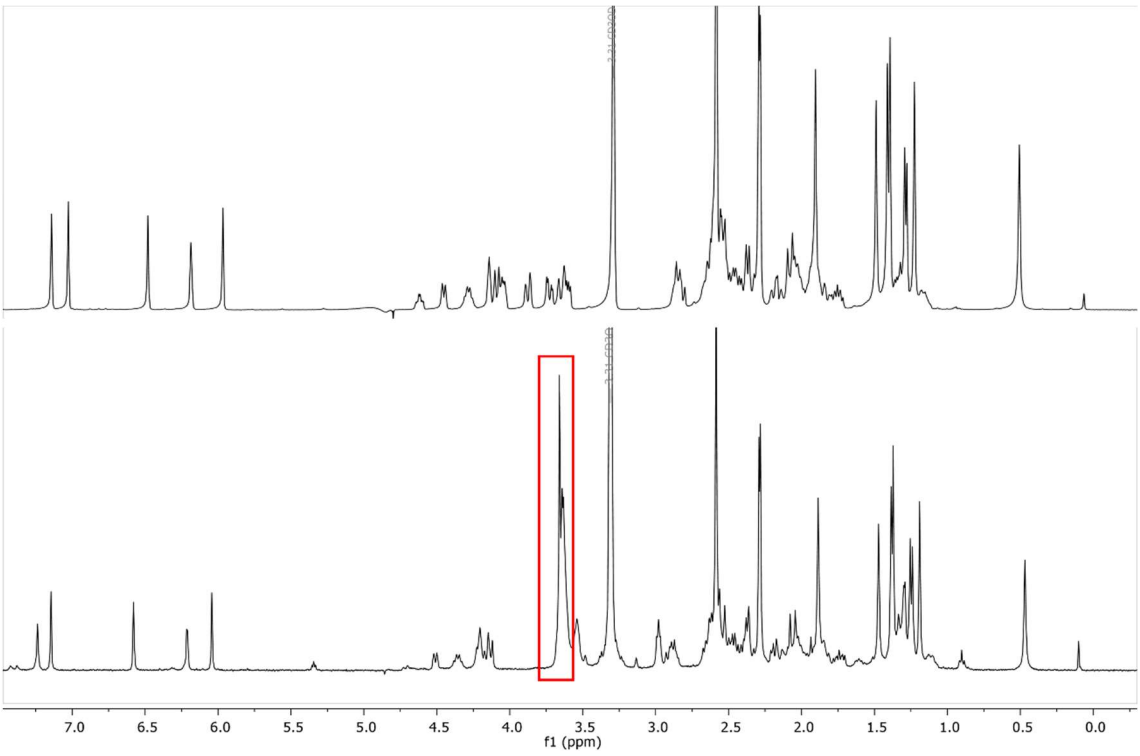

*Figure 32: ^{1}H NMR spectra of CNCbl (top) and **2** (bottom) obtained in MeOH-d_4. Peaks in the aromatic region of **2** at 6.04 (1H), 6.21 (1H), 6.58 (1H), 7.15 (1H) and 7.24 (1H) ppm can be assigned to C10, R1, B4, B2 and B7, respectively. The new resonance at 3.66 ppm assigned to the 12 O-CH_2 protons of the PEG linker is highlighted.*

The formation of **2** was achieved in high yields (78%). Analysis by ^{1}H NMR spectroscopy and LC-MS indicates a purity of ≥95%.

2.3.2 Synthesis and analysis of CNCbl-linker-NBD-X conjugates

NBD-X contains the fluorescent 7-nitrobenz-2-oxa-1,3-diazole moiety attached to hexanoic acid, providing a free carboxylic acid suitable for coupling to CNCbl. This fluorophore was selected based on the commercial availability, price, structure simplicity and spectral properties. The spectral overlap of NBD-X emission and CNCbl absorbance was selected to probe the fluorescence quenching phenomenon that has been observed by CNCbl when bound to fluorescent molecules.

Compound 3

The synthesis of **3** was achieved by using the crude compound **1** as a starting material in addition to the peptide coupling reagents 1-ethyl-3-(3-

dimethylaminopropyl)carbodiimide (EDC), 1-hydroxybenzotriazole (HOBt), Et_3N and NBD-X in a 1:1.5:3:5 mol ratio at 40°C in anhydrous DMSO(Scheme 4).

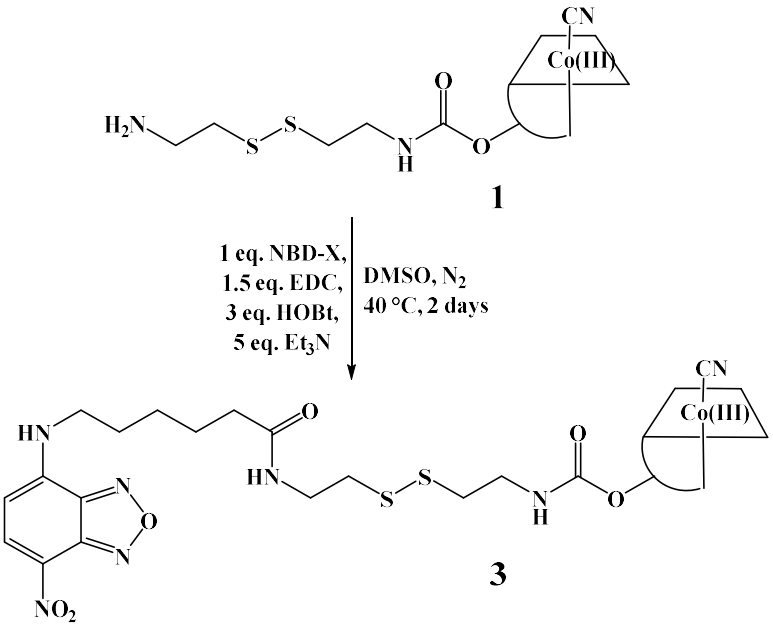

*Scheme 4: Synthetic scheme for the synthesis of **3**.*

EDC is a common reagent employed in peptide coupling reactions and was utilised here to activate the carboxylic acid to form a more reactive *O*-acylisourea intermediate (Scheme 5). The *O*-acylisourea is then readily substituted by primary amines resulting in a peptide bond. This was employed to form a bond between the -COOH functionalised NBD-X and the $-NH_2$ of **1**. EDC is commonly used in stoichiometric ratios and was utilised in a 1.5 mol excess in this reaction. However, the *O*-acylisourea intermediate can undergo *O,N*-acyl migration and form the unreactive *N*-acyl-urea derivative, inhibiting the formation of the **3** (Scheme 5).[35]

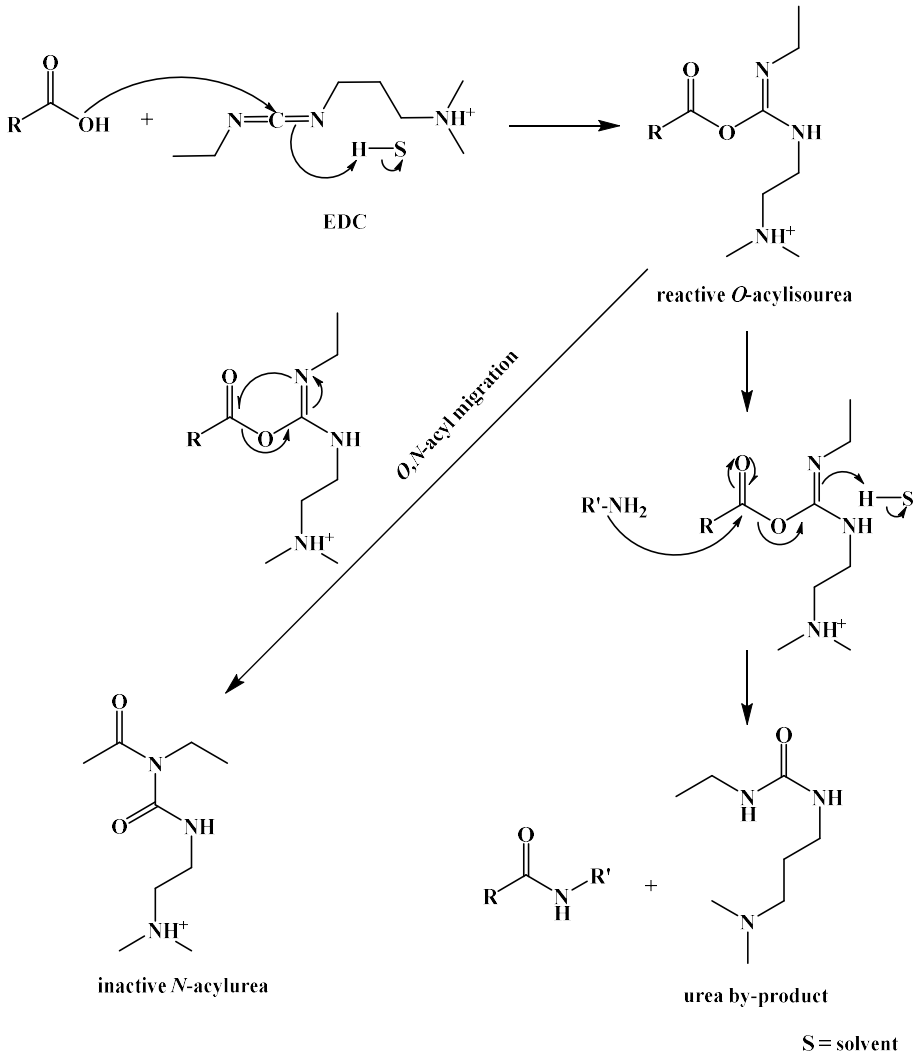

Scheme 5: Mechanism of action of EDC during peptide coupling showing the O,N-acyl migration, forming the unreactive N-acyl-urea derivative. SH represents a solvent molecule.

To prevent this, the addition of excess HOBt was employed to rapidly convert the *O*-acylisourea to the corresponding benzotriazole active ester, therefore limiting the formation of the inactive *N*-acylurea side product. This concept was also trialled utilising *N*-hydroxysuccinimide (NHS) in place of HOBt to form the corresponding succinimidyl ester from the *O*-acylisourea, but this was found to result in lower yields (~15% compared to ~50%) of the desired product.

The conversion of **1** to **3** reached completion within 2 days, as followed by LC-MS chromatography. Four main peaks were evident at 19.5, 20.6, 25.3 and 26.5 min (Figure 33).

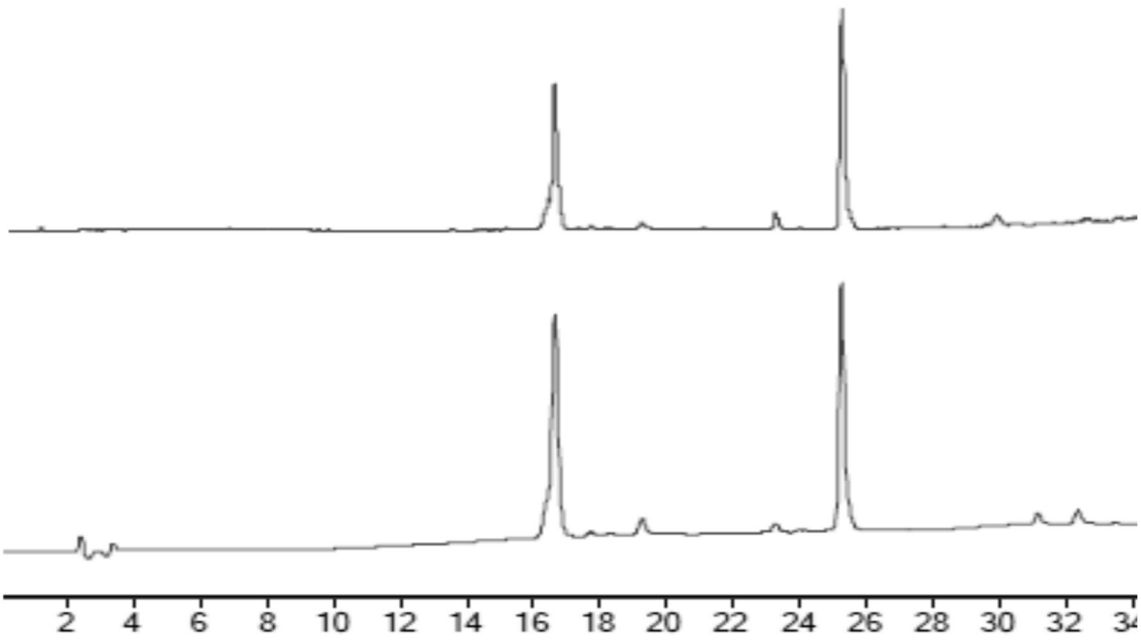

*Figure 33: LC-MS TIC (top) and DAD (361 nm, bottom) chromatograms of the crude **3** (LC-MS method 3). The major peaks can be assigned as CNCbl (16.2 min, $C_{63}H_{88}CoN_{14}O_{14}P$, calcd. m/z $[M+H]^+$ = 1355.6 and $[M+2H]^{2+}$ = 678.3; found 1355.4 and 678.5) and **4** ($C_{80}H_{110}CoN_{20}O_{19}PS_2$, calcd. m/z $[M+H]^+$ = 1809.7 and $[M+2H]^{2+}$ = 905.3 and $[M+3H]^{3+}$ = 603.9, found 905.6 and 604.1).*

Two separate peaks were found to be consistent with the desired product, eluting at 23.8 and 25.1 min. The starting material **1** did show evidence of peak splitting when analysed by LC-MS, but no clear peak separation was observed. The peak separation for the products differs by a full minute, indicating that it isn't caused by peak fronting. The formation of a peptide bond between the **1** and NBD-X moiety does not form a chiral centre. The possibility of 5'-OH and 2'-OH bound isomers of **1** is therefore likely, with the synthesis of **1** at the 5'-OH site more favourable than the 2'-OH site due to steric hindrance. Due to the smaller amount of product being observed at 23.8 min, this was assigned to the 2'-OH functionalised product. No efforts were made to prevent the 2'-OH isomer from forming.

After precipitation of the crude product mixture into 1:1 CH_2Cl_2; Et_2O, a red precipitate was collected and the unreacted NBD-X fluorophore was observed in the filtrate as a yellow solution. Compound **3** was purified by reversed-phase C18 chromatography. The first bands to elute from the column were the red CNCbl and **1** starting materials at 10%

CH_3CN/H_2O. The next band to elute was the orange product **3**, at 35% CH_3CN/H_2O. The final dilute band remaining on the column was the remaining yellow NBD-X fluorophore. The orange product was analysed by LC-MS where one peak was retained at 25.1 min, confirmed to be **3** ($C_{80}H_{110}CoN_{20}O_{19}PS_2$ calcd. *m/z* $[M+2H]^{2+}$ = 905.3 and $[M+3H]^{3+}$ = 603.9, found 905.3 and 604.1, Figure 34).

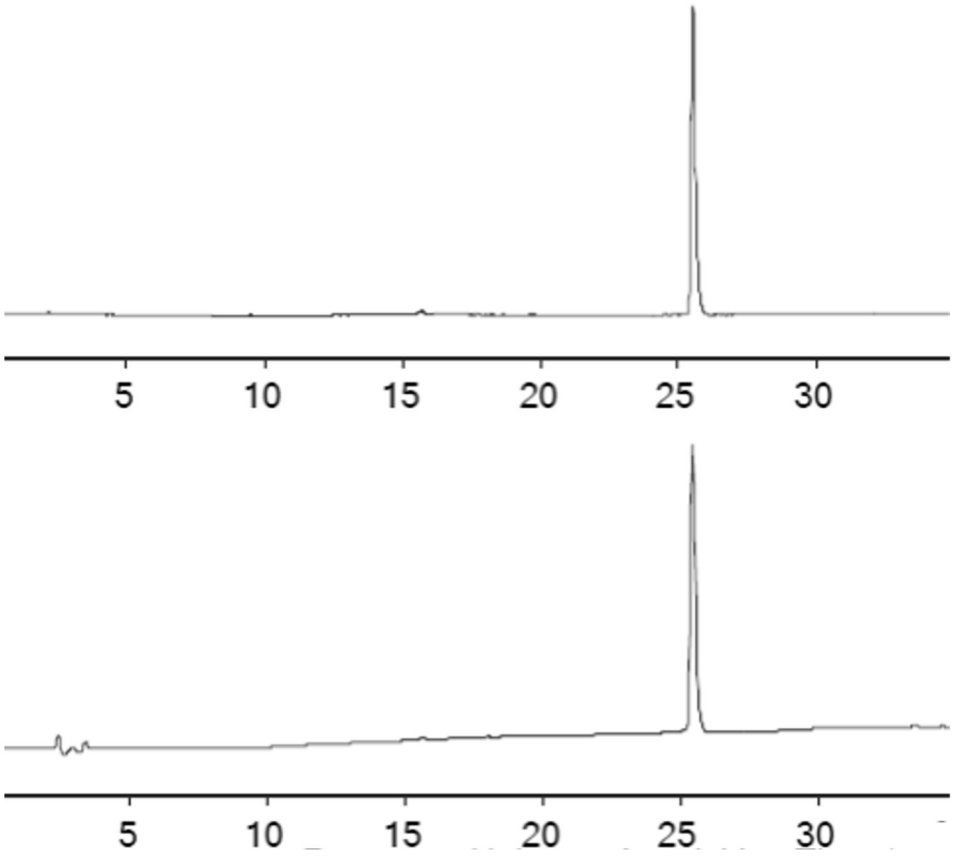

Figure 34: LC-MS TIC (top) and DAD (361 nm, bottom) chromatograms of purified compound ***3*** *($C_{80}H_{110}CoN_{20}O_{19}PS_2$, calcd. m/z $[M+2H]^{2+}$ = 905.3 and $[M+3]^{3+}$ = 603.9, found 905.3 and 604.1 at 25.1 min, LC-MS method 3).*

^{1}H and COSY NMR spectroscopic analysis was carried out in both MeOH-d_4 and DMSO-d_6 to further assess the purity of **3**. The spectra obtained in MeOH-d_4 were first used to identify the NBD-X resonances as CNCbl protons show no correlations by COSY analysis. NBD-X correlations in the COSY spectrum are shown in Figure 35. The doublet peaks at 6.36 (J = 8.9, 1H) and 8.52 (J = 8.8, 1H) ppm have been assigned to protons **a** and **b** of NBD-X, respectively (Figure 35). Unconjugated NBD-X has two multiplets in

the aromatic region of the ^{1}H NMR spectrum at 6.33 and 8.52 ppm (obtained in MeOH-d_4), analogous to that observed in **3**.

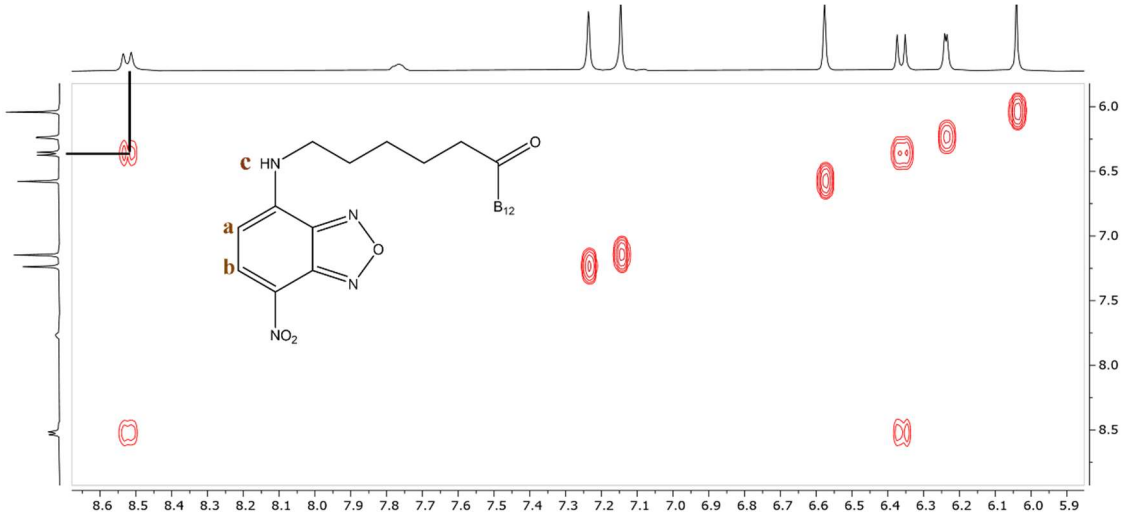

*Figure 35: Aromatic region of the COSY spectra of **3** obtained in MeOH-d_4, highlighting the correlation for the NBD-X protons at 6.36 (1H, **a**) and 8.52 (1H, **b**) ppm.*

Compound **3** showed five remaining peaks in the aromatic region of the ^{1}H NMR spectrum in MeOH-d_4 (Figure 36). The protons of the CNCbl moiety of **3** have been assigned as 6.04 (1H, C10), 6.24 (1H, R1), 6.58 (1H, B4), 7.15 (1H, B2) and 7.24 (1H, B7) ppm. The peak observed at 7.67 ppm is broad and integrates for less than one proton; furthermore, it shows no correlation with other protons in the COSY spectrum. These two factors suggest that the proton at 7.67 ppm is likely due to the partially exchanged NH moiety (**c**) of the NBD-X fluorophore (Figure 35). When compared to **1**, the ^{1}H NMR resonances of the protons located on the CNCbl moiety are similar.

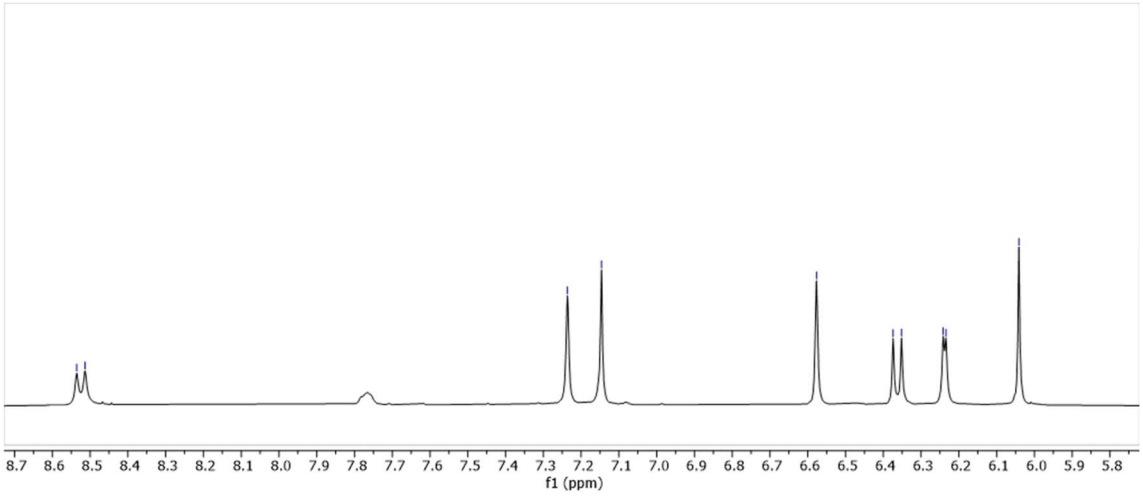

*Figure 36: Aromatic region of the ^{1}H NMR spectrum of **3** in MeOH-d_4. The peaks are assigned as 6.04 (1H, C10), 6.24 (1H, R1), 6.36 (J = 8.9, 1H, **a**) 6.58 (1H, B4), 7.15 (1H, B2), 7.24 (1H, B7) and 8.52 ppm (J = 8.8, 1H, **b**).*

Analysis of the low-field region of the ^{1}H NMR spectrum of **3**, although complex, showed additional resonances from the NBD-X moiety. The ^{1}H NMR spectrum of NBD-X has four distinct peaks in the low field region at 2.28 (m, 2H, **h**), 1.80 (m, 2H, **e**), 1.68 (m, 2H, **g**), 1.50 ppm (m, 2H, **f**) that correspond to the protons of the hexanoic acid chain (Figure 37). The multiplet peak expected for protons **d** resonate under the MeOD-d_4 solvent peak and have not been observed. A careful analysis of the low-field region of **3** shows evidence of the NBD-X proton multiplets at 1.69, 1.80 and 2.23 ppm (Figure 37). These peaks are not present in the starting material, **1**. Although integrations could not confidently be made due to overlapping signals from the CNCbl moiety, the splitting patterns remained consistent. The final peak expected at 1.50 ppm can be partially identified underneath a large overlapping CNCbl peak.

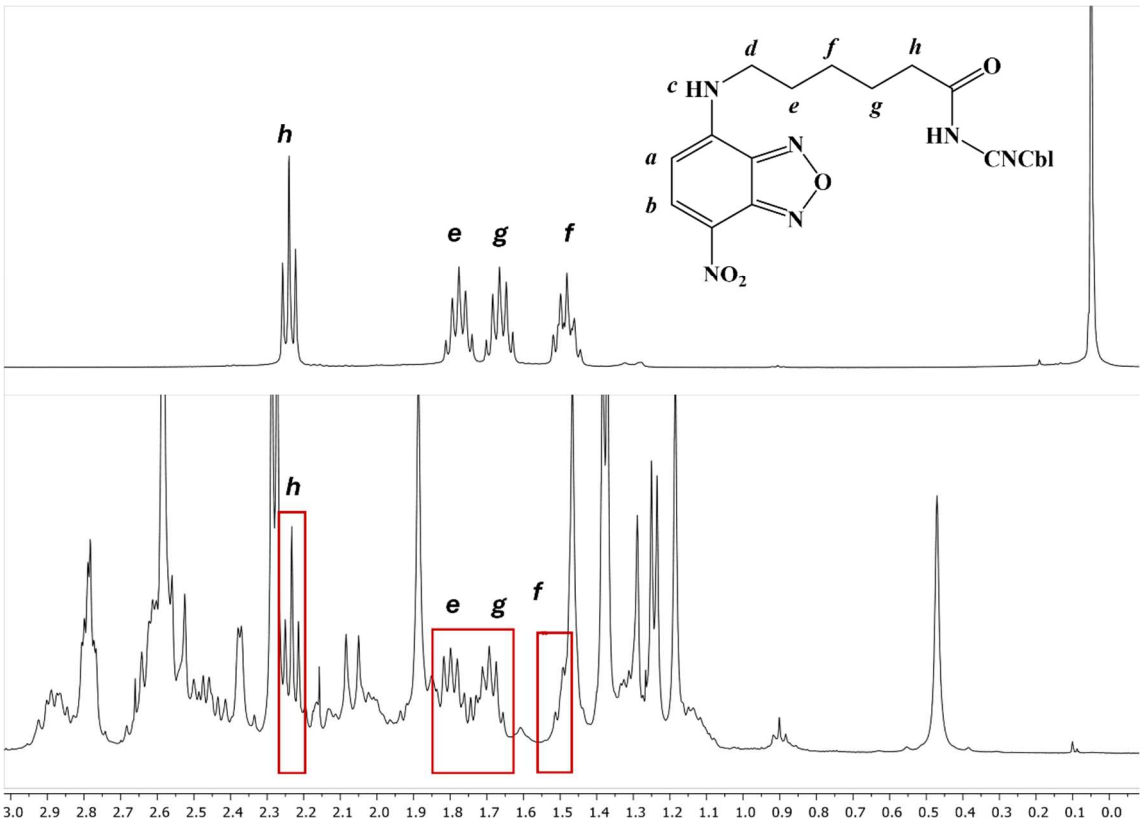

*Figure 37: Low-field region of the ^{1}H NMR spectrum of NBD-X (top) and **3** (bottom) obtained in MeOD-d_4. The highlighted peaks at 1.69 (**g**), 1.80 (**e**) and 2.23 (**h**) ppm of **3** can be assigned to the NBD-X moiety with arrows highlighting the resonance at ~1.50 (**f**) ppm that overlaps with a CNCbl peak. The inset shows a simplified structure of **3** with protons labelled.*

NMR spectra were also obtained in DMSO-d_6 where ^{1}H, ^{13}C, COSY and HSQC spectroscopy experiments assisted in peak assignments. Initially, the two proton resonances of the NBD-X fluorophore were identified. The COSY spectrum identified the two neighbouring protons (**a** and **b**) of the NBD-X moiety of **3** resonating at 6.38-6.41 and 8.47-8.50 ppm, respectively (Figure 38). These were assigned to the NBD-X moiety as COSY experiments of CNCbl and **1** starting materials showed no correlations for aromatic protons in their respective COSY spectra.

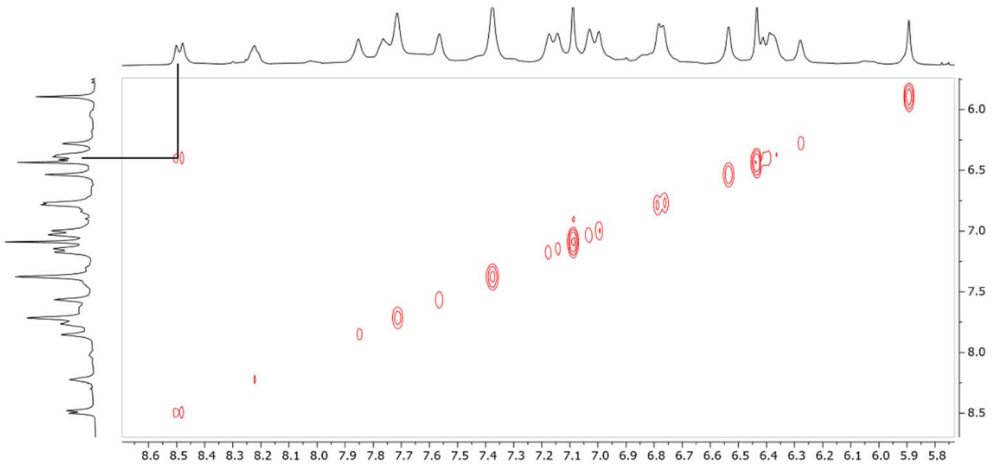

*Figure 38: Aromatic region of the COSY spectrum for **3** in DMSO-d_6 highlighting the NBD-X proton correlations at 6.41-6.43 and 8.47-8.50 ppm assigned to protons **a** and **b** of NBD-X, respectively.*

Further analysis was performed using HSQC, where the NBD-X proton signals were used to identify carbons to which they are directly bonded. The carbon peaks have been assigned as 99.22 (**a**) and 137.91 (**b**) ppm (Figure 39). HQSC analysis allowed for the assignment of the carbon peaks directly bonded to the five protons of the CNCbl moiety that resonate in the aromatic region (Figure 25). These proton resonances have been assigned as 5.89 (C10), 6.28 (R1), 6.43 (B4), 7.08 (B2) and 7.37 ppm (B7) (Figure 39). The corresponding carbon peaks are 93.59, 85.98, 116.38, 142.22 and 111.46 ppm. These assignments agree with the expected order of peaks for both proton and carbon resonances of CNCbl and the synthesised compound **1**.[23]

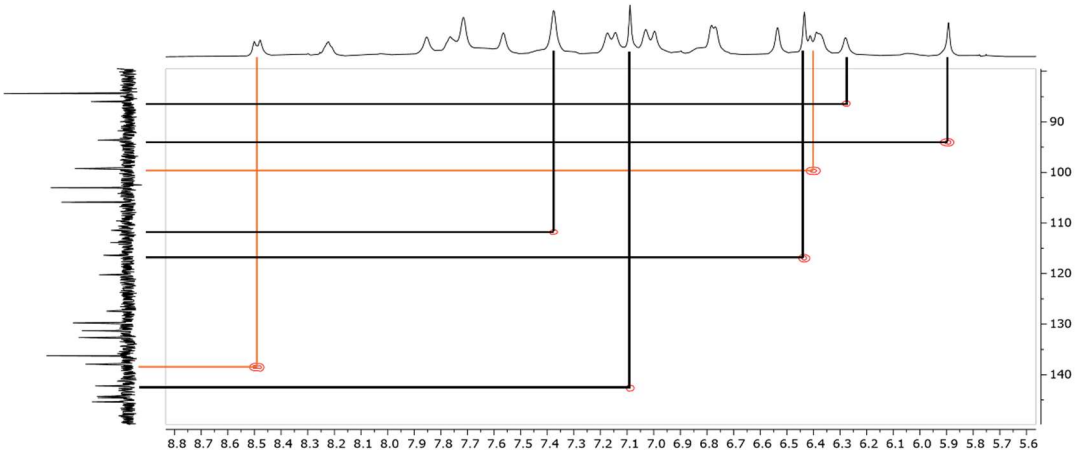

*Figure 39: HSQC spectrum of the aromatic protons of **3** and the carbons they are bonded to in DMSO-d_6, highlighting the NBD-X (orange) and the CNCbl moiety correlations (black).*

Initial stability studies were carried out for compound **3**. Solutions of **3** were prepared in Dulbecco's Modified Eagle Medium (DMEM) and Lysogeny broth (LB) at 16 µM. The solutions were incubated at 37°C with shaking for 24 h. LC-MS analysis of the solutions before and after incubation were the same. This indicated that compound **3** was stable in biological conditions for 24 h.

The formation of **3** was achieved in moderate yields (54%). Analysis by ^{1}H NMR spectroscopy and LC-MS indicates a purity of ≥95%.

Compound 4

The synthesis of **4** was carried out using the same methodology employed for the synthesis of **3**. Crude compound **2** was used as the starting material.

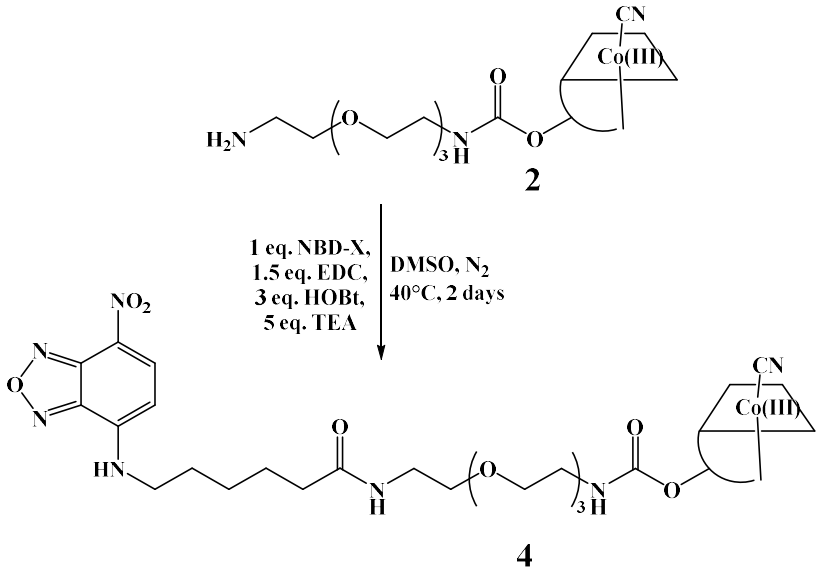

*Figure 40: Synthetic scheme for the synthesis of **4**.*

Reaction progress was followed by LC-MS chromatography where two major peaks were evident at 16.2 and 24.9 min. Interestingly two smaller peaks were also found at 19.2 and 23.1 min (Figure 42). The peak at 16.2 min was CNCbl remaining in the crude **2** starting material ($C_{63}H_{88}CoN_{14}O_{14}P$, calcd. *m/z* $[M+H]^+$ = 1355.6 and $[M+2H]^{2+}$ = 678.3; found 1355.4 and 678.5). The other large peak eluting at 24.9 min corresponded to the product ($C_{84}H_{118}CoN_{20}O_{22}P$, calcd. *m/z* $[M+H]^+$ = 1850.8, $[M+2H]^{2+}$ = 925.9 and $[M+3H]^{3+}$ = 617.6; found 1850.5, 925.5 and 617.5). The smaller peak at 23.1 min also had *m/z* values consistent with the desired product. This phenomenon of two product peaks for CNCbl

bound NBD-X was also observed for the previous product, **3**. The peak at 23.1 min likely represents the 2'-OH functionalised isomer formed during the reaction of **2**. Functionalisation at the 2'-OH is less favourable than the 5'-OH due to steric hindrance by the corrin ring. However, this has still occurred but to a lesser extent. The small peak eluting at 19.2 min was assigned to the CNCbl-PEG-CNCbl dimer that also forms to a small extent during the synthesis of **2** ($C_{136}H_{192}Co_2N_{30}O_{33}P_2$, calcd. *m/z* $[M+2H]^{2+}$ = 1478.1, $[M+3H]^{3+}$ = 985.8 and $[M+4H]^{4+}$ = 739.6; found 1477.7, 985.6, 739.3).

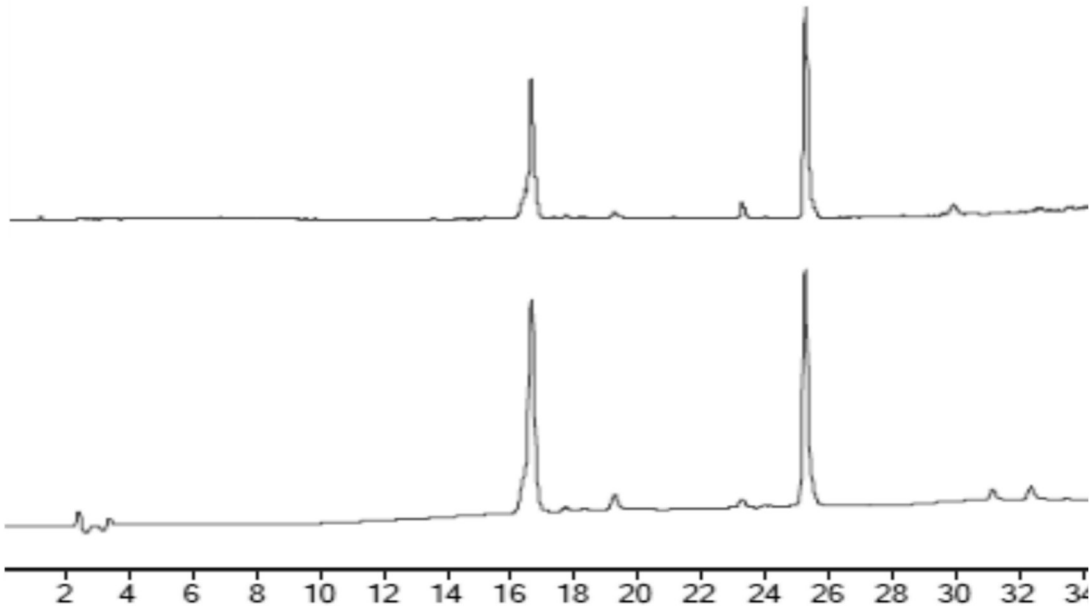

*Figure 41: LC-MS TIC (top) and DAD (361 nm, bottom) chromatograms of the crude compound **4** (LC-MS method 3). The major peaks can be assigned as CNCbl (16.2 min, $C_{63}H_{88}CoN_{14}O_{14}P$, calcd. m/z $[M+H]^+$ = 1355.6 and $[M+2H]^{2+}$ = 678.3; found 1355.4 and 678.5) and **4** (23.1 min, $C_{84}H_{118}CoN_{20}O_{22}P$, calcd. m/z $[M+H]^+$ = 1850.8, $[M+2H]^{2+}$ = 925.9 and $[M+3H]^{3+}$ = 617.6; found 1850.5, 925.5 and 617.5).*

Upon precipitation of the reaction solution into Et_2O and CH_2Cl_2 (1:1, RT), the same yellow filtrate (unreacted NBD-X) and red precipitate were observed as seen during the synthesis of **3**. Furthermore, the order of elution of the peaks was the same, with a red band (CNCbl) followed by an orange band (**4**) eluting from the reversed-phase C18 column. The orange fraction was analysed by LC-MS and assigned to the product ($C_{84}H_{118}CoN_{20}O_{22}P$, calcd. *m/z* $[M+H]^+$ = 1850.8, $[M+2H]^{2+}$ = 925.9 and $[M+3H]^{3+}$ = 617.6; found 1850.5, 925.5 and 617.5, Figure 42).

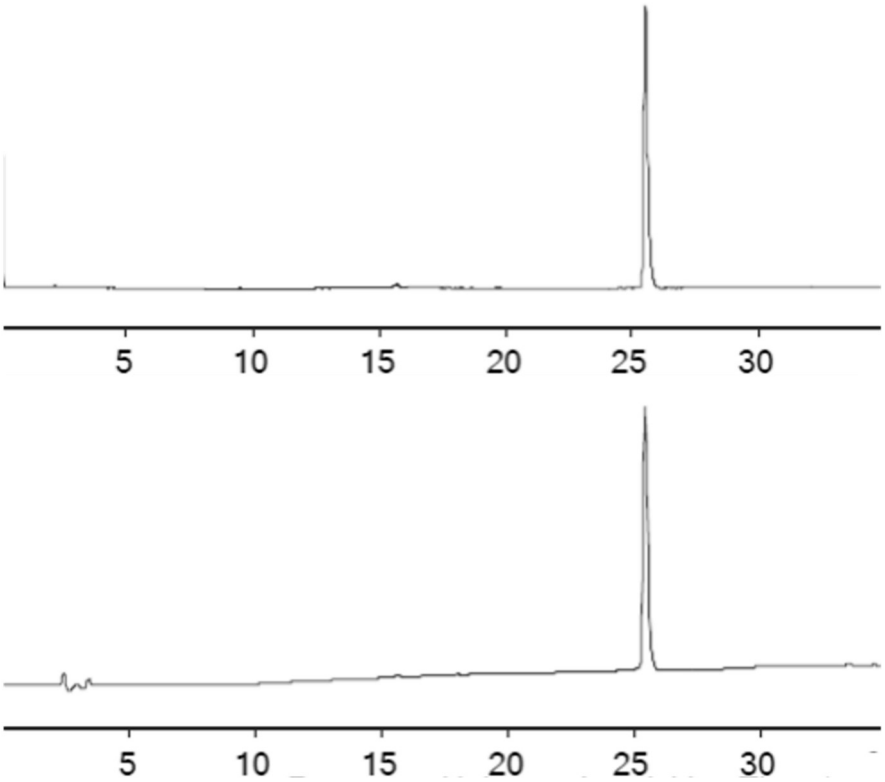

Figure 42: LC-MS TIC (top) and DAD (361 nm, bottom) chromatograms of purified compound ***4*** *($C_{84}H_{118}CoN_{20}O_{22}P$, calcd. m/z $[M+H]^+$ = 1850.8, $[M+2H]^{2+}$ = 925.9 and $[M+3H]^{3+}$ = 617.6; found 1850.5, 925.5 and 617.5, LC-MS method 3).*

^{1}H NMR spectroscopic analysis was carried out in MeOH-d_4 to further assess the purity of **4**. Analogous to that seen for **3**, the five proton resonances of CNCbl in the aromatic region are observed at 6.04 (1H, C10), 6.23 (1H, R1), 6.58 (1H, B4), 7.15 (1H, B2) and 7.24 ppm (1H, B7). The two aromatic resonances of the NBD-X moiety are again observed at 6.36 (J = 8.9) and 8.52 (J = 8.9) ppm, each corresponding to one proton (Figure 43).

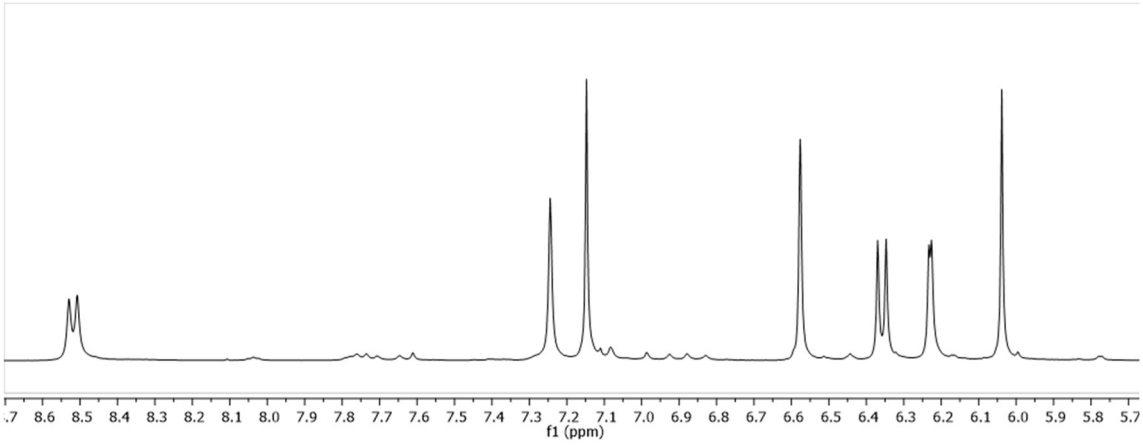

*Figure 43: Aromatic ^{1}H NMR spectrum of **4** obtained in MeOH-d_4. The peaks can be assigned as 6.04 (1H, C10), 6.23 (1H, R1), 6.35-6.37 (1H, **a**), 6.58 (1H, B4), 7.15 (1H, B2), 7.24 (1H, B7) and 8.51-8.53 (1H, **b**) ppm.*

COSY analysis showed correlations in the aromatic region for the multiplets resonating 6.36 (J = 8.9) and 8.52 (J = 8.9) ppm, further supporting their assignment to NBD-X (Figure 44).

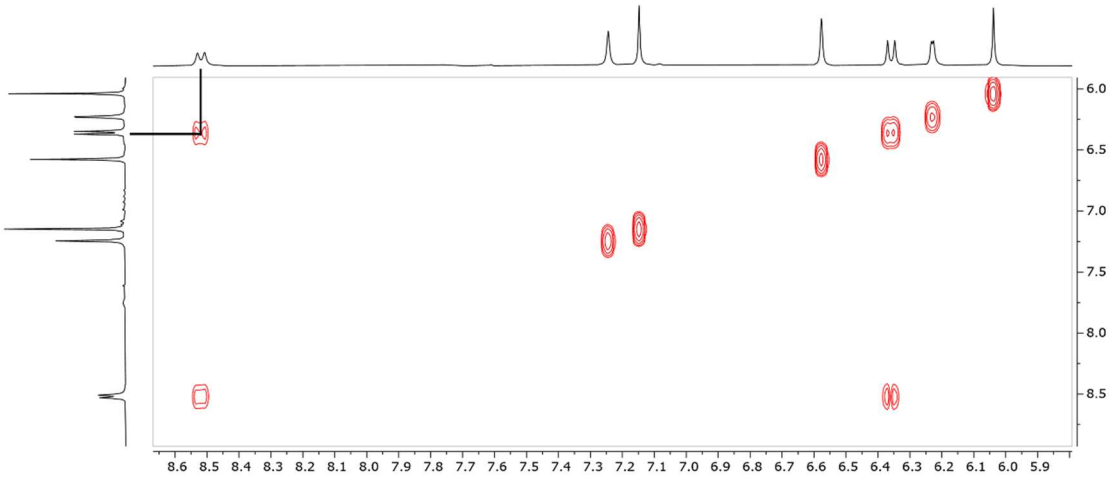

*Figure 44: Aromatic region of the COSY spectrum for **4** obtained in MeOH-d_4 highlighting correlations between the NBD-X protons at 6.35 (J = 8.9, 1H, **a**) and 8.51 (j = 8.9, 1H, **b**) ppm.*

Analogous to that observed in **3**, analysis of the low-field region of the ^{1}H NMR spectrum of **4** showed additional resonances of the NBD-X moiety. The ^{1}H NMR spectrum of NBD-X has four distinct peaks in the low field region at 2.28 (m, 2H, **h**), 1.80 (m, 2H, **e**), 1.68 (m, 2H, **g**), 1.50 ppm (m, 2H, **f**) that correspond to the hexanoic acid chain. Peaks

expected for **d** overlap with the MeOH-d_4 solvent peak and have not been shown. The spectrum of **4** shows these NBD-X protons at 1.69, 1.80 and 2.23 ppm (Figure 45). These peaks are not present in the starting material **2**. Although integrations could not confidently be made due to overlapping signals from CNCbl, the splitting patterns remained consistent. The final peak expected at 1.50 ppm can be partially identified underneath a large overlapping CNCbl peak.

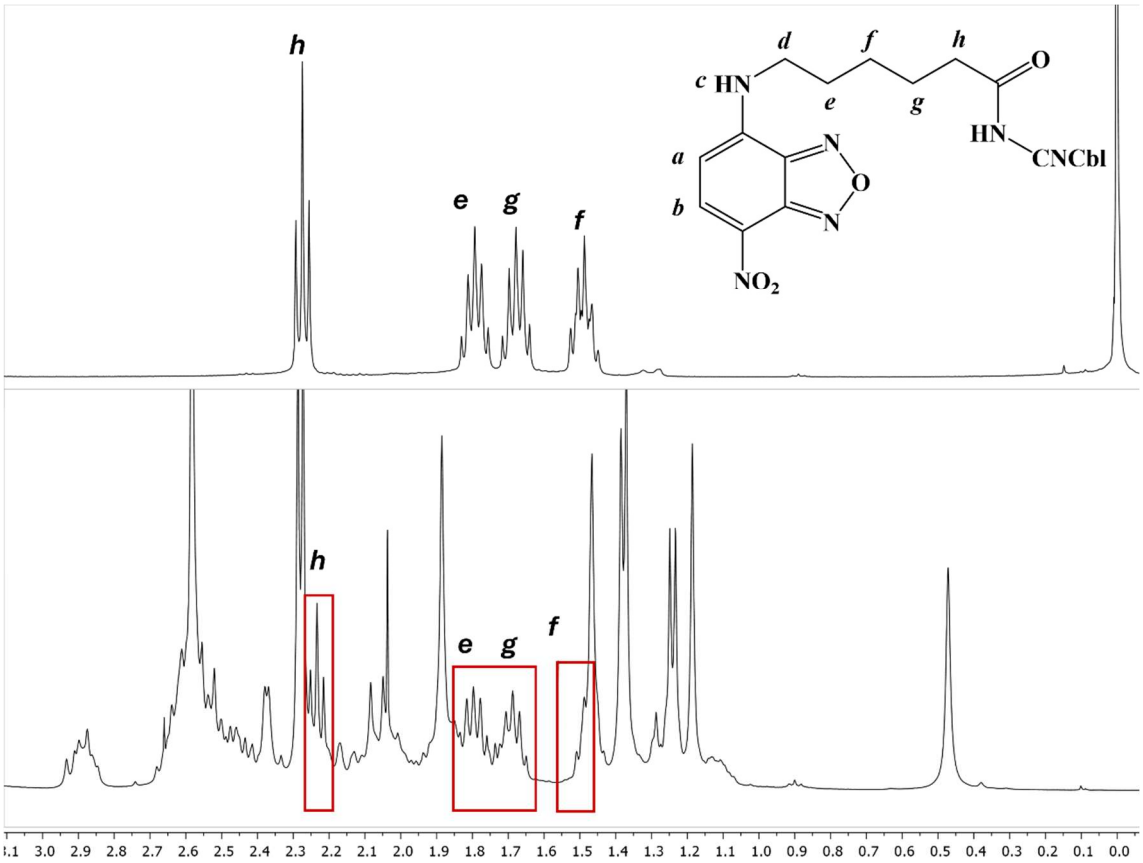

*Figure 45: Low-field region of the ^{1}H NMR spectrum of NBD-X (top) and **4** (bottom) in MeOD-d_4. The highlighted regions of **4** can be assigned to the NBD-X moiety.*

NMR spectroscopic analysis was then performed in DMSO-d_6 to obtain a ^{13}C spectrum. COSY correlations were identified for the NBD-X protons at 6.39-6.40 and 8.49-8.51 ppm. HSQC analysis then allowed for the corresponding NBD-X carbon resonances to be assigned at 99.73 and 138.16 ppm. The five CNCbl proton resonances have been assigned as 5.89 (C10), 6.20 (R1), 6.43 (B4), 7.06 (B2) and 7.29 (B7) ppm (Figure 46). The corresponding carbon peaks are assigned as 93.73, 86.12, 116.54, 142.33 and 111.37 ppm respectively. These resonances are similar to the starting material, compound **2** and CNCbl.

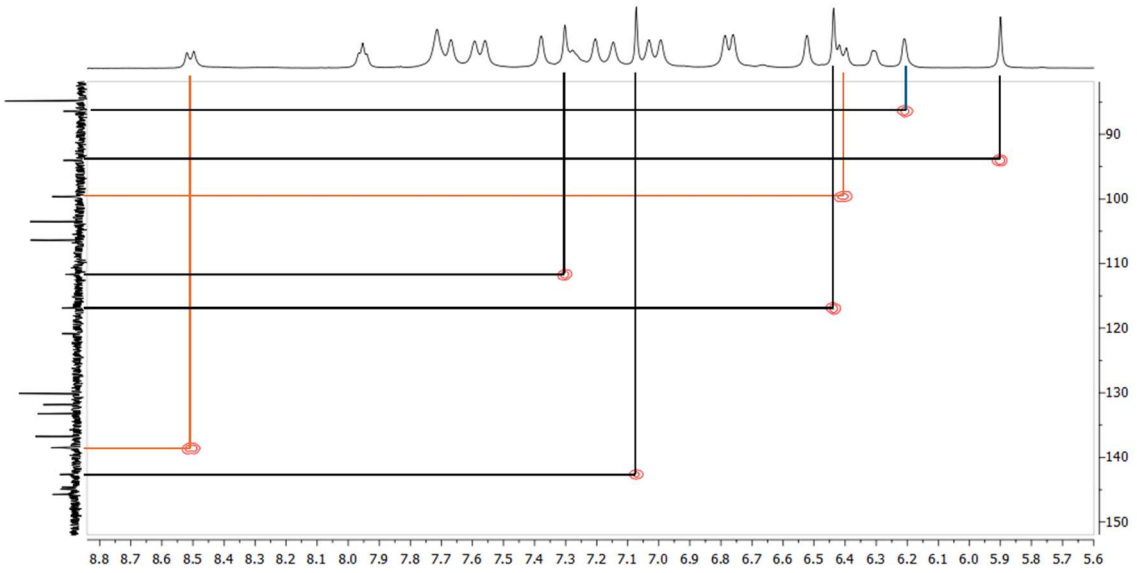

*Figure 46: HSQC spectrum of the aromatic protons and the corresponding carbons of **4** obtained in DMSO-d_6, highlighting the NBD-X (orange) and CNCbl (black) correlations. The remaining proton peaks can be assigned to the amide protons of the NBD-X and CNCbl moieties.*

The formation of **4** was achieved in high yields (89%). Analysis by ^{1}H NMR and LC-MS indicates a purity of $\geq$ 95%.

2.3.3 Synthesis and analysis of CNCbl-linker-sulfo-Cyanine5 conjugates

Compounds **5** and **6** incorporate the sulfo-Cyanine5 fluorophore. Sulfo-Cyanine5 belongs to the cyanine family of fluorescent dyes. Cyanine fluorophores are commonly employed in biological studies due to their high molar extinction coefficients and red-shifted absorbance and emission spectra.[36] The cyanine scaffold consists of two nitrogen-containing heterocycles connected through a conjugated polymethine chain (Figure 47). Tuning of the photophysical properties of these dyes is achieved by modifying the length of the central π-conjugated chain and/or the terminal groups. The sulfo-Cyanine5 fluorophore is an example of this modification, containing a 5-carbon methine chain and two sulfonated residues. One large drawback of cyanine dyes is their limited solubility in aqueous solution, which is imperative in biological studies.[37] To address this, sulfo substituents have been added to the benzyl moieties of Cyanine5.[38] Adding these sulfo substituents significantly increases aqueous solubility, fluorescence quantum yields and lifetimes (caused by hydrophobic dye aggregation).[37]

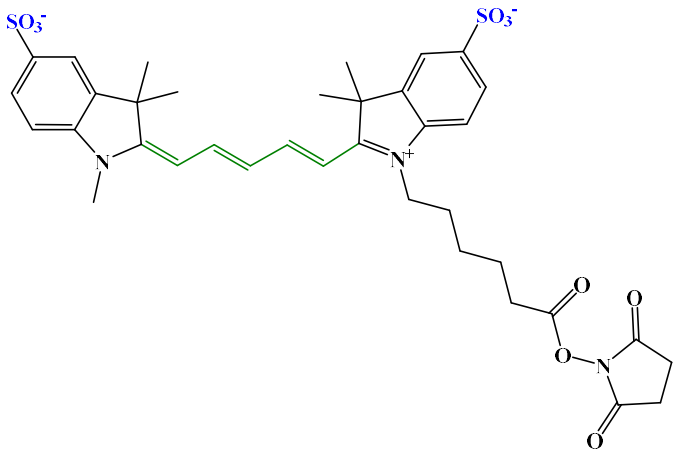

Figure 47: Structure of sulfoCyanine5-NHS ester emphasizing the sulfo substituents (blue) and the 5-carbon methine chain (green).

Compound 5.

The synthesis of **5** was more straightforward than that of the NBD-X conjugates as the sulfo-Cyanine5 was purchased as the more reactive NHS ester. The synthesis was carried out using sulfo-Cyanine5 as the limiting reagent (Scheme 6). The reaction was carried out in anhydrous DMSO at 40°C and was complete after 24 h. Sulfo-Cyanine5 has been conjugated previously to CNCbl by Cannon M.J. in 2001 using commercially available sulfo-Cyanine5-NHS ester via a 1,6-diaminohexane linker.[39] A similar synthetic procedure has been used here for the synthesis of **5,** except that Et_3N was added, lower equivalents of sulfo-Cyanine5-NHS ester (0.7 eq. vs 1 eq.) used, and the reaction temperature was increased to 40°C.

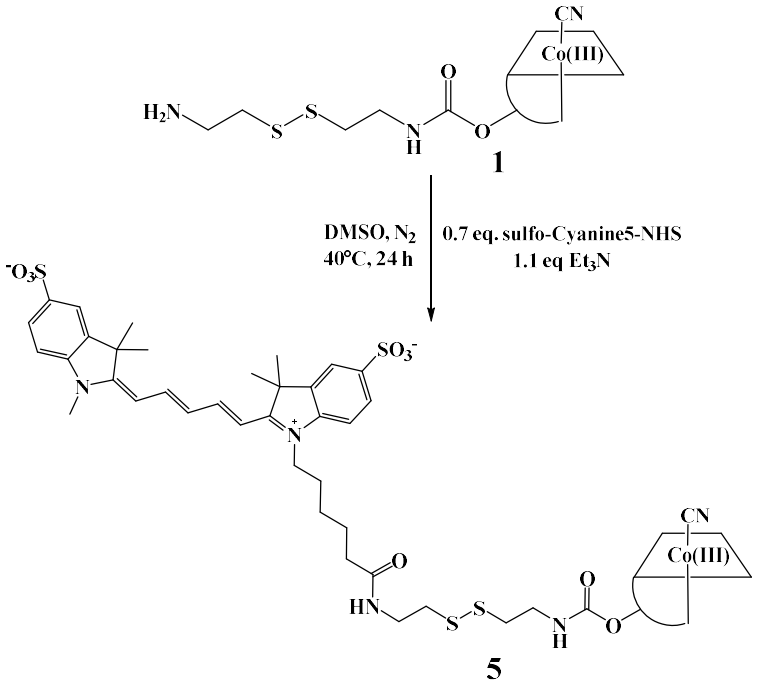

*Scheme 6: Synthetic scheme for the synthesis of **5***

The reaction was followed by LC-MS. LC-MS analysis for this conjugate proved more challenging as no peaks were observed in the total ion count (TIC) chromatogram. However, peaks were observed using diode array detection (DAD, 361 nm). Since the sulfo-Cyanine5 fluorophore is negatively charged and the resulting conjugate, **5** is also negatively charged so LC-MS analysis was carried out in both the negative and positive ionization modes. No peaks were observed in the TIC chromatograms in either ionisation mode. For the earlier compounds all analyte samples had been prepared in CH_3OH (concentrations of 10 ppm) as this proved to be the best solvent for both the CNCbl conjugates and the non-polar fluorophores. Due to the water solubility of the sulfo-Cyanine5 fluorophore, H_2O was also trialled as the solvent for sample preparation. This resulted in peaks observable in the TIC chromatogram at the same retention times as peaks observed in the DAD chromatogram. The use of CH_3OH as a solvent, and in this case as a dilution matrix, can result in ion suppression (Figure 48).[40]

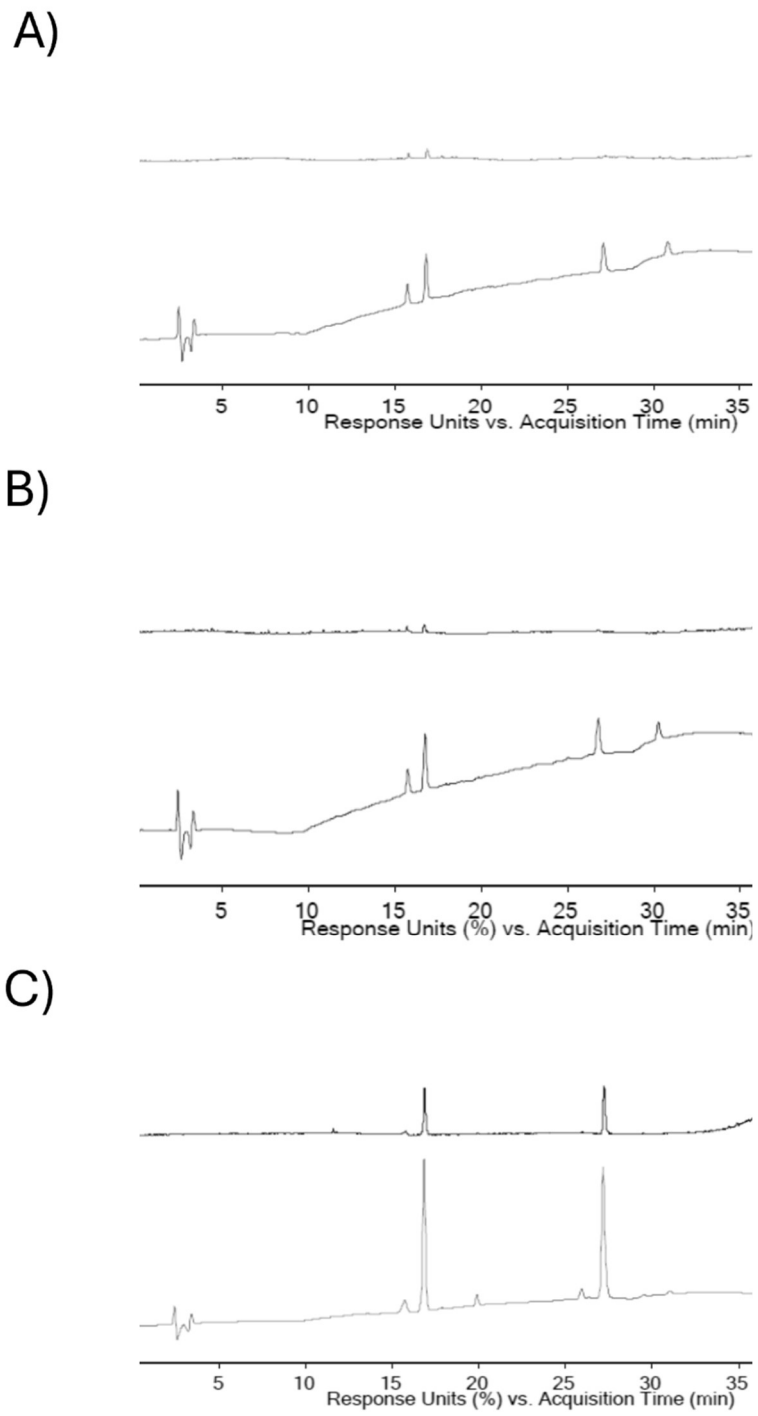

*Figure 48: LC-MS chromatograms of crude compound **5** (LC-MS method 3). A) Prepared in CH_3OH, TIC chromatogram (top) and DAD chromatogram (bottom) in the positive ionisation mode. B) prepared in CH_3OH, TIC chromatogram (top) and DAD chromatogram (bottom) in the negative ionisation mode. C) prepared in H_2O, TIC chromatogram (top) and DAD chromatogram (bottom) in the positive ionisation mode.*

The LC-MS chromatograms for the sample prepared in H_2O showed two major peaks at 16.6 and 26.9 min (Figure 48C). The peak eluting at 16.6 min is from the unreacted CNCbl in the crude **1** reactant ($C_{63}H_{88}CoN_{14}O_{14}P$, calcd. *m/z* $[M+H]^+$ = 1355.6 and $[M+2H]^{2+}$ = 678.3 found 1355.4 and 678.5). Eluting at 26.9 min was the product **5** ($C_{100}H_{133}CoN_{18}O_{22}PS_4$, calcd. *m/z* $[M+3H]^{2+}$ = 1079.9 and $[M+4H]^{3+}$ = 720.3; found 1080.1 and 720.3).

The crude product solution was precipitated into a 1:1 solution of CH_2Cl_2:Et_2O, and a blue solid was collected. Unlike the NBD-X fluorophore, free sulfo-Cyanine5 is not soluble in the organic precipitation solvent (CH_2Cl_2 and Et_2O), and therefore no unreacted sulfo-Cyanine5 was found in the filtrate. The crude blue solid was loaded onto a reversed-phase C18 chromatography column by dissolution in the minimal volume of H_2O. During purification, the first two red bands that eluted (10% CH_3CN in H_2O) were from CNCbl and the starting material **1**. Compound **5** eluted as a large blue band at 50% CH_3CN in H_2O. Purity was confirmed by LC-MS (Figure 49). Two small peaks were identified in the LC-MS DAD chromatogram but were not observed in the TIC chromatogram. Since *m/z* values were not available for the impurity peaks, they were not identified. However, the areas of the small peaks were used to assess the purity of compound **5** as 92%. The purified compound **5** was analysed further by ^1H NMR spectroscopy.

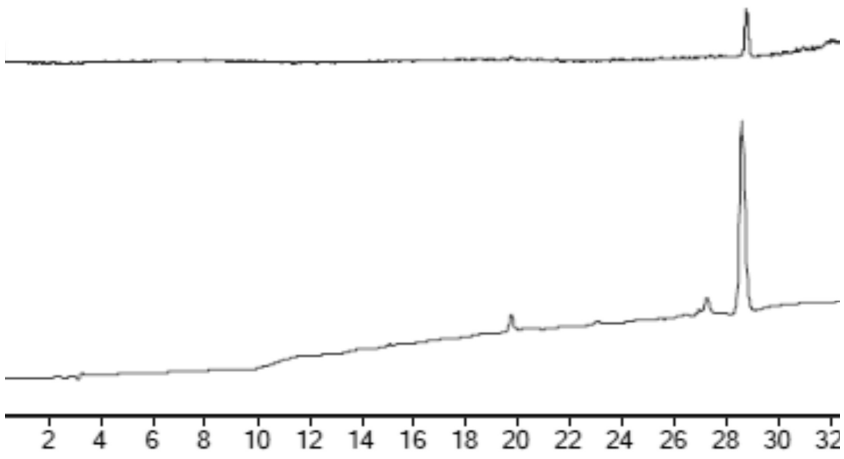

*Figure 49: LC-MS of purified **5** (LC-MS method 3). The peak at 28.6 min can be assigned to **5** ($C_{100}H_{133}CoN_{18}O_{22}PS_4$, calcd. m/z $[M+3H]^{2+}$ = 1079.9 and $[M+4H]^{3+}$ = 720.3; found 1079.8 and 720.3).*

The ^{1}H NMR spectrum in MeOH-d_4 showed resonances in the aromatic region (Figure 50). The ^{1}H NMR spectrum has five proton resonances at 6.02 (1H, C10), 6.25 (1H, R1), 6.56 (1H, B4), 7.12 (1H, B2) and 7.26 (1H, B7) ppm. These chemical shifts are similar to the protons of the reactant **1** and CNCbl. The remaining five peaks in the ^{1}H NMR spectrum can be assigned to the sulfo-Cyanine5 moiety.

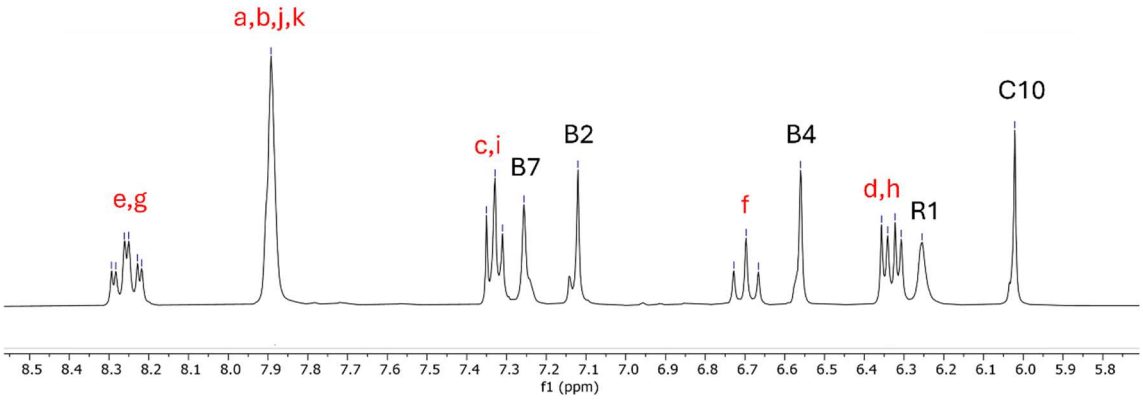

*Figure 50: Aromatic ^{1}H NMR spectrum of **5** in MeOH-d_4. Multiplets from the sulfo-Cyanine5 moiety (red) are observed at 8.22-8.29 (2H, **e** and **g**), 7.89 (4H, **a**, **b**, **j** and **k**), 7.33-7.35 (2H, **c** and **i**), 6.67-6.73 (1H, **f**) and 6.31-6.36 ppm (2H, **d** and **h**). Peaks assigned to the corrin ring and nucleotide of CNCbl are assigned as 6.02 (1H, C10), 6.25 (1H, R1), 6.56 (1H, B4), 7.12 (1H, B2) and 7.26 ppm (1H, B7).*

The COSY NMR experiment showed correlations between the multiplets resonating at 8.22-8.29 ppm, 6.67-6.73 ppm and 6.31-6.36 ppm (

Figure 51). Integrations and splitting patterns suggest that the multiplet at 6.67-6.73 corresponds to the proton **f**, with **e** and **j** overlapping in the correlated multiplet at 8.22-8.29 ppm and **d** and **h** overlapping at 6.31-6.36 ppm (Figure 52). The final two multiplet at 7.33-7.35 and 7.89 ppm show correlations in the COSY spectrum. The multiplet at 7.89 ppm has been assigned to the overlapping protons **a**, **b**, **j** and **k** with the correlated peak at 7.33-7.35 ppm assigned to **c** and **i**. (Figure 50).

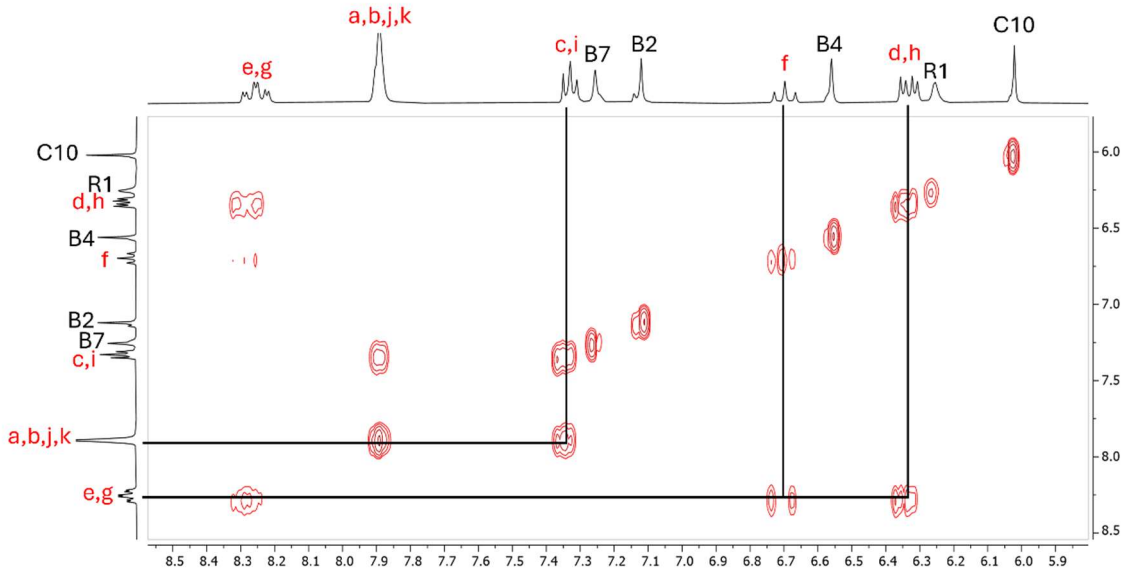

*Figure 51: Aromatic COSY spectrum of **5** in MeOH-d_4. Correlations were observed for the sulfo-Cyanine5 moiety protons **c**/**i** and **a**/**b**/**j**/**k** in addition to correlations between **e**/**g**, **f** and **d**/**h**.*

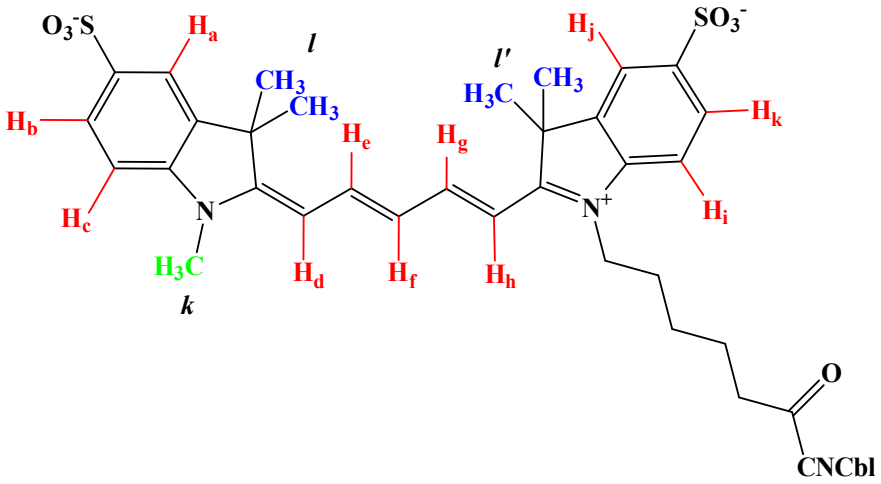

*Figure 52: Structure of **5**, highlighting the aromatic protons (red) and select low-field protons (blue and green) of the sulfo-Cyanine5 moiety. CNCbl-linker atoms have been simplified to CNCbl for clarity.*

Further analysis of the low-field region of the ^{1}H NMR spectrum was undertaken. The NHS ester of sulfo-Cyanine5 has large peaks at 1.73 (multiplet, 12H, **l**/**l'**), 2.85 (singlet, 4H) and 3.65 (singlet, 3H, **k**) ppm (Figure 53). The multiplet at 1.73 ppm has been assigned to the four CH_3 moieties **l**/**l'**, with the peak at 3.65 ppm assigned to the *N*-CH_3 protons, **k** (Figure 52). The peak at 2.85 ppm has been assigned to the four protons of the

NHS ester moiety. Analysis of the corresponding low-field region of **5** showed the sulfo-Cyanine5-associated methyl protons at 1.73 and 3.65 ppm (Figure 53). The absence of the peak at 2.85 ppm in compound **5** confirms the absence of the NHS ester moiety as expected upon formation of **5**.

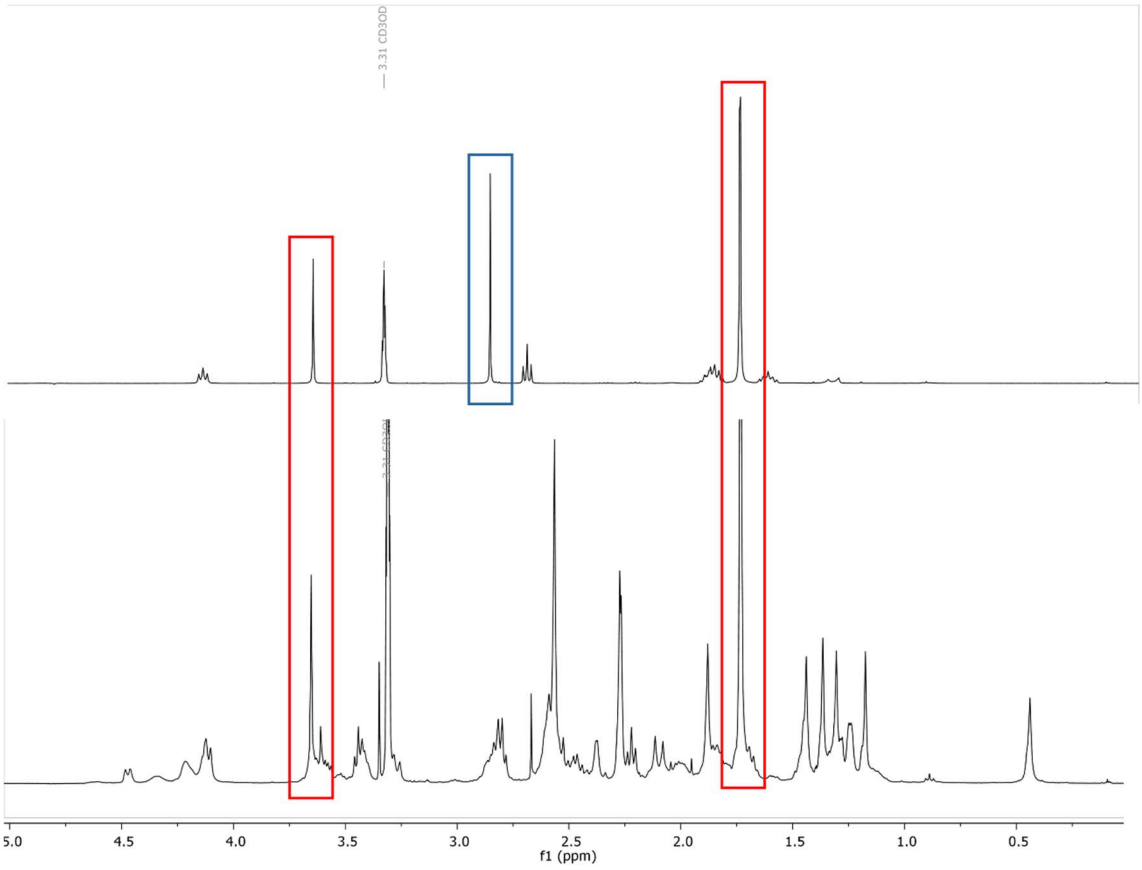

*Figure 53: Low-field ^{1}H NMR spectrum of sulfo-Cyanine5 NHS ester (top) and **5** (bottom). Peaks assigned to the four CH_3 groups (1.73 ppm, **l/l'**, Figure 52) and the N-CH_3 (3.65 ppm, **k**, Figure 52) group in both sulfo-Cyanine5 and **5** highlighted in red. The NHS ester protons are highlighted in blue, absent from **5**.*

The correlations in the COSY experiment obtained in MeOH-d_4 allowed for the assignment of the corresponding sulfo-Cyanine5 moiety peaks in the ^{1}H NMR spectrum obtained in DMSO-d_6. The COSY spectra showed correlations between the multiplet at 8.30-8.37 ppm (1H) and resonances at 6.28-6.32 (2H) and 6.58-6.61 (2H) ppm (Figure 54). The signals at 6.28-6.32 and 6.58-6.61 ppm are broad which indicates they could be due to overlapping ^{1}H residues. This is likely due to amide proton signals from the CNCbl moiety resonating at the same chemical shifts as the sulfo-Cyanine5 protons. However, the COSY correlations supported the assignment of the protons at 8.30-8.37 ppm as **e** and **g**, 6.28-6.32 ppm as **f** and 6.58-6.61 ppm as **d** and **h**. The splitting patterns are difficult to

observe due to peak overlapping. Correlations between protons at 7.30-7.33 (2H) and 7.62-7.66 (2H) ppm indicate that these resonances correspond to four of the six aromatic protons on the benzyl residue. The overlapping multiplets at 7.27-7.33 ppm have been assigned to **c** and **i**, the multiplet at 7.62-7.66 ppm assigned to **b** and **k**. The remaining protons, **a** and **j**, have been assigned to the singlet at 7.80 (2H) ppm. In the ^{1}H NMR spectrum of compound **5** in MeOH-d_4 (Figure 50), the broad peak at 7.89 ppm integrated for four protons, and was assigned to **a**, **b**, **j** and **k**. In DMSO-d_6 protons **b**/**k** and **a**/**j** resonate separately. The aromatic sulfo-Cyanine5 protons have the same order with respect to increasing chemical shift as was observed in MeOH-d_4.

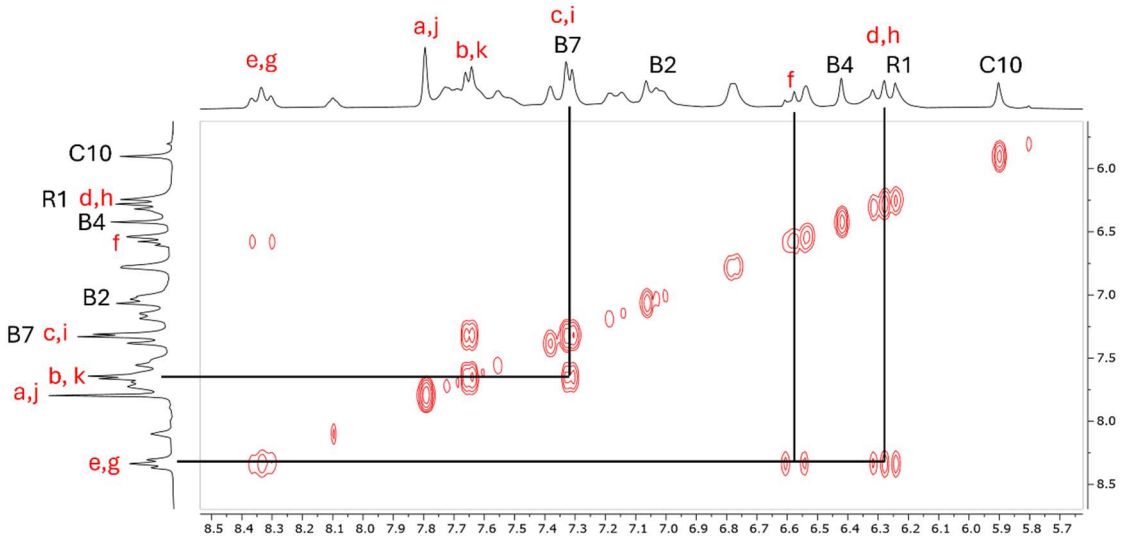

*Figure 54: Aromatic region of the COSY spectrum of **5** obtained in DMSO-d_6. Correlations were observed for the sulfo-Cyanine5 moiety protons **c**/**i** and **b**/**k** in addition to correlations between **e**/**g**, **f** and **d**/**h**.*

HSQC NMR analysis allowed for the partial assignment of the aromatic peaks for the sulfo-Cyanine5, corrin ring and nucleotide protons of **5**. The aromatic proton multiplet of the sulfo-Cyanine5 moiety are 6.24-6.32 (**d**/**h**), 6.58-6.61 (**f**), 7.31-7.33 (**c**/**i**), 7.64-7.66 (**b**/**k**), 7.89 (**a**/**j**) and 8.30-8.37 ppm (**e**/**g**) (Figure 55). The R1 and B7 proton resonances of the CNCbl moiety overlap with the sulfo-Cyanine5 peaks. Corresponding carbon peaks have been assigned as 103.8/103.5 (**d**/**h**), 125.9 (**f**), 126.2/126.2 (**b**/**k**), 119.9/119.9 (**a**/**j**) and 154.4 ppm (**e**/**g**). It was expected that the proton resonances for **e** and **g** would correlate to two separate carbon signals. Due to the low resolution of the ^{13}C NMR spectrum of **5** or overlapping ^{13}C peaks, only one carbon peak was observed. Furthermore,

two separate carbon resonances correlating to the protons at 7.31-7.33 ppm were not observed. The aromatic proton peaks of CNCbl have been assigned as 5.90 (C10), 6.24 (R1), 6.42 (B4), 7.07 (B2) and 7.31 ppm (B7). The corresponding carbon peaks of CNCbl are 93.73, 86.12, 116.48, 142.30, and 110.29 ppm; similar chemical shifts were observed in both CNCbl and **1** starting materials.

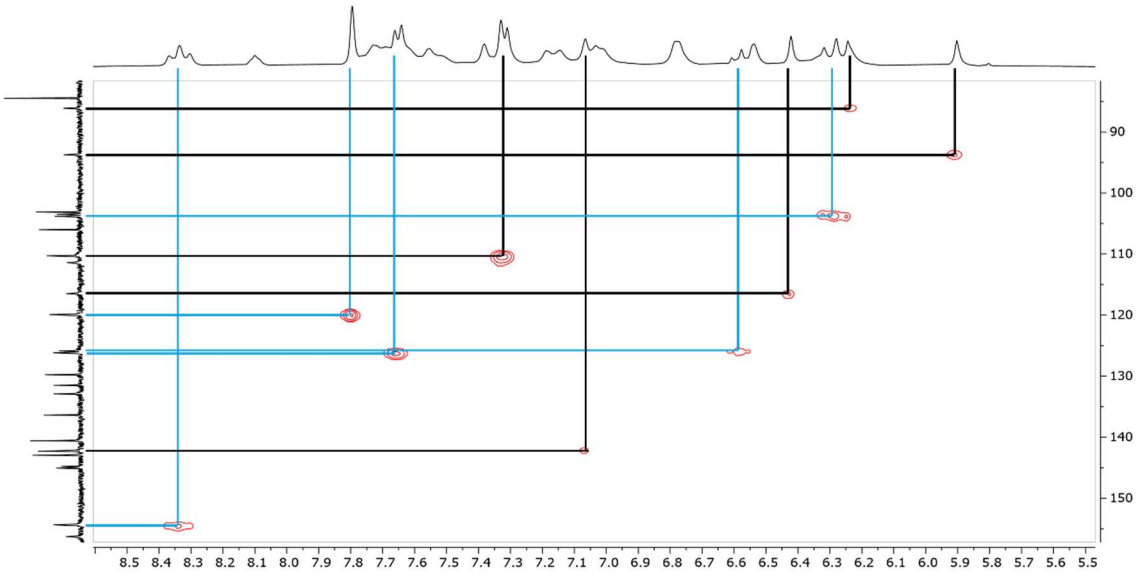

*Figure 55: HSQC of the aromatic protons and the corresponding carbons of **5** with highlighted sulfo-Cyanine5 (blue) and CNCbl (black) moiety correlations.*

The formation of **5** was achieved in high yields (92%). Analysis by ^{1}H NMR spectroscopy and LC-MS indicates a purity ≥ 92%.

Compound 6.

The synthesis of **6** was analogous to that of the synthesis of **5**. Sulfo-Cyanine5 was once again used as the limiting reagent (Scheme 7). The reaction was carried out in anhydrous DMSO at 40°C and proceeded to completion within 24 h.

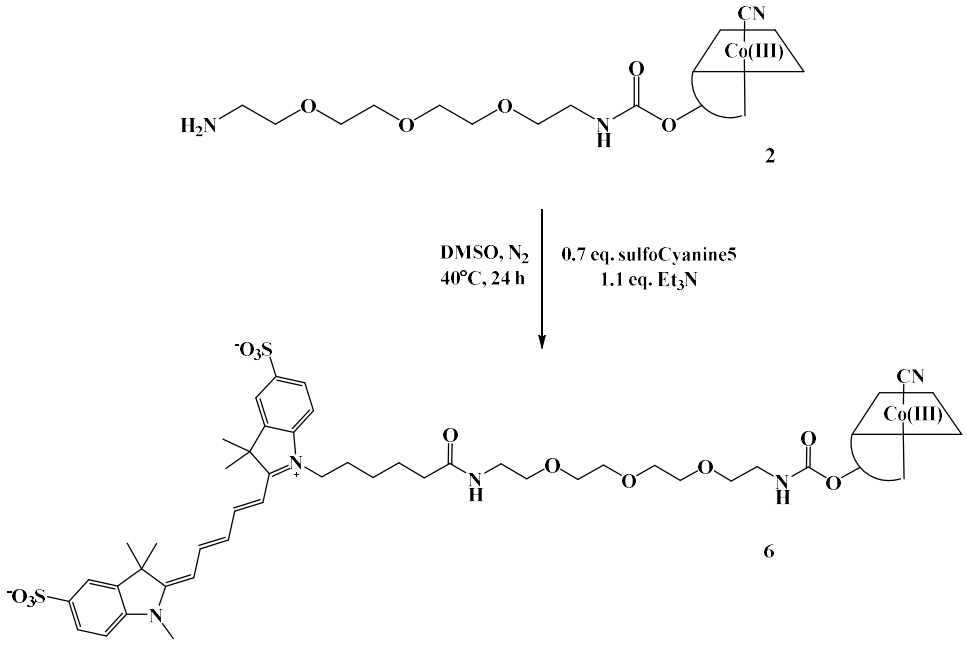

*Scheme 7: Synthetic scheme for the synthesis of **6**.*

Analysis of the crude product mixture was carried out by LC-MS (Figure 56). Once again, preparation of the product in H_2O rather than CH_3OH gave the best TIC chromatogram. The peak eluting at 15.6 min was assigned to the reactant **2** ($C_{72}H_{106}CoN_{16}O_{18}P$, calcd. *m/z* $[M+2H]^{2+}$ = 787.4; found 787.3). The large peak at 16.9 min represents the unreacted CNCbl in the crude reactant **2** ($C_{63}H_{88}CoN_{14}O_{14}P$, calcd. *m/z* $[M+H]^{+}$ = 1355.6 and $[M+2H]^{2+}$ = 678.3 found 1355.5 and 678.4). The small peak at 19.6 min was from the CNCbl-PEG-CNCbl dimer ($C_{136}H_{192}Co_2N_{30}O_{33}P_2$, calcd. *m/z* $[M+2H]^{2+}$ = 1478.1, $[M+3H]^{3+}$ = 985.8 and $[M+4H]^{4+}$ = 739.6; found 1478.0, 985.9 and 739.6). The desired product **6** was the major peak at 25.9 min ($C_{104}H_{141}CoN_{18}O_{25}PS_2$, calcd. *m/z* $[M+3H]^{2+}$ = 1100.0 and $[M+4H]^{3+}$ = 733.6, found 1099.9 and 733.5).

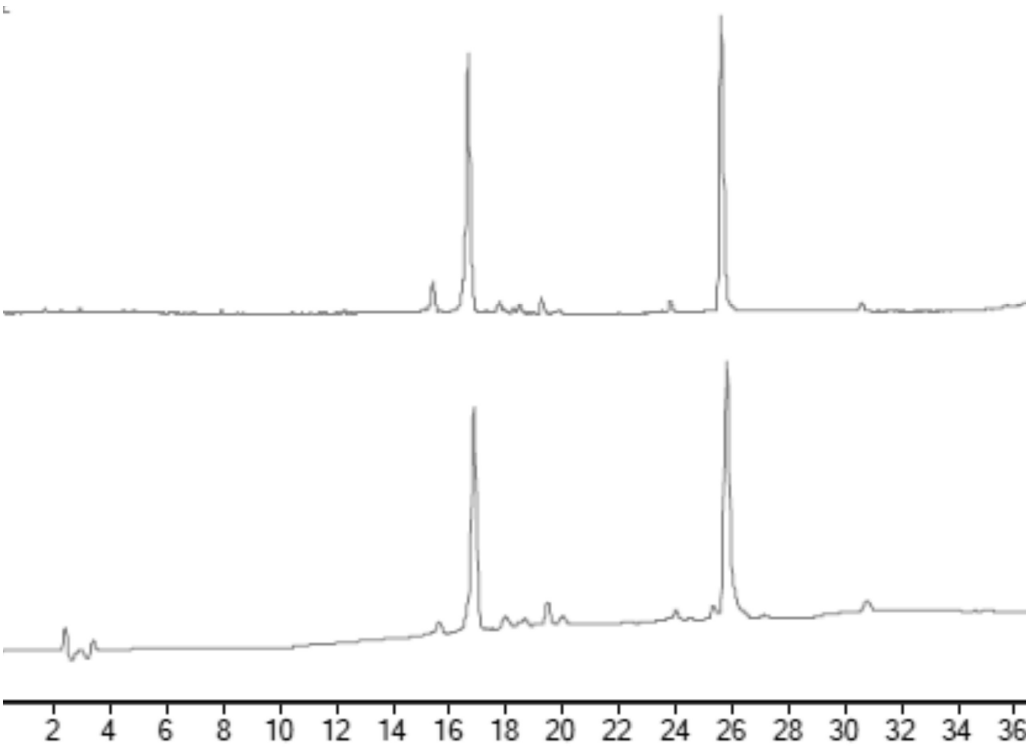

Figure 56: LC-MS TIC (top) and DAD (bottom, 361 nm) chromatograms of crude ***6*** *(LC-MS method 3). The peak at 25.9 min can be assigned to* ***6*** *($C_{104}H_{141}CoN_{18}O_{25}PS_2$, calcd. m/z $[M+3H]^{2+}$ = 1100.0 and $[M+4H]^{3+}$ = 733.6; found 1099.9 and 733.5)*

The crude product solution was precipitated into a 1:1 v/v solution of CH_2Cl_2:Et_2O, and a blue solid was collected. Sulfo-Cyanine5 is not soluble in the organic precipitation solvent. The filtrate remained colourless indicating no sulfo-Cyanine5 was dissolved in the filtrate. During purification by reversed-phase C18 chromatography, the first bands to elute were red and were from the CNCbl, CNCbl-PEG-CNCbl dimer and unreacted **2** (10% v/v CH_3CN in H_2O). The product eluted as a large blue band at 50% v/v CH_3CN in H_2O. The purity was confirmed by LC-MS, with a large peak observed at 25.9 min ($C_{104}H_{141}CoN_{18}O_{25}PS_2$, calcd. *m/z* $[M+3H]^{2+}$ = 1100.0 and $[M+4H]^{3+}$ = 733.6; found 1099.6 and 733.7) (Figure 57). The compound associated with the small peak at 23.9 min could not be identified. Relative peak areas were used to estimate the purity of **6** as 94%.

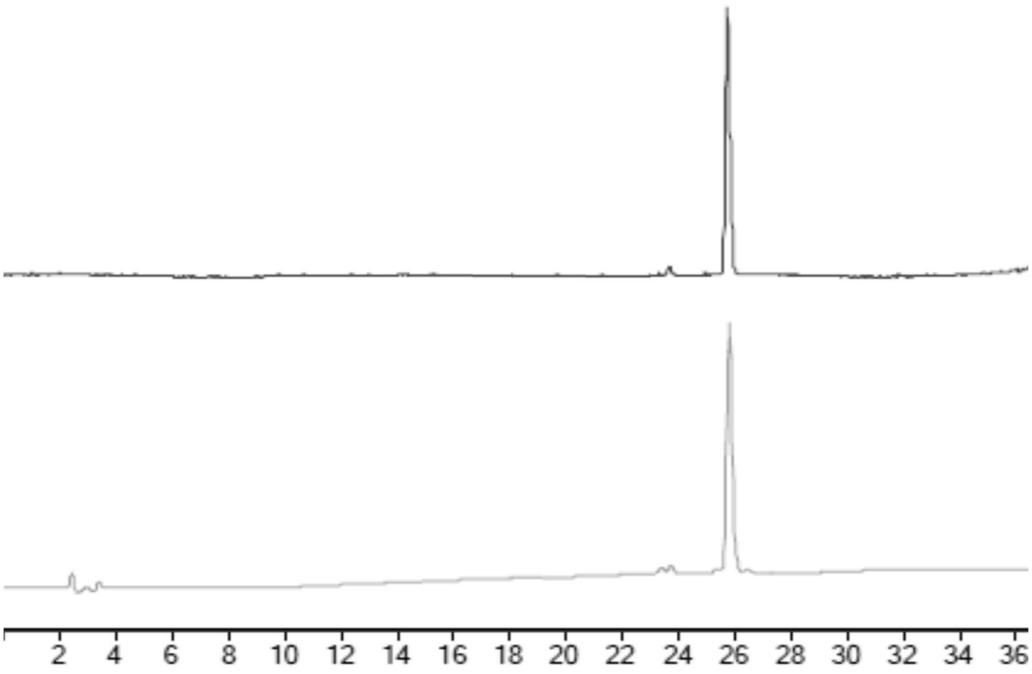

Figure 57: LC-MS TIC (top) and DAD (bottom, 361 nm) chromatograms of pure ***6*** *(LC-MS method 3). The peak at 25.9 min can be assigned to* ***6*** *($C_{104}H_{141}CoN_{18}O_{25}PS_2$, calcd. m/z $[M+3H]^{2+}$ = 1100.0 and $[M+4H]^{3+}$ = 733.6; found 1099.6 and 733.7).*

To further assess the purity of **6**, ^{1}H NMR analyses were undertaken. The ^{1}H NMR spectrum obtained in MeOH-d_4 (Figure 58) was utilised to determine the purity. The proton resonances at 6.03 (1H, C10), 6.23 (1H, R1), 6.58 (1H, B4), 7.14 (1H, B2) and 7.24 ppm (1H, B7) can be assigned to the CNCbl moiety. The remaining five multiplets can be assigned to the sulfo-Cyanine5 moiety, 6.31-6.35 (2H **d** and **h**), 6.65-6.71 (1H, **f**), 7.32-7.34 (2H, **c** and **i**), 7.88-7.91 (4H, **a**, **b**, **j** and **k**) and 8.24-8.31 ppm (2H, **e** and **g**), analogous to the assignments in **5**. COSY NMR analysis supported these assignments, with correlations between the proton resonances at 8.24-8.31, 6.65-6.71 and 6.31-6.35 ppm. Correlations were also evidenced between the protons at 7.88-7.91 and 7.32-7.34 ppm.

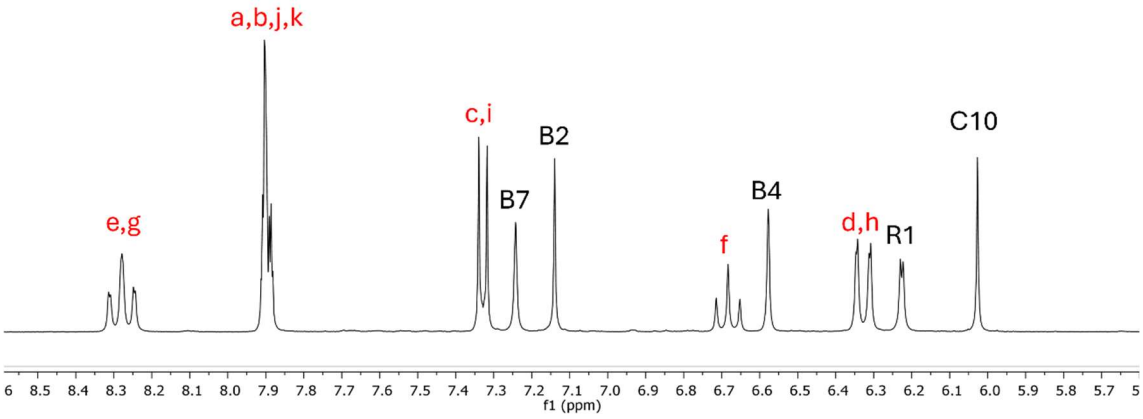

*Figure 58: Aromatic region of the ^{1}H NMR spectrum of **6** obtained in MeOH-d_4. Peaks can be assigned as 6.03 (1H, C10), 6.23 (1H, R1), 6.31-6.35 (2H, **d/h**), 6.58 (1H, B4), 6.65-6.71 (1H, **f**), 7.14 (1H, B2), 7.24 (1H, B7), 7.32-7.34 (2H, **c/i**), 7.88-7.91 (4H, **a**, **b**, **j** and **k**) and 8.24-8.31 ppm (2H, **e/g**).*

Further analysis of the low-field region of the ^{1}H NMR spectrum was undertaken for both compound **6** and the sulfo-Cyanine5 starting material. The NHS ester of sulfo-Cyanine5 has large peaks at 1.73 (multiplet, 12H, **l/l'**), 2.85 (singlet, 4H) and 3.63 (singlet, 3H, **k**) ppm (Figure 59). The multiplet at 1.73 ppm has been assigned to the four CH_3 moieties highlighted (**l/l'**), with the peak at 3.63 ppm assigned to the *N*-CH_3 moiety (**k**) (Figure 52). The peak at 2.85 ppm has been assigned to the four protons of the NHS ester moiety. Analysis of the corresponding low-field region of **6** showed the sulfo-Cyanine5-associated protons at 1.73 and 3.63 ppm (Figure 59). The absence of the peak at 2.85 ppm confirms the absence of the NHS ester moiety as expected upon formation of **6**.

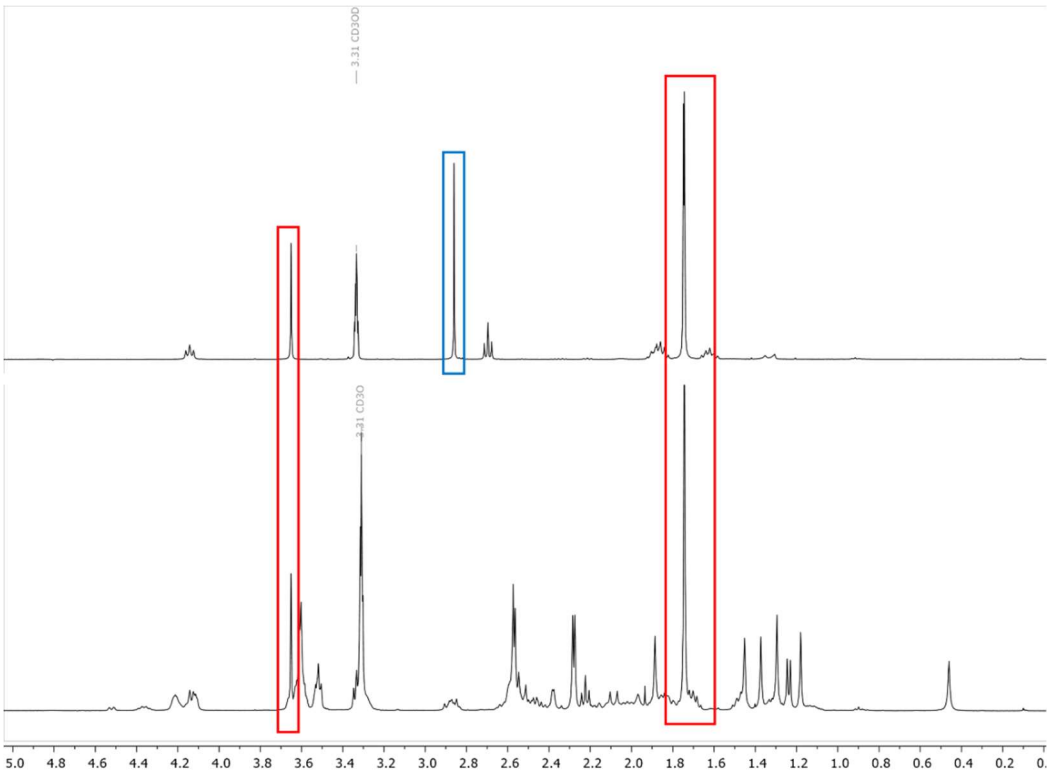

*Figure 59: Low-field ^{1}H NMR of sulfo-Cyanine5 NHS ester (top) and **6** (bottom). Peaks assigned to the four CH_3 groups (**l/l'**, Figure 52) and the N-CH_3 (**k**, Figure 52) group in both sulfo-Cyanine5 and **6** highlighted in red. The NHS ester protons are highlighted in blue, absent from **6**.*

The COSY spectra obtained in DMSO-d_6 showed correlations between the multiplet at 8.32-8.38 (2H) and resonances at 6.29-6.34 (2H) and 6.57-6.60 (2H) ppm (Figure 60). These peaks have been assigned as follows; 8.30-8.37 ppm (**e** and **g**), 6.28-6.32 ppm (**f**) and 6.58-6.61 ppm (**d** and **h**). The splitting patterns are difficult to observe due to peak overlapping. Correlations between protons at 7.30-7.33 (2H) and 7.62-7.66 (2H) ppm indicate that these resonances correspond to four of the six aromatic protons on the benzyl residue. The peak at 7.33-7.33 ppm has been assigned to protons **c/i** and the peak at 7.62-7.66 ppm assigned to **b/k**. The remaining protons, **a** and **j**, have been assigned to the singlet at 7.80 (2H) ppm Unlike the ^{1}H NMR spectrum in MeOH-d_4, the peak at 7.89 ppm integrated for four protons, and was assigned to **a**, **b**, **j** and **k**. Except for **b/k** and **a/j** resonating separately, the aromatic sulfo-Cyanine5 protons show in the same order as was observed in MeOH-d_4. These assignments are consistent with the similar conjugate, compound **5**.

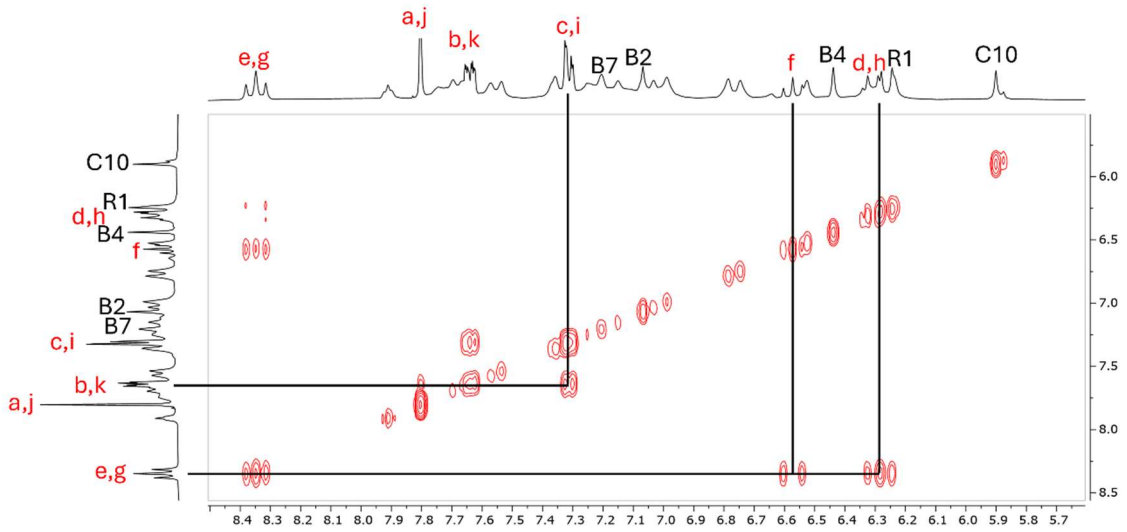

*Figure 60: COSY NMR spectrum of **6** in DMSO-d_6. The peaks can be assigned as 5.90 (C10), 6.23 (R1), 6.29-6.34 (**d/h**), 6.42 (B4), 6.57-6.60 (**f**), 7.07 (B2), 7.31 (B7), 7.30-7.33 (**c/i**), 7.62-7.66 (**b/k**), 7.80 (**a/j**) and 8.32-8.38 (**e/f**) ppm.*

A HSQC NMR experiment allowed for the partial assignment of the aromatic peaks for the sulfo-Cyanine5, corrin ring and nucleotide protons of **6**. The aromatic protons of the sulfo-Cyanine5 moiety are 6.29-6.34 (**d** and **h**), 6.57-6.60 (**f**), 7.30-7.33 (**c** and **i**), 7.62-7.66 (**b** and **k**), 7.80 (**a** and **j**) and 8.32-8.38 (**e** and **g**) ppm (Figure 61). The R1 and B7 proton resonances of the CNCbl moiety overlap with the sulfo-Cyanine5 peaks, also observed in compound **5**. Corresponding carbon peaks have been assigned as 103.45/103.62 (**d/h**), 125.71 (**f**), 126.05/126.10 (**b/k**), 119.86/119.95 (**a/j**) and 154.24 ppm (**e/g**). Individual carbon resonances for protons **c** and **i**, and **e** and **g** were not observed and most likely overlap. The aromatic proton peaks of CNCbl have been assigned as 5.90 (C10), 6.24 (R1), 6.44 (B4), 7.07 (B2) and 7.33 ppm (B7). The corresponding carbon peaks of CNCbl are 93.65, 85.94, 116.42, 142.07, and 110.17 ppm, consistent with the chemical shifts peaks observed for CNCbl and the **2** reactant.

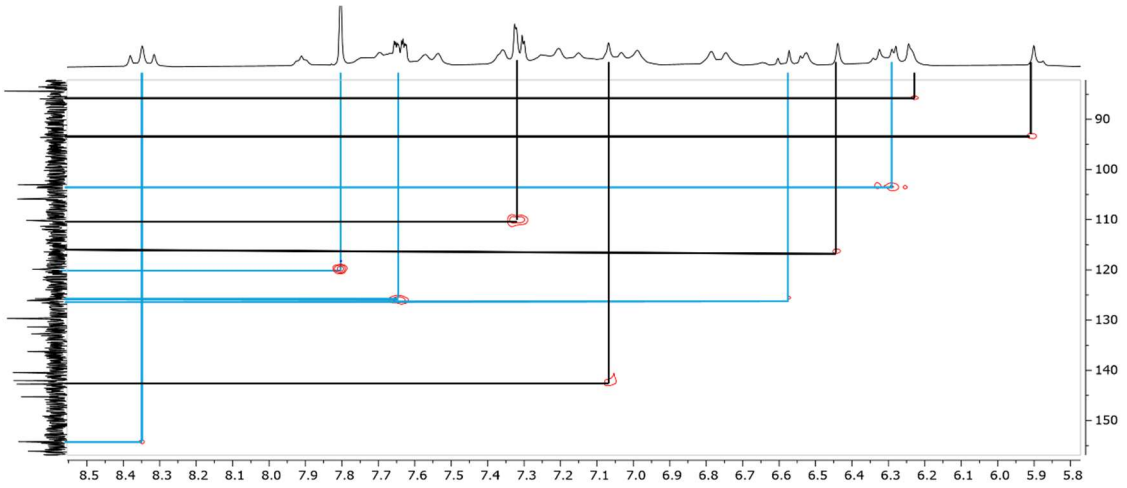

Figure 61: HSQC spectrum of the aromatic protons and the corresponding carbons of ***6*** *with correlations highlighted for the sulfo-Cyanine5 (blue) and CNCbl (black) moieties.*

The synthesis of **6** was achieved in high yields (89%). Analysis by ^{1}H NMR spectroscopy and LC-MS indicates a purity of ≥94%.

2.3.4 Synthesis and analysis of CNCbl-linker-Cyanine7 conjugates

Compounds **7** and **8** incorporate the Cyanine7 fluorophore. Cyanine7 is a red/near-infrared emitting fluorophore based upon the fluorescent cyanine scaffold. The near-infrared emission of Cyanine7 has made this molecule suitable for a wide range of biological studies and applications, with a particular interest in its tumour-targeting properties.[41–43] The commercially available Cyanine7 used in this research is an NHS ester, providing a rapid reactive site for addition to CNCbl by peptide bond formation.

Compound 7

The synthesis of compound **7** is analogous to that of compounds **5** and **6** (Scheme 8). Cyanine7-NHS ester was utilised as the limiting reagent. The reaction was followed by LC-MS and reached completion within 24 h.

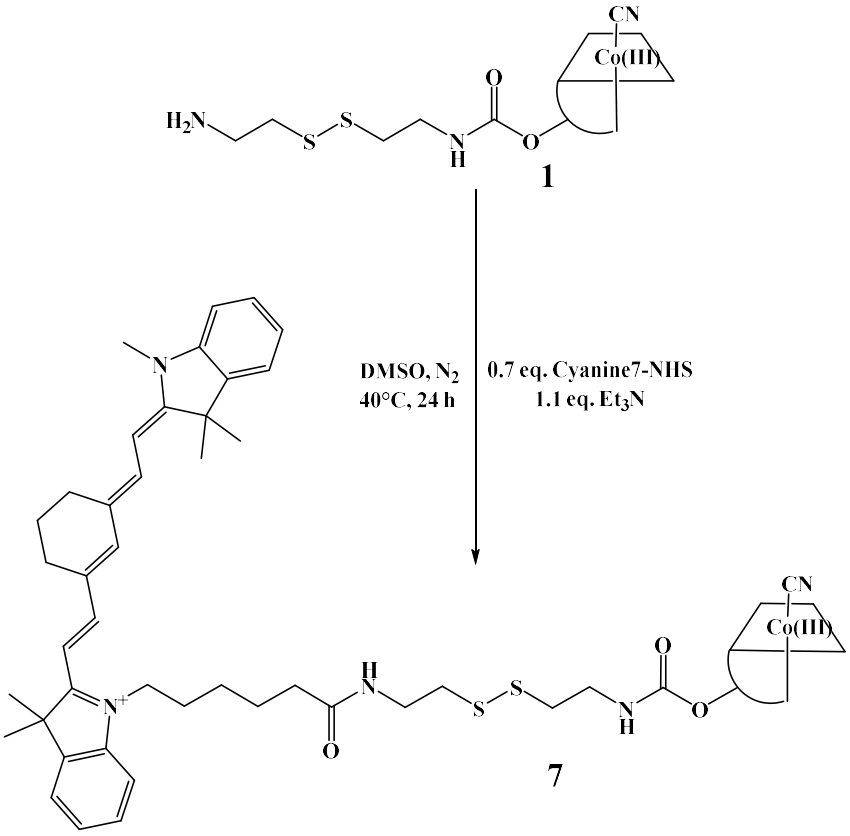

Scheme 8: Synthetic scheme for the synthesis of 7.

The LC-MS analysis of the crude product solution showed three large peaks at 15.6, 16.8 and 30.7 min (Figure 62). The peak at 15.6 min is remaining **1** starting material ($C_{68}H_{98}CoN_{16}O_{15}PS_2$, calcd. *m/z* $[M+H]^+$ =1533.7 and $[M+2H]^{2+}$ = 767.3; found 1534.3 and 767.4). The peak at 16.8 min is from CNCbl impurity in the starting material, **1** ($C_{63}H_{88}CoN_{14}O_{14}P$, calcd. *m/z* $[M+H]^+$ =1355.6 and $[M+2H]^{2+}$ = 678.3; found 1355.6 and 678.5). The desired product eluted at 30.7 min ($C_{105}H_{141}CoN_{18}O_{16}PS_2$, calcd. *m/z* $[M+H]^{2+}$ = 1033.0 and $[M+2H]^{3+}$ = 689.0; found 1033.0 and 689.0).

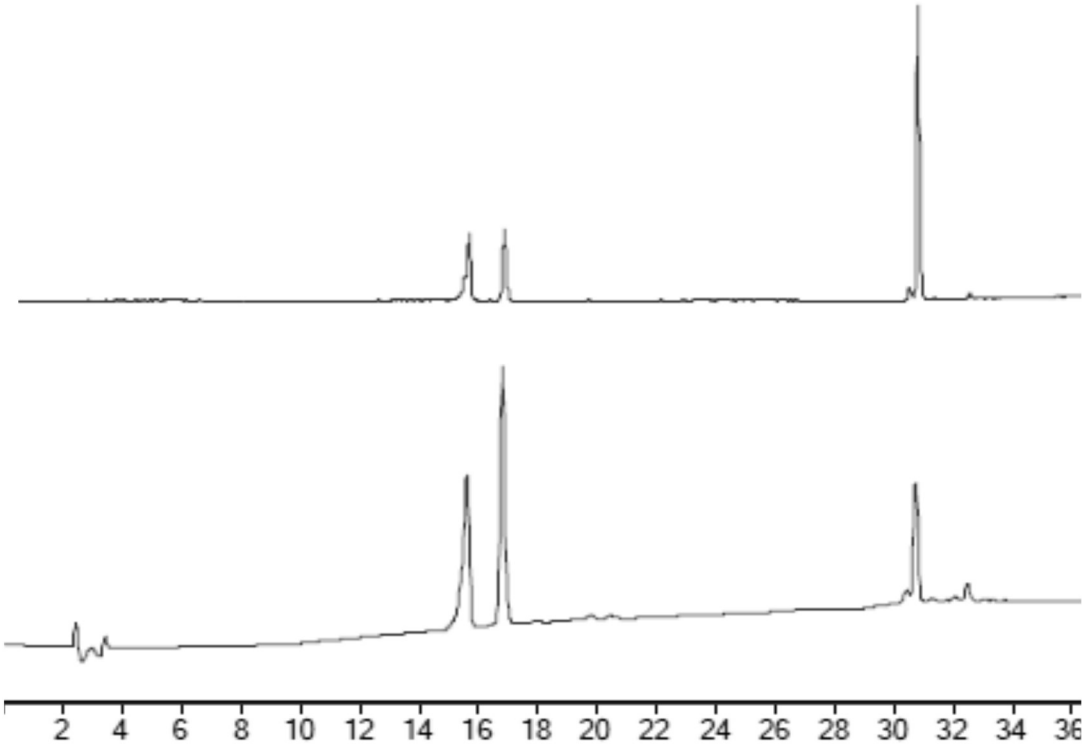

*Figure 62: LC-MS TIC (top) and DAD (bottom, 361 nm) chromatograms of crude **7** (LC-MS method 3). The peaks at 15.6 and 16.9 min can be assigned to **1** and CNCbl, respectively. The peak at 30.7 min is assigned to the product, **7** ($C_{105}H_{141}CoN_{18}O_{16}PS_2$, calcd. m/z $[M+H]^{2+}$ = 1033.0 and $[M+2H]^{3+}$ = 689.0; found 1033.0 and 689.0).*

Upon precipitation of the crude product solution into CH_2Cl_2:Et_2O (1:1 v/v), a dark charcoal-coloured precipitate was collected. The filtrate was light green from the remaining unreacted Cyanine7-NHS ester. Purification of **7** was carried out by reversed-phase C18 chromatography. The solid required dissolution into an H_2O/CH_3CN solvent mixture (9:1 v/v) to ensure a small solvent volume suitable for column loading. An initial red band was collected at ~10% CH_3CN/H_2O which contains unreacted **1** and CNCbl. Multiple attempts were made to purify these conjugates in H_2O/CH_3CN, but it was observed that both the product, **7**, and any remaining Cyanine7 products would adhere to the reversed-phase C18 silica. These compounds would remain on the column at 100% CH_3CN and could only be removed using DMSO. However, both Cyanine7 and **7** travelled through the LC-MS reversed-phase column as discrete bands. Following the addition of formic acid to the aqueous phase of the preparative reversed-phase C18 column, the product eluted as an indigo band at ~80% CH_3CN in H_2O (0.1% v/v formic acid in H_2O). It was found that the addition of formic acid to the aqueous phase was

required to purify all Cyanine7 derivatives. The indigo band was taken to dryness and LC-MS confirmed the presence of pure **7** eluting at 30.7 min ($C_{105}H_{141}CoN_{18}O_{16}PS_2$, calcd. *m/z* $[M+H]^{2+}$ = 1033.0 and $[M+2H+CH_3OH]^{3+}$ = 699.4; found 1032.9 and 699.5 (Figure 63).

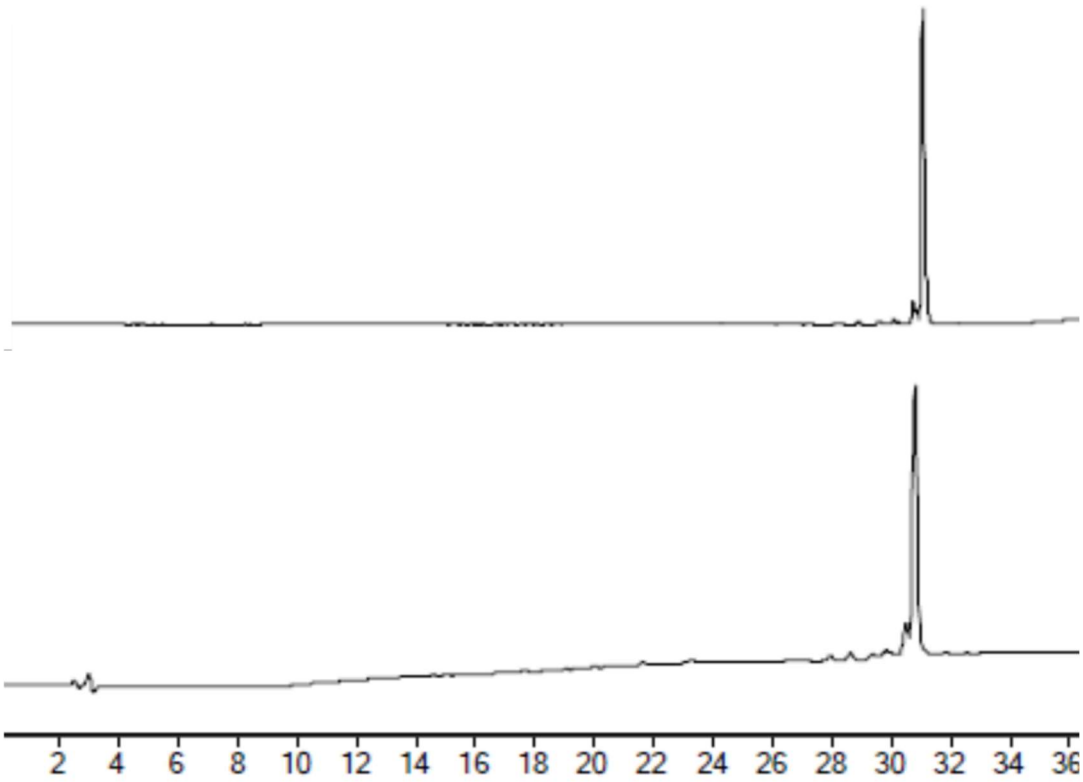

Figure 63: LC-MS TIC (top) and DAD (361 nm, bottom) chromatograms of pure 7. The peak at 30.7 min is assigned to 7 ($C_{105}H_{141}CoN_{18}O_{16}PS_2$, calcd. m/z $[M+H]^{2+}$ = 1033.0 and $[M+2H+CH_3OH]^{3+}$ = 699.4; found 1032.9 and 699.5 (LC-MS method 3).

NMR spectroscopic analysis of the **7** conjugate was first carried out in MeOH-d_4. ^{1}H and COSY spectra were recorded. The complexity of the Cyanine7 fluorophore and the resulting ^{1}H NMR spectrum did not allow for the full assignment of the aromatic proton signals. To aid in the analysis of the spectra, the ^{1}H NMR spectrum of Cyanine7-NHS ester was also recorded (Figure 65). Peaks were observed at 7.74-7.77 (2H), 7.46-7.47 (3H), 7.37-7.41 (2H), 7.21-7.27 (4H) and 6.14-6.20 ppm (2H). The COSY spectrum of Cyanine7-NHS ester showed correlations between the protons at 7.74-7.77 (2H) and 6.14-6.20 ppm (2H). These peaks have been assigned to the protons of the methine chain, **a/e** and **b/d**, respectively (Figure 64). Correlations were also observed between the multiplets

at 7.46-7.47 (3H), 7.37-7.41 (2H) and 7.21-7.27 ppm (4H). These peaks have been assigned to the eight protons of the benzyl moieties of Cyanine7. Integrations suggest that the multiplet at 7.46-7.47 can also be assigned to proton **c** of the methine chain.

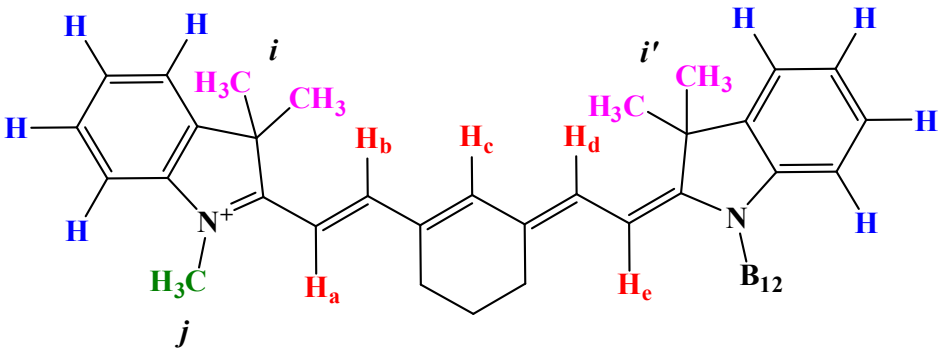

*Figure 64: Structure of Cyanine7 moiety highlighting the aromatic protons (blue and red). Four diagnostic CH_3 moieties have been highlighted in purple (**i/i'**) and the N-CH_3 moiety highlighted in green (**j**).*

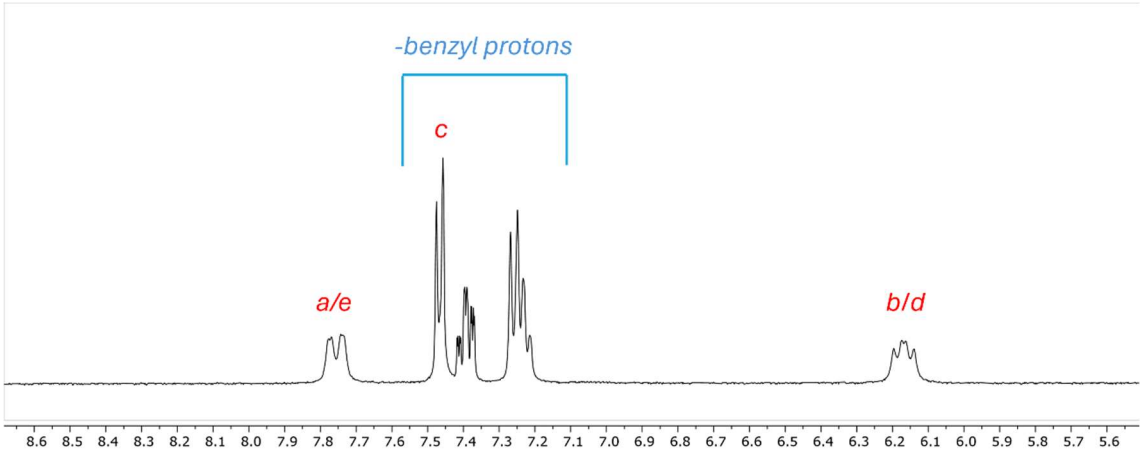

*Figure 65: Aromatic region of the ^{1}H NMR spectrum of commercially purchased Cyanine-7 NHS in MeOH-d_4. Peaks are observed at 7.75 ppm (m, **a/e**, 2H), 7.46 (m, **c** and benzyl group, 3H), 7.39 (m, 2H, benzyl group), 7.25 (m, 4H, benzyl group) and 6.17 ppm (m, **b/d**, 2H). See Figure 64 for assignments.*

Upon conjugation to CNCbl, similar characteristic Cyanine7 proton signals were identified (Figure 66). Correlations in the COSY spectrum assisted in assigning the peaks as 7.73-7-78 (m, 2H, **a** and **e**) and 6.15-6.19 ppm (m, 2H, **b** and **d**) (Figure 67). The three proton resonances at 7.45-7.47, 7.37-7.42 and 7.21-7.27 ppm show correlations in the COSY spectrum and can be assigned to the eight protons of the benzyl moieties. The peak at 7.73-7.78 ppm, which previously appeared as a broad doublet, in Figure 65, now

presents as a multiplet. Furthermore, the protons at 7.21-7.27 and 6.15-6.19 ppm integrate to 5H and 3H, rather than the 4H and 2H shown in Figure 65. This is due to overlapping with the two CNCbl proton signals at 7.21 (B4) and 6.22 ppm (R1). The remaining CNCbl protons are observed at 6.03 (C10), 6.57 (B4) and 7.14 ppm (B2). These resonances are similar to those observed for both **1** and CNCbl.

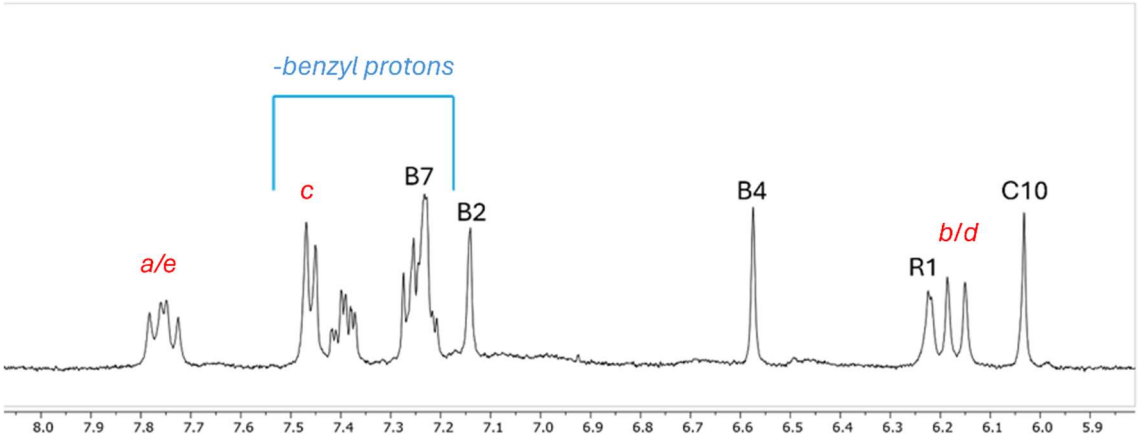

*Figure 66: Aromatic region of the ^{1}H NMR spectrum of **7** obtained in MeOH-d_4. Peaks have been assigned as 6.03 (C10, 1H), 6.15-6.19 (**b/d**, 2H), 6.22 (R1, 1H), 6.57 (B4, 1H), 7.14 (B2, 1H), 7.21-7.27 (B7 and benzyl protons, 5H), 7.37-7.42 (benzyl protons, 2H), 7.45-7.47 (**c** and benzyl protons, 3H) and 7.73-7.78 (2H, **a/e**) ppm.*

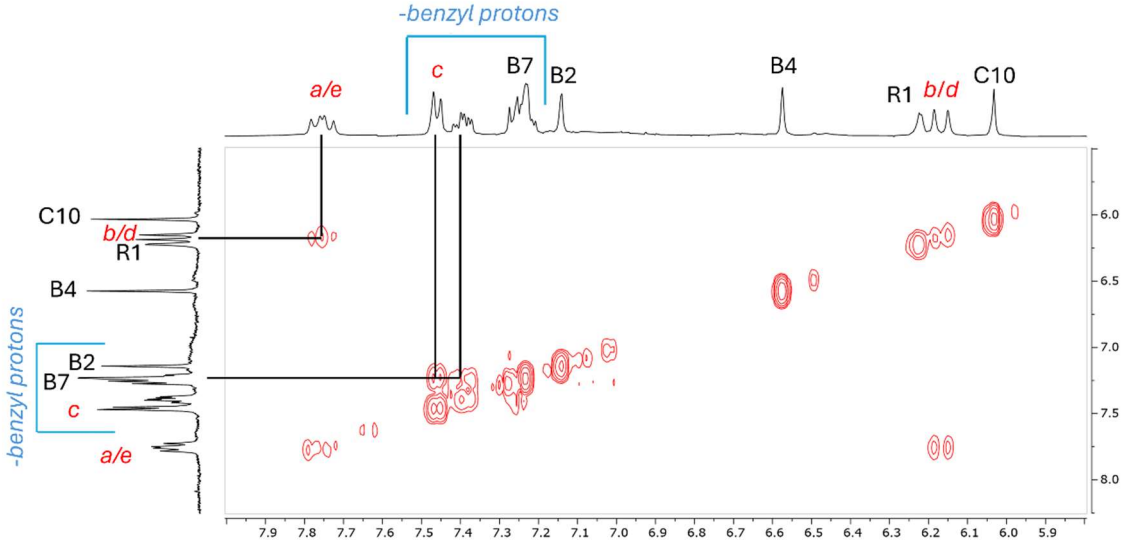

*Figure 67: Aromatic regions of the COSY spectrum of **7** in MeOH-d_4 highlighting correlations between Cyanine7 proton residues at 6.15-6.19 (m, **b/d**, 2H) and 7.73-7.78 ppm (m, 2H, **a/e**). Correlations are highlighted between peaks assigned to the eight protons of the benzyl moieties at 7.21-7.27 (m, 5H), 7.37-7.42(m, 2H) and 7.45-7.47 ppm (m, 3H).*

Further analysis of the low-field region of the ^{1}H NMR spectra was undertaken for both compound **7** and the Cyanine7-NHS starting material. The NHS ester of Cyanine7 has large peaks at 1.71 (m, 12H, **i/i'**), 2.83 (s, 4H) and 3.60 (s, 3H, **j**) ppm (Figure 68). This is similar to what was found for the sulfo-Cyanine5 moiety. The peak at 1.71 ppm has been assigned to the four CH_3 moieties (**i/i'**), with the peak at 3.60 ppm assigned to the N-CH_3 protons (**j**) (Figure 64). The peak at 2.83 ppm has been assigned to the four protons of the NHS ester moiety. Analysis of the corresponding low-field region of **7** showed the Cyanine7-associated protons at 1.71 (12H) and 3.60 (3H) ppm (

Figure 68). The absence of the peak at 2.85 ppm confirms the absence of the NHS ester moiety as expected upon formation of **7**.

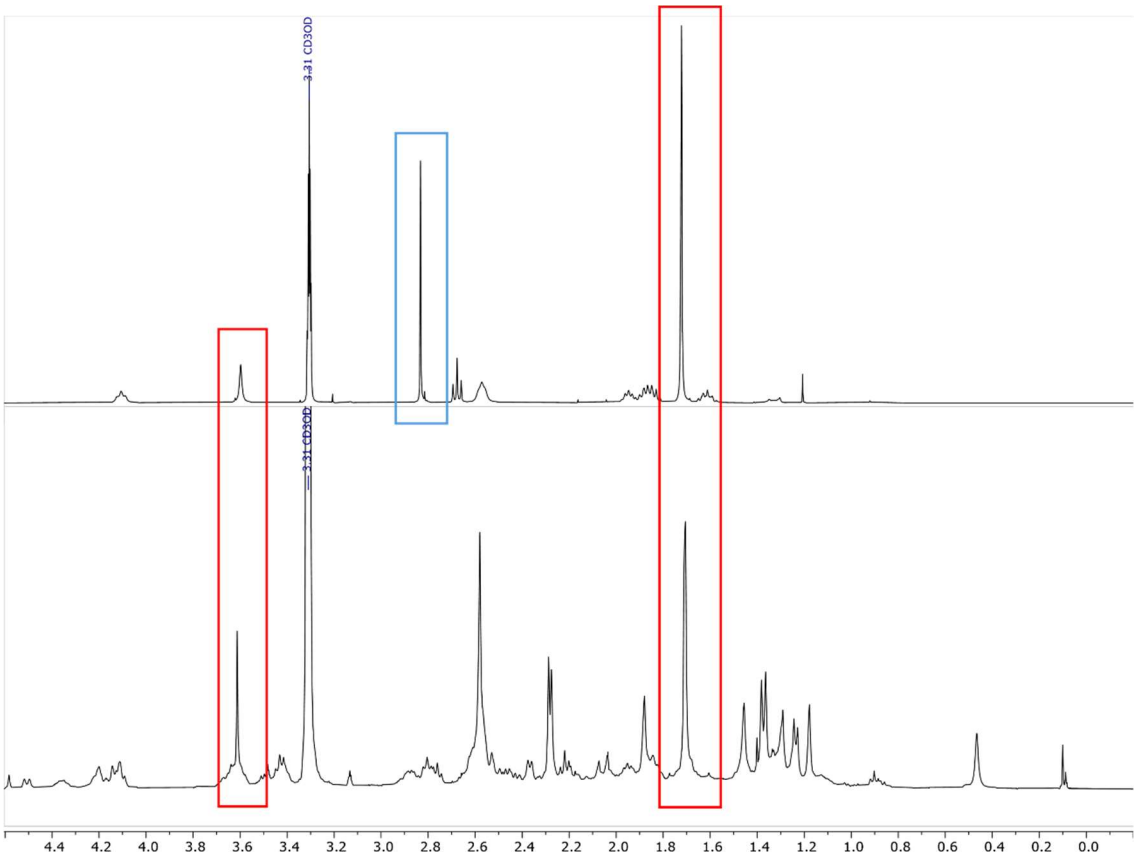

*Figure 68: Low-field ^{1}H NMR spectra of Cyanine7-NHS ester (top) and **7** (bottom). Peaks were assigned to the four CH_3 groups (m, 12H, **i/i'**) and the N-CH_3 (s, 3H, **j**) group in Cyanine7-NHS and **7** highlighted in red. The NHS ester protons are highlighted in blue and are absent in **7**.*

Further NMR spectroscopic analysis was conducted in DMSO-d_6 where the ^{1}H NMR spectrum became more complex. However, the COSY analysis allowed for the

identification of the proton multiplets corresponding to the Cyanine7 moiety as 7.71-7.66, 7.58-7.56, 7.41-7.39, 7.24-7.19 and 6.17-6.13 ppm (2H) (Figure 69). The peaks at 7.71-7.66 and 6.17-6.13 ppm (2H) show correlations in the COSY spectrum and have been assigned as **a/e** and **b/d**, respectively. These peaks are expected to integrate to two protons each, however, the peaks between 7.71-7.66 ppm integrate to four protons as this overlaps with amide protons of CNCbl. The peaks at 7.58-7.56, 7.41-7.39 and 7.24-7.19 ppm show correlations in the COSY spectrum and have been assigned to the two benzyl moieties of Cyanine7. Proton **c** could not be confidently identified as it has no correlations in the COSY spectrum and likely overlaps with other Cyanine7 and amide protons of CNCbl. The aromatic protons on the CNCbl moiety have been assigned as 5.88 (C10, 1H), 6.27 (R1, 1H), 6.43 (B4, 1H), 7.08 (B2, 1H) and 7.35 (B7) ppm. The peak corresponding to B7 has not been integrated as it overlaps with Cyanine7 and amide proton resonances.

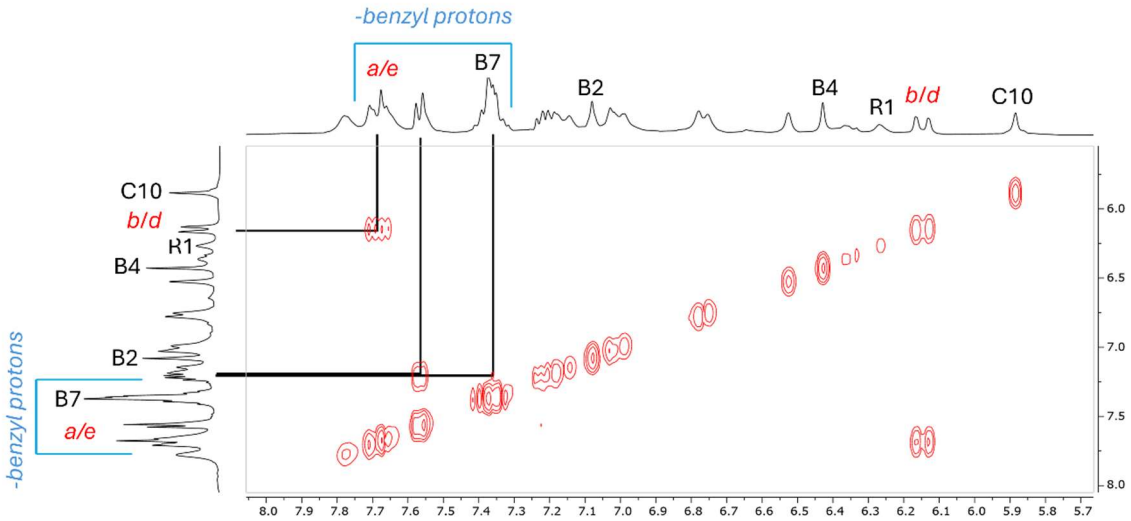

*Figure 69: Aromatic region of the COSY NMR spectrum of **7**. The correlations between the Cyanine7 protons are highlighted. Peaks have been assigned to 7.71-7.66 (m, 2H, **a/e**), 7.56-7.68 (m, 3H, benzyl protons and **c**), 7.41-7.32 (m, 2H, benzyl protons), 7.24-7.19 (m, benzyl protons and B7, 5H), 7.08 (B2, 1H), 6.43 (B4, 1H), 6.27 (R1, 1H), 6.17-6.13 (**b/d**, 2H) and 6.03 (C10, 1H) ppm.*

Finally, HSQC analysis allowed for the assignment of correlations for protons and their corresponding carbon signals of the Cyanine7 moiety. Carbon peaks that correlate to the Cyanine7 proton signals are 99.64, 100.14, 122.27, 122.38, 124.39, 124.46, 128.36, 128.39, 147.27 and 147.77 ppm (Figure 70). Thirteen carbon atoms are expected to be present in the aromatic region of the ^{13}C NMR spectrum of **7**; however, only ten peaks

were observed. The low signal-to-noise in the carbon spectrum and the pseudo symmetry of the Cyanine7 molecule are the likely causes of missing and/or overlapping carbon peaks. The remaining five HSQC correlations have been assigned to the expected CNCbl residues. Protons are assigned as 5.88 (C10), 6.27 (R1), 6.43 (B4), 7.08 (B2) and 7.35 (B7) ppm. Correlated carbon peaks are 93.35, 85.98, 116.36, 142.24 and 110.85 ppm, respectively. These chemical shifts are very similar to both CNCbl and compound **1**.

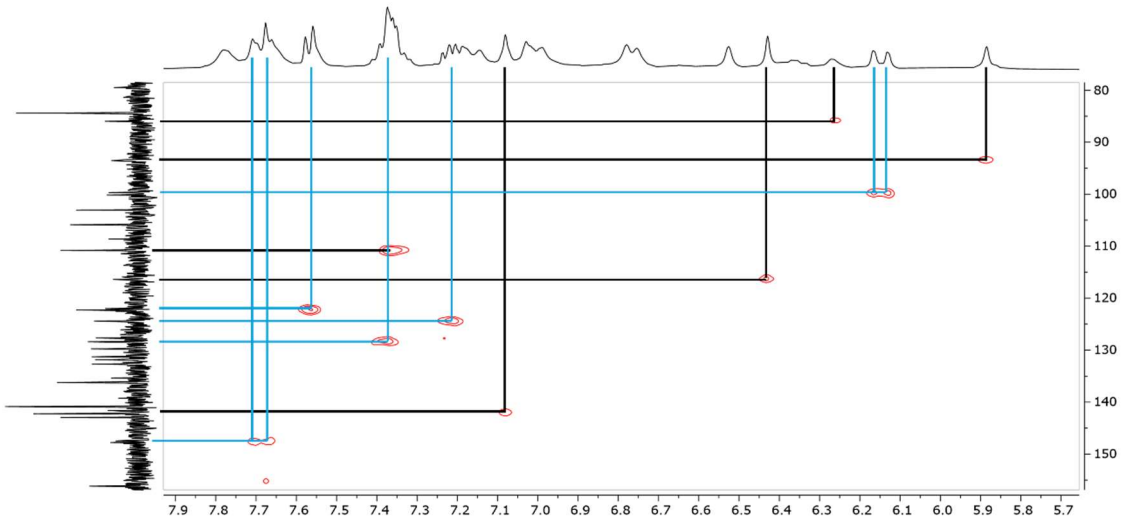

Figure 70: Aromatic region of the HSQC spectrum of 7 highlighting correlations for CNCbl (black) and Cyanine7 (blue).

The formation of **7** was achieved in moderate yields (60%). Analysis by ^{1}H NMR spectroscopy and LC-MS indicates purity of ≥ 95%.

Compound 8

The synthesis of compound **8** is analogous to that of compounds **5**, **6** and **7** (Scheme 9). Cyanine7-NHS ester was utilised as the limiting reagent. The reaction was followed by LC-MS and reached completion within 24 h.

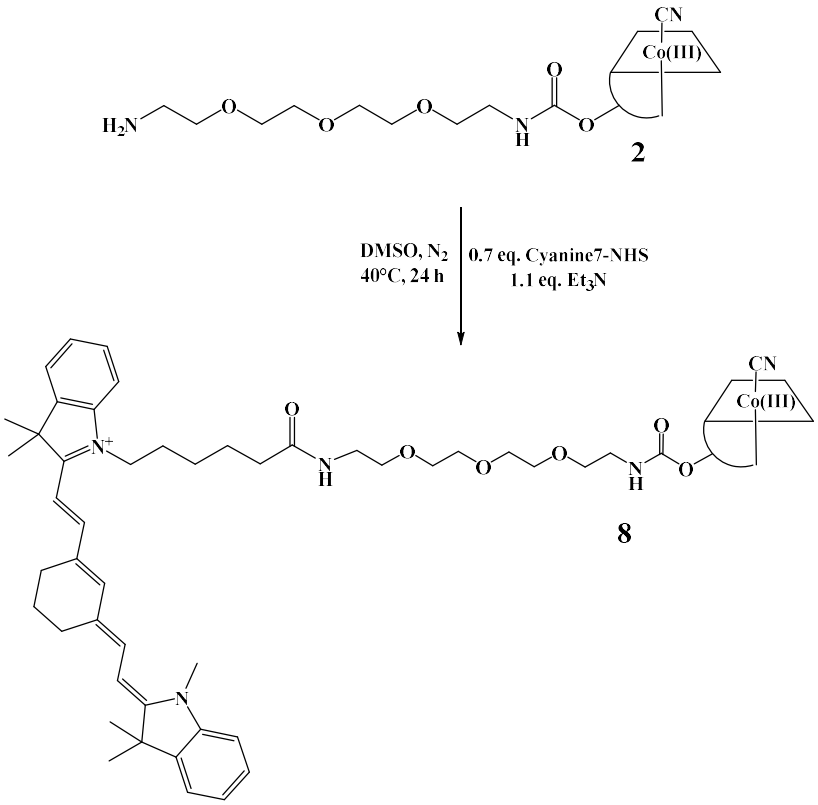

*Scheme 9: Synthetic scheme for the synthesis of **8**.*

Analysis of the crude product mixture was carried out by LC-MS. Two peaks were observed at 16.9 and 30.6 min (Figure 71). The peak at 16.9 min is assigned to unreacted CNCbl from the crude **2** starting material ($C_{63}H_{88}CoN_{14}O_{14}P$, calcd. *m/z* $[M+H]^+$ = 1355.6 and $[M+2H]^{2+}$ = 678.3; found 1355.4 and 678.4). A small peak was observed in the DAD at 19.8 min but was not observed in the TIC chromatogram. The retention time of this peak suggests that it is the CNCbl-PEG-CNCbl dimer previously observed in the syntheses **2**, **4** and **6** (retained at 19.8 min in all analyses). The desired product retains at 30.6 min ($C_{109}H_{149}CoN_{18}O_{19}P$, calcd. *m/z* $[M+H]^{2+}$ = 1053.0 and $[M+2H]^{3+}$ = 702.3; found 1052.8 and 702.2).

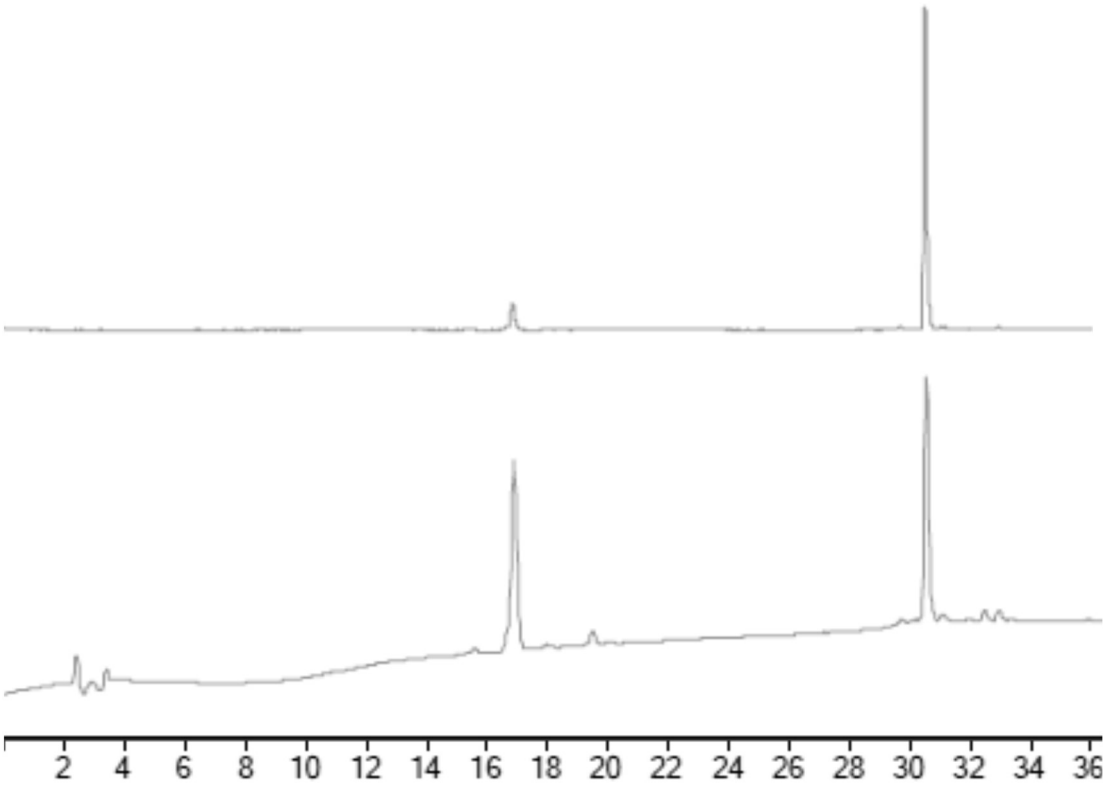

*Figure 71: LC-MS TIC (top) and DAD (bottom, 361 nm) chromatograms of crude **8** (LC-MS method 3). Peaks at 16.9 and 19.6 min can be assigned to CNCbl and the CNCbl-PEG-CNCbl dimer, respectively. The peak at 30.6 min is assigned to **8** ($C_{109}H_{149}CoN_{18}O_{19}P$, calcd. m/z $[M+H]^{2+}$ = 1053.0 and $[M+2H]^{3+}$ = 702.3; found 1052.8 and 702.2).*

Purification of **8** was carried out by reversed-phase C18 chromatography. Two coloured bands were collected, one red and the other indigo. Analogous to that seen during the purification of **7**, adding formic acid was necessary to elute the Cyanine7-containing product. The indigo band was taken to dryness and analysed for purity by LC-MS (Figure 72). One single peak eluting at 30.7 min was assigned to **8** ($C_{109}H_{149}CoN_{18}O_{19}P$, calcd. *m/z* $[M+H]^{2+}$ = 1053.0 and $[M+2H]^{2+}$ = 702.3; found 1052.7 and 702.3). No other peaks were identified in either the TIC or the DAD chromatogram, and the purity was estimated as $\geq$ 95%.

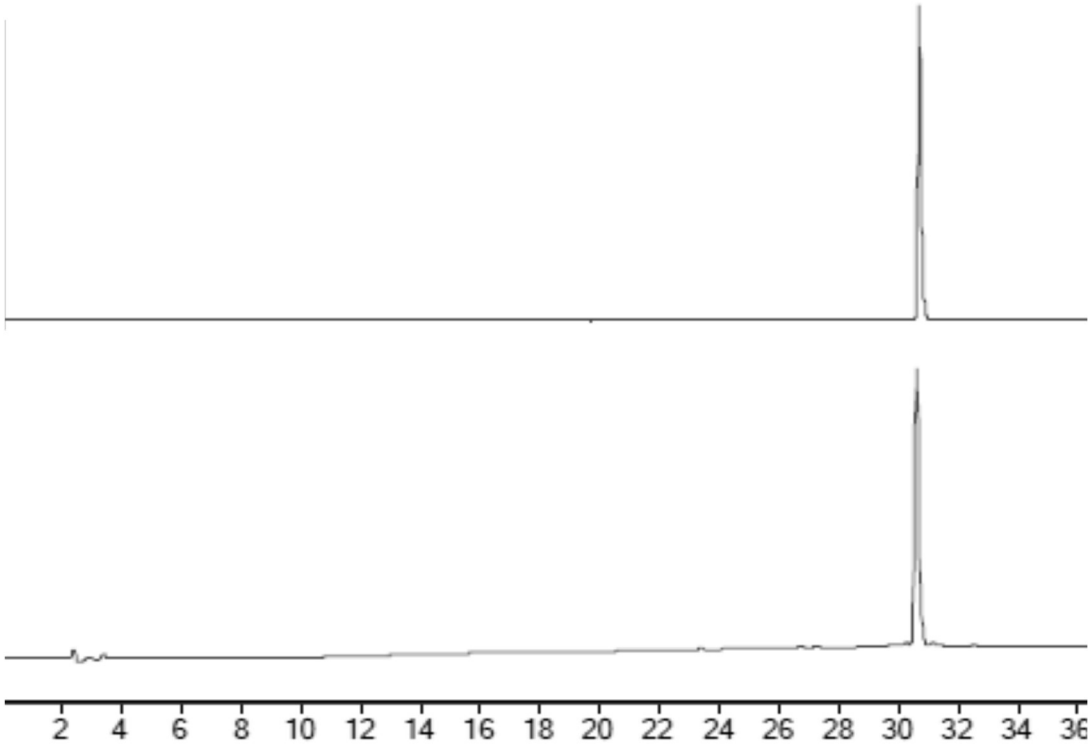

*Figure 72: LC-MS TIC (top) and DAD (bottom, 361 nm) chromatograms of pure **8** (LC-MS method 3). The peak at 30.7 min can be assigned to **8** ($C_{109}H_{149}CoN_{18}O_{19}P$, calcd. m/z $[M+H]^{2+}$ = 1053.0 and $[M+2H]^{2+}$ = 702.3; found 1052.7 and 702.3).*

NMR analysis was first carried out in MeOH-d_4 to further assess the purity of **8**. As observed previously in **7**, the aromatic signals for the Cyanine7 residue can be distinguished from the CNCbl peaks by COSY analysis. The CNCbl protons do not show COSY correlations whereas the Cyanine7 protons do (Figure 67). As observed in both Cyanine7 and compound **7**, correlations are observed between the methine chain protons at 7.71-7.78 and 6.15-6.19 ppm. The remaining protons of the benzyl moieties of Cyanine7 at 7.47-7.45, 7.42-7.37 and 7.27-7.21 ppm also showed correlations in the COSY spectrum.

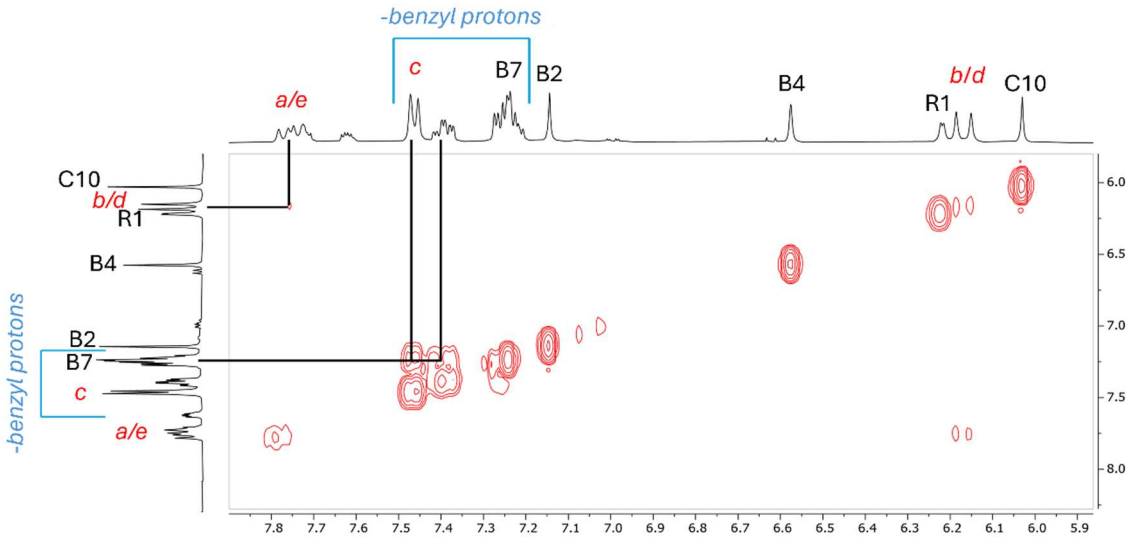

*Figure 73: COSY spectrum of the aromatic region for **8** obtained in MeOH-d_4 highlighting correlations between the Cyanine7 protons.*

The characteristic Cyanine7 protons for **8** have been assigned as 7.78-7.71 (m, 2H, **a** and **e**), 7.47-7.45 (m, 3H, benzyl moieties and **c**), 7.42-7.37 (m, 2H, benzyl moieties), 7.27-7.21 (m, 5H, benzyl moieties and B7) and 6.19-6.15 (m, 2H, **b** and **d**) ppm (Figure 74, see Figure 64 for assignments). As observed in compound **7**, the resonance at 7.21-7.27 ppm contains overlapping peaks for B7 of CNCbl and four benzyl protons of the Cyanine7 moiety. The CNCbl peaks are assigned as 6.03 (s, C10, 1H), 6.22 (m, R1, 1H), 6.58 (s, B4, 1H), 7.14 ppm (s, B2, 1H) and 7.26 ppm (s, B7, 1H). The ^{1}H NMR spectrum does show the presence of impurities with smaller peaks at 7.62, 6.99 and 6.62 ppm. The largest impurity peak at 7.62 ppm integrated for 0.05 protons in comparison to the other product peaks. The impurity is unlikely to be due to unreacted Cyanine7 fluorophore as the proton signals do not correspond to those seen in Figure 65. Cyanine7 is prone to degradation by light, it is proposed that the impurity peaks represent a small amount of degradation products. Compound **8** was columned a total of three times; after each column the impurities decreased. Due to the significant loss of compound during column chromatography (~10% loss per column) and the impurity being absent in the LC-MS chromatogram, the product was determined to be ≥95% pure.

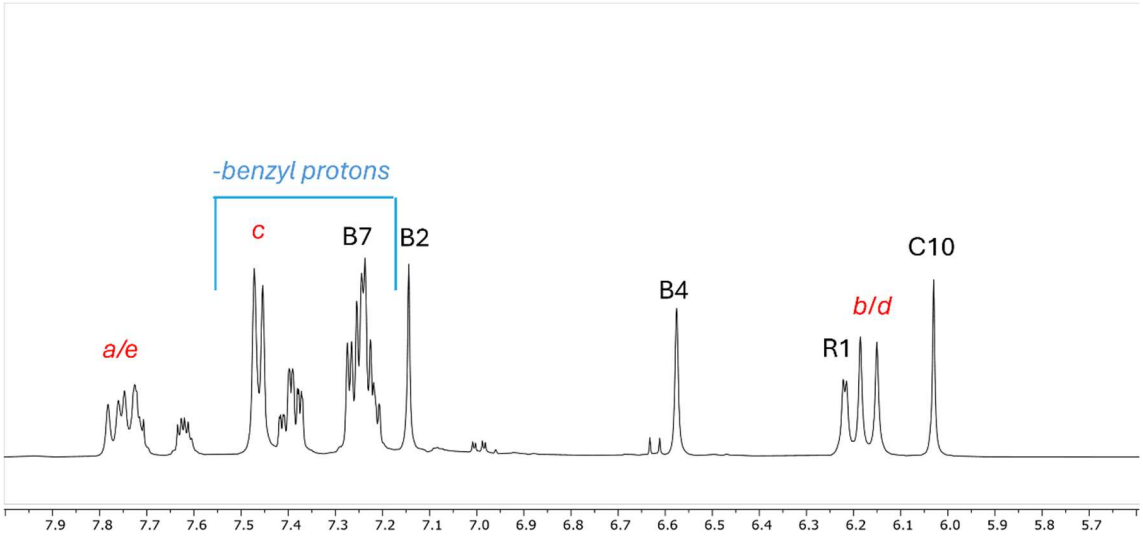

*Figure 74: Aromatic ^{1}H NMR spectrum of **8** obtained in MeOH-d_4. Peaks have been assigned as 7.78-7.71 (m, 2H, **a/e**), 7.47-7.45 (m, 3H, benzyl moieties and **c**), 7.42-7.37 (m, 2H, benzyl moieties), 7.27-7.21 (m, 5H, benzyl moieties and B7), 7.14 (s, 1H, B7), 6.58 (s, 1H, B4), 6.22 (m, 1H, R1), 6.19-6.15 (m, 2H, **b/d**) and 6.03 ppm (s, 1H, C10). Small impurities are observed at 7.62, 6.99 and 6.62 ppm, likely from Cyanine7 degradation products.*

Investigation into the low-field region of the ^{1}H NMR spectrum obtained in MeOD-d_4 further supported the formation of compound **8**. Characteristic peaks for the Cyanine7-NHS ester starting material have been assigned at 1.71 (m, 12H, **i/i'**), 2.83 (s, 4H) and 3.60 (s, 3H, **j)** ppm (Figure 68). The multiplet at 1.71 ppm corresponds to the four CH_3 moieties highlighted (**i/i'**), with the peak at 3.61 ppm assigned to the N-CH_3 protons (**j**) (Figure 64). The peak at 2.83 ppm has been assigned to the four protons of the NHS ester moiety. Analysis of the corresponding low-field region of **8** showed the Cyanine7-associated protons at 1.71 (12H, **i/i'**), and 3.61 (3H, **j**) ppm (

Figure 68). The absence of the peak at 2.85 ppm confirms the absence of the NHS ester moiety as expected upon formation of **8**.

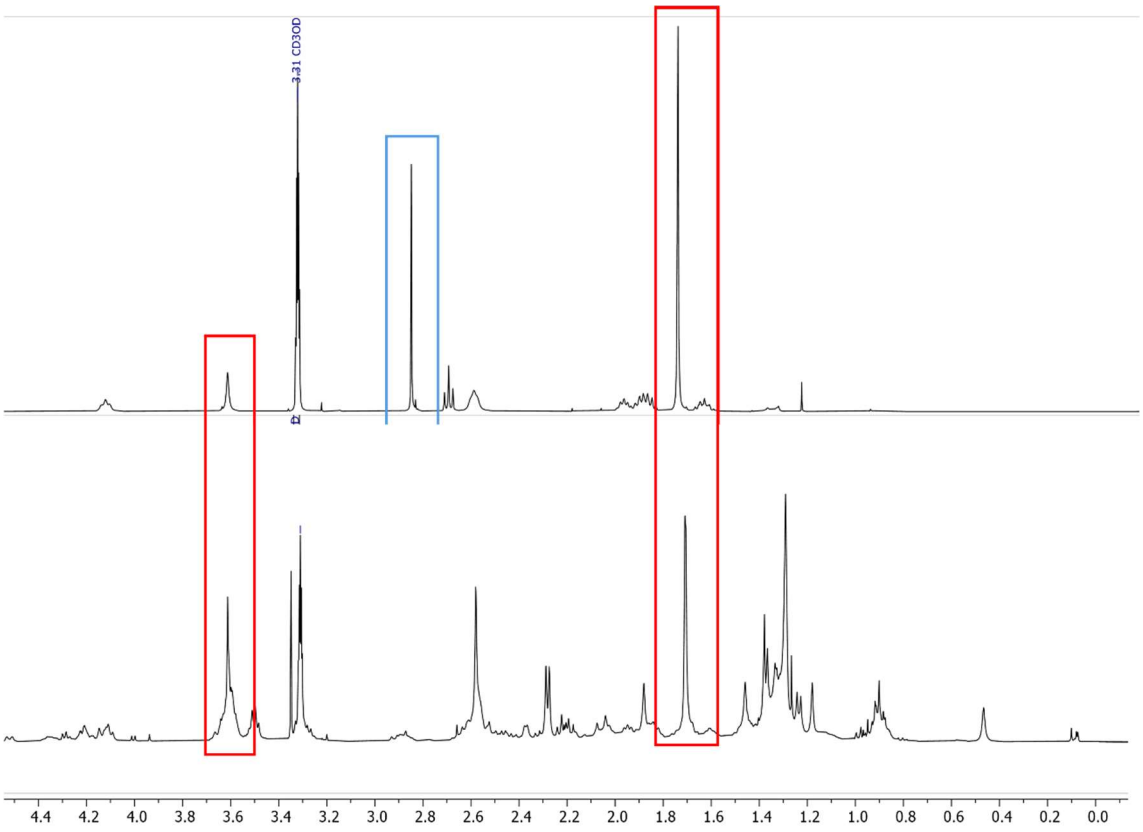

*Figure 75: Stacked low-field region of the ^{1}H NMR spectra of Cyanine7-NHS ester (top) and **8** obtained in MeOD-d_4. Peaks were assigned to the four CH_3 groups (**i/i'**, Figure 64) and the N-CH_3 (**j**, Figure 64) group in both Cyanine7 and **8** highlighted in red. The NHS ester protons are highlighted in blue, absent from **8**.*

Further NMR spectroscopic analysis was conducted in DMSO-d_6 where the ^{1}H NMR spectrum became more complex. The COSY spectrum obtained in DMSO-d_6 showed correlations between the three multiplets at 7.58-7.56, 7.39-7.35 and 7.24-7.19 ppm which have been assigned to the benzyl moiety protons of Cyanine7. Correlations were observed for peaks at 7.71-7.66 and 6.16-6.13 ppm which have been assigned to **a/e** and **b/d**, respectively (see Figure 64 for assignments). The proton **f** could not be confidently assigned due to the complexity of the spectrum and the lack of correlation in the COSY spectrum. Proton signals of the nucleotide and corrin ring of CNCbl have been assigned at 5.89 (s, 1H, C10), 6.23 (m, 1H, R1), 6.43 (s, 1H, B4), 7.08 (s, 1H, B2) and 7.35 ppm (B7). The peak for B7 overlaps with the Cyanine7 peaks between 7.35 and 7.39 ppm and integrations could not be determined.

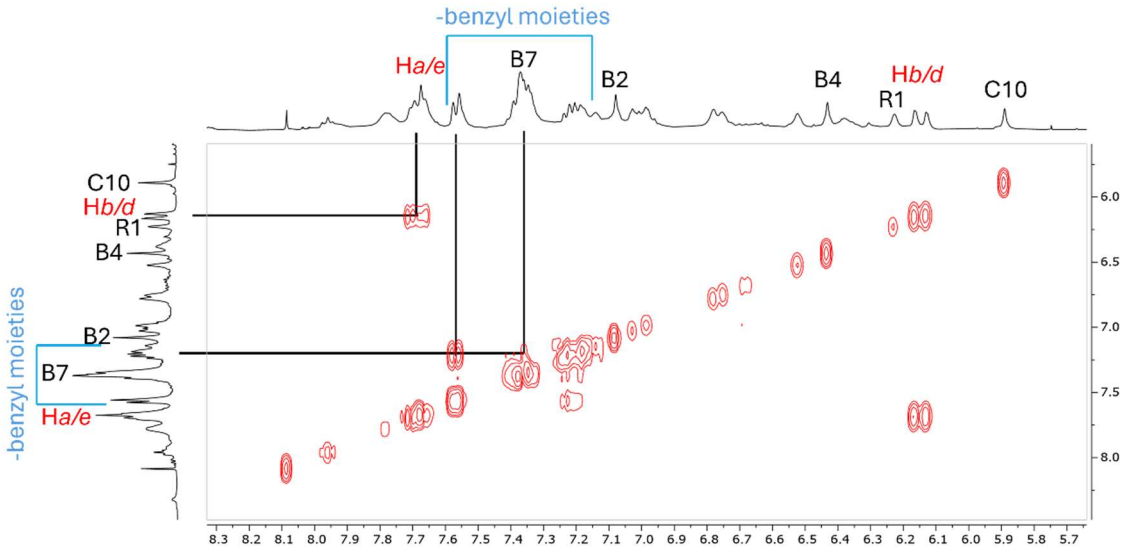

*Figure 76: COSY spectrum of **8** obtained in DMSO-d_6. Correlations between the Cyanine7 protons are highlighted. Peaks are assigned as 7.71-7.66 (**a/e**), 7.58-7.56 (benzyl protons), 7.39-7.35 (benzyl protons and B7), 7.24-7.19 (benzyl protons), 7.08 (B2), 6.43 (B4), 6.23 (R1), 6.16-6.13 (**b/d**) and 5.89 ppm (C10).*

The HSQC spectrum obtained in DMSO-d_6 was used to assign the five CNCbl carbon peaks associated with the nucleotide, ribose and corrin ring. These have been assigned as 93.49 (C10), 85.74 (R1), 116.26 (B4), 142.11 (B2) and 110.83 (B7) ppm (Figure 77). The peak positions are very similar to both CNCbl and compound **2**. The proton signals for Cyanine7 were used to identify corresponding carbon signals as 99.68, 100.15, 122.29, 122.35, 122.39, 124.41, 124.54, 128.41, 128.46, 147.49 and 147.78 ppm (Figure 77). Again, 13 ^{13}C carbon peaks were expected in the aromatic region of the NMR spectrum for the Cyanine7 moiety; however, only 11 were observed. This is likely due to overlapping carbon peaks.

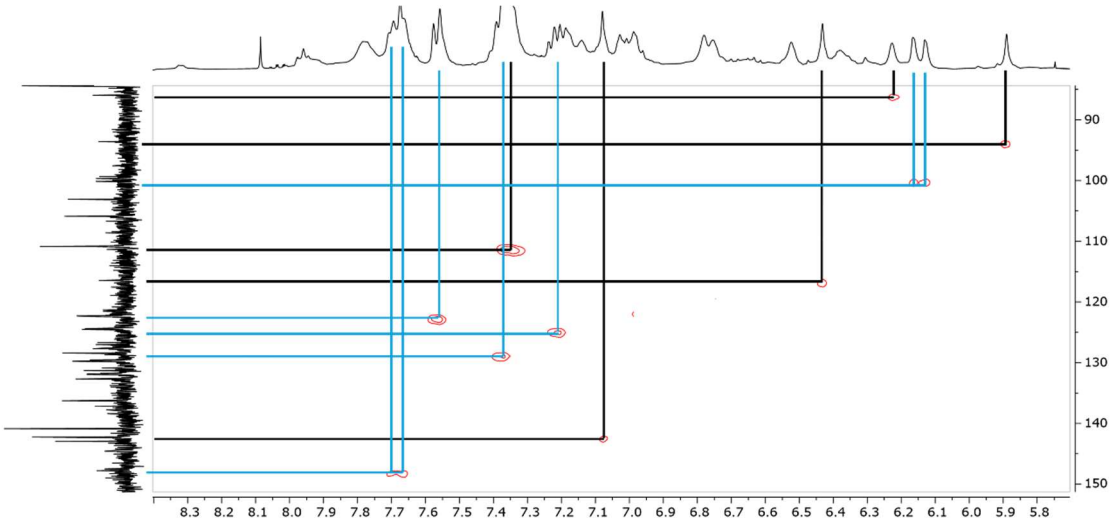

Figure 77: HSQC spectrum of the aromatic proton region of ***8*** *obtained in DMSO-d_6. Correlations between the Cyanine7 protons and carbons are shown in blue, and correlations for the CNCbl moiety protons and carbons are shown in black.*

The formation of **8** was achieved in high yields (86%). Analysis by ^{1}H NMR spectroscopy and LC-MS indicates a purity of ≥95%.

2.4 Conclusion

The synthesis of CNCbl-linker conjugates containing both cystamine and polyethylene glycol linkers (conjugates **1** and **2**) has been outlined with yields of 78-80%. Attachment of the linkers to CNCbl was achieved by carbamate bond formation between the 5'-OH group of CNCbl and the primary amine of the desired linker, facilitated by CDT. A robust purification method was developed for the CNCbl-linker molecules by preparative reversed-phase C18 chromatography, allowing ~200 mg of crude material to be purified at once. The synthesis of novel CNCbl-linker-fluorophore conjugates of commercially available NBD-X, sulfo-Cyanine5-NHS and Cyanine7-NHS fluorophores has been recorded (conjugates **3-8**) with yields between 54-92%. Synthesis of the fluorescent conjugates was achieved by amide coupling. Attachment of the NBD-X fluorophore to the CNCbl-linker molecule was carried out using EDC and HOBt as coupling reagents. HOBt was necessary to prevent the formation of the unreactive *N*-acyl urea byproduct of EDC. Sulfo-Cyanine5 and Cyanine7 were purchased as activated NHS esters which readily underwent substitution by the amine of the CNCbl-linker molecules with no need for EDC or HOBt. LC-MS chromatography was utilised throughout to analyse crude

reaction mixtures. Analysis of the sulfo-Cyanine5 conjugates showed CH_3OH supressed ionisation but this could be remedied by using pure H_2O. Purification of the CNCbl conjugates proved to be a difficult task. A robust reversed-phase C18 purification procedure has been developed for the difficult-to-purify CNCbl conjugates. Purification of Cyanine7 and Cyanine7-containing compounds required the addition of formic acid (0.1% v/v) in the aqueous component. Stability studies were carried out for **3** over 24 h at 37°C (with shaking) in multiple biological media. No changes or degradation was observed by LC-MS, indicating the conjugates are stable in biological conditions. All conjugates have been analysed by LC-MS chromatography, ^{1}H, ^{13}C and 2D NMR spectroscopy in addition to HRMS to confirm both the identity and purity of each sample (≥90%).

2.4.1 References

(1) Proinsias, K.; Giedyk, M.; Gryko, D. Vitamin B_{12}: Chemical Modifications. *Chem. Soc. Rev.* **2013**, *42* (16), 6605–6619. https://doi.org/10.1039/c3cs60062a.
(2) Gruber, K.; Puffer, B.; Kräutler, B. Vitamin B_{12}-Derivatives—Enzyme Cofactors and Ligands of Proteins and Nucleic Acids. *Chem. Soc. Rev.* **2011**, *40* (8), 4346–4363. https://doi.org/10.1039/c1cs15118e.
(3) Bridwell-Rabb, J.; Drennan, C. L. Vitamin B_{12} in the Spotlight Again. *Curr. Opin. Chem. Biol.* **2017**, *37*, 63–70. https://doi.org/10.1016/j.cbpa.2017.01.013.
(4) Lawrence, A. D.; Nemoto-Smith, E.; Deery, E.; Baker, J. A.; Schroeder, S.; Brown, D. G.; Tullet, J. M. A.; Howard, M. J.; Brown, I. R.; Smith, A. G.; Boshoff, H. I.; Barry, C. E.; Warren, M. J. Construction of Fluorescent Analogs to Follow the Uptake and Distribution of Cobalamin (Vitamin B 12) in Bacteria, Worms, and Plants. *Cell Chemical Biology*. https://doi.org/10.1016/j.chembiol.2018.04.012.
(5) Mundwiler, S.; Spingler, B.; Kurz, P.; Kunze, S.; Alberto, R. Cyanide-Bridged Vitamin B_{12}-Cisplatin Conjugates. *Chem. - Eur. J.* **2005**, *11* (14), 4089–4095. https://doi.org/10.1002/CHEM.200500117.
(6) Ruiz-Sánchez, P.; Mundwiler, S.; Alberto, R. Syntheses of Fluorescent Vitamin B_{12}-Pt(II) Conjugates and Their Pt(II) Release in a Spectroelectrochemical Assay. *CHIMIA* **2007**, *61* (4), 190. https://doi.org/10.2533/chimia.2007.190.
(7) Vortherms, A. R.; Kahkoska, A. R.; Rabideau, A. E.; Zubieta, J.; Andersen, L. L.; Madsen, M.; Doyle, R. P. A Water Soluble Vitamin B_{12}-Re(i) Fluorescent Conjugate for Cell Uptake Screens: Use in the Confirmation of Cubilin in the Lung Cancer Line A549. *Chem. Commun.* **2011**, *47* (35), 9792. https://doi.org/10.1039/c1cc13615a.
(8) Fedosov, S. N.; Fedosova, N. U.; Kräutler, B.; Nexø, E.; Petersen, T. E. Mechanisms of Discrimination between Cobalamins and Their Natural Analogues during Their Binding to the Specific B_{12}-Transporting Proteins. *Biochemistry* **2007**, *46* (21), 6446–6458. https://doi.org/10.1021/BI062063L.
(9) McGreevy, J. M.; Cannon, M. J.; Grissom, C. B. Minimally Invasive Lymphatic Mapping Using Fluorescently Labeled Vitamin B_{12}. *J. Surg. Res.* **2003**, *111* (1), 38–44. https://doi.org/10.1016/S0022-4804(03)00093-3.
(10) Gendron, L. N.; Zites, D. C.; LaRochelle, E. P. M.; Gunn, J. R.; Pogue, B. W.; Shell, T. A.; Shell, J. R. Tumor Targeting Vitamin B_{12} Derivatives for X-Ray Induced Treatment of Pancreatic Adenocarcinoma. *Photodiagnosis Photodyn. Ther.* **2020**, *30*, 101637. https://doi.org/10.1016/j.pdpdt.2019.101637.
(11) Viola-Villegas, N.; Rabideau, A. E.; Bartholoma, M.; Zubieta, J.; Doyle, R. P. Targeting the Cubilin Receptor through the Vitamin B_{12} Uptake Pathway: Cytotoxicity and Mechanistic Insight through Fluorescent Re(I) Delivery. *J. Med. Chem.* **2009**, *52* (16), 5253–5261. https://doi.org/10.1021/JM900777V.
(12) Kalaiyarasan, G.; Joseph, J. Determination of Vitamin B_{12} via pH-Dependent Quenching of the Fluorescence of Nitrogen Doped Carbon Quantum Dots. *Microchim. Acta* **2017**, *184* (10), 3883–3891. https://doi.org/10.1007/s00604-017-2421-y.
(13) Haghdoost, M. M.; Sauvageau, E.; Oguadinma, P.; Tran, H. V.; Lefrancois, S.; Castonguay, A. Cu-Catalyzed Click Conjugation of Cobalamin to a BODIPY-Based Fluorophore: A Versatile Tool to Explore the Cellular Biology of Vitamin B_{12}. *J. Inorg. Biochem.* **2020**, *210*. https://doi.org/10.1016/j.jinorgbio.2020.111105.
(14) Fredericksen, J.; Brasch, N. Synthesis of Fluorescent Conjugates of Vitamin B_{12}; Auckland University of Technology, **2019**.
(15) Fredericksen, J.; Brasch, N.; Seale, B. Developing Fluorescent Vitamin B_{12} Analogues as Tools to Assess the Potential of Vitamin B_{12} in the Delivery of Antimicrobial Agents; Auckland University of Technology, **2020**.

(16) Ng, Y. M.; Mat Yusuf, S. N. A.; Chiu, H. I.; Lim, V. Redox-Sensitive Linear and Cross-Linked Cystamine-Based Polymers for Colon-Targeted Drug Delivery: Design, Synthesis, and Characterisation. *Pharmaceutics* **2020**, *12* (5), 461. https://doi.org/10.3390/pharmaceutics12050461.
(17) Thomas, J. D.; Burke, T. R. Application of a Water-Soluble Pyridyl Disulfide Amine Linker for Use in Cu-Free Click Bioconjugation. *Tetrahedron Lett.* **2011**, *52* (33), 4316–4319. https://doi.org/10.1016/j.tetlet.2011.06.042.
(18) de Weers, O.; Beurret, M.; van Buren, L.; Oomen, L. A.; Poolman, J. T.; Hoogerhout, P. Application of Cystamine and *N*,*N* ‘-Bis(Glycyl)Cystamine as Linkers in Polysaccharide−Protein Conjugation. *Bioconjug. Chem.* **1998**, *9* (3), 309–315. https://doi.org/10.1021/bc9702011.
(19) Równicki, M.; Wojciechowska, M.; Wierzba, A. J.; Czarnecki, J.; Bartosik, D.; Gryko, D.; Trylska, J. Vitamin B_{12} as a Carrier of Peptide Nucleic Acid (PNA) into Bacterial Cells. *Sci. Rep.* **2017**, *7* (1). https://doi.org/10.1038/s41598-017-08032-8.
(20) Russell-Jones, G. J.; Westwood, S. W.; Habberfield, A. D. Vitamin B_{12} Mediated Oral Delivery Systems for Granulocyte-Colony Stimulating Factor and Erythropoietin. *Bioconjug. Chem.* **1995**, *6* (4), 459–465. https://doi.org/10.1021/bc00034a016.
(21) Wierzba, A.; Wojciechowska, M.; Trylska, J.; Gryko, D. Vitamin B_{12} Suitably Tailored for Disulfide-Based Conjugation. *Bioconjug. Chem.* **2016**, *27* (1), 189–197. https://doi.org/10.1021/acs.bioconjchem.5b00599.
(22) Giovengo, A. S. B_{12} Conjugates for Intracellular Tracking and Drug Delivery. **2019**, Kent State University,
(23) Horton, R. A.; Bagnato, J. D.; Grissom, C. B. Structural Determination of 5′-OH α-Ribofuranoside Modified Cobalamins via 13C and DEPT NMR. *J. Org. Chem.* **2003**, *68* (18), 7108–7111. https://doi.org/10.1021/jo0340399.
(24) Wahab, M. F.; Armstrong, D.; Patel, D. C. Peak Shapes and Their Measurements: The Need and the Concept Behind Total Peak Shape Analysis. *LCGC North America* **2017**, *35* (12), 846–853.
(25) Dolan, J. Peak Fronting . . . Some of the Time. *LCGC North America*. **2013**, *31* (12), 992–997.
(26) Bonnett, R.; Godfrey, J. M.; Redman, D. G. Cobyric Acid and Related Compounds from Vitamin B_{12}. *J Am Chem Soc.* **1969**, *8*, 1163-1166. https://doi.org/10.1039/J39690001163.
(27) Brodie, J. D.; Poe, M. Proton Magnetic Resonance Studies of Vitamin B_{12}. Proton Magnetic Resonance Spectra of Some Cobalamins and Cobinamides. *Biochemistry* **1971**, *10* (5), 914–922. https://doi.org/10.1021/bi00781a029.
(28) Chandra, T.; Brown, K. L. Vitamin B_{12} and α-Ribonucleosides. *Tetrahedron* **2008**, *64* (1), 9–38. https://doi.org/10.1016/j.tet.2007.08.061.
(29) Calafat, A. M.; Marzilli, L. G. Investigations of B_{12} Derivatives with Inorganic Ligands Using 2D NMR Spectroscopy. Ligand-Responsive Shifts Suggest That the Deoxyadenosyl Moiety in Coenzyme B_{12} Has a Steric Trans Influence. *J Am Chem Soc* **1993**, *115*, 9182–9190.
(30) Chemaly, S. M. Use of ^{13}C and ^{1}H NMR to Determine in Detail the Structures of the Base-off Vitamin B_{12} Complexes Dicyanocobinamide and Dicyanocobalamin. *Polyhedron* **2019**, *174*, 114162. https://doi.org/10.1016/j.poly.2019.114162.
(31) Zhou, K.; Zelder, F. Identification of Diastereomeric Cyano–Aqua Cobinamides with a Backbone-Modified Vitamin B_{12} Derivative and with ^{1}H NMR Spectroscopy. *Eur. J. Inorg. Chem.* **2011**, *2011* (1), 53–57. https://doi.org/10.1002/EJIC.201001146.
(32) Banerjee, S. S.; Aher, N.; Patil, R.; Khandare, J. Poly(Ethylene Glycol)-Prodrug Conjugates: Concept, Design, and Applications. *J. Drug Deliv.* **2012**, *2012*, 1–17. https://doi.org/10.1155/2012/103973.

(33) Abuchowski, A.; van Es, T.; Palczuk, N. C.; Davis, F. F. Alteration of Immunological Properties of Bovine Serum Albumin by Covalent Attachment of Polyethylene Glycol. *J. Biol. Chem.* **1977**, *252* (11), 3578–3581. https://doi.org/10.1016/S0021-9258(17)40291-2.
(34) Pieńko, T.; Czarnecki, J.; Równicki, M.; Wojciechowska, M.; Wierzba, A. J.; Gryko, D.; Bartosik, D.; Trylska, J. Vitamin B_{12}-Peptide Nucleic Acids Use the BtuB Receptor to Pass through the Escherichia Coli Outer Membrane. *Biophys. J.* **2021**, *120* (4), 725–737. https://doi.org/10.1016/J.BPJ.2021.01.004.
(35) Merrifield, B. Solid-Phase Peptide Synthesis. In *Peptides*; Elsevier, **1995**; pp 93–169. https://doi.org/10.1016/B978-012310920-0/50004-8.
(36) Zhou, H.; Ren, T. Recent Progress of Cyanine Fluorophores for NIR-II Sensing and Imaging. *Chem. – Asian J.* **2022**, *17* (8). https://doi.org/10.1002/asia.202200147.
(37) Markova, L. I.; Terpetschnig, E. A.; Patsenker, L. D. Comparison of a Series of Hydrophilic Squaraine and Cyanine Dyes for Use as Biological Labels. *Dyes Pigments* **2013**, *99* (3), 561–570. https://doi.org/10.1016/j.dyepig.2013.06.022.
(38) Mujumdar, S. R.; Mujumdar, R. B.; Grant, C. M.; Waggoner, A. S. Cyanine-Labeling Reagents: Sulfobenzindocyanine Succinimidyl Esters. *Bioconjug. Chem.* **1996**, *7* (3), 356–362. https://doi.org/10.1021/bc960021b.
(39) Cannon, M. J. Protein Binding, Cellular Localization, and Tissue Uptake of Breast Cancer Targeted Fluorescent Cobalamin Analogs. Ph.D., The University of Utah, United States -- Utah. **2001**
(40) Annesley, T. M. Methanol-Associated Matrix Effects in Electrospray Ionization Tandem Mass Spectrometry. *Clin. Chem.* **2007**, *53* (10), 1827–1834. https://doi.org/10.1373/clinchem.2007.090811.
(41) Jiang, C.; Cai, H.; Peng, X.; Zhang, P.; Wu, X.; Tian, R. Targeted Imaging of Tumor-Associated Macrophages by Cyanine 7-Labeled Mannose in Xenograft Tumors. *Mol. Imaging* **2017**, *16*, 153601211668949. https://doi.org/10.1177/1536012116689499.
(42) Zhang, L.; Jia, H.; Liu, X.; Zou, Y.; Sun, J.; Liu, M.; Jia, S.; Liu, N.; Li, Y.; Wang, Q. Heptamethine Cyanine–Based Application for Cancer Theranostics. *Front. Pharmacol.* **2022**, *12*. https://doi.org/10.3389/fphar.2021.764654.
(43) Xiao, L.; Zhang, Y.; Liu, Z.; Yang, M.; Pu, L.; Pan, D. Synthesis of the Cyanine 7 Labeled Neutrophil-Specific Agents for Noninvasive near Infrared Fluorescence Imaging. *Bioorg. Med. Chem. Lett.* **2010**, *20* (12), 3515–3517. https://doi.org/10.1016/j.bmcl.2010.04.136.

Chapter 3 Synthesis and characterisation of fluorescent cobinamide conjugates

3.1 Introduction

This chapter investigates the synthesis and characterisation of novel cobinamide (Cbi) linker conjugates incorporating polyethylene glycol and cystamine linkers. The subsequent synthesis and characterisation of Cbi-linker-fluorophore conjugates incorporating NBD-X, sulfo-Cyanine5 and Cyanine7 is also presented. The synthesis of Cbi derivatives is sparsely documented in the literature.[1–3] In short, Cbi derivatives have focused on modification of the amide side chains or the secondary alcohol. There are a few examples where therapeutic peptides have been conjugated to Cbi and uptake has been assessed in bacterial cell lines.[1,4] The goal of this work is to synthesise fluorescent Cbi conjugates. The Cbi-linker-fluorophore conjugates will then allow the uptake, movement and localisation of this vitamin B_{12} precursor to be tracked within different cell lines.

3.1.1 Synthesis of Cbi-linker molecules

The addition of a linker to Cbi in this research serves two functions. It provides a suitable synthetic functionality (amine) for conjugating a fluorophore and, more importantly, to limit the attached cargo from inhibiting Cbi uptake within cells.[1] The secondary alcohol of Cbi is a convenient site to conjugate the linker. This methodology is based on a literature procedure.[1] The linkers employed in the syntheses are analogous to those used in Chapter 2 for the CNCbl-linker conjugates. This will allow for a direct comparison of cellular uptake between Cbi and Cbl fluorescent conjugates in cell lines in the future. The linkers employed here are the disulfide-containing cystamine linker and the short polyethylene glycol-based linker 1,11-diamino-3,6,9-trioxaundecane (Figure 78).

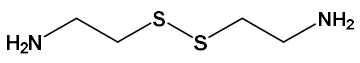

cystamine

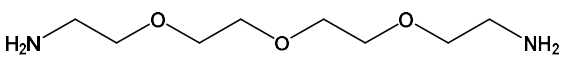

1,11-diamino-3,6,9-trioxaundecane

Figure 78: Structures of the linkers cystamine and 1,11-diamine-3,6,9-trioxaundecane employed in this study.

3.1.2 Synthesis of Cbi-fluorophore conjugates

To the best of our knowledge, no fluorescent Cbi conjugates are published in the literature. The conjugation of a fluorophore to the Cbi-linker has been achieved in this work by peptide bond formation. The selected fluorophores are the same as those used in Chapter 2. Each fluorophore contains either a carboxylic acid or *N*-hydroxysuccinamide ester (NHS) suitable for peptide coupling (Figure 79).

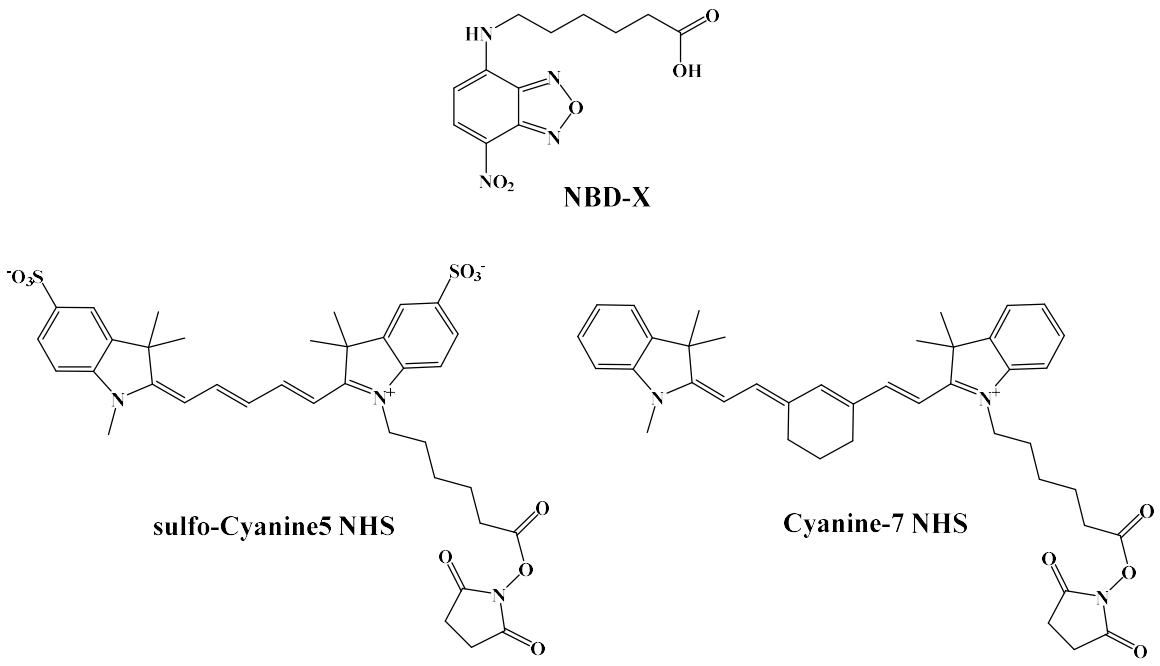

Figure 79: Structures of 6-(N-(7-Nitrobenz-2-oxa-1,3-diazol-4-yl)amino)hexanoic acid (NBD-X), sulfo-Cyanine5 NHS and Cyanine7 NHS esters.

3.2 Experimental

3.2.1 Chemicals

See Chapter 2, section 2.2.1. Silica gel 60 (0.015-0.040 mm), utilised for dry column vacuum chromatography (DCVC) was purchased from EMD Millipore corporation.

3.2.2 Instrumentation

See Chapter 2, section 2.2.2.

3.2.3 General methods

See Chapter 2, section 2.2.3.

Cbi compounds were used as the limiting reagent in all syntheses unless otherwise stated. Dry column vacuum chromatography (DCVC) was used for the purification of dicyanocobinamide ($(CN)_2$Cbi). The column was prepared by dry packing silica (LiChroprep RP-18 40-63 μm) onto a fritted column (13 cm x 3.5 cm). The surface of the silica was flattened using the back of a syringe piston. Tight packing was ensured by fitting a round bottom flask to the bottom of the column and applying a vacuum under the frit overnight. Packing was checked by running hexane (100 mL) through the column to ensure an even solvent band was observed moving through stationary phase. The crude product was dissolved in minimal EtOH (5 mL) and isopropanol (40 mL). Sonication for 10 min was required for complete dissolution. The purple solution was then loaded onto the dry column, ensuring the silica surface was not disturbed. Cotton wool was placed on top of the column to ensure the addition of the mobile phase did not disturb the silica surface. The column was washed with a mobile phase solvent mixture of CH_3OH/CH_2Cl_2 (100 mL aliquots, 15-30% CH_3OH increasing by 2.5% CH_3OH after each addition). The column was taken to dryness by vacuum before increasing the CH_3OH component of the mobile phase. The product eluted at 32.5% CH_3OH. Each product fraction was collected in separate round bottom flasks (~7 fractions in total) and each fraction was taken to dryness by rotary evaporation. The purity of each fraction was established by ^{1}H NMR spectroscopy. Pure fractions were dissolved in minimal CH_3OH and precipitated into Et_2O The precipitate was washed with Et_2O (3 x 15 mL aliquots).

3.2.4 LC-MS methods

Four LC-MS programs were used for the analysis of both the crude and pure products. The mobile phase consisted of milliQ H_2O + 0.1% formic acid (solvent A) and CH_3CN + 0.1% formic acid (solvent B). The mobile phase programs used are as below.

Method 1: 0-2 min isocratic elution 95:5 A:B, 2-30 min from 95:5 to 65:35 A:B and 30-31 from 65:35 to 10:90 A:B.

Method 2: 0-2 min isocratic elution 95:5 A:B, 2-30 min from 95:5 to 80:20 A:B, 30-35 min isocratic elution of 80:20 A:B.

Method 3: 0-5 min isocratic elution 95:5 A:B, 2-25 min from 95:5 to 65:35 A:B, 25-35 min from 65:35 to 10:90 A:B, 35-43 min of isocratic elution at 10:90 A:B.

3.2.5 Synthetic methods

Synthesis of $(CN)_2$Cbi (9)

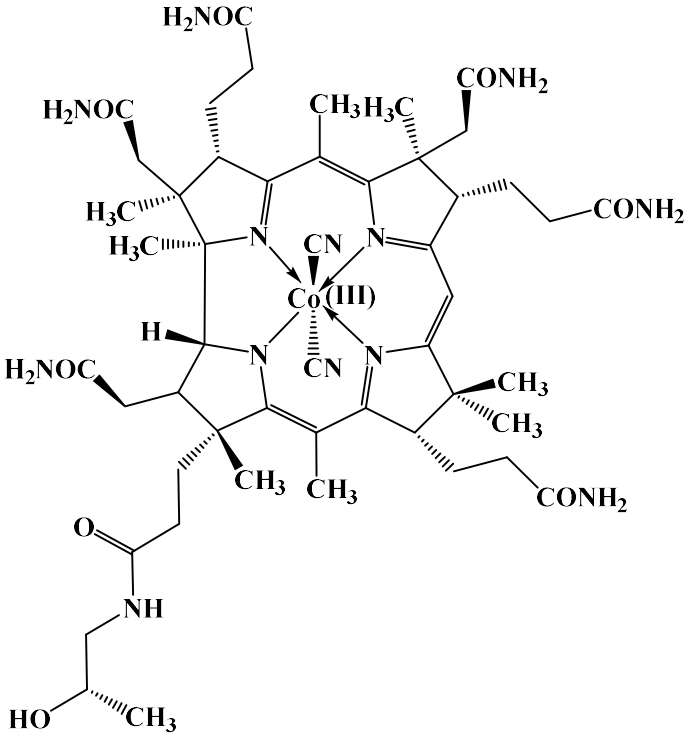

*Figure 80: Structure of $(CN)_2$Cbi **9**.*

Compound **9** was synthesised using a previously published procedure.[1] Cyanocobalamin (CNCbl, 200 mg, 148 µmol) and NaCN (200 mg, 4.08 mmol) were added to CH_3OH (12 mL) in a J Young tube. The J Young tube was sealed and sonicated for 30 min to dissolve all the solid NaCN. The solution was stirred at 50°C for 16 h and taken to dryness by rotary evaporation. The solid was dissolved in CH_3OH (4.0 mL) and IPA (40 mL) and loaded onto a DCVC (dry column vacuum chromatography) column. Fractions were taken to dryness by rotary evaporation and assessed for purity by ^{1}H NMR spectroscopy. Pure fractions were combined by dissolution in the minimal volume of CH_3OH and precipitated by dropwise addition into EtOAc (100 mL). The precipitate was filtered, washed with EtOAc (2 x 10 mL) then released with CH_3OH and taken to dryness (see general methods for full DCVC methodology). A purple powder was obtained (86 mg) in a 56% yield and ≥98% purity was established by LC-MS and ^{1}H NMR spectroscopy.

^{1}H NMR (400 MHz, MeOD) δ = 5.81 (s, 1H), 4.20 – 4.04 (m, 1H), 3.88 – 3.77 (m, 2H), 3.62 – 3.52 (m, 1H), 3.29 – 3.17 (m, 2H), 3.13 – 2.94 (m, 2H), 2.65 – 2.61 (m, 2H), 2.59

– 2.00 (m, 25H), 2.00 – 1.79 (m, 4H), 1.71 (s, 3H), 1.52 (s, 6H), 1.44 (s, 3H), 1.32 – 1.23 (m, 5H), 1.20 (s, 3H), 1.17 – 1.11 (m, 3H) ppm.

^{13}C NMR (101 MHz, DMSO) δ 175.92, 175.74, 175.47, 174.62, 174.24, 173.54, 172.84, 172.81, 171.74, 171.55, 171.31, 163.39, 162.28, 132.20, 129.72, 103.08, 101.84, 90.22, 82.46, 74.77, 65.16, 58.21, 55.06, 53.73, 52.92, 48.64, 48.47, 46.66, 46.08, 45.59, 42.90, 41.46, 40.15, 39.94, 39.73, 39.52, 39.31, 39.10, 38.89, 38.43, 35.27, 32.66, 32.28, 31.86, 31.31, 31.11, 30.79, 27.21, 25.27, 25.13, 21.69, 21.12, 19.45, 18.34, 17.76, 16.29, 15.33, 14.93 ppm.

Synthesis of cyanocobinamide (CNCbi, 10)

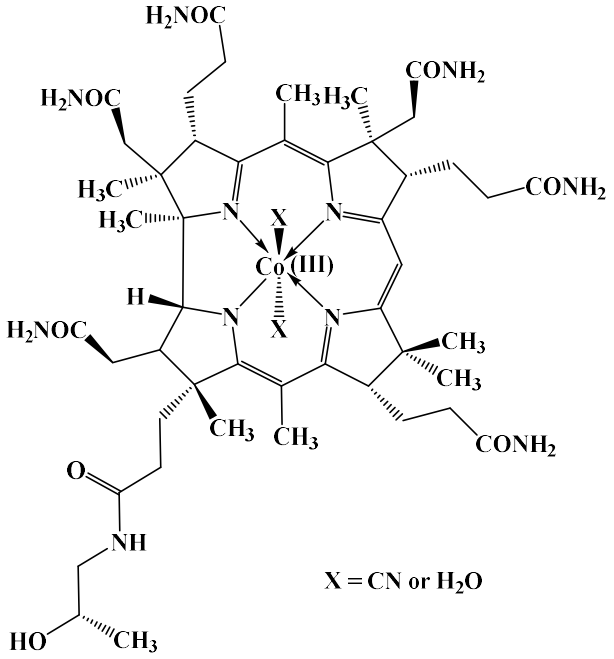

*Figure 81: Structure of CNCbi **10**.*

Compound **10** was synthesised using a previously established procedure.[1] Compound **9** (150 mg, 144 µmol) and $AgNO_3$ (26.9 mg, 158 µmol) were dissolved in H_2O (20 mL) and stirred for 10 min. The solution was left to stand for 1 h and a white precipitate was observed. The solution was filtered, and the red filtrate was collected and taken to dryness by rotary evaporation. The compound was desalted to remove any remaining $AgNO_3$ and taken to dryness. A red powder was obtained (124 mg) in an 85% yield and ≥ 98% purity was established by LC-MS and ^{1}H NMR spectroscopy.

^{1}H NMR (400 MHz, D_2O) δ = 6.50 (s, 0.4H), 6.43 (s, 0.6H), 4.28 – 4.18 (m, 1H), 4.13 – 4.04 (m, 2H), 4.02 – 3.96 (m, 1H), 3.96 – 3.86 (m, 2H), 3.72 – 3.61 (m, 2H), 3.59 – 3.53 (m, 1H), 3.36 (s, 2H), 3.32 – 3.22 (m, 2H), 3.22 – 3.14 (m, 2H), 3.14 – 3.01 (m, 2H), 2.86 – 2.50 (m, 14H), 2.50 – 2.24 (m, 18H), 2.24 – 2.03 (m, 12H), 2.02 – 1.88 (m, 4H), 1.88 – 1.74 (m, 5H), 1.74 – 1.68 (m, 5H), 1.64 – 1.54 (m, 9H), 1.49 – 1.37 (m, 4H), 1.37 – 1.35 (m, 2H), 1.35 – 1.31 (m, 6H), 1.19 – 1.12 (m, 7H) ppm.

CNCbi-(1,11-diamine-3,6,9-trioxaundecane) (Cbi-PEG-NH_2, 11)

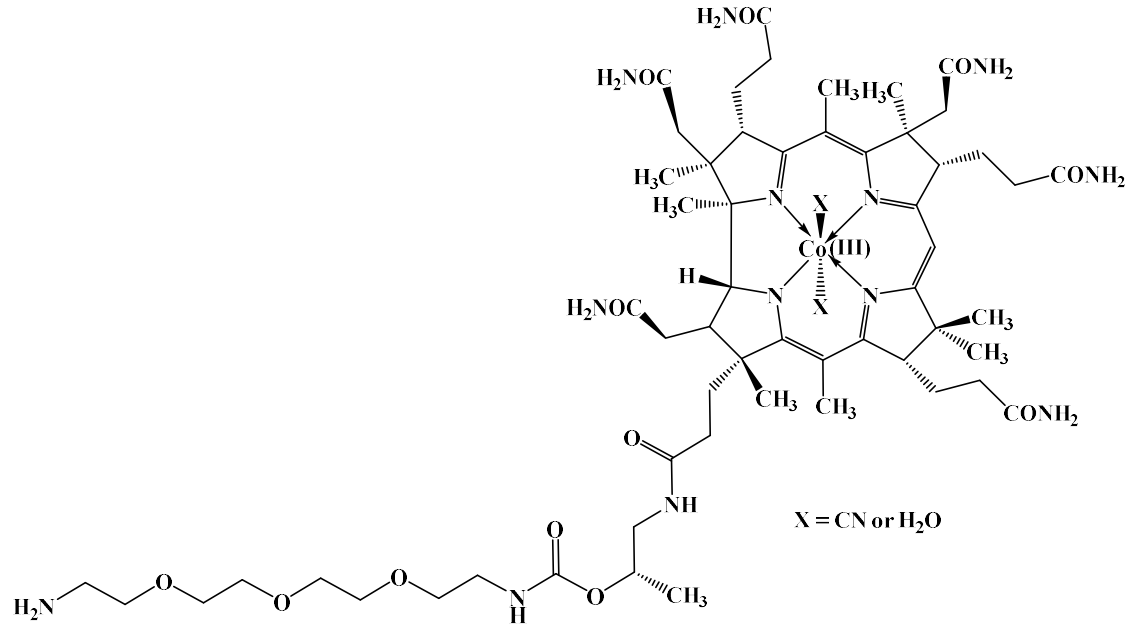

*Figure 82: Structure of **11**.*

Compound **9** (51.1 mg, 48.0 µmol) and 1,1-carbonyl-di(1,2,4-triazole) (CDT, 152.5 mg, 96.0 mmol) were dissolved in anhydrous DMSO (2 mL) and stirred for 30 min at 40°C. 1,11-Diamine-3,6,9-trioxaundecane (179.8 µL, 96.0 mmol) and Et_3N (46.7 µL, 7 mol eq.) were dissolved in anhydrous DMSO (1 mL) before addition to the solution of **9**. The solution was stirred for 1 h at 40°C. The crude product was precipitated by dropwise addition into EtOAc (~100 mL), filtered and washed with EtOAc (2 x 10 mL). The dark purple solid was released from the filter with CH_3OH and taken to dryness by rotary evaporation. The crude product was desalted to remove excess CDT and linker and analysed by LC-MS. A purple powder was obtained (56.9 mg) in a 92% yield and ~95% purity established by LC-MS.

CNCbi-(2-(2-aminoethyldisulfanyl)ethanamine) (CNCb1-cys-NH_2, 12)

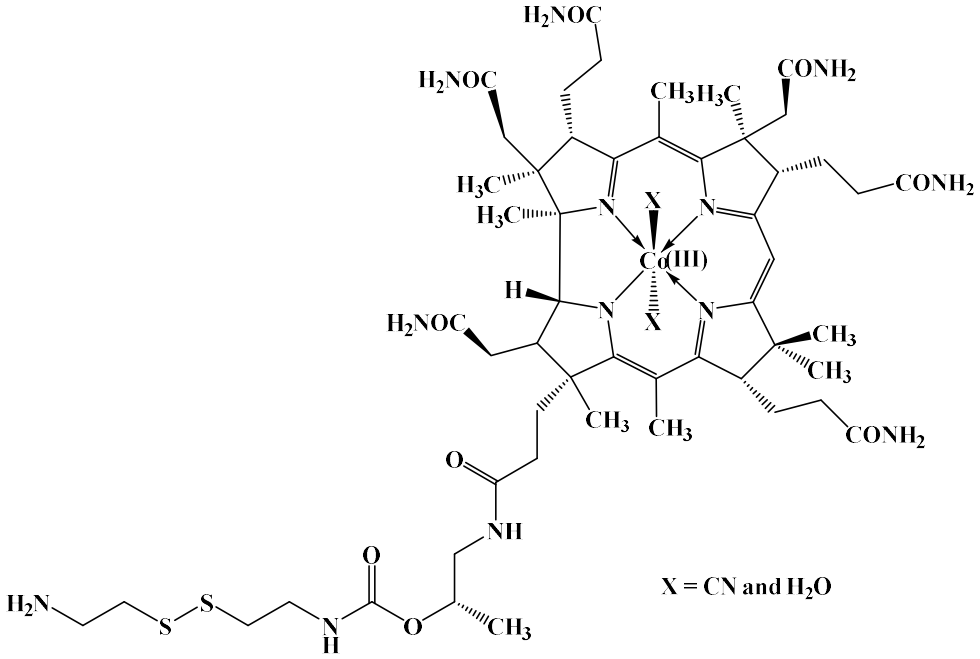

*Figure 83: Structure of **12**.*

Compound **10** (20.4 mg, 19.2 µmol) and CDT (61.4 mg, 38.4 mmol) were dissolved in anhydrous DMSO (1 mL) and stirred for 30 min at 40°C. Cystamine dihydrochloride (73.1 mg, 38.4 mmol) and Et_3N (133.9 µL, 50 mol eq.) were dissolved in anhydrous DMSO (1 mL) before being added dropwise to the reaction solution. The solution was stirred for 1 h at 40°C. The crude product was precipitated by dropwise addition into EtOAc, (80 mL), and isolated by centrifugation (5000 rpm, 5 min). The supernatant was discarded and the red solid dissolved in the minimal volume of CH_3 and taken to dryness by rotary evaporation. The crude product was desalted to remove any remaining cystamine and then analysed by LC-MS. A red powder was obtained (21.5 mg). Attempts to purify **12** were made by reversed-phase C18 chromatography, normal-phase chromatography and DCVC. The compound was unable to be purified so the yield and purity were not obtained.

CNCbi-PEG-NBD-X (13)

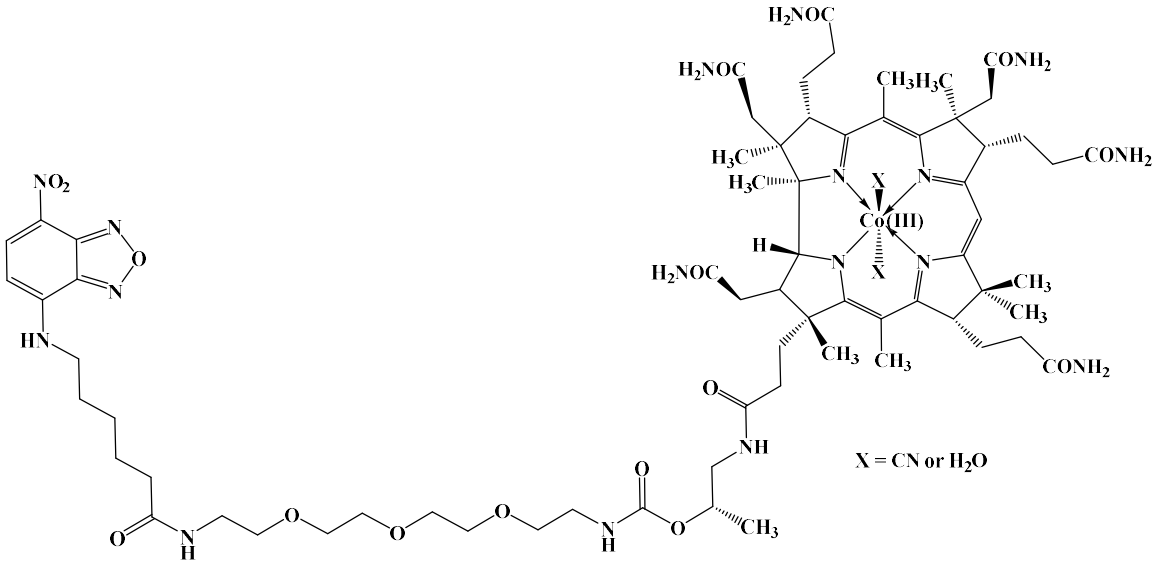

*Figure 84: Structure of **13**.*

Compound **11** (49.0 mg, 38.8 µmol), 1-hydroxybenzotriazole hydrate (HOBt, 22.5 mg, 155 µmol), 1-ethyl-3-(3-dimethylaminopropyl)carbodiimide (EDC, 16.1 mg, 77.8 µmol), 6-(*N*-(7-nitrobenz-2-oxa-1,3-diazol-4-yl)amino)hexanoic acid (NBD-X, 12.5 mg, 38.8 µmol) and Et_3N (22 µL, 3.0 mol eq.) were dissolved in anhydrous DMSO (2 mL) and stirred at 40°C for 24 h. A further 1.0 equivalent (5.6 mg) of HOBt was added and the mixture was stirred at 40 °C for a further 24 h. The crude product was precipitated by dropwise addition into EtOAc (150 mL), filtered and washed with EtOAc (2 x 10 mL). The orange precipitate was released from the filter with CH_3OH and taken to dryness by rotary evaporation. The crude product was purified by reversed-phase C18 chromatography. The product eluted as an orange band at 50% CH_3CN in H_2O. An orange powder was obtained (17.1 mg) in a 42% yield and ≥ 90% purity was established by LC-MS and ^{1}H NMR spectroscopy. HRMS ESI *m/z* calcd. for $[M]^+$ $C_{70}H_{102}O_{16}N_{18}Co$ 1509.7053; found 1509.7019.

^{1}H NMR (400 MHz, MeOD) δ = 8.57 – 8.50 (m, 1H), 6.42 – 6.33 (m, 1H), 3.70 – 3.56 (m, 8H), 3.56 – 3.47 (m, 5H), 3.37 – 3.32 (m, 9H), 3.27 – 3.23 (m, 2H), 2.74 – 2.66 (m, 4H), 2.53 – 2.49 (m, 2H), 2.49 – 2.44 (m, 3H), 2.41 – 2.37 (m, 3H), 2.27 – 2.15 (m, 5H), 2.05 – 2.00 (m, 2H), 1.94 (s, 2H), 1.86 – 1.74 (m, 5H), 1.73 – 1.65 (m, 5H), 1.65 – 1.54 (m, 7H), 1.53 – 1.43 (m, 4H), 1.39 – 1.27 (m, 17H), 1.22 – 1.16 (m, 4H), 0.94 – 0.86 (m, 2H) ppm.

CNCbi-cys-NBD-X (14)

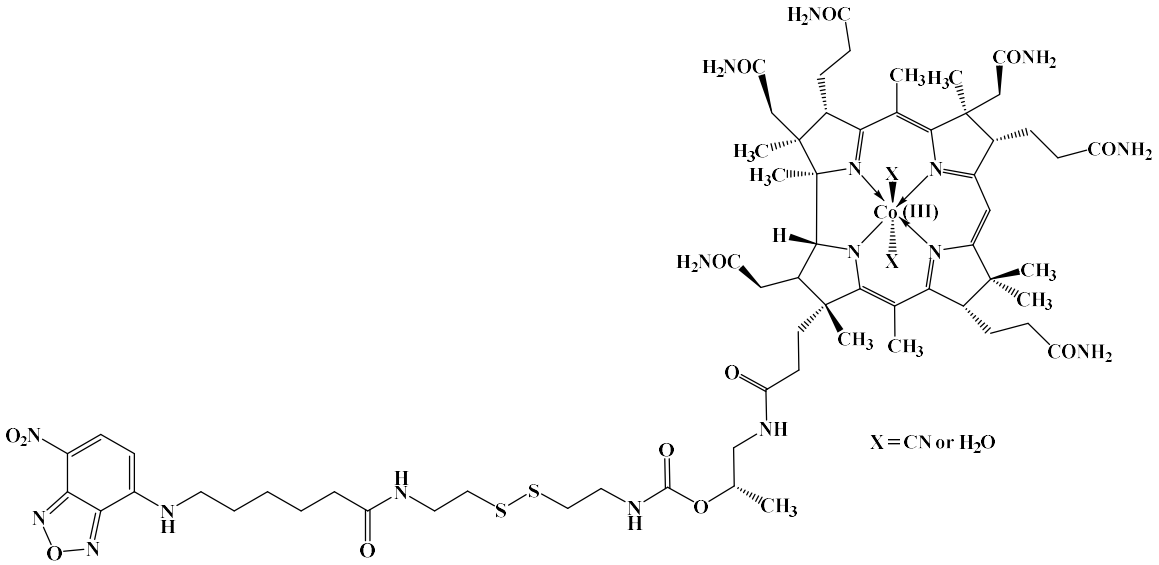

*Figure 85: Structure of **14**.*

Compound **12** (25.4 mg, 21.2 µmol), HOBt (8.61 mg, 63.7 µmol), EDC (4.51 mg, 77.8 µmol), NBD-X (4.43 mg, 23.1 µmol) and Et_3N (6.5 µL, 3 mol eq.) were dissolved in anhydrous DMSO (2 mL) and stirred at 40°C for 24 h. An additional 1.0 equivalent (1.61 mg) of HOBt was added and the mixture was stirred at 40°C for a further 24 h. The crude product was precipitated by dropwise addition into EtOAc (150 mL), filtered and washed with EtOAc (2 x 10 mL). The orange precipitate was released from the filter with CH_3OH and taken to dryness by rotary evaporation. The sample was purified by reversed-phase C18 chromatography. The product eluted as an orange band at 55% CH_3CN in H_2O. An orange powder was obtained (6.34 mg) in a 27% yield and ≥ 97% purity was established by LC-MS and ^{1}H NMR spectroscopy. HRMS ESI *m/z* $[M]^+$ calcd. for $C_{66}H_{94}O_{13}N_{18}CoS_2$ 1469.6013; found 1469.6022.

^{1}H NMR (400 MHz, MeOD) δ = 8.53 (d, *J*=9.0, 1H), 6.36 (d, *J*=8.7, 1H), 3.67 – 3.57 (m, 15H), 3.55 – 3.40 (m, 11H), 3.37 – 3.32 (m, 5H), 3.31 – 3.27 (m, 9H), 3.27 – 3.25 (m, 1H), 2.96 – 2.90 (m, 1H), 2.81 – 2.72 (m, 3H), 2.66 (s, 2H), 2.49 – 2.43 (m, 3H), 2.39 – 2.35 (m, 2H), 2.27 – 2.15 (m, 5H), 1.93 (s, 3H), 1.85 – 1.75 (m, 4H), 1.73 – 1.55 (m, 9H), 1.51 – 1.42 (m, 4H), 1.36 – 1.24 (m, 10H), 1.24 – 1.16 (m, 5H), 1.16 – 1.09 (m, 3H), 0.93 – 0.83 (m, 2H) ppm.

CNCbi-PEG-sulfo-Cyanine5 (15)

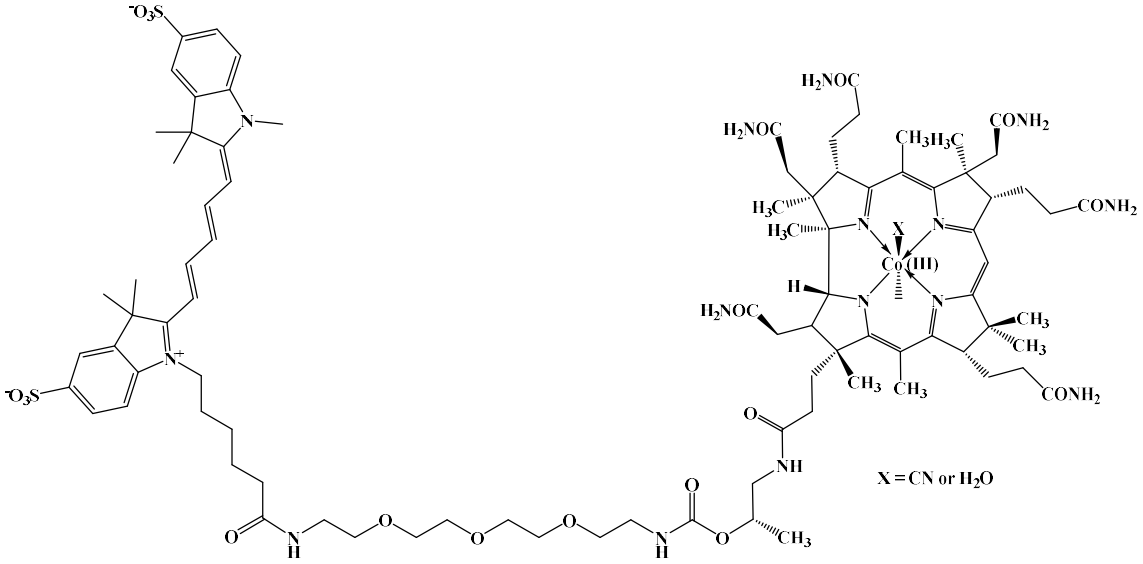

*Figure 86: Structure of **15**.*

Compound **11** (49.0 mg, 38.8 µmol), sulfo-Cyanine5-NHS ester (purchased from Lumiprobe, Cat #43320, 25.9 mg, 35.0 µmol) and Et_3N (11 µL, 1.1 mol eq.) were dissolved in anhydrous DMSO (2 mL) and stirred at 40°C for 24 h. The crude product was precipitated by dropwise addition into EtOAc (150 mL), filtered and washed with EtOAc (2 x 10 mL). The deep blue solid was then released from the filter with the minimal volume of CH_3OH and H_2O (10:1) and taken to dryness by rotary evaporation. The product was purified by reversed-phase C18 chromatography. The product eluted as a deep blue band at 50% CH_3CN in H_2O. A dark blue powder was obtained (39.3 mg) in a 63% yield and ≥ 95% purity was established by LC-MS and ^1H NMR spectroscopy. HRMS ESI *m/z* $[M+2Na]^{2+}$ calcd. for $C_{90}H_{125}O_{19}N_{16}CoS_2Na_2$ 951.3932; found 951.3930.

^1H NMR (400 MHz, D_2O) δ = 8.01 – 7.97 (m, 1H), 7.80 – 7.70 (m, 5H), 7.28 – 7.22 (m, 2H), 6.58 – 6.44 (m, 1H), 6.38 – 6.25 (m, 1H), 6.23 – 6.13 (m, 2H), 4.01 – 3.96 (m, 2H), 3.67 – 3.64 (m, 3H), 3.55 – 3.48 (m, 9H), 3.47 – 3.34 (m, 5H), 3.27 – 3.09 (m, 8H), 2.68 – 2.56 (m, 4H), 2.47 – 2.39 (m, 4H), 2.34 – 2.20 (m, 6H), 2.19 – 2.12 (m, 4H), 2.12 – 1.89 (m, 7H), 1.74 – 1.70 (m, 3H), 1.62 – 1.56 (m, 6H), 1.55 – 1.35 (m, 5H), 1.34 – 1.10 (m, 7H), 1.10 – 0.96 (m, 4H) ppm.

CNCbi-PEG-Cyanine7 (16)

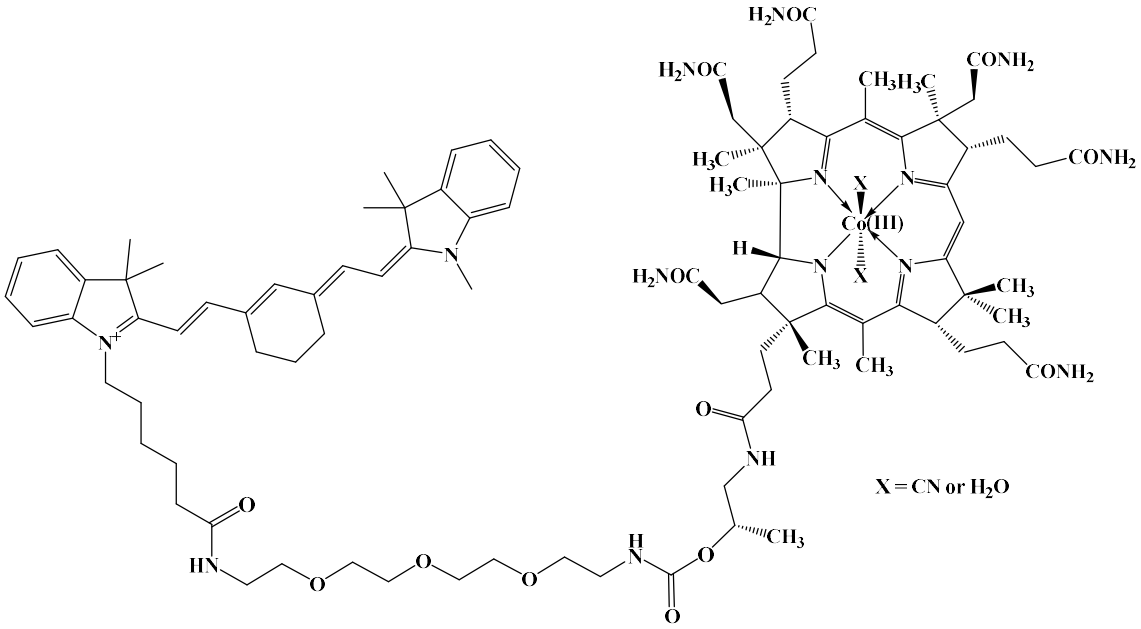

*Figure 87: Full structure of **16**.*

Compound **11** (48.8 mg, 38.7 µmol), Cyanine7-NHS ester (10.5 mg, 77.4 µmol) and Et_3N (11 µL) were dissolved in anhydrous DMSO (2 mL) and stirred at 40°C for 24 h. The crude product was precipitated by dropwise addition into EtOAc (150 mL), filtered and washed with EtOAc (2 x 10 mL). The green/black solid was released from the filter with CH_3OH and taken to dryness by rotary evaporation. The product was purified by reversed-phase C18 chromatography. The product eluted as a blue/green band at 60% CH_3CN in H_2O with 0.1% formic acid. A dark green solid was obtained (12.5 mg) in an 18.3% yield and 95% purity was established by LC-MS and ^1H NMR spectroscopy. HRMS ESI *m/z* $[M]^{2+}$ calcd. for $C_{95}H_{133}O_{13}N_{16}Co$ 882.4779; found 882.4760.

^1H NMR (400 MHz, MeOD) δ = 7.80 – 7.69 (m, 2H), 7.49 – 7.35 (m, 5H), 7.29 – 7.18 (m, 4H), 6.20 – 6.12 (m, 2H), 4.12 – 4.07 (m, 2H), 3.70 – 3.59 (m, 11H), 3.57 – 3.47 (m, 9H), 3.37 – 3.32 (m, 6H), 3.29 (s, 6H), 2.60 – 2.53 (m, 4H), 2.52 – 2.48 (m, 3H), 2.40 (s, 4H), 2.30 – 2.18 (m, 5H), 2.18 – 2.13 (m, 2H), 2.06 – 2.02 (m, 2H), 1.99 – 1.91 (m, 4H), 1.89 – 1.82 (m, 4H), 1.74 – 1.65 (m, 5H), 1.60 (s, 5H), 1.53 – 1.43 (m, 6H), 1.42 – 1.32 (m, 5H), 1.32 – 1.27 (m, 5H), 1.26 – 1.14 (m, 2H) ppm.

Results and Discussion

3.2.6 Synthesis of 11 and 12

Dicyanocobinamide (**9**) was required for the synthesis of compounds **11** and **12**. The synthesis of **9** was achieved using an established procedure within our research group which was slightly modified from a literature procedure.[1,5] In short, commercially available CNCbl and the equivalent mass of NaCN were dissolved in EtOH. This required sonication for ~30 min to ensure complete dissolution of the solid NaCN, which was instrumental to the success of the reaction. The reaction solution was prepared in a J Young tube and heated with stirring at 50°C for 16 h. An immediate colour change from red to purple was observed upon adding NaCN to CNCbl, indicating coordination of a second CN^- ligand to the Co(III) centre to form dicyanocobalamin ($(CN)_2Cbl^-$).[6] Nucleophilic attack at the phosphodiester of dicyanocobalamin by excess CN^- produces dicyanocobinamide ($(CN)_2Cbi$, **9**, Scheme 10). Synthetic attempts were also carried out using KCN as the CN^- source, which resulted in lower yields (~20% vs 50% using KCN vs NaCN).

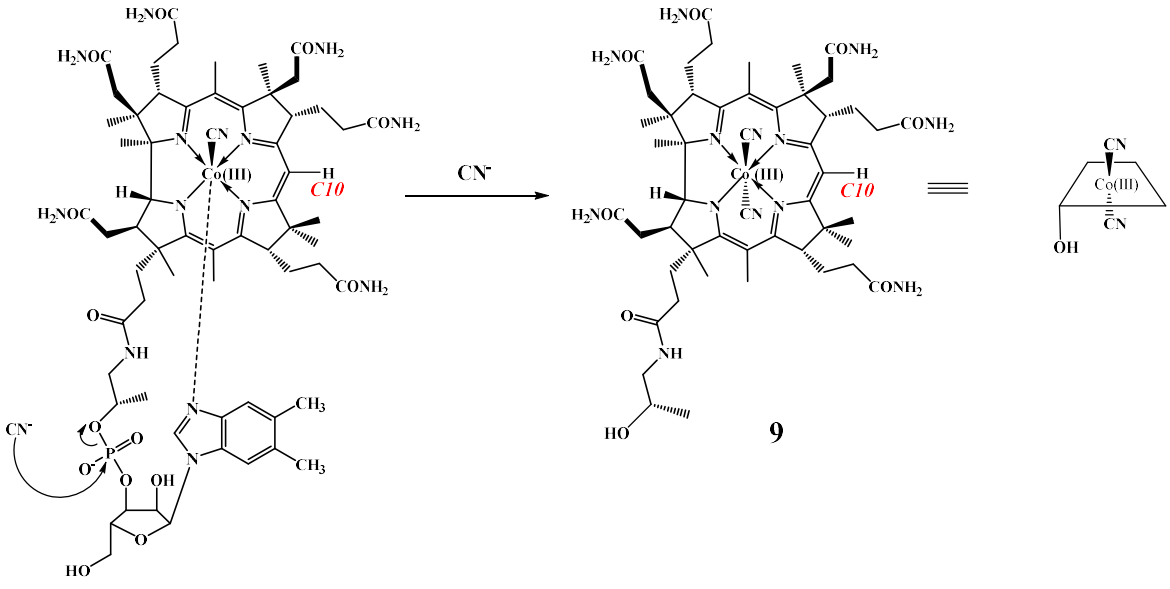

*Scheme 10: Synthesis of **9** from CNCbl. The C10 proton of both CNCbl and $(CN)_2$Cbi has been highlighted.*

Compound **9** was purified by dry column vacuum chromatography (DCVC). DCVC chromatography proved the most effective column chromatography method to separate **9**

from the closely eluting $(CN)_2Cbl^-$. Yields obtained ranged between 50-60%. The purity of the final product was analysed by ^1H NMR spectroscopy in MeOH-d_4. As mentioned in Chapter 2, using a protic NMR solvent such as MeOH-d_4 results in deuterium exchange of the amide protons on the corrin ring, considerably simplifying the aromatic region of the ^1H NMR spectrum. This is useful for the determination of purity for CNCbl and Cbi conjugates.

The formation of **9** was confirmed by a single proton in the aromatic region of the ^1H NMR spectrum at 5.81 ppm, the C10 proton of the corrin ring (Figure 88).[5,7] No other signals are present in the aromatic region for **9** whereas $(CN)_2Cbl^-$ and CNCbl have five resonances due to protons on the ribose and 5,6-dimethylbenzimidazole moieties.

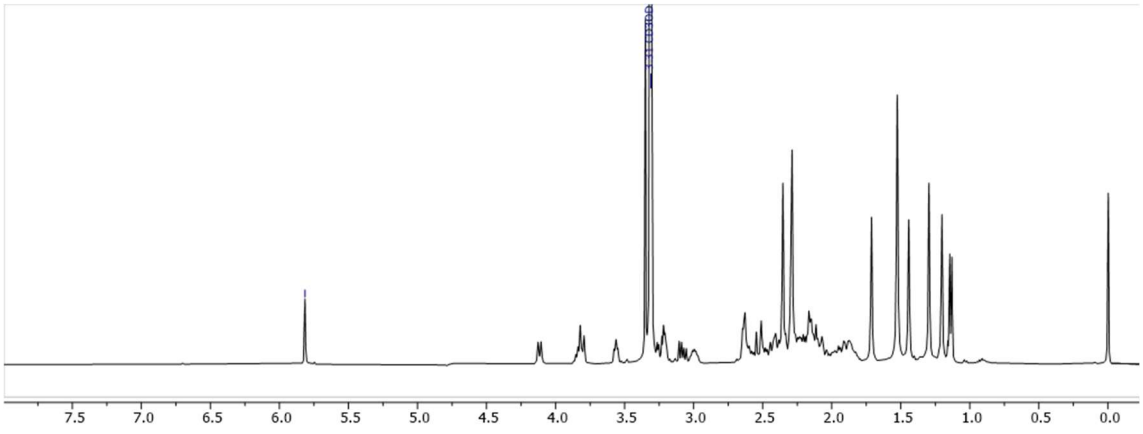

*Figure 88: ^1H NMR spectrum of **9** obtained in MeOH-d_4 showing one characteristic peak from the C10 proton at 5.81 ppm.*

Compound **9** was also analysed by LC-MS. Two peaks eluting at 15.0 and 20.8 min are from the two isomers of cyanocobinamide (CNCbi) ($C_{50}H_{72}CoN_{13}O_8$, calcd. *m/z* $[M\text{-}CN]^+$ = 1015.5 and $[M\text{-}CN+H]^{2+}$ = 508.3; found 1015.4 and 508.3, Figure 89). The two isomers formed are α-cyano-β-aquacobinamide and α-aqua-β-cyanocobinamide (Figure 90). Upon dissolving **9** in H_2O, or H_2O containing formic acid, one of the CN^- ligands of $(CN)_2Cbi$ is substituted for a solvent molecule, giving the two CNCbi isomers. The remaining CN^- is lost under the LC-MS experimental conditions .[8]

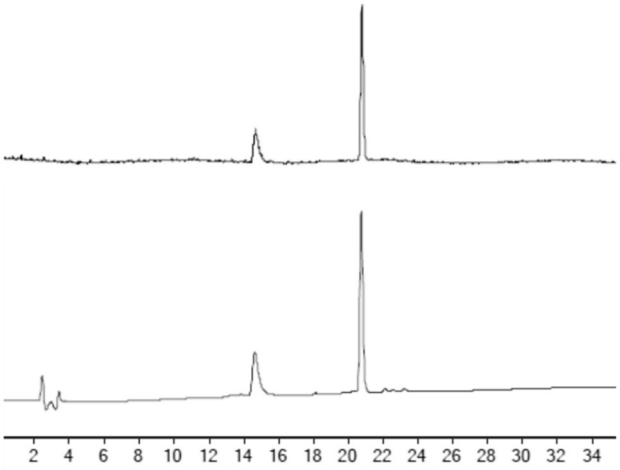

*Figure 89: LC-MS TIC (top) and DAD (361 nm, bottom) chromatograms of **9** showing two peaks at 15.0 and 20.8 min which can be assigned to the α-cyano-β-aquacobinamide and α-aqua-β-cyanocobinamide isomers ($C_{50}H_{72}CoN_{13}O_8$, calcd. m/z $[M\text{-}CN]^+$ =1015.5 and $[M\text{-}CN+H]^{2+}$ = 508.3; found 1015.4 and 508.3, LC-MS method 1).*

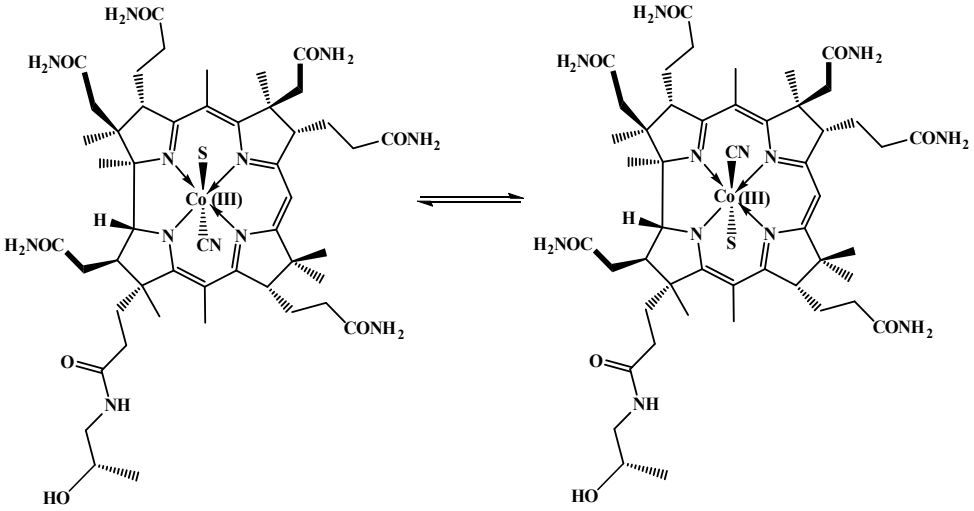

*Figure 90: Structures of the α-cyano-β-aquacobinamide and α-aqua-β-cyanocobinamide isomers formed when **9** is dissolved in H_2O, S = a solvent molecule.*

Compound 11

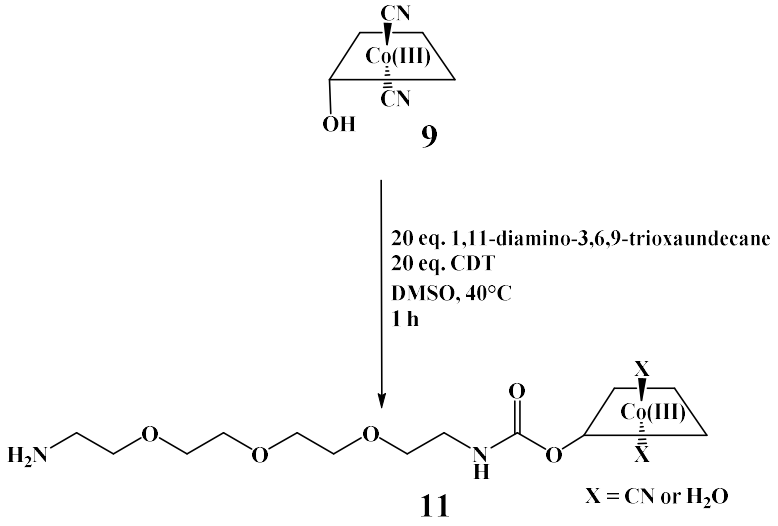

*Scheme 11: Synthetic procedure for the synthesis of **11**.*

The synthesis of **11** was achieved by modification of a previously published literature procedure.[8] Compound **9** and CDT (20 eq.) were stirred in the minimal volume of anhydrous DMSO at 40°C. After 30 min, 1,11-diamino-3,6,9-trioxaundecane (20 eq.) was added and the mixture stirred for 1 h. The product was precipitated into EtOAc and filtered. Excess 1,11-diamino-3,6,9-trioxaundecane was evident in the precipitate as the crude sample was isolated as a purple oil (1,11-diamino-3,6,9-trioxaundecane is a viscous liquid). Multiple attempts were made to purify the product using reversed-phase C18 chromatography. Initial attempts were carried out using a mobile phase analogous to the one used for purification of the CNCbl-linker compounds (H_2O + 0.1% formic acid and CH_3CN + 0.1% formic acid); however, none of these attempts resulted in the pure compound being isolated. LC-MS analysis of the crude product showed more peaks in the total ion count (TIC) chromatogram than the diode array detector (DAD) chromatogram at 361 nm (Figure 91). The DAD chromatogram at 361 nm is particularly useful for identifying CNCbl and CNCbi complexes due to the large γ absorbance band in both complexes at this wavelength.[9,10] This is a common analysis technique used to identify CNCbl and CNCbl analogues.[3,11] Peaks observed in the TIC chromatogram and not the DAD at 361 nm indicate that they are not CNCbi products, and are likely due to 1,11-diamino-3,6,9-trioxaundecane byproducts. The two large peaks at 14.5 and 18.4 min in the DAD chromatogram can be assigned to the α-cyano-β-aquacobinamide and α-aqua-β-cyanocobinamide isomers of **11** ($C_{58}H_{90}CoN_{14}O_{12}$, calcd. *m/z* $[M\text{-}CN+H]^{2+}$ = 617.3;

found 617.4). Peaks in the DAD at 13.5 and 19.9 min are assigned to the α-cyano-β-aquacobinamide and α-aqua-β-cyanocobinamide isomers CNCbi ($C_{50}H_{72}CoN_{13}O_8$, calcd. *m/z* $[M\text{-}CN]^+$ =1015.5 and $[M\text{-}CN+H]^{2+}$ = 508.3; found 1015.4 and 508.3).

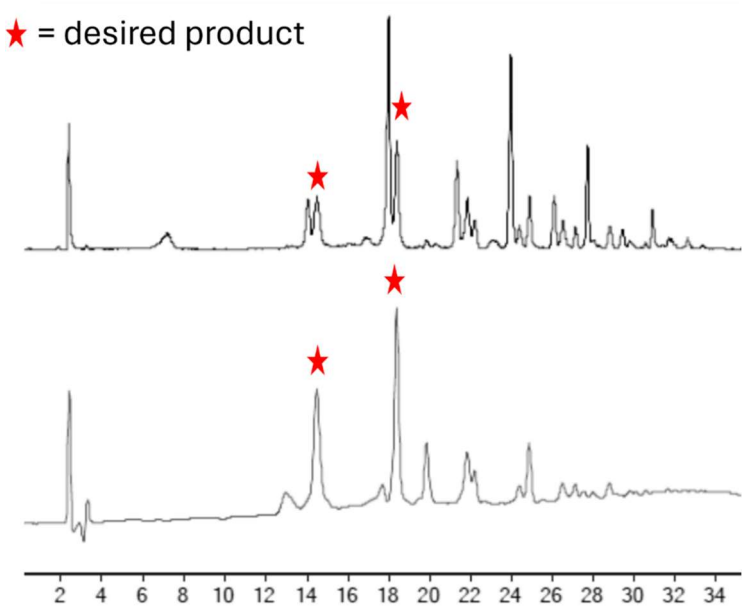

Figure 91: LC-MS TIC (top) and DAD (361 nm, bottom) chromatograms of crude ***11*** *(LC-MS method 1). Peaks of interest at 14.5 and 18.4 min can be assigned to the α-cyano-β-aquacobinamide and α-aqua-β-cyanocobinamide isomers of* ***11*** *($C_{58}H_{90}CoN_{14}O_{12}$, calcd. m/z $[M\text{-}CN+H]^{2+}$ = 617.3; found 617.4).*

The peaks at 21.9 and 24.9 are assigned to the α-cyano-β-aqua and α-aqua-β-cyano isomers of a product where three 1,11-diamino-3,6,9-trioxaundecane linkers have been linked to CNCbi sequentially (Cbi-$(PEG)_3$ $C_{76}H_{126}CoN_{18}O_{20}$, calcd. *m/z* $[M\text{-}CN]^+$ = 1670.0, $[M\text{-}CN+H]^{2+}$ = 835.4 and $[M\text{-}CN+2H]^{2+}$ = 557.3; found 835.5 and 557.4, Figure 92). This has occurred through carbamate bond formation between the Cbi and the amine-containing linker, followed by nucleophilic substitution of two further linkers by urea bond formation (Scheme 12). It is noted in the literature that CDT facilitates urea bond formation between two amine residues.[12]

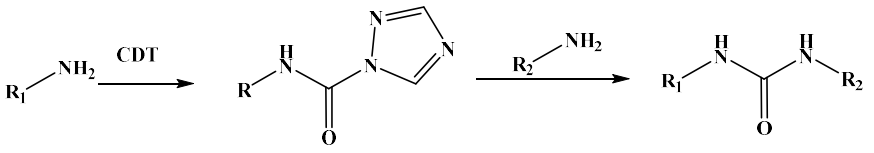

Scheme 12: Urea bond formation facilitated by CDT in the presence of two primary amines.[12]

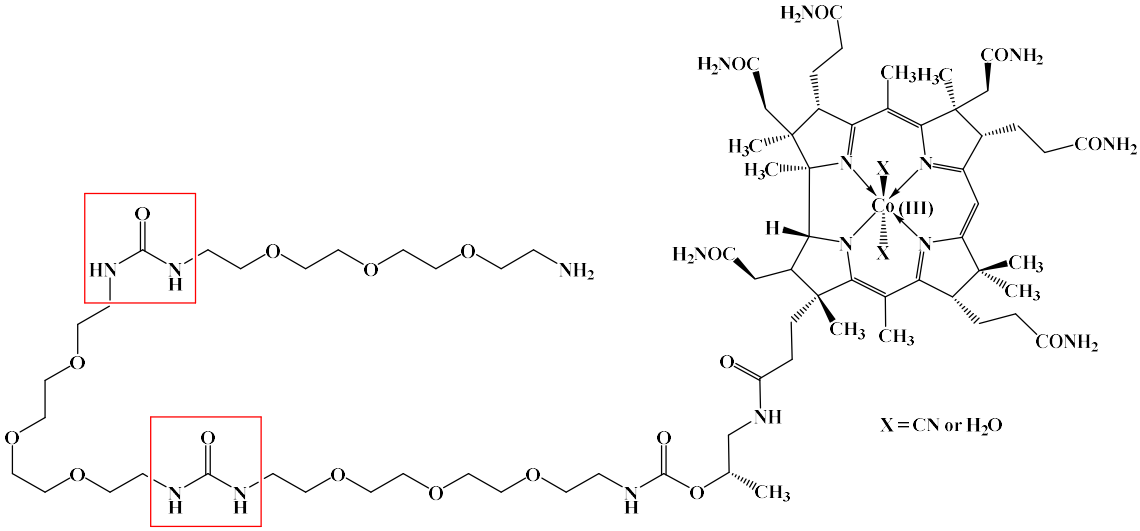

Figure 92: Structure of the CNCbi product incorporating three 1,11-diamino-3,6,9-trioxaundecane linkers (CNCbi-(PEG)$_3$), conjugated via urea bond formation, highlighted in red.

Using peak areas in the DAD chromatogram, the CNCbi compound containing three 1,11-diamino-3,6,9-trioxaundecane linkers was not a major product (the limitations of peak area to estimate the relative amounts of compounds is discussed in Chapter 2). Due to this, efforts were not made to prevent the formation of CNCbi-(PEG)$_3$.

High mol equivalents of both CDT and 1,11-diamino-3,6,9-trioxaundecane were required during this synthesis to maximise product formation. Compared to the synthesis of CNCbl-linker compounds where three mol equivalents of CDT and linker are utilised, higher mol equivalents are required due to the reduced reactivity of CNCbi vs CNCbl. The OH moiety functionalised in CNCbl is primary whereas the OH residue of CNCbi is secondary. The high excess of 1,11-diamino-3,6,9-trioxaundecane resulted in many peaks observed in the TIC (and not the DAD), likely due to the polymerisation of the polyethylene glycol units. To remove the polymerised 1,11-diamino-3,6,9-trioxaundecane impurities, the crude product was instead desalted using a silica plug with copious volumes of H_2O (~200 mL per 30 mg of crude material). Analysis of the desalted

compound by LC-MS confirmed that these impurities were removed. The peaks at 17.5 and 21.0 min can be assigned to the α-cyano-β-aqua and α-aqua-β-cyano isomers of **11** ($C_{58}H_{90}CoN_{14}O_{12}$, calcd. *m/z* $[M\text{-}CN+H]^{2+}$ = 617.3; found 617.4, Figure 93). Two further peaks eluting at 16.2 and 22.2 min represent the α-cyano-β-aqua and α-aqua-β-cyano isomers of CNCbi ($C_{50}H_{72}CoN_{13}O_8$, calcd. *m/z* $[M\text{-}CN]^+$ =1015.5 and $[M\text{-}CN+H]^{2+}$ = 508.3; found 1015.4 and 508.3). One final peak was found in the TIC chromatogram at 23.8 min but is not present in the DAD chromatogram. The *m/z* value of this peak was 412.2 and could not be identified.

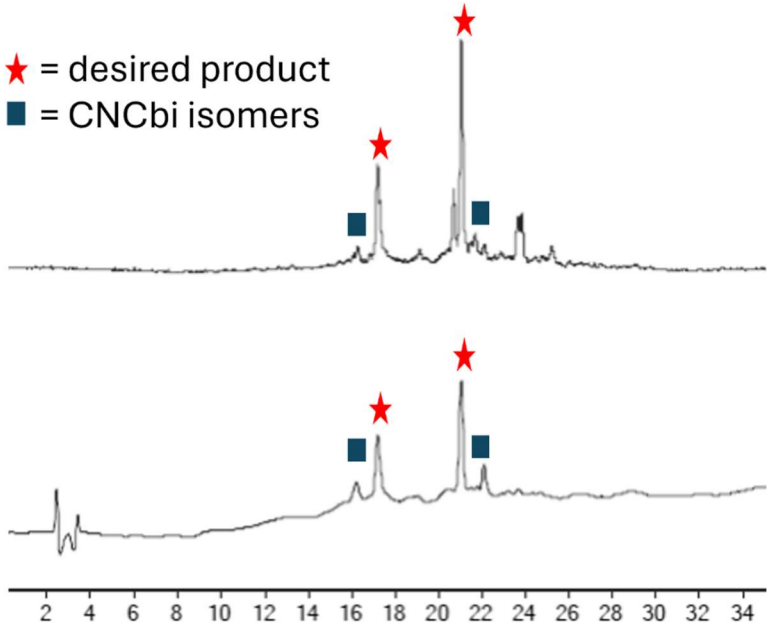

*Figure 93: LC-MS TIC (top) and DAD (361 nm, bottom) chromatograms of desalted **11** (LC-MS method 1). The peaks at 17.5 and 21.0 min can be assigned to the α-cyano-β-aqua and α-aqua-β-cyano isomers of **11** ($C_{58}H_{90}CoN_{14}O_{12}$, calcd. m/z, $[M\text{-}CN+H]^{2+}$ = 617.3; found 617.4). The peaks at 16.2 and 22.2 min represent the α-cyano-β-aqua and α-aqua-β-cyano isomers of CNCbi ($C_{50}H_{72}CoN_{13}O_8$, calcd. m/z $[M\text{-}CN]^+$ =1015.5 and $[M\text{-}CN+H]^{2+}$ = 508.3; found 1015.4 and 508.3).*

The ^{1}H NMR spectrum of the crude desalted product in MeOH-d_4 showed similarities with **9** in the aromatic region. The proton resonances in this region for the isomers of **11** are located at 5.50 and 5.57 ppm, from the C10 proton of the α-cyano-β-aqua and α-aqua-β-cyano isomers of the desired product.[13] Furthermore, a new multiplet at 3.54 ppm is observed (Figure 94), assigned to the CH_2 residues of the attached 1,11-diamino-3,6,9-trioxaundecane linker.

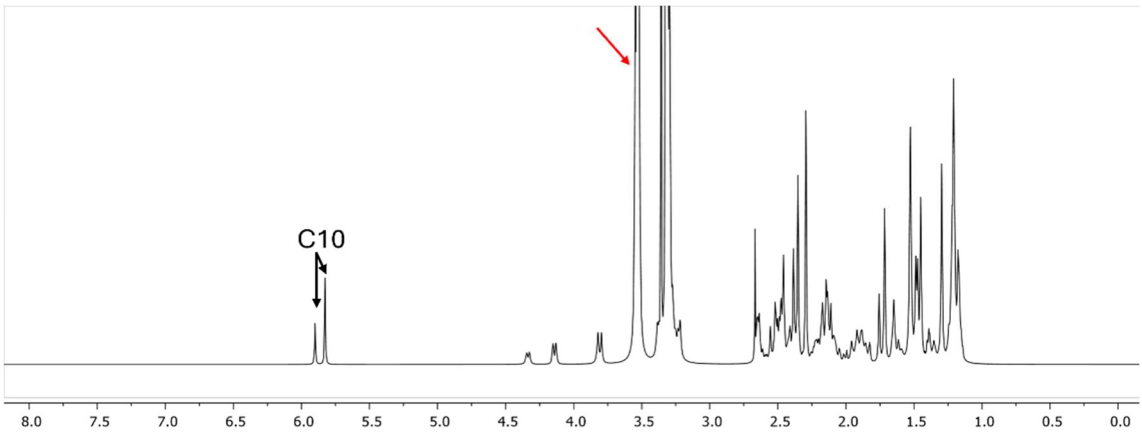

*Figure 94: ^{1}H NMR spectrum of **11** obtained in MeOH-d_4. The C10 proton of the α-cyano-β-aqua and α-aqua-β-cyano isomers of **11** resonate at 5.50 and 5.57 ppm. The methylene protons of the linker at 3.54 ppm is also highlighted.*

Examples of Cbi conjugates are limited in the literature and their purity is not always determined. Using a combination of LC-MS and ^{1}H NMR spectroscopy, the presence of **11** was confirmed. Multiple attempts to purify **11** were made but were not successful. Desalting the crude reaction mixture over a silica plug removed most of the impurities (established by LC-MS and ^{1}H NMR spectroscopy), giving a compound that was suitable for further synthesis.

Compound 12

Initial attempts to synthesise **12** were carried out using conditions similar to those used for the synthesis of **11**. Higher mole equivalents of Et_3N were required for this reaction (50 eq.) as the cystamine reagent used was a dihydrochloride salt (Scheme 13). Compound **9** was dissolved in the minimal volume of anhydrous DMSO together with 20 eq CDT and a deep purple solution was observed. Cystamine.2HCl was dissolved in anhydrous DMSO, Et_3N added and this solution was added to the solution of **9**.

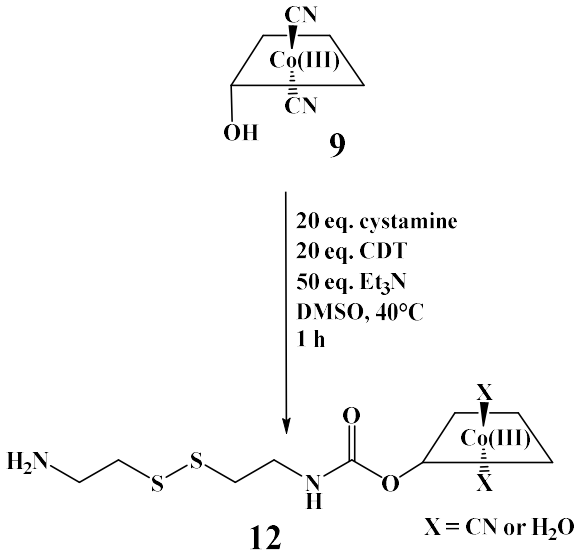

*Scheme 13: Synthetic procedure for the synthesis of **12**.*

Upon addition of the cystamine solution to **9** and CDT, an immediate colour change from deep purple to amber orange was observed. A pale orange precipitate was obtained from the reaction and the LC-MS analysis of the crude product indicated that neither **9** or **12** was present. Furthermore, the ^{1}H NMR spectrum of the crude solid obtained after precipitation showed many broad overlapping peaks, both in the aromatic and low-field regions. The observed colour change to orange can result from the reductive decomposition of the corrin ring.[14] Multiple experimental conditions were tested to synthesise **12** from **9**, by modification of the methodology used for the synthesis of **11**, (Table 3) but none proved successful.

*Table 3: Reaction conditions trialled for the synthesis of **12** from **9**.*

Mol equivalents of reagent				**Reaction time**
9	CDT	Cystamine.2HCl	Et_3N	
1	20	20	10	5 min
1	20	20	30	5 min
1	20	20	50	5 min
1	20	30	10	30 min

1	20	20	30	30 min
1	20	20	50	30 min
1	20	20	10	1 h
1	20	20	30	1 h
1	20	20	50	1 hr
1	20	20	10	6 h
1	20	20	30	6 h
1	20	20	50	6 h
1	3	3	8	1 h
1	3	3	8	6 h
1	3	3	8	16 h

It is proposed that the reduced cystamine linker catalyses the decomposition of the corrin ring. Compound **9** contains two axially bound CN^- ligands. At lower pH conditions (pH ≤6.5) one of the CN^- ligands is substituted by a solvent molecule, resulting in free HCN ions in the solution (Figure 95).[15,16] This phenomenon has been observed throughout this research during LCMS analysis of Cbi products.

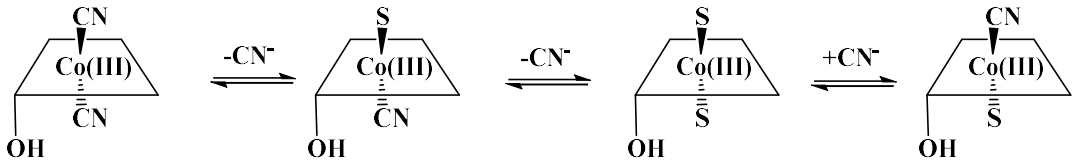

Figure 95: Equilibria for $(CN)_2$Cbi in co-ordinating solvents (S = solvent molecule).

It is well established that disulfides, including cystine, are cleaved by CN^- as a result of nucleophilic attack at the disulfide, resulting in a thiol and thiocyanate.[17,18] The stability of cystamine in the presence of cyanide was investigated in DMSO-d_6 by ^{1}H NMR spectroscopy. DMSO-d_6 was used as the solvent as this was the solvent used in the attempted synthesis of **12**. The ^{1}H NMR spectrum of cystamine.2HCl in DMSO-d_6 showed two multiples at 3.03 and 3.08 ppm, each representing two CH_2 residues, integrating for 4H (Figure 96). NaCN (~1 mg) was subsequently added to the same NMR

sample and the ^{1}H NMR spectrum recorded. The addition of NaCN resulted in the complete decomposition of cystamine (Figure 96). Hence, cystamine.2HCl is unstable in the presence of cyanide.

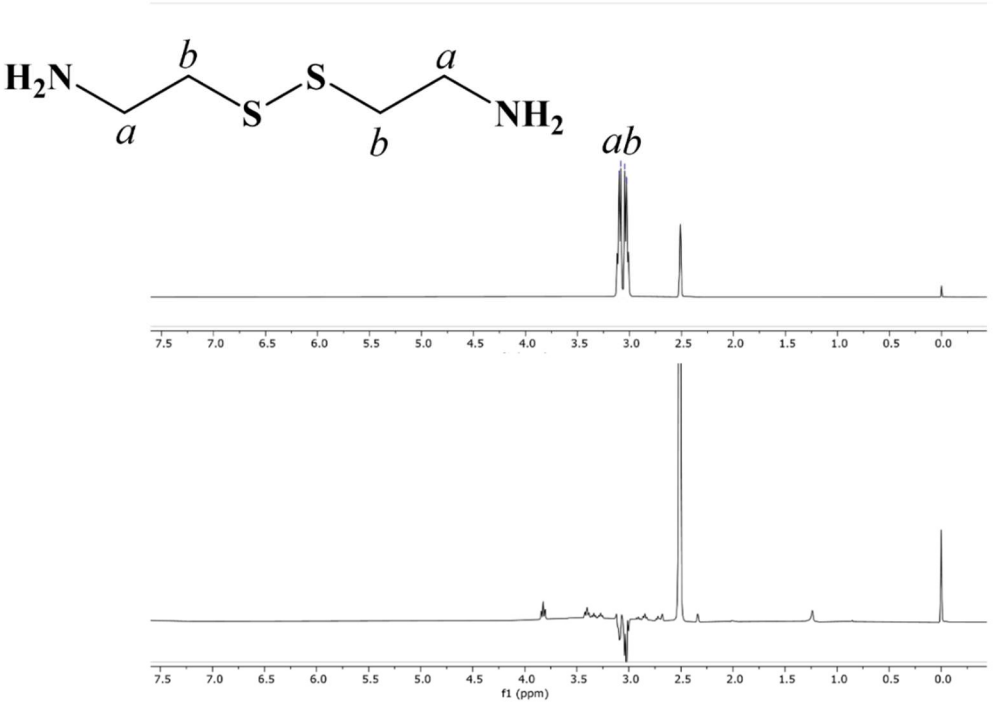

Figure 96: ^{1}H NMR spectrum of cystamine (top) and cystamine + NaCN (bottom) in DMSO-d_6. The two multiplets in the upper spectrum are from the CH_2 protons of cystamine.2HCl, at 3.03 (4H) and 3.08 (4H) ppm.

Nucleophilic attack of cyanide at the disulfide of the cystamine generates the thiol cysteamine. It is well known that this can reduce Co(III) corrinoid complexes.[19,20] We propose that upon substitution of one of the cyanido ligands of **9** with a solvent ligand, the released cyanide can cleave the disulfide of the cystamine, generating cysteamine (Figure 97). Cysteamine reduces the Co(III) centre in addition to reductive decomposition of the macrocycle.

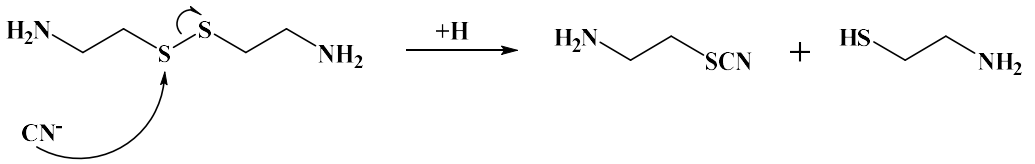

Figure 97: Proposed reaction of cystamine with cyanide forming 1-thiocyanato-2-aminoethane and cysteamine, respectively.

To prevent the cleavage of the disulfide linker, **9** was converted to the isomers of CNCbi (**10**), where one CN^- ligand was removed by the addition of one mol equivalent of $AgNO_3$ (Scheme 14).[21] $AgNO_3$ efficiently traps one of the two CN^- ligands, forming an insoluble AgCN precipitate.[22] An immediate colour change from purple to red is observed upon the addition of 1.1 mol eq. $AgNO_3$ with stirring. After 10 min without stirring a white precipitate is observed which was removed by filtration. The filtrate was dried by rotary evaporation and **10** was obtained as a red solid.

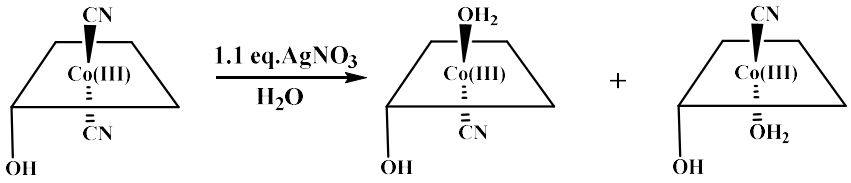

*Scheme 14: Synthetic procedure for the synthesis of **10**.*

Two proton resonances were observed in the ^1H NMR spectrum at 6.45 and 6.38 ppm for the C10 protons of the corrin ring of the two α-cyano-β-aqua and α-aqua-β-cyano isomers of **10** (Figure 98). These resonances agree with the literature.[13]

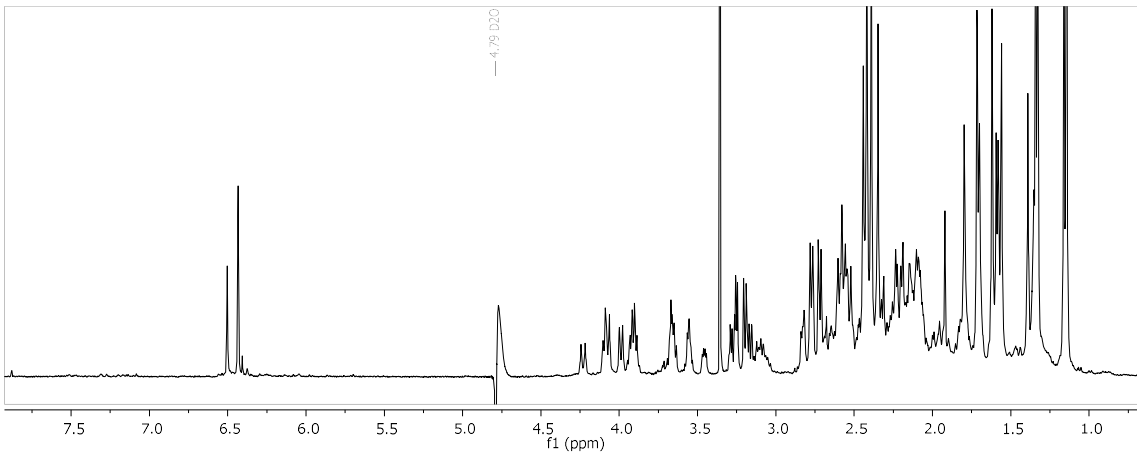

*Figure 98: ^{1}H NMR spectrum of **10** in D_2O. Peaks at 6.45 and 6.38 ppm are assigned to the two C10 protons of the α-cyano-β-aqua and α-aqua-β-cyano isomers of **10**.*

To synthesise **12, 10** and CDT (20 eq.) were stirred in the minimal volume of anhydrous DMSO at 40°C. After 30 min a solution of cystamine.2HCl (20 eq.), and Et_3N (50 eq.) were added the solution and left to stir for 1 h (Scheme 15). No colour change was observed after the addition of cystamine.HCl.

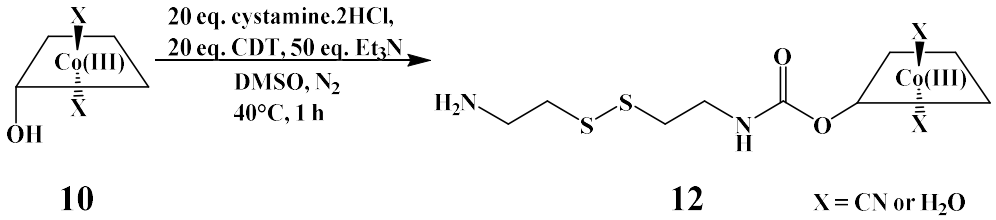

*Scheme 15: Synthetic procedure for the synthesis of **12**.*

The crude red product was precipitated into EtOAc and the solid was isolated by centrifugation. Centrifugation was utilised here as filtration of the crude material was unsuccessful due to a fine white precipitate blocking the filter. Analysis of the crude product mixture by LC-MS identified the presence of the isomers of **12** at 16.2 and 19.6 min ($C_{54}H_{82}CoN_{14}O_9S_2$ calcd. *m/z* $[M+H]^{2+}$ = 597.3, found 597.3, Figure 99). The peaks at 15.4 and 20.6 min were assigned to the starting material **10** ($C_{50}H_{72}CoN_{13}O_8$, calcd. *m/z* $[M\text{-}CN]^+$ =1015.5 and $[M\text{-}CN+H]^{2+}$ = 508.3; found 1015.4 and 508.3). Many peaks in the chromatogram could not be identified and represented ~55% of the total area of the DAD chromatogram at 361 nm. It is likely that side reactions initiated by the cyanide-

induced cleavage of the disulfide were still occurring. However, the desired product was formed, and it was decided to purify the crude mixture.

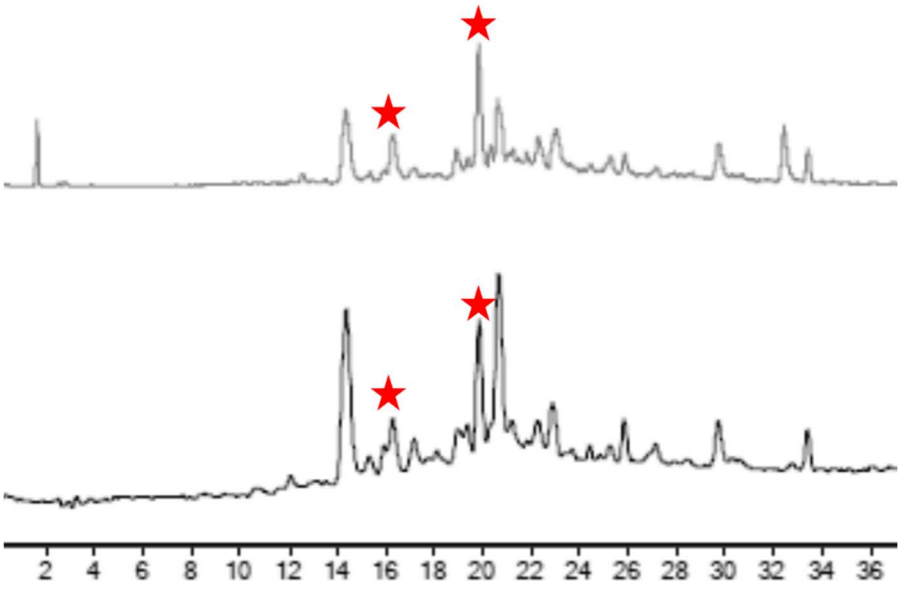

Figure 99: LC-MS TIC (top) and DAD (361 nm, bottom) chromatograms of crude ***12*** *(LC-MS method 1). The peaks of interest at 16.2 and 19.2 min are assigned to the α-cyano-β-aqua and α-aqua-β-cyano isomers of* ***12*** *($C_{54}H_{82}CoN_{14}O_9S_2$ calcd. m/z $[M+H]^{2+}$ = 597.3, found 597.3).*

Many attempts were made to purify the crude product **12** by reversed-phase C18 chromatography using a range of mobile phase solvents (CH_3CN and H_2O, CH_3CN and H_2O + 0.1% formic acid, CH_3OH and H_2O, CH_3OH and H_2O + 0.1% formic acid and CH_3CN in phosphate buffer (0.05 M, pH 7)) but the pure compound could not be isolated. Additional attempts at purification by normal phase silica chromatography and dry column vacuum chromatography were also unsuccessful. The crude sample was instead thoroughly desalted using a reversed-phase C18 silica plug with excess H_2O (~200 mL per 50 mg of crude compound) and released from the silica with CH_3OH. After desalting, the LC-MS chromatogram of the compound showed fewer impurities (Figure 100). The peaks at 16.4 and 19.8 min correspond to the α-cyano-β-aqua and α-aqua-β-cyano isomers of **12** ($C_{54}H_{82}CoN_{14}O_9S_2$ calcd. *m/z* $[M+H]^{2+}$ = 597.3, found 597.3). The peaks at 15.2 and 20.9 min are assigned to the starting material, **10** ($C_{50}H_{72}CoN_{13}O_8$, calcd. *m/z* $[M-CN]^+$ =1015.5 and $[M-CN+H]^{2+}$ = 508.3; found 1015.3 and 508.3).

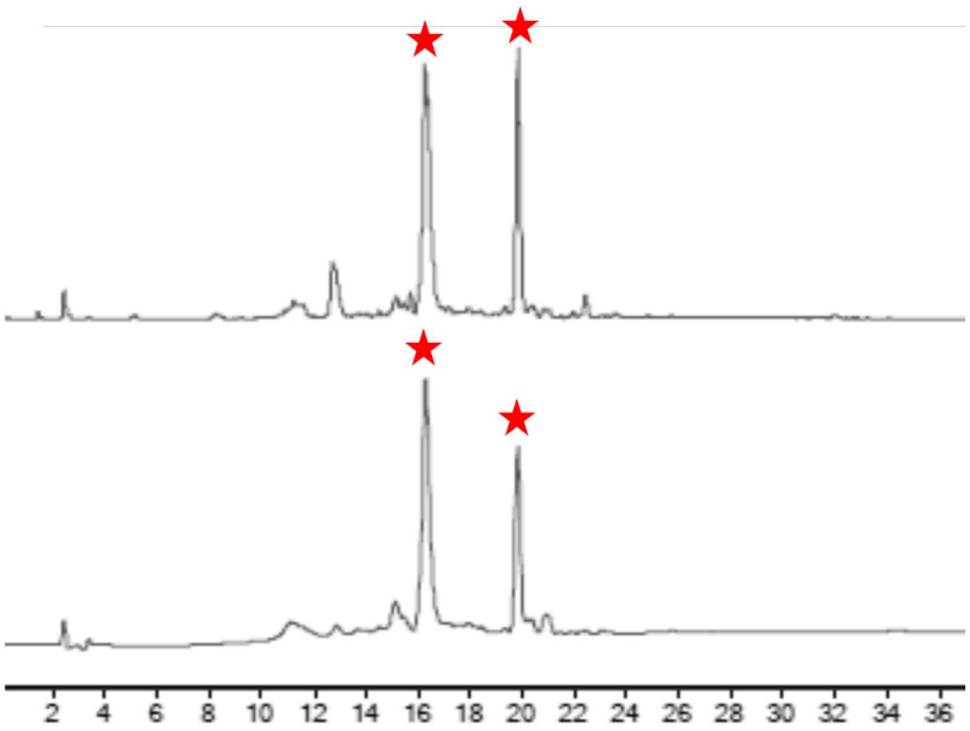

Figure 100: LC-MS TIC (top) and DAD (361 nm, bottom) chromatograms of desalted ***12*** *(LC-MS method 1). The peaks eluting at 16.4 and 19.8 min are from the the α-cyano-β-aqua and α-aqua-β-cyano isomers of* ***12*** *($C_{54}H_{82}CoN_{14}O_9S_2$ calcd. m/z $[M+H]^{2+}$ =597.3, found 597.3).*

The ^{1}H NMR spectrum was obtained for the desalted product to confirm that the macrocycle had not decomposed since this had occurred during the earlier attempts to synthesise **12**. The ^{1}H NMR spectrum showed proton resonances at 6.43 and 6.50 ppm, from the C10 protons of the α-cyano-β-aqua and α-aqua-β-cyano isomers of **12**. These chemical shifts agree well with the C10 chemical shifts of compounds **9** and **11**, indicating an intact corrin ring. The new proton resonances at 3.00 (4H) and 3.44 (4H) ppm provide further confirmation of the successful conjugation of the cystamine linker. These multiplets are assigned to the four methylene protons of cystamine.

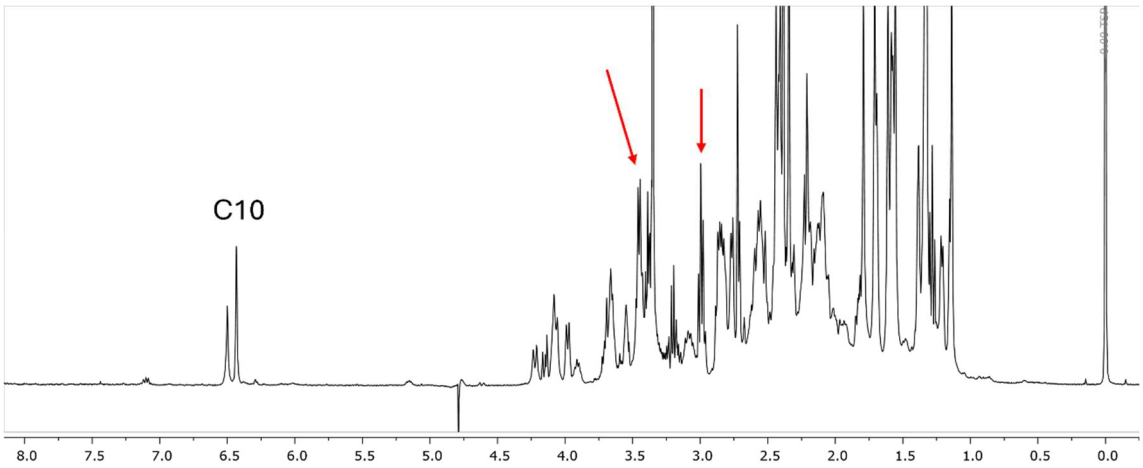

*Figure 101: ^{1}H NMR spectrum of **12** (crude) obtained in D_2O, referenced to TSP. Peaks at 6.43 and 6.50 ppm are assigned to the C10 protons of the α-cyano-β-aqua and α-aqua-β-cyano isomers of **12**. The new peaks highlighted at 3.00 and 3.44 ppm are assigned to the four CH_2 protons of the cystamine linker.*

It was then decided that the desalted product would be functionalised by the addition of a fluorophore since separation of the product from **12** and other impurities would be easier to achieve due to a decrease in the polarity of the compound upon conjugation of the fluorophore.

To summarise, functionalisation of Cbi with the cystamine linker was challenging, affording low yields and purity. Although the compound was not successfully purified, desalting the crude reaction mixture over a reversed-phase C18 silica plug removed most of the impurities (determined by LC-MS). Despite the synthetic difficulty, ^{1}H NMR spectroscopy and LC-MS confirmed the successful synthesis **12**.

3.2.7 Synthesis and analysis of the NBD-X conjugates of Cbi

Compound 13

The synthesis of **13** was carried out using the same synthetic procedure as described for compounds **3** and **4** in Chapter 2. Utilising the peptide coupling agents EDC and HOBt resulted in formation of a peptide bond between the terminal amine of **11** and the carboxylic acid of NBD-X (Scheme 16).

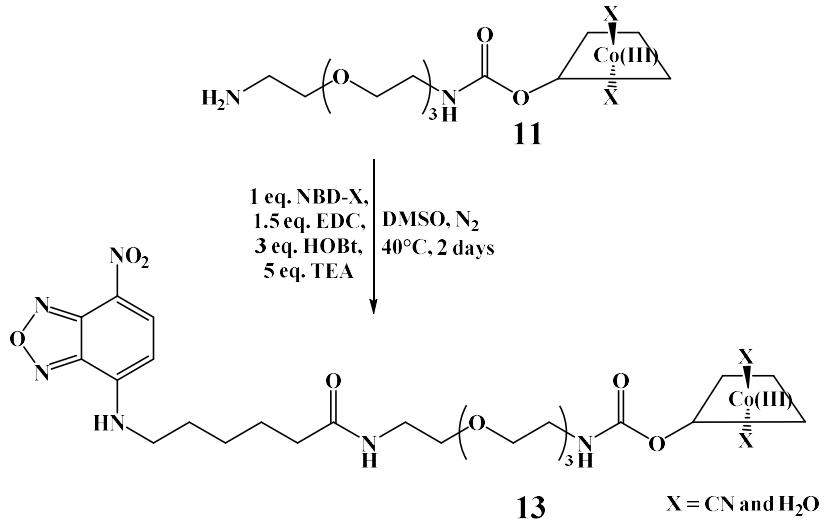

*Scheme 16: Synthetic method for the synthesis of **13**.*

The reaction progress was monitored by LC-MS chromatography with the reaction reaching completion after 48 h, by monitoring the consumption of **11** (Figure 102). Peaks representing the starting material, **11**, were observed at 14.3 and 15.0 min (*m/z* values of 1233.6 and 617.3). The TIC and DAD (361 nm) showed clear differences in the number of peaks, with more peaks present in the TIC. Peaks at 22.4 and 23.3 min were assigned to the α-cyano-β-aqua and α-aqua-β-cyano isomers of **13** ($C_{70}H_{102}CoN_{18}O_{16}$ calcd. *m/z* $[M]^+$ = 1509.7, $[M+H]^{2+}$ = 755.4 and $[M+2H]^{3+}$ = 503.9; found 1509.7, 755.5 and 504.1). The compounds responsible for the other peaks retaining between 22-24 and 30-32 min could not be identified.

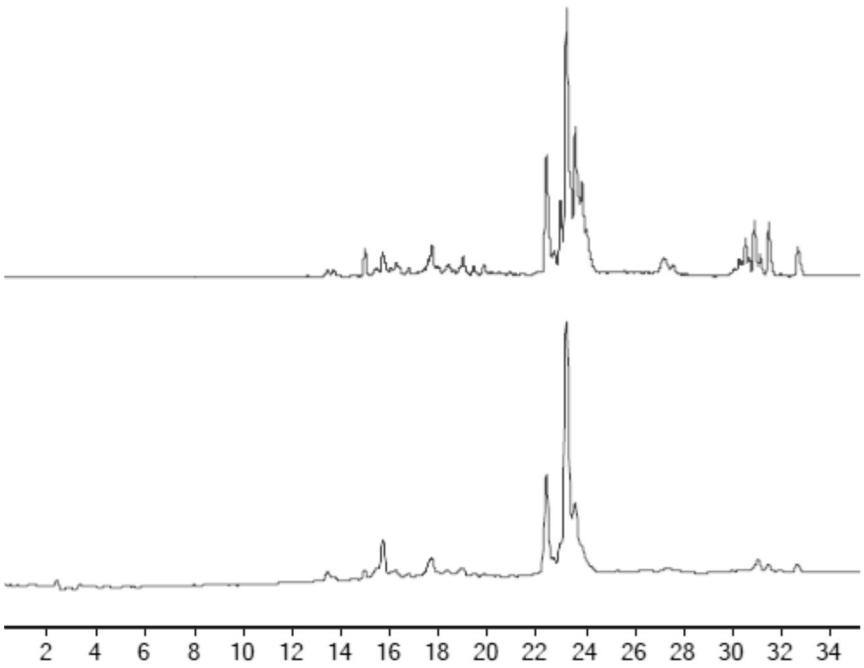

*Figure 102: LC-MS TIC (top) and DAD (361 nm, bottom) chromatograms of crude **13** (LC-MS method 3). Peaks at 22.4 and 23.3 min were assigned to the α-cyano-β-aqua and α-aqua-β-cyano isomers of **13** ($C_{70}H_{102}CoN_{18}O_{16}$ calcd. m/z $[M]^+$ = 1509.7, $[M+H]^{2+}$ = 755.4 and $[M+2H]^{3+}$ = 503.9; found 1509.7, 755.5 and 504.1).*

Compound **13** was purified by reversed-phase C18 chromatography. Two deep orange bands were collected at 60% CH_3CN in H_2O. The orange fractions were combined and analysed by LC-MS (Figure 103). Two peaks were present in the DAD (361 nm) chromatogram at 22.3 and 23.1 min from the α-cyano-β-aqua and α-aqua-β-cyano isomers of **13** ($C_{70}H_{102}CoN_{18}O_{16}$ calcd. *m/z* $[M]^+$ = 1509.7, $[M+H]^{2+}$ = 755.4 and $[M+2H]^{3+}$ = 503.9; found 1509.7, 755.5 and 504.1). However, close analysis of the TIC chromatogram showed overlapping peaks, with three smaller peaks at 22.7, 22.9 and 23.6 min.

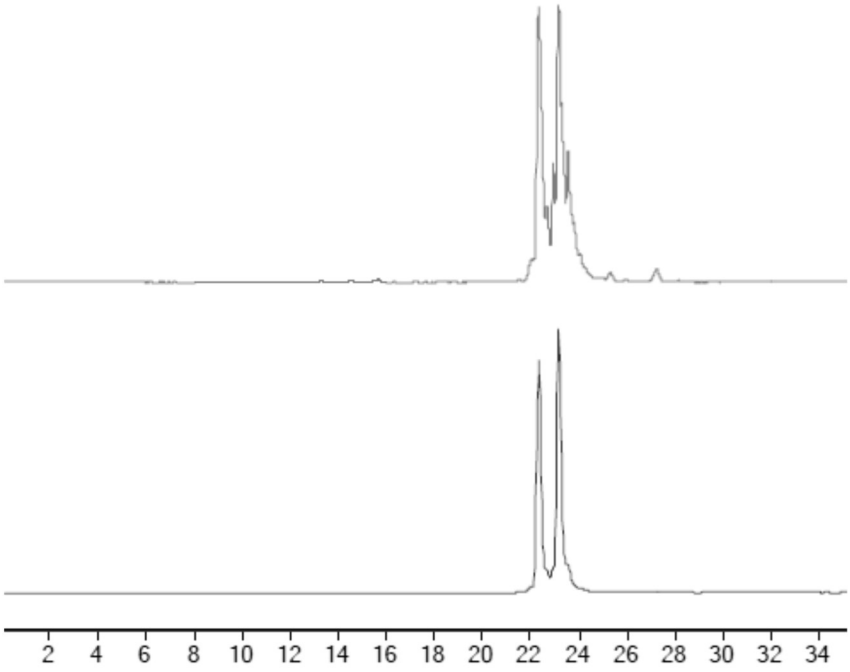

*Figure 103: LC-MS TIC (top) and DAD (361 nm, bottom) chromatograms of pure **13** (LC-MS method 3). Peaks at 22.4 and 23.3 min were assigned to the α-cyano-β-aqua and α-aqua-β-cyano isomers of **13** ($C_{70}H_{102}CoN_{18}O_{16}$ calcd. m/z $[M]^+$ = 1509.7, $[M+H]^{2+}$ = 755.4 and $[M+2H]^{3+}$ = 503.9; found 1509.7, 755.5 and 504.1).*

The peaks at 22.9 and 23.6 min both had *m/z* values of 973.9 and 649.6, corresponding to a 2+ and 3+ species from the same compound. These peaks are likely α-cyano-β-aqua and α-aqua-β-cyano isomers of the same Cbi derivative. This impurity has been assigned to a product incorporating three PEG linkers as observed during the synthesis of **11** ($C_{88}H_{138}CoN_{22}O_{24}$ calcd. *m/z* $[M+H]^{2+}$ = 974.0 and $[M+2H]^{3+}$ = 649.7; found 973.9 and 649.6, Figure 104). Interestingly the DAD (361 nm) chromatogram does not show the presence of these peaks, indicating they are present in a small quantity. This is an assumption based on compound **13** and the additional product having the same molar absorbance co-efficient at 361 nm, which is reasonable given that the macrocycle absorbs at this wavelength and is the same for all Cbi compounds. Due to the closely overlapping retention times, this product was not purified further.

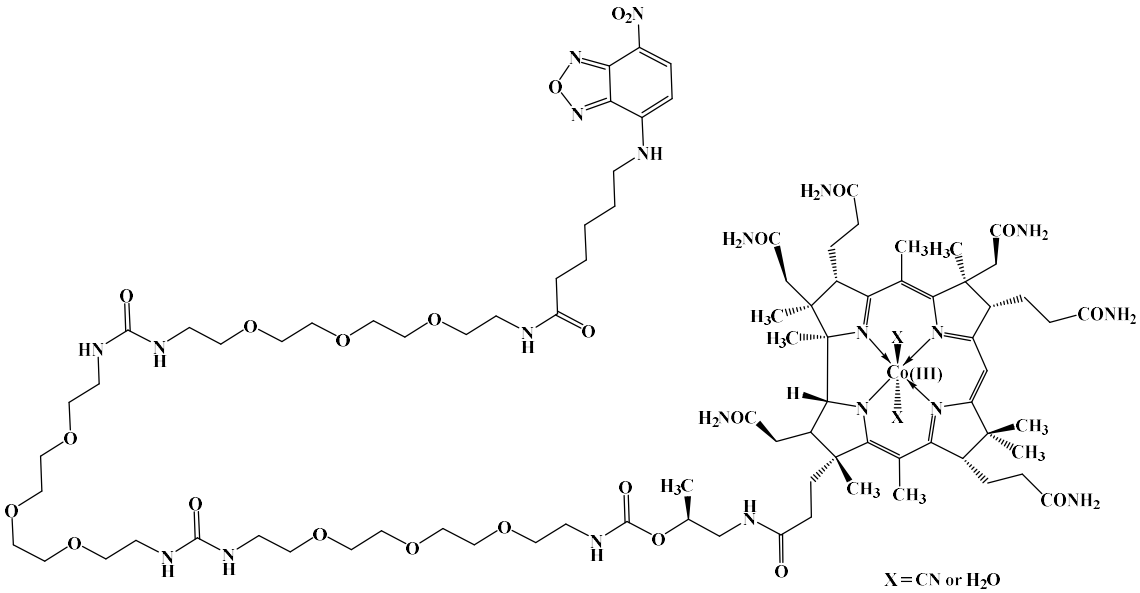

Figure 104: Structure of CNCbi-(PEG)$_3$-NBD-X impurity incorporating three 1,11-diamino-3,6,9-trioxaundecane linkers.

^{1}H NMR spectroscopy analysis of **13** was carried out in MeOH-d_4 and two resonances were identified in the aromatic region (Figure 105). The doublets resonating at 8.53 (J = 9.0, 1H) and 6.35 (J = 9.0, 1H) ppm showed correlations in the COSY spectra and are the adjacent protons of the NBD-X fluorophore. However, the peak at 6.35 ppm integrated for 1.2 protons and there is another overlapping peak to the left. This other peak is the C10 proton of the CNCbi corrin ring. The multiplet at 6.35 ppm should therefore integrate to two protons, not 1.2 as observed. The C10 proton of the corrin ring is known to undergo electrophilic substitution, the most notable example being the substitution of H for Cl at this position upon exposure to HOCl.[23] The C10 proton of CNCbl can undergo exchange in protic deuterated solvents; however, this requires acidic conditions. Studies on deuterium exchange are limited for Cbi. This exchange was only investigated for methylCbi and ethylCbi where deuterium exchange rates were dependent on the axial ligand (half-lives of 10 and 30 min, respectively).[24,25] Although the NMR spectrum of **13** was recorded in MeOH-d_4 with no added acid, proton-deuterium exchange of the C10 proton is likely occurring.

Additional evidence of NBD-X coordination can be seen in the low-field region of the ^{1}H NMR spectrum. NBD-X contains a hexyl chain extending from the chromophore. The protons of this chain resonate at 2.28 (t, J = 7.3 Hz, 2H), 1.80 (p, J = 7.4 Hz, 2H), 1.68

(p, J = 7.4 Hz, 2H) and 1.50 ppm (tt, J = 9.9, 5.9 Hz, 2H), in MeOH-d_4 for NBD-X itself (Chapter 2, Figure 37). These peaks are found in the ^{1}H NMR spectrum of **13** at 2.25 (overlapping), 1.80 (2H), 1.69 (2H) and 1.47 ppm (2H) (Figure 105).

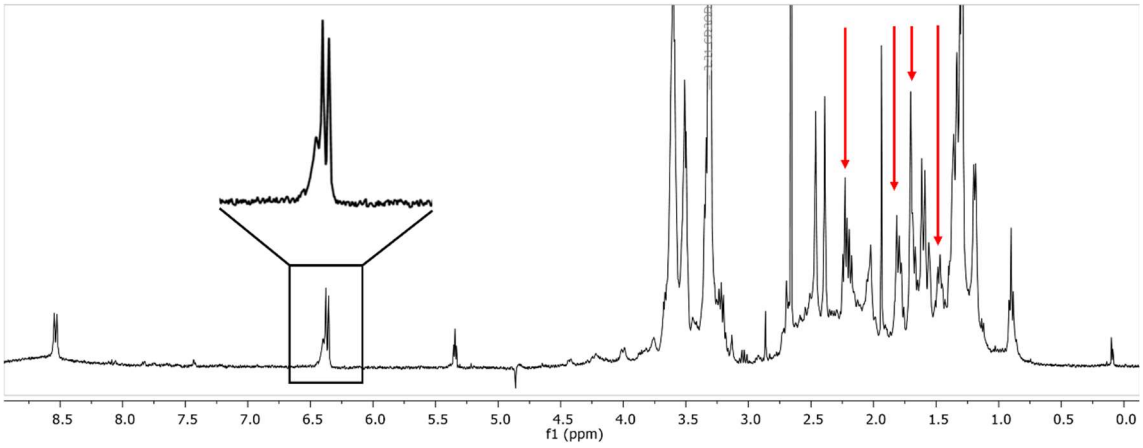

*Figure 105:^{1}H NMR spectrum of **13** obtained in MeOH-d_4. Peaks at 8.53 (1H) and 6.35 ppm (expanded in inset) are assigned to the aromatic protons of the NBD-X chromophore. The highlighted peaks in the low field region (2.23, 1.80 (2H), 1.69 (2H) and 1.47 ppm (2H)) are assigned to the protons on the hexyl chain of NBD-X.*

Due to the low yields of product and therefore a limited mass of the pure compound, ^{13}C NMR analysis was not undertaken. However, ^{1}H NMR and LC-MS analysis indicate a purity of ≥90%. HRMS analysis confirmed the product identity ($C_{70}H_{102}O_{16}N_{18}Co$ $[M]^+$ = 1509.7019 (calcd. *m/z* = 1509.7053)).

Compound 14

The synthesis of **14** employed the same methodology as that used for compounds **3** and **4** (Chapter 2) and compound **13**. Desalted **12** was dissolved in the minimal volume of anhydrous DMSO together with the NBD-X fluorophore and the peptide coupling reagents EDC and HOBt.

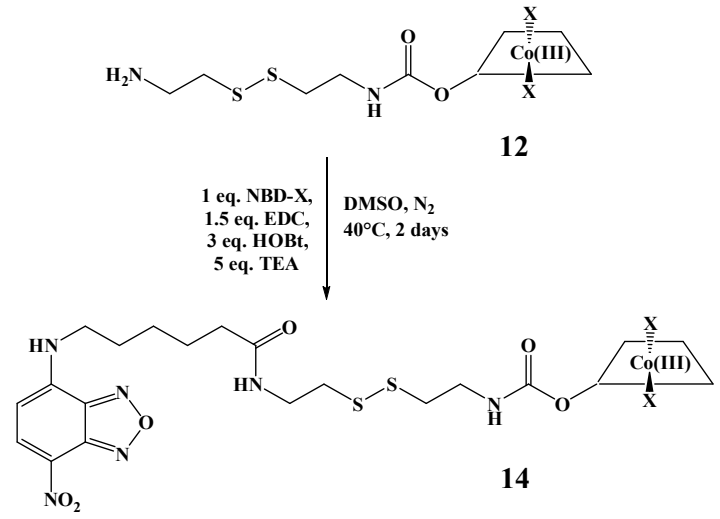

*Scheme 17: Synthetic method for the synthesis of **14**.*

The reaction progress was monitored by LC-MS. After 24 h there was minimal evidence of the starting material, **12**, (12.2 and 13.8 min, Figure 106). The peaks eluting at 23.9 and 24.9 min are assigned to the α-cyano-β-aqua and α-aqua-β-cyano isomers of **14** ($C_{66}H_{94}CoN_{18}O_{13}S_2$ calcd. *m/z* $[M]^+$ = 1469.6 and $[M+H]^{2+}$ = 735.3; found 1469.5 and 735.3). Smaller impurity peaks were identified at 15.5 and 16.6 min (*m/z* value of 653.9). As these peaks were also present in both the DAD at 361 nm and TIC of the starting material, they are likely due to a Cbi associated impurity from the crude **12** reactant.

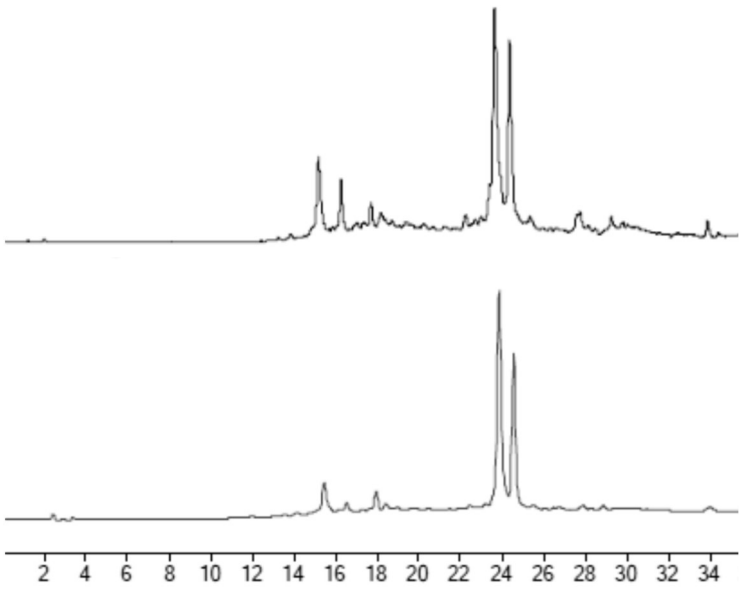

*Figure 106: LC-MS TIC (top) and DAD (361 nm, bottom) chromatograms of the crude **14** product (LC-MS method 3). Peaks at 23.9 and 24.9 min are assigned to the α-cyano-β-aqua and α-aqua-β-cyano isomers of **14** ($C_{66}H_{94}CoN_{18}O_{13}S_2$ calcd. m/z $[M]^+$ = 1469.6 and $[M+H]^{2+}$ = 735.3; found 1469.5 and 735.3).*

Conjugate **14** was purified by reversed-phase C18 chromatography. In total, **14** was columned three times to remove all traces of impurities. The final column maintained an isocratic mobile phase of 55% CH_3CN in H_2O. This isocratic elution method proved the most successful; however, the bands were not well separated during the column and small 8 mL fractions were collected. Direct injection MS analysis of these fractions identified the desired product. The pure fractions (those showing only *m/z* peaks of **14**) were combined and taken to dryness. LC-MS analysis of the combined fractions showed two peaks eluting at 23.1 and 24.1 min (Figure 107), corresponding to the α-cyano-β-aqua and α-aqua-β-cyano isomers of compound **14** ($C_{66}H_{94}CoN_{18}O_{13}S_2$ calcd. *m/z* $[M]^+$ = 1469.6 and $[M+H]^{2+}$ = 735.3; found 1469.5 and 735.3).

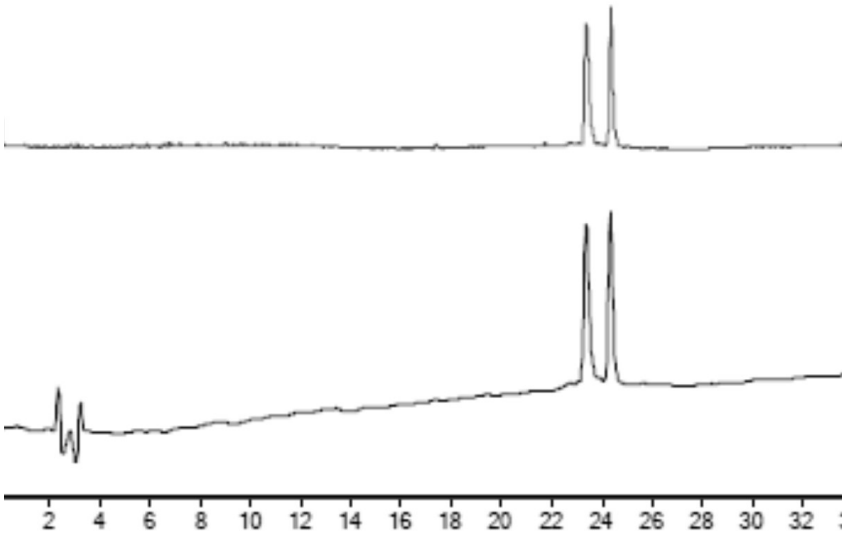

*Figure 107: LC-MS TIC (top) and DAD (361 nm, bottom) chromatograms of pure **14** (LC-MS method 3). The peaks at 23.9 and 24.9 min are assigned to the α-cyano-β-aqua and α-aqua-β-cyano isomers of **14** ($C_{66}H_{94}CoN_{18}O_{13}S_2$ calcd.* m/z *$[M]^+$ = 1469.6 and $[M+H]^{2+}$ = 735.3; found 1469.5 and 735.3).*

Although the yield obtained from the synthesis of **14** was low (~6 mg of product), this was sufficient for further analysis by ^{1}H NMR spectroscopy. The doublets resonating at 8.54 (J = 9.0, 1H) and 6.37 (J = 8.9, 1H) ppm show correlations in the COSY spectrum. These represent the two protons of the NBD-X chromophore with both peaks integrating for 1H (Figure 108). Two proton resonances are expected at approximately 6.45 and 6.38 ppm for the C10 proton of the corrin ring for the two α-cyano-β-aqua and

α-aqua-β-cyano isomers. However, these C10 peaks were absent from the ^{1}H NMR spectrum of **13**, which is likely the result of proton exchange with the deuterium in the solvent. Furthermore, four methylene peaks of the NBD-X moiety are observed in the ^{1}H NMR spectrum of **14** at 2.23, 1.79, 1.68 and 1.47 ppm, analogous to that observed in compound **13**. These peaks could not be integrated due to overlapping resonances with CNCbi protons.

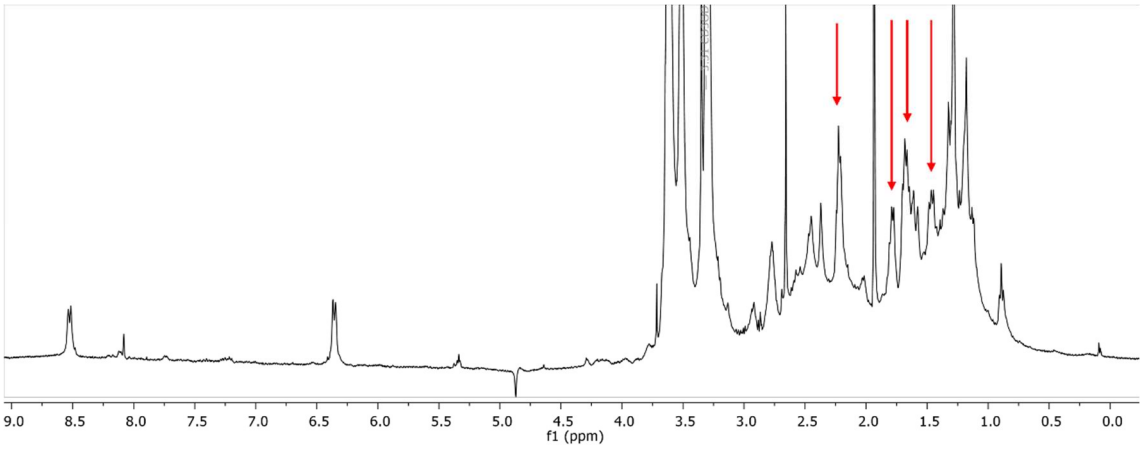

*Figure 108: ^{1}H NMR spectrum of **14** obtained in MeOD-d_4. Doublets in the aromatic region are assigned to the chromophore of NBD-X at 8.52 (J = 9.0, 1H) and 6.37 ppm (J = 8.7, 1H). The highlighted peaks at 2.23, 1.79, 1.68 and 1.47 are four methylenes of the hexyl chain on NBD-X.*

Due to low yields, ^{13}C NMR analysis was not undertaken. LC-MS and ^{1}H NMR spectroscopy of **14** suggest a purity of ≥90%. HRMS confirmed the identity of the compound ($C_{66}H_{94}O_{13}N_{18}CoS_2$ calcd. *m/z* $[M]^+$ 1469.6013, found 1469.6022).

3.2.8 Synthesis and analysis of the sulfo-Cyanine5 conjugate of Cbi

Compound 15

The synthesis of **15** was achieved by peptide bond formation between the amine functionalised linker of the Cbi conjugate, **11** and the NHS ester of the sulfo-Cyanine5 fluorophore (Scheme 18). EDC and HOBt coupling reagents, employed in the synthesis of **13** and **14**, were not required as the sulfo-Cyanine5 molecule is an active NHS ester. In the presence of Et_3N, nucleophilic substitution of the NHS moiety by the linker amine readily occurs. Sulfo-Cyanine5 was used as the limiting reagent and the reaction was carried out in anhydrous DMSO at 40°C. The reaction reached completion within 24 h.

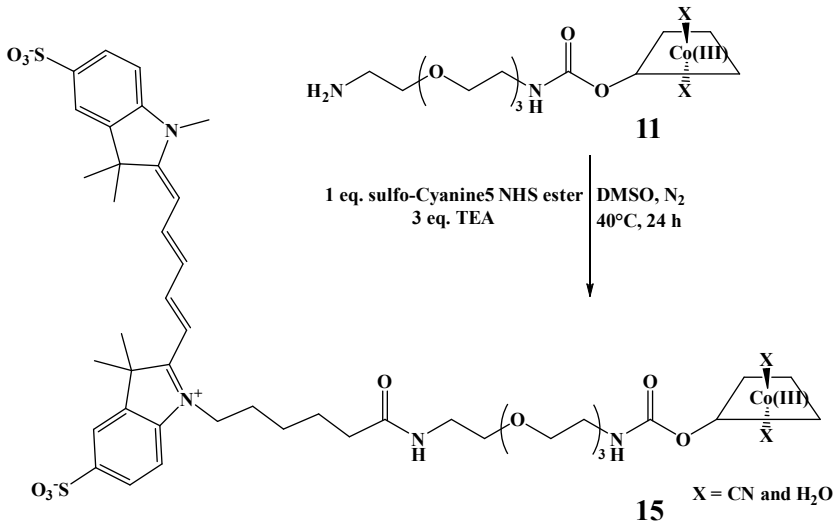

*Scheme 18: Synthetic method for the synthesis of **15**.*

The crude product was analysed by LC-MS. As established in Chapter 2 with the CNCbl-sulfo-Cyanine5 conjugates, dissolving **15** in H_2O for injection into the LC-MS instrument was necessary to obtain a signal in the TIC chromatogram. Numerous peaks were observed between 22-25 min (Figure 109). The peaks retained at 22.8 and 23.4 min are assigned to the α-cyano-β-aqua and α-aqua-β-cyano isomers of **15** ($C_{90}H_{125}CoN_{16}O_{19}S_2$ calcd. *m/z* $[M+H]^+$ = 1857.8, $[M+2H]^{2+}$ = 929.4 and $[M+3H]^{3+}$ = 620.3; found 1858.3, 929.7 and 620.1).

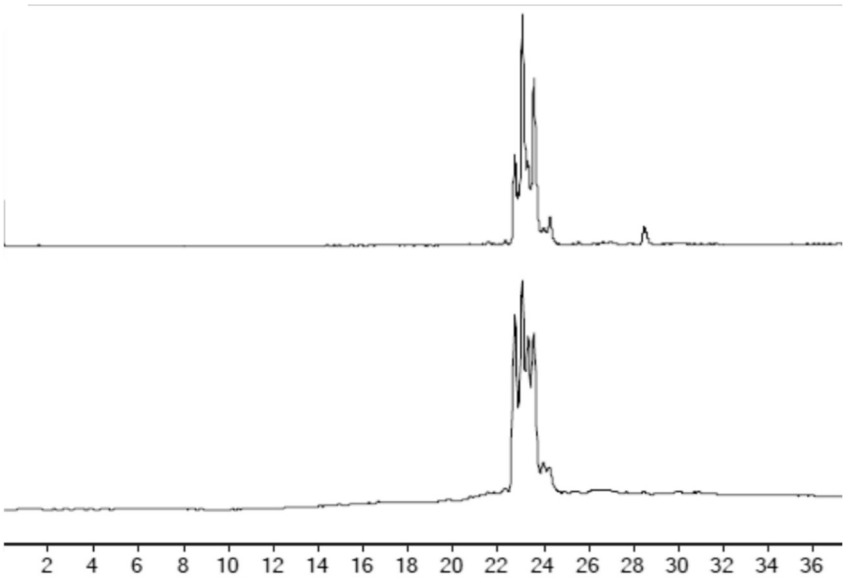

*Figure 109: LC-MS TIC (top) and DAD (361 nm, bottom) chromatograms the of crude product **15** (LC-MS method 3). The peaks at 22.8 and 23.4 min are assigned to the α-cyano-β-aqua and α-aqua-β-cyano isomers of **15** ($C_{90}H_{125}CoN_{16}O_{19}S_2$ calcd. m/z $[M+H]^+$ = 1857.8, $[M+2H]^{2+}$ = 929.4 and $[M+3H]^{3+}$ = 620.3; found 1858.3, 929.7 and 620.1).*

The two closely retaining peaks at 23.1 and 23.6 min were assigned to a side product incorporating three 1,11-diamino-3,6,9-trioxaundecane linkers ($C_{108}H_{161}CoN_{20}O_{27}S_2$ calcd. *m/z* $[M+2H]^{2+}$ = 1148.0 and $[M+3H]^{3+}$ = 765.7; found 1147.9 and 165.7, Figure 110).

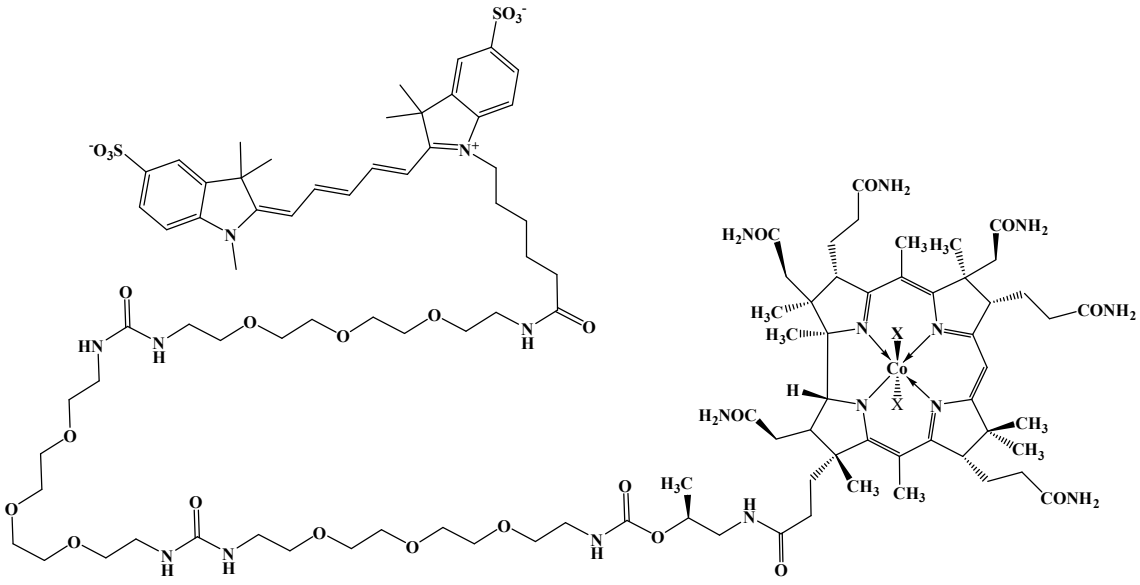

Figure 110: Structure of the CNCbi-(PEG)$_3$-sulfo-Cyanine5 side product containing three 1,11-diamino-3,6,9-trioxaundecane linkers.

Purification of **15** was achieved by reversed-phase C18 chromatography. The purification was run in isocratic conditions with 50% CH_3CN in H_2O to remove the closely eluting impurities. A single very broad blue band slowly eluted from the stationary phase with no clear band separation observed. Small fractions (~5 mL) were collected until the eluant was a pale blue colour. All collected fractions were subjected to direct injection MS. Fractions containing only **15** (*m/z* = 1858.3, 929.7 and 620.1) were combined and taken to dryness by rotary evaporation. LC-MS analysis of the combined pure fractions identified two peaks eluting at 22.7 and 23.4 min, assigned to the isomers of **15** ($C_{90}H_{125}CoN_{16}O_{19}S_2$ calcd. *m/z* $[M+H]^+$ = 1857.8, $[M+2H]^{2+}$ = 929.4 and $[M+3H]^{3+}$ = 620.3; found 1858.3, 929.7 and 620.1). The isocratic purification method proved effective in removing the Cbi-(PEG)$_3$-sulfo-Cyanine5 impurity.

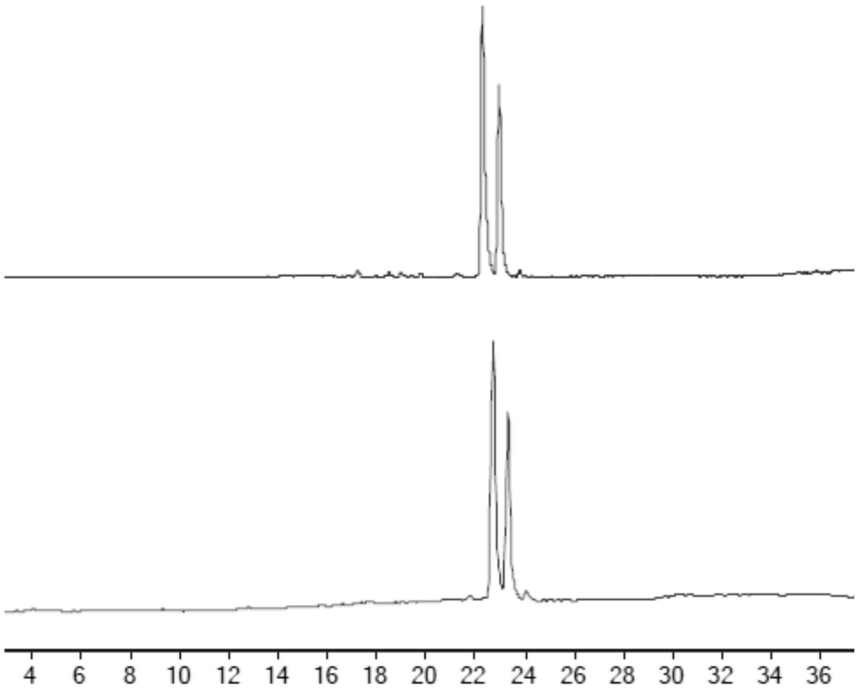

*Figure 111: LC-MS TIC (top) and DAD (361 nm, bottom) chromatograms of pure **15** (LC-MS method 3). Peaks at 22.7 and 23.4 min are assigned to the α-cyano-β-aqua and α-aqua-β-cyano isomers of **15** ($C_{90}H_{125}CoN_{16}O_{19}S_2$ calcd. m/z $[M+H]^+$ = 1857.8, $[M+2H]^{2+}$ = 929.4 and $[M+3H]^{3+}$ = 620.3; found 1858.3, 929.7 and 620.1).*

^{1}H NMR spectroscopic analysis of **15** was carried out in D_2O owing to its greater solubility in this solvent rather MeOH-d_4. COSY analysis was used previously to identify the aromatic protons of the fluorophores for both Cbi and Cbl conjugates. However, compound **15** did not show any correlations in the COSY spectrum. This analysis was run multiple times, and the spectra were all truncated at 5.00 ppm. To gain insight into the aromatic residues of sulfo-Cyanine5, the ^{1}H NMR spectrum of the sulfo-Cyanine5-NHS ester was taken in D_2O and directly compared with the spectrum of **15** (Figure 112). Similarities were observed for the resonances at 6.15-6.19 (m, 2H), 6.45-6.52 (m, 1H), 7.30-7.34 (m, 2H), 7.78-7.86 (m, 4H) and 7.89-8.05 ppm (m, 2H) in both spectra. These multiplets are assigned to the protons of sulfo-Cyanine5-NHS, **d/h**, **f**, **c/i**, **a/b/j/k**, and ***e*/*g*** respectively (Figure 113, red). Two other signals are present in the aromatic ^{1}H NMR spectrum of **15** at 6.29 and 6.36 ppm. These peaks have been assigned to the C10 protons of the α-cyano-β-aqua and α-aqua-β-cyano isomers of **15**. However, these two peaks are expected to integrate to one proton in total but instead integrate to 0.3 and 0.2,

respectively. It is likely that the C10 protons are partially exchanged with deuterium from the solvent, as was observed for **13** and **14**, accounting for the smaller integral.

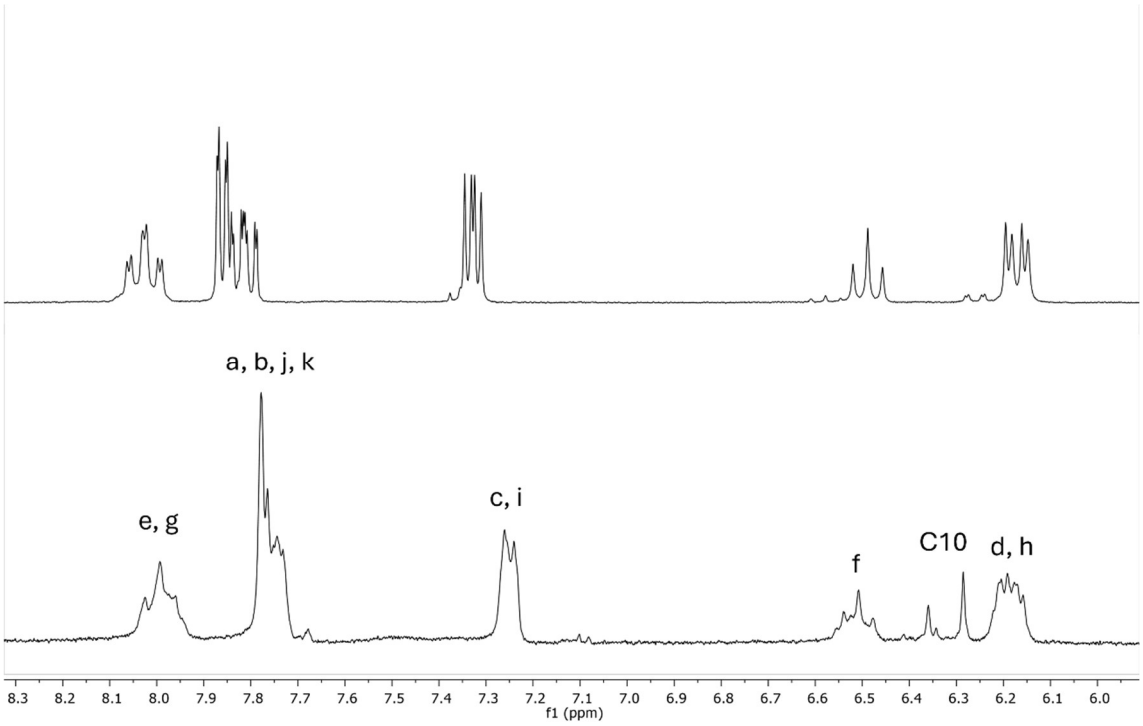

*Figure 112: Aromatic ^{1}H NMR spectra of sulfo-Cyanine5 NHS ester (top) and **15** (bottom) in D_2O. Multiplets are assigned as 6.15-6.19 (2H, m, **d** and **h**), 6.45-6.52 (1H, m, **f**), 7.30-7.34 (2H, m, **c** and **i**), 7.78-7.86 (1H, m, **a**, **b**, **j** and **k**) and 7.89-8.05 ppm (2H, m, **e** and **g**) in both spectra. The peaks at 6.29 and 6.36 ppm are assigned to the C10 protons of the α-cyano-β-aqua and α-aqua-β-cyano isomers of **15**.*

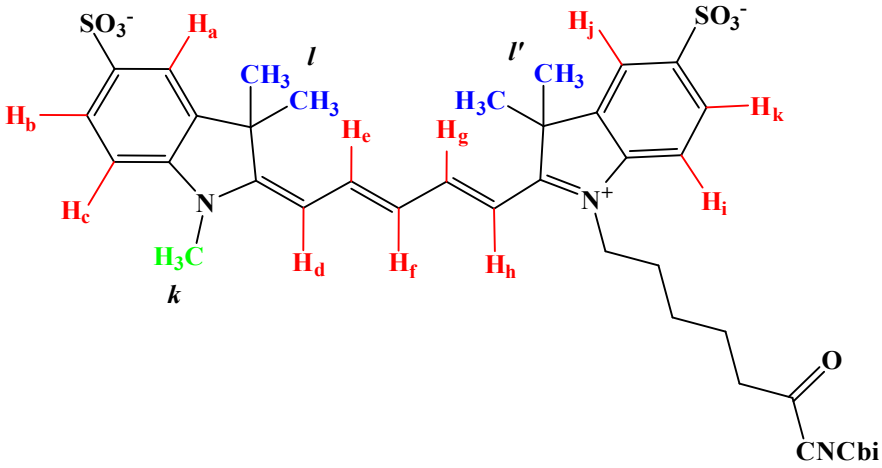

*Figure 113: Structure of **15**, highlighting the aromatic protons (**a-j**, red) and select low-field protons (**l, l'** and **k**, blue and green) of the sulfo-Cyanine5 moiety. CNCbi-linker atoms have been simplified to CNCbi for clarity.*

Analysis of the low field ^{1}H NMR spectrum of both the sulfo-Cyanine5-NHS ester and **15** further supported the successful synthesis of the conjugate (Figure 114). Sulfo-Cyanine5-NHS has three intense methyl peaks at 1.66 (12H), 2.89 (4H) and 3.57 ppm (3H). These peaks can be assigned to the four CH_3 substituents (***l/l'***, Figure 113), the four succinimide protons of the NHS ester and the *N*-CH_3 (***k***, Figure 113) group of sulfo-Cyanine5-NHS. The peaks corresponding to the four CH_3 groups and the *N*-CH_3 moiety are observed in **15** at 1.68 (12H) and 3.55 (overlapping) ppm. The peak at 2.89 corresponding to the NHS-ester protons is absent from **15**, as expected.

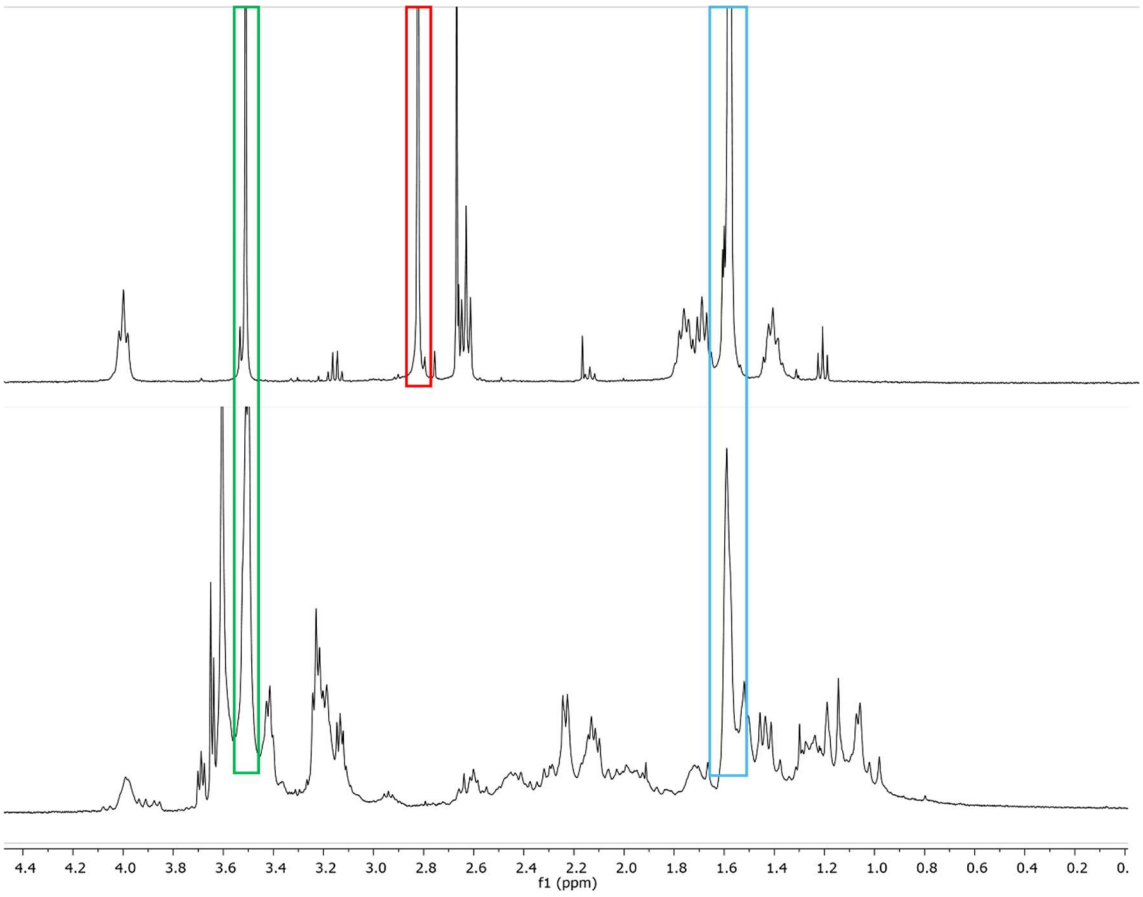

*Figure 114: Low-field ^{1}H NMR spectra of sulfo-Cyanine5-NHS ester (top) and **15** (bottom) in D_2O. The peaks assigned to the four CH_3 (**l/l'**, Figure 113) and the N-CH_3 (**k**, Figure 113) in both sulfo-Cyanine5-NHS and **15** are highlighted in blue and green, respectively. The NHS ester protons of sulfo-Cyanine5-NHS are highlighted in red and are absent from **15**.*

Due to the limited amount of product obtained the ^{13}C NMR spectrum was not recorded for **15**. ^{1}H NMR spectroscopy and LC-MS analysis suggest a purity of ≥95%. HRMS

confirmed the identity of **15** ($C_{90}H_{125}O_{19}N_{16}CoS_2$ $[M+2Na]^{2+}$ = 951.3930 (calcd. *m/z* = 951.3932)).

3.2.9 Synthesis and analysis of the Cyanine7 conjugate of Cbi

Compound 16

The synthesis of **16** was achieved using crude **11** as the starting material, together with the Cyanine7-NHS ester (Scheme 19). Cyanine7-NHS was utilised as the limiting reagent, in addition to Et_3N. The reaction was carried out in DMSO under N_2 at 40°C for 24 h.

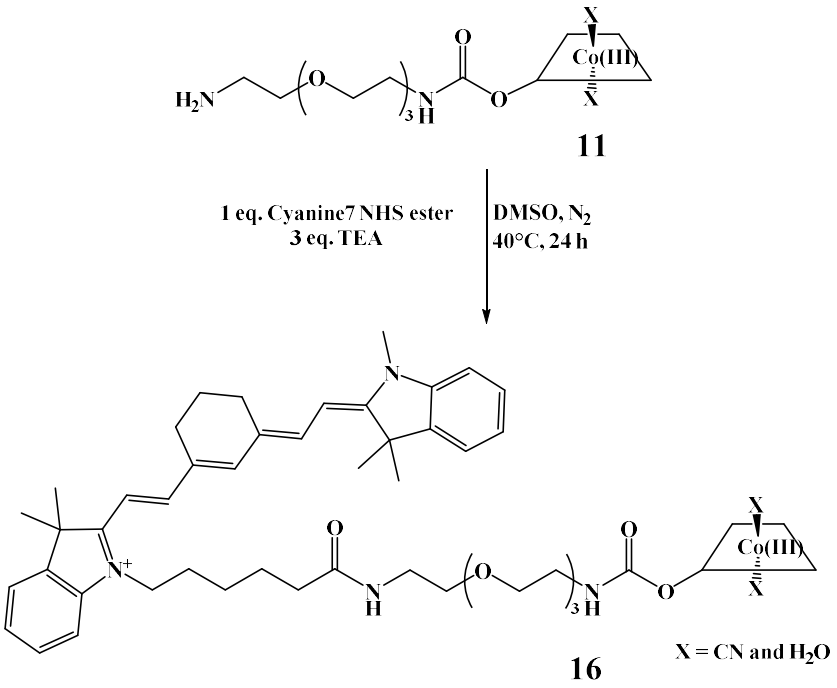

*Scheme 19: Synthetic method for the synthesis of **16**.*

Reaction progress was monitored by LC-MS and reached completion after 24 h. The crude product had four major peaks in the LC-MS chromatograms at 29.8, 31.7, 32.8 and 33.2 min (Figure 115). The peak at 29.8 min was from **16** ($C_{95}H_{133}CoN_{16}O_{13}$ calcd. *m/z* $[M]^{2+}$ = 883.0 and $[M+H]^{3+}$ = 589.0; found 882.7 and 588.8). The peaks eluting at 32.7 and 33.2 min were assigned to hydrolysed Cyanine7-COO^- ($C_{37}H_{45}N_2O_2$ calcd. *m/z* $[M]^+$ = 549.3; found 549.4) and the Cyanine7-NHS ester ($C_{41}H_{48}N_3O_4$ calcd. *m/z* $[M]^+$ = 646.4; found 646.3), respectively (Figure 116). The final peak eluting at 31.7 min had *m/z* values of 532.6 and 709.7, likely corresponding to a 3+ and 4+ peak from the same parent compound but could not be identified. During the synthesis of **13** and **15**, the Cbi-$(PEG)_3$-

fluorophore side product was observed in LC-MS chromatograms. The Cbi-$(PEG)_3$-Cyanine7 conjugate has *m/z* values of 725.7 and 544.6 (calcd. $[M+H]^{3+}$ and $[M+2H]^{4+}$ for $C_{112}H_{169}CoN_{19}O_{21}$), which are significantly different from 709.7 and 532.6.

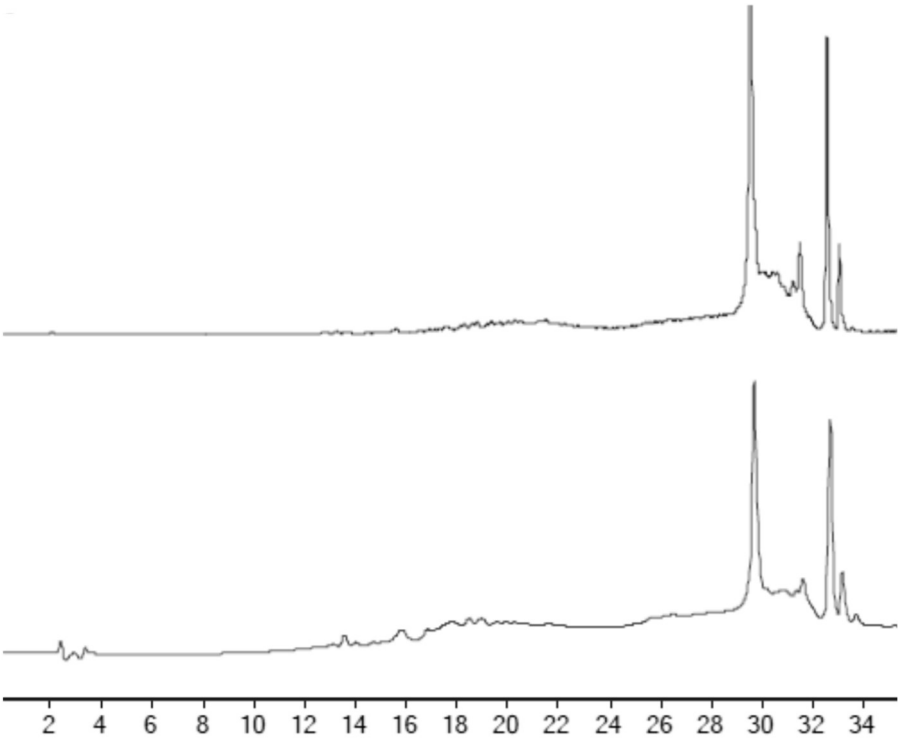

Figure 115: LC-MS TIC (top) and DAD (361 nm, bottom) chromatograms of the crude product ***16*** *(LC-MS method 3). The peak eluting at 29.8 min has been assigned to* ***16*** *($C_{95}H_{133}CoN_{16}O_{13}$ calcd. m/z $[M]^{2+}$ = 883.0 and $[M+H]^{3+}$ = 589.0; found 882.7 and 588.8).*

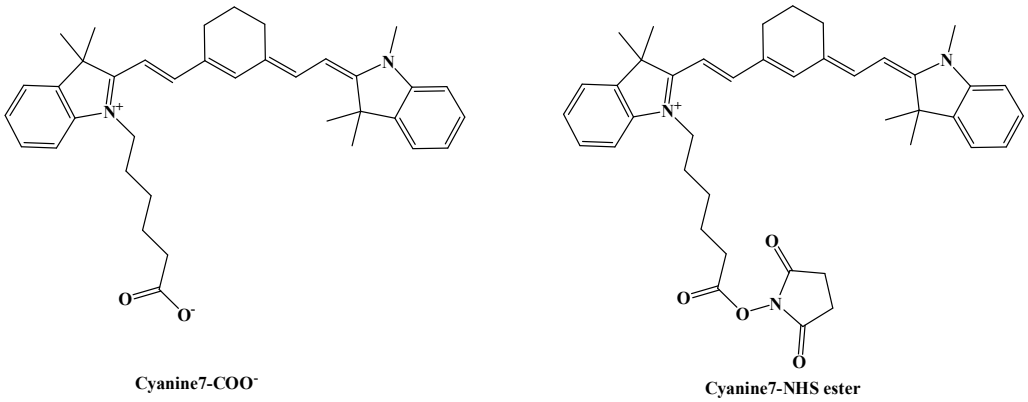

Figure 116: Structures of Cyanine7-COO^- and Cyanine7-NHS.

The purification of **16** proved to be challenging. The crude product was columned by reversed-phase C18 chromatography three times to remove impurities observed in the aromatic region of the ^{1}H NMR spectrum. The final reversed-phase C18 column was run under isocratic conditions of 60% CH_3CN in H_2O with 0.1% formic acid added to both the organic and aqueous mobile phase. Compound **16** eluted from the stationary phase as a dull green band and was taken to dryness by rotary evaporation. LC-MS was used to determine the purity of **16** (Figure 117). Two peaks retained at 29.7 and 30.7 min from the α-cyano-β-aqua and α-aqua-β-cyano isomers of **16** ($C_{95}H_{133}CoN_{16}O_{13}$ calcd. *m/z* $[M]^{2+}$ = 883.0 and $[M+H]^{3+}$ = 589.0; found 882.7 and 588.8).

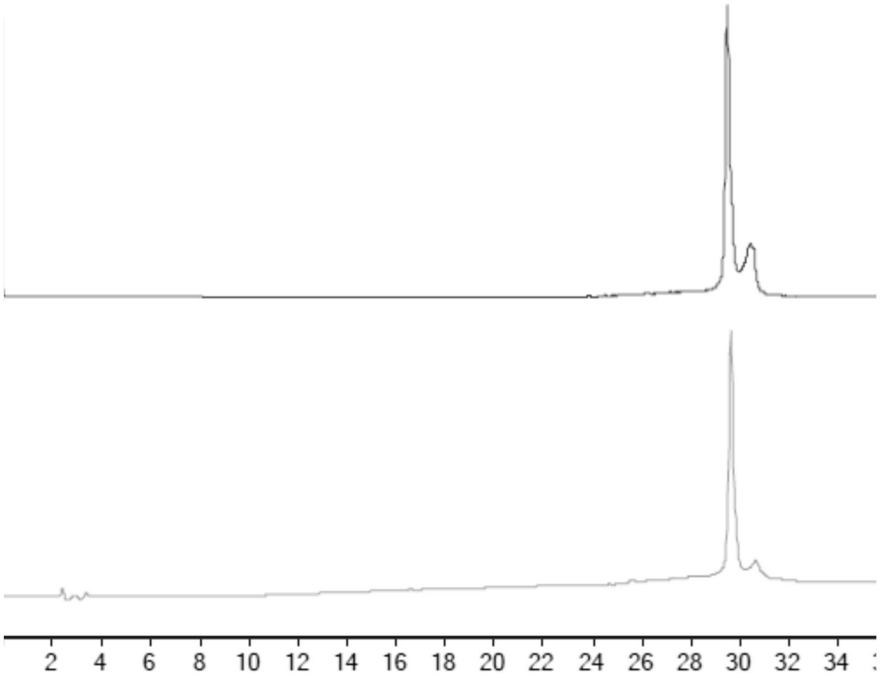

*Figure 117: LC-MS TIC (top) and DAD (361 nm, bottom) chromatograms of pure **16** (LC-MS method 3). The peaks eluting at 29.7 and 30.7 min have been assigned to the α-cyano-β-aqua and α-aqua-β-cyano isomers of **16** ($C_{95}H_{133}CoN_{16}O_{13}$ calcd. m/z $[M]^{2+}$ = 883.0 and $[M+H]^{3+}$ = 589.0; found 882.7 and 588.8).*

^{1}H NMR spectroscopy in MeOH-d_4 was undertaken to further assess the purity of **16**. In the COSY experiment, no coupling was observed for **16** above 5.00 ppm. The aromatic region of the ^{1}H NMR spectrum of **16** and Cyanine7-NHS were compared (Figure 118). The proton signals at 6.14-6.20 (m, 2H), 7.23-7.26 (m, 4H), 7.37-7.47 (m, 5H) and 7.71-7.78 ppm (m, 2H) were present in both Cyanine7-NHS and **16**.

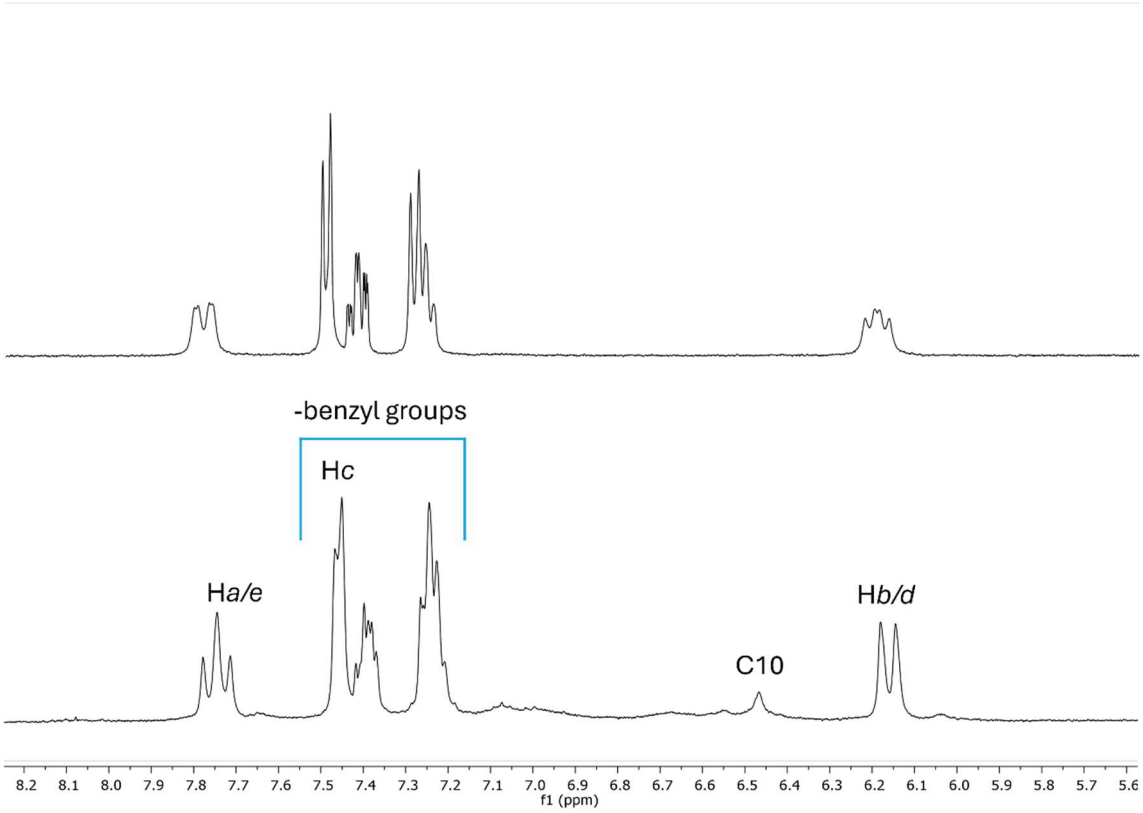

*Figure 118: Aromatic region of the ^{1}H NMR spectrum of the Cyanine7-NHS ester (top) and **16** (bottom) in MeOH-d_4. Multiplets have been assigned as 6.47-6.20 (2H, m, **d** and **b**), 7.23-7.26 (4H, m, benzyl protons), 7.37-7.47 (4H, m, benzyl protons), 7.72 (1H, m, **c**) and 7.71-7.78 ppm (2H, m, **a** and **e**) for both Cyanine7-NHS and **16**. The peak at 6.47 ppm of **16** has been assigned to the C10 proton of the corrin ring.*

Peaks assignments for the Cyanine7 protons of **16** are **d**/**b** (6.47-6.20, m, 2H), benzyl moiety (7.23-7.26, m, 4H and 7.37-7.47, m, 4H) overlapping with **c** (7.72 ppm, 1H) and **a**/**e** (7.71-7.78 ppm, m, 2H) (Figure 119). The proton signal at 6.47 (s, 0.4H) was assigned to the C10 proton of the corrin ring. As observed for all the Cbi fluorophore conjugates, the C10 proton is prone to deuterium exchange, resulting in an area corresponding to 0.4 rather than 1H. The C10 proton of a second isomer of Cbi was not observed, possibly due to proton-deuterium exchange.

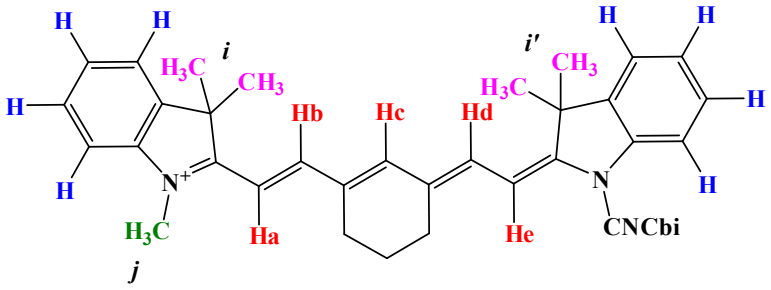

*Figure 119: Structure of compound **16** highlighting the aromatic protons, the four diagnostic CH_3 moieties (**i/i'**, purple) and the N-CH_3 (**j**, green).*

The low-field region of the ^{1}H NMR spectrum of **16** was also analysed. The distinct peak at 1.71 ppm (s, 12H) is present in both Cyanine7-NHS and **16** and is from the four CH_3 protons, **i** and **i'** (Figure 119). A further peak at 3.60 ppm (3H) corresponding to the *N*-CH_3 protons of Cyanine7-NHS (**j**) is likely overlapping with another larger peak at 3.60 ppm from **16**. Cyanine7-NHS also has a large peak at 2.83 ppm (s, 4H) from the four NHS ester protons. This signal is not present in **16**, due to peptide bond formation.

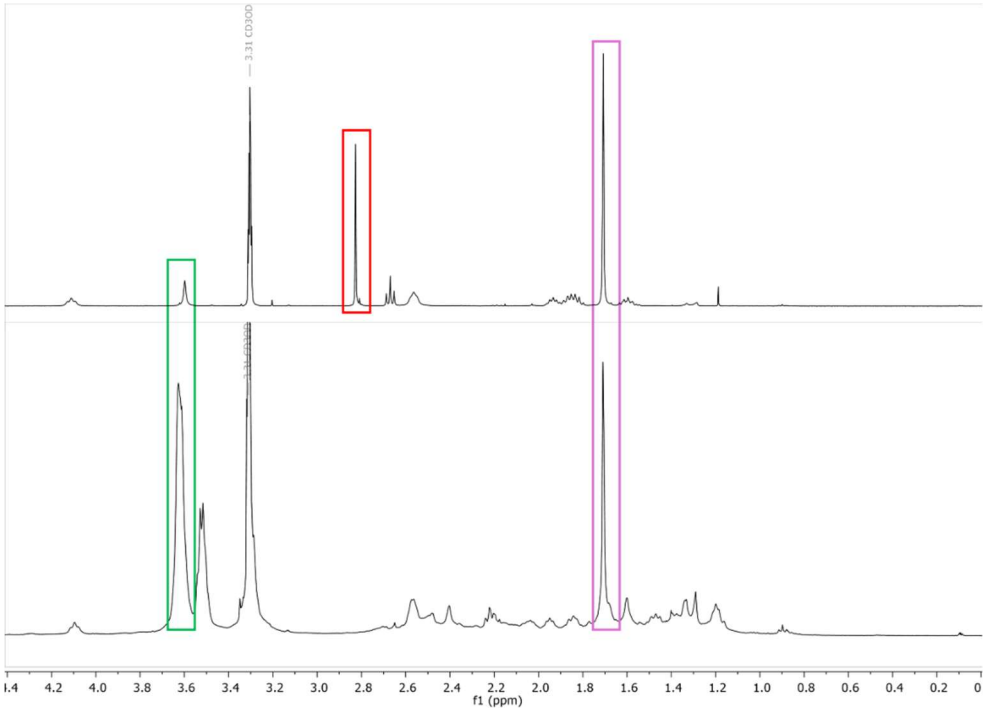

*Figure 120: Low-field region of the ^{1}H NMR spectra of Cyanine7-NHS ester (top) and **16** (bottom) in MeOH-d_4. Peaks can be assigned to the four CH_3 groups (**i/i'**, pink, Figure 119) and the N-CH_3 (**j**, green, Figure 119) substituent in both Cyanine7-NHS and **16**. The NHS ester protons of Cyanine7-NHS are highlighted in red, absent from **16**.*

Due to limited amount of compound **16**, the ^{13}C NMR spectrum was not recorded. Analysis by ^{1}H NMR and LCMS indicate a purity of ≥95%, however, difficulty during purification resulted in a low yield of 18.3%. HRMS analysis confirmed the identity of **16** ($C_{95}H_{133}O_{13}N_{16}Co$ $[M]^{2+}$ calcd. *m/z* 882.4779, found 882.4760).

3.3 Conclusion

This chapter presents the synthesis and characterisation of Cbi-linker compounds (**11** and **12**) incorporating the 1,11-diamino-3,6,9-trioxaundecane and cystamine linkers. Purification of **11** and **12** by normal-phase silica and DCVC chromatography methods were unsuccessful. Purification by reversed-phase C18 chromatography was also unsuccessful. These methodologies were therefore replaced by thorough desalting using a reversed-phase C18 silica plug to remove some impurities. Due to the inability to purify the Cbi-linker compounds, yields were not obtained for these syntheses.

The crude Cbi-linker molecules were functionalised with a fluorescent group NBD-X, sulfo-Cyanine5 or Cyanine7. Purification of the Cbi-linker-fluorophore conjugates was also challenging. Reversed-phase C18 chromatography under isocratic conditions allowed for purity above 90% to be obtained. All fluorescent conjugates have been analysed by LC-MS, ^{1}H NMR spectroscopy and HRMS to confirm the identity and purity of each sample. Yields obtained for the Cbi-fluorophore conjugates ranged from 18-63%, which is significantly lower than the CNCbl-linker-fluorophore derivatives (conjugates **3-8**) which had yields of 54-92%. Interestingly, ^{1}H NMR analysis of compounds **13-16** in both MeOH-d_4 and D_2O showed proton-deuterium exchange of the C10 proton of the corrin ring. Proton-deuterium exchange resulted in ^{1}H NMR peak for the C10 proton to not be observed (compound **14**) or have a reduced peak area (integration of <0.4H for compounds **13** and **15-16**). However, proton-deuterium exchange was not observed for the Cbi and Cbi-linker compounds **9-12**.

3.4 References

(1) Równicki, M.; Wojciechowska, M.; Wierzba, A. J.; Czarnecki, J.; Bartosik, D.; Gryko, D.; Trylska, J. Vitamin B_{12} as a Carrier of Peptide Nucleic Acid (PNA) into Bacterial Cells. *Sci. Rep.* **2017**, *7* (1). https://doi.org/10.1038/s41598-017-08032-8.
(2) Lawrence, A. D.; Nemoto-Smith, E.; Deery, E.; Baker, J. A.; Schroeder, S.; Brown, D. G.; Tullet, J. M. A.; Howard, M. J.; Brown, I. R.; Smith, A. G.; Boshoff, H. I.; Barry, C. E.; Warren, M. J. Construction of Fluorescent Analogs to Follow the Uptake and Distribution of Cobalamin (Vitamin B_{12}) in Bacteria, Worms, and Plants. *Cell Chemical Biology.* **2018**. https://doi.org/10.1016/j.chembiol.2018.04.012.
(3) Proinsias, K. ó; Giedyk, M.; Sharina, I. G.; Martin, E.; Gryko, D. Synthesis of New Hydrophilic and Hydrophobic Cobinamides as NO-Independent sGC Activators. *ACS Med. Chem. Lett.* **2012**, *3* (6), 476–479. https://doi.org/10.1021/ML300060N.
(4) Doyle, R. Peptide Drug Improvement Using Vitamin B_{12} and Haptocorrin Binding Substrate Conjugates. US20220184218A1, June 16, 2022. https://patents.google.com/patent/US20220184218A1/en (accessed 2025-02-03).
(5) Müller, G.; Müller, O. N, O-Acylwanderung Bei Cobinamid - Gewinnung von Cobyrsäure Aus Cobamiden. **1966**. https://doi.org/10.1515/znb-1966-1212.
(6) Hannibal, L.; Bunge, S. D.; van Eldik, R.; Jacobsen, D. W.; Kratky, C.; Gruber, K.; Brasch, N. E. X-Ray Structural Characterization of Imidazolylcobalamin and Histidinylcobalamin: Cobalamin Models for Aquacobalamin Bound to the B_{12} Transporter Protein Transcobalamin. *Inorg. Chem.* **2007**, *46* (9), 3613–3618. https://doi.org/10.1021/ic070022n.
(7) Proinsias, K. ó; Karczewski, M.; Zieleniewska, A.; Gryko, D. Microwave-Assisted Cobinamide Synthesis. *J. Org. Chem.* **2014**, *79* (16), 7752–7757. https://doi.org/10.1021/JO501364B.
(8) Wierzba, A. J.; Maximova, K.; Wincenciuk, A.; Równicki, M.; Wojciechowska, M.; Nexø, E.; Trylska, J.; Gryko, D. Does a Conjugation Site Affect Transport of Vitamin B_{12}–Peptide Nucleic Acid Conjugates into Bacterial Cells? *Chem. – Eur. J.* **2018**, *24* (70), 18772–18778. https://doi.org/10.1002/chem.201804304.
(9) Salerno, E. V.; Miller, N. A.; Konar, A.; Li, Y.; Kieninger, C.; Kräutler, B.; Sension, R. J. Ultrafast Excited State Dynamics and Fluorescence from Vitamin B_{12} and Organometallic [Co]–C≡C–R Cobalamins. *J. Phys. Chem. B* **2020**, *124* (30), 6651–6656. https://doi.org/10.1021/acs.jpcb.0c04886.
(10) Butler, P. A.; Murtaza, S.; Kräutler, B. Partial Synthesis of CoαCoβ-Dicyano-176-Norcobinamide. *Monatshefte Chem.* **2006**, *137* (12), 1579–1589. https://doi.org/10.1007/s00706-006-0556-3.
(11) Chromiński, M.; Gryko, D. "Clickable" Vitamin B_{12} Derivative. *Chem. – Eur. J.* **2013**, *19* (16), 5141–5148. https://doi.org/10.1002/chem.201203899.
(12) Reber, S.; Blumer, N.; Leuenberger, D.; Fleischer, T.; Renneberg, D.; Abele, S.; Schäfer, G. Scalable Synthesis of C5aR1 Antagonist ACT-1014-6470 via N7-Selective Reductive Amination of an Unprotected Pyrazole Starting Material and Intramolecular Urea Formation with 1,1′-Carbonyl-Di(1,2,4-Triazol) (CDT). *Org. Process Res. Dev.* **2024**, *28* (6), 2269–2283. https://doi.org/10.1021/acs.oprd.3c00492.
(13) Chemaly, S. M. Use of 13C and 1H NMR to Determine the Structure of the Diastereomeric Cobalt Corrinoids Aquacyanocobinamide and Aquacyanocobester. *Polyhedron* **2020**, *175*, 114203. https://doi.org/10.1016/j.poly.2019.114203.
(14) Greenawald, L. A.; Boss, G. R.; Reeder, A.; Bell, S. Development of a Hydrogen Sulfide End-of-Service-Life Indicator for Respirator Cartridges Using Cobinamide. *Sens. Actuators B Chem.* **2016**, *230*, 658–666. https://doi.org/10.1016/j.snb.2016.02.129.

(15) Maitra, D.; Ali, I.; Abdulridha, R. M.; Shaeib, F.; Khan, S. N.; Saed, G. M.; Pennathur, S.; Abu-Soud, H. M. Kinetic Studies on the Reaction between Dicyanocobinamide and Hypochlorous Acid. *PLoS ONE* **2014**, *9* (11), e110595. https://doi.org/10.1371/journal.pone.0110595.
(16) Marques, H. M.; Bradley, J. C.; Brown, K. L.; Brooks, H. Placing Hydroxide in the Thermodynamic *Trans* Influence Order of the Cobalt Corrinoids: Equilibrium Constants for the Reaction of Some Ligands with Aquahydroxocobinamide. *Inorganica Chim. Acta* **1993**, *209* (2), 161–169. https://doi.org/10.1016/S0020-1693(00)85137-3.
(17) Wood, J. L.; Cooley, S. L. Detoxication of cyanide by cystine. *J. Biol. Chem.* **1956**, *218* (1), 449–457. https://doi.org/10.1016/S0021-9258(18)65908-3.
(18) Boyde, T. R. C. The Reaction between Cyanide and the Mixed Disulfide of Cysteine and Penicillamine. *J. Chem. Soc. C Org.* **1968**, No. 0, 2751–2753. https://doi.org/10.1039/J39680002751.
(19) Jacobsen, D. W.; Troxell, L. S.; Brown, K. L. Catalysis of Thiol Oxidation by Cobalamins and Cobinamides: Reaction Products and Kinetics. *Biochemistry* **1984**, *23* (9), 2017–2025. https://doi.org/10.1021/bi00304a021.
(20) Dereven'kov, I. A.; Salnikov, D. S.; Makarov, S. V.; Boss, G. R.; Koifman, O. I. Kinetics and Mechanism of Oxidation of Super-Reduced Cobalamin and Cobinamide Species by Thiosulfate, Sulfite and Dithionite. *Dalton Trans.* **2013**, *42* (43), 15307–15316. https://doi.org/10.1039/C3DT51714D.
(21) Lisboa, L. Developing an Efficient Procedure to Synthesise the Vitamin B_{12} Derivative, Diaquacobinamide, Auckland University of Technology, **2017**.
(22) Professor, P. A.; Dr, M. S. *Chemistry: The Molecular Nature of Matter and Change*; McGraw-Hill Education, **2017.**
(23) Dereven'kov, I. A.; Osokin, V. S.; Hannibal, L.; Makarov, S. V.; Khodov, I. A.; Koifman, O. I. Mechanism of Cyanocobalamin Chlorination by Hypochlorous Acid. *JBIC J. Biol. Inorg. Chem.* **2021**, *26* (4), 427–434. https://doi.org/10.1007/s00775-021-01869-5.
(24) Brown, K. L.; Peck, S. Heteronuclear NMR Studies of Cobalamins. 7. Protonation of the Corrin Ring in Sulfuric Acid/Water Mixtures. *Inorg. Chem.* **1987**, *26* (25), 4143–4145. https://doi.org/10.1021/ic00272a001.
(25) Hill, H. a. O.; Mann, B. E.; Pratt, J. M.; Williams, R. J. P. The Chemistry of Vitamin B_{12}. Part VII. Further Studies of the Proton Magnetic Resonance Spectra of Some Corrinoids. *J. Chem. Soc. Inorg. Phys. Theor.* **1968**, No. 0, 564–567. https://doi.org/10.1039/J19680000564.

Chapter 4 Fluorescence studies of CNCbl and CNCbi conjugates incorporating NBD-X, sulfo-Cyanine5 and Cyanine7

4.1 Introduction

A series of 5'-OH bound CNCbl-linker-fluorophore and CNCbi-linker-fluorophore conjugates have been synthesised, utilising three fluorophores - 7-nitrobenz-2-oxa-1,3-diazole hexanoic acid (NBD-X), sulfo-Cyanine5 and Cyanine7. These fluorophores were selected to emit in a wide range of the visible and near-infrared spectrum. This chapter concerns the determination of the fluorescence quantum yields for six CNCbl-linker-fluorophore and four CNCbi-linker-fluorophore conjugates. Emission and absorption spectroscopy studies have also been carried out to investigate the fluorescence quenching mechanism for the CNCbl and CNCbi conjugates of NBD-X.

4.2 Experimental

4.2.1 Sample preparation

Reference solutions were prepared using commercially available fluorescein (Sigma-Aldrich, cat #46955), sulfo-Cyanine5 (Lumiprobe, cat# 46955) and 1,3,3-trimethyl-2-[7-(1,3,3-trimethylindol-1-ium-2-yl)hepta-2,4,6-trienylidene]indole iodide (HITCI, Sigma-Aldrich, cat# 252034), purchased from Merek and Lumiprobe. The CNCbl/CNCbi-linker-fluorophore samples had purities of ≥95% as established by LC-MS chromatography. All solutions were prepared in analytical grade CH_3OH, EtOH or 0.1 M NaOH in milliQ H_2O directly before absorbance and fluorescence measurements were recorded (less than 1 h in solution). Solutions were protected from light.

Stock solutions for UV/Vis and fluorescence measurements were prepared by dissolving ~1 mg of sample or reference in 10 mL volumetric flasks with the required solvent. Further dilutions were made from the stock sample by aliquoting appropriate volumes into 10 mL volumetric flasks to obtain absorbance values between 0.005-0.01 at the excitation wavelength. UV/Vis and fluorescence spectra were recorded in quartz cuvettes.

LC-MS analysis were obtained using milliQ H_2O + 0.1% formic acid (solvent A) and CH_3CN + 0.1% formic acid (solvent B) with the following mobile phase program: 0-5

min isocratic elution 95:5 A:B, 2-25 min 95:5 to 65:35 A:B, 25-35 min 65:35 to 10:90 A:B and 35-43 min isocratic elution 10:90 A:B.

4.2.2 Instrumentation

Absorbance spectra were obtained using an Agilent Cary 100 UV/Vis spectrophotometer. The cell compartment was maintained at 25.0ºC by a thermostatted control. All spectra were plotted with Origin64 2024. Fluorescence emission spectra were obtained using a Varian Cary Eclipse Fluorescence spectrophotometer. The cell compartment was maintained at 25.0ºC by a thermostatted control. To check the photostability of each sample, the absorbance was taken before and after fluorescence measurements.

See Section 2.2.2 for details on the LC-MS instrumentation.

4.2.3 General methods

Determination of the fluorescence quantum yields was achieved by fitting the data to equation (1)

$$\phi_s = \phi_r \left(\frac{m_s}{m_r}\right)\left(\frac{\eta_s^2}{\eta_r^2}\right) \qquad (1)$$

where Φ represents the fluorescence quantum yield, m is the slope of the integrated fluorescence emission against absorbance at the excitation wavelength, η is the refractive index of the solvent, s denotes sample and r denotes reference. The error for each term was converted to a percentage error. All percentage errors were combined to determine the absolute error of fluorescence quantum yields.

4.3 Results and Discussion

4.3.1 Determination of fluorescence quantum yields of the CNCbl and CNCbi conjugates of NBD-X

The gold standard for determining the fluorescence quantum yield uses an integrating sphere system.[1,2] However, the fluorescence quantum yield determination in this work has been achieved using the relative fluorescence quantum yield method. This method is robust and commonly used.[1,2]

Fluorescein reference

The fluorescent reference dye used for the determination of the quantum yield of compounds **3**, **4**, **13** and **14** was 3',6'-dihydroxyspiro[2-benzofuran-3,9'-xanthene]-1-one (fluorescein). Fluorescein is commonly utilised to determine fluorescence quantum yields and has a published quantum yield of 0.925 ± 0.015 in 0.1 M NaOH.[3] The excitation wavelength selected in this work was 470 nm where both NBD-X and fluorescein absorb strongly. Five solutions of fluorescein with different concentrations (0.626-1.41 µM in 0.1 M NaOH) were measured for both absorbance and fluorescent emission (Figure 121). The integrated fluorescence intensity was plotted against the absorbance at 470 nm for each sample. The data was fitted to a straight line with an intercept at (0,0) and the slope was determined. The refractive index (η) of 0.1M NaOH is 1.334 (± 0.004).[4] This data was used as the reference for the quantum yield determination of all NBD-X-containing conjugates.

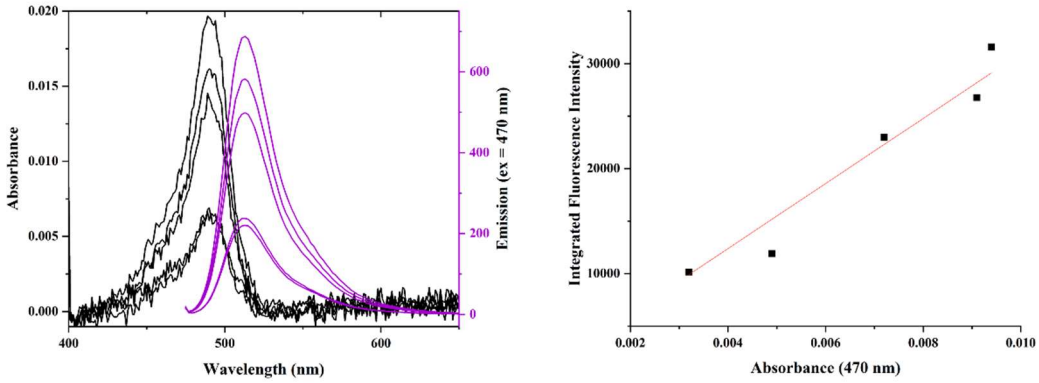

Figure 121: Left: absorbance (black) and emission (purple) spectra of fluorescein (0.626-1.41 µM, 0.1M NaOH). Right: plot of integrated fluorescence emission versus the absorbance at the excitation wavelength (470 nm). The data is fitted to a straight line passing through the origin, giving a gradient of (3.10 ± 0.14) x 10^6. The Pearson's correlation of the linear fit is 0.99.

NBD-X fluorophore

The fluorescence quantum yield of NBD-X is not published in the literature. To compare the fluorescence quantum yield of the CNCbl-linker-NBD-X and CNCbi-linker-NBD-X to the unbound NBD-X moiety, the fluorescence quantum yield of NBD-X was determined. The absorbance and emission profiles of five solutions of NBD-X in analytical grade CH_3OH were recorded (Figure 122). The excitation wavelength was maintained at 470 nm. The refractive index (η) of CH_3OH is 1.3270 (± 0.0005).[5] The

fluorescence quantum yield of NBD-X was calculated using equation (1), giving 0.287 ± 0.022.

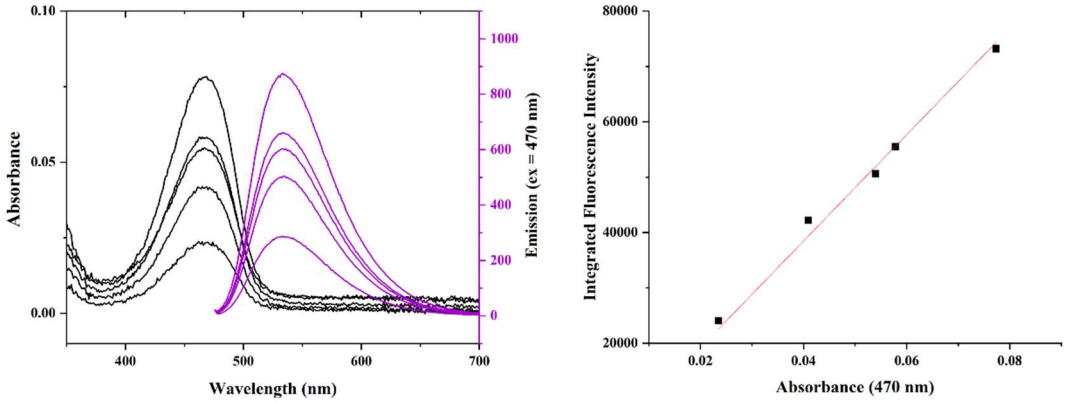

Figure 122: Left: absorbance (black) and emission (purple) spectra of NBD-X (0.871-3.47 μM, CH_3OH). Right: plot of integrated fluorescence emission versus the absorbance at the excitation wavelength (470 nm). The data were fitted to a straight line passing through the origin. The Pearson's correlation of the linear fit is 0.99. Data was fit to equation (1) where $\Phi_r = 0.925 \pm 0.015$, $m_s = (9.60 \pm 0.15) \times 10^5$, $m_r = (3.10 \pm 0.14) \times 10^6$, $\eta_s = 1.3270 (\pm 0.0005)^5$ and $\eta_r = 1.334 (\pm 0.004)^4$, giving $\phi_s = 0.287 \pm 0.022$.

Compound 3

The fluorescence quantum yield of compound **3** was determined using an analogous experimental procedure. Absorbance and excitation spectra were obtained for five solutions (in CH_3OH). The integrated fluorescence intensity of each solution was plotted against the absorbance at the excitation wavelength (470 nm). The data were fitted to a straight line with an intercept at (0,0) and the gradient determined (Figure 123). The calculated fluorescence quantum yield of 0.011 ± 0.001, using equation (1).

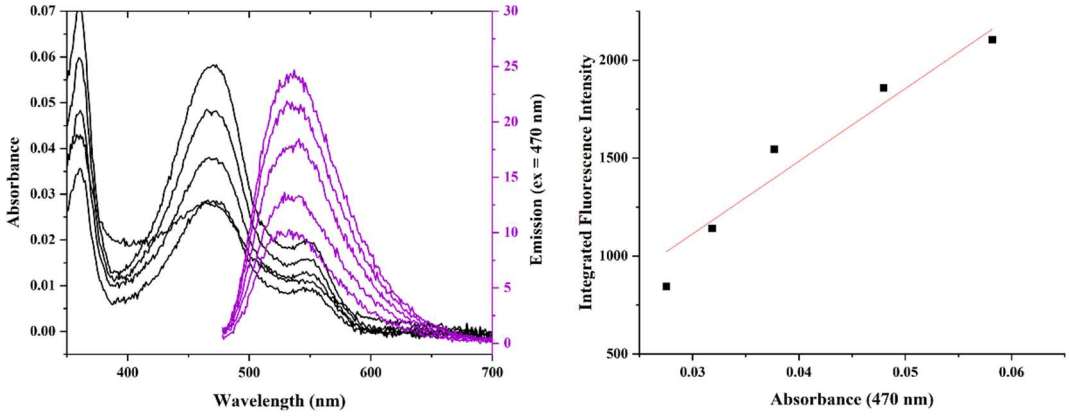

*Figure 123: Left: absorbance (black) and emission (purple) spectra of **3** (0.471-2.82 µM, CH_3OH). Right: plot of integrated fluorescence emission versus the absorbance at the excitation wavelength (470 nm). The data is fitted to a straight line passing through the origin. The Pearson's correlation of the linear fit is 0.99. The fluorescence quantum yield was determined using equation (1) where $\Phi_r = 0.925 \pm 0.015$, $m_s = (3.71 \pm 0.13) \times 10^4$, $m_r = (3.10 \pm 0.14) \times 10^6$, $\eta_s = 1.3270 (\pm 0.0005)^5$ and $\eta_r = 1.334 (\pm 0.004)^4$ giving $\phi_s = 0.011 \pm 0.001$.*

Compound 4

Compound **4** was analysed using the same methodology for **3** and NBD-X. Absorbance values of five solutions (in CH_3OH) at 470 nm were plotted against the integrated fluorescence intensity. The data were fitted to a straight line with an intercept at (0,0) (Figure 124). The fluorescence quantum yield was determined to be 0.007 ± 0.001 using equation (1).

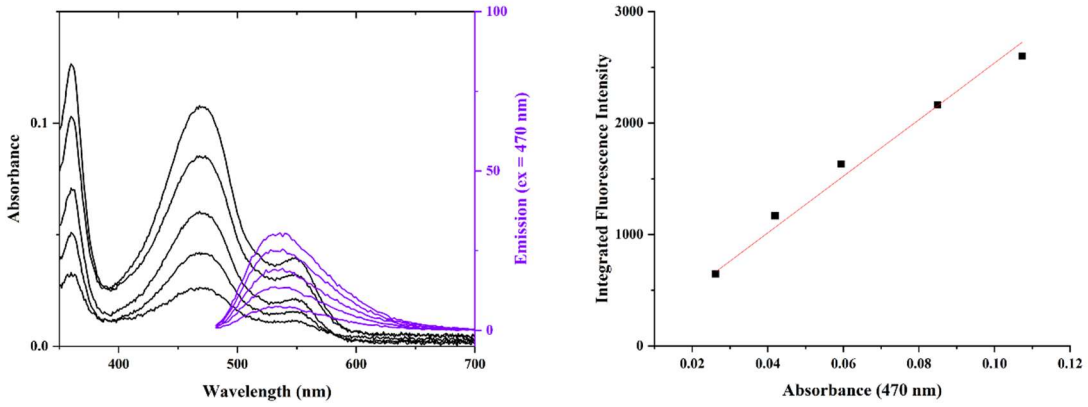

*Figure 124: Left: absorbance (black) and emission (purple) spectra of **4** (0.703-3.50 µM, CH_3OH). Right: plot of integrated fluorescence emission versus the absorbance at the excitation*

wavelength (470 nm). The data is fitted to a straight line passing through the origin. The Pearson's correlation of the linear fit is 0.99. The fluorescence quantum yield was determined using equation (1) where Φ_r = 0.925 ± 0.015, m_s = (2.37 ± 0.14) x 10^4, m_r = (3.10 ± 0.14) x 10^6, η_s = 1.3270 (± 0.0005)[5] and η_r = 1.334 (± 0.004)[4], giving ϕ_s = 0.007 ± 0.001.

Compound 13

The fluorescence quantum yield for **13** was determined in CH_3OH, using fluorescein as the reference. The absorbance at 470 nm was plotted against the integrated fluorescence intensity for five samples. The data were fitted to a straight line with an intercept at (0,0) (Figure 125). The fluorescence quantum yield was determined as 0.019 ± 0.002 using equation (1).

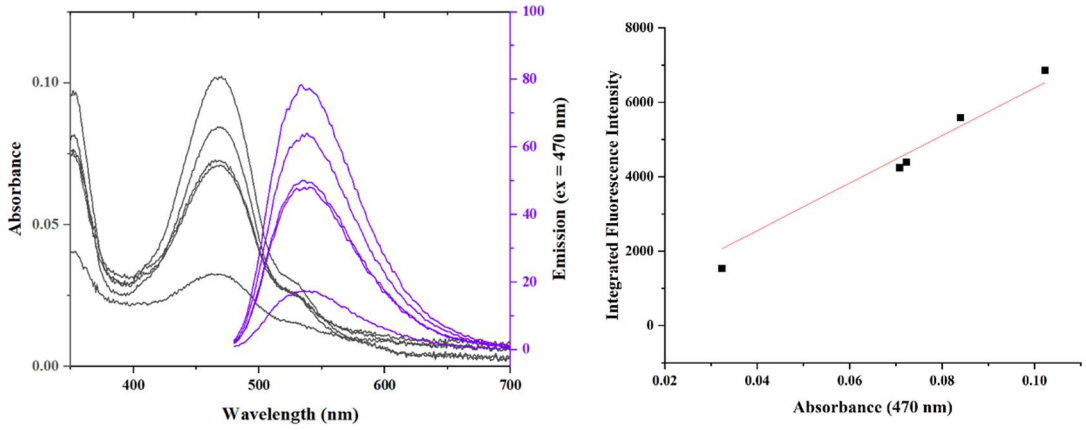

*Figure 125: Left: absorbance (black) and emission (purple) spectra of **13** (1.11-5.53 µM, CH_3OH). Right: plot of integrated fluorescence emission versus the absorbance at the excitation wavelength (470 nm). The data is fitted to a straight line passing through the origin. The Pearson's correlation of the linear fit is 0.99. The fluorescence quantum yield was determined using equation (1) where Φ_r = 0.925 ± 0.015, m_s = (1.16 ± 0.02) x 10^4, m_r = (3.10 ± 0.14) x 10^6, η_s = 1.3270 (± 0.0005)[5] and η_r = 1.334 (± 0.004)[4] giving ϕ_s = 0.019 ± 0.002.*

Compound 14

The fluorescence quantum yield of **14** was determined in CH_3OH. The integrated fluorescence intensity (excitation wavelength at 470 nm) was plotted against the absorbance at 470 nm for five solutions (Figure 126). The data were fitted to a straight line with an intercept at (0,0). The fluorescence quantum yield was determined to be 0.035 ± 0.003 using equation (1).

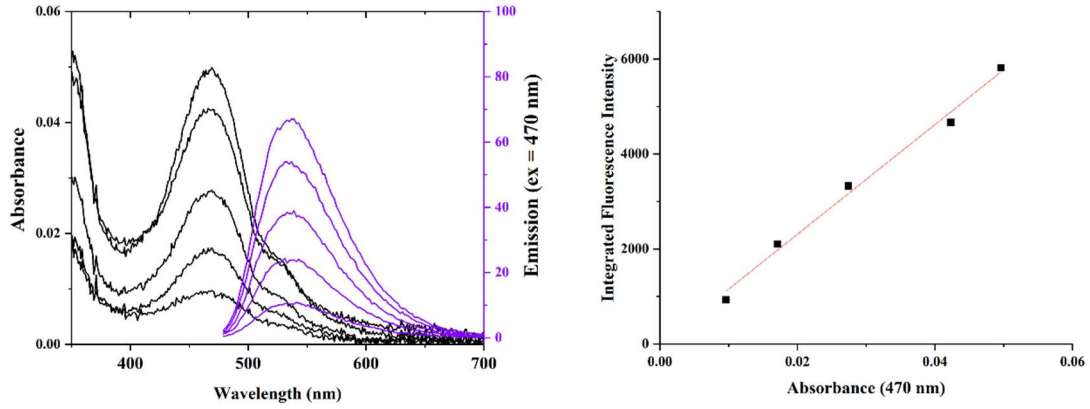

*Figure 126: Left: absorbance (black) and emission (purple) spectra of **14** (0.142.1.21 μM, CH_3OH). Right: plot of integrated fluorescence emission versus the absorbance at the excitation wavelength (470 nm). The data is fitted to a straight line passing through the origin. The Pearson's correlation of the linear fit is 0.99. The fluorescence quantum yield was determined using equation (1) where $\Phi_r = 0.925 \pm 0.015$, $m_s = (6.38 \pm 0.22) \times 10^4$, $m_r = (3.10 \pm 0.14) \times 10^6$, $\eta_s = 1.3270 (\pm 0.0005)^5$ and $\eta_r = 1.334 (\pm 0.004)^4$, giving $\phi_s = 0.035 \pm 0.003$.*

The fluorescence quantum yields of the CNCbl and CNCbi conjugates of NBD-X have been determined using fluorescein as a reference and are summarised in Table 4. All CNCbl and CNCbi conjugates have a significantly lower fluorescence quantum yield than the free NBD-X fluorophore. This indicates that the CNCbl and CNCbi moieties are quenching the fluorescence of the NBD-X moiety in the conjugates. Quenching was more pronounced for the CNCbl conjugates **3** and **4**, with a reduction in the fluorescence quantum yield from 0.29 to 0.011 and 0.007, respectively. Fluorescence quenching is greater for the conjugates containing the 1,11-diamino-3,6,9-trioxaundecane linker compared to the cystamine analogues of CNCbl and CNCbi. It is proposed that the longer 1,11-diamino-3,6,9-trioxaundecane linker provides greater flexibility than the shorter cystamine linker. This increased linker length would potentially allow for greater folding, allowing the CNCbl/CNCbi corrin ring and NBD-X to be spatially close to each other. Energy transfer between the excited NBD-X fluorophore and the CNCbl/CNCbi would result in a lower fluorescence quantum yield.

Table 4: Fluorescence quantum yields of NBD-X conjugates of CNCbl and CNCbi obtained in CH_3OH using fluorescein as the reference.

Compound	Fluorescence quantum yield
3 (CNCbl-Cy-NBD-X)	0.011 ± 0.001
4 (CNCbl-PEG-NBD-X)	0.007 ± 0.001
13 (CNCbi-PEG-NBD-X)	0.019 ± 0.002
14 (CNCbi-Cy-NBD-X)	0.035 ± 0.003
NBD-X	0.287 ± 0.022

4.3.2 Visible spectroscopy studies to assess a potential association between the free NBD-X fluorophore and CNCbl ground state molecules

Significantly reduced fluorescence quantum yields were observed for the CNCbl and CNCbi conjugates of NBD-X compared to the NBD-X fluorophore. Quenching by the corrin ring of CNCbl has been observed by others for numerous fluorescent moieties upon conjugation to CNCbl.[6–9] Many mechanisms have been suggested for this fluorescence quenching, commonly separated into static or dynamic mechanisms. Static quenching refers to the interaction between the donor and acceptor in the ground state, resulting in a non-fluorescent complex. Dynamic quenching describes an interaction between the acceptor and the donor molecule in the excited state.[10,11] Static quenching can lead to a change in the absorbance spectrum compared to the solutions of the individual components (donor and acceptor). This can be studied by UV/Vis spectroscopy.

To probe if static quenching is occurring between CNCbl and NBD-X due to an association occurring between these moieties in the conjugates, absorbance spectroscopy studies were carried out between free NBD-X and CNCbl. The visible spectra of separate solutions of CNCbl and NBD-X were recorded in CH_3OH (27.7 μM) and the absorbance spectra were added together using the Cary 100 instrument software (Figure 127). An absorbance spectrum was also obtained for an equimolar CNCbl and NBD-X solution (CH_3OH, 27.7 μM). There were no differences between these spectra. This was repeated with increasing concentrations of CNCbl (NBD-X:CNCbl 1:1.5, 1:2, 1:3, 1:5, see Appendix). No change was observed in the absorbance spectra when CNCbl and NBD-X were in separate solutions and the spectra added together or in the same solution. Since

there is no evidence for an association between free CNCbl and NBD-X in their ground states, this does not support static quenching being the main mechanism of fluorescence quenching for the CNCbl-linker-NBD-X and CNCbi-linker-NBD-X conjugates.

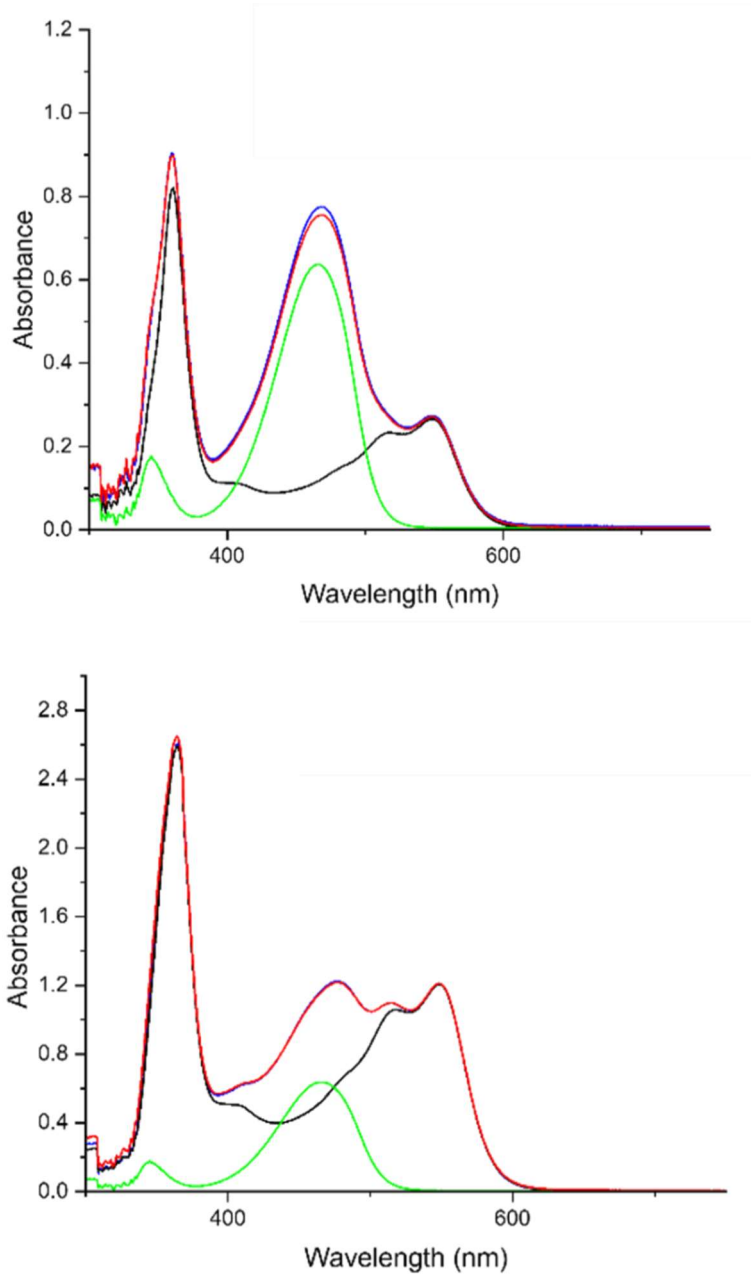

Figure 127: Top: Visible spectra of CNCbl (27.7 µM, black), NBD-X (27.9 µM, green) and a solution of CNCbl and NBD-X (27.7 and 27.9 µM, respectively, blue). Combined visible spectra of CNCbl and NBD-X (27.9 µM, red). All solutions were recorded in CH_3OH at 25.0 °C. Bottom: Visible spectra of CNCbl (142 µM, black), NBD-X (27.9 µM, green) and a 1:5 solution of NBD-X and CNCbl (27.9 µM and 142 µM, respectively, blue). Combined visible spectra of CNCbl (142 µM) and NBD-X (27.9 µM, red). All solutions were recorded in CH_3OH at 25.0 °C.

4.3.3 Emission spectroscopy studies to determine if free CNCbl quenches the fluorescence of NBD-X

Emission spectroscopy studies were undertaken to probe for energy transfer between the free NBD-X fluorophore in the excited state and CNCbl. The emission spectrum of NBD-X was first obtained (Figure 128). Emission spectra were then recorded for solutions of NBD-X (1.28 µM) and CNCbl (1.28-12.8 µM). As the concentration of CNCbl increases, the fluorescence emission of NBD-X decreases. The integrated fluorescence emission peak areas were used to determine the percentage reduction in fluorescence upon the addition of CNCbl, with the NBD-X peak area in the absence of CNCbl set to 100%. The 1:1 NBD-X:CNCbl solution experienced a 1% decrease in fluorescence, with 1:5 NBD-X:CNCbl showing a 10% reduction and 1:10 NBD-X:CNCbl showing a 15% reduction in emission. This indicates that there is an interaction between NBD-X in the excited state and CNCbl, resulting in fluorescence quenching.

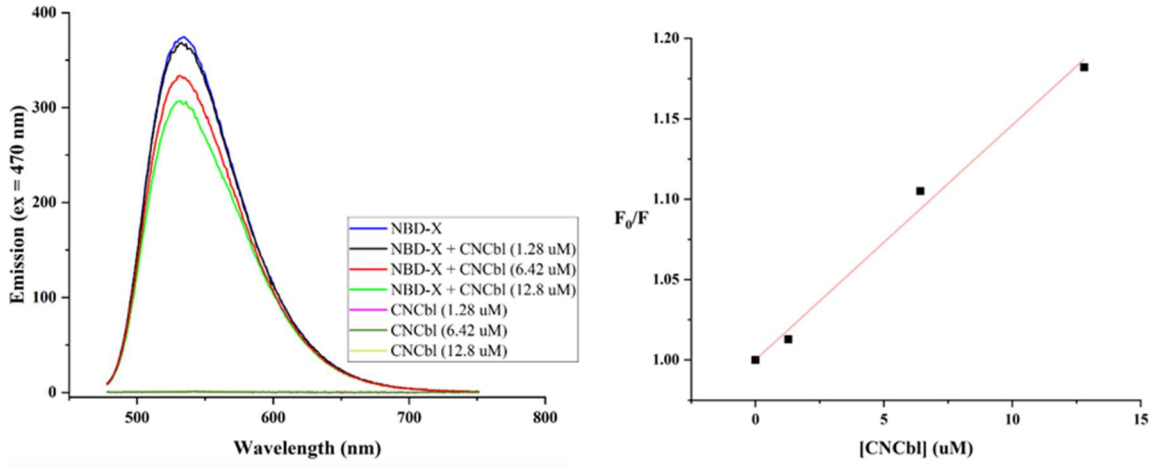

Figure 128: Left: Fluorescence emission studies of NBD-X (1.28 µM) in the presence of CNCbl (0, 1.28, 6.42 and 12.8 µM). All solutions were prepared in CH_3OH and recorded at 25.0°C. Emission spectra (excitation at 470 nm) of NBD-X (1.28 µM, blue), NBD-X & CNCbl (1.28 µM and 1.28 µM, 1:1, black), NBD-X & CNCbl (1.28 µM and 6.42 µM, 1:5, red) and NBD-X & CNCbl (1.28 µM and 12.8 µM, 1:10, green). Emission of CNCbl (1.28 µM, pink), CNCbl (6.42 µM, dark green) and CNCbl (12.8 µM, yellow) are overlapping. Right: Stern-Volmer plot of NBD-X (1.28 µM) emission in the presence of increasing concentrations of CNCbl (0, 1.28, 6.42 and 12.8 µM) in CH_3OH at 25.0°C. Data were fitted to a straight line with an intercept at (0,1), giving a Pearsons coefficient of 0.99.

4.4 Fluorescence emission studies of the NBD-X conjugates following cleavage of the cystamine linker

A component of this work was to develop a chemically responsive series of CNCbl and CNCbi complexes that would cleave to release their cargo in cellular environments. The disulfide-containing cystamine linker is known to undergo reductive cleavage in the cytoplasm of cells by glutathione (GSH).[12,13] The significantly lower fluorescence quantum yield of the NBD-X conjugates of both CNCbl and CNCbi compared to the NBD-X species released upon cleavage of the disulfide of the linker provides a convenient mechanism by which to confirm that cleavage occurs upon exposure to GSH.

4.4.1 Spectral studies of NBD-X conjugates 3, 4 and 14

Solutions of compounds **3** (CNCbl-cy-NBD-X) and **14** (CNCbi-cy-NBD-X) were prepared in an aqueous solution of carbonate buffer (0.050 M, pH 10.0) at concentrations of 1.0 μM. The UV/Vis and fluorescence emission spectra (excitation at 470 nm) were recorded. Analogous solutions were made with the addition of reduced glutathione (GSH, 5.0 mM), similar to the concentration found in cytosolic compartments in cells (0.1-10 mM).[14,15] The UV/Vis and fluorescence spectra of solutions containing GSH were measured immediately and after 2 h at room temperature, with the solutions protected from light (Figure 129). After the addition of GSH to **3** and **14**, a large increase in the fluorescence intensity is observed, consistent with a significant increase in the distance between the CNCbl/CNCbi and NBD-X moieties. After linker cleavage, the CNCbl/Cbi and NBD-X chromophores diffuse away from each other, decreasing the efficiency of fluorescence quenching.

Upon exposure to GSH, an unexpected increase was observed for the absorbance peak of **3** and **14** centred ~480 nm (Figure 129). Closer inspection of the absorbance spectra shows that the peak/shoulder at 550 nm for **3** and 530 nm for **14** are at similar absorbance values before and after the addition of GSH. These peak/shoulders can be attributed to CNCbl and CNCbi, respectively. As the absorbance of this peak/shoulder for both CNCbl and CNCbi does not significantly change upon the addition of GSH, it suggests the large change of the peak/shoulder at ~480 nm for both systems is associated with the NBD-X moiety. The *N*-hexyl chain of NBD-X can readily undergo nucleophilic attack. It is proposed that the *N*-hexyl chain of NBD-X is cleaved by thiolates (RS^-) produced upon cleavage of the disulfide of **3** and **14** by GSH (Scheme 20 and Scheme 21).

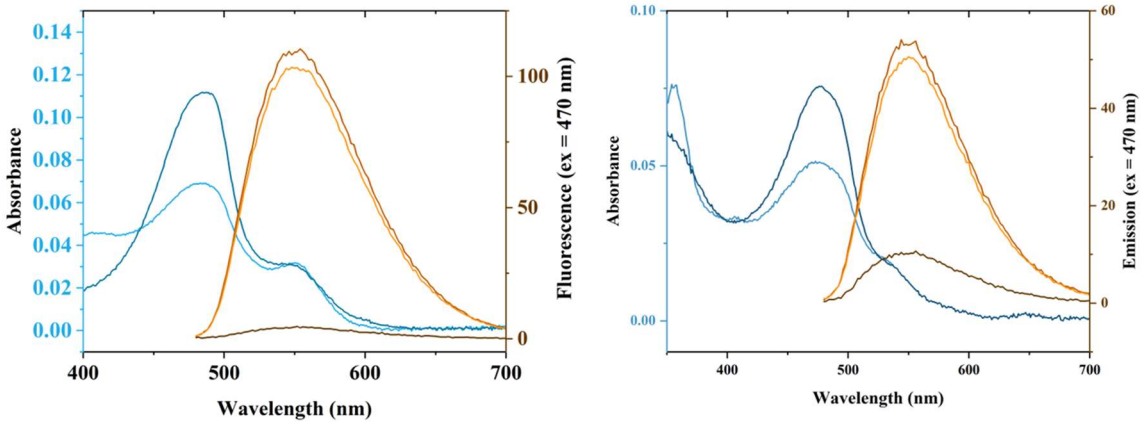

*Figure 129: Left: absorbance spectra of **3** (1.0 μM) in carbonate buffer (0.050 M, pH 10.0) without GSH (light blue) and with GSH (dark blue, 5 mM) and the corresponding fluorescence emission spectra of **3** (1.0 μM) in carbonate buffer (0.050 M, pH 10.0) without GSH (brown), immediately after the addition of GSH (yellow, 5 mM) and 2 h after GSH addition (orange). Right: absorbance spectra of **14** (1.0 μM) in carbonate buffer (0.050 M, pH 10.0) without GSH (light blue) and with GSH (dark blue, 5 mM) and the corresponding fluorescence emission spectra of **14** (1.0 μM) in carbonate buffer (0.05M, pH 10) without GSH (brown), immediately after the addition of GSH (yellow, 5 mM) and 2 h after GSH addition (orange).*

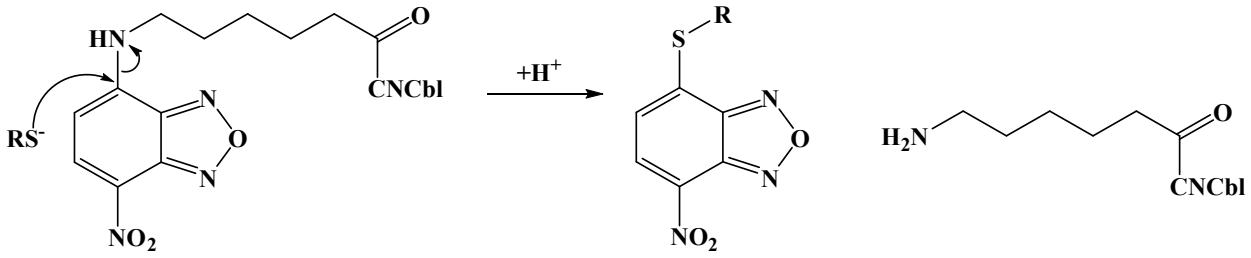

Scheme 20: Proposed nucleophilic attack of NBD-X by the thiolates produced following reductive cleavage of the CNCbl-linker-NBD-X or CNCbi-linker-NBD-X by GSH, Scheme 21.

LC-MS analysis of glutathione-treated NBD-X conjugates 3 and 4

Compound **3** was analysed by LC-MS before and after the addition of GSH. This was carried out to confirm cystamine cleavage upon exposure to GSH. GSH can attack either S centre of cystamine, giving rise to a free thiol (CNCbl-S^- or (NBD-X)-S^-) and glutathione adduct with a disulfide bond (CNCbl-SSG or (NBD-X)-SSG, Scheme 21).

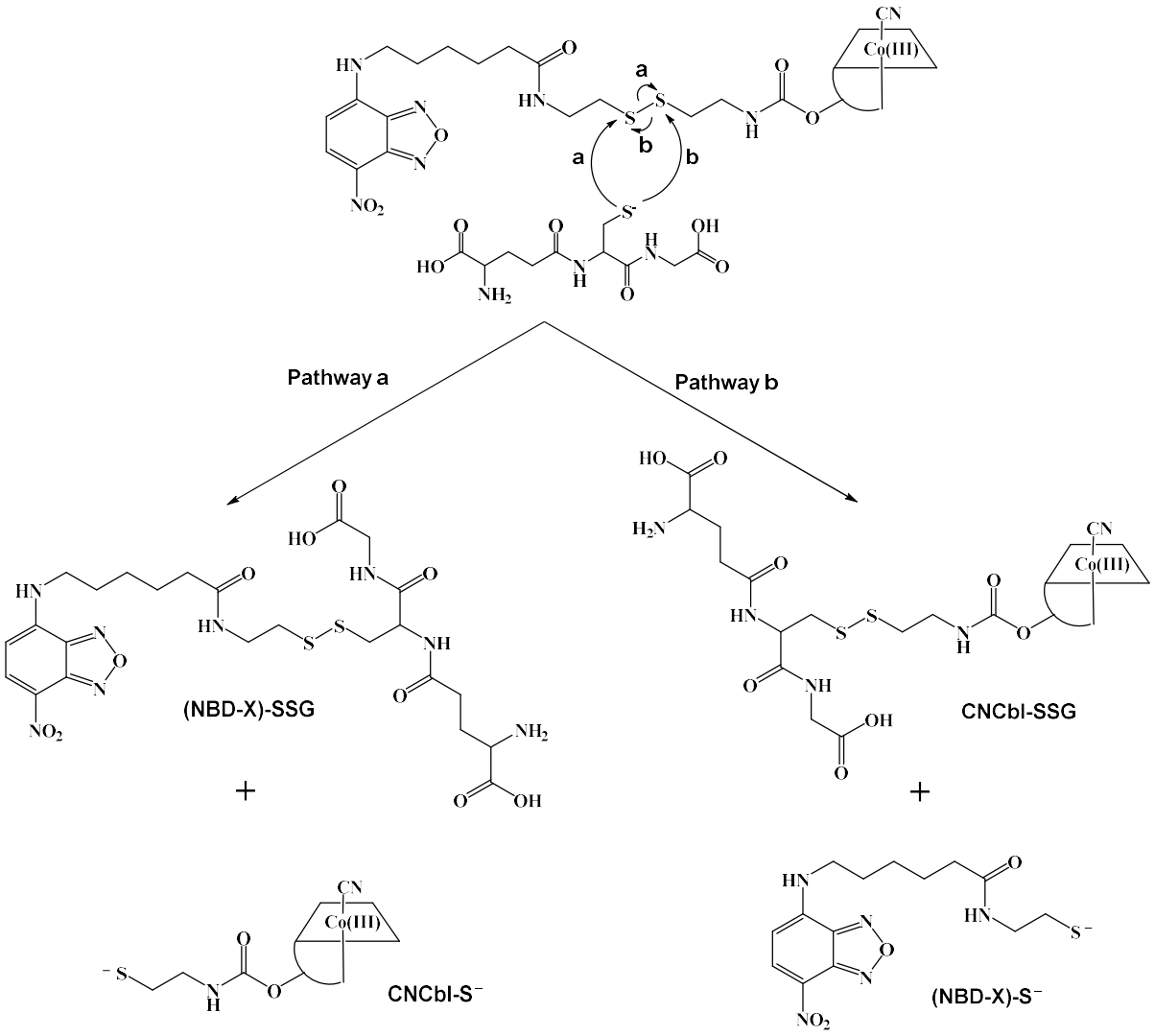

*Scheme 21: Cystamine linker cleavage of **3** by GSH, producing the thiolates CNCbl-S⁻ or (NBD-X)-S⁻, and the corresponding disulfide (NBD-X)-SSG and CNCbl-SSG products.*

The solutions utilised for fluorescence analysis upon exposure to GSH were injected into the LC-MS instrument. Compound **3**, which was not exposed to GSH, showed two peaks in the LC-MS chromatogram (Figure 130). The peak at 26.6 min is assigned to compound **3** ($C_{80}H_{110}CoN_{20}O_{19}PS_2$, calcd. *m/z* $[M+H]^+$ = 1809.7, $[M+2H]^{2+}$ = 905.4 and $[M+3H]^{3+}$ = 603.9; found 1809.4, 905.6 and 604.1). A second peak at 16.9 min can be assigned to a degradation product of **3** ($C_{74}H_{109}CoN_{17}O_{16}PS_2$ calcd. *m/z* $[M+2H]^{2+}$ = 823.8 and $[M+3H]^{3+}$ = 549.6; found 824.0 and 549.7). This product is formed by the loss of the fluorescent NBD moiety as shown in Scheme 21, as a result of base-catalysed C-N bond cleavage. After the addition of GSH, the area of the product peak at 26.6 min is greatly diminished. The peaks at 17.0 and 19.0 min can be assigned to the two possible CNCbl

fragments after GSH-induced cleavage of the cystamine linker. The peak at 17.0 min is the newly formed disulfide-containing CNCbl-SSG complex ($C_{76}H_{108}CoN_{18}O_{21}PS_2$ calcd. *m/z* $[M+H]^+$ = 1763.7, $[M+2H]^{2+}$ = 882.3 and $[M+3H]^{3+}$ = 588.6; found 1763.6, 882.5 and 588.8) whereas 19.0 min corresponds to the free thiol CNCbl-SH cleaved product ($C_{66}H_{93}CoN_{15}O_{15}PS$ calcd. *m/z* $[M+H]^+$ = 1458.6 and $[M+2H]^{2+}$ = 729.8; found 1458.9 and 729.3), Scheme 22.

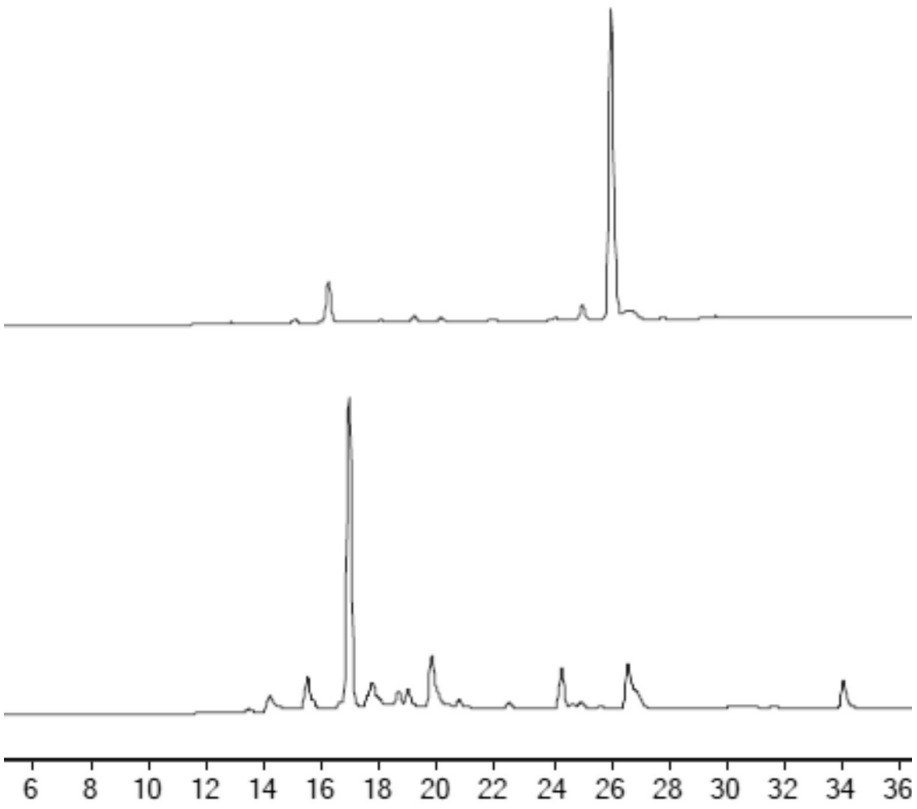

*Figure 130: LC-MS DAD chromatograms (361 nm) of **3** obtained after treatment without (top) and with 5 mM GSH (bottom) in carbonate buffer (0.050 M, pH 10.0). Newly formed peaks after GSH addition at 17.0 and 19.0 min are assigned to the disulfide-containing CNCbl-SSG complex (CNCbl-SSG, $C_{76}H_{108}CoN_{18}O_{21}PS_2$ calcd. m/z $[M+2H]^+$ = 1763.6; $[M+2H]^{2+}$ = 882.3 and $[M+3H]^{3+}$; found 1763.6, 882.5 and 588.8) and the free thiol CNCbl product (CNCbl-SH, $C_{66}H_{93}CoN_{15}O_{15}PS$ calcd. m/z $[M+H]^+$ = 1458.6 and $[M+2H]^{2+}$ = 729.8; found 1458.9 and 729.39).*

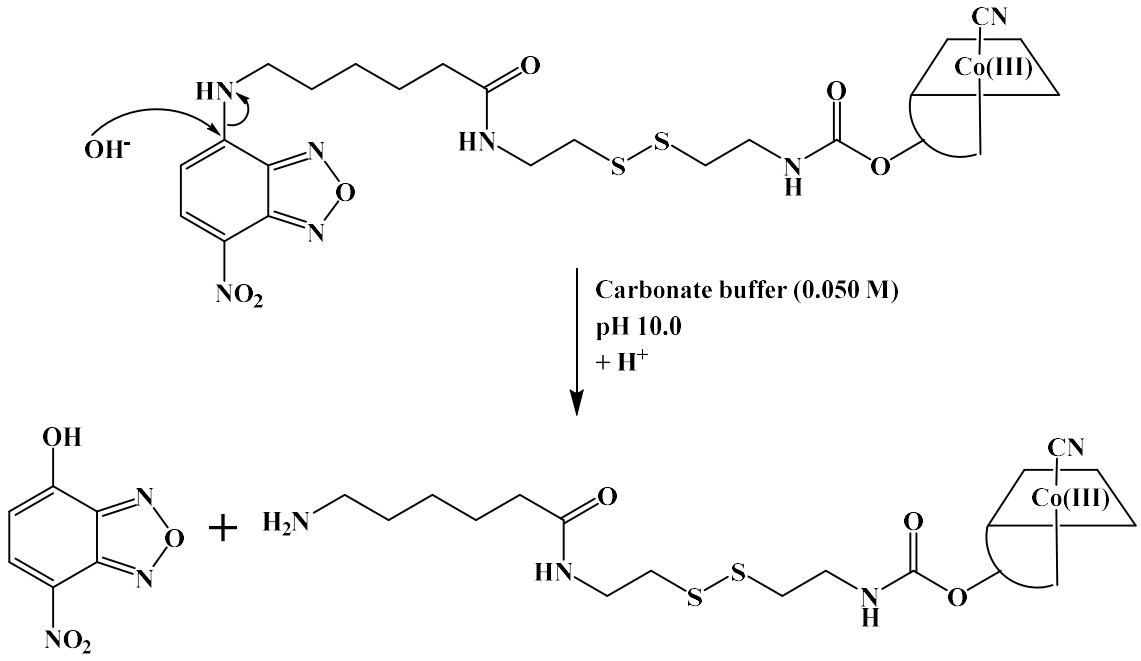

*Scheme 22: Proposed base hydrolysis of compound **3** in carbonate buffer (0.050 M, pH 10.0).*

Treatment of compound **3** with GSH resulted in the expected disulfide bond cleavage of the cystamine linker. This bond cleavage leads to separation of the CNCbl and NBD-X moieties, resulting in the large increase in fluorescence observed in Figure 129. LC-MS analysis also showed a small amount of base-catalysed hydrolysis for compound **3** in basic solution.

To determine if base hydrolysis also occurs for the non-disulfide linked CNCbl-linker-NBD-X conjugate, the stability of compound **4** in pH 10.0 buffer in the presence and absence of 5 mM GSH was determined. Before treatment with GSH, the LC-MS showed two peaks (Figure 131). The peak eluting at 25.6 min can be assigned to compound **4** ($C_{84}H_{118}CoN_{20}O_{22}P$ calcd. *m/z* $[M+H]^+$ = 1849.8, $[M+2H]^{2+}$ = 925.4 and $[M+3H]^{3+}$ = 617.3; found 1850.1, 925.6 and 617.4) As seen for compound **3**, compound **4** also showed evidence of degradation in basic solution. The peak eluting at 16.0 min can be assigned to the base hydrolysis-associated degradation product of **4** shown in Scheme 23 ($C_{78}H_{117}CoN_{17}O_{19}P$ calcd. *m/z* $[M+2H]^{2+}$ = 843.9 and $[M+3H]^{3+}$ = 562.9; found 844.0 and 563.0). After the addition of GSH, the degradation product was more prevalent along with other impurities that could not be identified retaining between 20-24 min. Compound **4**, however, was also observed eluting at 25.6 min ($C_{84}H_{118}CoN_{20}O_{22}P$ calcd. *m/z* $[M+H]^+$ = 1849.8, $[M+2H]^{2+}$ = 925.4 and $[M+3H]^{3+}$ = 617.3; found 1850.1, 925.6 and 617.4). The

increase in degradation products after treatment with GSH can be linked to the extended time compound **4** was left in solution at pH 10.0. The GSH-treated sample was allowed to react for ~5 h before being analysed.

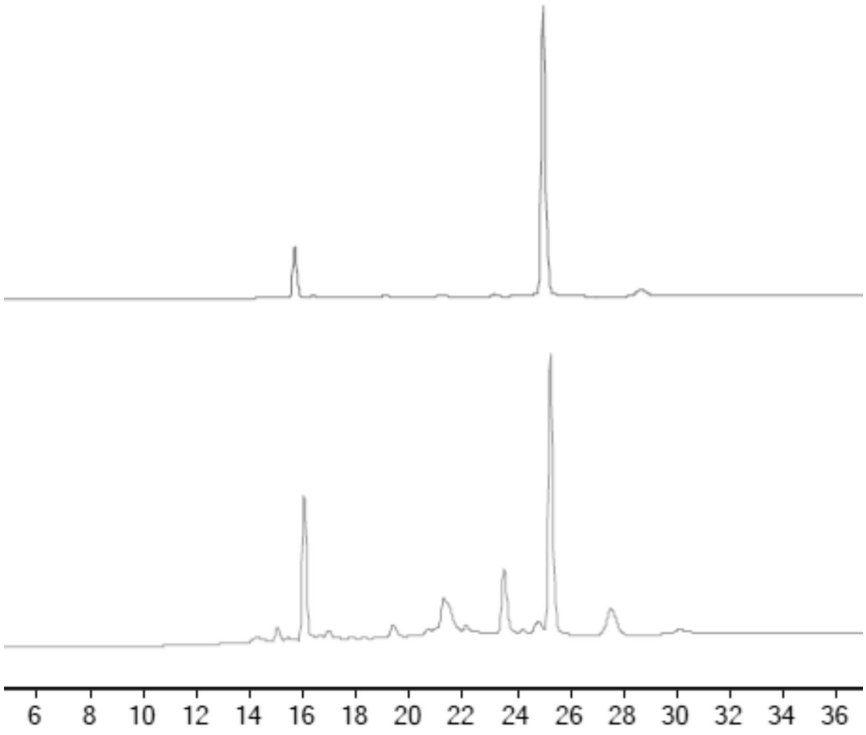

*Figure 131: LC-MS DAD chromatograms (361 nm) of **4** obtained after treatment without (top) and with 5 mM GSH (bottom) in carbonate buffer (0.05 M, pH 10). The peak eluting at 25.6 min is assigned to **4** ($C_{84}H_{118}CoN_{20}O_{22}P$ calcd. m/z $[M+H]^+$ = 1849.8, $[M+2H]^{2+}$ = 925.4 and $[M+3H]^{3+}$ = 617.3; found 1850.1, 925.6 and 617.4).*

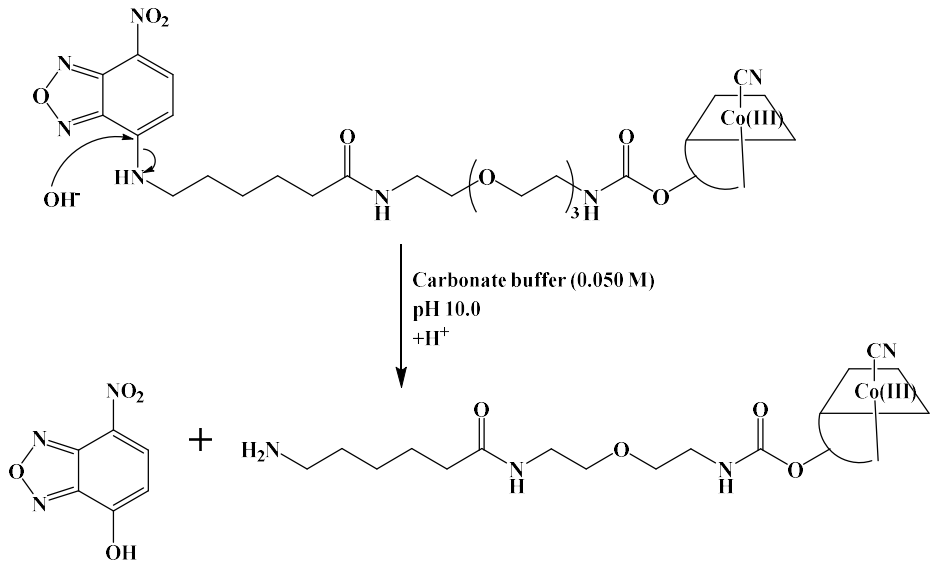

*Scheme 23: Proposed base hydrolysis of compound **4** in carbonate buffer (0.050 M, pH 10.0).*

The LC-MS results for both **3** and **4** show that these compounds undergo nucleophilic attack by base resulting in C-N bond cleavage. Compound **3** undergoes the expected disulfide bond cleavage of the cystamine linker after the addition of GSH. Compound **4** does not have a disulfide bond and was therefore a suitable compound to confirm that base hydrolysis occurs for these systems in alkaline solution. There was increased degradation of **4** compared to **3**, probably due to the extended time in solution at pH 10.0. The fluorescence studies were undertaken immediately after preparation, to limit interference from the base-hydrolysed degradation product of NBD-X. The increase in fluorescence of **3** upon exposure to GSH is due to GSH-catalysed cystamine linker cleavage.

4.4.2 Determination of the fluorescence quantum yields for the CNCbl and CNCbi conjugates of sulfo-Cyanine5

Sulfo-Cyanine5-NHS reference

The reference dye selected to determine the fluorescence quantum yields of **5**, **6** and **14** was the sulfo-Cyanine5-NHS dye itself. This fluorophore has a reported fluorescence quantum yield of 0.30 in EtOH (no error in this value was published).[16] As the fluorophore in this case is identical to that of the conjugates, this ensures excellent spectral overlap of both absorbance and emission spectra of the reference and CNCbl/CNCbi conjugates. Sulfo-Cyanine5-NHS has a smaller Stokes shift than fluorescein. However, excitation of sulfo-Cyanine5-NHS at 600 nm ensures that the complete emission peak is observed. The concentrations of sulfo-Cyanine5-NHS ranged from 0.231-0.540 μM, giving absorbance values between ~0.02-0.07 at 600 nm (Figure 132). The integrated fluorescence intensity and absorbance (at 600 nm) was plotted and fitted to a straight line with the intercept at (0,0). The refractive index (η) of EtOH was 1.3604 (±0.0003).[5] The slope of the plot of integrated fluorescence intensity versus absorbance together with the reported fluorescence quantum yield and refractive indices were used to determine the fluorescence quantum yields of the CNCbl and CNCbi conjugates of sulfo-Cyanine5.

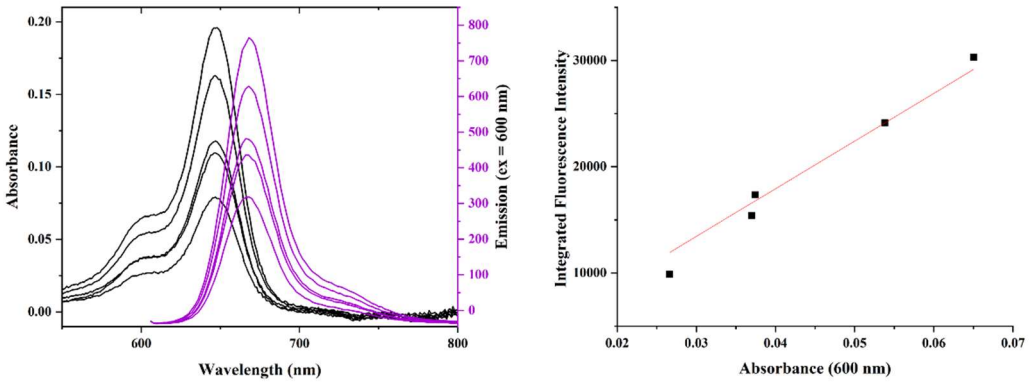

Figure 132: Left: absorbance (black) and emission (purple) spectra of sulfo-Cyanine5-NHS ester (0.231-0.540 μM) in EtOH. Right: plot of integrated fluorescence intensity versus the absorbance at the excitation wavelength (600 nm). The data are fitted to a straight line passing through the origin, giving a gradient of (4.48 ± 0.13) x 10^5. The Pearson's correlation of the linear fit is 0.99.

Sulfo-Cyanine5 in CH_3OH

The fluorescence quantum yield for sulfo-Cyanine5-NHS published in the literature was obtained in EtOH (0.30 (no error reported)).[16] The CNCbl/CNCbi conjugates of sulfo-Cyanine5 have minimal solubility in EtOH, therefore CH_3OH was the solvent used for determining the fluorescent quantum yields. To compare the fluorescence quantum yields of the conjugates to the sulfo-Cyanine5 fluorophore, the fluorescence quantum yield of sulfo-Cyanine5-NHS ester was determined in CH_3OH. Solutions of sulfo-Cyanine5 were prepared in CH_3OH (0.534-1.63 μM) and the absorbance and emission spectra were recorded. The absorbance at 600 nm was plotted against the integrated fluorescence intensity. The data were fitted to a straight line with an intercept at (0,0). The fluorescence quantum yield was determined as 0.34 ± 0.02 using equation (1).

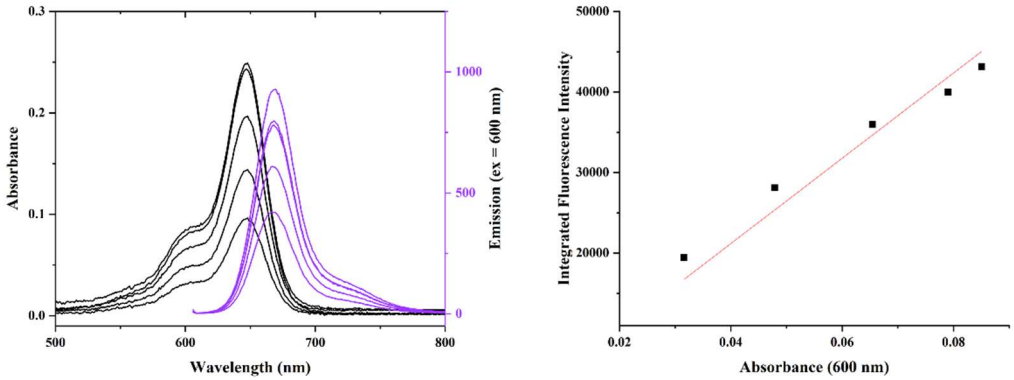

Figure 133: Left: absorbance (black) and emission (purple) spectra of sulfo-Cyanine5-NHS ester (0.534-1.63 μM, CH_3OH). Right: plot of integrated fluorescence emission versus the absorbance at the excitation wavelength (600 nm). The data is fitted to a straight line passing through the origin. The Pearson's correlation of the linear fit is 0.99. The fluorescence quantum yield was determined using equation (1) where $\Phi_r = 0.30$,[16] $m_s = (5.30 \pm 0.17) \times 10^5$, $m_r = (4.48 \pm 0.13) \times 10^5$, $\eta_s = 1.3270 (\pm 0.0005)$[5] and $\eta_r = 1.3604 (\pm 0.0003)$[5], giving $\phi_s = 0.34 \pm 0.02$.

Compound 5

Five solutions of compound **5** were prepared in CH_3OH and the absorbance spectra were obtained. Fluorescence emission spectra were obtained using 600 nm as the excitation wavelength. The integrated fluorescence intensity was plotted against absorbance at the excitation wavelength (600 nm) and the data fitted to a straight line with the intercept (0,0) (Figure 134). The obtained gradient and refractive index of CH_3OH (1.3270 ± 0.0005)[5] were used to calculate the fluorescence quantum yield of compound **5** giving 0.28 ± 0.01 using equation (1).

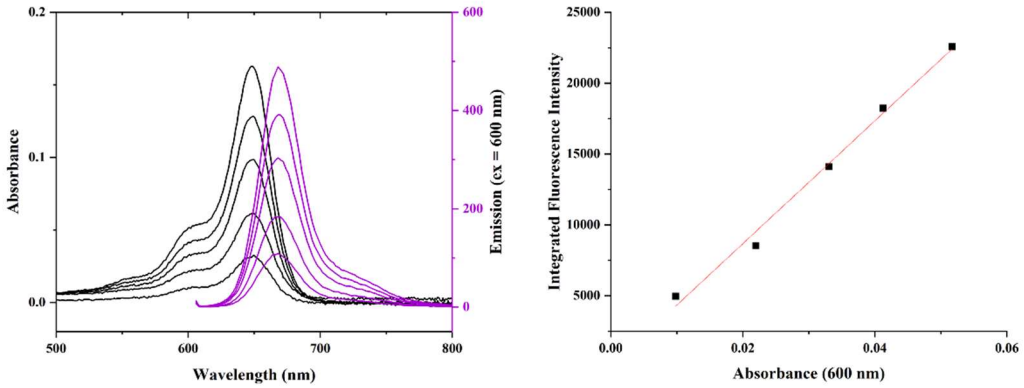

*Figure 134: Left: absorbance (black) and emission (purple) profiles of **5** (0.173-0.851 μM) in CH_3OH. Right: plot of integrated fluorescence emission versus the absorbance at the excitation wavelength (600 nm). The data is fitted to a straight line passing through the origin. The Pearson's correlation of the linear fit is 0.99. The fluorescence quantum yield was determined using equation (1) where $\Phi_r = 0.30$,[16] $m_s = (4.34 \pm 0.08) \times 10^4$, $m_r = (4.38 \pm 0.13) \times 10^5$, $\eta_s = 1.3270 (\pm 0.0005)$[5] and $\eta_r = 1.3604 (\pm 0.0003)$[5], giving $\phi_s = 0.28 \pm 0.01$.*

Compound 6

The fluorescence quantum yield of **6** was determined using the same methodology used for **5**. Five solutions were prepared in CH_3OH and the absorbance and emission spectra were obtained (excitation at 600 nm, Figure 135). The integrated fluorescence intensity was plotted against the absorbance at 600 nm and the data fitted to a straight line with the intercept at (0,0). The fluorescence quantum yield was calculated as 0.29 ± 0.02 using equation (1).

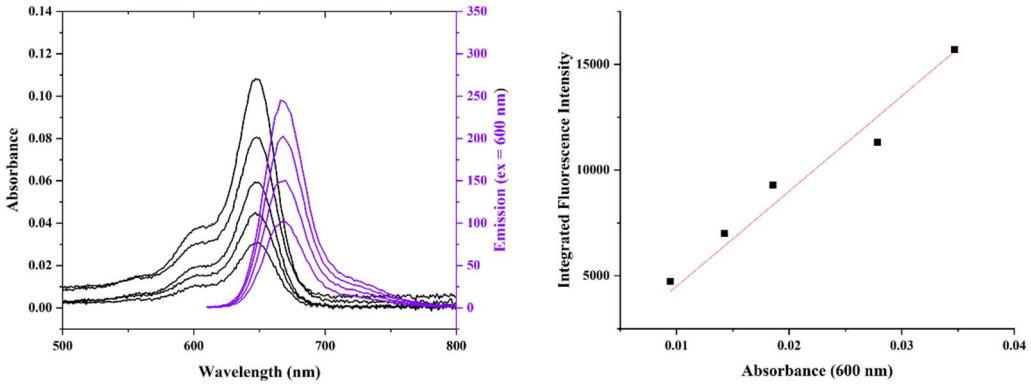

*Figure 135: Left: absorbance (black) and emission (purple) profiles of **6** (0.162-0.584 μM) in CH_3OH. Right: plot of integrated fluorescence emission versus the absorbance at the excitation*

wavelength (600 nm). The data is fitted to a straight line passing through the origin. The Pearson's correlation of the linear fit is 0.99. The fluorescence quantum yield was determined using equation (1) where Φ_r = 0.30,[16] m_s = (4.50 ± 0.17) x 10^4, m_r = (4.38 ± 0.13) x 10^5 , η_s = 1.3270 (± 0.0005)[5] and η_r = 1.3604 (±0.0003)[5], giving ϕ_s = 0.29 ± 0.02.

Compound 15

Compound **15** has the sulfo-Cyanine5 fluorophore attached to CNCbi. Absorbance and emission spectra (excitation at 600 nm) were obtained for five solutions in CH_3OH (Figure 136). The absorbance values were plotted against the integrated fluorescence intensity and the data fitted to a straight line with the intercept at (0,0). The fluorescence quantum yield was calculated as 0.22 ± 0.01 using equation (1).

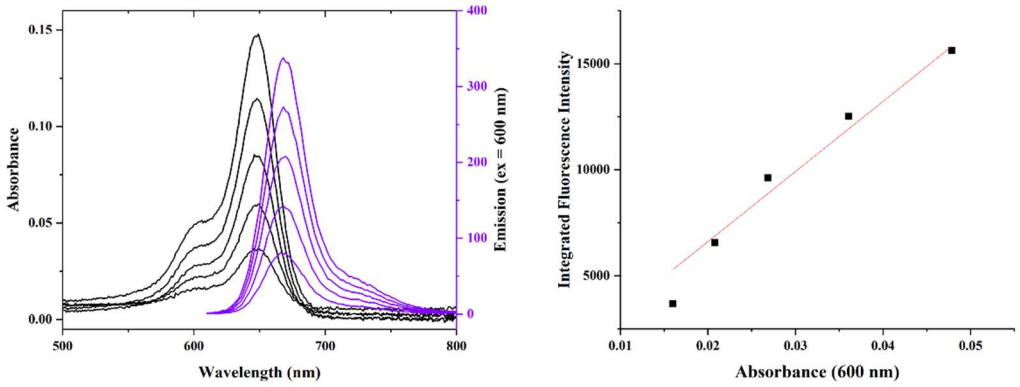

*Figure 136: Left: absorbance (black) and emission (purple) profiles of **15** (0.193-0.142 µM in CH_3OH). Right: plot of integrated fluorescence emission versus the absorbance at the excitation wavelength (600 nm). The data is fitted to a straight line passing through the origin. The Pearson's correlation of the linear fit is 0.99. The fluorescence quantum yield was determined using equation (1) where Φ_r = 0.30,[16] m_s = (3.31 ± 0.13) x 10^4, m_r = (4.38 ± 0.13) x 10^5 , η_s = 1.3270 (± 0.0005)[5] and η_r = 1.3604 (±0.0003)[5], giving ϕ_s = 0.22 ± 0.01.*

The fluorescence quantum yields of compounds **5**, **6** and **15** are summarized in Table 5. The values for **5** and **6** are the same within experimental error. The fluorescence quantum yield of the CNCbi conjugate (**15**) is lower than the CNCbl analogues. The fluorescence quantum yield of sulfo-Cyanine5-NHS ester was published in EtOH[16], so the quantum yield of free sulfo-Cyanine5-NHS in CH_3OH was experimentally determined to allow comparison with the quantum yields of **5**, **6** and **15**.

Table 5: Fluorescence quantum yields of CNCbl and CNCbi conjugates of sulfo-Cyanine5 obtained in CH_3OH.

Compound	Fluorescence quantum yield
5 (CNCbl-Cy-sulfo-Cyanine5)	0.28 ± 0.01
6 (CNCbl-PEG-sulfo-Cyanine5)	0.29 ± 0.02
15 (CNCbi-PEG-sulfoCyanine5)	0.22 ± 0.01
sulfo-Cyanine5-NHS ester	0.34 ± 0.02

The fluorescence quantum yields of **5** and **6** are over one order of magnitude larger than the value reported in the literature for a CNCbl-linker-sulfo-Cyanine5 conjugate (0.011 ± 0.001)[17,11] incorporating a diaminohexane linker between CNCbl and sulfo-Cyanine5. The experimental procedure used by us was more robust as five solutions were utilised to obtain the value, where as a single solution was used to obtained the value for the CNCbl-diaminohexane-sulfo-Cyanine5 conjugate. More importantly, the absorbance value of the solution (1 μM) used for the fluorescence quantum yield determination was 0.62. A maximum absorbance value of 0.1 is recommended for quantum yield determinations, so the inner filter effect is negligible.[1,2]

The fluorescence quantum yields of **5**, **6** and **15** (0.22-0.29) make these molecules suitable for use in cellular-imaging studies. Furthermore, the excellent quantum yields together with the high molar extinction coefficient of the sulfo-Cyanine5 fluorophore (2.71 x 10^5 L mol^{-1} cm^{-1} at 646 nm) ensures that a strong fluorescent signal will be emitted.[18,19]

4.4.3 Determination of fluorescence quantum yields of CNCbl and Cbi conjugates of Cyanine7

1,1',3,3,3',3'-hexamethylindotricarbocyanine iodide (HITCI) reference

The reference dye selected for the Cyanine7 conjugates **7**, **8** and **15** was HITCI. HITCI is structurally similar to the appended Cyanine7 molecule used in this research (Figure 137). Furthermore, HITCI and Cyanine7 have similar absorbance and emission spectra with excitation maxima at 750 and 756 nm, respectively (Figure 138). HITCI has a published fluorescence quantum yield of 0.283 ± 0.017 in EtOH.[20]

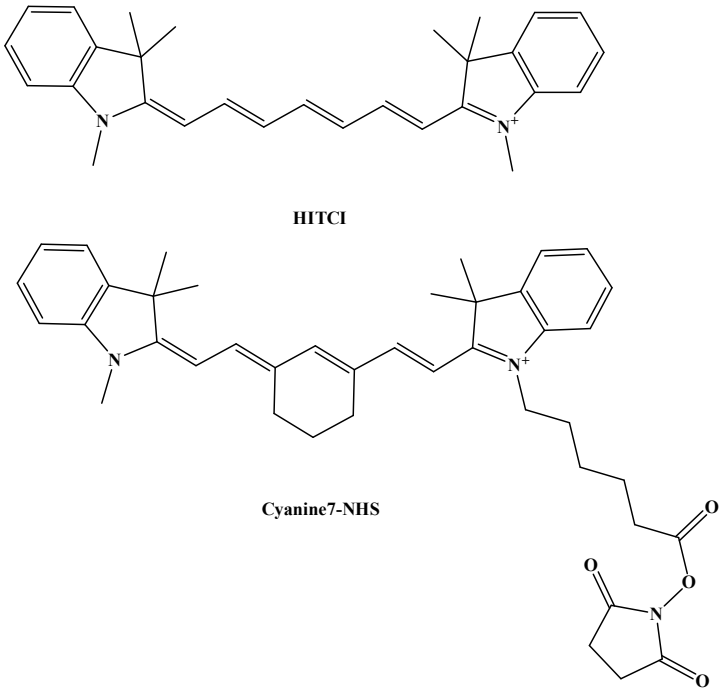

Figure 137: Structures of HITCI and Cyanine7-NHS.

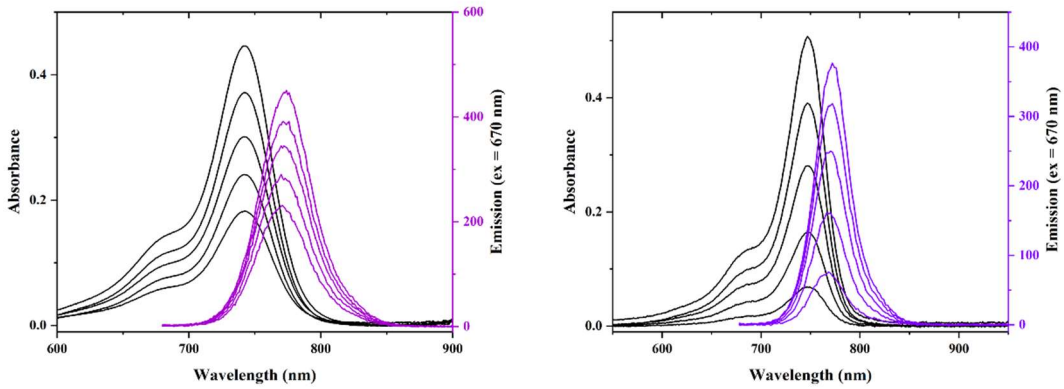

Figure 138: Absorbance (black) and emission (purple, excitation at 670 nm) spectra of HITCI (EtOH, left) and Cyanine7-NHS (CH_3OH, right) obtained at 25.0 °C.

Like sulfo-Cyanine5, HITCI has a shoulder in the absorbance spectrum at ~670 nm which was selected as the excitation wavelength. This excitation wavelength permitted the full fluorescence emission spectrum to be measured. Five solutions of HITCI were prepared and the absorbance and emission spectra recorded (in EtOH, Figure 139). The integrated fluorescence intensity versus absorbance (at 670 nm) were fitted to a straight line with the intercept at (0,0).

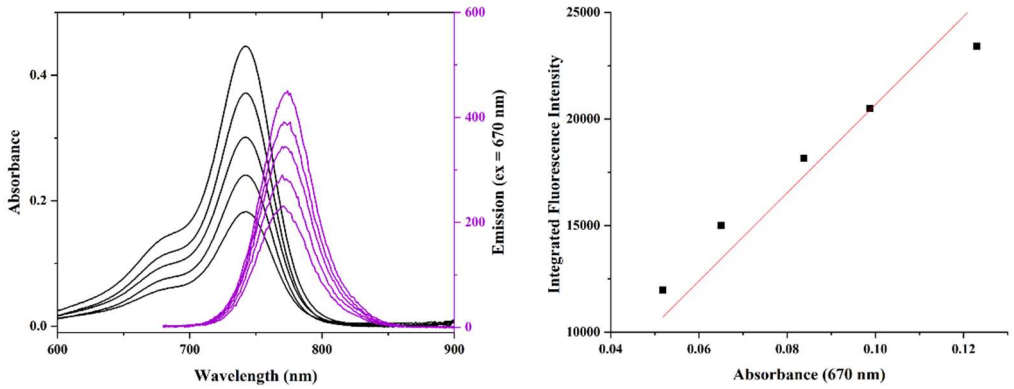

Figure 139: Left: absorbance (black) and emission (purple) spectra of HITCI (0.331-0.724 µM in EtOH). Right: plot of integrated fluorescence intensity versus the absorbance at the excitation wavelength (670 nm). The data was fitted to a straight line passing through the origin, giving a (2.07 ± 0.08) x 10^5 gradient. The Pearson's correlation of the linear fit is 0.99.

Cyanine7-NHS

The fluorescence quantum yield of Cyanine7-NHS has not been published in the literature. To compare the fluorescence quantum yield of the CNCbl and CNCbi conjugates of Cyanine7 to the unbound Cyanine7-NHS molecule, the fluorescence quantum yield of Cyanine7-NHS was determined. Five solutions of Cyanine7-NHS were prepared in CH_3OH and the absorbance and emission spectra were obtained (Figure 140). The absorbance data at 670 nm was plotted against the integrated fluorescence intensity for each sample. The data was fitted to a straight line with an intercept at (0,0). The fluorescence quantum yield value for Cyanine7-NHS was determined as 0.24 ± 0.04 using equation (1).

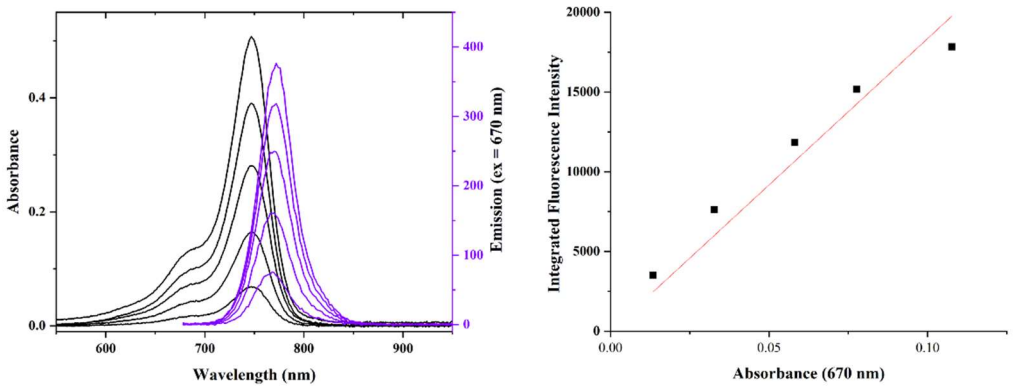

Figure 140: Left: absorbance (black) and emission (purple) spectra of Cyanine7-NHS (0.202-1.43 μM in CH_3OH). Right: plot of integrated fluorescence intensity versus the absorbance at the excitation wavelength (670 nm). The data were fitted to a straight line passing through the origin. The Pearson's correlation of the linear fit is 0.99. The fluorescence quantum yield was determined using equation (1) where $\Phi_r = 0.283 \pm 0.017$, $m_s = (1.84 \pm 0.10) \times 10^5$, $m_r = (2.07 \pm 0.08) 10^5$, $\eta_s = 1.3270 (\pm 0.0005)^5$ and $\eta_r = 1.3604 (\pm 0.0003)^5$, giving $\phi_s = 0.24 \pm 0.04$.

Compound 7

The absorbance and emission spectra of five solutions of **7** were recorded in CH_3OH (Figure 141). The integrated fluorescence intensity was plotted against the absorbance at 670 nm. The fluorescence quantum yield was determined as 0.22 ± 0.03 using equation (1).

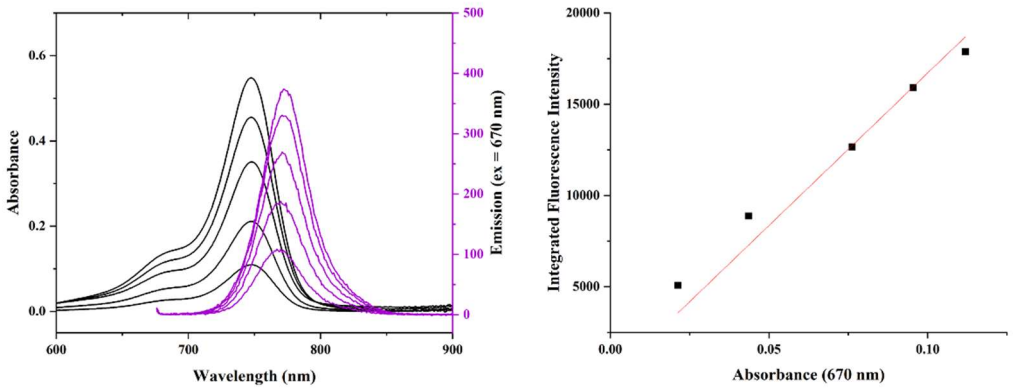

Figure 141: Left: absorbance (black) and emission (purple) spectra of 7 (0.586-1.74 μM in CH_3OH). Right: plot of integrated fluorescence intensity versus the absorbance at the excitation wavelength (670 nm). The data was fitted to a straight line passing through the origin. The Pearson's correlation of the linear fit is 0.99. The fluorescence quantum yield was determined

using equation (1) where Φ_r = 0.283 ± 0.017, m_s = (1.67 ± 0.07) x 10^5, m_r = (2.07 x ± 0.08) 10^5, η_s = 1.3270 (± 0.0005)[5] and η_r = 1.3604 (±0.0003),[5] giving ϕ_s = 0.22 ± 0.03.

Compound 8

Five solutions of **8** were prepared in CH_3OH and the emission and absorbance spectra were recorded (Figure 142). The absorbance at 670 nm was plotted against the integrated fluorescence intensity and the data fitted to a straight line with an intercept of (0,0). The fluorescence quantum yield was determined using equation (1) to be 0.25 ± 0.03.

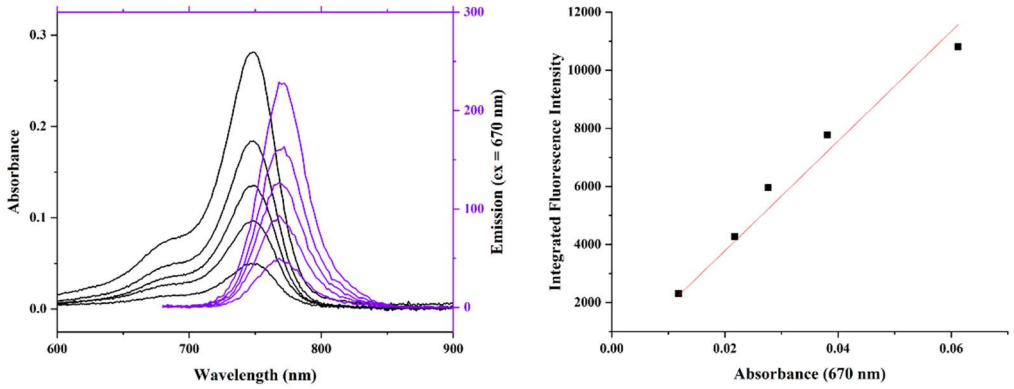

*Figure 142: Left: absorbance (black) and emission (purple) spectra of **8** (0.215-1.06 μM in CH_3OH). Right: plot of integrated fluorescence intensity versus the absorbance at the excitation wavelength (670 nm). The data was fitted to a straight line passing through the origin. The Pearson's correlation of the linear fit is 0.99. The fluorescence quantum yield was determined using equation (1) where Φ_r = 0.283 ± 0.017, m_s = (1.89 ± 0.07) x 10^5, m_r = (2.07 x ± 0.08) 10^5, η_s = 1.3270 (± 0.0005)[5] and η_r = 1.3604 (±0.0003)[5], giving ϕ_s = 0.25 ± 0.03.*

Compound 16

The absorbance and emission spectra of five solutions of **16** were recorded in CH_3OH. The data were fitted to a straight line with the intercept at (0,0) (Figure 143). The fluorescence quantum yield was established as 0.23 ± 0.03 using equation (1).

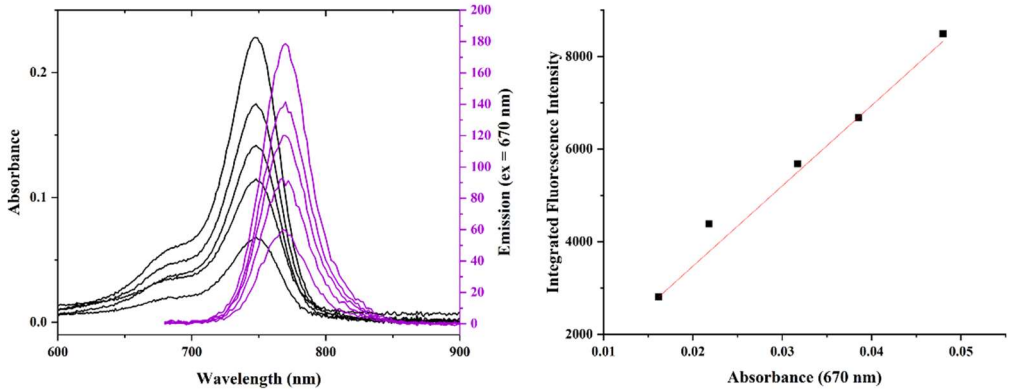

*Figure 143: Left: absorbance (black) and emission (purple) spectra of **16** (1.83-6.42 μM in CH_3OH). Right: plot of integrated fluorescence intensity versus the absorbance at the excitation wavelength (670 nm). The data were fitted to a straight line passing through the origin. The Pearson's correlation of the linear fit is 0.99. The fluorescence quantum yield was determined using equation (1) where $\Phi_r = 0.283 \pm 0.017$, $m_s = (1.73 \pm 0.06) \times 10^5$, $m_r = (2.07 \times \pm 0.08)\ 10^5$, $\eta_s = 1.3270\ (\pm 0.0005)^5$ and $\eta_r = 1.3604\ (\pm 0.0003)^5$, giving $\phi_s = 0.23 \pm 0.03$.*

Table 6 summarises the fluorescence quantum yields of Cyanine7-NHS and compounds **7**, **8** and **16**. The fluorescence quantum yields of all three Cyanine7 conjugates of CNCbl and CNCbi are the same within error as the free Cyanine7-NHS fluorophore. No fluorescence quenching is observed upon conjugation of Cyanine7 to CNCbl or CNCbi. There is no overlap between the absorbance spectra of CNCbl and CNCbi (<600 nm) and the emission spectrum of Cyanine7-NHS. This suggests that the quenching observed for the NBD-X systems may occur by FRET as quenching has only been observed where CNCbl/CNCbi absorbance spectra overlap with fluorescent emission.

Table 6: Fluorescence quantum yields of the CNCbl and CNCbi conjugates of Cyanine7, and free Cyanine7-NHS, in CH_3OH at 25.0°C.

Compound	Fluorescence quantum yield
7 (CNCbl-cy-Cyanine7)	0.22 ± 0.03
8 (CNCbl-PEG-Cyanine7)	0.25 ± 0.03
16 (CNCbi-PEG-Cyanine7)	0.23 ± 0.03
Cyanine7-NHS ester	0.24 ± 0.04

The Cyanine7 conjugates reported here are the first examples of near-infrared emitting CNCbl conjugates where the fluorescence quantum yield has been determined. A few other near-infrared fluorophores have been conjugated via a linker to the 5'-OH site of CNCbl in the literature; namely Atto725 (λ_{ex} 728, λ_{ex} 751 nm), Alexa700 (λ_{ex} 702, λ_{ex} 723 nm), DyLight800 (λ_{ex} 771, λ_{ex} 796 nm) and FL800 (λ_{ex} 775, λ_{ex} 792 nm).[21,22] The synthesis of these molecules has been well described but fluorescence quantum yield values were not determined. Although the fluorescent properties of these compounds were not discussed, irradiation of the CNCbl-fluorophore compounds afforded Co-C bond cleavage at the β-axial site. This indicates that photoinduced electron transfer from the excited state fluorophore to the corrin ring could also occur for these systems.

The fluorescence quantum yield of **7**, **8** and **16** make these compounds useful for cellular imaging experiments. Additionally, Cyanine7-NHS has a high molar extinction coefficient (1.99 x 10^5 mol^{-1} cm^{-1}) which ensures that strong fluorescent emission will occur.[23]

4.5 Discussion

Quenching of fluorescence has been observed for numerous fluorophores upon their coordination to vitamin B_{12} or a B_{12} analogue.[7,24,25] Static quenching which arises due to association between the fluorophore and B_{12} molecules in their ground states, was proposed by Hassanin et al. (2022).[26] This study found that increasing concentrations of aquacobalamin (from 0.1-7 eq.) resulted in a gradual linear reduction in the fluorescence of riboflavin. Riboflavin has similar absorbance maximum (λ_{max} = 400 nm) and emission maximum (λ_{max} = 530 nm) to NBD-X. Dynamic quenching mechanisms have also been proposed. Studies by Jacobsen et al. (1979) proposed that quenching occurs through a nonradiative energy transfer between the fluorophore and cobalamin.[27] Synthesis of fluorescent cobalamin derivatives by Grissom et al. achieved partial restoration of fluorescence after insertion of a 'rigid' linker, likening the quenching to occur via a contact-dependant mechanism (i.e. FRET).[25] Lawrence et al. (2016) suggested that fluorescence quenching occurs for these systems via photoinduced electron transfer (PeT), resulting in both Co-C and Co-S bond cleavage.[21,28,29]

Elucidating the quenching mechanism(s) for the CNCbl/Cbi conjugates requires an understanding of the photophysics of the parent molecule, CNCbl. Upon photoirradiation, the excited states of CNCbl undergo internal conversion to a lower energy state with

charge transfer (LMCT/MLCT) character, followed by non-radiative relaxation to the ground state.[30] Bond cleavage does not occur. CNCbl also fluoresces, albeit very weakly, as the competing internal conversion from the $\pi \rightarrow \pi^*$ state proceeds rapidly, preventing the observation of fluorescence under most conditions.[31,32] The photophysics of CNCbl is different from that of alkylcobalamins, where photoirradiation induces Co-C homolytic bond cleavage, generating cob(II)alamin and an alkyl radical.[31,32]

In static quenching the ground-state donor and acceptor associate to form a non-fluorescent complex prior to excitation of the donor. Transition metal complexes can form charge-transfer complexes with fluorophores.[33–35] To probe whether static quenching is occurring between CNCbl and NBD-X, visible spectroscopy studies were carried out for solutions of CNCbl/CNCbi and free NBD-X. The concentration of NBD-X was fixed (27.7 μM) and the CNCbl varied (ratio of the concentrations of NBD-X:CNCbl = 1:0, 1:1, 1:1.5, 1:2, 1:3 and 1:5, Figure 127). The combined visible spectra of the separate solutions of CNCbl and NBD-X were identical within experimental error to the spectra of equimolar solutions of CNCbl and NBD-X for all experimental conditions. Hence there was no evidence for association between the ground-state CNCbl/CNCbi molecules with free NBD-X. Importantly, there was also no evidence for ground-state association between the macrocycle and the fluorophore in the CNCbl/CNCbi-conjugates by ^{1}H NMR spectroscopy, with chemical shifts of the unbound CNCbl/CNCbi and NBD-X protons resonating in the aromatic region being the same as the CNCbl/CNCbi conjugates of NBD-X within experimental error (± 0.02 ppm).

Emission spectra were also recorded for free NBD-X in the presence of varying concentrations of CNCbl. A 1% reduction in fluorescence was observed upon the addition of 1 eq. CNCbl to a solution of NBD-X (1.24 μM). This is considerably smaller than the reduction in fluorescence observed for the CNCbl/CNCbi-NBD-X conjugates, where over one order of magnitude quenching was observed. The Stern-Volmer plot of the data is shown in Figure 128. The fluorescence intensity decreased linearly upon increasing the CNCbl concentration. This data suggests that fluorescence quenching occurs via one major mechanism.[26]

Dexter energy transfer, Förster resonance energy transfer (FRET) and photoinduced electron transfer (PeT) are dynamic fluorescence quenching mechanisms that depend on the distance between the donor and the acceptor. In Dexter energy transfer, electron

exchange occurs between the excited donor and acceptor molecules. This requires a close spatial contact of < 1 nm between the donor and acceptor (< 6 bond lengths).[10,11] Assuming a Poisson distribution for the excited state NBD-X molecules and the ground state CNCbl molecules in solution, the probability that a given molecule of species 1 (NBD-X) has a neighboring species 2 (CNCbl) with a concentration of c_2 (molecules.m^{-3}) within a volume of radius r can be calculated by:

$$P_{near} = 1 - e^{-c2\ \frac{4}{3}\pi r^3} \quad (2)$$

Using the experimental concentrations of CNCbl at 1.28 μM and 12.8 μM when r = 1 nm, the probability of CNCbl and NBD-X being near is 0.0003% and 0.003%, respectively. However, for the CNCbl/NBD-X system, a 1% reduction in fluorescence was observed when the concentration of the CNCbl was 1.28 μM, which is not consistent with the probabilities calculated above. This indicates that Dexter energy transfer is not occurring for free NBD-X/CNCbl solutions.

For PeT the excited donor molecule (the fluorophore in our case) transfers an electron to the acceptor. The Gibbs free energy change must be negative for PeT to be thermodynamically favorable and can be calculated using the Weller equation[36]:

$$\Delta G_{PET} = E_{ox}(\text{donor}) - E_{red}(\text{acceptor}) - E_o + C \quad (3)$$

where E_o is the energy of the donor's vibrationally relaxed excited state and C is the Coulombic term (which is ~ 0 in polar solvents[37]).

The E_{ox} value of NBD-X is not available in the literature; however, the structurally similar NBD-piperidine molecule has an E_{ox} of 1.58 V (Figure 144).[38] An assumption made here is that the E_{ox} of NBD-X and NBD-piperidine are similar. The redox potential is more negative in the excited state molecule.[39] The reduction potential for CNCbl is highly negative (-0.76 V).[40] Unlike alkylcobalamins, CNCbl is reduced from its Co(III) oxidation state directly to Co(I), since the rate of reduction of CNCbl to Co(II) is much slower than the rate of reduction of Co(II) to Co(I).[40] Using equation (3), the ΔG_{PET} value for PeT between NBD and CNCbl is -0.20 eV when the vibrationally relaxed excited state is 488 nm (estimated at 10% of the emission maximum). This indicates that PeT is thermodynamically favourable for this system. However, based on the probabilities calculated above and the short distance between the excited fluorophore and CNCbl

required for PeT to occur (1-3 nm)[41], it is unlikely that this mechanism occurs between free NBD-X and CNCbl.

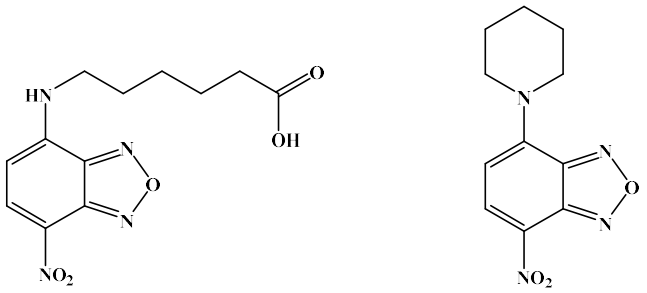

Figure 144: Structures of the NBD-X molecule used in this study (left) and a NBD-piperidine analogue with a published E_{ox} of 1.58 V.[38]

For FRET, dipole-dipole interactions between the donor and acceptor result in non-radiative energy transfer from the donor to the acceptor.[32] For FRET to be efficient, there must be significant spectral overlap of the donor's emission spectrum with the acceptor's absorbance spectrum.[32] The absorbance spectra of CNCbl and CNCbi overlap significantly with the NBD-X emission spectrum (Figure 145), whereas this is not the case for sulfo-Cyanine5 and especially Cyanine7. This supports the lower fluorescence quantum yields for the CNCbl-linker-NBD-X complexes **3** and **4** (0.011 and 0.007, respectively) compared to the NBD-X fluorophore (0.287). The absorbance spectrum of CNCbi overlaps less with the emission spectrum of NBD-X, consistent with the slightly higher fluorescence quantum yields for the CNCbi-linker-NBD-X complexes **13** and **14** (0.019 and 0.035, respectively, compared with 0.011 (**3**) and 0.007 (**4**)). Interestingly, the fluorescence quantum yield of the CNCbl-linker-sulfo-Cyanine5 complexes **5** and **6** (0.28 and 0.29, respectively) are slightly lower than the fluorescence quantum yield of sulfo-Cyanine5-NHS (0.34). Furthermore, the CNCbi-linker-sulfo-Cyanine5 complex **15** has a smaller fluorescence quantum yield of 0.22. There is no overlap between the absorbance spectrum of CNCbl/CNCbi and the emission spectrum of sulfo-Cyanine5. This suggests that FRET is not occurring for the sulfo-Cyanine5 complexes. The fluorescence quantum yields of both CNCbl/CNCbi-linker-Cyanine7 complexes **7**, **8** and **16** (0.22, 0.25 and 0.23, respectively) are the same within experimental error to the fluorescence quantum yield of Cyanine7 alone (0.24). This indicates that no fluorescence quenching occurred for these complexes.

FRET is strongly distance-dependent (α $1/r^6$, where r is the distance between the donor and acceptor) and occurs at donor-acceptor distances of 0.5-10 nm.[2,10,11,42] Equation (2) can be used to determine the likelihood that FRET is responsible for the observed quenching. In the emission studies of solutions containing NBD-X and CNCbl (Figure 128), the concentrations of CNCbl were 1.28, 6.42 and 12.8 μM. Using equation (2), the probabilities of the two molecules being within 10 nm of one another are 0.32%, 1.6% and 3.2%, respectively, at these three CNCbl concentrations. These values loosely align with what was observed experimentally, where a 1%, 10% and 15% reduction in fluorescence was observed at these concentrations (Figure 128). This suggests that fluorescence quenching between the free NBD-X and CNCbl molecules is likely to predominantly occur by FRET.

Additional experiments could confirm or refute FRET being the main mechanism of fluorescence quenching in this system. In PeT a charge-transfer intermediate is formed immediately after rapid electron transfer from the excited donor molecule to the acceptor, which should be observable by ultrafast transient absorption spectroscopy for these systems since the spectral characteristics of the Co(II) and Co(I) forms of CNCbl and CNCbi are very different from the Co(III) CNCbl/CNCbi.[31,43] The fluorescence quantum yield could also be determined in DMSO. For PeT, decreasing the solvent polarity decreases the stability of the charge-separated intermediate, making PeT less favourable in DMSO compared with CH_3OH. The fluorescence lifetime of free NBD-X in the presence of increasing concentrations of CNCbl could also be determined. For dynamic quenching mechanisms such as PeT and FRET, this lifetime will decrease, whereas it will be unchanged if static quenching is occurring [10,11,36]

The fluorescence of NBD-X is quenched by over one order of magnitude upon conjunction to CNCbl or CNCbi (Table 4), whereas a slight reduction in the fluorescence quantum yield was observed upon conjugating sulfo-Cyanine5 to CNCbl ($\leq$ 20%) or CNCbi ($\leq$ 35%, Table 5), and no quenching was detected when Cyanine7 was conjugated to CNCbl or CNCbi (Table 6). There is a significant overlap of the emission spectrum of NBD-X with the absorbance spectra of CNCbl and CNCbi (Figure 145). There is no overlap between the emission spectrum of sulfo-Cyanine5-NHS or Cyanine7-NHS and the absorbance spectra of CNCbl or CNCbi.

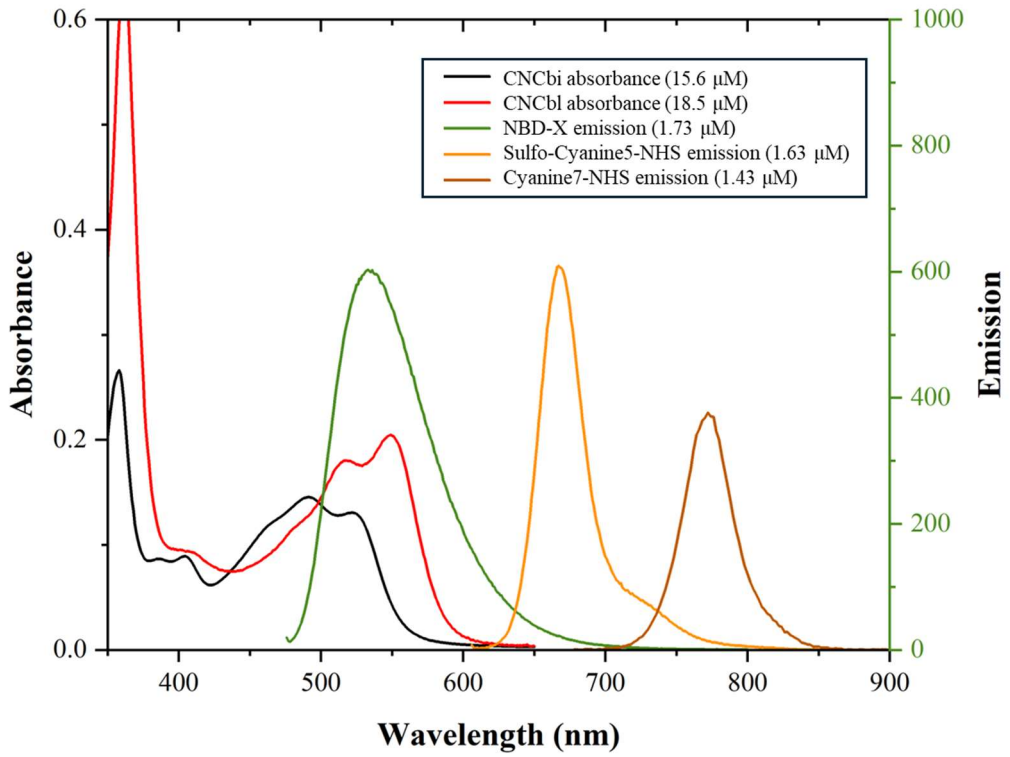

Figure 145: Absorbance spectra of CNCbl (18.5 µM, red) and CNCbi (15.6 µM, black) in CH_3OH, recorded at 25°C. Fluorescence emission spectra of NBD-X (1.73 µM, green, λ_{ex} = 470 nm), sulfo-Cyanine5-NHS (1.63 µM, orange, λ_{ex} = 600 nm) and Cyanine7-NHS (1.43 µM, brown, λ_{ex} = 670 nm) recorded in CH_3OH at 25°C.

The absorbance and emission spectroscopy studies for solutions of free CNCbl and NBD-X verses the CNCbl/CNCbi conjugates of NBD-X suggest a distance-dependent dynamic interaction between the two chromophores in solution. By tethering the NBD-X fluorophore to the CNCbl/CNCbi-linker, the distance between these two entities is reduced significantly compared to solutions of free CNCbl/CNCbi and NBD-X at the same concentration. This indicates that conjugating NBD-X to CNCbl via a linker dramatically improves the efficiency of fluorescence quenching. The linkers employed between the CNCbl/CNCbi moieties and NBD-X are flexible. These linkers could potentially allow molecular folding to occur, so the fluorescent NBD moiety is close to the corrin ring, with the 1,11-diamino-3,6,9-trioxaundecane linker allowing greater flexibility than cystamine due to its increased length. Attachment of the fluorescent molecule to CNCbl/CNCbi via these linkers likely decreases the distance between the two

chromophores. Equation (2) cannot be used in this system as the locations of the NBD-X and CNCbl/CNCbi in the conjugates are not independent, therefore, will not follow a Poisson distribution.

Quenching via FRET can be excluded for the Cyanine5 conjugates of CNCbl/CNCbi due to the lack of overlap between their respective emission and absorbance spectra. Fluorescence quenching of Cyanine5 and NBD-X could also occur via PeT or Dexter energy transfer, given that the distance between the donor and acceptor in these conjugates is potentially less than 1 nm. Both PeT and Dexter require electron transfer to occur between sulfo-Cyanine5 and CNCbl where Equation (3) can be used to indicate if PeT is thermodynamically favourable. The E_{ox} value of sulfo-Cyanine5 is not available in the literature, however, a structurally similar sulfo-Cyanine5 molecule has an E_{ox} of 0.628 V (Figure 146).[44] An assumption made here is that the E_{ox} of these related molecules are similar. Using equation (3), the ΔG_{PET} value for PeT between the sulfo-Cyanine5 and CNCbl is −0.55 eV when the energy of the vibrationally relaxed excited state is 640 nm (estimated as 10% of the emission maximum). This indicates that PeT is possible for the sulfo-Cyanine5 conjugates.

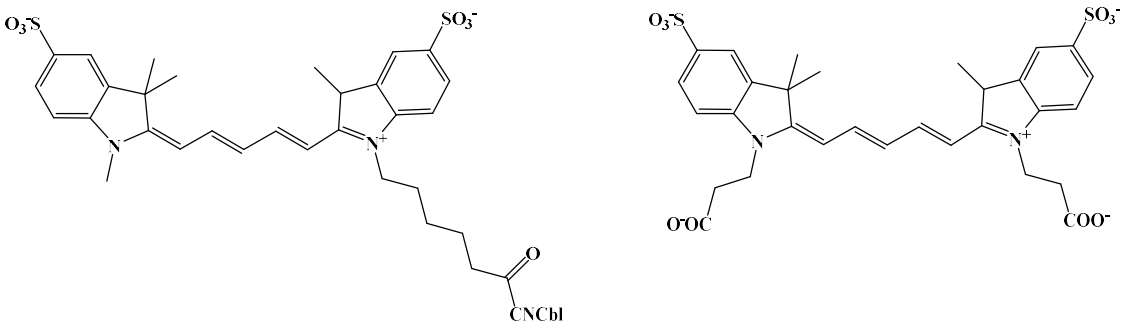

Figure 146: Structures of the sulfo-Cyanine5 molecule used in this study (left) and a structurally similar sulfo-Cyanine5 analogue with a published E_{ox} of 0.63 V.[44]

To elucidate the mechanism of quenching that occurs for the CNCbl/CNCbi-linker-NBD-X/sulfo-Cyanine5 conjugates, further studies need to be undertaken. Additional experiments could help determine whether FRET is the dominant quenching mechanism in the NBD-X system. Ultrafast transient absorption could provide insight into PeT or Dexter mechanisms, monitoring for the potential formation of Co(II) and/or Co(I) intermediates. Measuring the fluorescence quantum yield in a polar aprotic solvent such as DMSO could also provide insight. As discussed earlier, polar aprotic solvents make

PeT less favourable whilst having minimal impact of FRET as this is a dipole-dipole mediated process. To further differentiate between the various quenching mechanisms, the fluorescence lifetime of free NBD-X and sulfo-Cyanine5 can be measured in the presence of increasing concentrations of CNCbl. A reduction in lifetime would indicate a dynamic quenching process such as PeT or FRET, confirming the absence of a static mechanism. In addition, electrochemical measurements (e.g., cyclic voltammetry) can be used to determine the redox potentials of the donor NBD-X and sulfo-Cyanine5 molecules as similar analogues have been used in this analysis. Determining redox potentials for these specific donors could refute PeT as the quenching mechanism.

To summarize, the fluorescence quenching observed between free NBD-X and CNCbl molecules is tentatively proposed to occur predominantly via FRET. This is suggested due to the effective overlap of the NBD-X emission spectrum with the CNCbl absorbance spectrum. Although the Weller equation indicated that quenching via PeT is thermodynamically favourable for this system, the probability of NBD-X and CNCbl being within a 1 nm distance of each other was not significant (P = 0.0003% and 0.003% at CNCbl concentrations of 1.28 μM and 12.8 μM), indicating neither PeT nor Dexter energy transfer are likely to occur. The major fluorescent quenching mechanism for the CNCbl/Cbi-linker-NBD-X and sulfo-Cyanine5 conjugates is less obvious. Since FRET is likely for the free CNCbl/NBD-X system, the same mechanism may occur for the CNCbl/CNCbi-NBD-X conjugates, and may be highly efficient due to the reduction in the distance between the two chromophores as a result of conjugation of the two entities to each other. FRET is unlikely to occur for the CNCbl/CNCbi-linker-sulfoCyanine5 conjugates due to the lack of overlap between the donor emission spectrum and the CNCbl/CNCbi absorbance spectrum. However, a small amount of fluorescence quenching was observed for these conjugates, likely via PeT or Dexter energy transfer, where PeT was determined to be thermodynamically favorable using equation (3). No fluorescence quenching was observed for the CNCbl/CNCbi-Cyanine7 systems.

4.6 Conclusions

The fluorescence quantum yields have been determined for 1,11-diamino-3,6,9-trioxaundecane and cystamine-linked CNCbl and CNCbi conjugates of three fluorophores. The references used for the fluorescence quantum yield determinations

were fluorescein (for NBD-X conjugates), sulfo-Cyanine5-NHS and HITCI (for Cyanine7 conjugates). The fluorescence quantum yield of the Cyanine7 conjugates of CNCbl and CNCbi were the same as the unbound fluorophores. However, the fluorescence quantum yields of NBD-X conjugates of CNCbl and CNCbi were more than one order of magnitude lower than the unbound NBD-X fluorophore, indicating fluorescence quenching was occurring. Absorbance and fluorescence emission studies were also undertaken for solutions of CNCbl and NBD-X. There was no evidence for association of CNCbl and NBD-X by UV/Visible spectroscopy but adding more CNCbl did decrease fluorescence emission.

The fluorescence quenching of the NBD-X moiety in CNCbl-linker-NBD-X was utilised to confirm cystamine linker cleavage by GSH. Disulfide bond cleavage of cystamine by GSH was demonstrated by LC-MS and by a substantial increase in fluorescence upon the addition of GSH. NBD-X was also found to hydrolyse in basic solution (pH 10), resulting in the cleavage of the C-N bond, freeing the fluorescent NBD moiety from the hexanoic acid chain.

This chapter describes the fluorescent properties of a series of novel fluorescent CNCbl and CNCbi conjugates. The sulfo-Cyanine5 and Cyanine7 conjugates demonstrate robust fluorescence suitable for cellular studies by fluorescence microscopy. The chemically responsive cystamine-linked NBD-X conjugates are suitable for investigating the reductive environments within different cellular compartments, due to the significantly enhanced fluorescence upon cleavage of the disulfide bond of the linker.

4.7 References

(1) Würth, C.; Grabolle, M.; Pauli, J.; Spieles, M.; Resch-Genger, U. Relative and Absolute Determination of Fluorescence Quantum Yields of Transparent Samples. *Nat. Protoc.* **2013**, *8* (8), 1535–1550.
(2) Würth, C.; Grabolle, M.; Pauli, J.; Spieles, M.; Resch-Genger, U. Comparison of Methods and Achievable Uncertainties for the Relative and Absolute Measurement of Photoluminescence Quantum Yields. *Anal. Chem.* **2011**, *83* (9), 3431–3439.
(3) Magde, D.; Wong, R.; Seybold, P. G. Fluorescence Quantum Yields and Their Relation to Lifetimes of Rhodamine 6G and Fluorescein in Nine Solvents: Improved Absolute Standards for Quantum Yields *Photochem. Photobiol.* **2007**, *75* (4), 327–334.
(4) Olsen, A. L.; Washburn, E. R. An Interpolation Table for Refractive Index-Normality Relationship for Solutions of Hydrochloric Acid and Sodium Hydroxide. *Trans. Kans. Acad. Sci. 1903-* **1937**, *40*, 117–126. https://doi.org/10.2307/3625399.
(5) Chang, H.-J.; Munera, N.; Lopez-Zelaya, C.; Banerjee, D.; Beadie, G.; Stryland, E. W. V.; Hagan, D. J. Refractive Index Measurements of Liquids from 0.5 to 2 Using Rayleigh Interferometry. *Opt. Mater. Express* **2024,** *14* (5); 1253-1267. https://doi.org/10.1364/OME.519907.
(6) Lee, M.; Grissom, C. B. Design, Synthesis, and Characterization of Fluorescent Cobalamin Analogues with High Quantum Efficiencies. *Org. Lett.* **2009**, *11* (12), 2499–2502. https://doi.org/10.1021/ol900401z.
(7) Smeltzer, C. C.; Cannon, M. J.; Pinson, P. R.; Munger, J. D.; West, F. G.; Grissom, C. B. Synthesis and Characterization of Fluorescent Cobalamin (CobalaFluor) Derivatives for Imaging. *Org. Lett.* **2001**, *3* (6), 799–801. https://doi.org/10.1021/ol006825v.
(8) Jacobsen, D. W.; Digir, P. M.; M Huennekens, A. F. Adenosylcobalamin Analogues as Inhibitors of Ribonucleotide Reductase and Vitamin B_{12} Transport. *Mol. Pharmacol.* **1974**, *11*, 174–184.
(9) Santoro, G.; Zlateva, T.; Ruggi, A.; Quaroni, L.; Zobi, F. Synthesis, Characterization and Cellular Location of Cytotoxic Constitutional Organometallic Isomers of Rhenium Delivered on a Cyanocobalmin Scaffold. *Dalton Trans.* **2015**, *44* (15), 6999–7008. https://doi.org/10.1039/C4DT03598D.
(10) Gryczynski, Z. (Karol); Gryczynski, I. *Practical Fluorescence Spectroscopy*; Taylor & Francis Group: Milton, United Kingdom, 2019.
(11) Lakowicz, J. R. *Principles of Fluorescence Spectroscopy*; Springer: New York, NY, United States, 2011.
(12) Eisenberg, A. S.; Likhtina, I. V.; Znamenskiy, V. S.; Birke, R. L. Electronic Spectroscopy and Computational Studies of Glutathionylco(III)Balamin. *J. Phys. Chem. A* **2012**, *116* (25), 6851–6869. https://doi.org/10.1021/jp301294.
(13) Wierzba, A.; Wojciechowska, M.; Trylska, J.; Gryko, D. Vitamin B_{12} Suitably Tailored for Disulfide-Based Conjugation. *Bioconjug. Chem.* **2016**, *27* (1), 189–197. https://doi.org/10.1021/acs.bioconjchem.5b00599.
(14) Montero, D.; Tachibana, C.; Rahr Winther, J.; Appenzeller-Herzog, C. Intracellular Glutathione Pools Are Heterogeneously Concentrated. *Redox Biol.* **2013**, *1* (1), 508–513. https://doi.org/10.1016/j.redox.2013.10.005.
(15) Vázquez-Meza, H.; Vilchis-Landeros, M. M.; Vázquez-Carrada, M.; Uribe-Ramírez, D.; Matuz-Mares, D. Cellular Compartmentalization, Glutathione Transport and Its Relevance in Some Pathologies. *Antioxidants* **2023**, *12* (4), 834. https://doi.org/10.3390/antiox12040834.

(16) Mujumdar, R. B.; Ernst, L. A.; Mujumdar, S. R.; Lewis, C. J.; Waggoner, A. S. Cyanine Dye Labeling Reagents: Sulfoindocyanine Succinimidyl Esters. *Bioconjug. Chem.* **1993**, *4* (2), 105–111. https://doi.org/10.1021/bc00020a001.
(17) Cannon, M. J. Protein Binding, Cellular Localization, and Tissue Uptake of Breast Cancer Targeted Fluorescent Cobalamin Analogs. Ph.D., The University of Utah, United States -- Utah, **2001**.
(18) Martins, C. D. F.; Raposo, M. M. M.; Costa, S. P. G. Synthesis and Characterization of a Water-Soluble Pentamethine Indocyanine Dye for Peptide Labeling. *Chem. Proc.* **2022**, *8* (1), 91. https://doi.org/10.3390/ecsoc-25-11768.
(19) Martins, C. D. F.; Raposo, M. M. M.; Costa, S. P. G. A Sulfo-Cyanine Dye as a Colorimetric Chemosensor for Metal Cation Recognition. *Eng. Proc.* **2022**, *27* (1), 12. https://doi.org/10.3390/ecsa-9-13219.
(20) Rurack, K.; Spieles, M. Fluorescence Quantum Yields of a Series of Red and Near-Infrared Dyes Emitting at 600−1000 Nm. *Anal. Chem.* **2011**, *83* (4), 1232–1242. https://doi.org/10.1021/ac101329h.
(21) Hughes, R. M.; Marvin, C. M.; Rodgers, Z. L.; Ding, S.; Oien, N. P.; Smith, W. J.; Lawrence, D. S. Phototriggered Secretion of Membrane Compartmentalized Bioactive Agents. *Angew. Chem.* **2016**, *128* (52), 16314–16317. https://doi.org/10.1002/ange.201609731.
(22) Shell, T. A.; Lawrence, D. S. Vitamin B_{12}: A Tunable, Long Wavelength, Light-Responsive Platform for Launching Therapeutic Agents. *Acc. Chem. Res.* **2015**, *48* (11), 2866–2874. https://doi.org/10.1021/acs.accounts.5b00331.
(23) Son, T.; Kim, M.; Choi, M.; Nam, S. H.; Yoo, A.; Lee, H.; Han, E. H.; Hong, K. S.; Park, H. S. Advancing Fluorescence Imaging: Enhanced Control of Cyanine Dye-Doped Silica Nanoparticles. *J. Nanobiotechnology* **2024**, *22* (1), 347. https://doi.org/10.1186/s12951-024-02638-7.
(24) Lawrence, A. D.; Nemoto-Smith, E.; Deery, E.; Baker, J. A.; Schroeder, S.; Brown, D. G.; Tullet, J. M. A.; Howard, M. J.; Brown, I. R.; Smith, A. G.; Boshoff, H. I.; Barry, C. E.; Warren, M. J. Construction of Fluorescent Analogs to Follow the Uptake and Distribution of Cobalamin (Vitamin B_{12}) in Bacteria, Worms, and Plants. *Cell Chem. Biol.* **2018**, *25* (8), 941-951.e6. https://doi.org/10.1016/j.chembiol.2018.04.012.
(25) Lee, M.; Grissom, C. B. Design, Synthesis, and Characterization of Fluorescent Cobalamin Analogues with High Quantum Efficiencies. *C J Lab Clin Med* **2004**, *43* (1), 799. https://doi.org/10.1021/ol900401z.
(26) Hassanin, H. A. Investigation on the Interaction of Riboflavin with Aquacobalamin (Vitamin B_{12}): A Fluorescence Quenching Study. *J. Photochem. Photobiol. Chem.* **2022**, *430*, 113968.
(27) Jacobsen, D. W.; Holland, R. J.; Montejano, Y.; Huennekens, F. M. Cryptofluorescent Analogs of Cobalamin Coenzymes: Synthesis and Characterization. *J. Inorg. Biochem.* **1979**, *10* (1), 53–65. https://doi.org/10.1016/S0162-0134(00)81005-3.
(28) Welfare, J. G.; Mortelliti, M. J.; McGlade, C. A.; Hartman, T. W.; Dempsey, J. L.; Lawrence, D. S. Assessment of Photoreleasable Linkers and Light-Capturing Antennas on a Photoresponsive Cobalamin Scaffold. *J. Org. Chem.* **2022**, *87* (8), 5076–5084. https://doi.org/10.1021/acs.joc.1c02931.
(29) Rodgers, Z. L.; Shell, T. A.; Brugh, A. M.; Nowotarski, H. L.; Forbes, M. D. E.; Lawrence, D. S. Fluorophore Assisted Photolysis of Thiolato-Cob(III)Alamins. *Inorg. Chem.* **2016**, *55* (5), 1962–1969. https://doi.org/10.1021/acs.inorgchem.5b02036.
(30) Chemaly, S. M. Cobalamins and the Spectrochemical Series. *Dalton Trans.* **2008**, No. 42, 5766–5773. https://doi.org/10.1039/B806927A.
(31) Salerno, E. V.; Miller, N. A.; Konar, A.; Li, Y.; Kieninger, C.; Kräutler, B.; Sension, R. J. Ultrafast Excited State Dynamics and Fluorescence from Vitamin B_{12} and

Organometallic [Co]–C≡C–R Cobalamins. *J. Phys. Chem. B* **2020**, *124* (30), 6651–6656. https://doi.org/10.1021/acs.jpcb.0c04886.
(32) Kozlowski, P. M.; Garabato, B. D.; Lodowski, P.; Jaworska, M. Photolytic Properties of Cobalamins: A Theoretical Perspective. *Dalton Trans.* **2016**, *45* (11), 4457–4470. https://doi.org/10.1039/C5DT04286K.
(33) Shakya, S.; Khan, I. M. Charge Transfer Complexes: Emerging and Promising Colorimetric Real-Time Chemosensors for Hazardous Materials. *J. Hazard. Mater.* **2021**, *403*, 123537. https://doi.org/10.1016/j.jhazmat.2020.123537.
(34) Yam, V. W.-W.; Chan, A. K.-W.; Hong, E. Y.-H. Charge-Transfer Processes in Metal Complexes Enable Luminescence and Memory Functions. *Nat. Rev. Chem.* **2020**, *4* (10), 528–541. https://doi.org/10.1038/s41570-020-0199-7.
(35) Lee, H.; Hancock, R. D.; Lee, H.-S. Role of Fluorophore–Metal Interaction in Photoinduced Electron Transfer (PET) Sensors: Time-Dependent Density Functional Theory (TDDFT) Study. *J. Phys. Chem. A* **2013**, *117* (50), 13345–13355. https://doi.org/10.1021/jp406624p.
(36) Weller, A. Photoinduced Electron Transfer in Solution: Exciplex and Radical Ion Pair Formation Free Enthalpies and their Solvent Dependence. *Zeitschrift für Physikalische Chemie* **1982**, *133*, 93–98. https://doi.org/10.1024/zpch.1982.133.1.093
(37) Rumble, C. A.; Licari, G.; Vauthey, E. Molecular Dynamics Simulations of Bimolecular Electron Transfer: Testing the Coulomb Term in the Weller Equation. *J. Phys. Chem. B* **2020**, *124* (44), 9945–9950. https://doi.org/10.1021/acs.jpcb.0c09031.
(38) Raissi, H.; Chérif, I.; Ayachi, H.; Said, A. H.; Hassen, F.; Ayachi, S.; Boubaker, T. Structure-Property Relationships in Benzofurazan Derivatives: A Combined Experimental and DFT/TD-DFT Investigation; *IntechOpen*, **2021**. https://doi.org/10.5772/intechopen.99246.
(39) Jr, W. E. J.; Fox, M. A. Determination of Excited-State Redox Potentials by Phase-Modulated Voltammetry. *ACS Publications*. **1994**, *98* (19), 5095–5099. https://doi.org/10.1021/j100070a025.
(40) Marques, H. M. The Inorganic Chemistry of the Cobalt Corrinoids – an Update. *J. Inorg. Biochem.* **2023**, *242*, 112154. https://doi.org/10.1016/j.jinorgbio.2023.112154.
(41) Portela, C. F.; Brunckova, J.; Richards, J. L.; Schöllhorn, B.; Iamamoto, Y.; Magde, D.; Traylor, T. G.; Perrin, C. L. Distance Dependence of Photoinduced Electron Transfer in Metalloporphyrin Dimers. *J. Phys. Chem. A* **1999**, *103* (49), 10540–10552. https://doi.org/10.1021/jp991766s.
(42) Clegg, R. M. Chapter 1 Förster Resonance Energy Transfer—FRET What Is It, Why Do It, and How It's Done. In *Laboratory Techniques in Biochemistry and Molecular Biology*; **2009**; *33*, 1–57. https://doi.org/10.1016/S0075-7535(08)00001-6.
(43) Hamza, M. S. A.; Pratt, J. M. The Chemistry of Vitamin B_{12}. Part 29. Co-Ordination of Imidazoles and 1,2,4-Triazole by Aquacyanocobinamide. *J. Chem. Soc. Dalton Trans.* **1994**, *9*, 1373–1376. https://doi.org/10.1039/DT9940001373.
(44) Oushiki, D.; Kojima, H.; Terai, T.; Arita, M.; Hanaoka, K.; Urano, Y.; Nagano, T. Development and Application of a Near-Infrared Fluorescence Probe for Oxidative Stress Based on Differential Reactivity of Linked Cyanine Dyes. *J. Am. Chem. Soc.* **2010**, *132* (8), 2795–2801. https://doi.org/10.1021/ja910090v.x

Chapter 5 Synthesis and characterisation of vitamin B_{12} conjugates of the antibiotics ciprofloxacin and gentamicin

5.1 Introduction

The use of CNCbl as a carrier molecule for different types of cargo into cells has been investigated by many research groups.[1–3] An emerging field concerns the delivery of molecules including nanoparticles, peptide nucleic acids or antibiotics into bacteria using CNCbl.[3–7] This chapter presents the synthesis and characterisation of novel CNCbl-linker-antibiotic conjugates of the established broad-spectrum antibiotics with known cytoplasmic targets, gentamicin and ciprofloxacin.[8–11] CNCbl-linker-ciprofloxacin conjugates have been synthesised using two functional groups of ciprofloxacin - either the carboxylic acid or the secondary amine of the piperazine. CNCbl-linker-gentamicin conjugates were synthesised by peptide bond formation between CNCbl-linker-COOH molecules and an amino group of gentamicin.

The procedures for the synthesis of the CNCbl-linker compounds described in Chapter 2 have been extended using linkers with a terminal carboxylic acid which are suitable for peptide coupling to amine functionalities of gentamicin or ciprofloxacin. The linkers 3-[2-[2-(2-aminoethoxy)ethoxy]ethoxy]propanoic acid and 3-[(2-aminoethyl)dithio]propionic acid were conjugated to CNCbl by carbamate bond formation (Figure 147).

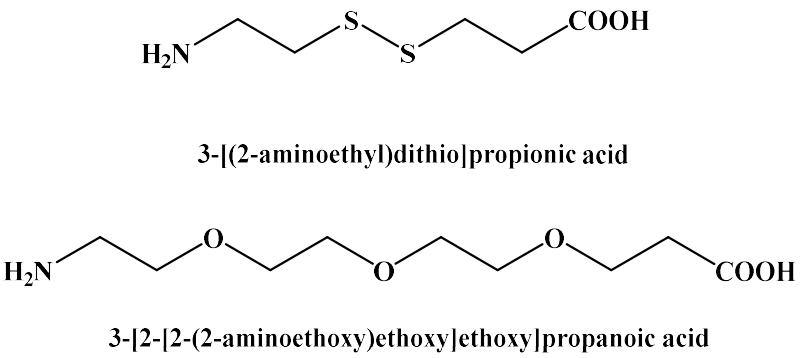

Figure 147: Structures of 3-[2-[2-(2-aminoethoxy)ethoxy]ethoxy]propanoic acid and 3-[(2-aminoethyl)dithio]propionic acid.

CNCbl-linker compounds incorporating a terminal carboxylic acid were conjugated to a primary amine of gentamicin or the secondary amine of ciprofloxacin (Figure 147). Gentamicin C1a was selected for this work, and offers multiple amino groups suitable for CNCbl-linker conjugation by peptide coupling. The CNCbl-linker compounds **1** and **2** (Chapter 2), which incorporate a linker with a terminal amine, were also coupled to the carboxylic acid of ciprofloxacin.

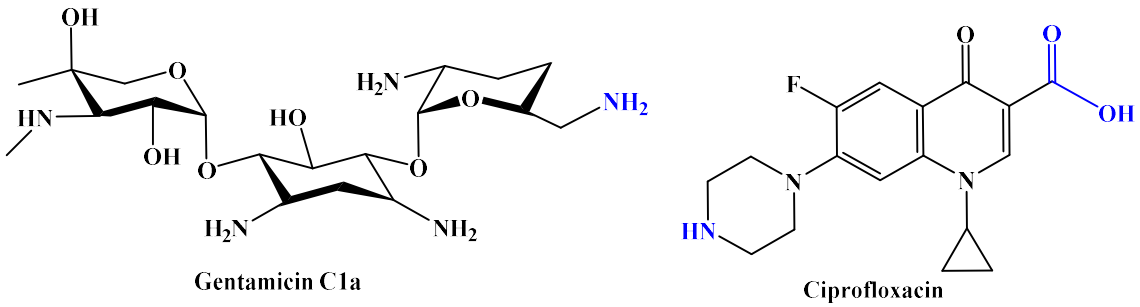

Figure 148: Structures of commercially available gentamicin C1a and ciprofloxacin. Functional groups utilised for conjugation to CNCbl are highlighted in blue.

5.2 Experimental

Chemicals

Ciprofloxacin, di-*tert*-butyl decarbonate, propargyl bromide, 3-[2-[2-(2-aminoethoxy)ethoxy]ethoxy]propanoic acid, 2-(1H-benzotriazole-1-yl)-1,1,3,3-tetramethyluronium hexafluorophosphate and 3-[(2-aminoethyl)dithio]propionic acid HCl were purchased from AK Scientific. Gentamicin C1a was purchased from BioSynth. All other chemicals were purchased from Merck or AK Scientific. Solvents were purchased from ECP, ThermoFisher or Scharlau. Anhydrous solvents were stored under N_2 in a glove box. Ultra-pure water was obtained from a Purite Purewater 200 system. NMR solvents (MeOH-d_4, DMSO-d_6 and D_2O) were purchased from Eurisotop and stored at 4 °C. Reversed-phase silica (LiChroprep RP-18 40-63 µm) was purchased from Merck.

Instrumentation

Refer to Section 2.2.2 for instrumentation details.

General methods

Refer to Section 2.2.2 for general methods.

LC-MS experiments

Four LC-MS methods were developed for the analysis of CNCbl-linker and CNCbl-linker-antibiotic conjugates. The mobiles phase consisted of milliQ water +0.1 % formic acid (A), milliQ water (B) and CH_3CN + 0.1% formic acid (C). The mobile phase programs are below.

Method 1: 0-5 min isocratic elution 95:5 A:C, 2-25 min from 95:5 to 65:35 A:C, 25-35 min from 65:35 to 10:90 A:C, 35-43 min isocratic elution at 10:90 A:C.

Method 2: 0.-2 min isocratic elution of 95:5 A:C, 2-30 min from 95:5 to 80:20 A:C, 30-35 isocratic elution of 80:20 A:C, 35-36 min from 80:20 to 10:90 A:C, 36-44 isocratic elution of 10:90 A:C.

Method 3: 0.-2 min isocratic elution of 95:5 A:C, 2-30 min from 95:5 to 70:30 A:C, 30-35 isocratic elution of 70:30 A:C, 35-36 min from 70:30 to 10:90 A:C, 36-44 isocratic elution of 10:90 A:C.

Method 4: 0-2 min isocratic elution 95:5 B:C, 2-20 min from 95:5 to 65:35 B:C, 20-25 min isocratic elution of 65:35 B:C, 25-26 min from 65:35 to 10:90 B:C, 26-32 isocratic elution of 10:90 B:C.

5.2.1 Synthetic methods

Boc-ciprofloxacin (C1)

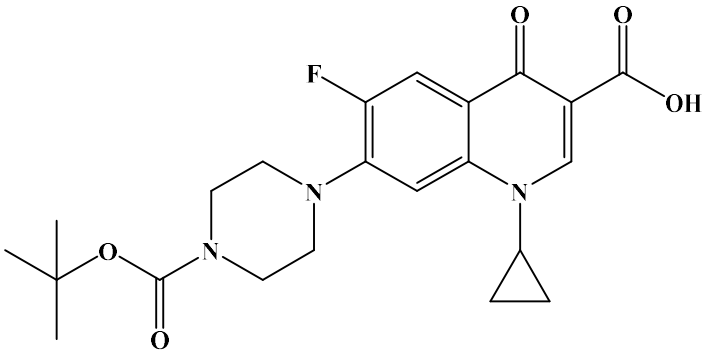

*Figure 149: Structure of Boc-ciprofloxacin (**C1**).*

Compound **C1** was synthesised following a literature procedure.[12] Ciprofloxacin (500 mg) and di-*tert*-butyl decarbonate (Boc_2O, 433 mg, 1.1 eq.) were dissolved in a 1:1 solution of H_2O and dioxane (8 mL). Aqueous NaOH (1 M, 2.25 mL) was added dropwise with stirring. The reaction was followed by TLC (15:1 CH_2Cl_2:CH_3OH) and stained with phosphomolybdic acid. The reaction reached completion in 1 h. Three-quarters of the solvent was removed by rotary evaporation. The remaining aqueous layer was acidified (pH 4-5) with saturated succinic acid solution. The product was then extracted by CH_2Cl_2 (3 x 100 mL). The organic layer was dried over Na_2SO_4, filtered, and taken to dryness. A white solid was obtained in a 94% yield with ≥95% purity (^{1}H NMR spectroscopy). ^{1}H NMR (400 MHz, $CDCl_3$) 8.79 (s, 1H), 8.06 (m, 1H), 7.37 (m, 1H), 3.67 (t, J = 5.1 Hz, 4H), 3.53 (tt, J = 7.2, 3.9 Hz, 1H), 3.32 – 3.25 (m, 4H), 1.49 (s, 9H), 1.45 – 1.32 (m, 2H), 1.25 – 1.16 (m, 2H) ppm.

Boc-Ciprofloxacin-propargyl ester (C2)

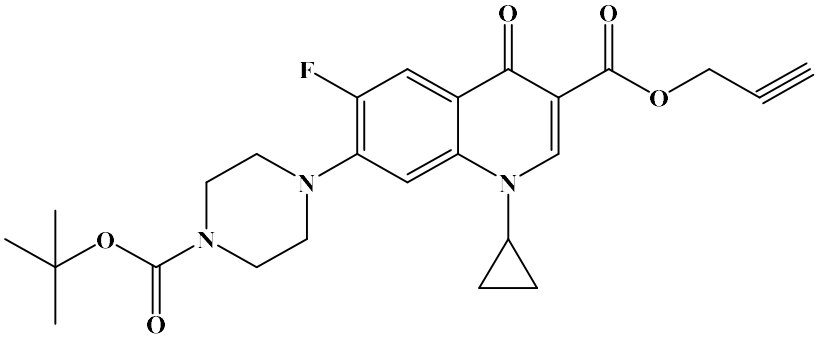

*Figure 150: Structure of Boc-ciprofloxacin-propargyl ester (**C2**).*

Compound **C2** was produced following a literature procedure.[13] Compound **C1** (400 mg, 1 eq.) was dissolved in anhydrous DMF (10 mL), followed by the addition of $NaHCO_3$ (1.2 eq.) suspended in anhydrous DMF (10 mL) with stirring. Propargyl bromide (1.2 eq.) was added dropwise to the reaction mixture with stirring and the reaction mixture heated to 100°C for 3 days. The reaction was followed by TLC (9:1 CH_2Cl_2:CH_3OH with 1% NH_4OH). The solution was dried by rotary evaporation and columned by flash chromatography in CH_2Cl_2:CH_3OH 9:1 with 1% NH_4OH. The fractions containing the desired product were identified by TLC. The ^1H NMR spectrum in $CDCl_3$ was used to determine the purity of the product. A light brown solid was obtained in a 30.2% yield with ≥95% purity. ^1H NMR (400 MHz, $CDCl_3$) δ 8.57 (s, 1H), 8.08 (m, 1H), 7.28 (m, 1H), 4.92 (d, *J* = 2.4 Hz, 2H), 3.65 (dd, *J* = 6.3, 3.5 Hz, 4H), 3.42 (d, *J* = 2.4 Hz, 1H), 3.22 (m, 4H), 2.48 (t, *J* = 2.4 Hz, 1H), 1.50 (s, 9H), 1.34 (d, *J* = 6.5 Hz, 2H), 1.14 (dd, *J* = 9.3, 7.3 Hz, 2H) ppm.

Ciprofloxacin-propargyl ester (C3)

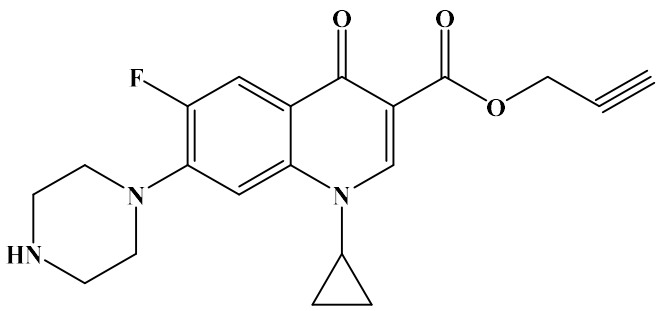

*Figure 151: Structure of ciprofloxacin-propargyl ester (**C3**).*

Deprotection was achieved following a literature procedure.[12] Compound **C2** (130 mg) was dissolved in TFA:CH_2Cl_2 (1:4, 5.0 mL) and stirred overnight at room temperature. The solution was diluted with CH_2Cl_2 (20 mL) and neutralised with saturated $NaHCO_3$. The organic layer was separated, dried over Na_2SO_4 and taken to dryness. A white solid was obtained in a 98% yield with ≥99% purity. ^{1}H NMR (400 MHz, $CDCl_3$) δ 8.57 (s, 1H), 8.06 (m, 1H), 7.28 (m, 1H), 4.92 (d, *J* = 2.4 Hz, 2H), 3.43 (dt, *J* = 7.1, 3.4 Hz, 1H), 3.24 (dd, *J* = 6.3, 3.5 Hz, 4H), 3.17 – 3.05 (m, 4H), 2.48 (t, *J* = 2.4 Hz, 1H), 1.33 (d, *J* = 6.5 Hz, 2H), 1.15 (dd, *J* = 9.3, 7.3 Hz, 2H) ppm.

CNCbl-(3-[2-[2-(2-aminoethoxy)ethoxy]ethoxy]propanoic acid) (CNCbl-PEG-$_{COOH}$, 17)

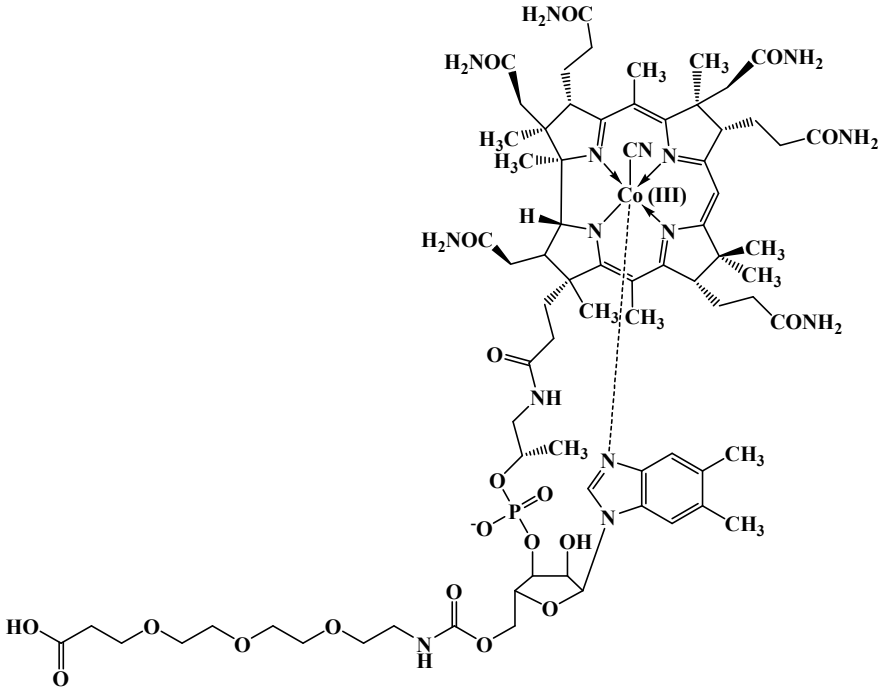

*Figure 152: Structure of **17**.*

CNCbl (101.2 mg, 73.8 µmol) and 1'1-carbonylditriazole (CDT, 39.2 mg, 221 µmol) were dissolved in anhydrous DMSO (2.0 mL) and stirred for 30 min at 40°C. 3-[2-[2-(2-Aminoethoxy)ethoxy]ethoxy]propanoic acid (48.1 mg, 221 µmol) was dissolved in minimal anhydrous DMSO (1.0 mL) and added to the CNCbl solution. The reaction was stirred for 6 h at 40°C. The crude product was precipitated by dropwise addition to Et_2O and CH_2Cl_2 (1:1, 200 mL). The precipitate was washed with Et_2O (2 x 10 mL), released from the filter with CH_3OH and taken to dryness by rotary evaporation. Purification was achieved by reversed-phase C18 chromatography. The product eluted as a red band at 17.5 % CH_3CN in H_2O. A red powder (84.4 mg) was obtained in a 70.5% yield. A purity of ≥95% was established by LC-MS and ^{1}H NMR spectroscopy.

^{1}H NMR (400 MHz, MeOD) δ = 7.78 (s, 1H), 7.25 (s, 1H), 7.15 (s, 1H), 6.57 (s, 1H), 6.25 – 6.20 (m, 1H), 6.03 (s, 1H), 4.55 – 4.49 (m, 1H), 4.26 – 4.10 (m, 4H), 3.76 – 3.71 (m, 1H), 3.71 – 3.64 (m, 2H), 3.64 – 3.63 (m, 1H), 3.63 – 3.60 (m, 8H), 3.60 – 3.49 (m, 5H), 3.31 – 3.25 (m, 4H), 2.96 – 2.82 (m, 3H), 2.70 – 2.63 (m, 3H), 2.63 – 2.56 (m, 10H), 2.56 – 2.54 (m, 2H), 2.54 – 2.50 (m, 3H), 2.49 – 2.42 (m, 3H), 2.37 (s, 2H), 2.31 – 2.26 (m, 7H), 2.23 – 2.15 (m, 1H), 2.10 – 1.97 (m, 5H), 1.91 – 1.86 (m, 4H), 1.86 – 1.80 (m,

2H), 1.78 – 1.68 (m, 2H), 1.47 (s, 3H), 1.40 – 1.35 (m, 7H), 1.32 – 1.22 (m, 5H), 1.19 (s, 4H), 1.15 – 1.08 (m, 1H), 0.47 (s, 3H) ppm.

^{13}C NMR (101 MHz, DMSO) δ 179.58, 178.29, 175.17, 173.96, 173.68, 173.34, 172.88, 172.62, 171.20, 171.11, 165.39, 164.70, 156.21, 142.26, 136.29, 132.72, 131.33, 129.75, 116.44, 111.38, 105.90, 103.09, 93.62, 86.01, 84.41, 79.38, 74.80, 72.75, 70.65, 69.85, 69.67, 69.64, 69.25, 68.88, 66.84, 63.04, 62.83, 58.65, 54.99, 54.05, 53.14, 50.38, 47.42, 46.60, 44.49, 42.13, 41.77, 40.43, 40.20, 40.15, 39.99, 39.94, 39.78, 39.73, 39.52, 39.31, 39.10, 38.89, 38.12, 35.69, 35.17, 34.00, 31.70, 31.61, 31.11, 29.93, 27.17, 25.79, 25.60, 20.02, 19.96, 19.92, 19.88, 18.76, 16.53, 16.42, 15.68, 15.10 ppm.

CNCbl-(3-[2-[2-(2-aminoethoxy)ethoxy]ethoxy]propanoic acid)-*N*-ciprofloxacin (CNCbl-PEG-*N*-cip, 18)

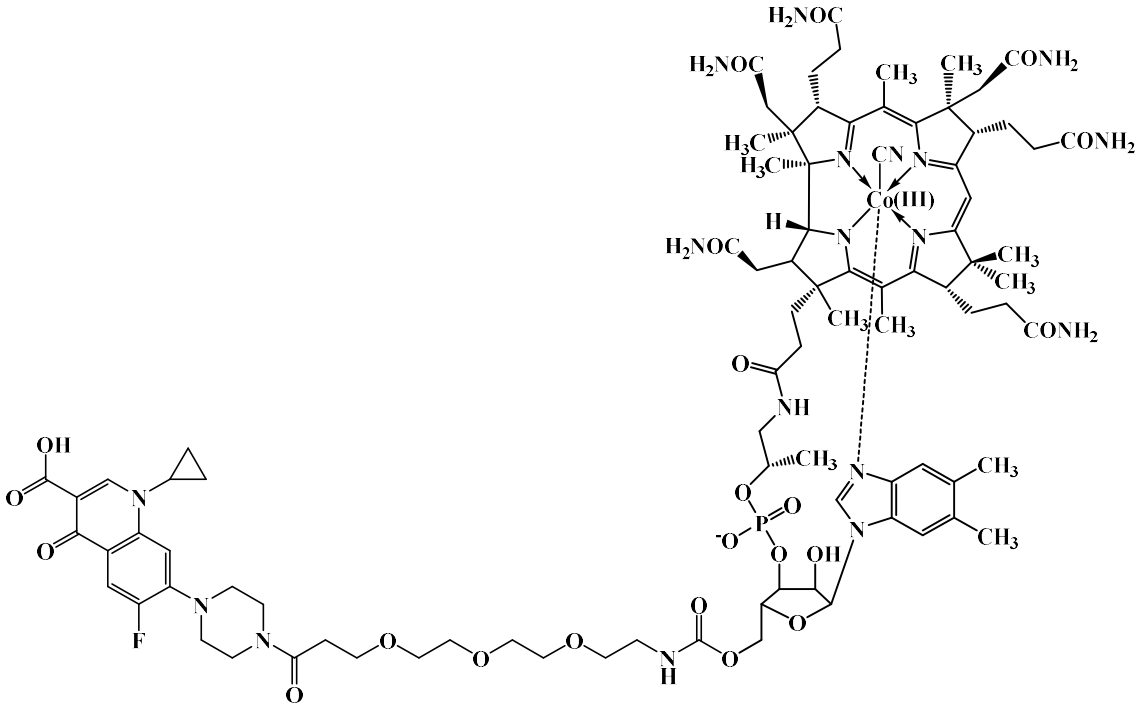

*Figure 153: Structure of **18.***

Compound **17** (30.3 mg, 18.7 µmol), ciprofloxacin (9.31 mg, 28.1 µmol), *N*-ethyl-*N'*-(3-dimethylaminopropyl)carbodiimide (EDC, 7.22 mg, 37.5 µmol), 1-hydroxybenzotrizole (HOBt, 15.2 mg, 112.4 µmol) and Et_3N (10.4 µL, 74.9 µmol) were dissolved in anhydrous DMSO (3.0 mL) and stirred at 40°C for 16 h. The crude product was precipitated by dropwise addition to Et_2O and CH_2Cl_2 (1:1, 50 mL). The precipitate was washed with Et_2O (2 x 10 mL), released from the filter with CH_3OH and taken to dryness by rotary evaporation. Purification was achieved by reversed-phase C18 chromatography. The product eluted as a red band at 45% CH_3CN in H_2O. A red powder (25.1 mg) was obtained in a 78.0% yield. A purity of ≥95% was established by LC-MS and ^{1}H NMR spectroscopy. HRMS ESI *m/z* $[M+2Na]^{2+}$ calculated for $C_{90}H_{121}CoN_{18}O_{22}PNa_2$ 980.3870, found 980.3865.

^{1}H NMR (400 MHz, MeOD) δ = 8.68 (s, 1H), 7.96 (d, *J*=13.4, 1H), 7.54 (d, *J*=7.3, 1H), 7.24 (s, 1H), 7.15 (s, 1H), 6.58 (s, 1H), 6.22 (d, *J*=3.0, 1H), 6.03 (s, 1H), 4.24 – 4.10 (m, 3H), 3.87 – 3.75 (m, 8H), 3.69 – 3.54 (m, 11H), 3.54 – 3.47 (m, 2H), 3.41 – 3.37 (m, 2H), 3.36 – 3.31 (m, 10H), 3.29 – 3.25 (m, 2H), 2.94 – 2.84 (m, 2H), 2.77 – 2.69 (m, 2H), 2.69

– 2.53 (m, 11H), 2.53 – 2.44 (m, 3H), 2.44 – 2.38 (m, 2H), 2.38 – 2.31 (m, 1H), 2.31 – 2.25 (m, 6H), 2.24 – 2.15 (m, 2H), 2.13 – 1.98 (m, 5H), 1.89 (s, 4H), 1.87 – 1.80 (m, 1H), 1.77 – 1.67 (m, 1H), 1.63 – 1.59 (m, 1H), 1.46 (s, 3H), 1.42 – 1.14 (m, 24H), 0.94 – 0.85 (m, 1H), 0.47 (s, 2H) ppm.

CNCbl-(1,11-diamine-3,6,9-trioxaundecane)-*O*-ciprofloxacin, (CNCbl-PEG-*O*-cip, 19)

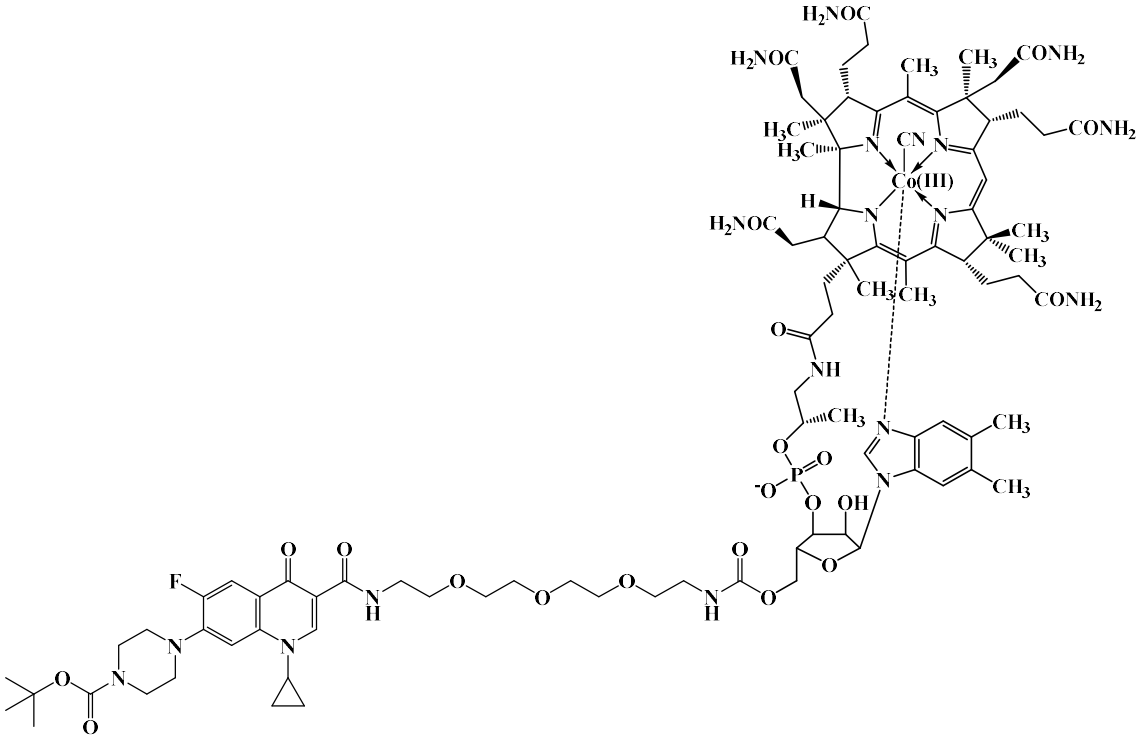

*Figure 154: Structure of **19**.*

Compound **2** (29.2 mg, 20.4 µmol), 2-(1H-benzotriazole-1-yl)-1,1,3,3-tetramethyluronium hexafluorophosphate (HBTU, 11.6 mg, 30.5 µmol), **C1** (13.2 mg, 30.5 µmol) and Et_3N (11.3 µL, 4 eq.) were dissolved in anhydrous DMSO (1.5 mL) and stirred at 40°C for 16 h. The crude product was precipitated by dropwise addition to Et_2O and CH_2Cl_2 (1:1, 80 mL). The precipitate was washed with Et_2O (2 x 10 mL), released from the filter with CH_3OH and taken to dryness by rotary evaporation. Purification was achieved by reversed-phase C18 chromatography. The product eluted as a red band at 45% CH_3CN in H_2O. A red powder (10.2 mg) was obtained in a 27.8% yield. A purity of ≥95% was established by LC-MS and ^{1}H NMR spectroscopy. HRMS ESI *m/z* $[M+2Na]^{2+}$ calculated for $C_{94}H_{130}CoN_{19}O_{22}PNa_2$ 1015.9238, found 1015.9246.

^{1}H NMR (400 MHz, MeOD) δ = 8.80 (s, 1H), 7.95 (d, *J*=13.4, 1H), 7.56 (d, *J*=7.3, 1H), 7.24 (s, 1H), 7.16 (s, 1H), 6.58 (s, 1H), 6.25 – 6.20 (m, 1H), 6.02 (s, 1H), 4.24 – 4.19 (m, 1H), 4.18 – 4.10 (m, 1H), 3.74 – 3.55 (m, 17H), 3.55 – 3.47 (m, 2H), 3.36 – 3.29 (m, 17H), 3.29 – 3.24 (m, 1H), 2.92 – 2.87 (m, 1H), 2.69 – 2.63 (m, 1H), 2.63 – 2.60 (m, 2H), 2.60 – 2.43 (m, 10H), 2.43 – 2.29 (m, 4H), 2.29 – 2.24 (m, 4H), 2.24 – 2.15 (m, 1H), 2.12

– 1.98 (m, 4H), 1.92 – 1.86 (m, 3H), 1.78 – 1.66 (m, 2H), 1.49 (s, 8H), 1.45 (s, 2H), 1.44 – 1.35 (m, 8H), 1.35 – 1.32 (m, 2H), 1.32 – 1.21 (m, 8H), 1.20 – 1.14 (m, 4H), 0.95 – 0.85 (m, 2H), 0.47 (s, 2H) ppm.

CNCbl-(2-(2-aminoethyldisulfanyl)ethanamine)-*O*-ciprofloxacin, (CNCbl-cys-*O*-cip, 20)

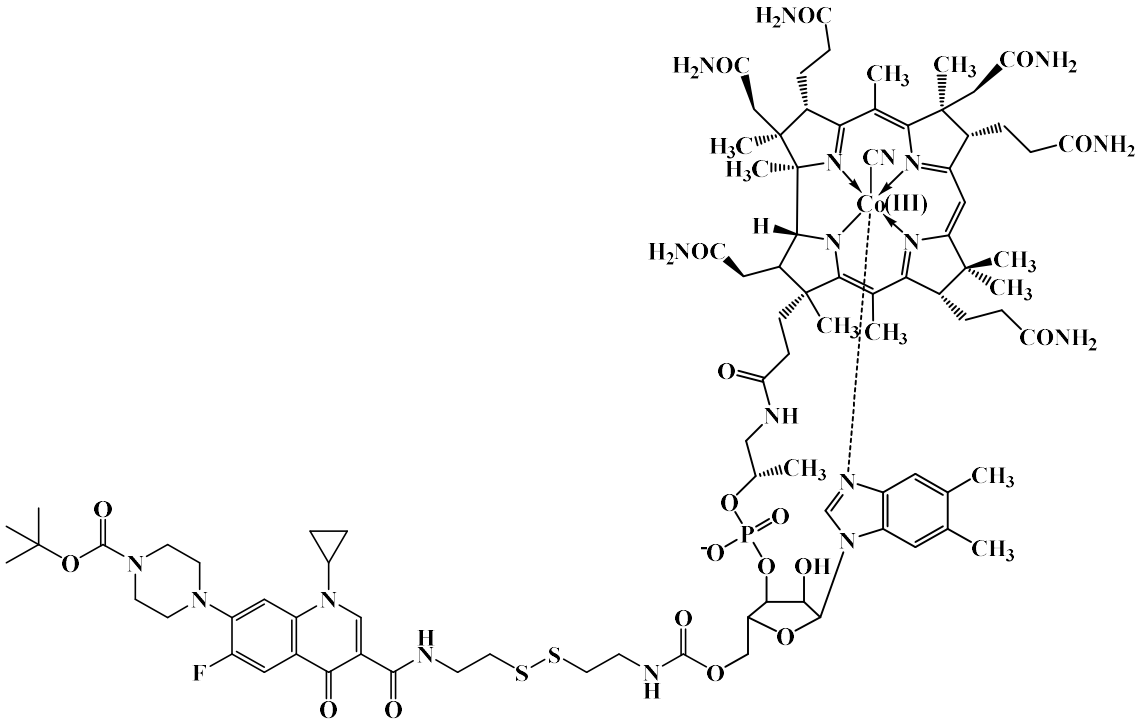

*Figure 155: Structure of **20**.*

Compound **1** (43.4 mg, 33.7 µmol), HBTU (19.2 mg, 50.5 µmol), **C1** (20.5 mg, 50.5 µmol) and Et_3N (18.8 µL, 4 eq.) were dissolved in anhydrous DMSO (2.5 mL) and stirred at 40°C for 16 h. The crude product was precipitated by dropwise addition to Et_2O and CH_2Cl_2 (1:1, 150 mL). The precipitate was washed with Et_2O (2 x 10 mL), released from the filter with CH_3OH and taken to dryness by rotary evaporation. Purification was achieved by reversed-phase C18 chromatography. The product eluted as a red band at 45% CH_3CN in H_2O. A red powder (18.3 mg) was obtained in a 33.2% yield. A purity of ≥95% was established by LC-MS and ^{1}H NMR spectroscopy. HRMS ESI *m/z* $[M+2Na]^{2+}$ calculated for $C_{90}H_{122}CoN_{19}O_{19}PS_2Na_2$ 995.8722, found 995.8717.

^{1}H NMR (400 MHz, MeOD) δ = 8.79 (s, 1H), 7.94 (d, *J*=13.4, 1H), 7.55 (d, *J*=7.3, 1H), 7.23 (s, 1H), 7.15 (s, 1H), 6.58 (s, 1H), 6.26 – 6.18 (m, 1H), 6.03 (s, 1H), 4.22 (s, 1H), 4.18 – 4.10 (m, 1H), 3.77 – 3.73 (m, 1H), 3.73 – 3.55 (m, 7H), 3.49 – 3.41 (m, 2H), 3.36 – 3.27 (m, 9H), 2.97 – 2.84 (m, 5H), 2.67 – 2.56 (m, 9H), 2.56 – 2.51 (m, 2H), 2.51 – 2.41 (m, 3H), 2.41 – 2.31 (m, 2H), 2.31 – 2.24 (m, 5H), 2.13 – 2.05 (m, 2H), 1.89 (s, 3H),

1.79 – 1.66 (m, 1H), 1.50 (s, 7H), 1.45 (s, 3H), 1.43 – 1.30 (m, 9H), 1.30 – 1.19 (m, 5H), 1.19 – 1.10 (m, 5H), 0.47 (s, 2H) ppm.

CNCbl-(1,11-diamine-3,6,9-trioxaundecane)-gentamicin (CNCbl-PEG-gent, 21)

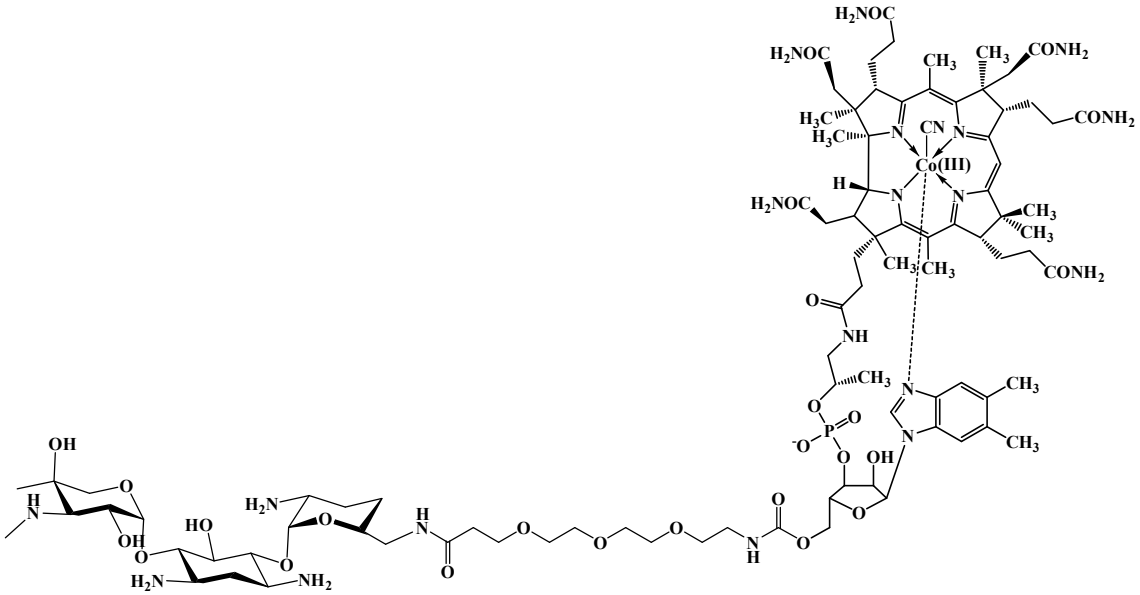

*Figure 156: Structure of **21**.*

Compound **17** (78.8 mg, 49.2 µmol), EDC (24.8 mg, 123 µmol), HOBt (26.5, 197 µmol), gentamicin C1a (33.8 mg, 73.7 µmol) and Et_3N (34.3 µL, 5 mol eq.) were dissolved in anhydrous DMSO (2.0 mL) and stirred at 40°C for 24 h. The precipitate was washed with Et_2O (2 x 10 mL), released from the filter with CH_3OH and taken to dryness by rotary evaporation. Purification was achieved by reversed-phase C18 chromatography. The product eluted as a red band at 22.5 % CH_3CN in (H_2O +0.1% formic acid). A red powder (15.3 mg) of was obtained in a 15.2% yield. A purity of ≥95% was established by LC-MS and ^{1}H NMR spectroscopy. HRMS ESI *m/z* $[M+2Na]^{2+}$ calculated for $C_{92}H_{142}O_{26}N_{20}CoNa_2P$ 1039.4629, found 1039.4637.

^{1}H NMR (400 MHz, D_2O) δ = 8.00 (d, *J*=7.7, 1H), 7.88 (d, *J*=7.6, 1H), 7.64 – 7.54 (m, 2H), 7.45 (s, 1H), 7.29 (s, 1H), 6.70 (s, 1H), 6.49 (d, *J*=3.1, 1H), 6.24 (s, 1H), 5.66 – 5.48 (m, 1H), 5.39 – 5.26 (m, 1H), 4.55 – 4.47 (m, 1H), 4.44 – 4.34 (m, 2H), 4.34 – 4.19 (m, 3H), 3.98 – 3.90 (m, 2H), 3.86 – 3.74 (m, 10H), 3.70 – 3.58 (m, 4H), 3.57 – 3.39 (m, 6H), 3.25 – 3.15 (m, 2H), 3.04 (s, 2H), 3.00 – 2.82 (m, 4H), 2.82 – 2.79 (m, 1H), 2.79 – 2.71 (m, 9H), 2.71 – 2.65 (m, 2H), 2.62 – 2.59 (m, 1H), 2.59 – 2.53 (m, 1H), 2.45 (s, 5H), 2.44 – 2.26 (m, 4H), 2.26 – 2.19 (m, 2H), 2.19 – 2.09 (m, 4H), 2.05 (s, 3H), 2.04 – 2.01 (m, 1H), 2.01 – 1.97 (m, 1H), 1.64 – 1.55 (m, 8H), 1.51 (s, 3H), 1.47 – 1.41 (m, 3H), 1.38 (s, 3H), 1.34 – 1.17 (m, 2H), 0.62 (s, 2H) ppm.

CNCbl-(3-(2-aminoethyldisulfanyl)propanoic acid) (CNCbl-cys$_{COOH}$, 22)

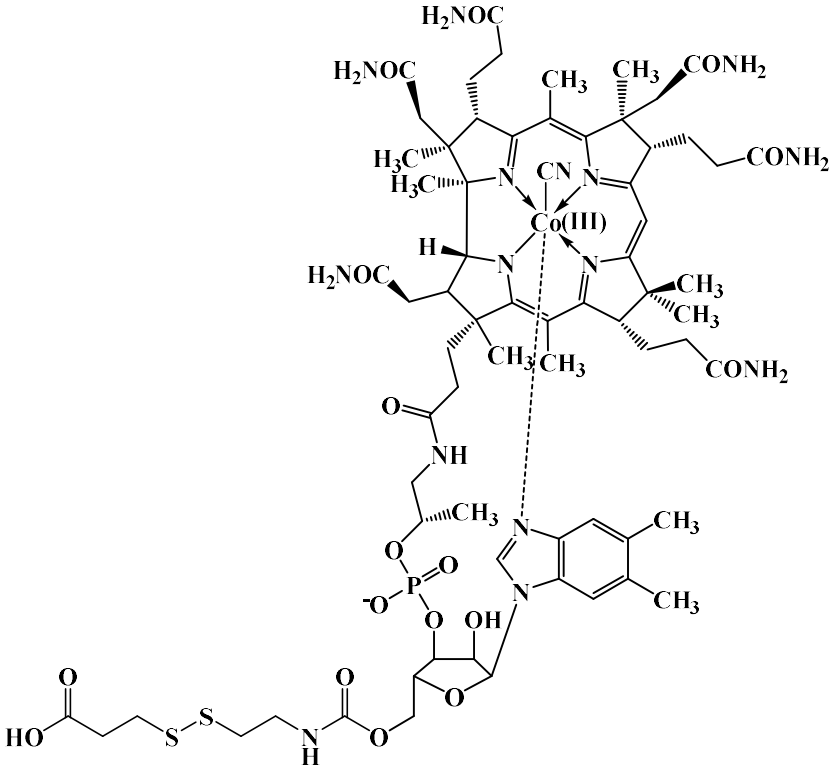

*Figure 157: Structure of **22**.*

CNCbl (103.1 mg, 73.8 µmol) and CDT (36.3, 221 µmol) were dissolved in anhydrous DMSO (2.0 mL) and stirred for 30 min at 40°C. 3-[(2-Aminoethyl)dithio]propionic acid HCl (48.2 mg, 221 µmol) was dissolved in minimal anhydrous DMSO (2.5 mL) and added to the CNCbl solution. The reaction was stirred for 6 h at 40°C. The crude product was precipitated by dropwise addition to Et_2O and CH_2Cl_2 (1:1, 200 mL). The precipitate was washed with Et_2O (2 x 10 mL), released from the filter with CH_3OH and taken to dryness by rotary evaporation. Purification was achieved by reversed-phase C18 chromatography. The product eluted as a red band at 15.0% CH_3CN in H_2O. A red powder (40.5 mg) was obtained in a 39.1% yield. A purity of ≥95% was established by LC-MS and ^{1}H NMR spectroscopy.

^{1}H NMR (400 MHz, MeOD) δ = 7.24 (s, 1H), 7.15 (s, 1H), 6.57 (s, 1H), 6.23 (d, *J*=2.9, 1H), 6.04 (s, 1H), 4.56 – 4.50 (m, 1H), 4.25 – 4.10 (m, 3H), 3.71 – 3.58 (m, 2H), 3.46 – 3.36 (m, 2H), 3.32 – 3.27 (m, 3H), 2.98 – 2.78 (m, 6H), 2.71 – 2.40 (m, 19H), 2.38 (s, 2H), 2.31 – 2.26 (m, 6H), 2.23 – 2.11 (m, 2H), 2.11 – 2.06 (m, 1H), 2.06 – 1.97 (m, 3H),

1.91 – 1.87 (m, 4H), 1.87 – 1.80 (m, 2H), 1.78 – 1.68 (m, 1H), 1.47 (s, 3H), 1.40 – 1.35 (m, 6H), 1.34 – 1.22 (m, 5H), 1.19 (s, 3H), 1.16 – 1.09 (m, 1H), 0.47 (s, 2H) ppm.

^{13}C NMR (101 MHz, DMSO) δ 179.58, 178.28, 175.19, 173.99, 173.68, 173.34, 172.89, 172.83, 172.59, 171.20, 171.12, 165.39, 164.73, 156.20, 142.25, 136.29, 132.74, 131.34, 129.73, 116.41, 111.44, 105.92, 103.07, 93.62, 86.01, 84.42, 79.42, 74.82, 72.74, 70.68, 68.87, 63.18, 58.66, 54.99, 54.06, 53.13, 50.39, 48.65, 47.40, 46.82, 46.60, 44.51, 42.14, 41.84, 40.43, 40.20, 40.15, 39.94, 39.73, 39.52, 39.31, 39.10, 38.89, 38.08, 35.16, 34.09, 33.88, 33.23, 31.69, 31.13, 30.75, 29.94, 27.20, 25.79, 25.61, 19.96, 18.76, 16.55, 16.44, 15.68, 15.12 ppm.

CNCbl-(2-(2-aminoethyldisulfanyl)ethanamine)-gentamicin (CNCbl-cys-gent, 23)

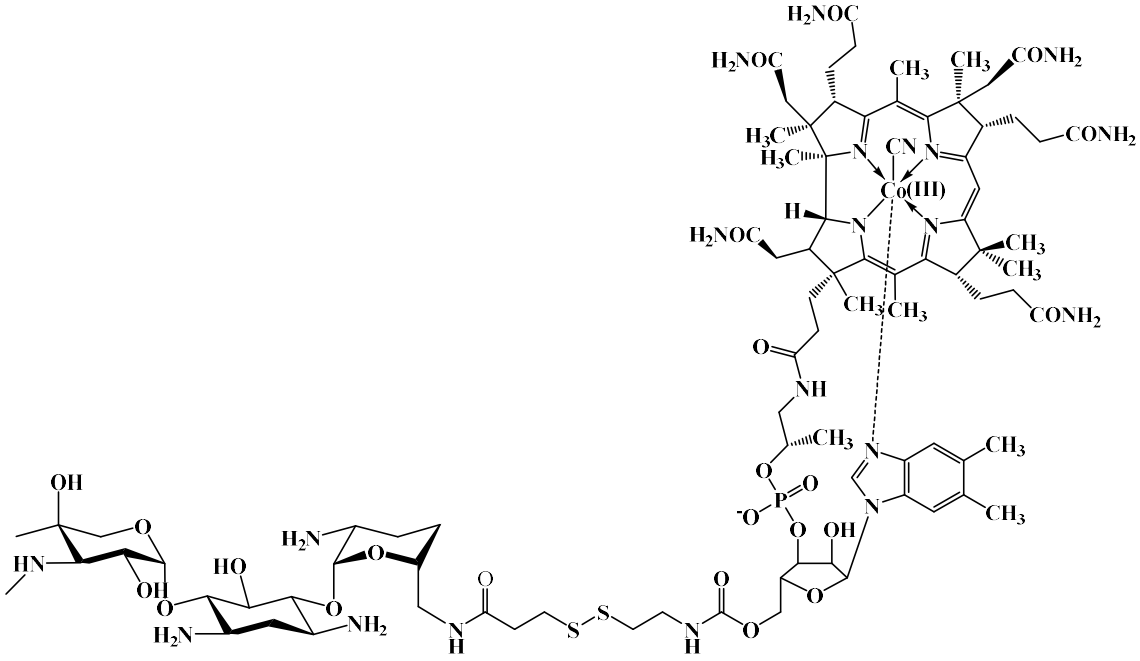

*Figure 158: Structure of **23**.*

Compound **22** (59.8 mg, 38.3 µmol), EDC (18.3 mg, 95.7 µmol), HOBt (22.8 mg, 153 µmol), gentamicin C1a (26.9 mg, 57.4 µmol) and Et_3N (26.7 µL, 5 mol eq.) were dissolved in anhydrous DMSO and stirred at 40°C for 24 h. The crude product was precipitated by dropwise addition to Et_2O and CH_2Cl_2 (1:1, 100 mL). The precipitate was washed with Et_2O (2 x 10 mL), released from the filter with CH_3OH and taken to dryness by rotary evaporation. Purification was achieved by reversed-phase C18 chromatography. The product eluted as a red band at 22.5% CH_3CN in (H_2O + 0.1% formic acid). A red powder (7.21 mg) was obtained in a 9.4% yield. A purity of ≥95% was established by LC-MS and ^{1}H NMR spectroscopy. HRMS ESI *m/z* $[M+2H]^{2+}$ calculated for $C_{88}H_{136}O_{23}N_{20}CoPS_2$ 997.4294, found 997.4290.

^{1}H NMR (400 MHz, D_2O) δ = 7.45 (s, 1H), 7.29 (s, 1H), 6.70 (s, 1H), 6.49 (d, *J*=3.1, 1H), 6.24 (s, 1H), 5.95 (d, *J*=3.6, 1H), 5.37 (d, *J*=3.9, 1H), 4.55 – 4.46 (m, 2H), 4.40 – 4.33 (m, 2H), 4.32 – 4.22 (m, 4H), 4.10 – 4.04 (m, 1H), 4.04 – 3.86 (m, 4H), 3.84 – 3.71 (m, 3H), 3.67 – 3.59 (m, 5H), 3.56 – 3.42 (m, 5H), 3.42 – 3.27 (m, 2H), 3.25 – 3.15 (m, 2H), 3.15 – 3.07 (m, 8H), 3.07 – 3.03 (m, 2H), 2.98 – 2.89 (m, 3H), 2.89 – 2.72 (m, 15H), 2.70 (s, 2H), 2.66 – 2.53 (m, 3H), 2.50 – 2.45 (m, 3H), 2.45 (s, 5H), 2.43 – 2.29 (m, 3H), 2.25 – 2.14 (m, 6H), 2.12 (s, 2H), 2.05 (s, 4H), 2.03 – 1.98 (m, 2H), 1.98 –

1.91 (m, 1H), 1.83 – 1.79 (m, 1H), 1.69 – 1.50 (m, 15H), 1.47 – 1.36 (m, 9H), 1.26 – 1.22 (m, 1H), 0.65 – 0.61 (m, 3H) ppm.

5.3 Results and Discussion

5.3.1 Synthesis and characterisation of CNCbl-ciprofloxacin conjugates 17-20

The first attempts to conjugate ciprofloxacin to CNCbl-linker (compound **2**) were carried out using the peptide coupling procedures established for the CNCbl-linker-fluorophore conjugates in Chapter 2. A ciprofloxacin-Zn nanoparticle has been published in the literature where EDC coupling was employed.[14] Compound **2** (20 mg) was dissolved in minimal anhydrous DMSO (2 mL) together with HOBt (4 eq.), EDC (2 eq.), Et_3N (4 eq.) and ciprofloxacin.HCl (limiting reagent) (Scheme 24). The reaction mixture was stirred at 40°C, which worked well for the earlier CNCbl reactions. Reaction progress was monitored by LC-MS over four days.

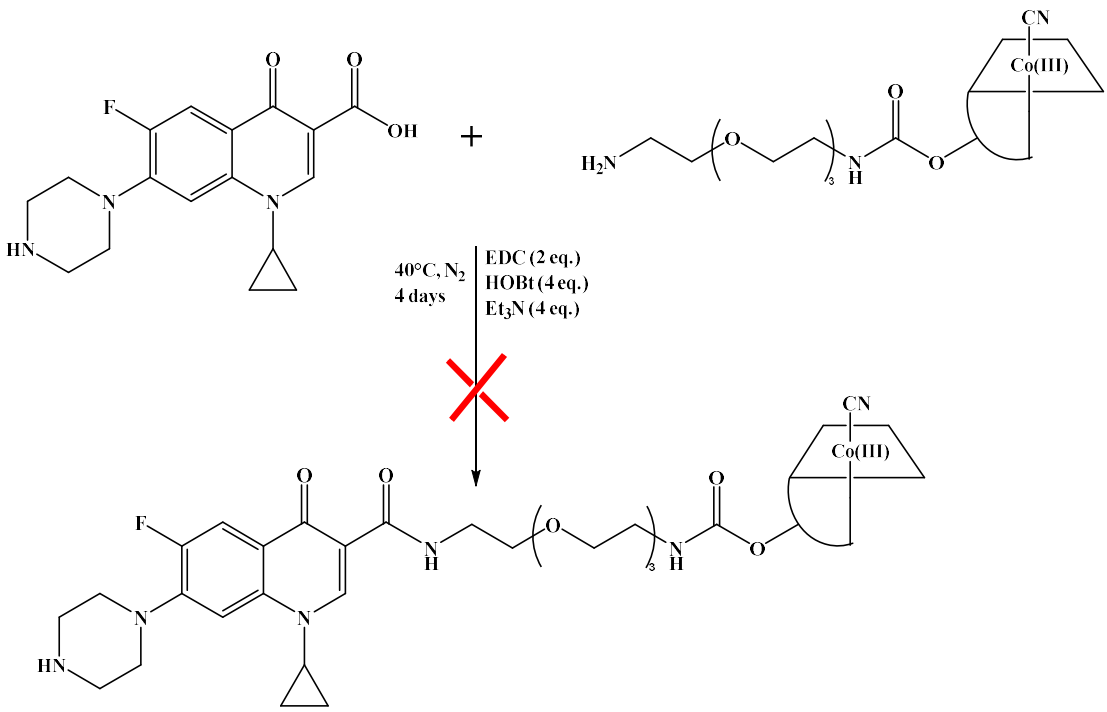

*Scheme 24: Attempted synthesis of the ciprofloxacin conjugate of **2**.*

Repeated LC-MS analysis of the reaction mixture over four days showed no evidence of the desired product being formed. Expected *m/z* values for the product $C_{90}H_{123}CoFN_{18}O_{20}P$, were $[M+H]^+$ = 1886.8, $[M+2H]^{2+}$ = 943.9 and $[M+3H]^{3+}$ = 629.6. However, LC-MS analysis showed one large peak eluting at 15.3 min, assigned to the unreacted starting material, **2** ($C_{72}H_{106}CoN_{16}O_{18}P$, calcd. *m/z* $[M+H]^+$ = 1573.7 and

$[M+2H]^{2+}$ = 787.4; found 1573.6 and 787.5, Figure 159). Several smaller peaks between 16-26 min were also observed in the LC-MS chromatograms (both the TIC and DAD (361 nm)), and are likely to correspond to CNCbl derivatives; however, none had the *m/z* values corresponding to the desired ciprofloxacin conjugate of CNCbl.

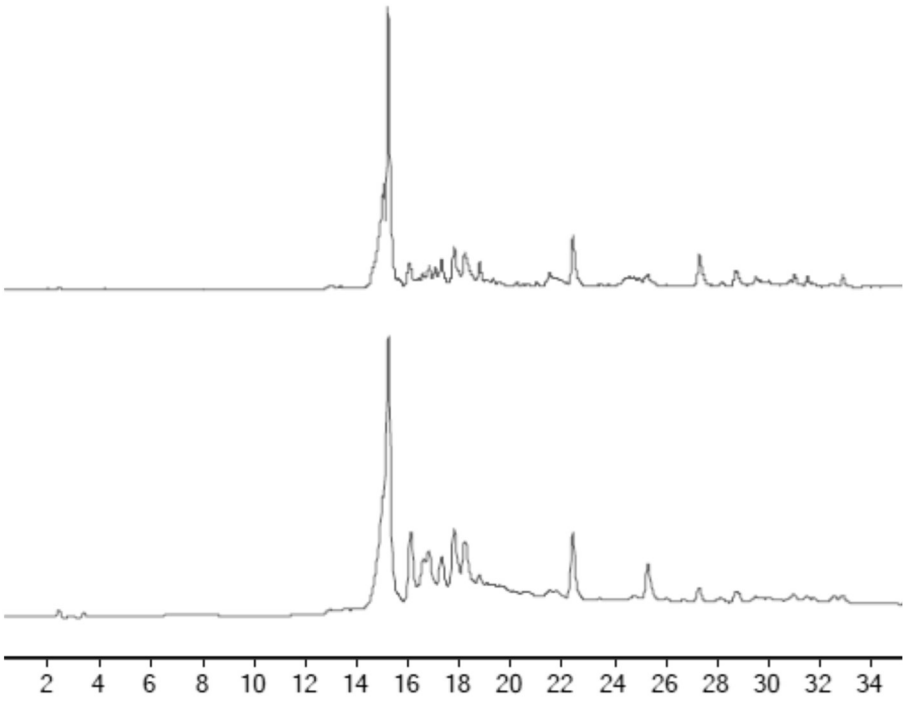

*Figure 159: LC-MS TIC (top) and DAD (361 nm, bottom) chromatograms of the initial attempted ciprofloxacin coupling to **2** using standard coupling procedures (Scheme 24, LC-MS method 1). The desired product could not be identified. The peak at 15.3 min can be assigned to the unreacted starting material, **2** ($C_{72}H_{106}CoN_{16}O_{18}P$, calcd. m/z $[M+H]^+$ = 1573.7 and $[M+2H]^{2+}$ = 787.4; found 1573.6 and 787.5).*

The same reaction conditions were attempted using the CNCbl-linker compound with a cystamine linker, compound **1**. Again, ciprofloxacin was used as the limiting reagent in addition to compound **1** (Scheme 25).

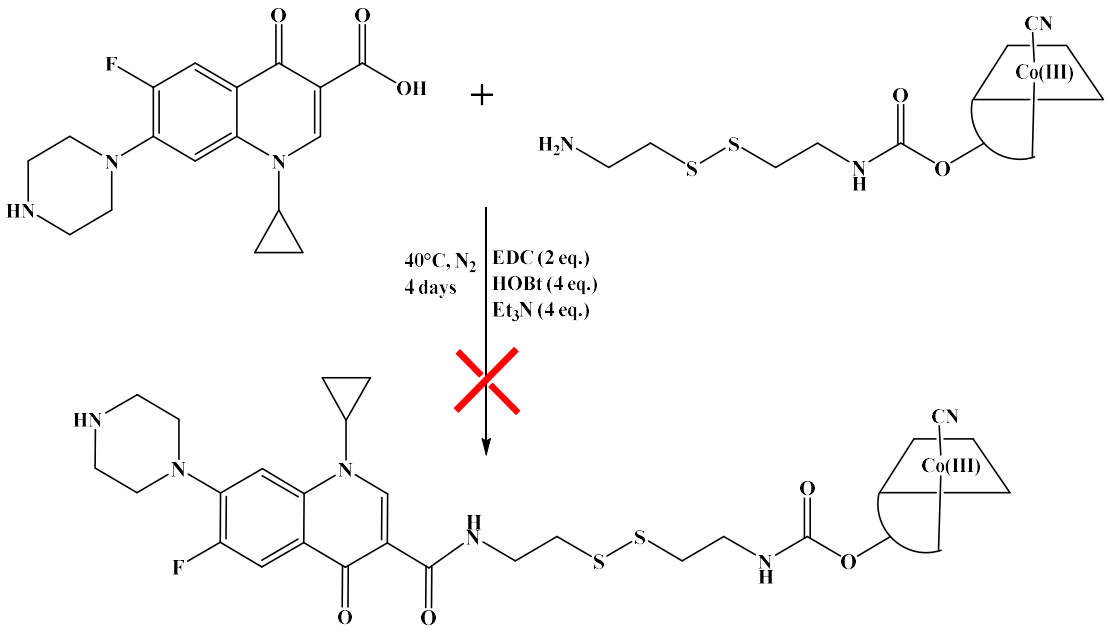

*Scheme 25: Attempted synthesis of a ciprofloxacin conjugate of **1**.*

The reaction progress was also followed by LC-MS over 4 days. The product was expected to have *m/z* values (calculated for $C_{86}H_{114}CoFN_{19}O_{19}PS$) of $[M+H]^+$ = 1859.7, $[M+2H]^{2+}$ = 930.4 and $[M+3H]^{3+}$ = 620.6. Many peaks were present in the LC-MS chromatogram, but none were found to represent the desired product (Figure 160). Furthermore, the starting material **1** had either degraded during the reaction or underwent undesired side reactions, as evidenced by the small peak corresponding to **1** at 15.8 min ($C_{68}H_{98}CoN_{16}O_{15}PS_2$, calcd. *m/z* $[M+H]^+$ = 1533.7 and $[M+2H]^{2+}$ = 767.3; found 1534.3 and 767.4).

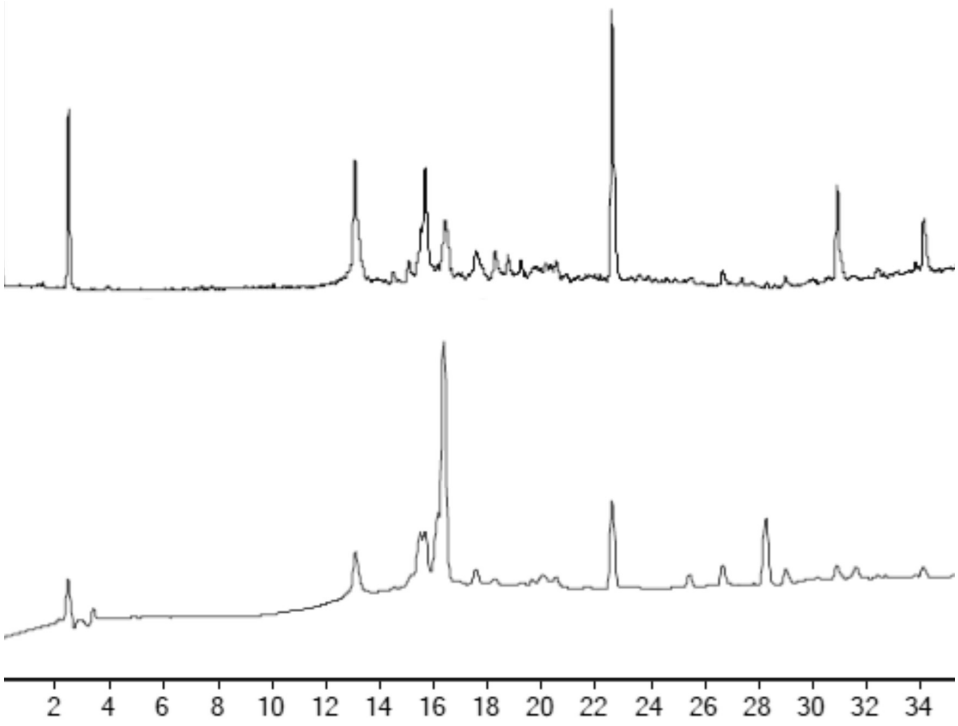

*Figure 160: LC-MS TIC (top) and DAD (361 nm, bottom) chromatograms of the attempted ciprofloxacin coupling to **1** using standard coupling procedures (Scheme 25, LC-MS method 1). The desired product could not be identified. A small peak from the starting material was observed at 15.8 min ($C_{68}H_{98}CoN_{16}O_{15}PS_2$, calcd. m/z $[M+H]^+$ = 1533.7 and $[M+2H]^{2+}$ = 767.3; found 1534.3 and 767.4).*

Both synthetic attempts proved to be unsuccessful. Modification of the reaction conditions was trialled using compound **2** as the CNCbl-linker starting material. The attempts focused on the variation of the mol equivalents and temperature, as summarised in Table 7. Each attempt was followed by LC-MS after 24 h and four days of stirring the reaction mixture. None of the desired product was identified in the reaction mixture for any attempt.

*Table 7: Summarised synthesis attempts to synthesise a ciprofloxacin conjugate of **2**. Each reaction mixture was analysed by LC-MS after 24 hr and 4 days of stirring. There was no evidence of the desired product for any of the syntheses.*

Attempt #	Mol. Equivalents of Reagents				
	2	EDC	HOBt	Ciprofloxacin	Temperature
1	1	4	8	1	40°C
2	1	4	8	3	40°C
3	1	4	8	1	r.t.
4	1	4	8	3	r.t

The same species in all synthesis attempts (using either **1** or **2** as the reactant) was observed by LC-MS at 22.5 min with the *m/z* value of 645.2. This species is unlikely to be a CNCbl-linker-ciprofloxacin conjugate as the *m/z* values of the product depend on the linker. It is therefore likely that this is a ciprofloxacin side product. The EDC-*N*-acyl urea adduct and HOBt intermediate of ciprofloxacin have different *m/z* values. In addition, a ciprofloxacin-ciprofloxacin (formed by carboxylate-piperazine amide bond formation) dimer also has different *m/z* values. Activation of the carboxylic acid of ciprofloxacin by EDC was therefore most likely unsuccessful.

To address this, the synthesis of the ciprofloxacin-NHS ester was attempted. Using NHS esters increased product yields compared to direct coupling of the corresponding carboxylic acid for the CNCbl-fluorophore conjugates. Boc protection of the piperazine NH moiety of ciprofloxacin was successfully carried out using a literature procedure to produce compound **C1** (Scheme 26).[12]

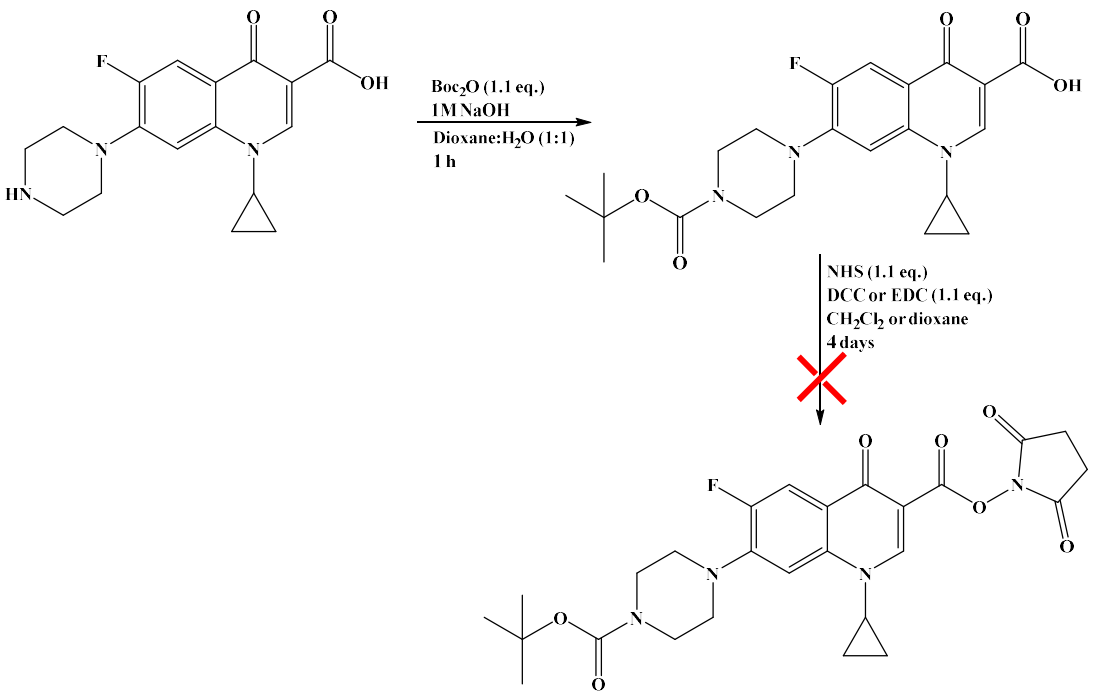

*Scheme 26: Synthesis of **C1** and the attempted synthesis of the Boc-ciprofloxacin-NHS ester. The reaction conditions trialled are summarised in Table 8.*

The ^{1}H NMR peaks of compound **C1** matched the literature values. The synthesis of the Boc-ciprofloxacin-NHS ester was then attempted following a literature procedure (Scheme 26).[11] Analysis of the crude product by TLC (15:1 CH_2Cl_2:CH_3OH), mass spectrometry and ^{1}H NMR spectroscopy showed the reaction was unsuccessful, with only unreacted **C1** found in the product mixture. Further attempts were made using EDC as the activating agent with the addition of Et_3N or by modifying reaction times and temperatures, as summarised in Table 8. The reaction products were analysed by TLC (15:1 CH_2Cl_2:CH_3OH) and mass spectrometry. No product could be detected in any of the attempts, and only unreacted starting material was present.

*Table 8: Synthetic attempts to produce the NHS ester of **C1**.*

	Mol. Equivalents of Reagents				
Attempt #	Boc-ciprofloxacin	Activating agent	Et_3N	Temperature	Reaction time
1	1	DCC, 1.1	0	4°C	48 h
2	1	DCC, 1.1	0	0°C	8 h

3	1	DCC, 1.1	0	r.t.	8 h
4	1	EDC, 1.1	2	4°C	48 h
5	1	EDC, 1.1	2	0°C	8 h
5	1	EDC, 1.1	2	r.t	8 h

Since this synthetic approach was unsuccessful, attempts were made to conjugate the 1,11-diamine-3,6,9-trioxaundecane linker to **C1**. If successful, the **C1**-linker molecule could be directly conjugated to CNCbl using the carbamate coupling procedures previously utilised for the other CNCbl conjugates. Reactions were trialled with **C1** using EDC as the initial coupling reagent (Scheme 27). The TLC of the product mixtures showed no new spots and mass spectrometry did not identify any new species being formed. Multiple conditions were tested and are summarised in Table 9. All trials were reacted for 48 h, followed by analysis by TLC and mass spectrometry. Trials **8-14** used *N,N′*-dicyclohexylmethanediimine (DCC) as the coupling reagent. This compound has the same mechanism of action as EDC with greater solubility in organic reagents and has previously successfully been used to activate the carboxylic acid of ciprofloxacin.[15] The desired product could not be detected for any of the conditions trialled. For the heated reaction mixtures (40°C and higher) a colour change in the solution from clear to yellow/brown was observed, with the deepest change in colour observed for the reflux reaction. Furthermore, the colour change coincided with multiple new peaks with high *m/z* values in the mass spectrum (>500 *m/z*). Reactions carried out lower than 40°C only showed peaks with *m/z* values corresponding to unreacted reagents. The observed colour change in the solution is likely due to the polymerisation of the polyethylene glycol linker.[16–18]

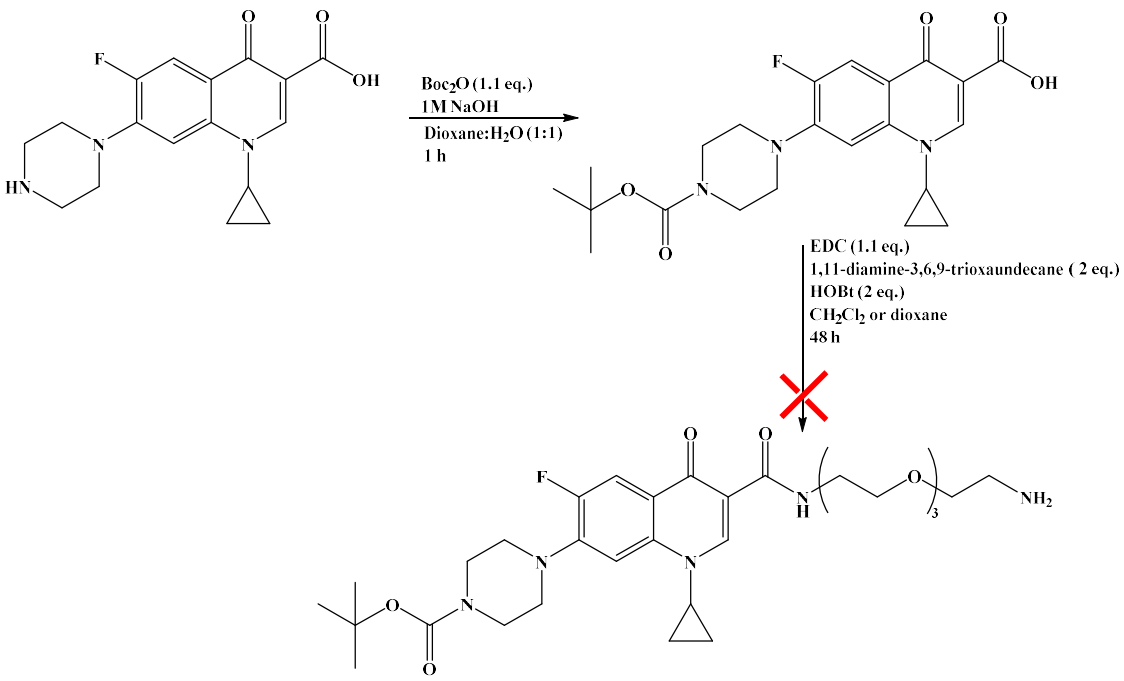

*Scheme 27: The attempted reaction of **C1** with 1,11-diamine-3,6,9-trioxaundecane. The reaction conditions are summarised in Table 9.*

*Table 9: Synthetic attempts to produce **C1**-1,11-diamine-3,6,9-trioxaundecane.*

	Mol. Equivalents of Reagents							
Attempt #	**C1**	DCC	EDC	Linker	Et_3N	HOBt	Solvent	Temperature
1	1	0	1.1	2	2	0	CH_2Cl_2	4°C
2	1	0	1.1	2	2	2	CH_2Cl_2	4°C
3	1	0	1.1	2	2	0	CH_2Cl_2	r.t.
4	1	0	1.1	2	2	2	CH_2Cl_2	r.t.
5	1	0	1.1	2	2	2	Dioxane	40°C
6	1	0	1.1	2	2	2	Dioxane	80°C
7	1	0	1.1	2	2	r.t	Dioxane	Reflux (~120°C)
8	1	1.1	0	2	2	0	CH_2Cl_2	4°C

9	1	1.1	0	2	2	2	CH_2Cl_2	4°C
10	1	1.1	0	2	2	0	CH_2Cl_2	r.t.
11	1	1.1	0	2	2	2	CH_2Cl_2	r.t.
12	1	1.1	0	2	2	2	Dioxane	40°C
13	1	1.1	0	2	2	2	Dioxane	80°C
14	1	1.1	0	2	2	r.t	Dioxane	Reflux (~120°C)

Amide bond formation at the carboxylic acid of ciprofloxacin unfortunately proved unsuccessful. Alkylation at the carboxylic acid to form a propargyl ester suitable for Cu-catalysed click chemistry was therefore explored. Alkylation of ciprofloxacin was achieved following a literature procedure (Scheme 28).[13] The ^{1}H NMR spectrum in $CDCl_3$ matched the spectrum in the literature.[13]

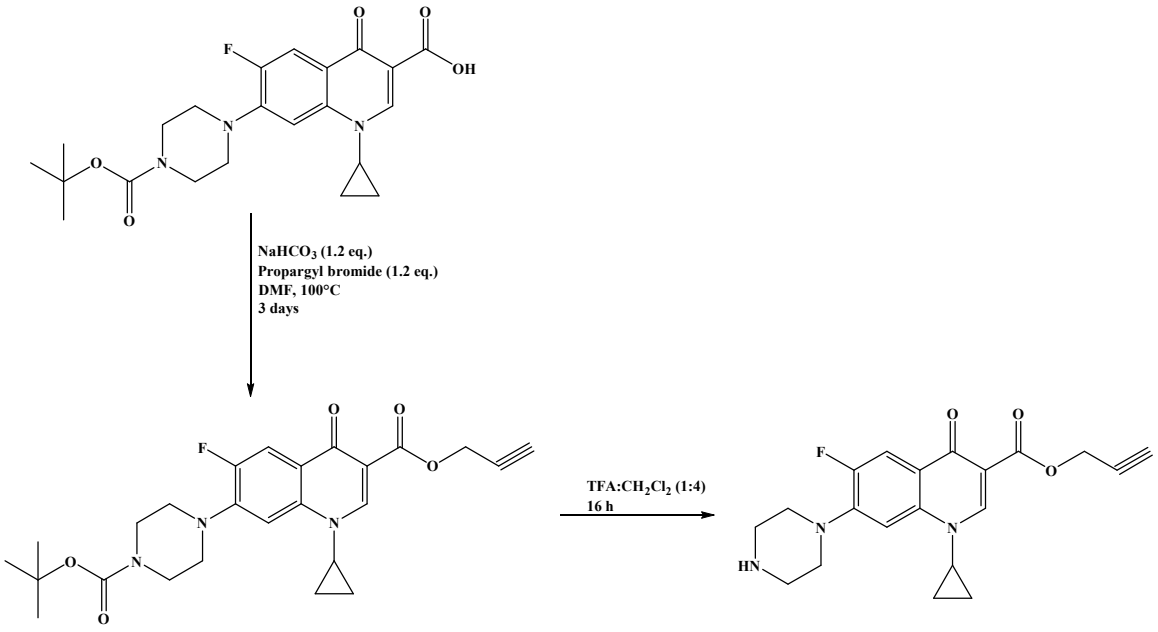

*Scheme 28: Synthesis of **C3**.*

Deprotection of the Boc group requires the addition of trifluoroacetic acid (TFA). Upon exposure to acid, including TFA, CNCbl can undergo acid hydrolysis of the amide side

chain of the nucleotide loop, producing cobyric acid (Figure 161).[19–22] This is not desired here as the selected coordination site of CNCbl is the 5'-OH group of the ribose ring on the nucleotide chain. The Boc-ciprofloxacin-propargyl ester was therefore deprotected before conjugation to CNCbl. Successful deprotection of Boc-ciprofloxacin-propargyl ester to produce compound **C3** was confirmed by ^{1}H NMR spectroscopy.

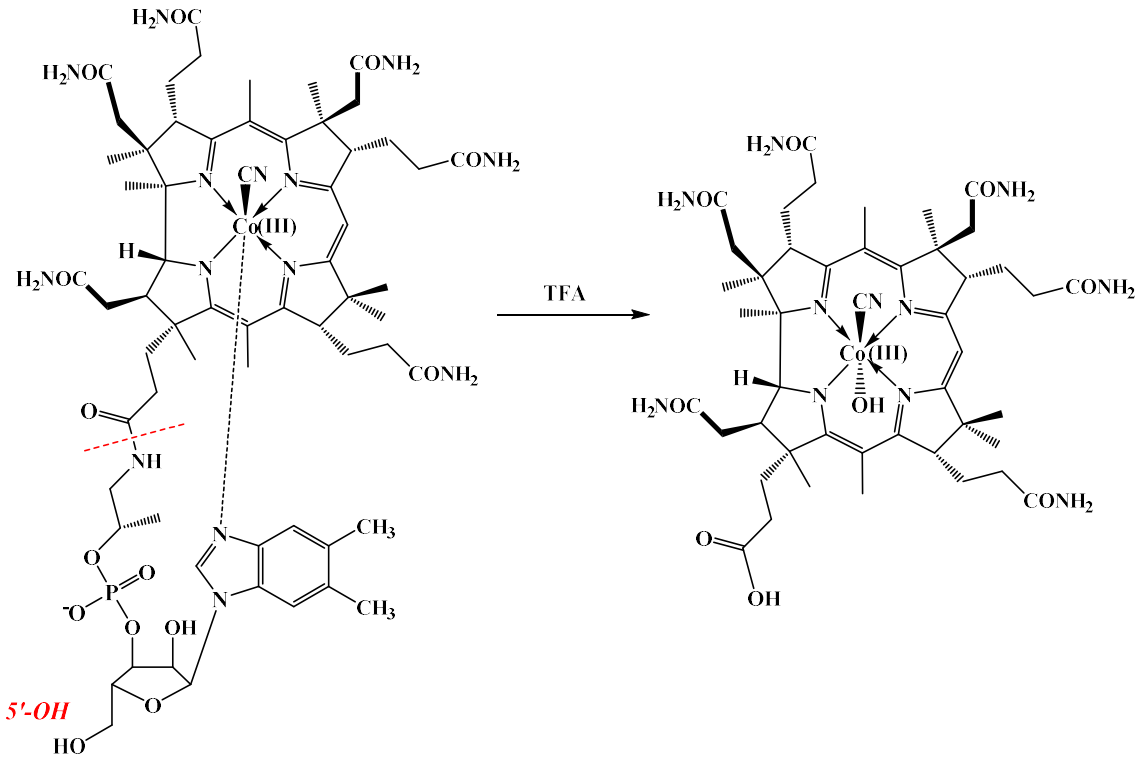

Figure 161: Acid hydrolysis of CNCbl by trifluoroacetic acid to form cobyric acid.

Research by others suggested that **C3** is suitable for conjugation to CNCbl by a copper-catalysed alkyne-azide cycloaddition reaction (CuAAC).[23–25] CNCbl was functionalised with an azide moiety at the 5'-OH site by a modified literature procedure.[26] The 5'-OH was converted to a good leaving group via mesylation, followed by nucleophilic substitution by azide.[27] CNCbl-N_3 (Figure 162) was then used as a suitable starting material for the CuAAC reaction with **C3**.

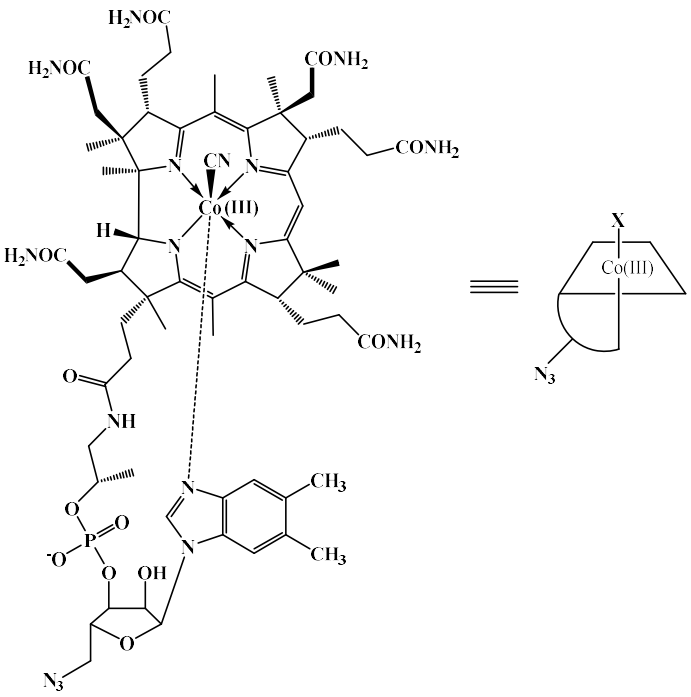

Figure 162: Structure of CNCbl-N_3 (left) and a simplified representation (right).[27]

Successful CuAAC reactions of CNCbl reported in the literature suggest using either CuI or $CuSO_4$/ascorbic acid as catalysts to produce high yields.[26,28] CuI (0.5 eq) was initially explored as a catalyst (Scheme 29).

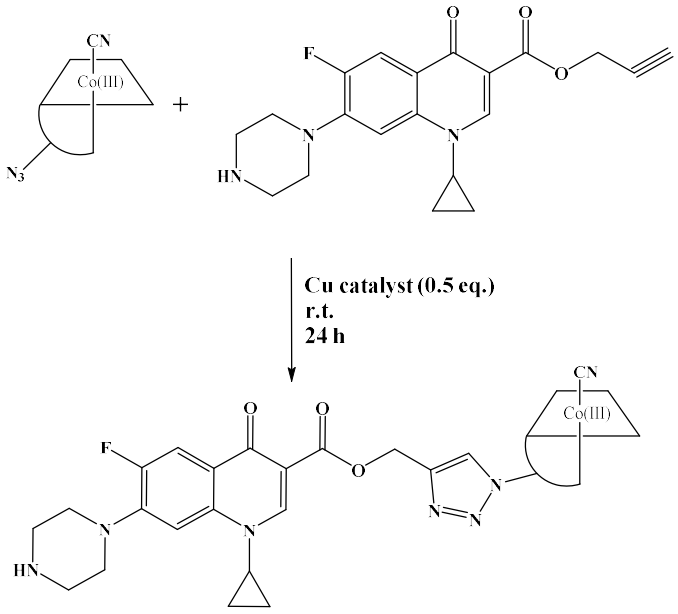

Scheme 29: Simplified reaction scheme for the synthesis of CNCbl-ciprofloxacin by copper-catalysed azide-alkyne cycloaddition. The complete reaction conditions are summarised in Table 10.

The LC-MS chromatogram, shown in Figure 163 (a), of the first trialled reaction (Table 10, **1**) showed two peaks. The peak eluting at 17.6 min (Figure 163, **1** and **2**) can be assigned to the CNCbl-N_3 starting material ($C_{64}H_{91}CoN_{17}O_{12}P$ calcd. *m/z* $[M+H]^+$ = 1380.6 and $[M+2H]^{2+}$ = 690.8; found 1380.6 and 690.9). The second peak at 16.6 min can be assigned to a CNCbl-triazole-OH fragment (Figure 164, $C_{66}H_{91}CoFN_{20}O_{16}P$ calcd. *m/z* $[M+H]^+$ = 1436.6 and $[M+2H]^{2+}$ = 718.8; found 1436.6 and 719.0) which is formed by hydrolysis of the ester of the desired product. A trial was also carried out using $CuSO_4$ as the copper catalyst (Table 10, **2**). In the trial using $CuSO_4$/sodium ascorbate as the catalyst, the CNCbl-N_3 starting material was observed at 17.6 min. This indicated that the CuAAC reaction had not occurred.

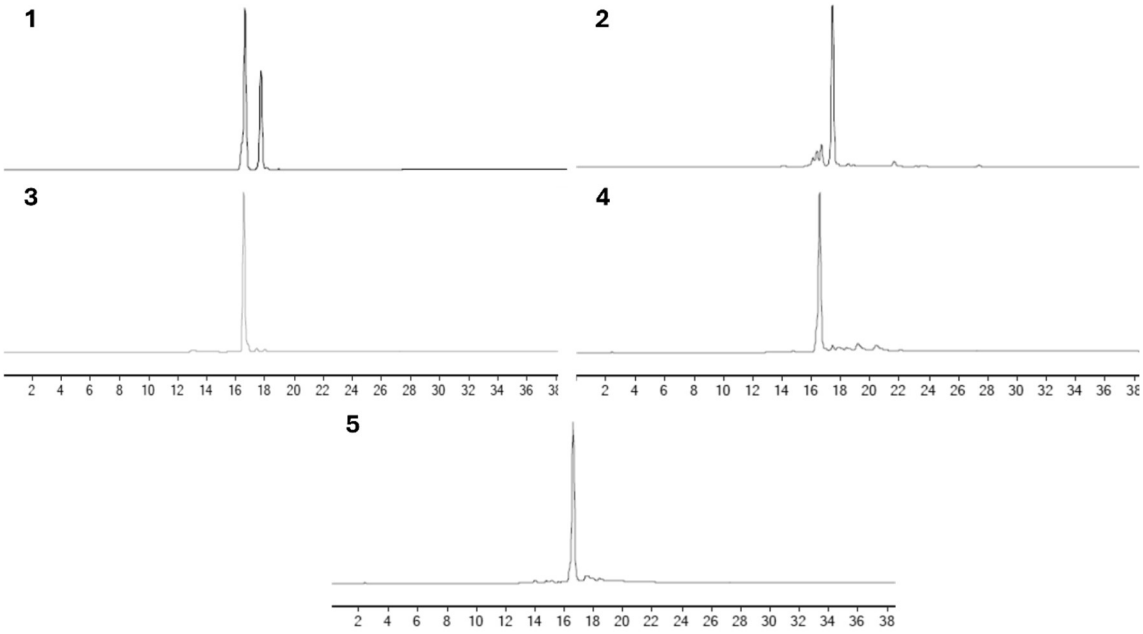

*Figure 163: LC-MS DAD (361 nm) chromatograms of trials **1-5** to synthesise a CNCbl-ciprofloxacin conjugate by copper-catalysed azide-alkyne cycloaddition (LC-MS method 1). The experimental conditions for each trial are summarised in Table 10. The peaks at 16.6 min can be assigned to an undesired CNCbl-triazole-OH product arising from hydrolysis and the peaks at 17.6 min are from the CNCbl-N_3 starting material.*

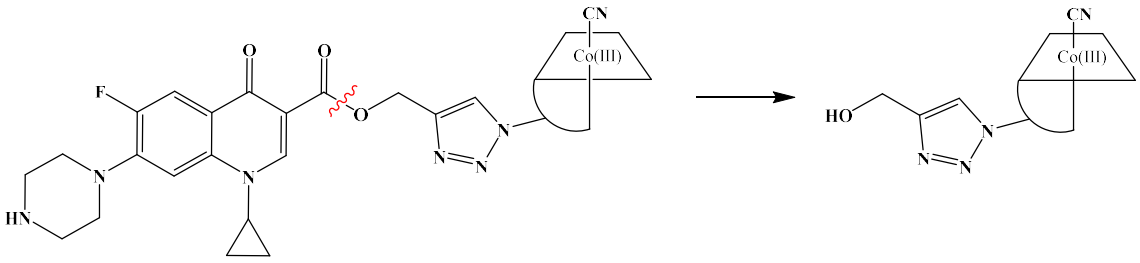

Figure 164: Ester cleavage of CNCbl-ciprofloxacin. This species was observed by LC-MS, eluting at 17.7 min in Figure 163.

Several further reaction conditions were trialled to determine if the ester bond cleavage could be avoided (attempts **3-5**, Table 10). The reactions focused primarily on different solvent systems to determine if the ester cleavage was solvent-dependent. It has been suggested that a proton source is required for CuAAC reactions.[29] In one synthesis (attempt **5**), amyl alcohol was trialled as a proton source in place of H_2O. These trials showed that CuI was the most effective catalyst for triazole formation using DMF as a solvent in the presence or absence of an added proton source (trials **3-5**). In aqueous conditions, DMF/buffers produced the best results. The CuAAC reactions under these conditions resulted in no remaining CNCbl-N_3 starting material, based on the LC-MS chromatogram at 361 nm. LC-MS allowed a direct comparison of each reaction outcome as the same mobile phase program was used. The observation of the CNCbl-triazole-OH species eluting at 17.6 min showed that the click reaction was successful, however, the ciprofloxacin moiety was subsequently hydrolysed at the ester.

Table 10: Synthetic attempts to produce CNCbl-ciprofloxacin by copper-catalysed azide-alkyne cycloaddition.

Attempt	Mol equivalents of Reactants				Catalyst	Solvent
	CNCbl-N_3	**C3**	TBTA	Sodium ascorbate		
1	1.2	1	0.5	-	CuI	DMF:H_2O (1:4)
2	1.2	1	-	4	$CuSO_4$	DMF:phosphate buffer (0.5M, pH 7) (1:1)
3	1.3	1	-	-	CuI	DMF:phosphate buffer (0.5M, pH 7) (1:1)

4	1.2	1	-	-	CuI	DMF
5	1.2	1	-	-	CuI	DMF:amyl alcohol (4:1)

[1-5] *The corresponding LC-MS chromatograms of the product solution for trials **1-5** are shown in Figure 163.*

Click-based reactions using **C3** as a starting material used the Boc protecting group for the amine.[13] Although the CuAAC reaction proved successful, ester cleavage also occurred either in the product or the **C3** reactant. Ester cleavage is typically acid or base catalysed.[30,31] The conditions trialled here included an aprotic solvent (entry **4**), preventing acid or base cleavage. LC-MS analysis routinely uses an aqueous mobile phase containing 0.1% formic acid. LC-MS analysis was therefore carried out without adding acid in the mobile phase; however, the resulting chromatograms were identical. This ruled out the acidic LC-MS mobile phase as the cause of ester cleavage. Another possibility is that the nucleophilic secondary amine on the piperazine ring of **C3** promotes ester cleavage (Scheme 30). This reaction could occur either before or after CuAAC. However, the stability of the **C3** product during deprotection in TFA and the ^{1}H NMR spectrum in $CDCl_3$ suggests that aminolysis occurs after CuAAC. It is suggested that following the CuAAC reaction, the cleaved -OR is stabilised as a leaving group, favouring amide bond formation.

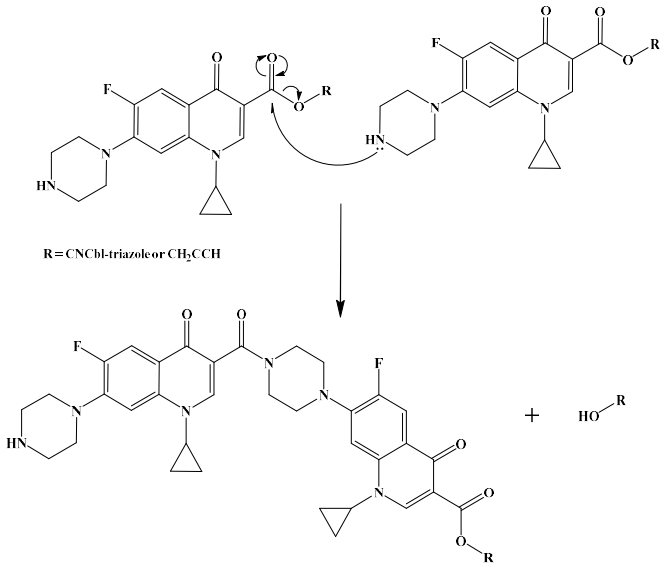

*Scheme 30: Aminolysis of the ester of **C3** or CNCbl-ciprofloxacin, tentatively proposed to occur by the amine of piperazine.*

Reactions with the Boc-protected ciprofloxacin-propargyl ester (**C2**) and CNCbl-N_3 were not undertaken. Removal of the Boc protecting group requires TFA and CNCbl is susceptible to acid catalysed cleavage.

Compound 17

Owing to the nucleophilic nature of the piperazine NH group (pK_a = 8.62[32]), the next synthetic attempts focused on utilising this functional group to couple to CNCbl. A suitable CNCbl-linker derivative incorporating a carboxylic acid was required to achieve this using amide coupling procedures. CNCbl was functionalised with a PEG-based 3-[2-[2-(2-aminoethoxy)ethoxy]ethoxy]propanoic acid linker (**17**, Scheme 31).

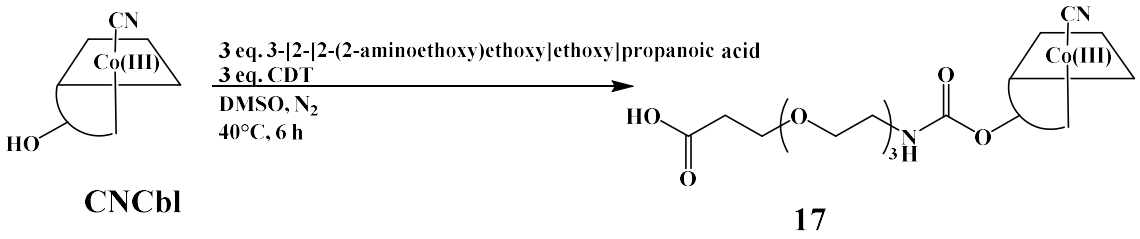

*Scheme 31: Synthetic scheme for the synthesis of **17**.*

Synthesis of **17** was achieved using the procedure established for other CNCbl-PEG molecules (Chapter 2) where CNCbl was the limiting reagent. The 5'-OH moiety was activated with CDT followed by nucleophilic substitution of the amino group of the 3-[2-[2-(2-aminoethoxy)ethoxy]ethoxy]propanoic acid linker. The reaction was followed by LC-MS and major peaks were observed at 22.9 and 29.7 min (Figure 165). The peak at 22.9 min is from the CNCbl starting material ($C_{68}H_{88}CoN_{16}O_{14}P$ calcd. *m/ z* $[M+H]^+$ = 1355.6 and $[M+2H]^{2+}$ = 678.4; found 1355.5 and 678.4). The peak at 29.7 min corresponds to **17** ($C_{73}H_{105}CoN_{15}O_{20}P$ calcd. *m/z* $[M+H]^+$ = 1602.7 and $[M+2H]^{2+}$ = 801.8; found 1603.5 and 802.0).

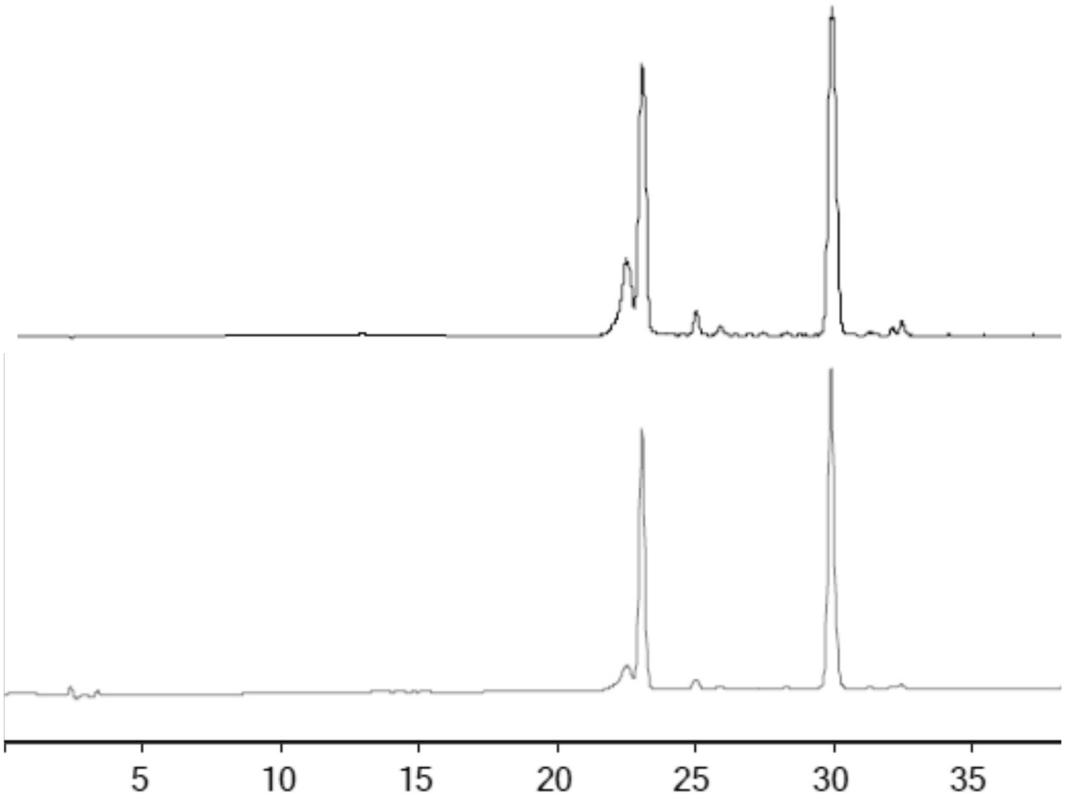

*Figure 165: LC-MS TIC (top) and DAD (361 nm, bottom) chromatograms of crude **17** (LC-MS method 3). The peak at 29.7 min is from the desired product ($C_{73}H_{105}CoN_{15}O_{20}P$ calcd. m/z $[M+H]^+$ = 1602.7 and $[M+2H]^{2+}$ = 801.8; found 1603.5 and 802.0).*

The product was purified by reversed-phase C18 chromatography, eluting as the second red band at 17.5% CH_3CN in H_2O. The purity was confirmed by LC-MS with one peak eluting at 40.1 min ($C_{73}H_{105}CoN_{15}O_{20}P$ calcd. *m/z* $[M+H]^+$ = 1602.7 and $[M+2H]^{2+}$ = 801.8; found 1603.5 and 801.9, Figure 166).

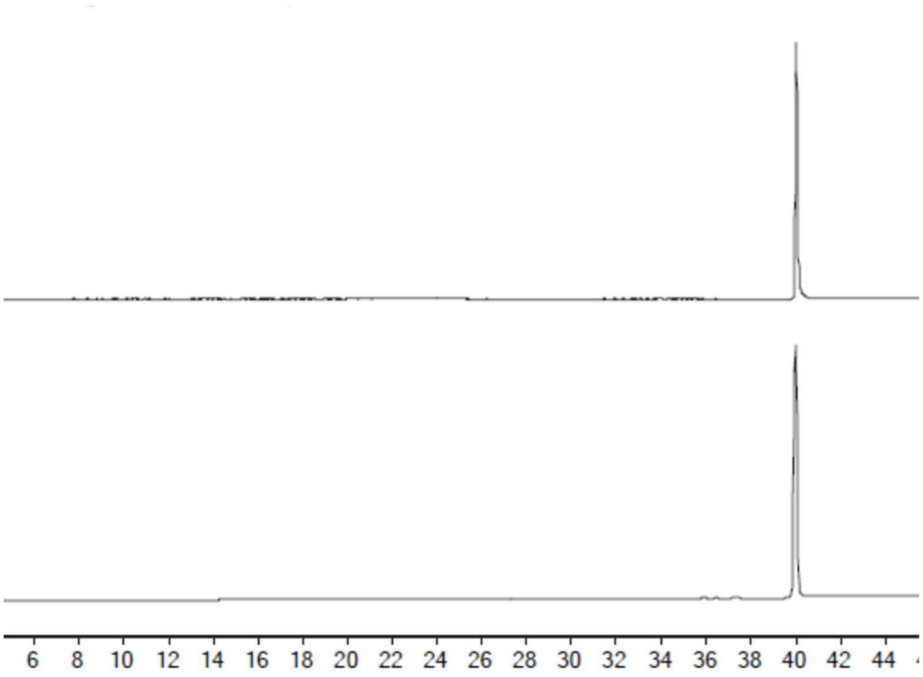

*Figure 166: LC-MS TIC (top) and DAD (361 nm, bottom) chromatograms of pure **17** (LC-MS method 2). The peak at 40.1 min is assigned to the product ($C_{73}H_{105}CoN_{15}O_{20}P$ calcd. m/z $[M+H]^+$ = 1602.7 and $[M+2H]^{2+}$ = 801.8; found 1603.5 and 801.9).*

Analysis by ^{13}C NMR spectroscopy is useful as the carbamate carbon gives rise to a distinctive resonance between 155-160 ppm.[33] The ^{13}C NMR spectrum of **17** was taken in DMSO-d_6, since the solubility of CNCbl and its derivatives is high (~20 mg per 500 µL). The new carbamate carbon resonance was observed at 156.21 ppm (Figure 167).

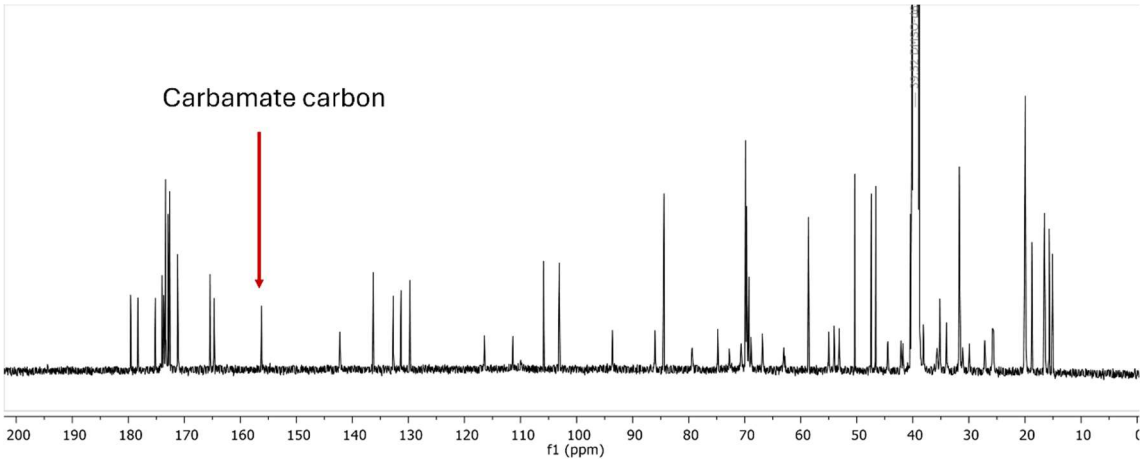

*Figure 167: ^{13}C NMR spectrum of **17** obtained in DMSO-d_6. The carbamate carbon resonating at 156.21 ppm is highlighted.*

HSQC NMR spectroscopy identified the aromatic protons and associated carbons of **17** as 5.89 (93.62), 6.23 (86.01), 6.43 (116.44), 7.08 (111.38) and 7.30 ppm (142.25 ppm). Most resonances had small or no changes in chemical shift upon conjugation of the linker to CNCbl (5.91 (93.40), 6.28 (85.39), 6.45 (116.23), 7.01 (111.35) and 7.32 ppm (142.34 ppm)). However, protons assigned to R1 and B2 did shift significantly upon conjugation to the linker, from 6.28 and 7.01 to 6.23 and 7.08 ppm, respectively. The protons (and corresponding carbons) of **17** have been assigned as C10, 5.89 (93.62); R1, 6.23 (86.01); B4, 6.43 (116.44); B2, 7.08 (111.38) and B7, 7.30 ppm (142.25 ppm).[33,34]

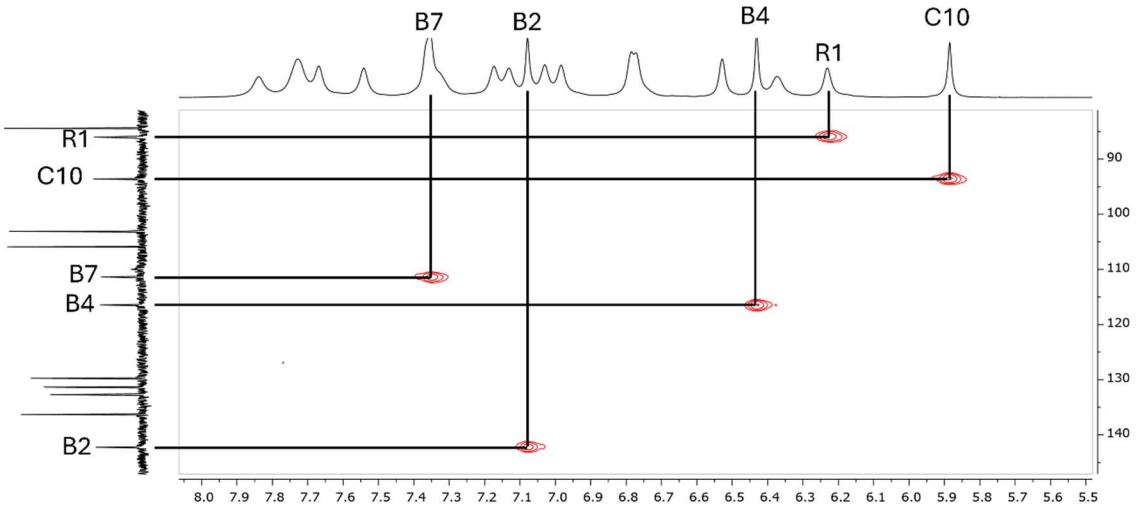

*Figure 168: HRMS NMR spectrum of **17** obtained in DMSO-d_6. The aromatic proton and corresponding carbons highlighted are assigned as C10, 5.89 (93.62); R1, 6.23 (86.01); B4, 6.43 (116.44); B2, 7.08 (111.38) and B7, 7.30 ppm (142.25 ppm).*

^{1}H NMR analysis was also carried out in MeOH-d_4, to determine the purity of the CNCbl conjugate. The ^{1}H NMR spectrum of **17** in MeOH-d_4 showed six resonances in the aromatic region at 6.03 (s, 1H), 6.23 (m, 1H), 6.57 (s, 1H), 7.15 (s, 1H), 7.25 (s, 1H) and 7.78 ppm (bs, 0.5H). The peaks at 6.03, 6.23, 6.57, 7.15 and 7.25 ppm can be assigned to protons C10, R1, B4, B2 and B7 of the CNCbl moiety. The chemical shifts of these protons are the same for **17** and CNCbl (Figure 169). The broad peak at 7.78 ppm is present in both CNCbl and **17**. This is assigned to a slowly exchanging NH proton of the CNCbl moiety. A new resonance was observed at 3.61 ppm (s, 12H) in **17**. This is assigned to the six CH_2 groups of the 3-[2-[2-(2-aminoethoxy)ethoxy]ethoxy]propanoic acid linker, analogous to that observed for **2** where a similar 1,11-diamine-3,6,9-trioxaundecane linker was employed (Section 2.3.1).

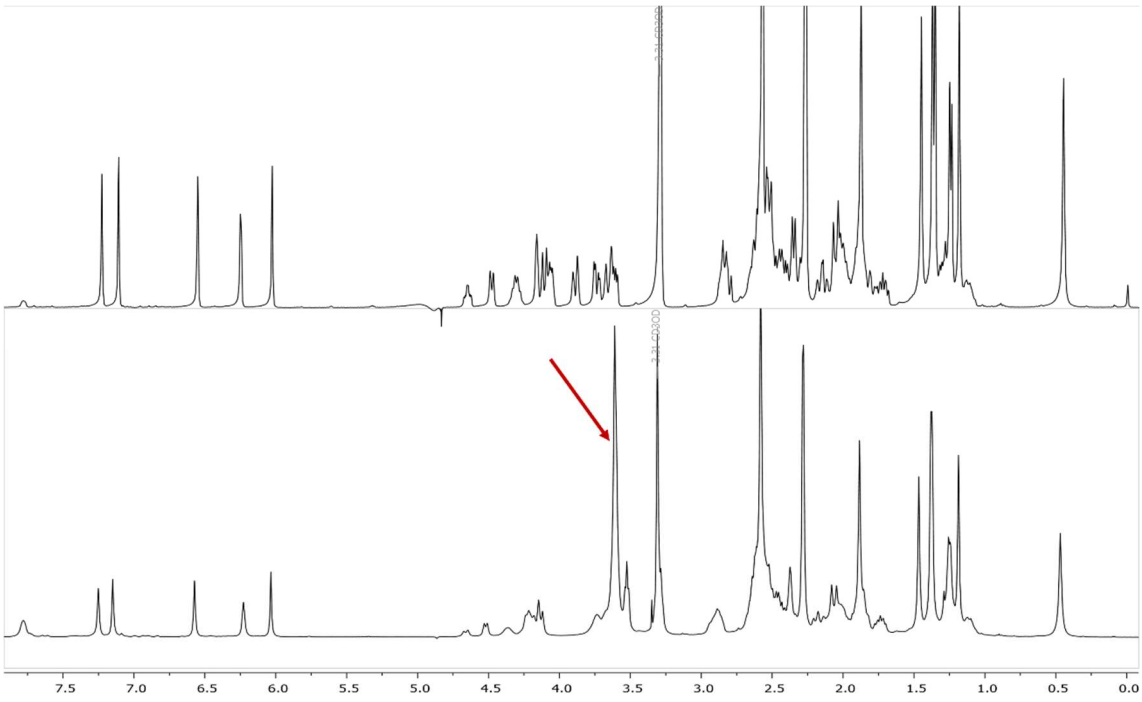

*Figure 169: ^{1}H NMR spectrum of CNCbl (top) and **17** (bottom) obtained in MeOH-d_4. The aromatic peaks of **17** at 6.03 (s, 1H), 6.23 (m, 1H), 6.57 (s, 1H), 7.15 (s, 1H) and 7.25 ppm (s, 1H) can be assigned as C10, R1, B4, B2 and B7. These remain unchanged upon conjugation of the linker. A new resonance at 3.61 ppm (s, 12H) is observed and assigned to the six methylene protons of the 3-[2-[2-(2-aminoethoxy)ethoxy]ethoxy]propanoic acid linker.*

To summarise, LC-MS analysis confirmed the formation of **17**, with a single peak and the expected *m/z* values (Figure 166). Further characterisation by ^{1}H and ^{13}C NMR spectroscopy supported the formation of **17** with a new carbamate carbon peak at 156.21 ppm (DMSO-d_6) and a new proton peak at 3.61 (s, 12H) ppm (MeOH-d_4) corresponding to six CH_2 groups of the 3-[2-[2-(2-aminoethoxy)ethoxy]ethoxy]propanoic acid linker. A purity of ≥95% was determined using the aromatic region of the ^{1}H NMR spectrum obtained in MeOH-d_4 and the LC-MS chromatogram.

Compound 18

Compound **17** has a terminal carboxylic acid moiety, suitable for amide coupling to the piperazine -NH group of ciprofloxacin. The amide coupling reagent employed earlier in this research for the synthesis of fluorescent CNCbl conjugates was EDC (a carbodiimide) or alternatively employing a reactive *N*-hydroxysuccinimide (NHS) ester of the fluorophore. Coupling of ciprofloxacin proved to be unsuccessful using these methods. A third amide coupling method was trialled for the synthesis of **18**, using aminium salts

as activating agents, namely *N*-[(1*H*-benzotriazol-1-yl)(dimethylamino)methylene]-*N*-methylmethanaminium hexafluorophosphate-*N*-oxide (HBTU) or *N*-[(dimethylamino)-1*H*-1,2,3-triazolo[4,5-*b*]pyridin-1-ylmethylene]-*N*-methylmethanaminium hexafluorophosphate-*N*-oxide (HATU) (Figure 170).[35–37] Both HBTU and HATU are useful for challenging peptide bond formation reactions.[36]

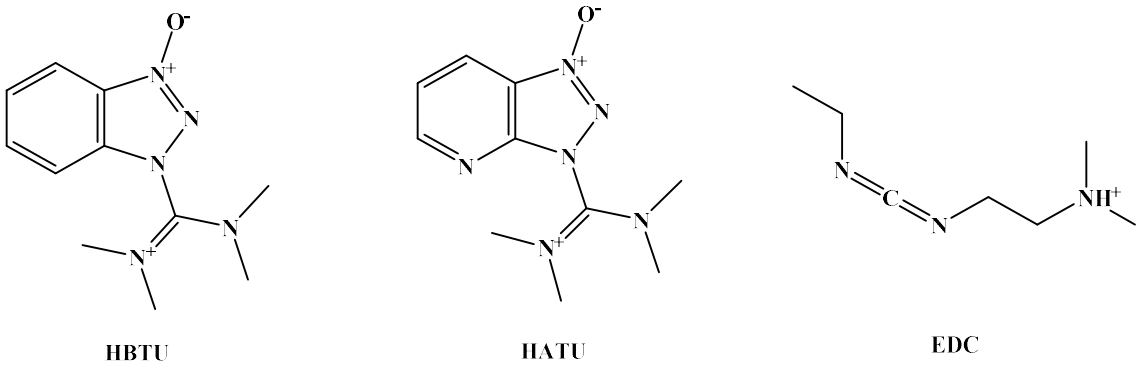

Figure 170: Structures of the peptide coupling reagents N-[(1H-benzotriazol-1-yl)(dimethylamino)methylene]-N-methylmethanaminium hexafluorophosphate-N-oxide (HBTU), N-[(dimethylamino)-1H-1,2,3-triazolo[4,5-b]pyridin-1-ylmethylene]-N-methylmethanaminium hexafluorophosphate-N-oxide (HATU) and N-ethyl-N'-(3-dimethylaminopropyl)carbodiimide (EDC).

Using EDC as a coupling reagent required the addition of 1-hydroxybenzotriazole (HOBt) to prevent the formation of the unreactive *N*-acylurea side product. This undesired side reaction is a common issue faced during carbodiimide couplings.[35] HATU and HBTU do not require HOBt. These reagents undergo a complex reaction to form the desired amide functionality where the limiting step is often the deprotonation of the carboxylic acid (Scheme 32). This has been achieved here by the addition of Et_3N.

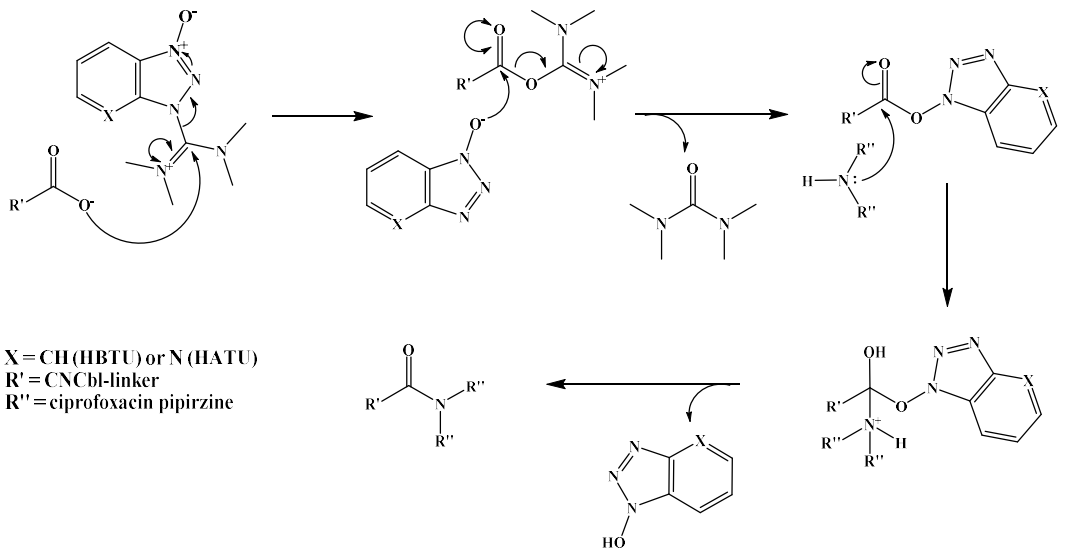

Scheme 32: Amide coupling mechanism of HBTU and HATU.

Synthetic attempts were carried out using **17** as the limiting reagent (Scheme 33) with either EDC, HBTU or HATU as the coupling reagents. All reactions were carried out in anhydrous DMSO under N_2 at 40°C for 16 h.

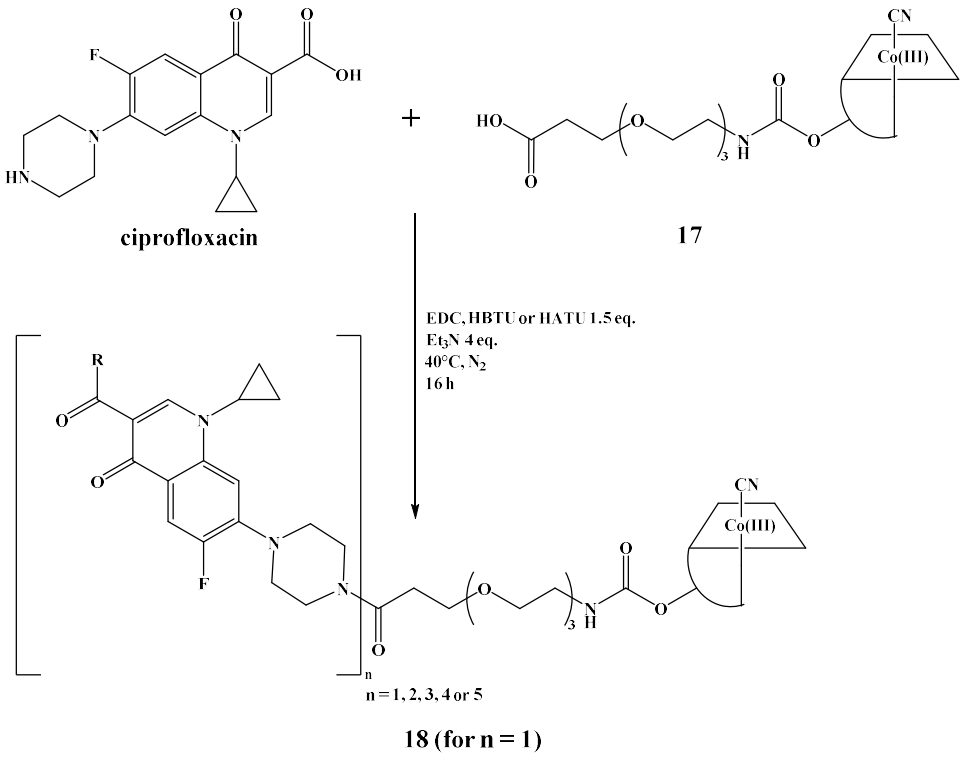

*Scheme 33: Synthesis of **18** using EDC, HBTU or HATU as coupling agents, resulting in an over-functionalised product. Multiple ciprofloxacin molecules are conjugated via amide bonds between the piperazine -NH and -COOH ciprofloxacin groups.*

Small peaks were identified in the LC-MS chromatograms of all reactions eluting at 16.6 min ($C_{63}H_{88}CoN_{14}O_{14}P$ calcd. *m/z* $[M+H]^+ = 1355.6$ and $[M+2H]^{2+} = 678.3$; found 1355.4 and 678.4) and 17.7 min ($C_{73}H_{105}CoN_{15}O_{20}P$ calcd. *m/z* $[M+H]^+ = 1602.7$ and $[M+2H]^{2+} = 801.8$; found 1602.5 and 801.9), assigned to the unreacted CNCbl and the compound **17** starting materials, respectively (Figure 171). The reactions using HBTU and HATU showed five further peaks eluting at 25.6, 28.4, 29.8, 30.3 and 30.6 min. The peak at 25.6 min could be assigned to the desired product, **18** ($C_{91}H_{124}CoFN_{18}O_{21}P$ calcd. *m/z* $[M+2H]^{2+} = 958.4$ $[M+3H]^{3+} = 639.3$; found 958.6 and 639.4).

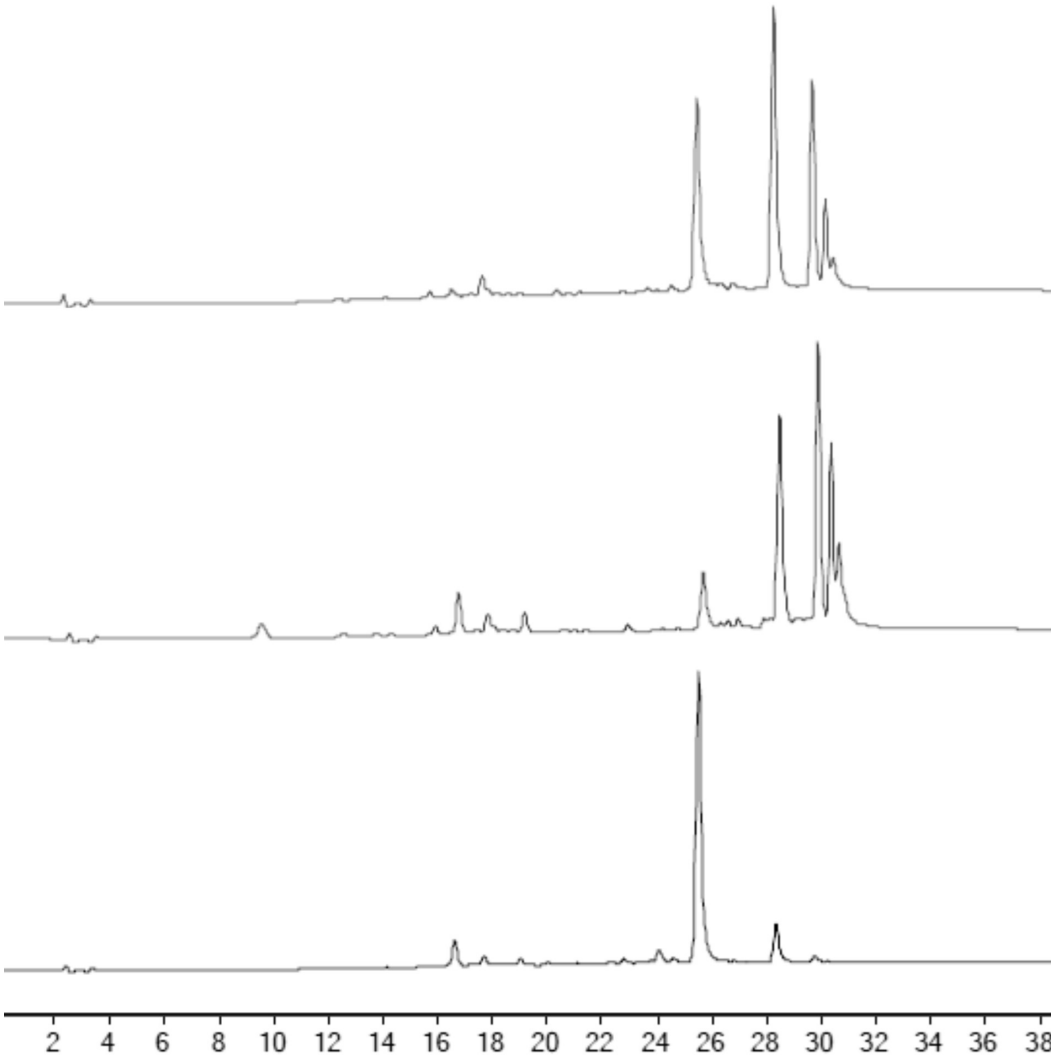

*Figure 171: LC-MS DAD (361 nm) chromatograms of crude **18**, with HBTU (top), HATU (middle) or EDC (bottom) as the coupling reagent (LC-MS method 1). The peak eluting at 25.6 min can be assigned to **18** ($C_{91}H_{124}CoFN_{18}O_{21}P$ calcd. m/z $[M+2H]^{2+} = 958.4$ $[M+3H]^{3+} = 639.3$; found 958.6 and 639.4).*

The peaks eluting at 28.4, 29.8, 30.3 and 30.6 min are from over-functionalised products (Scheme 33). Each of these peaks, in chronological order, contained an additional ciprofloxacin than the previous, with an amide bond formed between the piperazine amine and carboxylic acid of ciprofloxacin (Table 11). Unlike EDC, HBTU and HATU activated the ciprofloxacin carboxylic acid for nucleophilic substitution by another ciprofloxacin.

*Table 11: LC-MS peak assignments for the crude **18** product mixtures using HBTU or HATU as coupling reagents.*

Retention time (min)	Compound[a]	*n* (number of ciprofloxacin units)	Chemical formula	Calcd./observed *m/z*			
				$[M+H]^+$	$[M+2H]^{2+}$	$[M+3H]^{3+}$	$[M+4H]^{4+}$
28.4	CNCbl-PEG-Cip-Cip	2	$C_{107}H_{137}CoF_2N_{21}O_{24}P$	2229.9/-	1115.5/1115.8	744.0/743.8	-
29.8	CNCbl-PEG-Cip-Cip-Cip	3	$C_{124}H_{153}CoF_3N_{24}O_{26}P$	2543.1/-	1272.0/1271.9	848.4/848.3	636.5/636.5
30.3	CNCbl-PEG-Cip-Cip-Cip-Cip	4	$C_{141}H_{169}CoF_4N_{27}O_{28}P$	2856.1/-	1429.0/1428.8	952.7/952.7	715.0/714.8
30.6	CNCbl-PEG-Cip-Cip-Cip-Cip-Cip	5	$C_{158}H_{185}CoF_5N_{30}O_{30}P$	3169.3/-	1585.2/1585.1	1057.1/1057.0	793.1/793.1

a = CNCbl-linker-cargo, PEG = 3-[2-[2-(2-aminoethoxy)ethoxy]ethoxy]propanoic acid, Cip = ciprofloxacin.

The synthesis of **18** with EDC as the coupling reagent resulted a major peak eluting at 25.6 min assigned to the desired product ($C_{91}H_{124}CoFN_{18}O_{21}P$ calcd. *m/z* $[M+2H]^{2+}$ = 958.4 $[M+3H]^{3+}$ = 639.3; found 958.6 and 639.4, Figure 171, lower chromatogram). The smaller peak at 28.4 min is the di-functionalised product where two ciprofloxacin molecules are conjugated to CNCbl. Using EDC as the coupling reagent successfully formed the mono-functionalised product, rather than the over-functionalised products identified in the reactions using HBTU and HATU. The product from the EDC reaction was purified by reversed-phase C18 chromatography using (H_2O + 0.1% formic acid) and

CH_3CN as the mobile phase. Compound **18** eluted from the column at 45% CH_3CN as a red band and was taken to dryness by rotary evaporation. The purity of **18** was investigated by LC-MS. A prominent peak eluting at 25.6 min was observed ($C_{91}H_{124}CoFN_{18}O_{21}P$ calcd. *m/z* $[M+2H]^{2+}$ = 958.4 $[M+3H]^{3+}$ = 639.3; found 958.6 and 639.4, Figure 172).

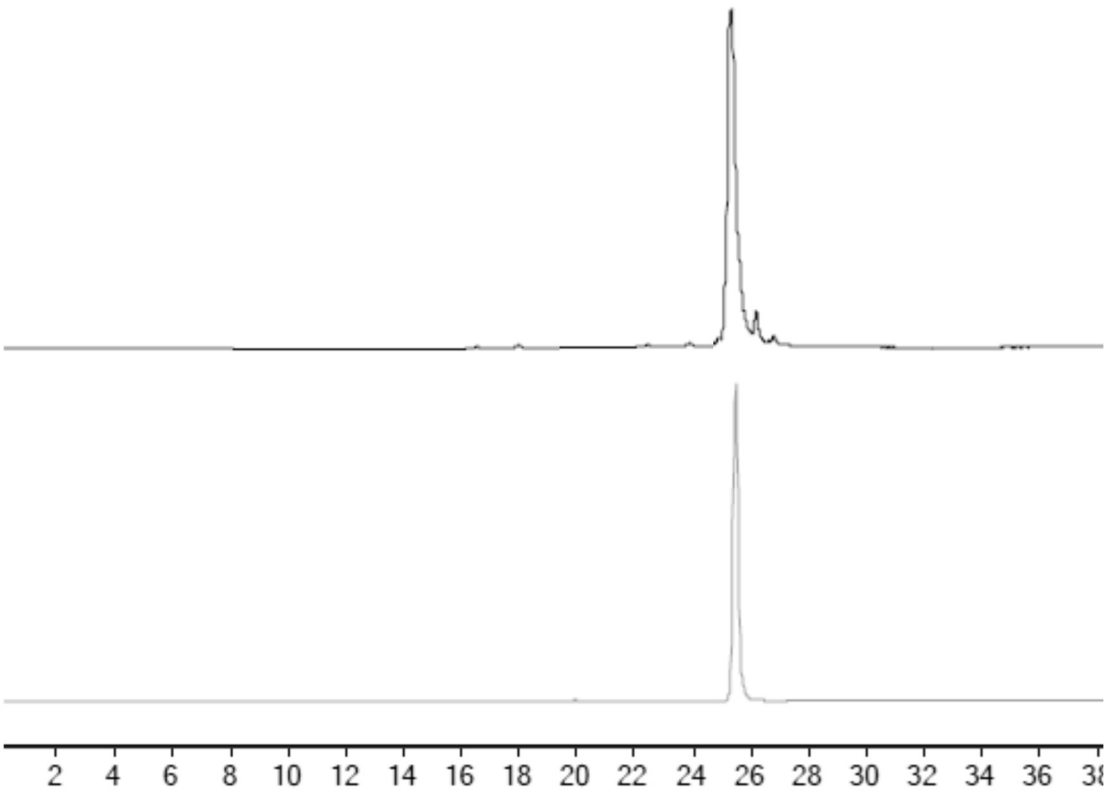

*Figure 172: LC-MS TIC (top) and DAD (361 nm, bottom) of pure **18** (LC-MS method 1). The peak eluting at 25.6 min is assigned to the product ($C_{91}H_{124}CoFN_{18}O_{21}P$ calcd. m/z = $[M+H]^+$ = 1914.8, $[M+2H]^{2+}$ = 958.4 $[M+3H]^{3+}$ = 639.3; found 958.6 and 639.4).*

The ^1H NMR spectrum of **18** was obtained in MeOH-d_4. The chemical shifts of the protons in the aromatic region are 6.03 (s, 1H, C10), 6.22 (m, 1H, R1), 6.58 (s, 1H, B4), 7.15 (s, 1H, B2) and 7.24 ppm (s, 1H, B7) (Figure 173). Three remaining proton resonances in the aromatic region are assigned to the protons of ciprofloxacin. The singlet resonating at 8.81 ppm (1H) is assigned to proton ***a*** due to the lack of neighbouring protons (Figure 174). Proton ***b*** and ***c*** are assigned to the doublets at 7.61 (1H, J = 7.31 Hz) and 7.96 ppm (1H, J = 13.3 Hz), respectively. Doublets are observed due to the splitting by the adjacent ^{19}F substituent (I = ½ for ^{19}F).

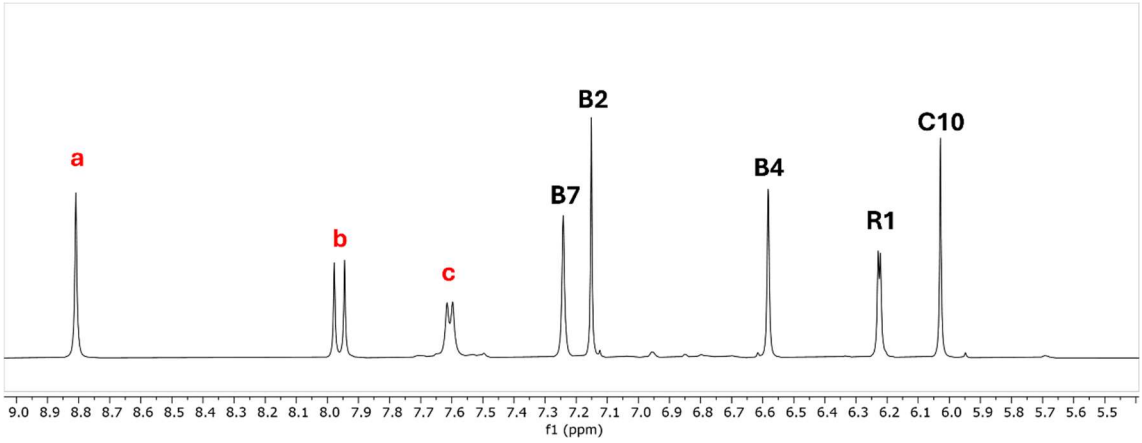

*Figure 173: Aromatic region of the ^{1}H NMR spectrum of **18** in MeOH-d_4. Peaks assigned to the CNCbl moiety are 6.03 (s, 1H, C10), 6.22 (m, 1H, R1), 6.58 (s, 1H, B4), 7.15 (s, 1H, B2) and 7.24 ppm (s, 1H, B7). Peaks assigned to ciprofloxacin are 7.61 (1H, d, J = 7.31 Hz, **c**), (7.96 ppm (1H, d, J = 13.3 Hz, **b**) and 8.81 ppm (s, 1H, **a**).*

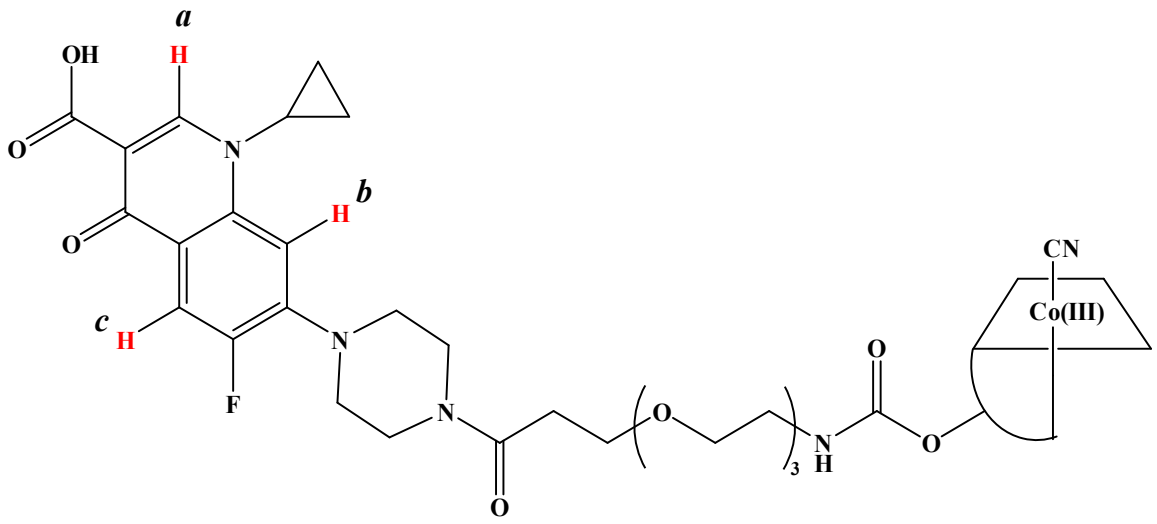

*Figure 174: Structure of **18** with the aromatic protons of ciprofloxacin labelled and highlighted in red.*

To summarise, the successful synthesis of a CNCbl-ciprofloxacin conjugate was achieved using the piperazine amine of ciprofloxacin as the coupling site. This was obtained in a 78% yield with a purity of ≥95% confirmed by both LC-MS and ^{1}H NMR spectroscopy. Finally, high-resolution mass spectrometry (HRMS) confirmed the successful synthesis of **18** as $C_{90}H_{121}CoN_{18}O_{22}PNa_2$ (*m/z* $[M+2Na]^{2+}$ calcd. 980.3870, found 980.3865).

Compound 19

Synthesis of a CNCbl-linker-ciprofloxacin conjugate using the -COOH moiety proved to be challenging as discussed at the beginning of this chapter. However, during the synthesis of the *N*-bound ciprofloxacin conjugate, it was observed that HBTU or HATU as amide coupling reagents, rather than EDC, resulted in CNCbl-linker-ciprofloxacin oligomers forming. Therefore, HBTU and HATU activate the carboxylic acid of ciprofloxacin, unlike EDC. Conjugating ciprofloxacin to CNCbl by amide bond formation at the -COOH moiety of ciprofloxacin was therefore attempted using HBTU. The first attempt at the synthesis of **19** was carried out using compound **2** (crude) as the limiting reagent in addition to ciprofloxacin (Scheme 34).

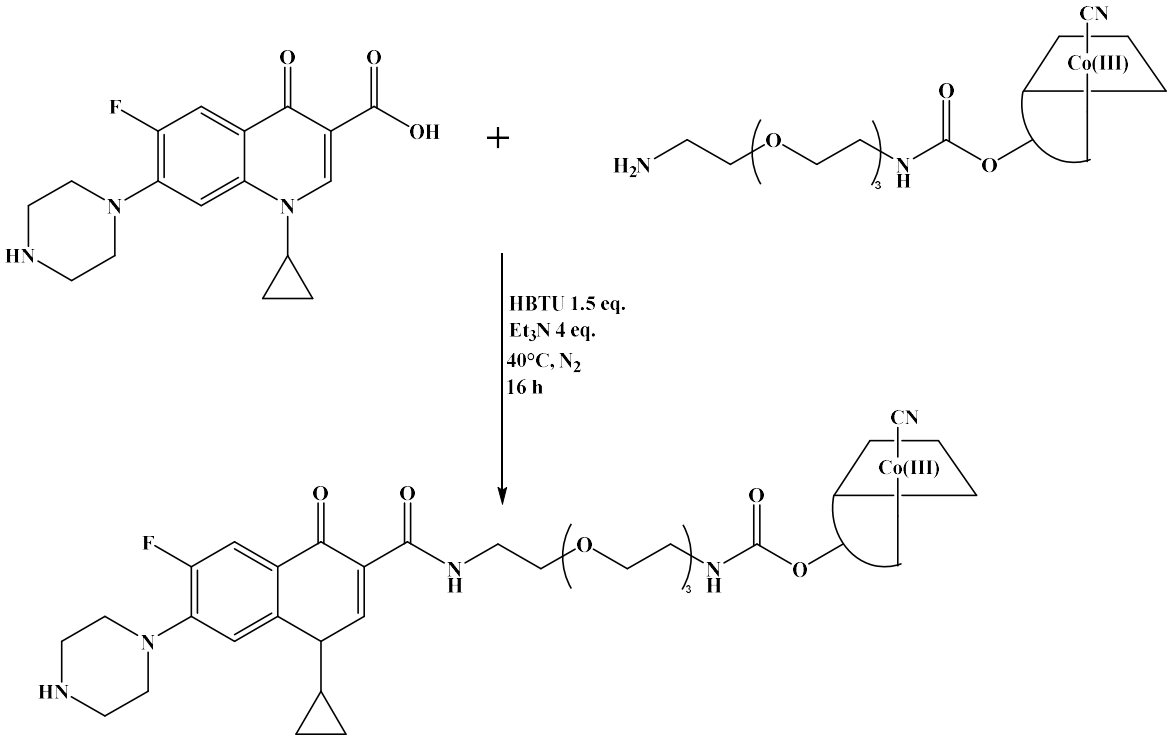

*Scheme 34: Synthetic scheme for the synthesis of **19**.*

The crude reaction solution was precipitated into Et_2O and CH_2Cl_2 (1:1) and filtered. The precipitate was released from the filter using minimal CH_3OH and taken to dryness. However, after washing the product off the filter using CH_3OH, a red filtrate was collected as expected but a pale pink solid remained on the filter. The red filtrate and pale pink solid were analysed by LC-MS. Both the solid and filtrate samples showed a main peak at 16.6 min where unreacted CNCbl is expected to retain ($C_{63}H_{88}CoN_{14}O_{14}P$ calcd. *m/z* $[M+H]^+$ = 1355.6 and $[M+2H]^{2+}$ = 678.3; found 1355.4 and 678.4). However, an

additional species also eluted at this retention time, with *m/z* values of 558.1, 836.5 and 1672.8. These three values likely correspond to $[M+3H]^{3+}$, $[M+2H]^{2+}$ and $[M+H]^{+}$ peaks of the same compound, but the structure of this species could not be deduced. Furthermore, there was no evidence of the starting material **2** or the desired product.

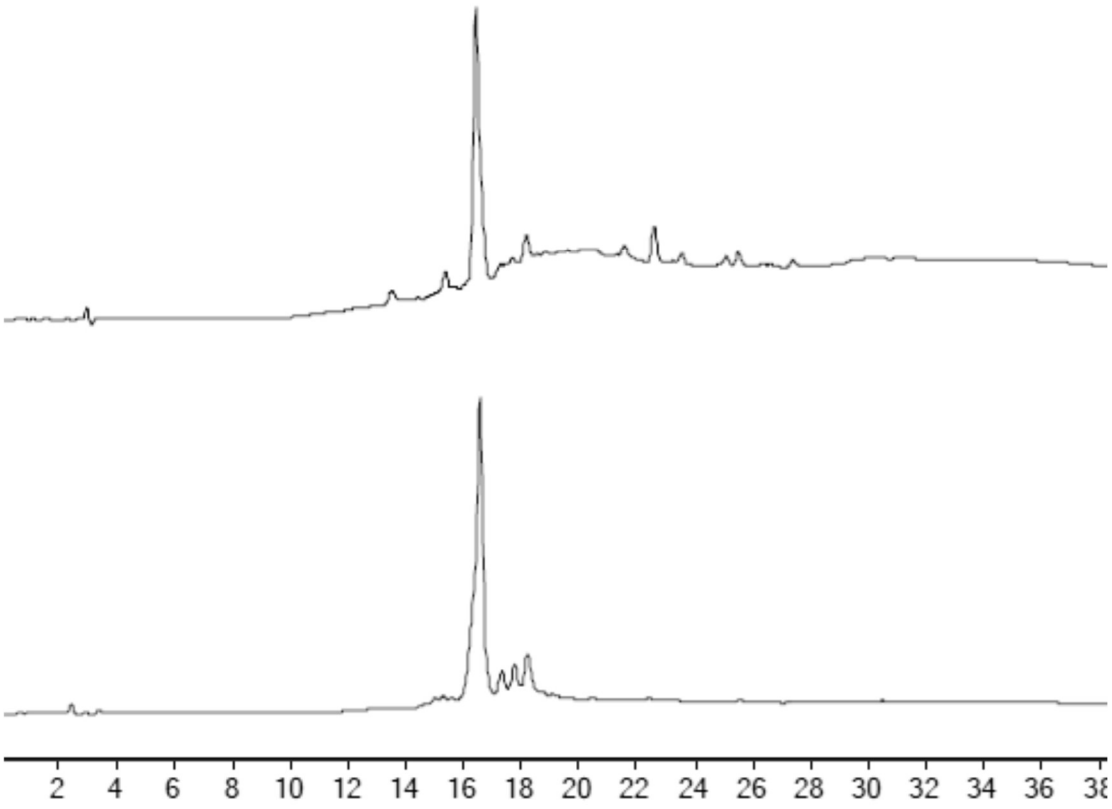

*Figure 175: LC-MS DAD (361 nm) chromatograms of the pale pink solid (top) and red filtrate (bottom) obtained after the synthesis attempt of **19** using ciprofloxacin (LC-MS method 1). The peak at 16.6 min can be assigned as unreacted CNCbl ($C_{63}H_{88}CoN_{14}O_{14}P$ calcd. m/z $[M+H]^{+}$ = 1355.6 and $[M+2H]^{2+}$ = 678.3; found 1355.4 and 678.4) from the crude starting material and an unknown product with m/z values of 558.1, 836.5 and 1672.8.*

During previous attempts to synthesise a CNCbl-ciprofloxacin conjugate, oligomers of ciprofloxacin were observed by amide bond formation between the carboxylic acid and piperazine -NH. The starting material used in the first synthetic attempt to produce **19** contained the unprotected piperazine-NH group. As the Boc protection of this group was successful, the reaction was repeated using **C1** as the starting material (Scheme 34). Upon precipitation of the crude reaction solution, no pale pink solid was observed as seen previously. LC-MS analysis of the crude red filtrate showed two peaks at 16.6 and 30.9

min (Figure 176). The peak at 16.6. min can be assigned to the unreacted CNCbl from the crude **2** starting material ($C_{63}H_{88}CoN_{14}O_{14}P$ calcd. *m/z* $[M+H]^+$ = 1355.6 and $[M+2H]^{2+}$ = 678.3; found 1355.4 and 678.4). The *m/z* values of 558.1, 836.5 and 1672.8 are also observed in this peak as seen in the previous synthesis using the unprotected ciprofloxacin starting material. This species is likely from an unidentified side product. The peak at 30.5 min can be assigned to compound **19** ($C_{94}H_{130}CoFN_{19}O_{22}P$ calcd. *m/z* $[M+2H]^{2+}$ = 994.4 and $[M+3H]^{3+}$ = 663.3; found 994.1 and 663.2).

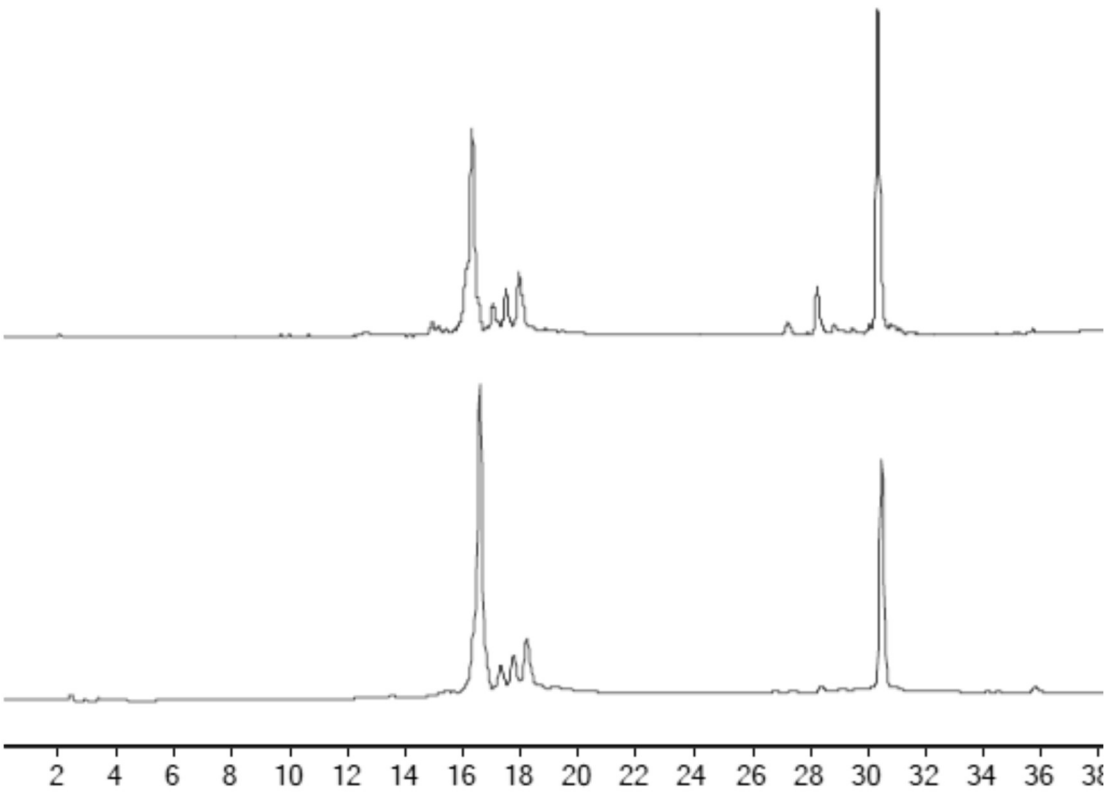

*Figure 176: LC-MS TIC (top) and DAD (361 nm, bottom) chromatograms of the crude reaction solution of **19** using **C1** as the starting material (LC-MS method 1). The peak at 16.6 min is assigned to unreacted CNCbl ($C_{63}H_{88}CoN_{14}O_{14}P$ calcd. m/z $[M+H]^+$ = 1355.6 and $[M+2H]^{2+}$ = 678.; found 1355.4 and 678.4) and the peak at 30.5 min is assigned to compound **19** ($C_{94}H_{130}CoFN_{19}O_{22}P$ calcd. m/z $[M+H]^+$ = 1987.9, $[M+2H]^{2+}$ = 994.4 and $[M+3H]^{3+}$ = 663.3; found 994.1 and 663.2).*

Using **C1** resulted in the formation of the desired product. Compound **19** was purified by reversed-phase C18 chromatography using (H_2O + 0.1% formic acid) and CH_3CN as the mobile phase. The desired compound eluted at 45% CH_3CN as a red band and was taken to dryness by rotary evaporation. LC-MS analysis of the purified compound identified

one peak eluting at 30.5 min (Figure 177). This peak was assigned to compound **19** ($C_{94}H_{130}CoFN_{19}O_{22}P$ calcd. *m/z* $[M+2H]^{2+}$ = 994.4 and $[M+3H]^{3+}$ = 663.3; found 994.1 and 663.2).

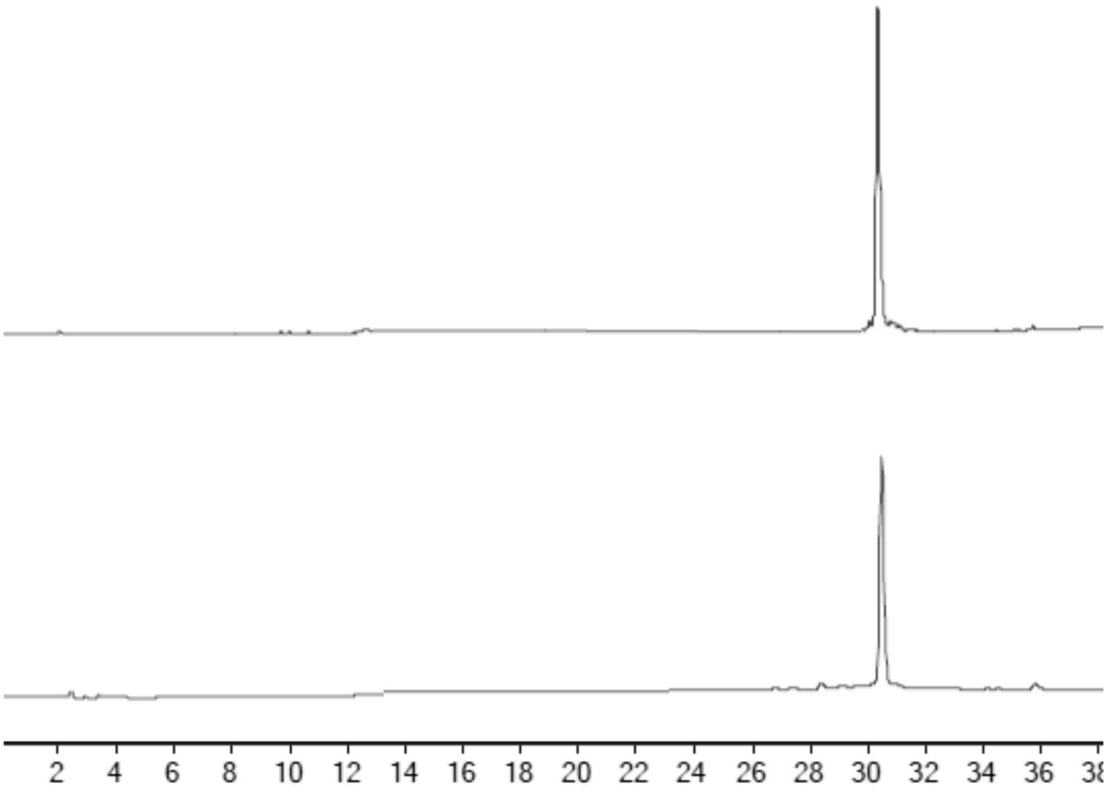

*Figure 177: LC-MS TIC (top) and DAD (361 nm, bottom) chromatograms of pure **19** (LC-MS method 1). The peak at 30.5 min is assigned to compound **19** ($C_{94}H_{130}CoFN_{19}O_{22}P$ calcd.* m/z *$[M+H]^+$ = 1987.9, $[M+2H]^{2+}$ = 994.4 and $[M+3H]^{3+}$ = 663.3; found 994.1 and 663.2).*

Compound **19** retained the Boc protecting group on the -N atom of the piperazine moiety. Deprotection was not carried out for two reasons, Boc deprotection requires the addition of trifluoroacetic acid (TFA) where CNCbl is known to be unstable.[19–22] Furthermore, TFA is known to cleave carbamate bonds.[13,38] Compound **19** has carbonates in two locations between the Boc group and ciprofloxacin, and the linker and CNCbl. Therefore, deprotection by TFA is likely to decompose the CNCbl-linker-ciprofloxacin product. ^{1}H NMR spectroscopy analysis of **19** was carried out in MeOH-d_4. The five aromatic protons of the CNCbl moiety are assigned as 6.02 (s, 1H, C10), 6.23 (m, 1H, R1), 6,58 (s, 1H, B4), 7.15 (s, 1H, B2) and 7.24 (s, 1H, B7) ppm (Figure 178). The three aromatic protons of ciprofloxacin are assigned as 7.55-7.57 (m, 1H, **c**), 7.93-7.97 (m, 1H, **b**) and

8.80 ppm (s, 1H, **a**, Figure 179). In addition to this, the methyl protons of the Boc protecting group can be observed at 1.49 ppm (s, 9H). The CNCbl and aromatic ciprofloxacin protons of **19** resonate at the same chemical shifts as compound **18** (6.03 (s, 1H, C10), 6.22 (m, 1H, R1), 6.58 (s, 1H, B4), 7.15 (s, 1H, B2) and 7.24 ppm (s, 1H, B7) 7.56 (d, 1H, J = 7.29 Hz, **b**), 7.95 (d, 1H, J = 13.4 Hz, **c**) and 8.81 ppm (s, 1H, **a**)). A peak is also observed at 7.68 ppm (bs, 0.5H). This is assigned to a slowly exchanging NH proton from the CNCbl moiety, observed earlier in this research for both CNCbl and other CNCbl-linker molecules.

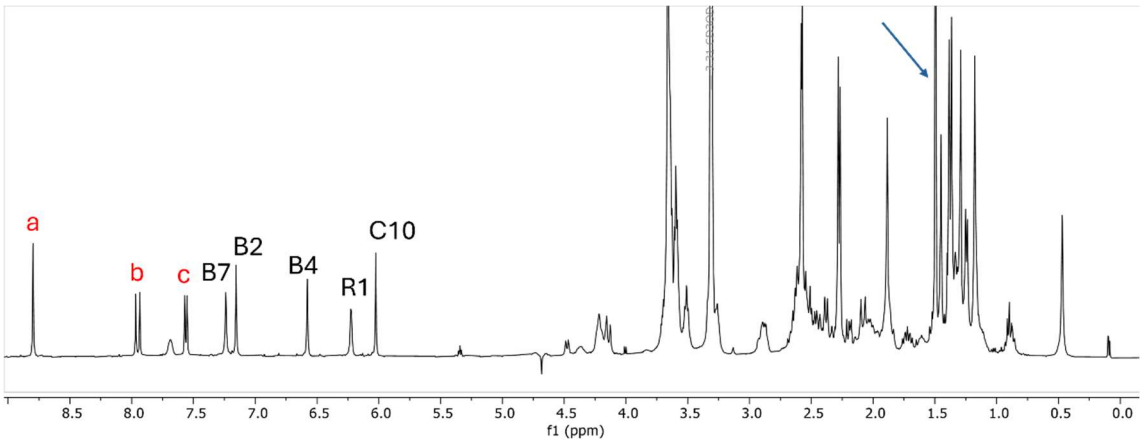

*Figure 178: ^{1}H NMR spectrum of **19** obtained in MeOH-d_4. Peaks assigned to the CNCbl moiety are 6.02 (s, 1H, C10), 6.23 (m, 1H, R1), 6,58 (s, 1H, B4), 7.15 (s, 1H, B2) and 7.24 (s, 1H, B7) ppm. The aromatic ciprofloxacin protons are labelled in red and assigned as 7.56 (d, 1H, J = 7.29 Hz, **b**), 7.95 (d, 1H, J = 13.4 Hz, **c**) and 8.81 ppm (s, 1H, **a**) with the three CH_3 protons of the Boc protecting group highlighted by the blue arrow (s, 9H).*

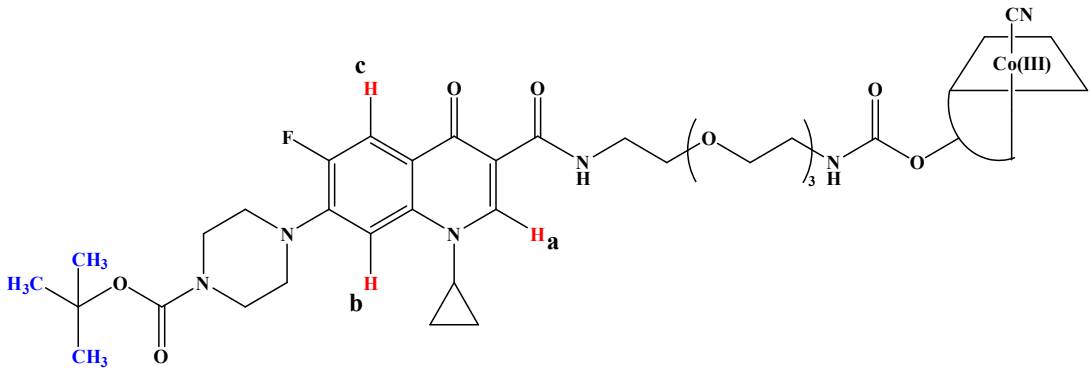

*Figure 179: Structure of **19** with the aromatic protons of ciprofloxacin highlighted in red and the three Boc CH_3 moieties highlighted in blue.*

To summarise, using **C1** as a starting material and HBTU as a coupling agent allowed for the successful synthesis of the *O*-bound Boc protected CNCbl-linker-ciprofloxacin conjugate, **19**, afforded in a 27.8% yield. The low yield reflects the lower reactivity of the carboxylic acid of ciprofloxacin. LC-MS and ^{1}H NMR spectroscopic analysis of compound **19** determined the purity of ≥95%. Finally, HR-MS analysis confirmed the identity of **19** (*m/z* $[M+2Na]^{2+}$ calculated for $C_{94}H_{130}CoN_{19}O_{22}PNa_2$ 1015.9238, found 1015.9246).

Compound 20

Synthesis of the *O*-bound CNCbl-ciprofloxacin conjugate proved successful with HBTU as the coupling reagent. Compound **19** used the 1,11-diamine-3,6,9-trioxaundecane-linked CNCbl starting material, compound **2**. For the synthesis of compound **20**, analogous reaction conditions were employed using the cystamine-linked CNCbl starting material, compound **1** (Scheme 35). Once again, either ciprofloxacin or **C1** were used as the starting material. Compound **1** was the limiting reagent, with HBTU (1.5 eq.), Et_3N (4.0 eq.) and the appropriate ciprofloxacin compound (1.5 eq.). All reagents were dissolved in anhydrous DMSO and the reaction mixture was stirred at 40 °C for 16 h.

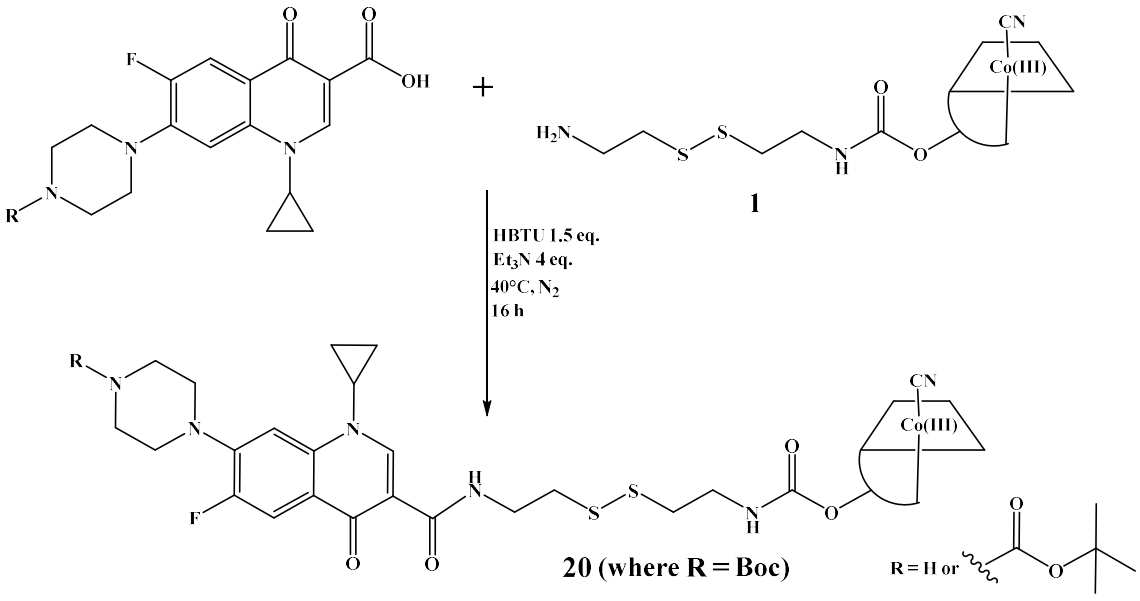

*Scheme 35: Synthetic scheme for the synthesis of **20**.*

LC-MS analysis of the crude reaction mixture using unprotected ciprofloxacin as the starting material showed similar results to that seen during the synthesis of **19**. Upon precipitation of the crude reaction solution, a red filtrate was obtained upon addition of

CH_3OH and a pale pink solid remained on the filter. The LC-MS chromatograms were obtained for both solid and filtrate (Figure 180). The largest peak in both solid and filtrate samples retained at 16.6 min and can be assigned to the unreacted CNCbl from the crude **1** starting material ($C_{63}H_{88}CoN_{14}O_{14}P$ calcd. *m/z* $[M+H]^+$ = 1355.6 and $[M+2H]^{2+}$ = 678.3; found 1355.5 and 678.4). Unreacted compound **1** can be assigned to the peak at 16.2 min ($C_{68}H_{98}CoN_{16}O_{15}PS_2$, calcd. *m/z* $[M+H]^+$ = 1534.3 and $[M+2H]^{2+}$ = 767.3; found $[M+H+CH_3CN]^+$ 1592.4 and $[M+2H+CH_3CN]^{2+}$ 797.6). Additional peaks were observed at 15.5, 17.6 and 19.8 min but the *m/z* values were not consistent with the desired compound. The main product is the unreacted CNCbl-linker molecule. The other side-product peaks indicate that other undesired chemistry is occurring.

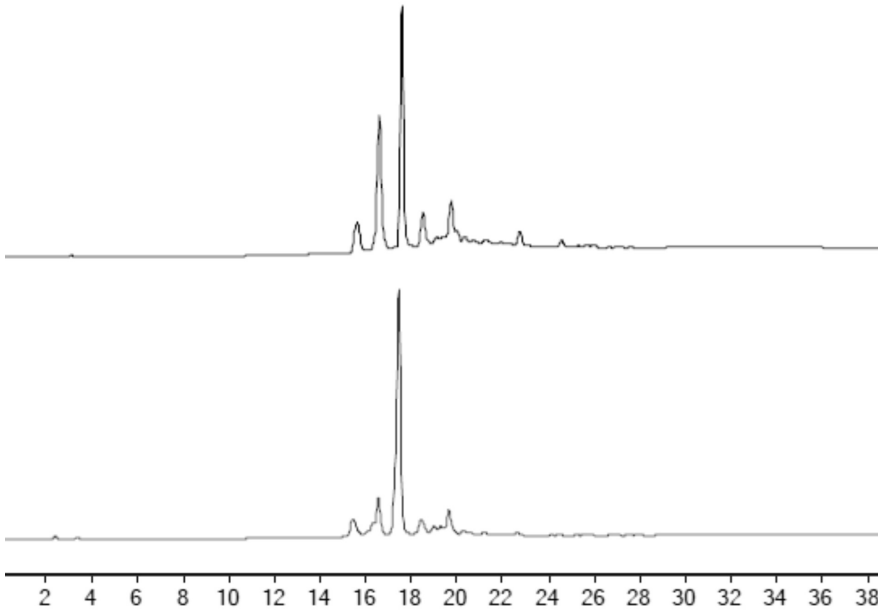

*Figure 180: LC-MS DAD (361 nm) chromatograms of the pale pink solid (top) and red filtrate (bottom) obtained after the synthesis attempt of **20** using unprotected ciprofloxacin (LC-MS method 1). The peaks at 16.2 and 16.3 mins can be assigned as CNCbl ($C_{63}H_{88}CoN_{14}O_{14}P$ calcd. m/z $[M+H]^+$ = 1355.6 and $[M+2H]^{2+}$ = 678.3; found 1355.5 and 678.4) and unreacted **1** ($C_{68}H_{98}CoN_{16}O_{15}PS_2$, calcd. m/z $[M+H]^+$ = 1534.3 and $[M+2H]^{2+}$ = 767.3; found $[M+H+CH_3CN]^+$ 1592.4 and $[M+2H+CH_3CN]^{2+}$ 797.6), respectively. The species eluting at 15.5, 17.6 and 19.8 min could not be identified.*

Synthesis using **C1** as the starting material together with compound **1** was more successful. Using analogous reaction conditions (Scheme 35), a red filtrate was obtained after precipitation of the crude reaction solution. LC-MS analysis of the crude product

showed multiple peaks between 15-20 min. The large peak at 16.6 min is assigned to the unreacted CNCbl ($C_{63}H_{88}CoN_{14}O_{14}P$ calcd. *m/z* $[M+H]^+$ = 1355.6 and $[M+2H]^{2+}$ = 678.3; found 1355.5 and 678.4). Other peaks retaining between 15-20 min have the same retention times and *m/z* values as observed during the synthesis using unprotected ciprofloxacin. This indicates that the starting material **1** decomposes during the synthesis. However, using **C1** was more successful. The large peak in the DAD chromatogram eluting at 31.1 min can be assigned to the desired compound ($C_{90}H_{122}CoFN_{19}O_{19}PS_2$ calcd. *m/z* $[M+2H]^{2+}$ = 974.4 and $[M+3H]^{3+}$ = 649.9; found 974.5 and 649.8). Multiple peaks are also observed between 29.1 and 30.1 min in the TIC chromatogram but are less obvious in the DAD chromatogram at 361 nm. The absorbance at 361 nm is often used to identify CNCbl-related products during LC-MS analysis as CNCbl has a large absorbance band at this wavelength.[1,26] Due to the diminished appearance of these peaks in the DAD chromatogram, they are likely not associated with a compound incorporating CNCbl or a closely related analogue.

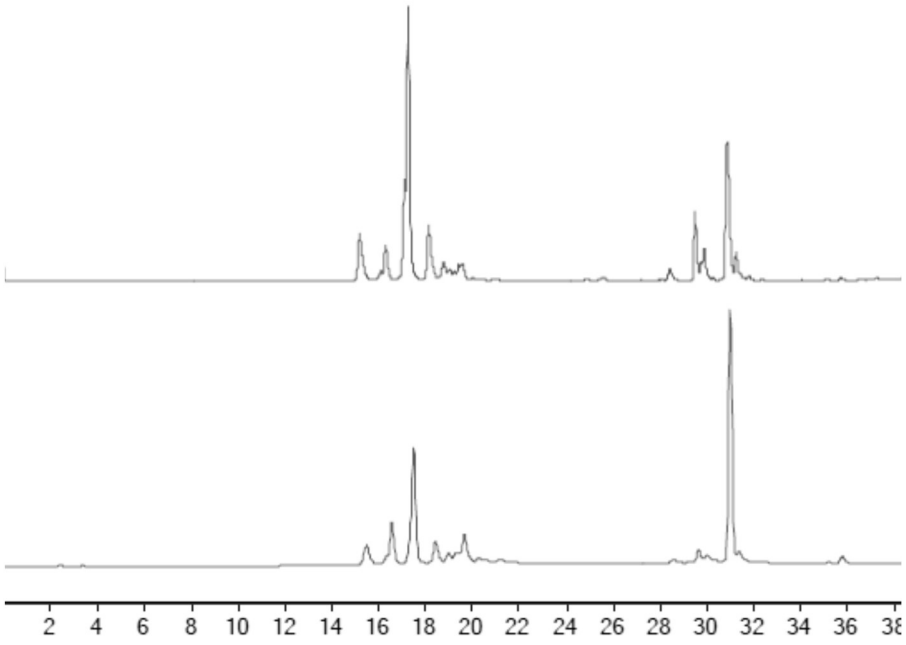

*Figure 181: LC-MS TIC (top) and DAD (361 nm, bottom) chromatograms of the crude reaction solution of **20** using Boc-ciprofloxacin as the starting material (LC-MS method 1). The peak at 16.6 min is assigned to unreacted CNCbl ($C_{63}H_{88}CoN_{14}O_{14}P$ calcd. m/z $[M+H]^+$ = 1355.6 and $[M+2H]^{2+}$ = 678.3; found 1355.4 and 678.4) and the peak at 31.1 min is assigned to compound **20** ($C_{90}H_{122}CoFN_{19}O_{19}PS$ calcd. m/z $[M+2H]^{2+}$ = 974.4 and $[M+3H]^{3+}$ = 649.9; found 974.5 and 649.8).*

Compound **20** was purified by reversed-phase C18 chromatography using (H_2O + 0.1% formic acid) and CH_3CN as the mobile phase. The desired compound eluted at 45% CH_3CN as a red band and was taken to dryness by rotary evaporation. LC-MS analysis of the purified compound identified one peak eluting at 31.3 min (Figure 182). This peak was assigned to compound **20** ($C_{90}H_{122}CoFN_{19}O_{19}PS$ calcd. *m/z* $[M+2H]^{2+}$ = 974.4 and $[M+3H]^{3+}$ = 649.9; found 974.5 and 649.8). Analogous to compound **19**, deprotection of the Boc moiety was not carried out due to concerns of decomposition in the presence of TFA.

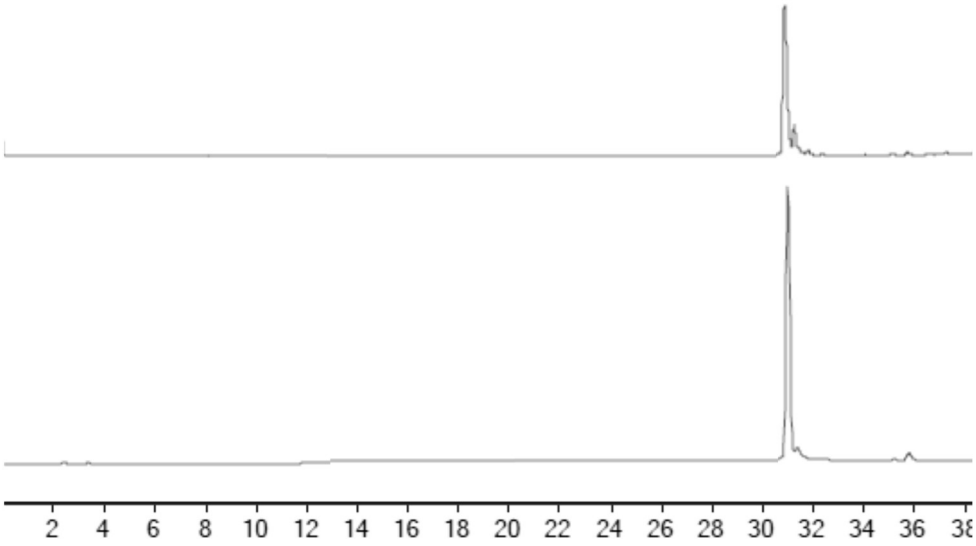

*Figure 182: LC-MS TIC (top) and DAD (361 nm, bottom) chromatograms of pure **20** (LC-MS method 1). The major peak at 31.1 min is assigned to compound **20** ($C_{90}H_{122}CoFN_{19}O_{19}PS$ calcd. m/z $[M+2H]^{2+}$ = 974.4 and $[M+3H]^{3+}$ = 649.9; found 974.5 and 649.8).*

^{1}H NMR spectroscopy analysis of **20** in MeOH-d_4 showed the five CNCbl peaks which resonate in the aromatic region at 6.03 (s, 1H, C10), 6.23 (m, 1H, R1), 6.58 (s, 1H, B4), 7.15 (s, 1H, B2) and 7.23 ppm (s, 1H, B7, Figure 183). The aromatic protons assigned to the ciprofloxacin molecule are assigned at 7.55 (d, 1H, *J*= 7.31, **c**), 7.94 (d, 1H, *J* = 13.37, **b**) and 8.79 ppm (s, 1H, **a**, Figure 184). Furthermore, the large singlet at 1.50 ppm (9H) can be assigned to the three CH_3 moieties of the Boc protecting group on the ciprofloxacin moiety.

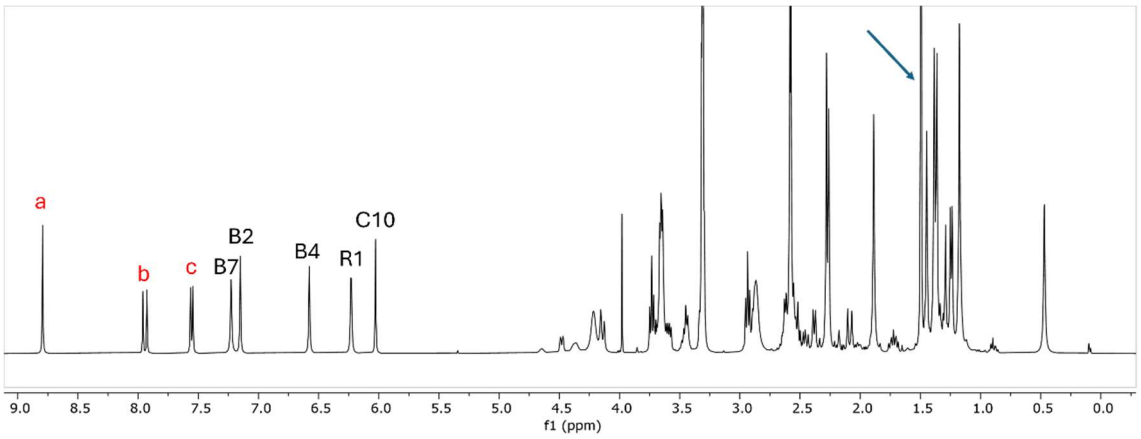

*Figure 183: ^{1}H NMR spectrum of **20** obtained in MeOH-d_4. Peaks assigned to the CNCbl moiety are 6.03 (s, 1H, C10), 6.23 (m, 1H, R1), 6.58 (s, 1H, B4), 7.15 (s, 1H, B2) and 7.23 ppm (s, 1H, B7). Aromatic protons of the ciprofloxacin moiety are shown in red and assigned as 7.55 (d, 1H, J= 7.31, **c**), 7.94 (d, 1H, J = 13.37, **b**) and 8.79 ppm (s, 1H, **a**) with the three low field CH_3 protons of Boc highlighted by the blue arrow at 1.50 ppm (s, 9H).*

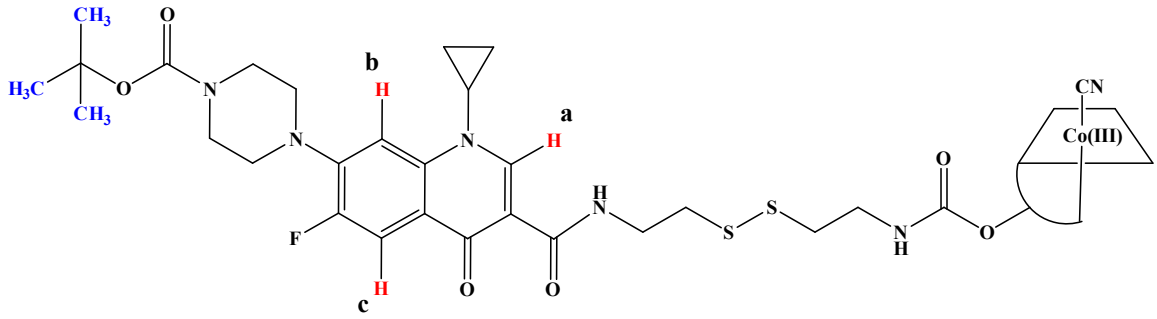

*Figure 184: Structure of **20** with the aromatic protons of ciprofloxacin highlighted in red and the three Boc CH_3 substituents highlighted in blue.*

To summarise, using **C1** as a starting material and HBTU as a coupling agent allowed for the successful synthesis of the *O*-bound Boc-protected CNCbl-linker-ciprofloxacin conjugate, **20**, obtained in a 33% yield. This conjugate contains the cleavable disulfide containing cystamine linker. LC-MS and ^{1}H NMR spectroscopic analysis of compound **20** determined the purity of ≥95%. Finally, HR-MS analysis confirmed $C_{90}H_{122}CoN_{19}O_{19}PS_2Na_2$.

Compound 21

The synthesis of a CNCbl-gentamicin conjugate was carried out using compound **17** as the limiting reagent (Scheme 36). The initial synthetic attempts employed EDC as the coupling reagent, which successfully activated the carboxylic acid of **17** in the synthesis

of compound **18**. As EDC is known to form an unreactive *N*-acyl-urea derivative (discussed in Chapter 2, compound **3**), HOBt was included in the reaction to prevent this. Gentamicin was used in excess (1.5 eq.) and the reaction was left to proceed at 45 °C for 24 h.

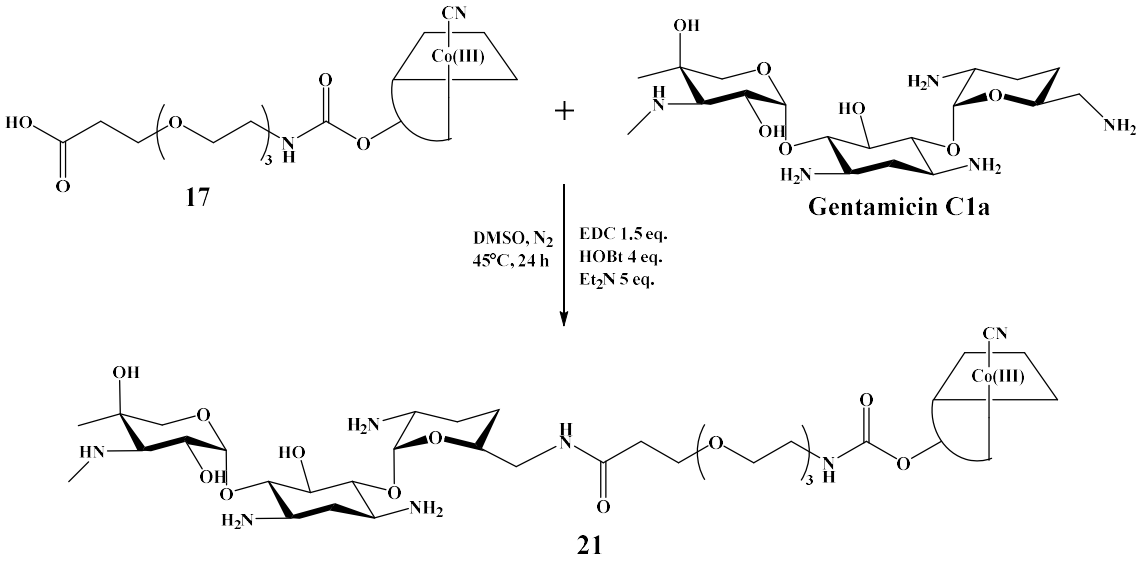

*Scheme 36: Synthetic scheme for the synthesis of compound **21**. This scheme shows conjugation at the terminal C1a amine of gentamicin.*

As an aminoglycoside, gentamicin C1a (Figure 185) contains one secondary and four primary amines. Conjugation to compound **17** is possible at any of these amine groups. Due to steric hindrance and a high pK_a, it is likely that amide coupling occurs at the amine highlighted in blue (Figure 185).[39] However, since no attempts were made to protect the other amine groups before coupling, the conjugation site was not controlled. Therefore, multiple CNCbl-gentamicin isomers are likely to be synthesised.

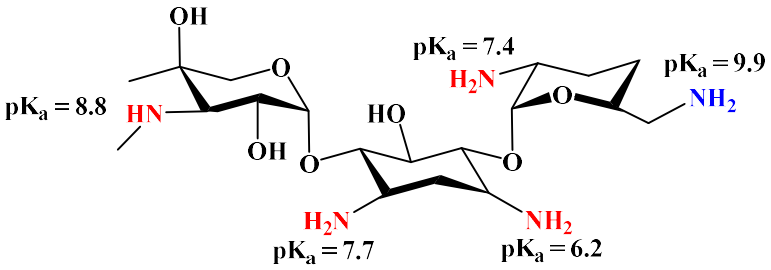

Figure 185: Structure and pK_a values of gentamicin C1a where the amine moieties are highlighted in red. The most reactive coupling site has been highlighted in blue.[39]

Throughout this research, LC-MS has been used to analyse the crude and pure reaction samples. However, LC-MS analysis of the crude reaction mixture for compound **21** proved difficult (Figure 186). Two broad peaks between 14-18 and 19-24 min are present in the TIC chromatogram. The DAD chromatogram at 361 nm, used to identify CNCbl derivatives, showed some evidence of separation for the large peak between 14-18 min but it was still broad. The *m/z* values across the peak between 14-18 min did show the desired product ($C_{92}H_{142}CoN_{20}O_{26}P$ calcd. *m/z* $[M+2H]^{2+}$ = 1018.0 and $[M+3H]^{3+}$ = 679.0; found 1017.9 and 678.8) along with other impurities that had a range of retention times within the 14-18 min time period. Although complex, the LC-MS results did not show the presence of compound **17**, indicating that the starting material had been consumed during the 24 h reaction.

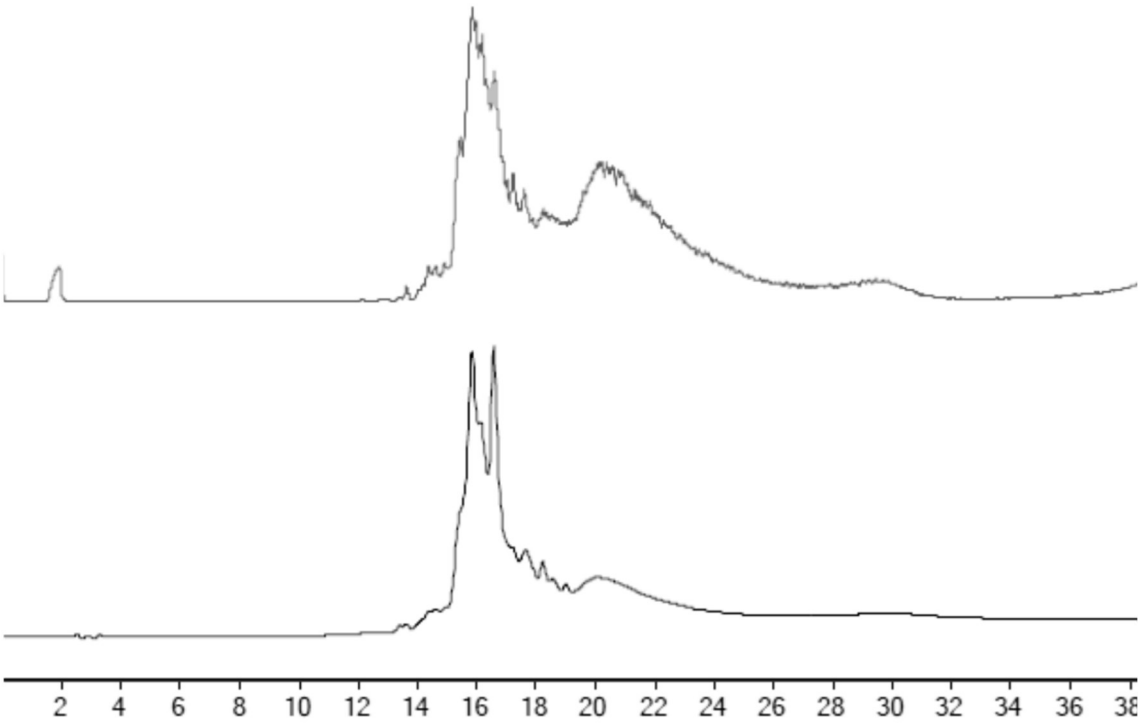

*Figure 186: LC-MS TIC (top) and DAD (361 nm, bottom) chromatograms of crude **21** obtained using LC-MS mobile phase method 1 in (H_2O+0.1% formic acid) and (CH_3CN+0.1% formic acid). Significant peak broadening is evident indicating numerous compounds are present. Impurities elute at 13.7, 15.1, 16.6 and 18.9 min based on their m/z values.*

Several attempts were made to improve the separation of the product mixture. Changes were made to the mobile phase method. Modifications included the removal of formic acid from both the H_2O and CH_3CN solvents or the exchange of CH_3CN for CH_3OH as

the organic solvent (Figure 187). The same mobile phase gradient program was used for all analyses. For clarity, only the TIC and extracted ion chromatograms (EIC) using *m/z* 1018 which corresponds to $[M+2H]^{2+}$ of the desired product, are shown in Figure 187, to identify where compound **21** elutes. Using CH_3OH as the organic component of the mobile phase was the least successful, as nothing eluted from the column until 95% CH_3OH was reached, and no peak separation was observed (Figure 187, **c**). The standard mobile phase components (H_2O+0.1% formic acid and CH_3CN+0.1% formic acid) resulted in a broad peak between 16-22 min (Figure 187, **a**). The EIC of this data shows that compound **21** elutes as a part of this broad peak, again with co-eluting impurities. The removal of formic acid from the mobile phase impacted the order of elution with compound **21** eluting between 22-30 min (Figure 187, **b**). The associated *m/z* values across this broad peak were the same and showed the presence of only compound **21** ($C_{92}H_{142}CoN_{20}O_{26}P$ calcd. *m/z* $[M+2H]^{2+}$ = 1018.0 and $[M+3H]^{3+}$ = 679.0; found 1017.9 and 678.8). The removal of formic acid from the mobile phase separated the impurities which eluted at 13.7, 15.1, 16.6 and 18.9 min. Only the peak at 16.6 min was also present in the DAD chromatogram at 361 nm and could be assigned to CNCbl from the crude **17** starting material ($C_{63}H_{88}CoN_{14}O_{14}P$ calcd. *m/z* $[M+H]^{+}$ = 1355.6 and $[M+2H]^{2+}$ = 678.3; found 1355.5 and 678.4).

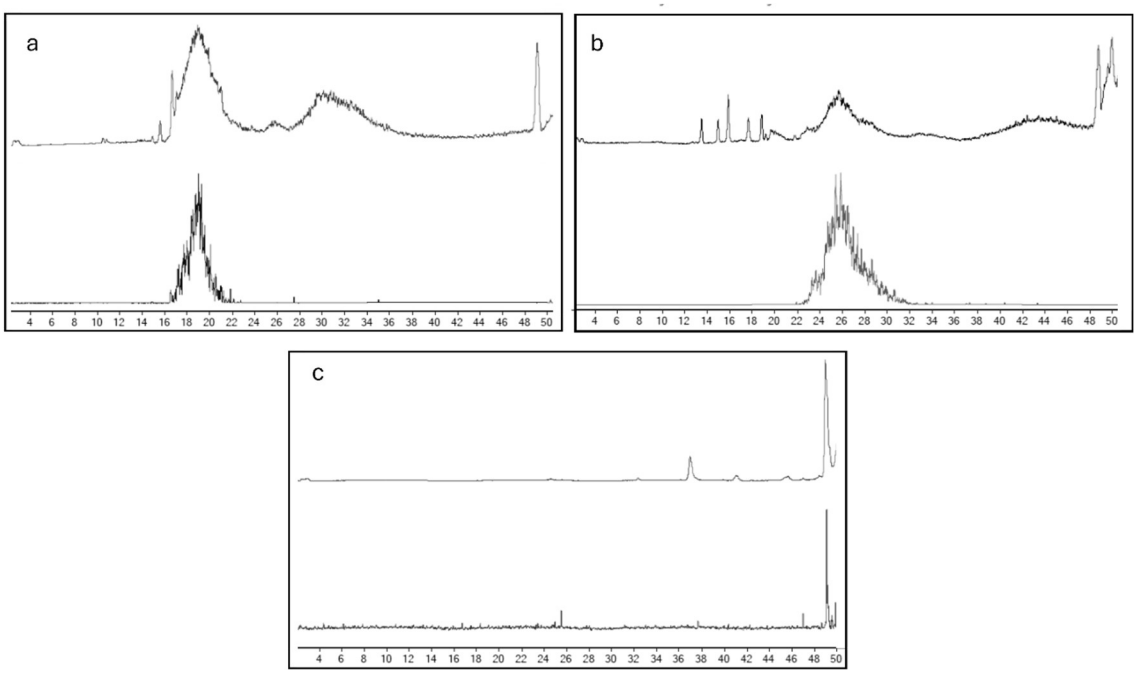

*Figure 187: LC-MS chromatograms of crude **21** with mobile phase modifications: a) TIC (top) and extracted ion chromatogram EIC, (1018 m/z, bottom, $C_{92}H_{142}CoN_{20}O_{26}P$ calcd. m/z $[M+2H]^{2+}$ = 1018.0) using (H_2O+0.1% formic acid) and (CH_3CN+0.1% formic acid) as the mobile phase, b) TIC (top) and EIC (1018 m/z, bottom) with H_2O and CH_3CN as the mobile phase and c) TIC (top) and EIC (1018 m/z, bottom) where (H_2O+0.1% formic acid) and CH_3OH were used as the organic mobile phase component.*

Although the use of H_2O and CH_3CN as the mobile phase proved effective in separating the impurities from **21**, the broad peak shape of the desired product remains. Gentamicin, an aminoglycoside antibiotic, is a highly polar molecule with multiple available ionisation sites, notably the four amine moieties. Aminoglycosides are notoriously difficult to analyse by LC-MS or HPLC methods, often displaying poor retention and resolution.[40,41] Many analytical methods have been published with a focus on the separation of aminoglycosides from serum and food samples. These methods use reversed-phase or ion-pairing HPLC/LC-MS over short time frames (2-10 min).[42–44]

Further experiments were undertaken using different column matrices to see if the peaks could be sharpened. Three additional analytical columns were trialled; Hypercarb (porous graphitic carbon stationary phase), ZIC-HILIC (zwitterionic hydrophilic interaction liquid ion-pair), Kinetex EVO C18 in addition to the Phenomenex Luna C18 column

(standard column used throughout this research). In addition to different column matrices, shorter mobile phase programs were used to decrease the contact time with the stationary phase and reduce peak broadening. The LC-MS chromatograms can be seen in Figure 188 (only the TIC chromatograms are shown for clarity). Each column required different solvent combinations; the mobile phase programs used are summarised in Table 12. The sample run through the Hypercarb graphite column showed minimal separation. Compound **21** eluted first as a broad peak between 10-11 min but overlapped with multiple impurities observed in the mass spectrum. The latter retaining peak between 16-21 min was absent in the DAD chromatogram at 361 nm and does not correspond to a CNCbl derivative. With the Kinetex EVO C18 column, the elution order was modified and compound **21** eluted between 10-14 min, again as a broad peak. This peak also co-eluted with an unidentified impurity between 10-11 min (*m/z* values of 994.6 and 1258.4). The ZIC-HILIC column was the least successful, with compound **21** not identified in either the TIC or DAD chromatograms. Five overlapping peaks were present between 9-12 min, but none had *m/z* values consistent with the desired compound. This was unexpected as a large number of literature procedures for the analysis of aminoglycoside antibiotics use this methodology.[40] It is suggested that upon conjugation to CNCbl, ion exchange chromatography is no longer effective. Finally, the sample run on the Phenomenex Luna C18 column, used ubiquitously throughout this research, with a shorter mobile phase program, showed the best analyte separation. Several sharp peaks retain between 11.5-14.5 min. The peak at 12.9 min in the DAD chromatogram at 361 nm can be assigned to unreacted CNCbl from the crude starting material ($C_{63}H_{88}CoN_{14}O_{14}P$ calcd. m/z $[M+H]^+$ = 1355.6 and $[M+2H]^{2+}$ = 678.3; found 1355.4 and 678.4). Compound **21** eluted as a broad peak between 15-17 min ($C_{92}H_{142}CoN_{20}O_{26}P$ calcd. *m/z* $[M+2H]^{2+}$ = 1018.0 and $[M+3H]^{3+}$ = 679.0; found 1017.9 and 678.8).

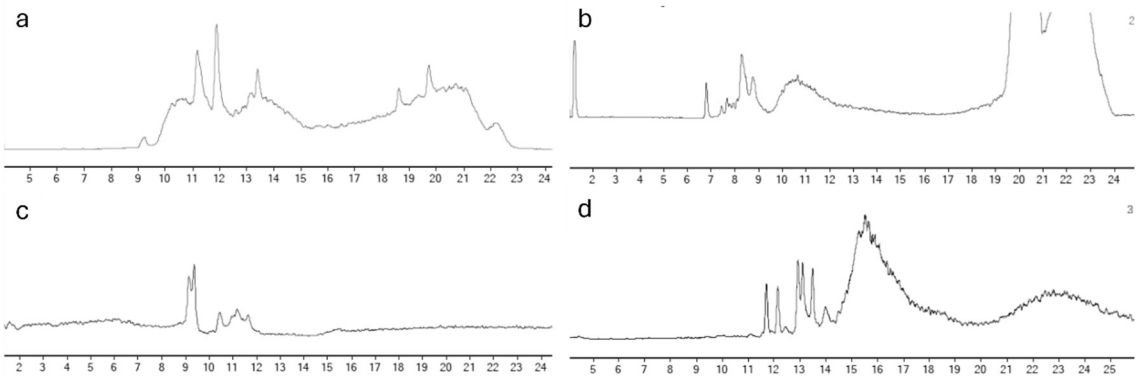

*Figure 188: LC-MS TIC chromatograms of crude **21** trialled on different analytical columns: a) Hypercarb (2.1 mm x100 mm), b) Kinetex EVO C18 (2.1 mm x 150 mm), c) ZIC-HILIC (2.1 mm x 150 mm), and d) Phenomenex Luna C18 (5 mm x 100 mm). Mobile solvents and programs are summarised in Table 12.*

*Table 12: LC-MS mobile phase methods for the analysis of crude **21** on different analytical columns.*

Column (dimensions)	Solvent A	Solvent B	Mobile phase program
Hypercarb (2.1 mm x100 mm)[a]	H_2O + 0.1% formic acid	CH_3CN + 0.1% formic acid	0-3 min 95:5 A:B, 3-6 min 95:5 to 65:35 A:B, 6-9 min 65:35 A:B, 9-12 min 65:35 to 20:80 A:B, 12-14 min 20:80 to 10:90 A:B.
Kinetex EVO C18 (2.1 mm x 150 mm)[b]	Ammonium formate (10 mM, pH 6.8)	CH_3CN + 0.1% formic acid	0-1 min 90:10 A:B, 1-8 min 90:10 to 50:50 A:B, 8-12 min 50:50 A:B, 12-15 min 50:50 to 10:90 A:B.
ZIC-HILIC (2.1 mm x 150 mm)[c]	Ammonium formate (10 mM, pH 6.8)	CH_3OH	0-2 min 15:85 A:B, 2-8 min 15:85 to 20:50 A:B, 8-15 min 50:50 A:B.

Phenomenex Luna C18 (5 mm x 100 mm)[d]	H_2O	CH_3CN	0-2 min 95:5 A:B, 2-20 min 95:5 to 35:65 A:B, 20-25 35:65 A:B, 25-26 35:65 to 90:10 A:B.

[a-d] *Refer to the corresponding LC-MS chromatograms shown in Figure 188.*

Several attempts have been made to improve peak shape and separation by LC-MS. The Phenomenex Luna C18 provided the best separation of analytes where H_2O and CH_3CN were used as the mobile phase. However, the peak shape could not be improved and compound **21** continued to elute as a broad peak. This highlights the difficulties faced during LC-MS or HPLC analysis of aminoglycoside compounds. Purification of compound **21** was achieved by reversed-phase C18 chromatography, using H_2O and CH_3CN as a solvent system and running a slow gradient from 0% to 50% CH_3CN, increasing by 5% organic solvent in 200 mL aliquots. The C18 stationary phase was shortened (5 cm height, 2 cm width), to minimise the compound contact time with the silica whilst retaining separation capabilities. When a coloured (red) band began to travel through the silica, the mobile phase was maintained until the band was removed and small fractions were collected (~5 mL). The fractions were then individually analysed by LC-MS using the optimised LC-MS program for this column in Table 12. Fractions containing the desired product with minimal impurities were combined and taken to dryness. The combined fractions were analysed by LC-MS. Compound **21** eluted as a broad peak between 13-16 min (Figure 189). A small broad peak between 11-12 min with *m/z* values of 1038.9 and 693.2 could be assigned to the CH_3CN adduct of compound **21** ($C_{92}H_{142}CoN_{20}O_{26}P$ calcd. *m/z* $[M+2H+CH_3CN]^{2+}$ = 1039.0 and $[M+3H+CH_3CN]^{3+}$ = 693.1; found 1038.9 and 693.0).

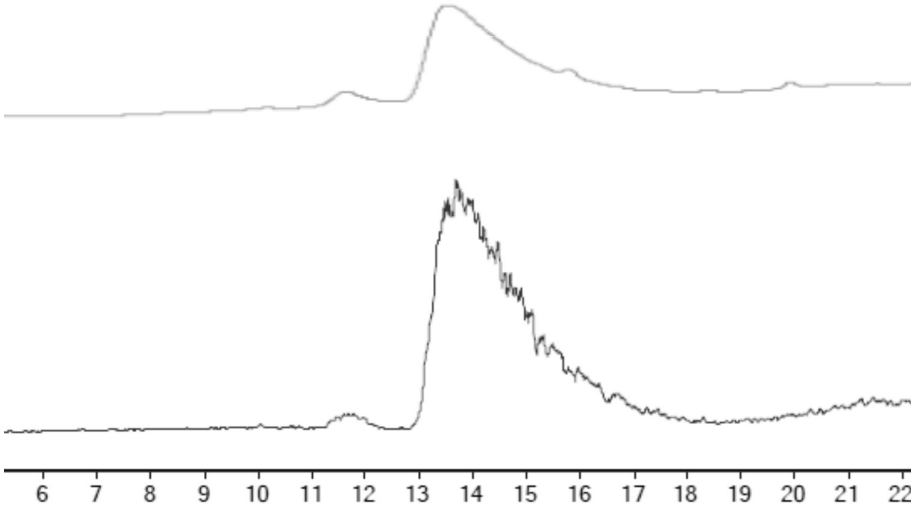

*Figure 189: LC-MS DAD (361 nm, top) and TIC (bottom) chromatograms of pure **21** using a Phenomenex Luna C18 column (LC-MS method 4). The broad peak between 13-16 min can be assigned to **21** ($C_{92}H_{142}CoN_{20}O_{26}P$ calcd. m/z $[M+2H]^{2+}$ = 1018.0 and $[M+3H]^{3+}$ = 679.0; found 1017.9 and 678.9).*

The broad peak of the desired product suggests that isomers of **21** may be present. Since isomers could not be resolved by LC-MS, further analysis by NMR spectroscopy was undertaken to investigate this further. ^{1}H NMR analysis was first carried out for gentamicin C1a in D_2O where peak assignments were made based on previously published values.[45] Proton peak assignments are made using atom numbering in Figure 190. The peaks are assigned as follows 5.35 (d, *J* = 3.6 Hz, 1H, ***20***), 5.28 (d, *J* = 4.0 Hz, 1H, ***1***), 4.22 (d, *J* = 12.6 Hz, 1H, ***5a***), 4.06 (m, 1H, ***24***), 3.98 (dd, *J* = 10.7, 4.0 Hz, 1H, ***2***), 3.79 (t, *J* = 9.3 Hz, 1H, ***12***), 3.57 – 3.39 (m, 3H, ***11/13/5b***), 3.07 (m, 3H, ***14/16/21***), 2.95 – 2.81 (m, 2H, ***25***), 2.76 (d, *J* = 10.7 Hz, 1H, ***3***), 2.71 (s, 3H, ***9***), 2.16 (dt, *J* = 13.1, 4.2 Hz, 1H, ***15 eq***), 1.93-1.51 (m, 4H, ***22/23***), 1.49 – 1.34 (m, 1H, ***15 ax***), 1.40 ppm (s, 3H, ***7***) (Figure 191). The protons at position 5 resonate at different locations (4.22 and overlapping with the multiplet at 3.57-3.39 ppm), due to equatorial or axial orientations but could not be assigned. The same can be seen for the protons at position 15, resonating at 2.16 and 1.34 ppm, respectively.

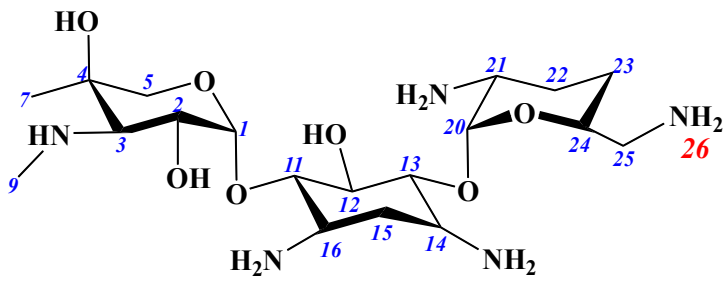

Figure 190: The structure of genatmicin C1a. The numbering scheme is shown in blue and the most basic and sterically accessible amine is highlighted as number 26 (pK_a = 9.9).

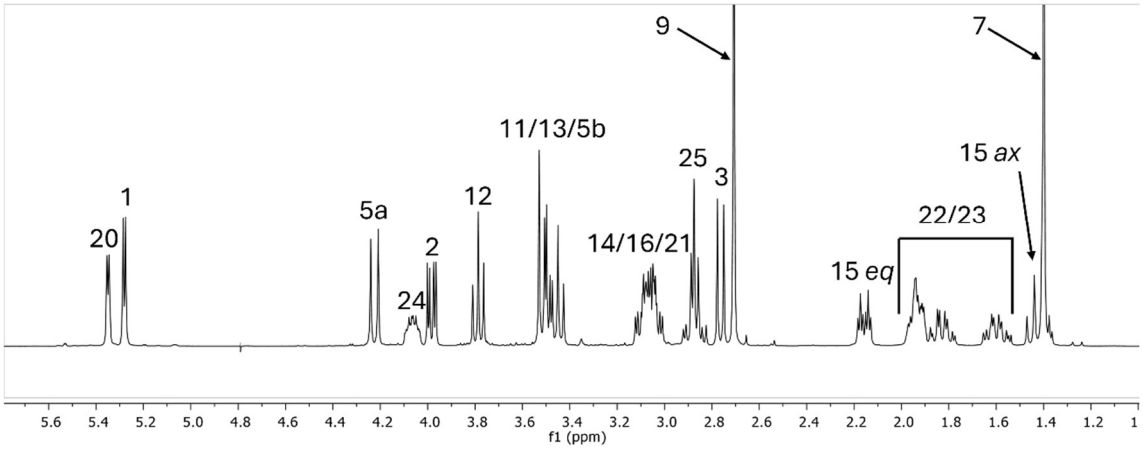

Figure 191: Assigned ^{1}H NMR spectrum of commercially purchased gentamicin C1a. The atomic numbering scheme is shown in Figure 190.

The ^{1}H NMR spectrum of **21** was also obtained in D_2O so a direct comparison with the gentamicin C1a spectrum could be made. The five aromatic signals of the CNCbl moiety have been assigned as 6.24 (s, 1H, C10), 6.49 (d, 1H, R1), 6.70 (s, 1H, B4), 7.26 (s, 1H, B4) and 7.45 ppm (s, 1H, B7, Figure 192). The two downfield peaks of gentamicin C1a were easily identified at 5.32 and 5.53 ppm. The broad peak observed in the LC-MS suggested that multiple isomers of **21** may have been formed. However, if different isomers of **21** were present, then more than two peaks for gentamicin would resonate between ~5-8 ppm of the ^{1}H NMR spectrum. This was not observed, indicating that only one isomer of **21** is present. The peaks at 5.32 (d, 1H, J = 4.0 Hz) and 5.53 (d, 1H, J = 3.2 Hz), ppm correspond to protons **1** and **20** of gentamicin but cannot be unequivocally assigned. However, J values compared to those of unconjugated gentamicin C1a tentatively suggest that the peak at 5.32 belongs to proton **1** (J = 4.0 Hz) and the peak at 5.53 ppm belongs to proton **20** (J = 3.6 Hz). A downfield shift of 0.18 ppm in the signal assigned to proton **20** supports the conjugation of gentamicin occurring at one of the

amine substituents of carbons 25, 21 or 14. The complex up-field NMR spectrum of CNCbl made the identification of gentamicin peaks challenging. However, the multiplet assigned to position **24** of unconjugated gentamicin seen at 4.06 ppm (1H, Figure 191) is no longer observed in the NMR spectrum of **21**. It is likely that this peak has shifted upon conjugation to CNCbl and overlaps with another peak in the spectrum. This suggests conjugation at the least sterically hindered amine highlighted in blue in Figure 190.

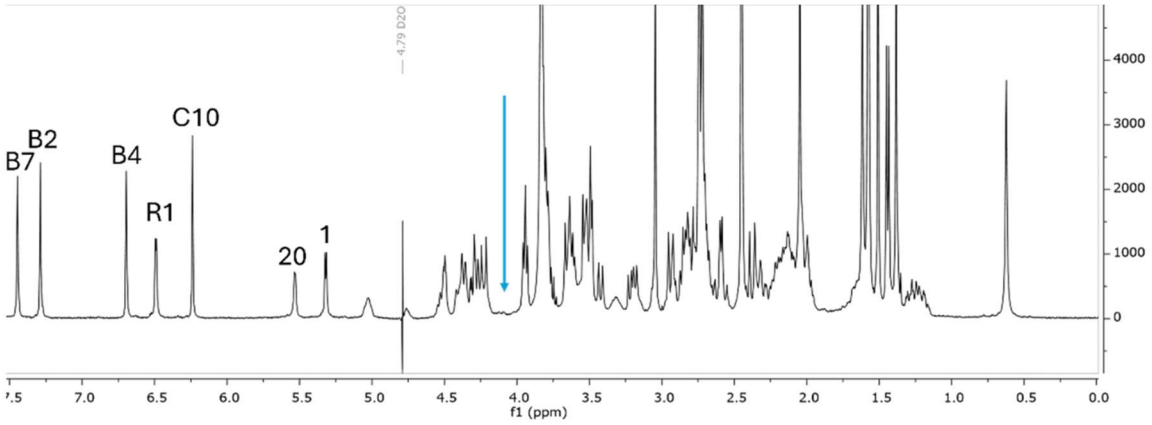

*Figure 192: ^{1}H NMR spectrum of **21** obtained in D_2O. Peak assignments of the CNCbl moiety are 6.24 (s, 1H, C10), 6.49 (d, 1H, R1), 6.70 (s, 1H, B4), 7.26 (s, 1H, B4) and 7.45 ppm (s, 1H, B7) with gentamicin protons at 5.53 (d, J = 3.2 Hz, 1H, **20**) and 5.32 ppm (d, J = 4.0 Hz, 1H, **1**) highlighted. The blue arrow highlights the missing resonance of gentamicin for the proton on carbon 24 at 4.06 ppm (m, 1H) in gentamicin itself.*

To summarise, the shift in protons **24** and **20** of gentamicin and the highest pK_a of amine **26** of gentamicin C1a indicate that one isomer of compound **21** was isolated, and it is most likely conjugated via the less sterically hindered amine. The formation of the CNCbl-gentamicin conjugate, **21**, was confirmed by HRMS ($C_{92}H_{142}O_{26}N_{20}CoNa_2P$ calcd. *m/z* for [M+2Na] 1039.4629, found 1039.4637). LC-MS and ^{1}H NMR analysis of the purified product support the formation of **21** with a purity of ≥95%.

Compound 22

The synthesis of the CNCbl-linker-ciprofloxacin conjugate **20** using a disulfide-containing linker suggested that a CNCbl-linker-gentamicin complex could be successfully synthesised using a similar synthetic approach. To synthesise compound **20**, the cystamine linker was employed. The terminal amines of the linker provide a site to

attach CNCbl via a carbamate bond and the carboxylic acid of ciprofloxacin by an amide bond. Gentamicin, however, does not have a carboxylic acid suitable for amide coupling. Rather than modify the complex gentamicin molecule, the cystamine analogue, 3-[(2-aminoethyl)dithio]propionic acid was substituted as the linker (Figure 193).

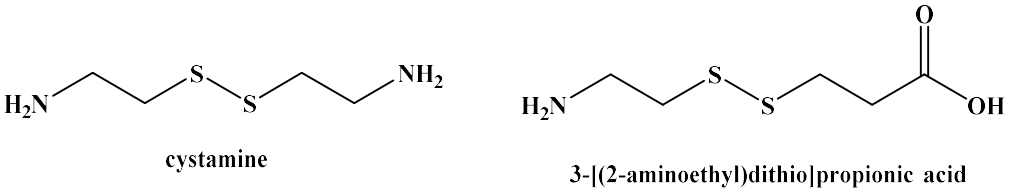

Figure 193: Structures of disulfide-containing linkers employed in this study, cystamine and 3-[(2-aminoethyl)dithio]propionic acid.

The initial attempt to synthesise **22** used the procedure employed for previous CNCbl-linker molecules. CNCbl was used as the limiting reagent, CDT added (3.0 eq.) and the solution stirred in anhydrous DMSO at 40°C for 30 min. A solution of 3-[(2-aminoethyl)dithio]propionic acid in DMSO (3.0 eq.) was then added to the CNCbl solution and the solution stirred for a further 6 h at 40 °C (Scheme 37).

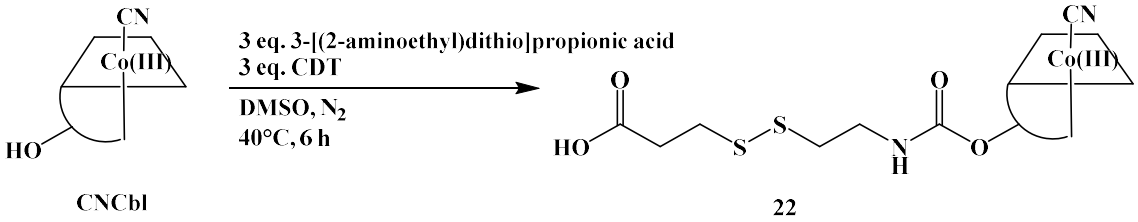

*Scheme 37: Synthetic scheme for the synthesis of **22**.*

The crude product solution was analysed by LC-MS. Four major peaks were identified. Interestingly, the first peak eluting at 21.2 min could be assigned to the CNCbl-cystamine containing product **1**, discussed in Chapter 2 ($C_{68}H_{98}CoN_{16}O_{15}PS_2$ calcd. *m/z* $[M+H]^+$ = 1534.3 and $[M+2H]^{2+}$ = 767.4; found 767.4). The peak at 23.0 min was from unreacted CNCbl ($C_{63}H_{88}CoN_{14}O_{14}P$ calcd. *m/z* $[M+H]^+$ = 1355.6 and $[M+2H]^{2+}$ = 678.3; found 1355.5 and 678.4). The large peak at 26.3 min corresponded to the methyl ester of CNCbl following activation by CDT ($C_{65}H_{90}CoN_{14}O16P$ calcd. *m/z* $[M+H]^+$ = 1413.6 and $[M+2H]^{2+}$ = 707.3; found 1413.7 and 707.3, Scheme 38). This intermediate is observed when CDT activation of the 5'-OH of CNCbl is successful but the linker fails to substitute

the triazole moiety. During the synthesis the crude solution is dissolved in CH_3OH following precipitation resulting in nucleophilic attack by CH_3OH on the intermediate (Scheme 38). The final peak eluting at 34.0 min can be assigned to the desired compound **22** ($C_{69}H_{97}CoN_{15}O_{17}PS_2$ calcd. *m/z* $[M+H]^+$ = 1562.6 and $[M+2H]^{2+}$ = 781.8; found 1562.7 and 781.9).

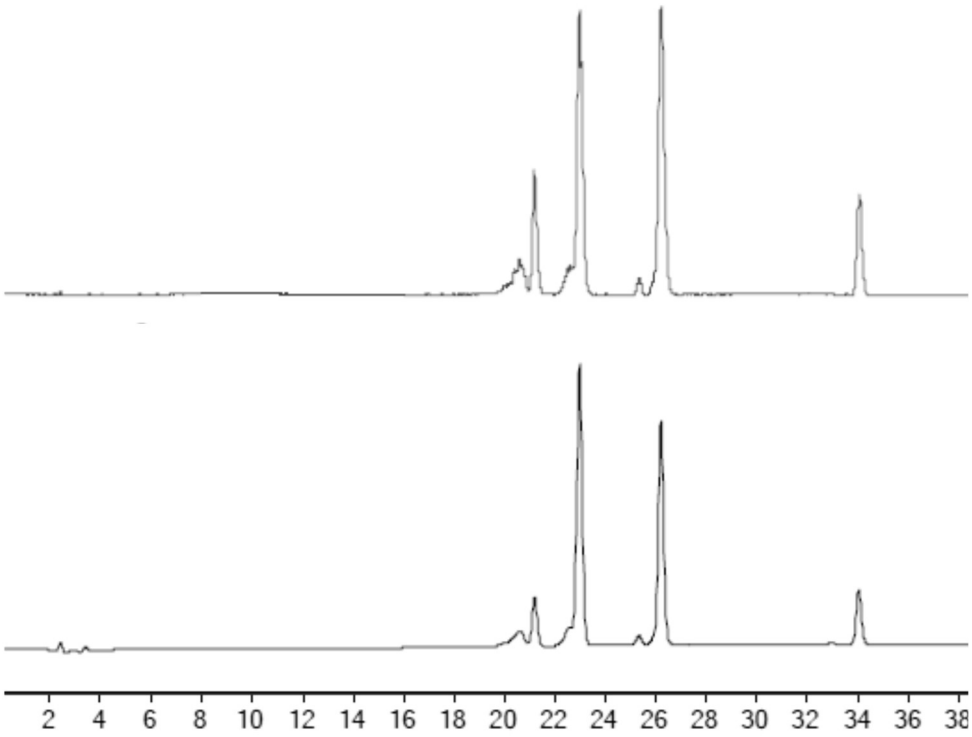

*Figure 194: LC-MS TIC (top) and DAD (361 nm, bottom) chromatograms of crude **22** using 3-[(2-aminoethyl)dithio]propionic acid (LC-MS method 2). The peak at 34.0 min can be assigned to compound **22** ($C_{69}H_{97}CoN_{15}O_{17}PS_2$ calcd. m/z $[M+H]^+$ = 1562.6 and $[M+2H]^{2+}$ = 781.8; found 1562.7 and 781.9).*

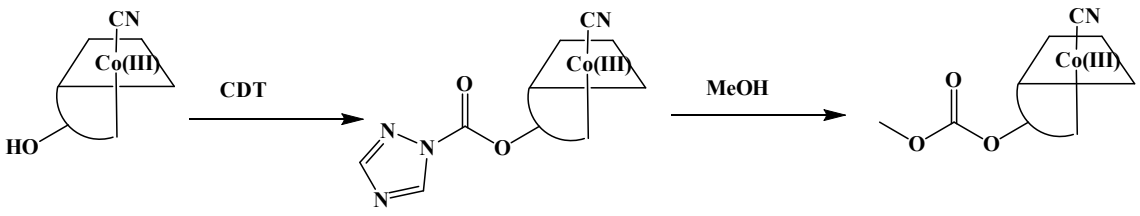

Scheme 38: Formation of a CNCbl-methyl ester after activation by CDT where the triazole moiety is substituted by CH_3OH rather than the -NH_2 of the linker.

The formation of compound **1** during the synthesis of **22** was unexpected. The ^{1}H NMR spectrum of the commercially purchased 3-[(2-aminoethyl)dithio]propionic acid was recorded in D_2O. Three multiplets were observed at 3.45 – 3.35 (m, 2H), 3.07 – 2.96 (m, 3H) and 2.84 ppm (m, 1H). Based on the structure of the linker, the multiplet peaks were expected to integrate to a total of eight protons (not including the exchanging OH and NH_2 protons, Figure 196). The obtained NMR spectrum however showed more complex splitting, and the peak integrations totalled six protons.

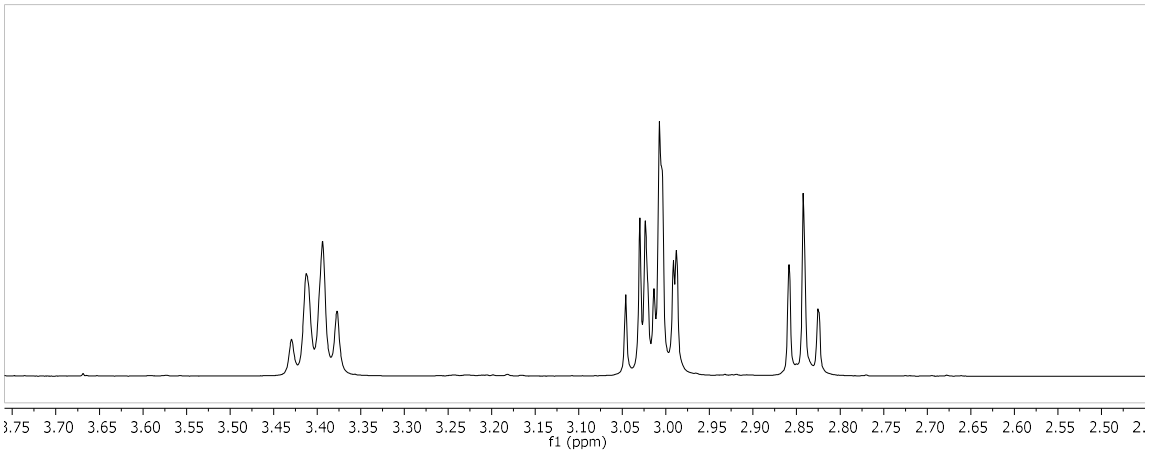

Figure 195: ^{1}H NMR spectrum of commercially purchased 3-[(2-aminoethyl)dithio]propionic acid obtained D_2O. Three multiplets were identified at 3.45–3.35 (2H), 3.07–2.96 (3H) and 2.84 ppm (1H).

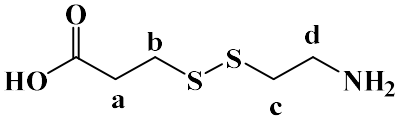

*Figure 196: Structure of 3-[(2-aminoethyl)dithio]propionic acid with non-exchanging protons labelled as **a-d**.*

3-[(2-Aminoethyl)dithio]propionic acid was then purchased as the HCl salt as this compound is likely more stable in the solid state. The ^{1}H NMR spectrum of 3-[(2-aminoethyl)dithio]propionic acid HCl was obtained in D_2O (Figure 197). Multiplets were observed at 3.43-3.37 (m, 2H), 3.05-2.96 (m, 4H) and 2.87-2.82 ppm (m, 2H) and assigned to protons **d**, (**c** + **b)** and **a**, respectively (Figure 196). The proton signals of the HCl salt display the expected splitting and integrations for the 3-[(2-aminoethyl)dithio]propionic acid linker.

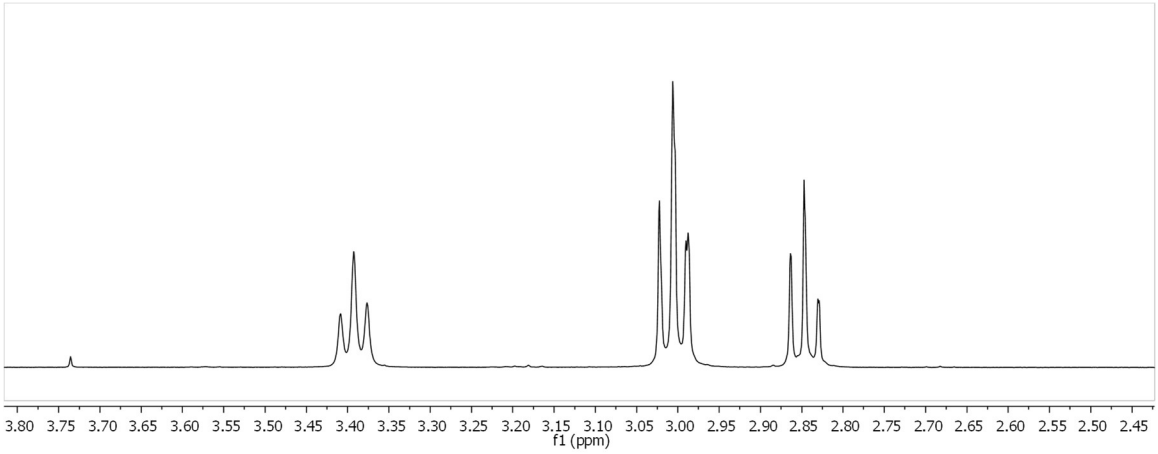

*Figure 197:[1]H NMR spectrum of commercially purchased 3-[(2-aminoethyl)dithio]propionic acid.HCl obtained in D_2O. Three multiplets were identified at 3.43-3.37 (m, 2H, **d**), 3.05-2.96 (m, 4H, **b**+**c**) and 2.87-2.82 ppm (m, 2H, **a**).*

Synthesis of **22** was attempted using the 3-[(2-aminoethyl)dithio]propionic acid HCl salt under analogous conditions to those used in the previous synthesis with the addition of Et_3N (5.0 eq.). The LC-MS chromatogram of the crude product showed two large peaks in the DAD chromatogram at 361 nm (Figure 198). The peak at 23.0 min is assigned to unreacted CNCbl ($C_{63}H_{88}CoN_{14}O_{14}P$ calcd. *m/z* $[M+H]^+$ = 1355.6 and $[M+2H]^{2+}$ = 678.3; found 1355.5 and 678.4) and the peak at 34.0 min can be assigned to compound **22** ($C_{69}H_{97}CoN_{15}O_{17}PS_2$ calcd. *m/z* $[M+H]^+$ = 1562.6 and $[M+2H]^{2+}$ = 781.8; found 1562.7 and 781.9). The use of 3-[(2-aminoethyl)dithio]propionic acid.HCl as the starting material was more successful in producing the desired compound. No evidence of the CNCbl-methyl ester was found in the LC-MS; however a small peak at 21.2 min could be assigned to compound **1** ($C_{68}H_{98}CoN_{16}O_{15}PS_2$ calcd. *m/z* $[M+H]^+$ = 1534.3 and $[M+2H]^{2+}$ = 767.4; found 767.4). Hence, the 3-[(2-aminoethyl)dithio]propionic acid.HCl must also contain a small amount of cystamine.

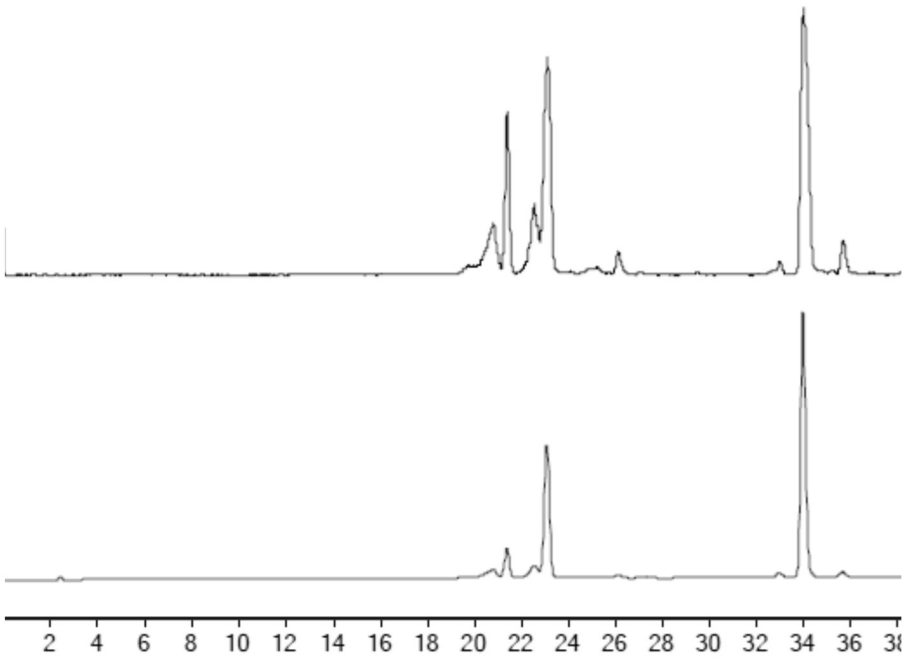

*Figure 198: LC-MS TIC (top) and DAD (361 nm, bottom) chromatograms of crude **22** using the 3-[(2-aminoethyl)dithio]propionic acid.HCl starting material (LC-MS method 2). The peak at 34.0 min can be assigned to compound **22** ($C_{69}H_{97}CoN_{15}O_{17}PS_2$ calcd. m/z $[M+H]^+$ = 1562.6 and $[M+2H]^{2+}$ = 781.8; found 1562.7 and 781.9).*

Purification of **22** was achieved by reversed-phase C18 chromatography with the desired compound eluting at 15% CH_3CN in (H_2O + 0.1% formic acid). LC-MS analysis of the purified product identified one peak eluting at 40.1 min corresponding to compound **22** ($C_{69}H_{97}CoN_{15}O_{17}PS_2$ calcd. *m/z* $[M+H]^+$ = 1562.6 and $[M+2H]^{2+}$ = 781.8; found 1562.7 and 781.9, Figure 199).

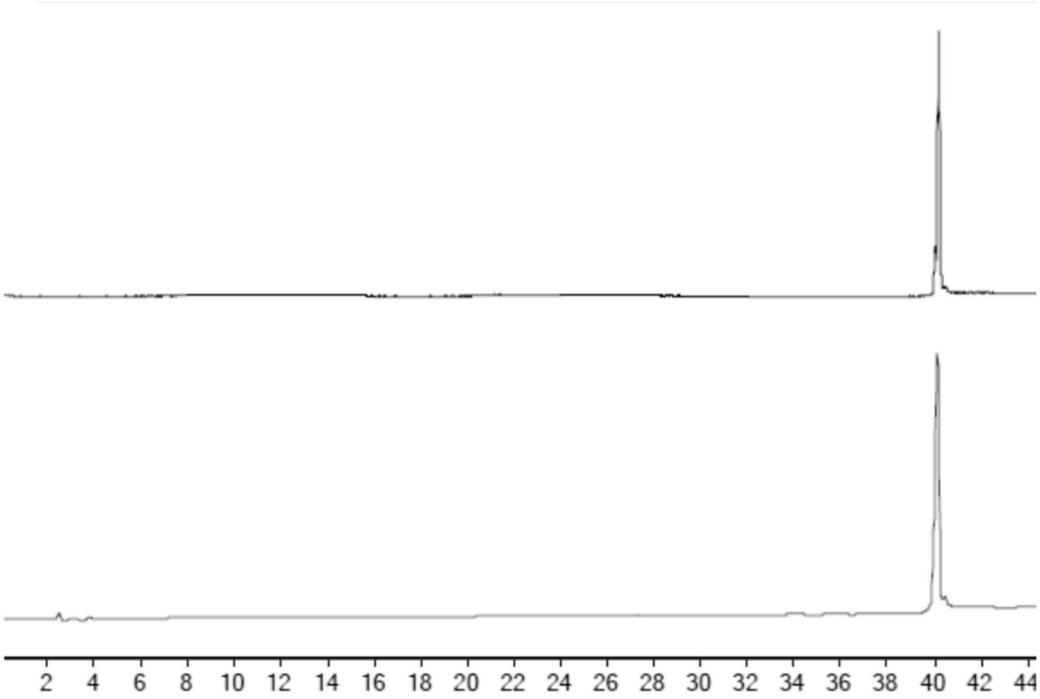

*Figure 199: LC-MS TIC (top) and DAD (361 nm, bottom) chromatograms of pure **22** (LC-MS method 2). The peak at 40.1 min can be assigned to compound **22** ($C_{69}H_{97}CoN_{15}O_{17}PS_2$ calcd. m/z $[M+H]^+$ = 1562.6 and $[M+2H]^{2+}$ = 781.8; found 1562.7 and 781.9).*

The ^{1}H NMR spectrum of **22** in MeOH-d_4 showed five peaks resonating in the aromatic region. These were assigned as 6.04 (s, 1H, C10), 6.23 (d, 1H, R1), 6.57 (s, 1H, B4), 7.15 (s, 1H, B2) and 7.24 ppm (s, 1H, B7, Figure 200). The broad peak at 7.77 ppm (0.81 H) can be assigned to a slowly exchanging -NH proton of CNCbl.

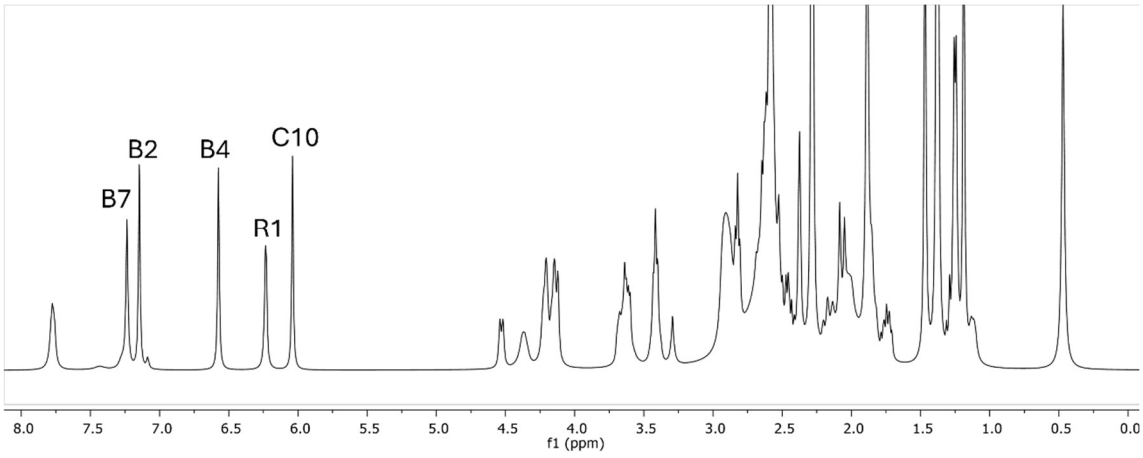

*Figure 200: ^{1}H NMR spectrum of **22** obtained in MeOH-d_4. The aromatic peaks can be assigned to the CNCbl protons 6.04 (s, 1H, C10), 6.23 (d, 1H, R1), 6.57 (s, 1H, B4), 7.15 (s, 1H, B2) and 7.24 ppm (s, 1H, B7).*

Further NMR analysis was carried out in DMSO-d_6 where a ^{13}C NMR spectrum can be obtained owing to greater solubility (~20 mg per 500 µL). The new carbamate carbon peak can be observed at 156.2 ppm (Figure 201).

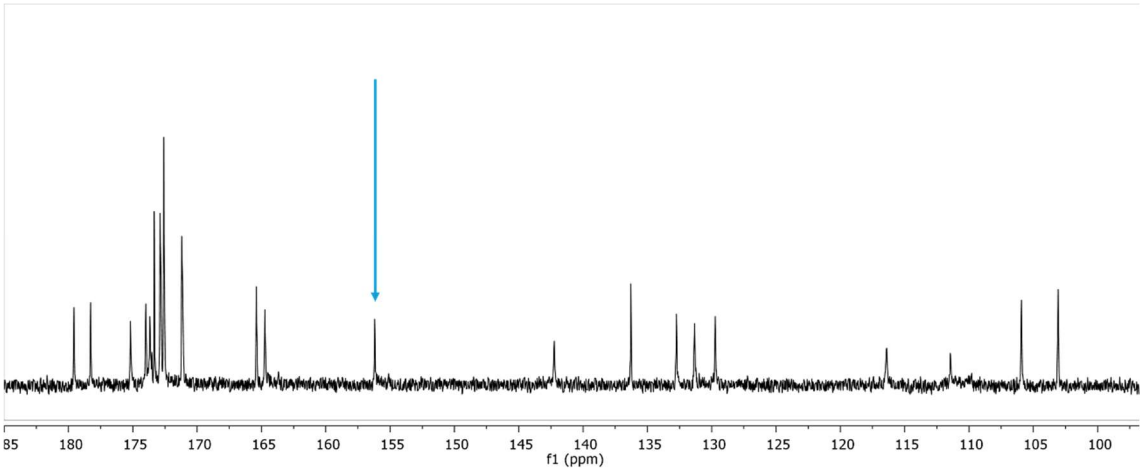

*Figure 201: Aromatic region of the ^{13}C NMR spectrum of **22** obtained in DMSO-d_6. A new resonance at 156.2 ppm is highlighted and is assigned to the newly formed carbamate carbon.*

Finally, 2D NMR analysis was carried out. This allowed for assignments of the aromatic protons C10, R1, B4, B2 and B7, and the corresponding carbons of the CNCbl moiety to be assigned as 5.88 (93.6), 6.25 (86.0), 6.43 (116.4), 7.08 (142.3) and 7.36 ppm (111.5 ppm). The aromatic proton and corresponding carbon resonances of the CNCbl moiety are similar after the conjugation of the 3-[(2-aminoethyl)dithio]propionic acid linker (peaks of CNCbl are (5.91 (93.4), 6.28 (85.4), 6.45 (116.2), 7.01 (111.4) and 7.32 ppm (142.3 ppm)).

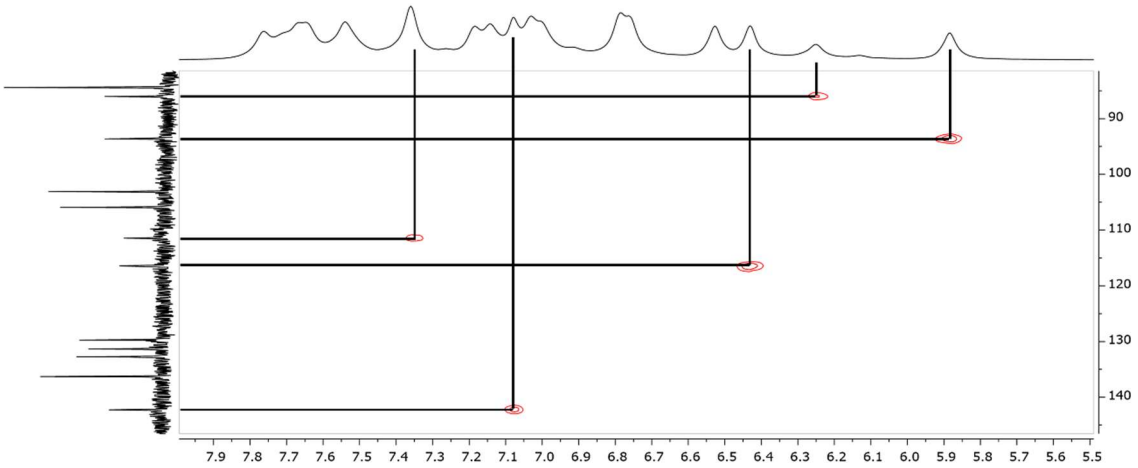

*Figure 202: Aromatic region of the 2D HSQC NMR spectrum of **22**. CNCbl moiety protons C10, R1, B4, B2 and B7, and corresponding the carbons are highlighted and assigned to peaks at 5.88 (93.6), 6.25 (86.0), 6.43 (116.4), 7.08 (142.3) and 7.36 ppm (111.5 ppm).*

To summarise, synthesis of a CNCbl-linker-gentamicin conjugate was achieved in a 39% yield. Fortuitously, one isomer of the product was formed although gentamicin offered multiple amines suitable for conjugation. Purification by reversed-phase C18 chromatography was difficult, but isocratic conditions permitted the pure compound to be isolated. LC-MS and ^{1}H NMR analysis of **22** indicated that the purity of the complex is ≥95%.

Compound 23

The successful synthesis of **22** allowed the previously established amide coupling procedures for gentamicin to be employed to synthesise a disulfide containing CNCbl-linker-gentamicin conjugate. Analogous reaction conditions used for the synthesis of **21** were used for the synthesis of **23** (Scheme 39).

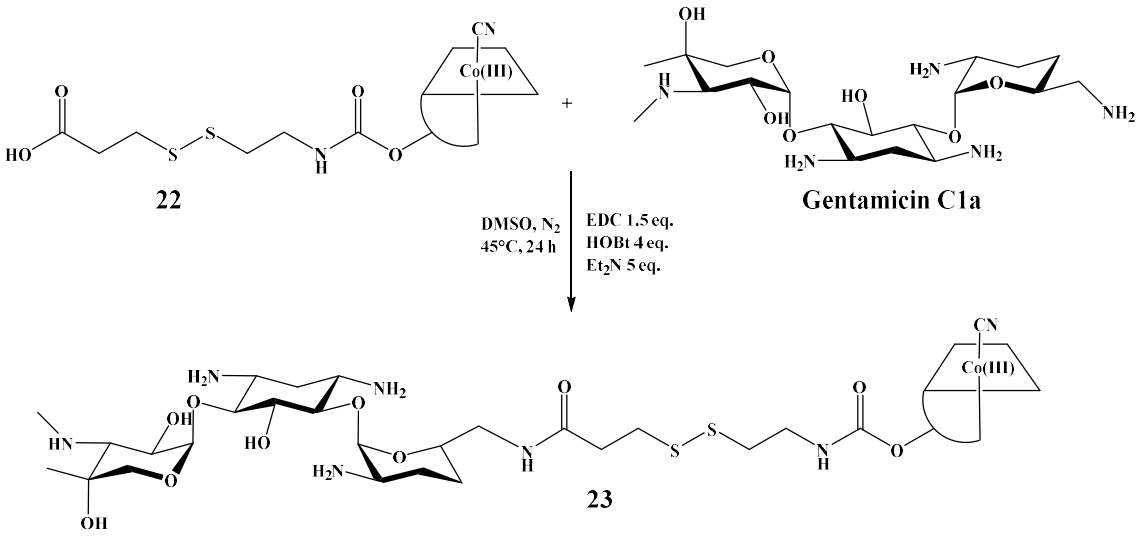

*Scheme 39: Synthetic scheme for the synthesis of **23**, assuming peptide bond formation occurs at the most nucleophilic amine of gentamicin C1a.*

LC-MS analysis of the crude product solution was carried out using the best conditions determined in Table 12 for compound **21**. The resulting chromatograms showed many overlapping peaks retaining between 10-18 min (Figure 203). Inspection of the *m/z* values of each peak showed that the starting material **22** (*m/z* = 1562.7 and 781.9) was no longer present. Furthermore, **23** was present between 14-17 min, together with impurities ($C_{88}H_{134}CoN_{20}O_{23}PS_2$ calcd. *m/z* $[M+2H]^{2+}$ = 997.6 and $[M+3H]^{3+}$ = 665.6; found 997.5 and 665.5). To further investigate the retention time of **23**, the EIC was obtained using *m/z* of 997 and 665 (representing calcd. *m/z* $[M+2H]^{2+}$ and $[M+3H]^{3+}$ where M = **23**). The EIC showed a broad peak between 14-17 min. As observed during the analysis of **21**, the CNCbl-linker-gentamicin complex does not elute as a sharp single peak in the LC-MS chromatograms.

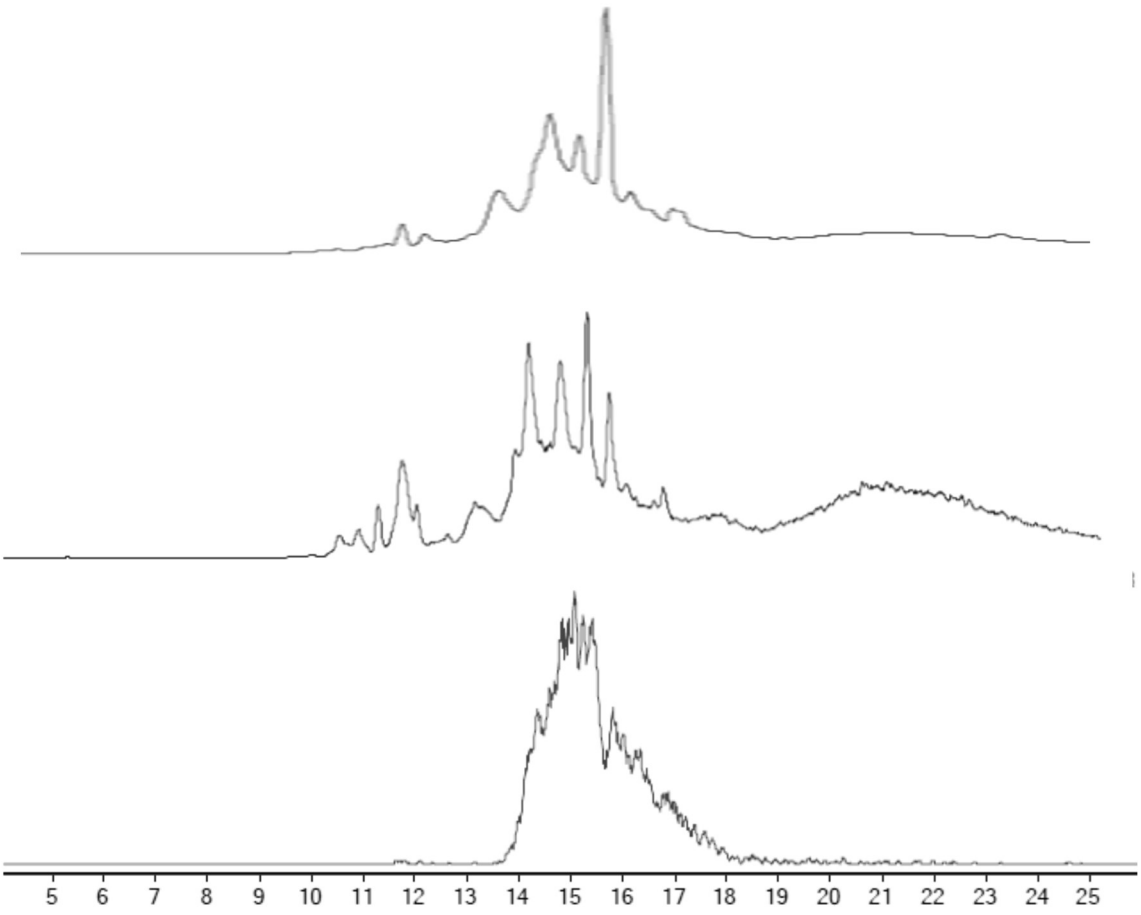

*Figure 203: LC-MS DAD (361 nm, top) TIC (middle) and EIC (997 m/z, bottom) of crude **23** (LC-MS method 4). The broad peak between 14-17 min can be assigned to **23** ($C_{88}H_{134}CoN_{20}O_{23}PS_2$ calcd. m/z $[M+2H]^{2+}$ = 997.6 and $[M+3H]^{3+}$ = 665.6; found 997.5 and 665.5).*

Although complex, the LC-MS results do indicate the successful synthesis of **23**. The product mixture was purified by reversed-phase C18 chromatography using a short column (5 cm height, 2 cm width) and H_2O and CH_3CN as the mobile phase. A weak gradient was used during purification. The desired compound eluted as a red band at 12.5% CH_3CN in H_2O and small (~3 mL) fractions were collected. Purification of **23** was difficult and required four columns to remove all impurities. LC-MS of the purified compound showed a broad peak eluting between 13-16 min (Figure 204). The *m/z* values across this peak were consistent with only compound **23** ($C_{88}H_{134}CoN_{20}O_{23}PS_2$ calcd. *m/z* $[M+2H]^{2+}$ = 997.6 and $[M+3H]^{3+}$ = 665.6; found 997.7 and 665.4).

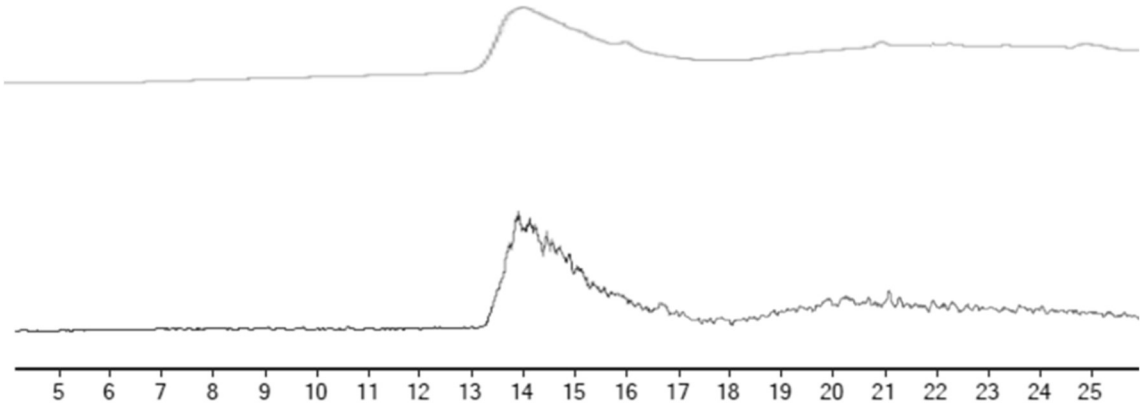

*Figure 204: LC-MS DAD (361 nm, top) and TIC (bottom) chromatogram of pure **23** (LC-MS method 4). The broad peak retaining between 13-16 min is assigned to **23** ($C_{88}H_{134}CoN_{20}O_{23}PS_2$ calcd. m/z $[M+2H]^{2+}$ = 997.6 and $[M+3H]^{3+}$ = 665.6; found 997.5 and 665.5).*

Gentamicin C1a contains many amine residues that would be susceptible to peptide bond formation. However, synthesis of **21** showed conjugation at the most nucleophilic amine (amine ***26***, Figure 190). Compound **23** was analysed by ^{1}H NMR spectroscopy in D_2O. The five aromatic resonances of the CNCbl moiety have been assigned as 6.24 (s, 1H, C10), 6.48 (d, 1H, R1), 6.70 (s, 1H, B4), 7.26 (s, 1H, B2) and 7.45 ppm (s, 1H, B7). The two downfield protons of the gentamicin moiety (**1** and **20**, Figure 190) resonate at 5.36 (d, 1H, J = 3.9 Hz) and 5.94 ppm (d, 1H, J = 3.6 Hz). When compared to the gentamicin starting material peaks at 5.35 (d, J = 3.6 Hz, 1H, ***20***) and 5.28 ppm (d, J = 4.0 Hz, 1H, ***1***), the likely assignments of the peak at 5.36 and 5.94 ppm in **23** are protons at positions ***1*** and ***20*** respectively (based on J value and peak height, Figure 190). The resonance of proton ***1*** is slightly shifted downfield upon conjugation to CNCbl from 5.28 ppm (unconjugated) to 5.36 and 5.32 ppm for compounds **21** and **23**, respectively. A larger shift is observed for proton ***20*** when conjugated to CNCbl, particularly for compound **23**, from 5.35 for unconjugated gentamicin to 5.53 in **21** and 5.94 ppm in **23**. This shift in resonance suggests conjugation at the least sterically hindered amine of gentamicin, analogous to that observed in compound **21**. The two peaks between 5.50 and 6.00 ppm for gentamicin further support the presence of only one isomer of compound **23**.

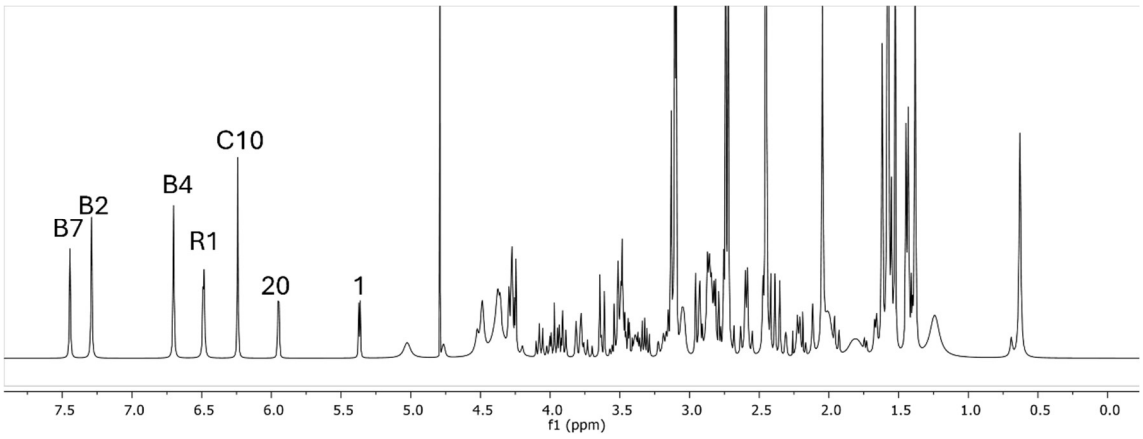

*Figure 205: ^{1}H NMR spectrum of **23** obtained in D_2O. Peaks assigned to the CNCbl moiety are 6.24 (s, 1H, C10), 6.48 (d, 1H, R1), 6.70 (s, 1H, B4), 7.26 (s, 1H, B2) and 7.45 ppm (s, 1H, B7). Peaks assigned to the gentamicin moiety are 5.36 (d, 1H, J = 3.9 Hz, **1**) and 5.94 ppm (d, 1H, J = 3.6 Hz, **20**).*

To summarise, LC-MS and ^{1}H NMR spectroscopy confirmed the purity of **23** was ≥95%. Complex purification by reversed-phase C18 chromatography, requiring four columns, afforded a low yield of 23%. However, HRMS analysis confirmed $C_{88}H_{136}O_{23}N_{20}CoPS_2$ was formed (calcd. for [M+2H] 997.4294, found 997.4290).

5.4 Conclusion

The synthesis and characterisation of CNCbl-linker molecules incorporating terminal carboxylic acids has been presented. These compounds have been analysed by LC-MS, ^{1}H NMR and ^{13}C NMR spectroscopy and were obtained in yields of 39-70% with purities ≥95%. Novel CNCbl conjugates of ciprofloxacin and gentamicin have also been synthesised. Conjugation of ciprofloxacin proved to be challenging when using the carboxylic acid functional group. Multiple synthetic strategies were trialled and HBTU was found to successfully activate the carboxylic acid functional group of ciprofloxacin. A second synthetic complication associated with the ciprofloxacin conjugates was its ability to polymerise, where the amine and carboxylic acid of two separate ciprofloxacin molecules form a peptide bond. Protecting the piperazine amine of ciprofloxacin prevented polymerisation from occurring. CNCbl-linker-ciprofloxacin compounds have been synthesised using either the carboxylic acid or piperazine -NH of ciprofloxacin. CNCbl-linker-gentamicin conjugates have been synthesised by peptide coupling at an amine of gentamicin. The analysis of the gentamicin compounds by LC-MS was

challenging. Compounds incorporating the gentamicin moiety showed significant peak broadening. Multiple analytical conditions were tested using different stationary and mobile phase combinations. Although optimised, LC-MS analysis still showed broadened peaks for the gentamicin analogues, highlighting the difficulties of aminoglycoside chromatography. ^{1}H NMR spectroscopy, however, proved useful for establishing the purity of the CNCbl-linker-gentamicin conjugates, and fortuitously indicated conjugation of gentamicin occurred only at the C1a amine moiety. Antibiotic conjugates of CNCbl were synthesised in yields of 9-78%, with the ciprofloxacin conjugates producing higher yields. Synthesis of the gentamicin conjugates proved the most challenging and afforded the lowest yields, likely owing to difficulties during purification. Purities of ≥95% were obtained for all conjugates, as determined by reversed-phase C18 chromatography and/or ^{1}H NMR spectroscopy. Finally, the successful synthesis of all of the CNCbl-linker-antibiotic conjugates was confirmed by HRMS.

5.5 References

(1) Proinsias, K.; Giedyk, M.; Gryko, D. Vitamin B_{12}: Chemical Modifications. *Chem. Soc. Rev.* **2013**, *42* (16), 6605–6619. https://doi.org/10.1039/c3cs60062a.
(2) Bridwell-Rabb, J.; Drennan, C. L. Vitamin B_{12} in the Spotlight Again. *Curr. Opin. Chem. Biol.* **2017**, *37*, 63–70. https://doi.org/10.1016/j.cbpa.2017.01.013.
(3) Równicki, M.; Wojciechowska, M.; Wierzba, A. J.; Czarnecki, J.; Bartosik, D.; Gryko, D.; Trylska, J. Vitamin B_{12} as a Carrier of Peptide Nucleic Acid (PNA) into Bacterial Cells. *Sci. Rep.* **2017**, *7* (1). https://doi.org/10.1038/s41598-017-08032-8.
(4) S, Z.; Zp, W.; X, W.; S, L.; G, W.; J, G.; Y, H. Synthesis of Vitamin B_{12}-Antibiotic Conjugates with Greatly Improved Activity against Gram-Negative Bacteria. *PubMed* **2020**.
(5) Równicki, M.; Dąbrowska, Z.; Wojciechowska, M.; Wierzba, A. J.; Maximova, K.; Gryko, D.; Trylska, J. Inhibition of Escherichia Coli Growth by Vitamin B_{12}–Peptide Nucleic Acid Conjugates. *ACS Omega* **2019**, *4* (1), 819–824. https://doi.org/10.1021/acsomega.8b03139.
(6) Giedyk, M.; Jackowska, A.; Równicki, M.; Kolanowska, M.; Trylska, J.; Gryko, D. Vitamin B_{12} Transports Modified RNA into E. Coli and S. Typhimurium Cells. *Chem. Commun.* **2019**, *55* (6), 763–766. https://doi.org/10.1039/c8cc05064c.
(7) Chen, Z.; Liang, Y.; Feng, X.; Liang, Y.; Shen, G.; Huang, H.; Chen, Z.; Yu, J.; Liu, H.; Lin, T.; Chen, H.; Wu, D.; Li, G.; Zhao, B.; Guo, W.; Hu, Y. Vitamin-B_{12}-Conjugated PLGA-PEG Nanoparticles Incorporating miR-532-3p Induce Mitochondrial Damage by Targeting Apoptosis Repressor with Caspase Recruitment Domain (ARC) on CD320-Overexpressed Gastric Cancer. *Mater. Sci. Eng. C* **2021**, *120*, 111722. https://doi.org/10.1016/j.msec.2020.111722.
(8) Chaves, B. J.; Tadi, P. Gentamicin. In *StatPearls*; StatPearls Publishing: Treasure Island (FL), **2024.**
(9) Gomarasca, M.; Martins, T. F. C.; Greune, L.; Hardwidge, P. R.; Schmidt, M. A.; Rüter, C. Bacterium-Derived Cell-Penetrating Peptides Deliver Gentamicin to Kill Intracellular Pathogens. *Antimicrob. Agents Chemother.* **2017**, *61* (4). https://doi.org/10.1128/AAC.02545-16/FORMAT/EPUB.
(10) Thai, T.; Salisbury, B. H.; Zito, P. M. Ciprofloxacin. In *StatPearls*; StatPearls Publishing: Treasure Island (FL), **2024.**
(11) Dahiya, S.; Chuttani, K.; K. Khar, R.; Saluja, D.; K. Mishra, A.; Chopra, M. Synthesis and Evaluation of Ciprofloxacin Derivatives as Diagnostic Tools for Bacterial Infection by Staphylococcus Aureus. **2009**. https://doi.org/10.1039/B908474F.
(12) Assali, M.; Joulani, M.; Awwad, R.; Assad, M.; Almasri, M.; Kittana, N.; Zaid, A. N. Facile Synthesis of Ciprofloxacin Prodrug Analogues to Improve Its Water Solubility and Antibacterial Activity. *ChemistrySelect* **2016**, *1* (6), 1132–1135. https://doi.org/10.1002/slct.201600091.
(13) Patel, U. K.; Tiwari, P.; Tilak, R.; Joshi, G.; Kumar, R.; Agarwal, A. Synthesis of Ciprofloxacin-Linked 1,2,3-Triazole Conjugates as Potent Antibacterial Agents Using Click Chemistry: Exploring Their Function as DNA Gyrase Inhibitors via in Silico- and in Vitro-Based Studies. *RSC Adv.* **2024**, *14* (24), 17051–17070. https://doi.org/10.1039/D4RA01332H.
(14) Patra, P.; Mitra, S.; Debnath, N.; Pramanik, P.; Goswami, A. Ciprofloxacin Conjugated Zinc Oxide Nanoparticle: A Camouflage towards Multidrug Resistant Bacteria. *Bull. Mater. Sci.* **2014**, *37* (2), 199–206. https://doi.org/10.1007/s12034-014-0637-6.
(15) Egorov, A. R.; Kurliuk, A. V.; Rubanik, V. V.; Kirichuk, A. A.; Khubiev, O.; Golubev, R.; Lobanov, N. N.; Tskhovrebov, A. G.; Kritchenkov, A. S. Chitosan-Based

Ciprofloxacin Extended Release Systems: Combined Synthetic and Pharmacological (In Vitro and In Vivo) Studies. *Molecules* **2022**, *27* (24), 8865. https://doi.org/10.3390/molecules27248865.
(16) Han, S.; Kim, C.; Kwon, D. Thermal/Oxidative Degradation and Stabilization of Polyethylene Glycol. *Polymer* **1997**, *38* (2), 317–323. https://doi.org/10.1016/S0032-3861(97)88175-X.
(17) Han, S.; Kim, C.; Kwon, D. Thermal Degradation of Poly(Ethyleneglycol). *Polym. Degrad. Stab.* **1995**, *47* (2), 203–208. https://doi.org/10.1016/0141-3910(94)00109-L.
(18) Paberit, R.; Rilby, E.; Göhl, J.; Swenson, J.; Refaa, Z.; Johansson, P.; Jansson, H. Cycling Stability of Poly(Ethylene Glycol) of Six Molecular Weights: Influence of Thermal Conditions for Energy Applications. *ACS Appl. Energy Mater.* **2020**, *3* (11), 10578–10589. https://doi.org/10.1021/acsaem.0c01621.
(19) Chandra, T.; Brown, K. L. Vitamin B_{12} and α-Ribonucleosides. *Tetrahedron* **2008**, *64* (1), 9–38. https://doi.org/10.1016/j.tet.2007.08.061.
(20) Bonnett, R.; Godfrey, J. M.; Redman, D. G. Cobyric Acid and Related Compounds from Vitamin B_{12}. *J. Chem. Soc. C Org.* **1969**, No. 8, 1163–1166. https://doi.org/10.1039/J39690001163.
(21) Riether, D.; Mulzer, J. Total Synthesis of Cobyric Acid: Historical Development and Recent Synthetic Innovations. *Eur. J. Org. Chem.* **2003**, *2003* (1), 30–45. https://doi.org/10.1002/1099-0690(200301)2003:1<30::AID-EJOC30>3.0.CO;2-I.
(22) R, B. The Chemistry of the Vitamin B_{12} Group. *Chem. Rev.* **1963**, *63* (6).
(23) Moses, J. E.; Moorhouse, A. D. The Growing Applications of Click Chemistry. *Chem. Soc. Rev.* **2007**, *36* (8), 1249–1262. https://doi.org/10.1039/B613014N.
(24) Hein, C. D.; Liu, X.-M.; Wang, D. Click Chemistry, a Powerful Tool for Pharmaceutical Sciences. *Pharm. Res.* **2008**, *25* (10), 2216. https://doi.org/10.1007/S11095-008-9616-1.
(25) Rostovtsev, V. V.; Green, L. G.; Fokin, V. V.; Sharpless, K. B. A Stepwise Huisgen Cycloaddition Process: Copper(I)-Catalyzed Regioselective "Ligation" of Azides and Terminal Alkynes. *Angew. Chem.* **2002**, *114* (14), 2708–2711.
(26) Chromiński, M.; Gryko, D. "Clickable" Vitamin B_{12} Derivative. *Chem. – Eur. J.* **2013**, *19* (16), 5141–5148. https://doi.org/10.1002/chem.201203899.
(27) Stackpole, B. J.; Brasch, Nicola E. Unpublished Manuscript.
(28) Haghdoost, M. M.; Sauvageau, E.; Oguadinma, P.; Tran, H.-V.; Lefrancois, S.; Castonguay, A. Cu-Catalyzed Click Conjugation of Cobalamin to a BODIPY-Based Fluorophore: A Versatile Tool to Explore the Cellular Biology of Vitamin B_{12}. *J. Inorg. Biochem.* **2020**, *210*, 111105. https://doi.org/10.1016/j.jinorgbio.2020.111105.
(29) Özen, C.; Tüzün, N. Ş. Mechanism of CuAAC Reaction: In Acetic Acid and Aprotic Conditions. *J. Mol. Catal. Chem.* **2017**, *426*, 150–157. https://doi.org/10.1016/j.molcata.2016.11.010.
(30) Cox, R. A. Chapter One - Revised Mechanisms for Simple Organic Reactions. In *Advances in Physical Organic Chemistry*; Williams, I. H., Williams, N. H., Eds.; Advances in Physical Organic Chemistry; Academic Press, **2012**; Vol. 46, pp 1–55. https://doi.org/10.1016/B978-0-12-398484-5.00001-8.
(31) Quinn, D. M.; Medhekar, R.; Baker, N. R. 5.06 - Ester Hydrolysis. In *Comprehensive Natural Products Chemistry*; Barton, S. D., Nakanishi, K., Meth-Cohn, O., Eds.; Pergamon: Oxford, **1999**; pp 101–137. https://doi.org/10.1016/B978-0-08-091283-7.00110-7.
(32) Moema, D.; Nindi, M. M.; Dube, S. Development of a Dispersive Liquid–Liquid Microextraction Method for the Determination of Fluoroquinolones in Chicken Liver by

High Performance Liquid Chromatography. *Anal. Chim. Acta* **2012**, *730*, 80–86. https://doi.org/10.1016/j.aca.2011.11.036.
(33) Horton, R. A.; Bagnato, J. D.; Grissom, C. B. Structural Determination of 5′-OH α-Ribofuranoside Modified Cobalamins via 13C and DEPT NMR. *J. Org. Chem.* **2003**, *68* (18), 7108–7111. https://doi.org/10.1021/jo0340399.
(34) Chemaly, S. M. Use of 13C and 1H NMR to Determine in Detail the Structures of the Base-off Vitamin B_{12} Complexes Dicyanocobinamide and Dicyanocobalamin. *Polyhedron* **2019**, *174*, 114162. https://doi.org/10.1016/j.poly.2019.114162.
(35) Dunetz, J. R.; Magano, J.; Weisenburger, G. A. Large-Scale Applications of Amide Coupling Reagents for the Synthesis of Pharmaceuticals. *Org. Process Res. Dev.* **2016**, *20* (2), 140–177. https://doi.org/10.1021/op500305s.
(36) El-Faham, A.; Albericio, F. Peptide Coupling Reagents, More than a Letter Soup. *Chem. Rev.* **2011**, *111* (11), 6557–6602. https://doi.org/10.1021/cr100048w.
(37) Merrifield, B. Solid-Phase Peptide Synthesis. In *Peptides*; Elsevier, **1995**; pp 93–169. https://doi.org/10.1016/B978-012310920-0/50004-8.
(38) Wuts, P. G. M.; Greene, T. W. *Greene's Protective Groups in Organic Synthesis*, 1st ed.; Wiley, **2006**. https://doi.org/10.1002/0470053488.
(39) Dagil, R.; O'Shea, C.; Nykjær, A.; Bonvin, A. M. J. J.; Kragelund, B. B. Gentamicin Binds to the Megalin Receptor as a Competitive Inhibitor Using the Common Ligand Binding Motif of Complement Type Repeats. *J. Biol. Chem.* **2013**, *288* (6), 4424–4435.
(40) Farouk, F.; Azzazy, H. M. E.; Niessen, W. M. A. Challenges in the Determination of Aminoglycoside Antibiotics, a Review. *Anal. Chim. Acta* **2015**, *890*, 21–43. https://doi.org/10.1016/j.aca.2015.06.038.
(41) Brozmanova, H.; Urinovska, R.; Safarcik, K.; Vsiansky, F.; Kacirova, I.; Grundmann, M. Liquid Chromatography-Tandem Mass Spectrometry Method for Quantification of Gentamicin and Its Individual Congeners in Serum and Comparison Results with Two Immunoanalytical Methods (Fluorescence Polarization Immunoassay and Chemiluminiscent Microparticle Immunoassay). *Clin. Chim. Acta* **2021**, *521*, 191–198. https://doi.org/10.1016/j.cca.2021.07.014.
(42) Amponsah, S. K.; Boadu, J. A.; Dwamena, D. K.; Opuni, K. F. M. Bioanalysis of Aminoglycosides Using High-Performance Liquid Chromatography. *ADMET DMPK* **2022**, *10* (1), 27–62. https://doi.org/10.5599/admet.1183.
(43) Bogialli, S.; Curini, R.; Di Corcia, A.; Laganà, A.; Mele, M.; Nazzari, M. Simple Confirmatory Assay for Analyzing Residues of Aminoglycoside Antibiotics in Bovine Milk: Hot Water Extraction Followed by Liquid Chromatography–Tandem Mass Spectrometry. *J. Chromatogr. A* **2005**, *1067* (1), 93–100. https://doi.org/10.1016/j.chroma.2004.10.033.
(44) Kaufmann, A.; Butcher, P.; Maden, K. Determination of Aminoglycoside Residues by Liquid Chromatography and Tandem Mass Spectrometry in a Variety of Matrices. *Anal. Chim. Acta* **2012**, *711*, 46–53. https://doi.org/10.1016/j.aca.2011.10.042.
(45) Deubner, R.; Schollmayer, C.; Wienen, F.; Holzgrabe, U. Assignment of the Major and Minor Components of Gentamicin for Evaluation of Batches. *Magn. Reson. Chem.* **2003**, *41* (8), 589–598. https://doi.org/10.1002/mrc.1222.

Chapter 6 Conclusion and Future Directions

Gram-negative bacteria are amongst the most clinically challenging multidrug-resistant pathogens and have become a serious global threat to human health. Most major antibiotics active against gram-negative pathogens enter the bacterial cell through passive processes. There is an urgent need for new antibiotic delivery technologies effective against gram-negative infections. Vitamin B_{12} has recently shown promise as a vehicle for the delivery of antibiotics into bacteria through the 'Trojan horse' approach, to potentially address the growing issue of antibiotic resistance.[1–5] A vitamin B_{12} conjugate of the antibiotic ampicillin was recently shown to be ~500 times more efficient than ampicillin itself at killing the gram-negative bacterium *E coli.*[1]

The thesis presents the synthesis of a series of conjugates of vitamin B_{12} (cyanocobalamin, CNCbl) and its naturally occurring analogue cyanocobinamide (CNCbi). Highly fluorescent CNCbl and CNCbi conjugates of the cyanine dyes sulfo-Cyanine5 and cyanine7 were synthesised, in addition to weakly fluorescent CNCbl and CNCbi conjugates of the fluorophore NBD-X. The CNCbl conjugates were derivatised at the 5'-alcohol of the ribose nucleoside of CNCbl. Vitamin B_{12} conjugates derivatised at this site and cobinamide conjugates derivatised at the alcohol are taken up efficiently by B_{12} uptake proteins in both bacterial (Btu) and mammalian systems (TC, IF and HC).[6,7] The fluorophores were conjugated to CNCbl and CNCbi via linker ligands, with the linkers conjugated to CNCbl via CDT-mediated carbamate bond formation. Two linkers were used: the disulfide containing cystamine linker and a short polyethylene glycol (PEG) linker. Polyethylene glycol linkers are known to be stable in biological conditions.[8,9] Conversely, the disulfide of cystamine will be cleaved in intracellular environments due to the presence of glutathione, releasing the fluorescent cargo from CNCbl.[10] The conjugation of NBD-X, sulfo-Cyanine5 or Cyanine 7 was achieved by peptide coupling to the terminal amine of the CNCbl-linker molecules.

Purification of large quantities (> 10 mg) of the products proved to be challenging. Most research groups have typically purified small quantities of the desired CNCbl conjugates using reversed-phase C18 HPLC, and the product yield is not always reported, especially in the older literature. More recently several groups have used preparative reversed-phase C18 column chromatography.[11-13] As part of this thesis, robust reversed-phase C18 column chromatography purification methods were developed to purify the compounds.

This methodology allowed for purification on a large scale (≤200 mg of crude material) in short time frames (1-2 h). Interestingly, the successful purification of CNCbl-linker-Cyanine7 conjugates (**7** and **8**) by column chromatography required the addition of formic acid to the mobile phase for the elution of Cyanine7 compounds despite the fluorophore not having any ionisation sites in the mildly acidic to alkaline pH range. CNCbl-linker molecules (**1** and **2**) were obtained in 78-80% yields with purities of ≥95%. CNCbl-linker-fluorophore conjugates **3**-**8** were achieved in yields of 54 to 92% with purities greater than 90%. The cystamine conjugates provided the lowest yields (**3** (CNCbl-cys-NBD-X) and **7** (CNCbl-cys-Cyanine7) being 54% and 60%, respectively). This is probably because of the instability of the disulfide of the cystamine linker during the reaction/purification. However, preliminary stability studies showed that CNCbl-cys-NBD-X was stable in biological media at 37°C for 24 h. Furthermore, all conjugates were stable in their dry state for ≥ one month.

Fluorescent conjugates of CNCbi were synthesised in this work using the secondary alcohol of CNCbi. To the best of our knowledge, these conjugates are the first examples CNCbi conjugates of fluorophores. The CNCbi-linker molecules incorporated both cystamine and PEG linkers. The synthesis of **12** (CNCbi-cystamine) was very challenging, with multiple reaction conditions being trialled. Modifying the $(CN)_2$Cbi starting material to CNCbi was essential for the successful synthesis of **12**. The removal of one cyanido ligand, known to be labile in solution, reduced undesired side reactions,[14,15] with the disulfide of cystamine susceptible to nucleophilic attack by cyanide. The formation of CNCbi conjugates incorporating PEG and cystamine linkers (**11** and **12**) was confirmed by LC-MS. A significant challenge faced with both CNCbi-linker molecules was purification of these molecules. Using the reversed-phase C18 column chromatography methodology developed for the purification of the CNCbl-linker and CNCbl-linker-fluorophore conjugates was unsuccessful for the purification of the CNCbi-linker conjugates despite many mobile phases being trialled. Purification by C18 reversed-phase column chromatography was replaced with thorough desalting using a reversed-phase C18 plug to remove a significant proportion of the non CNCbi impurities. The crude CNCbi-linker molecules purified by this method were then directly derivatised with the fluorophores NBD-X, sulfo-Cyanine5 or Cyanine7 by peptide coupling. Yields of 18-63% were obtained for the CNCbi-linker-fluorophore conjugates, with the CNCbi-cystamine (**14**, 27%) and the CNCbi-PEG-Cyanine7 conjugate **16** (18%) having the

lowest yields. In particular, the purification of **16** was laborious, requiring multiple reversed-phase C18 columns to obtain a purity of ≥90%. However, the synthesis of four CNCbi-linker-fluorophore conjugates was achieved with purities ranging from 90-97%.

An exciting result from this research was the high fluorescence quantum yields (>0.20) for the sulfo-Cyanine5 and Cyanine7 conjugates of both CNCbl and CNCbi. Significant fluorescence quenching was observed for the related NBD-X conjugates. Absorbance studies of solutions of free NBD-X and CNCbl indicated that static quenching is unlikely for the NBD-X conjugates of CNCbl and CNCbi. Fluorescence emission studies of solutions containing free NBD-X and increasing concentrations of CNCbl were undertaken. A Stern-Volmer plot of the emission data showed that the amount of quenching was proportional to the CNCbl concentration, suggesting that quenching occurs predominantly via one mechanism.[16] Due to the overlap of the emission of NBD-X and the absorbance spectra of CNCbl, quenching between the two molecules is suggested to occur via Förster resonance energy transfer (FRET).[17] However, the mechanism of fluorescence quenching for the CNCbl and CNCbi conjugates of fluorophores could not be deduced as both photoinduced electron transfer (PeT) and Dexter processes are also possible. Fluorescence quenching was observed primarily for the conjugates containing NBD-X with a minor reduction (≤25%) in fluorescence quantum yields of the sulfo-Cyanine5 conjugates.

The successful synthesis and characterisation of CNCbl conjugates of established antibiotics ciprofloxacin and gentamicin is also presented in this thesis. Ciprofloxacin conjugation was achieved at two sites, namely the carboxylic acid and the secondary amine. Initial attempts to couple ciprofloxacin to the carboxylic acid using 1-(3-dimethylaminopropyl)-3-ethylcarbodiimide (EDC) were unsuccessful. The carboxylic acid of ciprofloxacin was converted to an ester with a terminal alkyne group, and attempts were made to attach ciprofloxacin to CNCbl-N_3 by copper-catalysed azide-alkyne cycloaddition (CuAAC). Although the CuAAC reaction was successful, cleavage of the ester moiety occurred despite the modification of reaction conditions (buffered solution, removal of water and different Cu catalysts). Synthetic attempts then focused on conjugation to B_{12}-linker by the secondary amine of ciprofloxacin, with three peptide coupling reagents trialled. Using EDC resulted in formation of the desired CNCbl-linker-ciprofloxacin conjugate (**18**). However, using 2-(1H-benzotriazole-1-yl)-1,1,3,3-tetramethyluronium hexafluorophosphate (HBTU) as the coupling reagent resulted in the

polymerisation of ciprofloxacin. As HBTU successfully activates the carboxylic acid of ciprofloxacin, HBTU was subsequently employed to attach ciprofloxacin to the CNCbl-linker conjugates (**1** and **2**) by the carboxylic acid functional group (conjugates **19** and **20**). Synthesis of these molecules was challenging but successful, with yields of 78% for the *N*-bound ciprofloxacin conjugate (**18**) and 28-33% for the *O*-bound conjugates (**19** and **20**). Lower yields were afforded for the *O*-bound conjugates, reflecting the lower reactivity of the carboxylic group of ciprofloxacin.

Synthesis of CNCbl-linker-gentamicin conjugates was achieved by peptide coupling, employing EDC and CNCbl-linker molecules with terminal carboxylic acids (compounds **17** and **22**). Gentamicin, an aminoglycoside antibiotic, contains five amine functionalities, presenting the possibility of multiple product isomers forming. Analysis of the conjugates by LC-MS was difficult due to significant peak broadening. Numerous attempts were unsuccessfully made to overcome this by testing a wide range of mobile and stationary phase conditions. Purification of the conjugates was carried out using reversed-phase C18 column chromatography operating under isocratic conditions, albeit in low yields (15-39% for **21** and **23,** respectively). Analysis by ^{1}H NMR spectroscopy indicated that peptide coupling of gentamicin to CNCbl-linker had fortuitously occurred at a single amine functionality. This was deduced by the observation of two proton resonances corresponding to conjugated gentamicin in the downfield region of the ^{1}H NMR spectrum, both integrating for one proton as expected for a single product. Although the obtained yields of these conjugates were low, high purities of ≥95% were achieved.

6.1 Future Directions

Future work in our research group using the fluorescent conjugates of cyanocobalamin and cyanocobinamide synthesised in this thesis will focus on investigating the cellular uptake of these molecules into bacteria and mammalian cells using fluorescence microscopy. Some bacterial strains may exhibit a low fluorescence signal due to poor uptake efficiency, complicating fluorescence microscopy analysis. If encountered, alternative strategies such as confocal microscopy, flow cytometry, or fluorescence-activated cell sorting (FACS) could enhance detection sensitivity. Establishing bacterial uptake in representative gram-negative (*E. coli*) and gram-positive bacteria (*S. aureus*) is a crucial step towards validating this Trojan horse approach for delivering cargo into bacteria. Expanding these experiments to antibiotic-resistant bacterial strains will allow

the broader applicability and potential clinical relevance of this strategy to be investigated. Additionally, cell fractionation studies following incubation with the fluorescent conjugates will allow us to elucidate in which sub-cellular compartment(s) these conjugates localise. A comparative investigation of fluorescent CNCbl versus CNCbi conjugate selectivity in bacterial cells and mammalian cells will further inform potential therapeutic benefits and diagnostic applications, given the literature supporting uptake of CNCbi conjugates in hepatocytes only.

Further experiments are required to clarify the mechanism of fluorescence quenching observed for the NBD-X and sulfo-Cyanine5 conjugates with CNCbl/CNCbi. Although FRET appears likely for the NBD-X conjugates due to spectral overlap, alternative mechanisms should be explored, particularly for sulfo-Cyanine5. Fluorescence lifetimes of free and conjugated fluorophores would provide further insight into the mechanism(s) of quenching for these systems. A decrease in lifetime would indicate a dynamic quenching mechanism.[18] Repeating the Stern-Volmer plot at decreasing temperatures will demonstrate an increase in quenching for dynamic systems.[19] Conversely, a decrease in quenching with increasing temperatures occurs for static mechanisms due to complex destabilisation.[20] Experiments carried out at different temperatures and in solvents of varying polarity and viscosity can further distinguish between FRET, PeT and DEXTER quenching mechanisms. Polar aprotic solvents favour FRET due to enhanced dipole-dipole coupling interactions. PeT becomes less favourable as polarity decreases, as the charge-separated intermediate is destabilised, whereas DEXTER is relatively insensitive to polarity changes. Temperature changes impact both DEXTER and PeT mechanisms where FRET is often temperature independent. Photoinduced electron-transfer should also be investigated using cyclic voltammetry to determine the oxidation potentials (E_{ox}) of the fluorophores and the reduction potentials (E_{red}) of CNCbl/CNCbi, thereby evaluating the thermodynamic feasibility of photoinduced electron-transfer processes. Ultrafast transient absorption spectroscopy can be employed to further discriminate between photoinduced electron transfer (PeT) and Dexter energy transfer mechanisms. This will leverage the distinctive spectroscopic features of cobalamin and cobinamide spectra (Co(III), Co(II) and Co(I)) that emerge on the ultrafast timescale.[21] As PeT involves the transfer of an electron from the donor (fluorophore) to the acceptor (CNCbl), a change in the Co oxidation state will be observed which can be followed by UV/vis spectroscopy.[22] However, Dexter energy transfer involves electron transfer in both

directions; that is, electron transfer from the donor to the acceptor and from the acceptor to the donor.[23] Therefore, ultrafast transient absorbance spectroscopy should show evidence of a Co(III) → Co(II)/Co(I) → Co(III) conversion if Dexter energy transfer is occurring in these systems.

The CNCbl-linker-Cyanine3 conjugates of CNCbl and CNCbi could also be synthesised. Given the spectral properties of Cyanine3 (λ_{em} of Cyanine3 = 570 nm whereas CNCbl absorbs below 600 nm),[21] the photophysical properties of these conjugates could be compared with the corresponding SulfoCyanine5 and Cyanine 7 conjugates. That is, the importance of FRET as a mechanism for fluorescence quenching in these systems can be probed.

Finally, future experiments will include systematic testing of the antibacterial properties of the antibiotic conjugates of CNCbl synthesised in this thesis. Initial screening via disk assays will identify promising antibiotic conjugates, after which quantitative methods, including minimum inhibitory concentration (MIC) and minimum bactericidal concentration (MBC) determinations, will provide a rigorous assessment of efficacy. Comparative analyses with free antibiotics (gentamicin, ciprofloxacin) and existing clinical therapies will position the developed conjugates within the broader landscape of antimicrobial treatments. IC_{50} values for the CNCbl-linker-antibiotic conjugates in a range of mammalian cell types should also be established. If the CNCbl-linker antibiotic conjugates are effective, synthetic efforts should also be made to develop the corresponding CNCbi-linker-antibiotic conjugates.

6.2 Final statement

In summary, this thesis presents the synthesis of highly fluorescent conjugates of CNCbl and CNCbi, and ciprofloxacin and gentamycin conjugates of CNCbl. These molecules can be used to extend our understanding of the biological activity of conjugates of CNCbl and CNCbi, particularly in bacteria, and demonstrate the versatility of cobalamin and cobinamide as a chemical scaffold and delivery agent. Beyond the immediate next steps identified for this work, successful validation of the CNCbl and CNCbi conjugates synthesised in this thesis could enable their application as targeted diagnostic imaging agents, tools for studying the mechanisms of bacterial CNCbl/CNCbi metabolism, and potentially as scaffolds for developing selective antimicrobial therapies. Additionally,

insights gained from these investigations may inspire the synthesis and application of analogous conjugates targeting other clinically relevant systems.

(1) Zhao, S.; Wang, Z.-P.; Wen, X.; Li, S.; Wei, G.; Guo, J.; He, Y. Synthesis of Vitamin B_{12}-Antibiotic Conjugates with Greatly Improved Activity against Gram-Negative Bacteria. *Org. Lett.* **2020**, *22* (16), 6632–6636. https://doi.org/10.1021/acs.orglett.0c02403.
(2) Tillotson, G. S. Trojan Horse Antibiotics—A Novel Way to Circumvent Gram-Negative Bacterial Resistance? *Infect. Dis.* **2016**, *9*, 45–52. https://doi.org/10.4137/IDRT.S31567.
(3) Ij, S. A Trojan-Horse Strategy Including a Bacterial Suicide Action for the Efficient Use of a Specific Gram-Positive Antibiotic on Gram-Negative Bacteria. *PubMed* **2018**.
(4) Górska, A.; Sloderbach, A.; Marszałł, M. P. Siderophore–Drug Complexes: Potential Medicinal Applications of the 'Trojan Horse' Strategy. *Trends Pharmacol. Sci.* **2014**, *35* (9), 442–449. https://doi.org/10.1016/j.tips.2014.06.007.
(5) Równicki, M.; Wojciechowska, M.; Wierzba, A. J.; Czarnecki, J.; Bartosik, D.; Gryko, D.; Trylska, J. Vitamin B_{12} as a Carrier of Peptide Nucleic Acid (PNA) into Bacterial Cells. *Sci. Rep.* **2017**, *7* (1). https://doi.org/10.1038/s41598-017-08032-8.
(6) Giannella, R. A.; Broitman, S. A.; Zamcheck, N. Vitamin B_{12} Uptake by Intestinal Microorganisms: Mechanism and Relevance to Syndromes of Intestinal Bacterial Overgrowth. *J. Clin. Invest.* **1971**, *50* (5), 1100–1107. https://doi.org/10.1172/JCI106581.
(7) Borths, E. L.; Poolman, B.; Hvorup, R. N.; Locher, K. P.; Rees, D. C. In Vitro Functional Characterization of BtuCD-F, the Escherichia Coli ABC Transporter for Vitamin B_{12} Uptake. *Biochemistry* **2005**, *44* (49), 16301–16309. https://doi.org/10.1021/bi0513103.
(8) Chen, Z.; Liang, Y.; Feng, X.; Liang, Y.; Shen, G.; Huang, H.; Chen, Z.; Yu, J.; Liu, H.; Lin, T.; Chen, H.; Wu, D.; Li, G.; Zhao, B.; Guo, W.; Hu, Y. Vitamin-B_{12}-Conjugated PLGA-PEG Nanoparticles Incorporating miR-532-3p Induce Mitochondrial Damage by Targeting Apoptosis Repressor with Caspase Recruitment Domain (ARC) on CD320-Overexpressed Gastric Cancer. *Mater. Sci. Eng. C* **2021**, *120*, 111722. https://doi.org/10.1016/j.msec.2020.111722.
(9) Nieto-Orellana, A.; Li, H.; Rosiere, R.; Wauthoz, N.; Williams, H.; Monteiro, C. J.; Bosquillon, C.; Childerhouse, N.; Keegan, G.; Coghlan, D.; Mantovani, G.; Stolnik, S. Targeted PEG-Poly(Glutamic Acid) Complexes for Inhalation Protein Delivery to the Lung. *J. Controlled Release* **2019**, *316*, 250–262. https://doi.org/10.1016/j.jconrel.2019.10.012.
(10) Wierzba, A.; Wojciechowska, M.; Trylska, J.; Gryko, D. Vitamin B_{12} Suitably Tailored for Disulfide-Based Conjugation. *Bioconjug. Chem.* **2016**, *27* (1), 189–197. https://doi.org/10.1021/acs.bioconjchem.5b00599.
(11) Proinsias, K.; Gryko, D. T.; Hisaeda, Y.; Martin, E.; Sessler, J. L.; Gryko, D. Vitamin B_{12} Derivatives as Activators of Soluble Guanylyl Cyclase. **2012**. *55* (20), 8943-8947. https://doi.org/10.1021/jm3006959
(12) Jackowska, A.; Gryko. Vitamin B_{12} Derivatives Suitably Tailored for the Synthesis of Photolabile Conjugates. **2021**, *23* (13), 4940-4944. https://doi.org/10.1021/acs.orglett.1c00839
(13) Butler, P.; Ebert, M-O.; Lyskowski, A.; Gruber, K.; Kratky, C.; Kraulter, B. Vitamin B_{12}: a methyl group without a job?. **2006**, *45* (6), 989-993. https://doi.org/10.1002/anie.200502638
(14) Argü, J. E.; Costentin, C.; Griveau, S.; Savé, J.-M. Role of Protonation and of Axial Ligands in the Reductive Dechlorination of Alkyl Chlorides by Vitamin B_{12} Complexes. Reductive Cleavage of Chloroacetonitrile by Co(I) Cobalamins and Cobinamides. *J. Am. Chem. Soc.* **2005**, *127*, 5049–5055. https://doi.org/10.1021/ja042940f.

(15) Baldwin, D. A.; Betterton, E. A.; Pratt, J. M. The Chemistry of Vitamin B_{12}. Part 20. Diaquocobinamide : pK Values and Evidence for Conformational Isomers. *J. Chem. Soc. Dalton Trans.* **1983**, No. 2, 217–223. https://doi.org/10.1039/DT9830000217.
(16) El-Daly, S. A.; El-Hallag, I. S. Photophysical Parameters, Photodecomposition, Fluorescence Quenching and Convolutive Voltammetry of 7-Diethylaminocoumarin (DEAC) Laser Dye -Journal of the Korean Chemical Society | Korea Science. *J. Korean Chem. Soc.* **2010**, *54* (1), 13–22.
(17) Clegg, R. M. Chapter 1 Förster Resonance Energy Transfer—FRET What Is It, Why Do It, and How It's Done. In *Laboratory Techniques in Biochemistry and Molecular Biology*; Fret and Flim Techniques; Elsevier, 2009; Vol. 33, pp 1–57. https://doi.org/10.1016/S0075-7535(08)00001-6.
(18) Berezin, M. Y.; Achilefu, S. Fluorescence Lifetime Measurements and Biological Imaging. *Chem. Rev.* **2010**, *110* (5), 2641–2684. https://doi.org/10.1021/cr900343z.
(19) Gryczynski, Z. (Karol); Gryczynski, I. *Practical Fluorescence Spectroscopy*; Taylor & Francis Group: Milton, United Kingdom, **2019.**
(20) Lakowicz, J. R. *Principles of Fluorescence Spectroscopy*; Springer: New York, NY, UNITED STATES, 2011.
(21) Salerno, E. V.; Miller, N. A.; Konar, A.; Li, Y.; Kieninger, C.; Kräutler, B.; Sension, R. J. Ultrafast Excited State Dynamics and Fluorescence from Vitamin B_{12} and Organometallic [Co]–C≡C–R Cobalamins. *J. Phys. Chem. B* **2020**, *124* (30), 6651–6656. https://doi.org/10.1021/acs.jpcb.0c04886.
(22) Weller, A. Photoinduced Electron Transfer in Solution: Exciplex and Radical Ion Pair Formation Free Enthalpies and their Solvent Dependence. *Zeitschrift für Physikalische Chemie* **1982**, *133*, 93–98. https://doi.org/10.1024/zpch.1982.133.1.093
(23) Cravcenco, A.; Ye, C.; Gräfenstein, J.; Börjesson, K. Interplay between Förster and Dexter Energy Transfer Rates in Isomeric Donor–Bridge–Acceptor Systems. *J. Phys. Chem. A* **2020**, *124* (36), 7219–7227. https://doi.org/10.1021/acs.jpca.0c05035.
(24) *Cy3 Dye - NZ*. https://www.thermofisher.com/au/en/home/life-science/cell-analysis/fluorophores/cy3-dye.html (accessed 2025-03-04).

Appendix

NMR spectra

CNCbl

^{1}H NMR MeOD-d_4

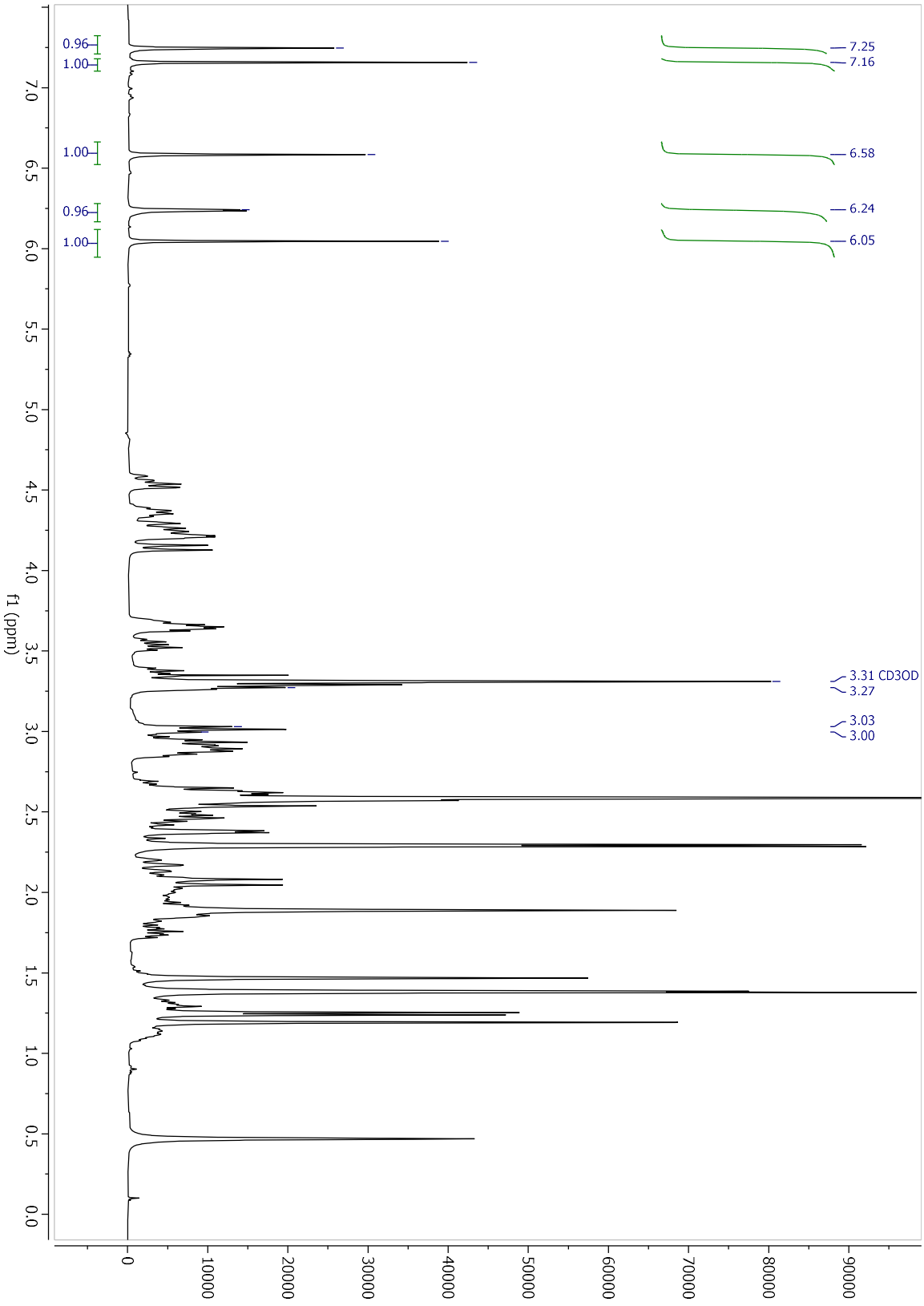

^{1}H NMR DMSO-d_6

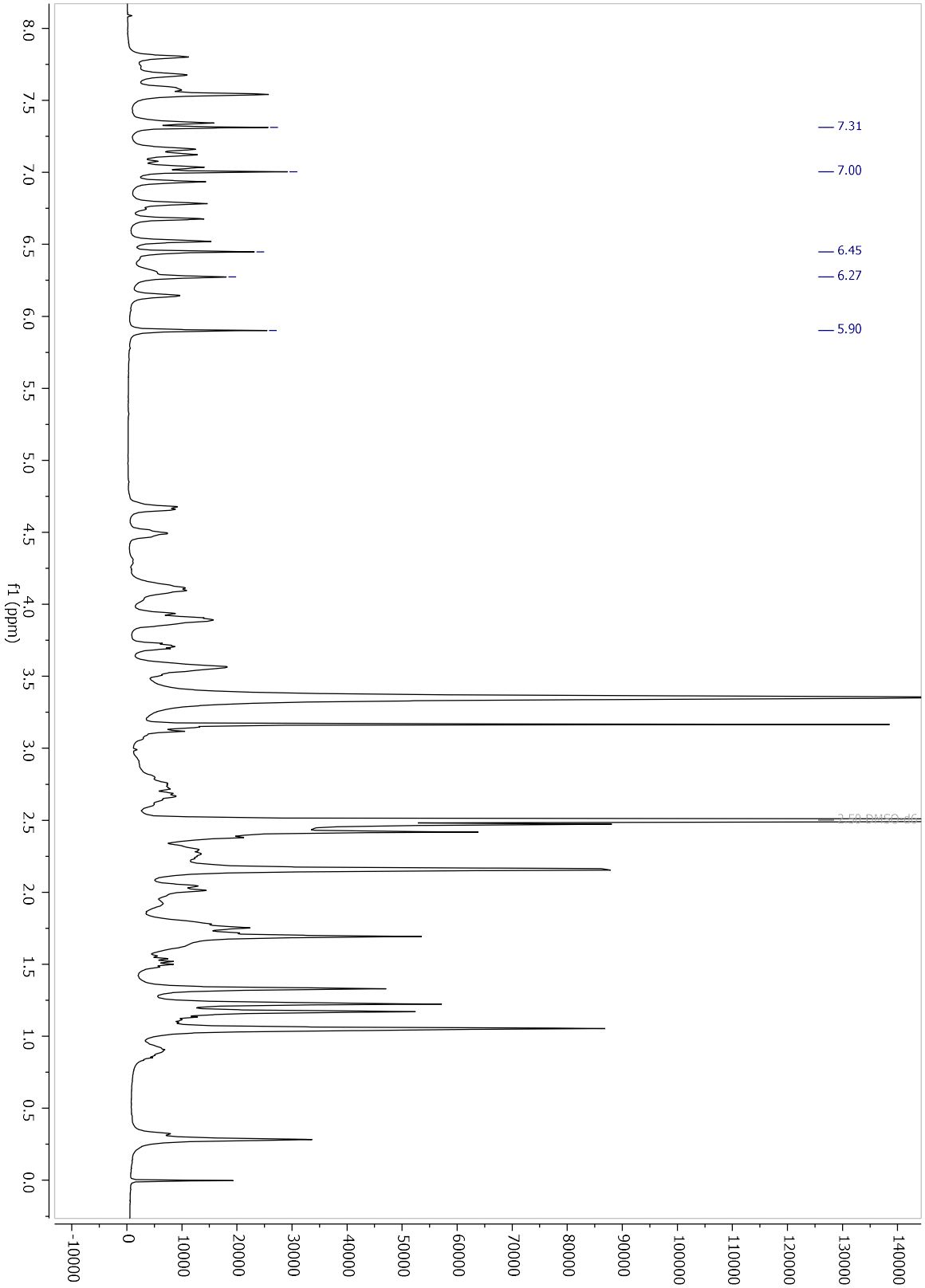

^{13}C NMR DMSO-d_6

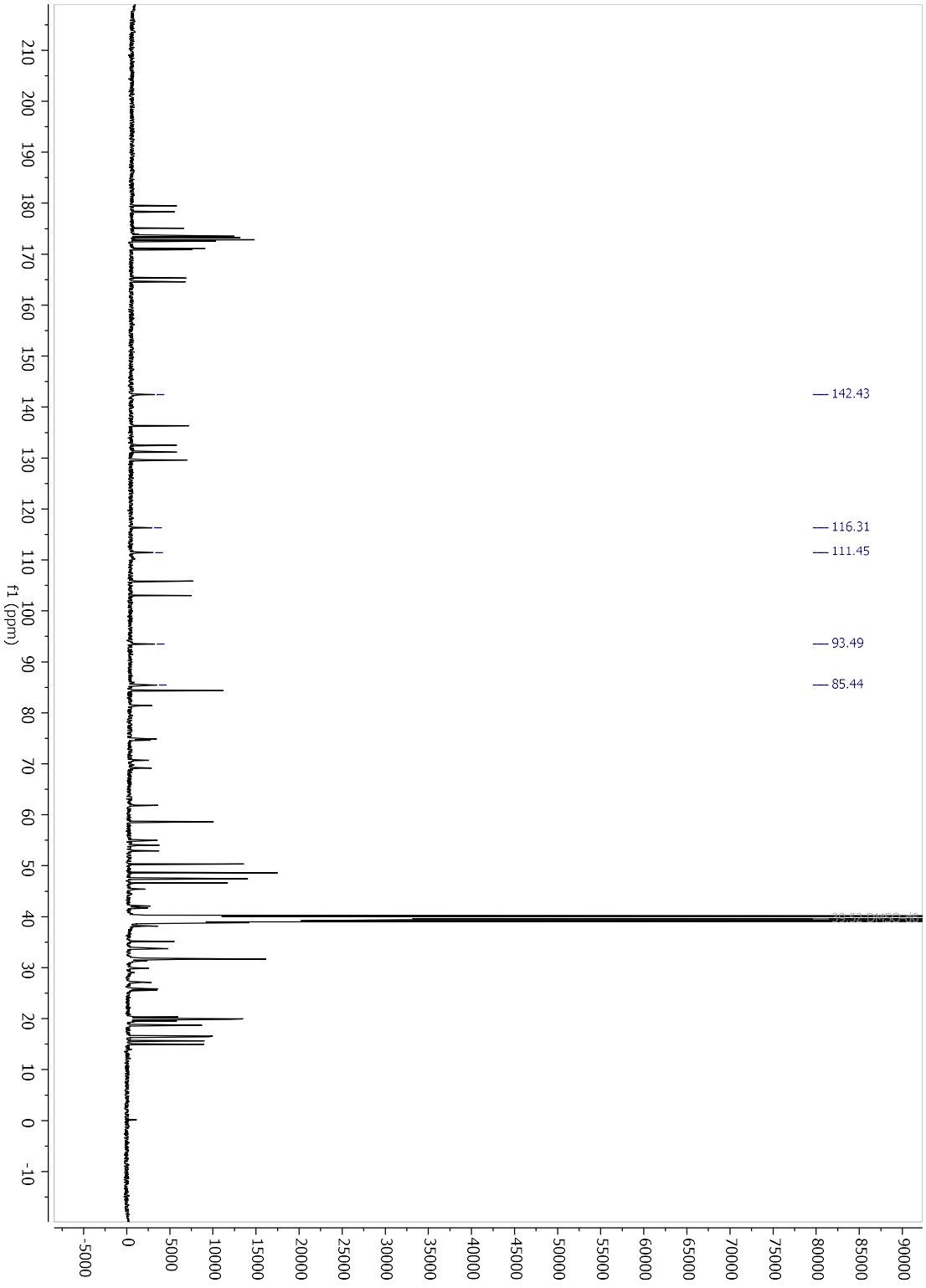

Compound 1

^{1}H NMR MeOD-*d*$_{4}$

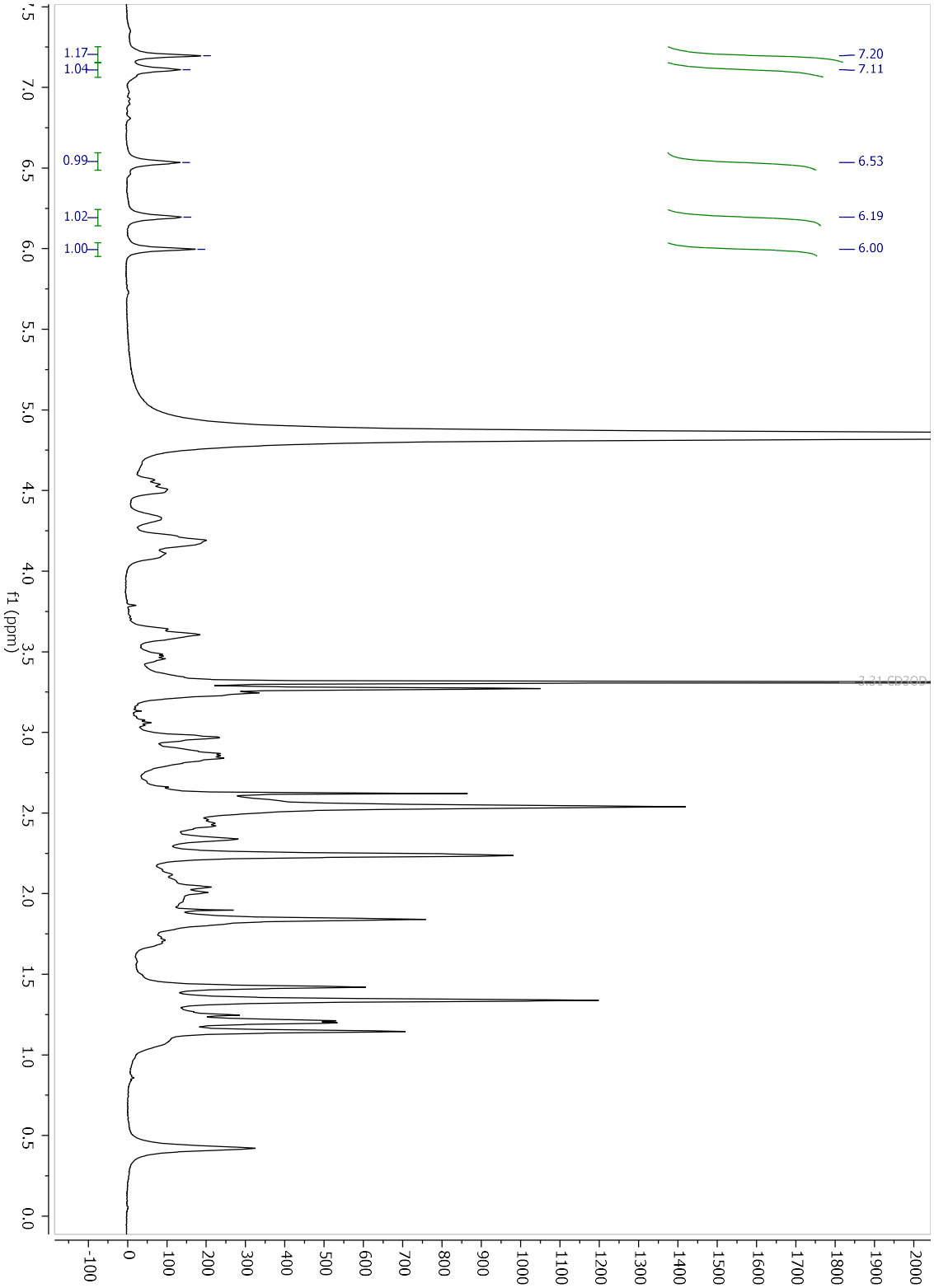

^{1}H NMR DMSO-d_6

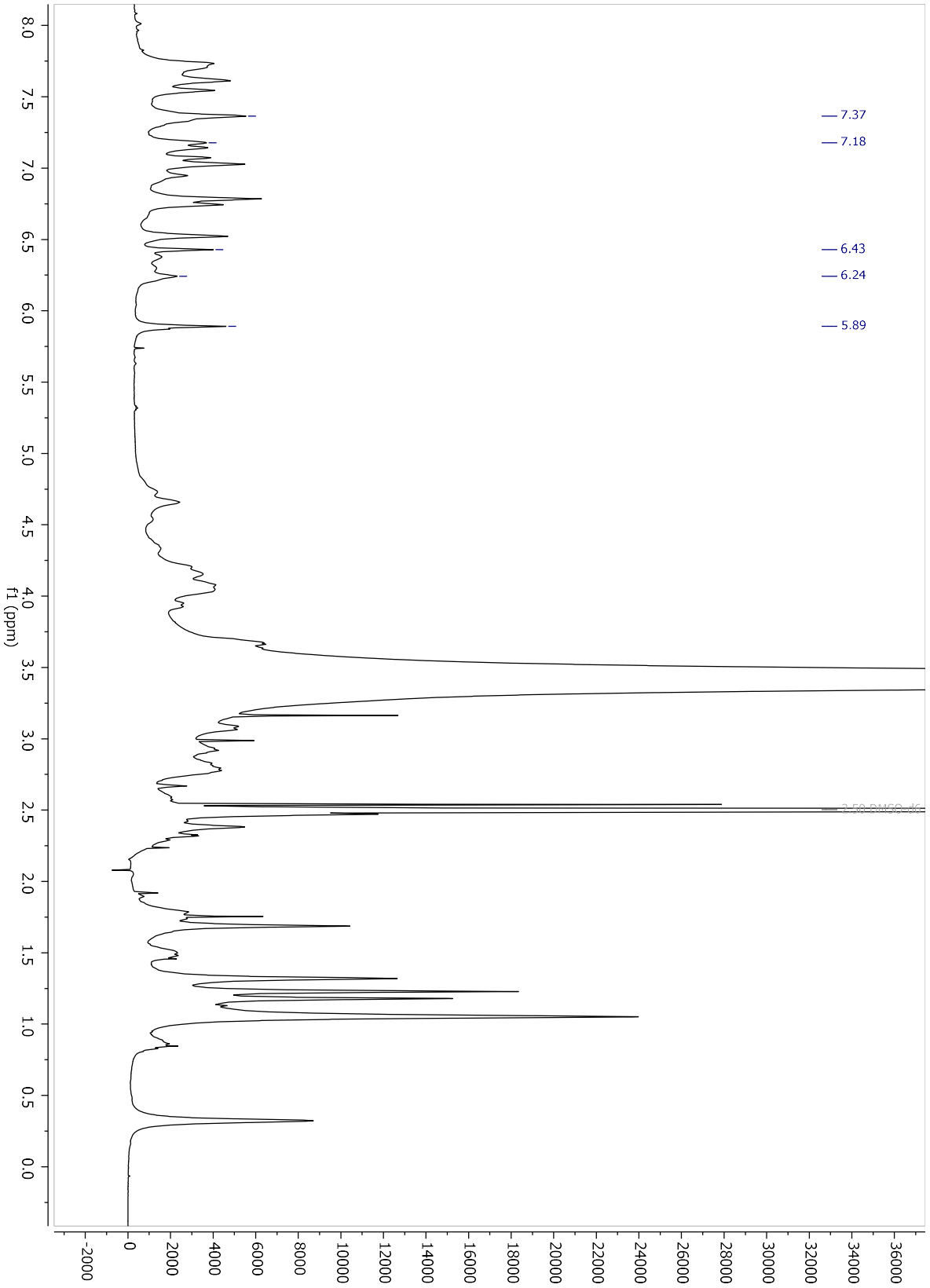

^{13}C NMR DMSO-*d*$_6$

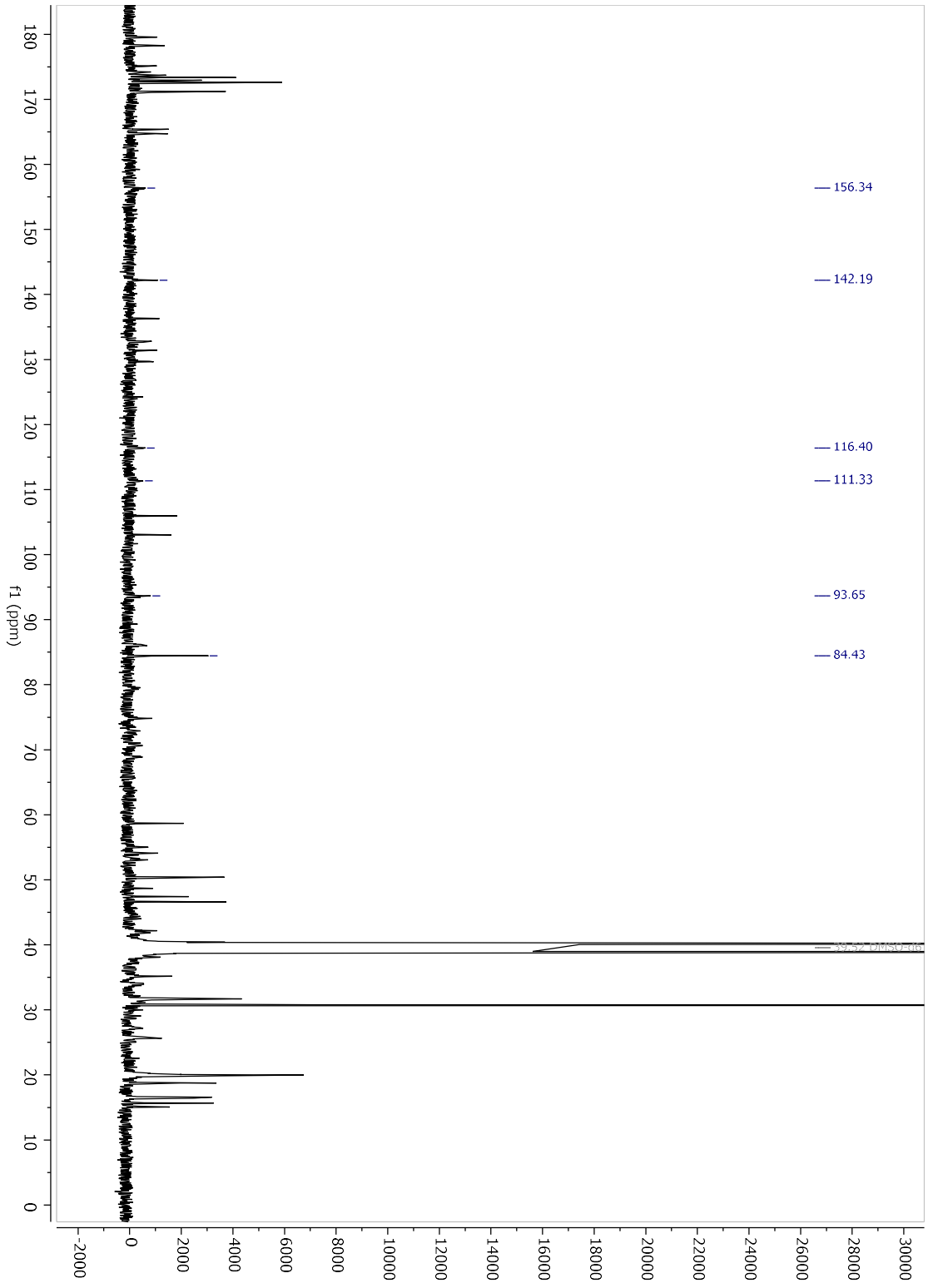

Compound 2

^{1}H NMR MeOD-d_4

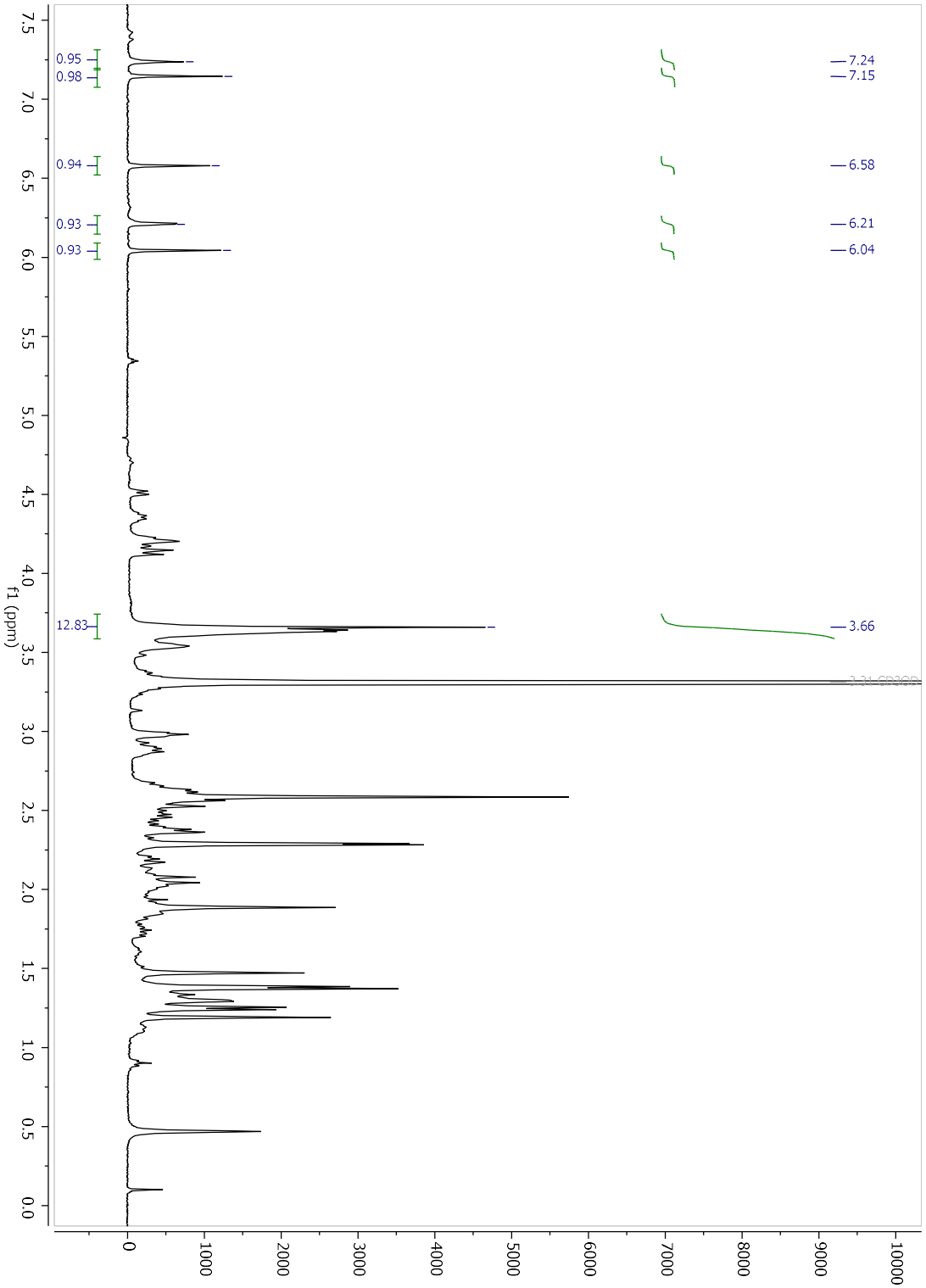

^{1}H NMR DMSO-*d*$_{6}$

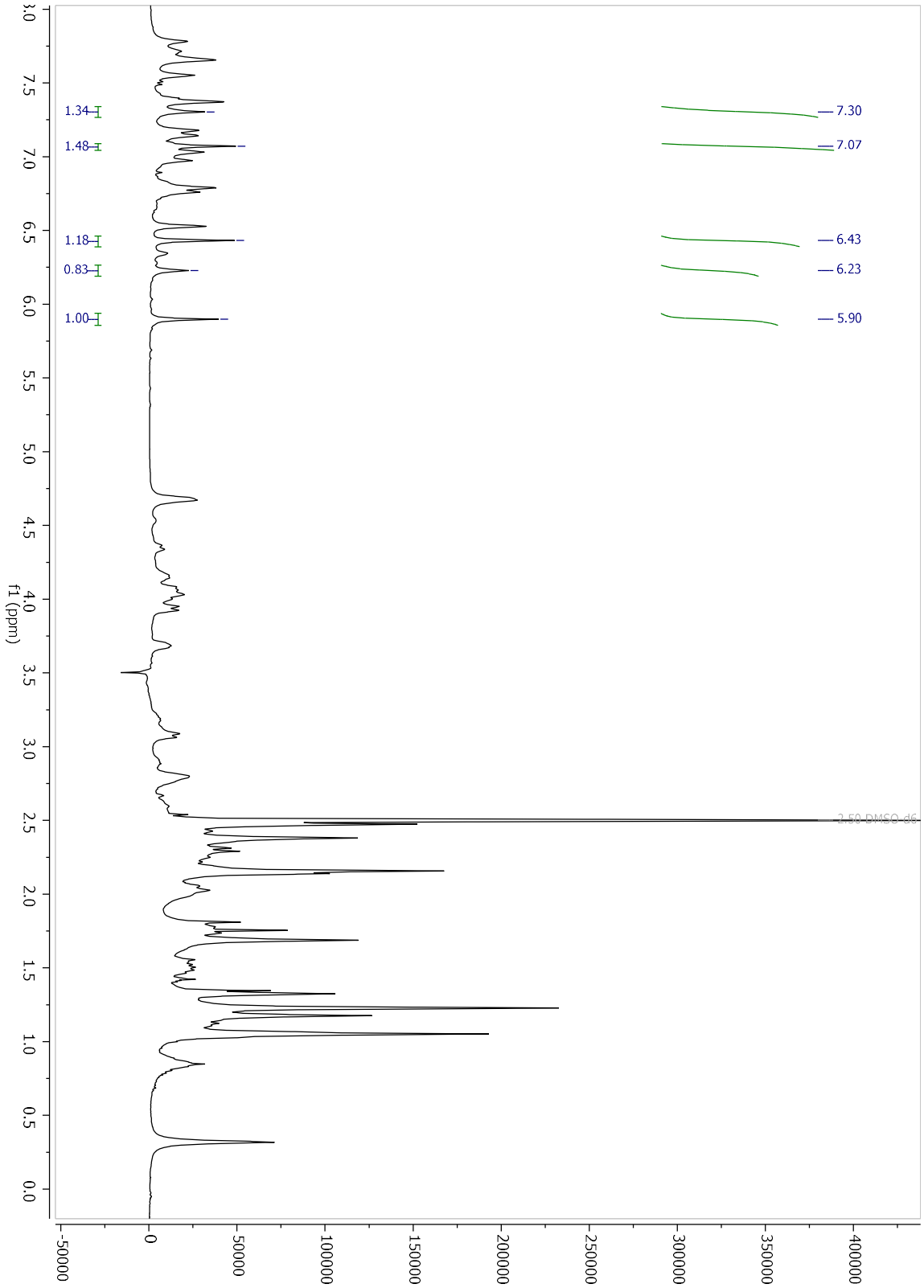

^{13}C NMR DMSO-d_6

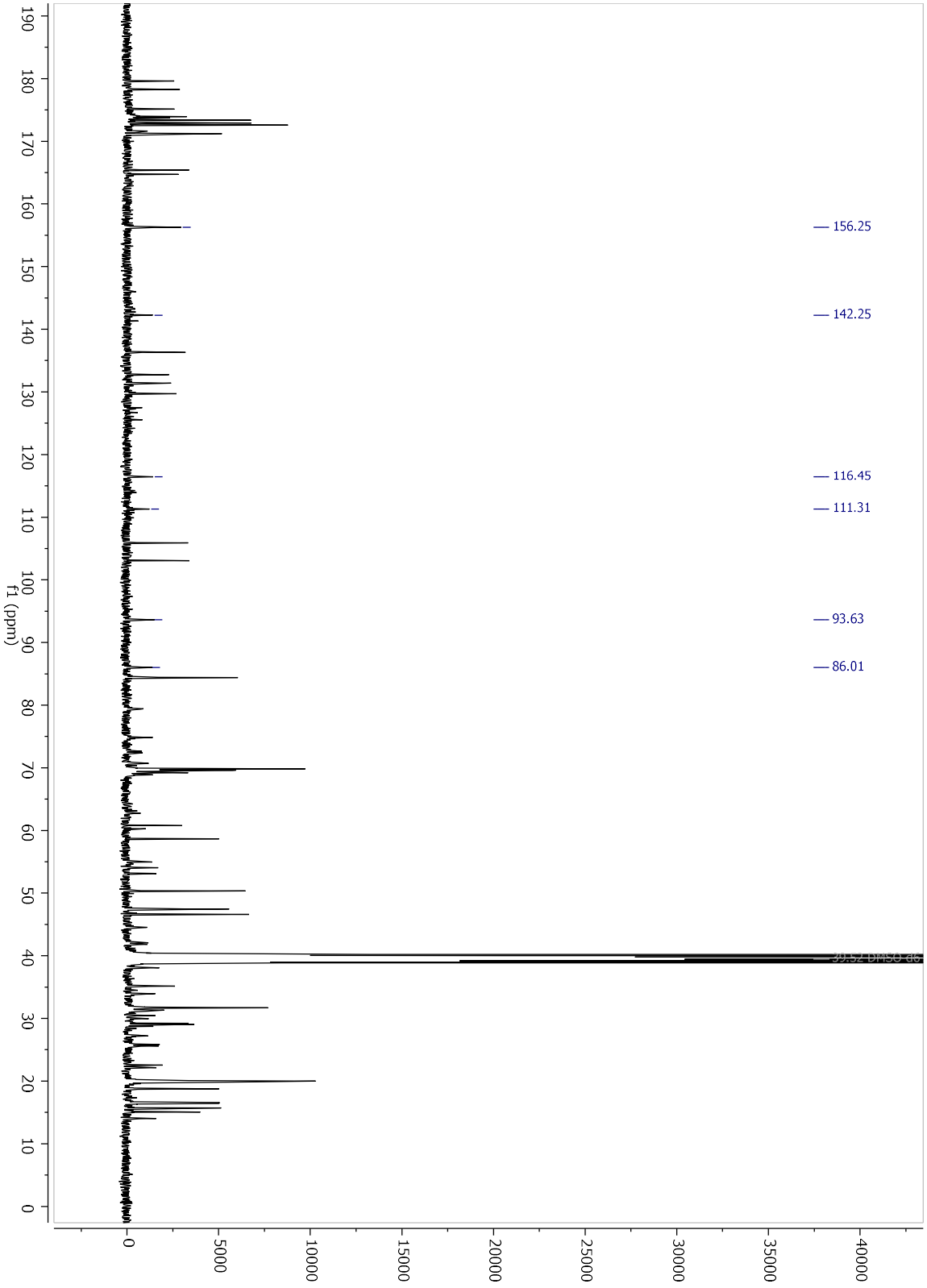

Compound 3

^{1}H NMR MeOD-d_4

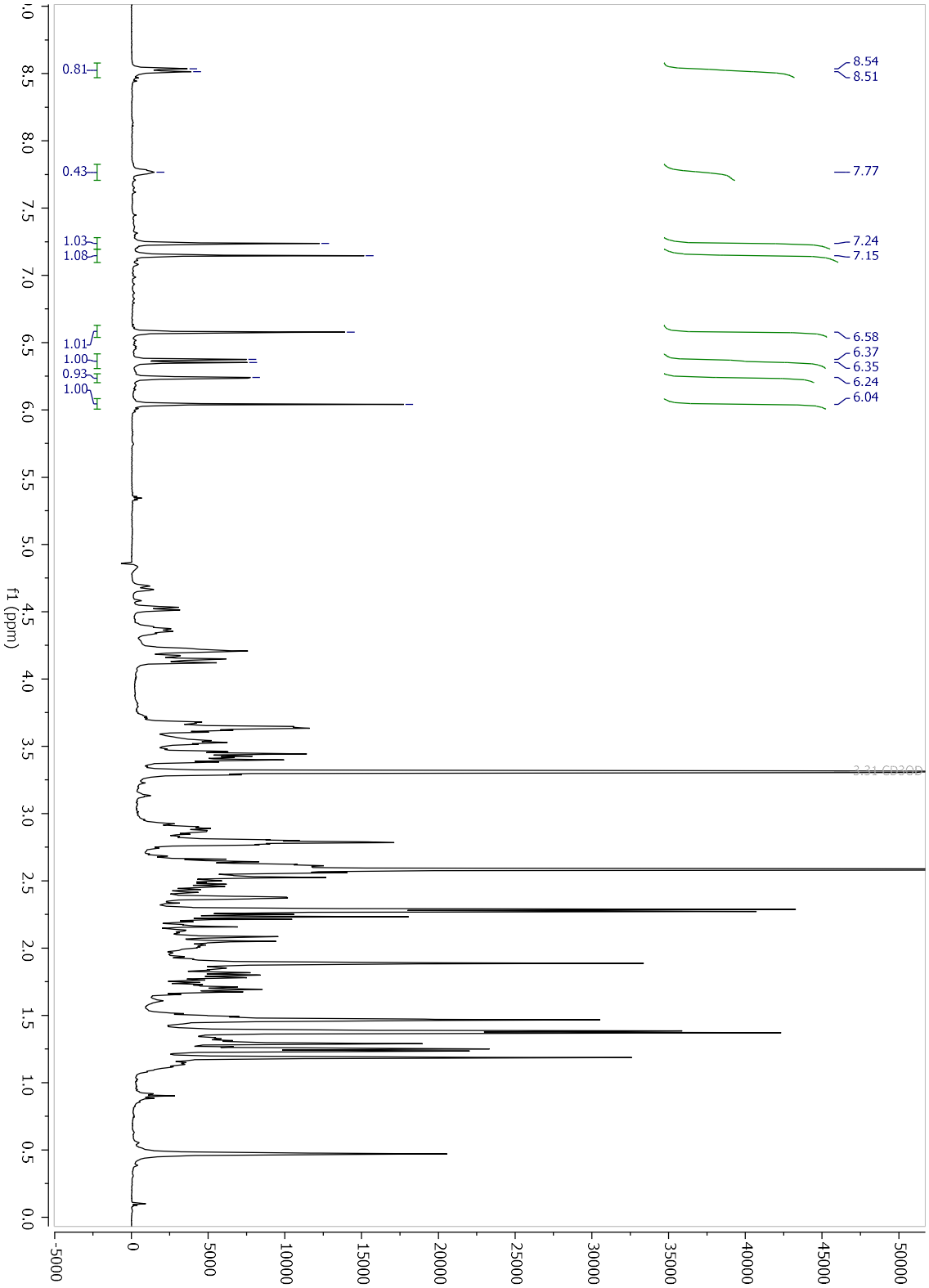

^{1}H NMR DMSO-*d*$_{6}$

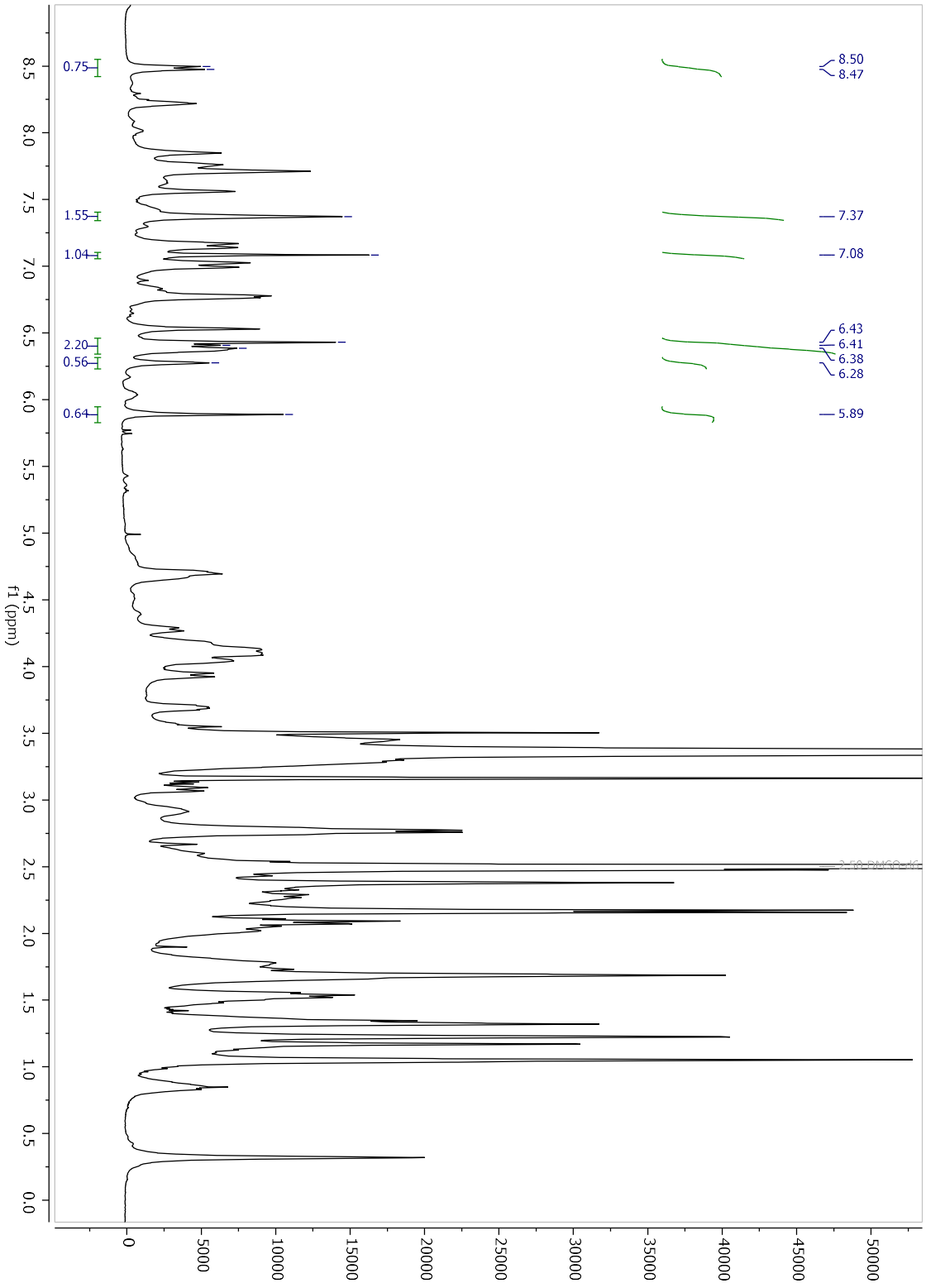

^{13}C NMR DMSO-d_6

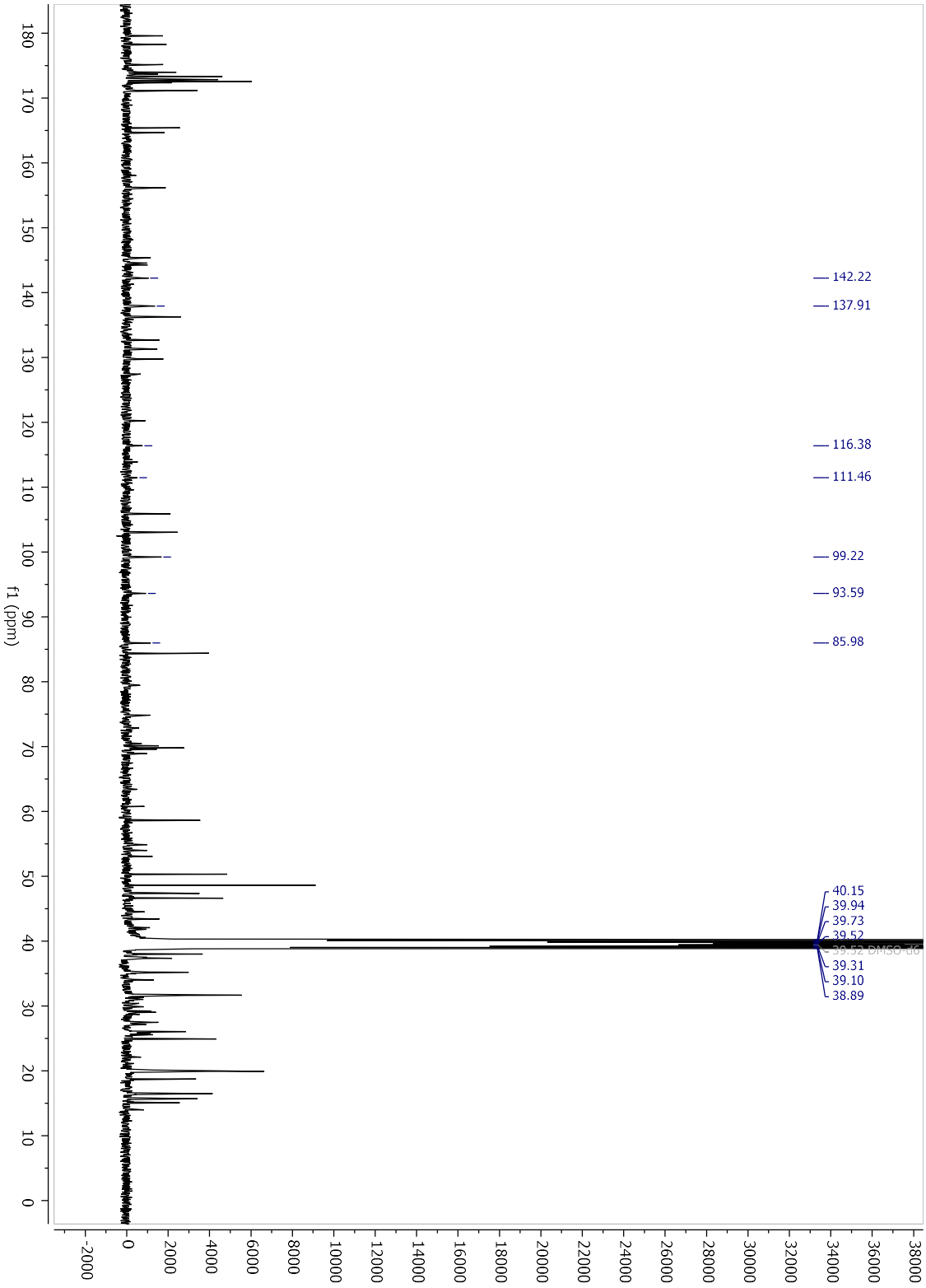

Compound 4

^{1}H NMR MeOD-*d*$_4$

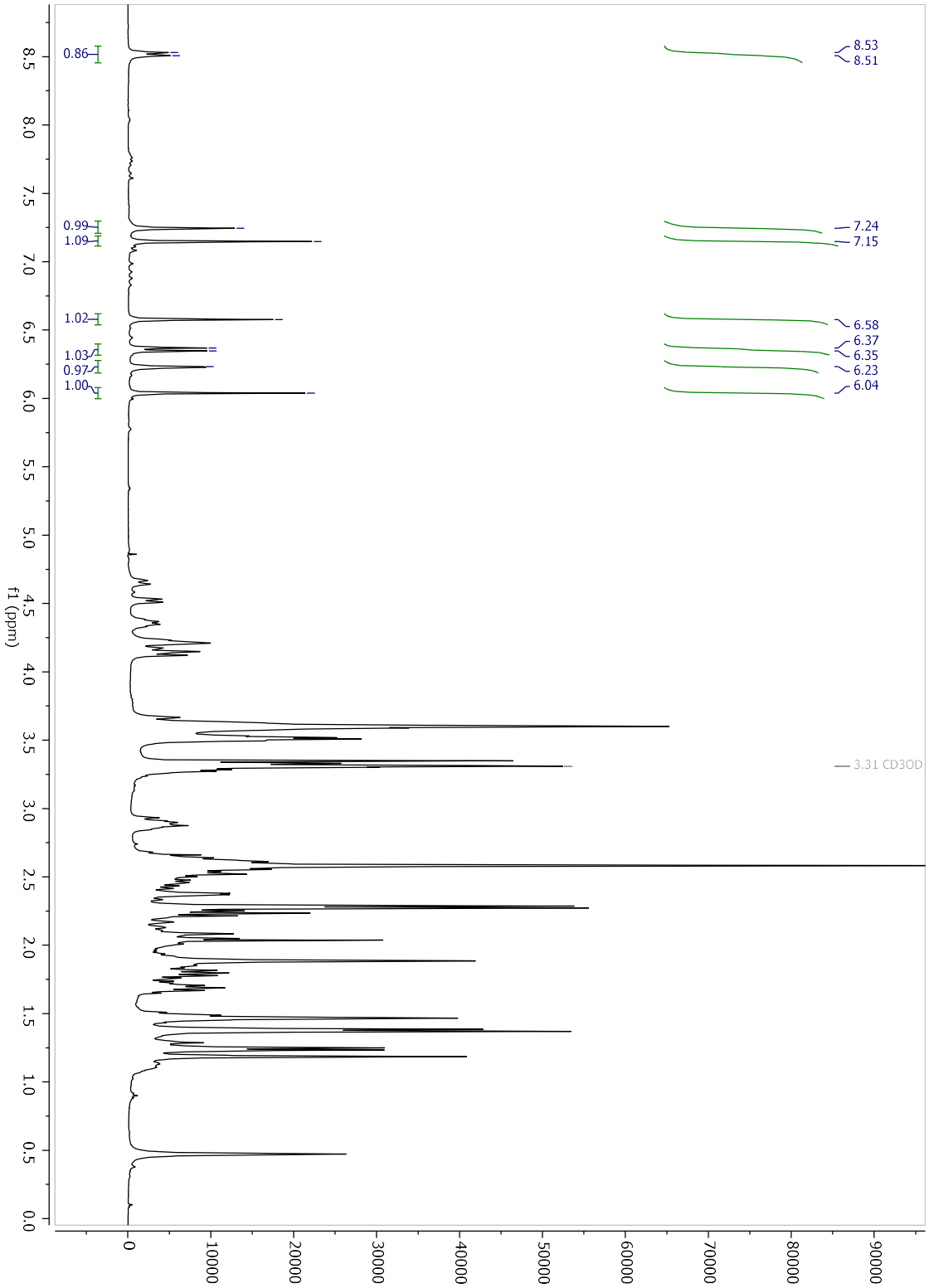

^{1}H NMR DMSO-*d*$_{6}$

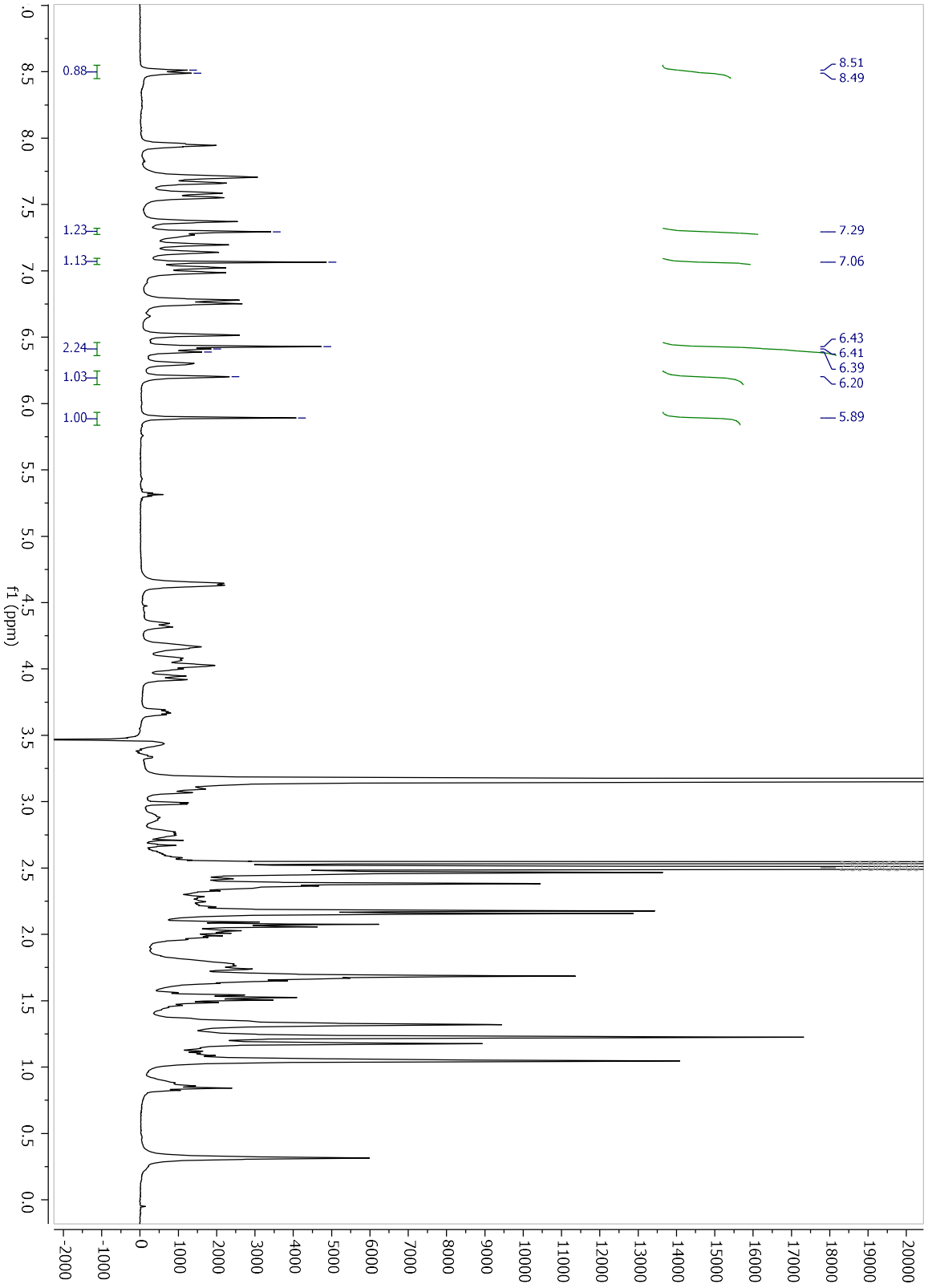

^{13}C NMR DMSO-d_6

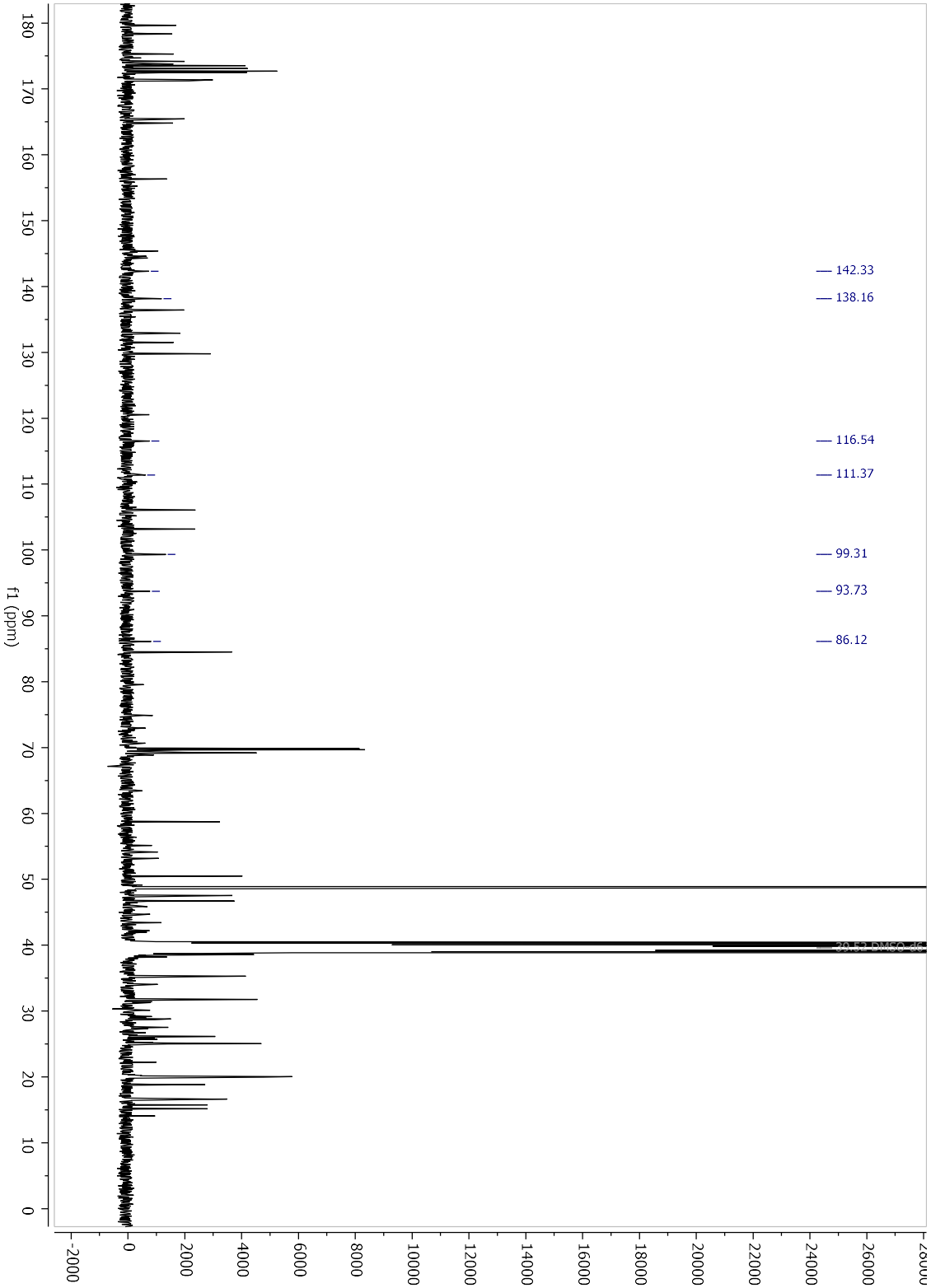

Compound 5

^{1}H NMR MeOD-d_4

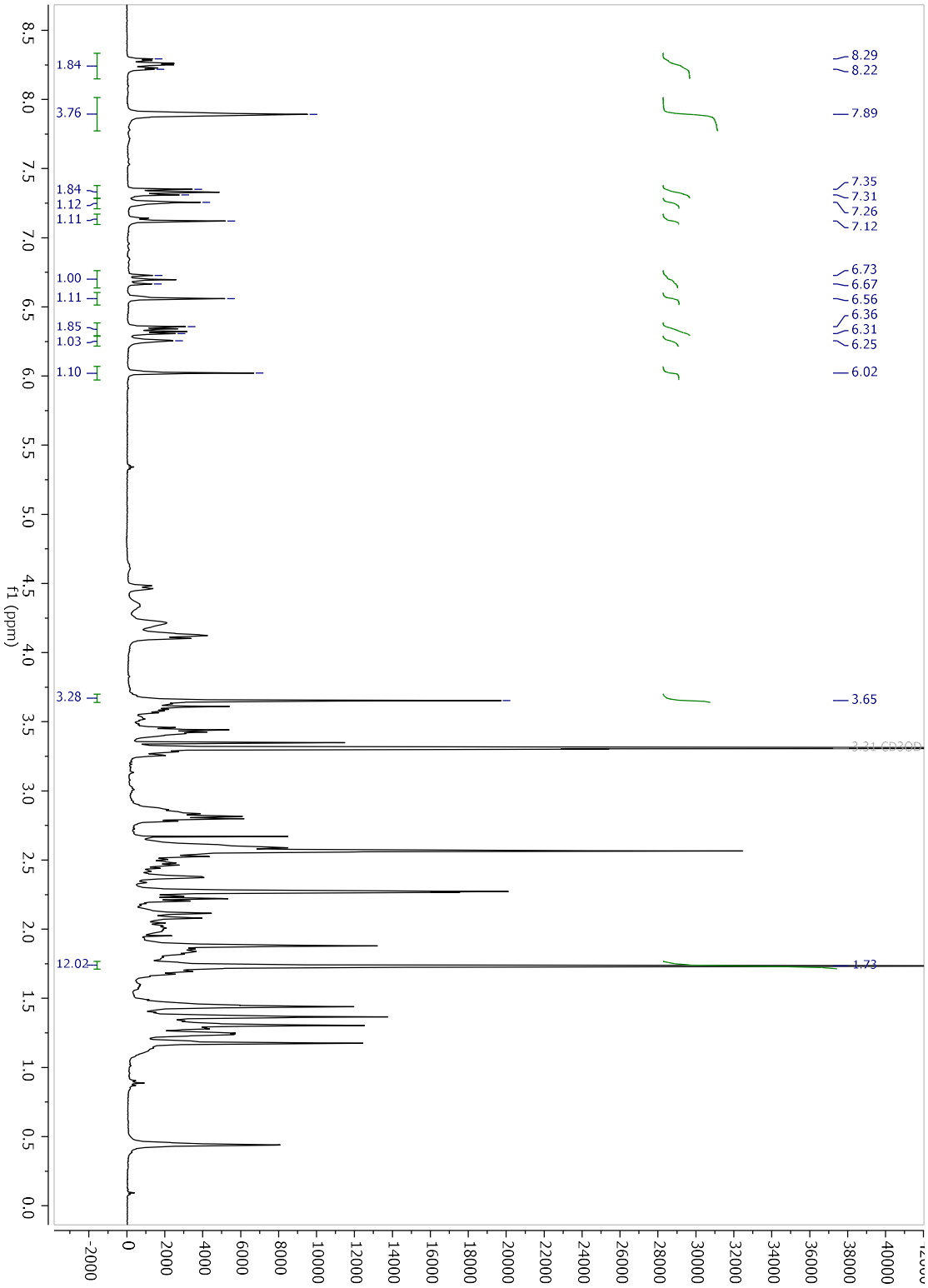

^{1}H NMR DMSO-d_6

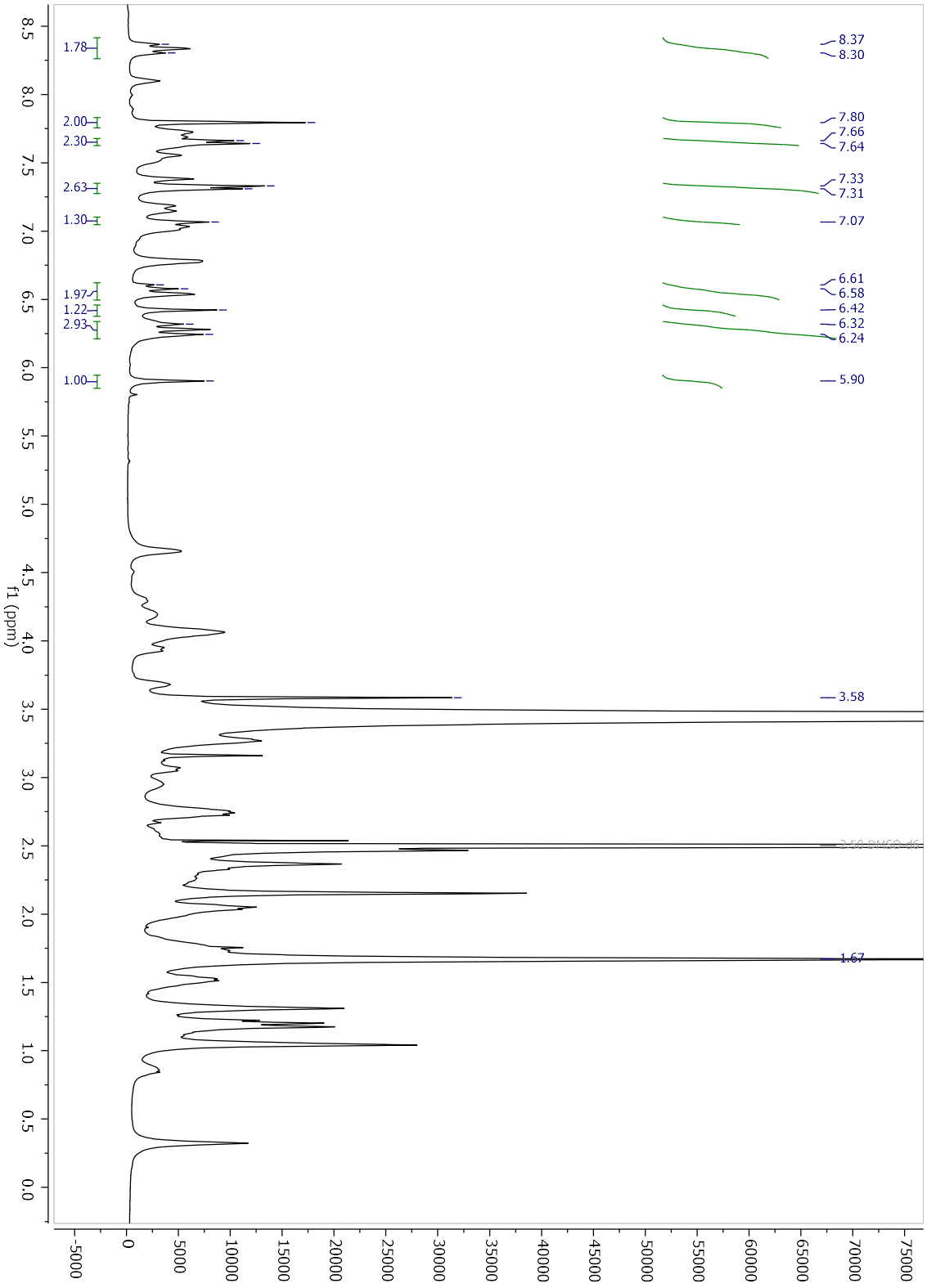

^{13}C NMR DMSO-d_6

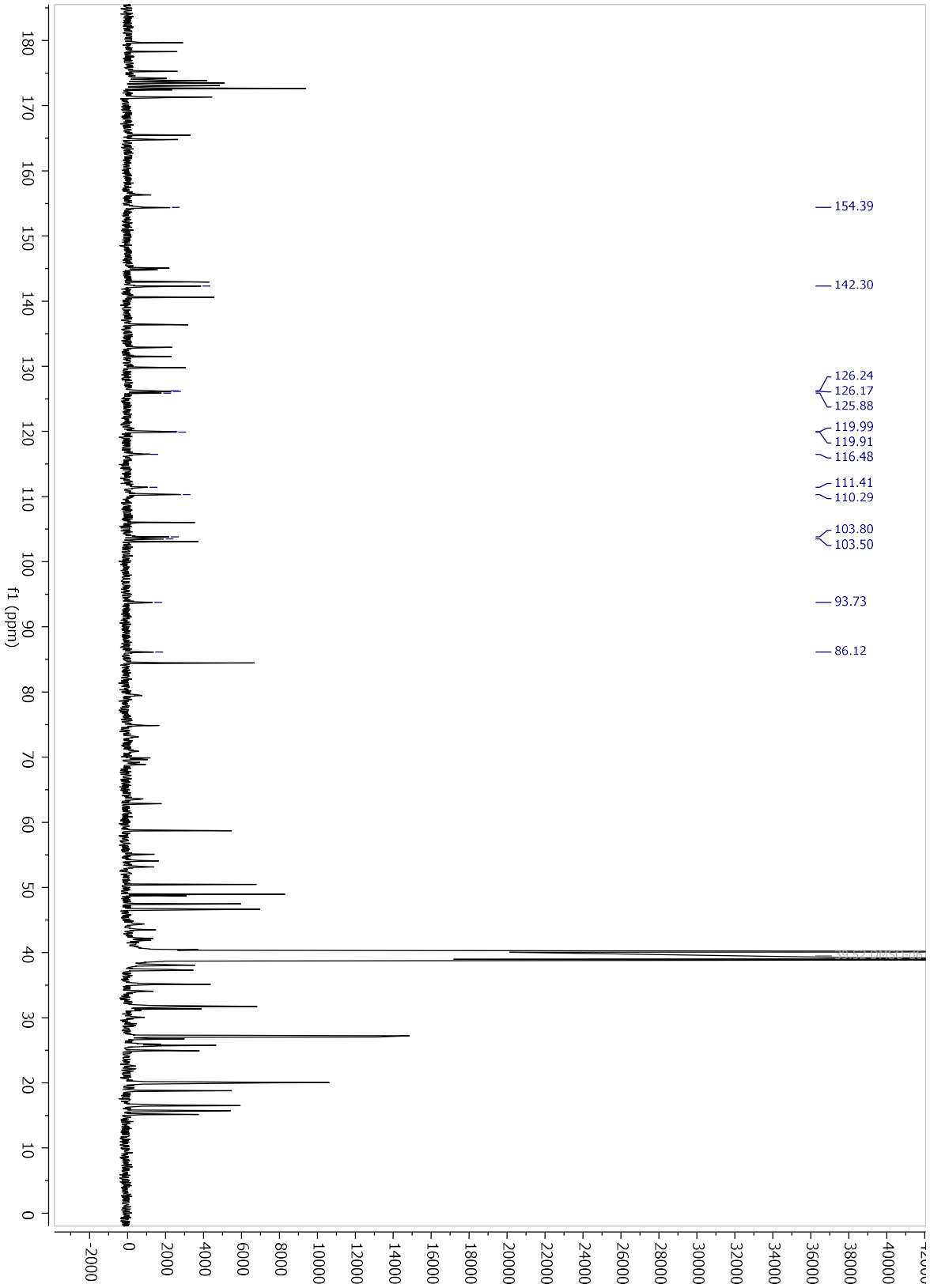

Compound 6

^{1}H NMR MeOD-d_4

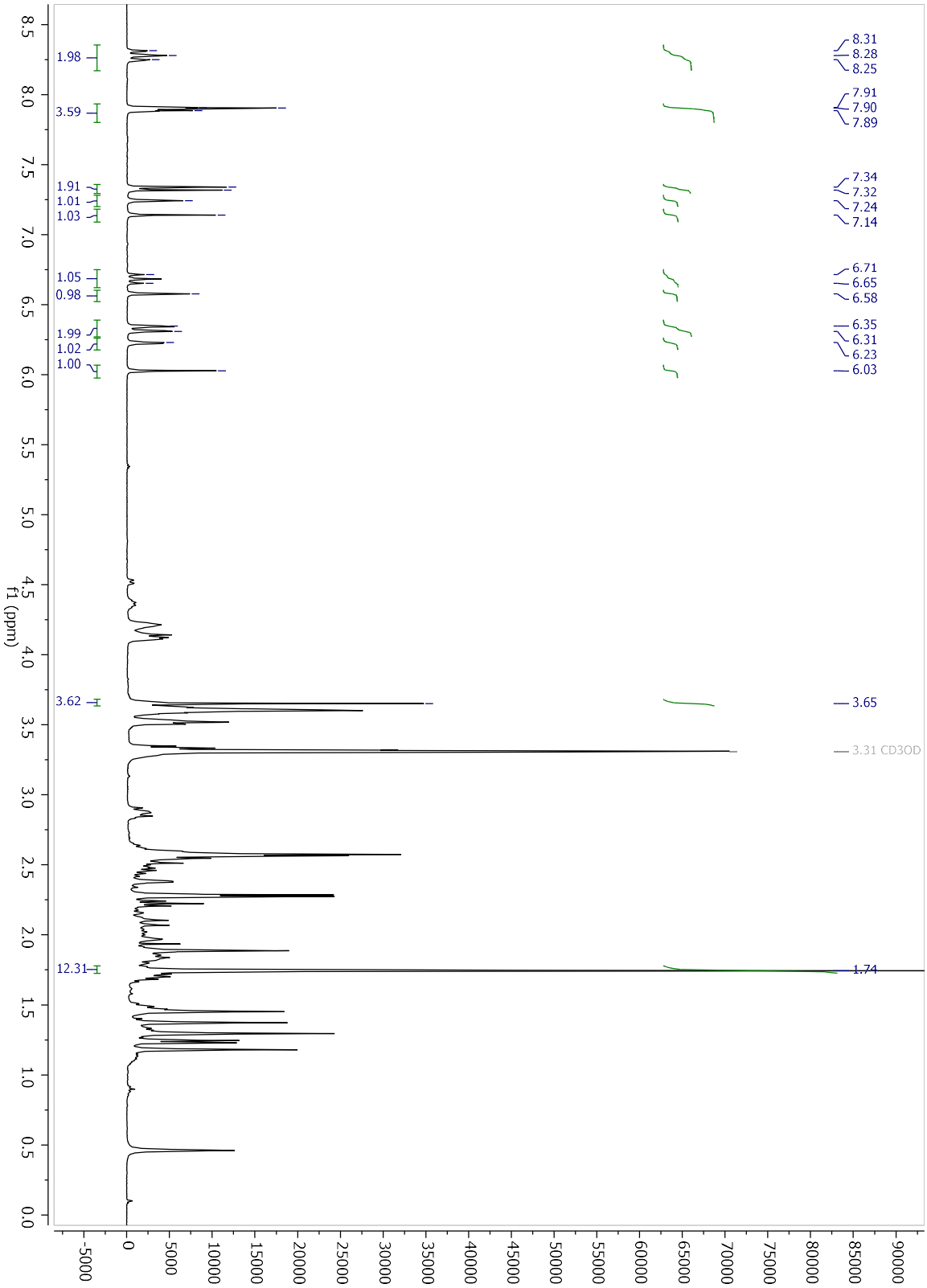

^{1}H NMR DMSO-*d*$_{6}$

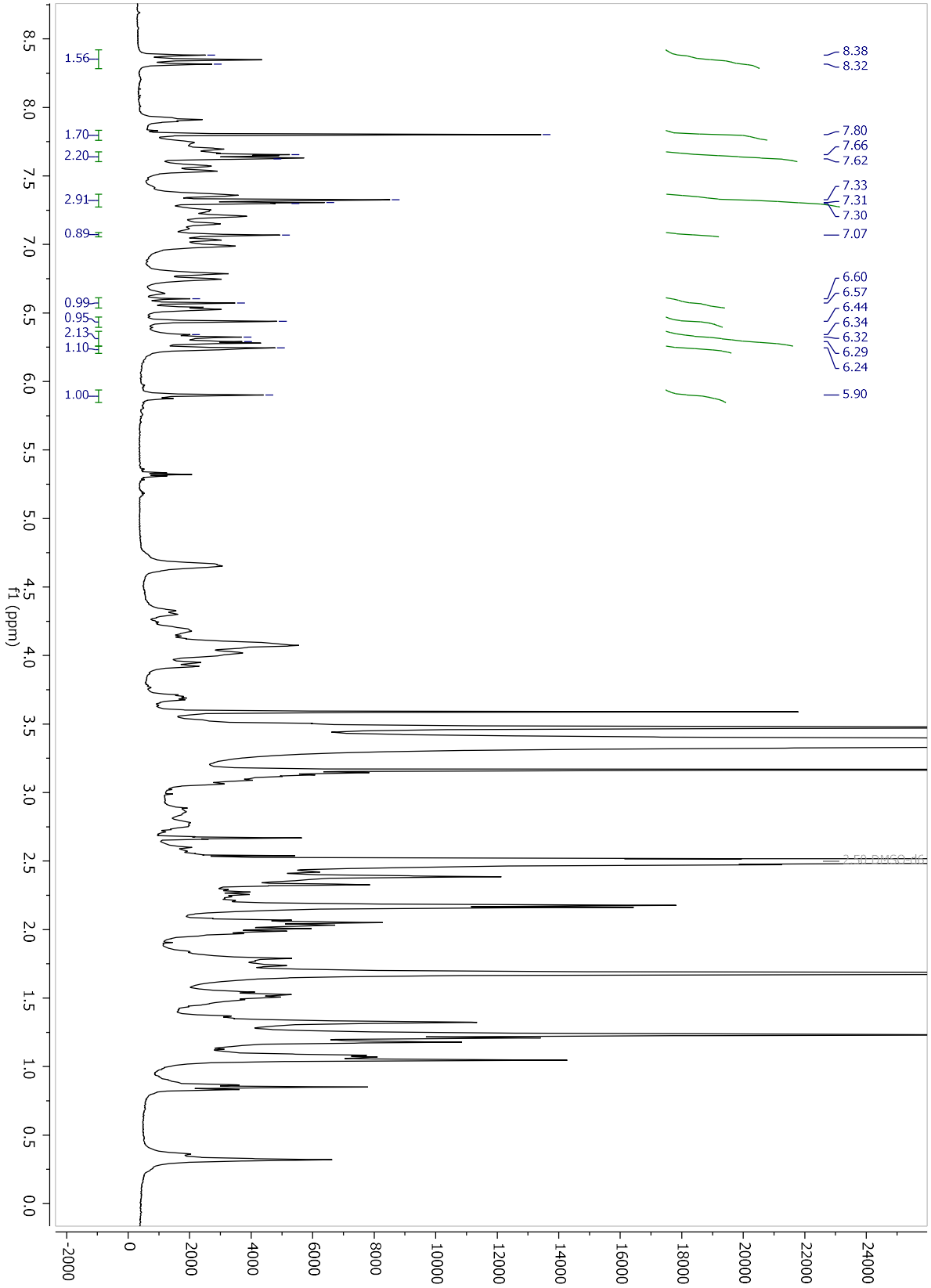

^{13}C NMR DMSO-*d*$_6$

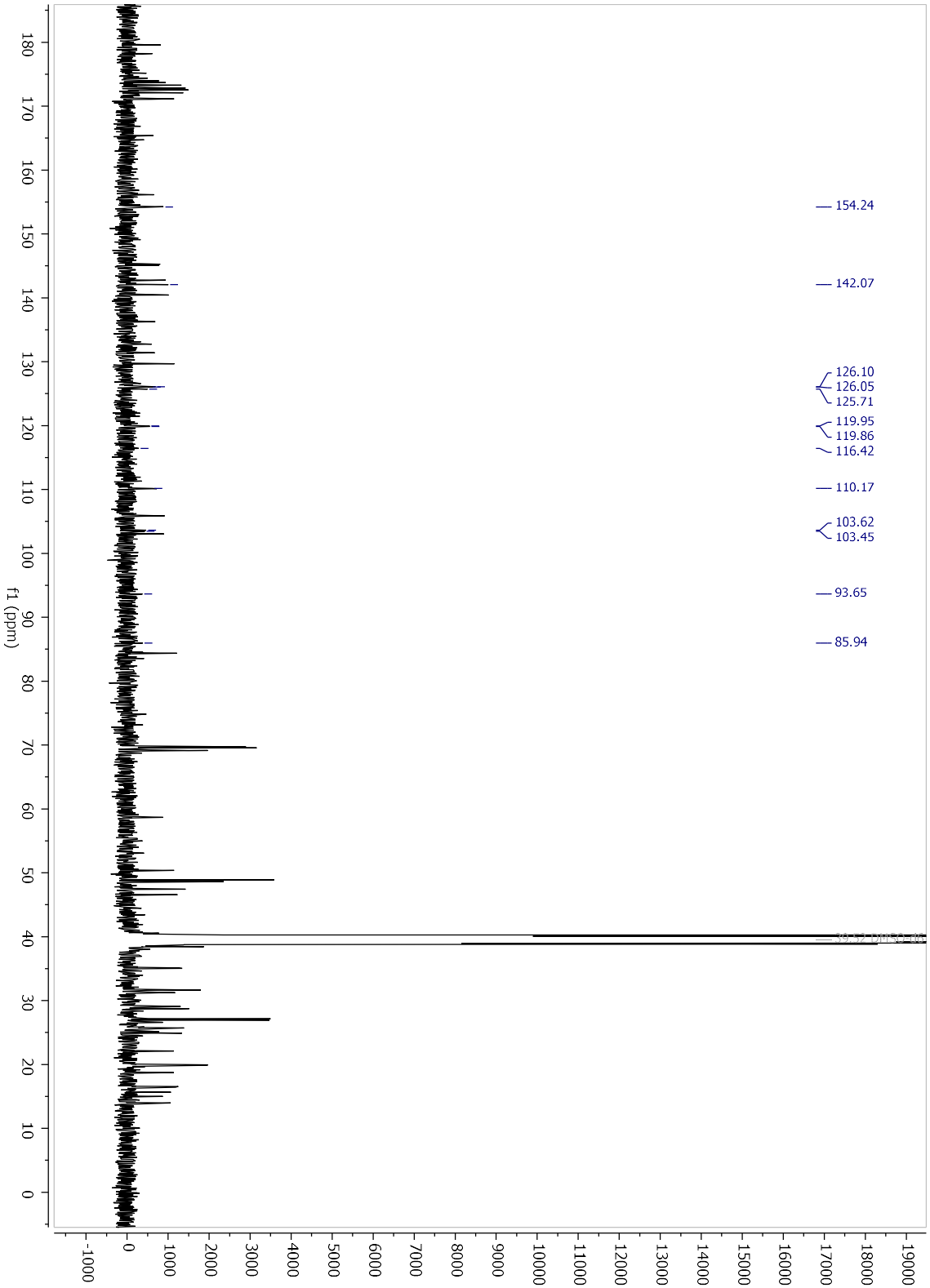

Compound 7

^{1}H NMR MeOD-*d*$_4$

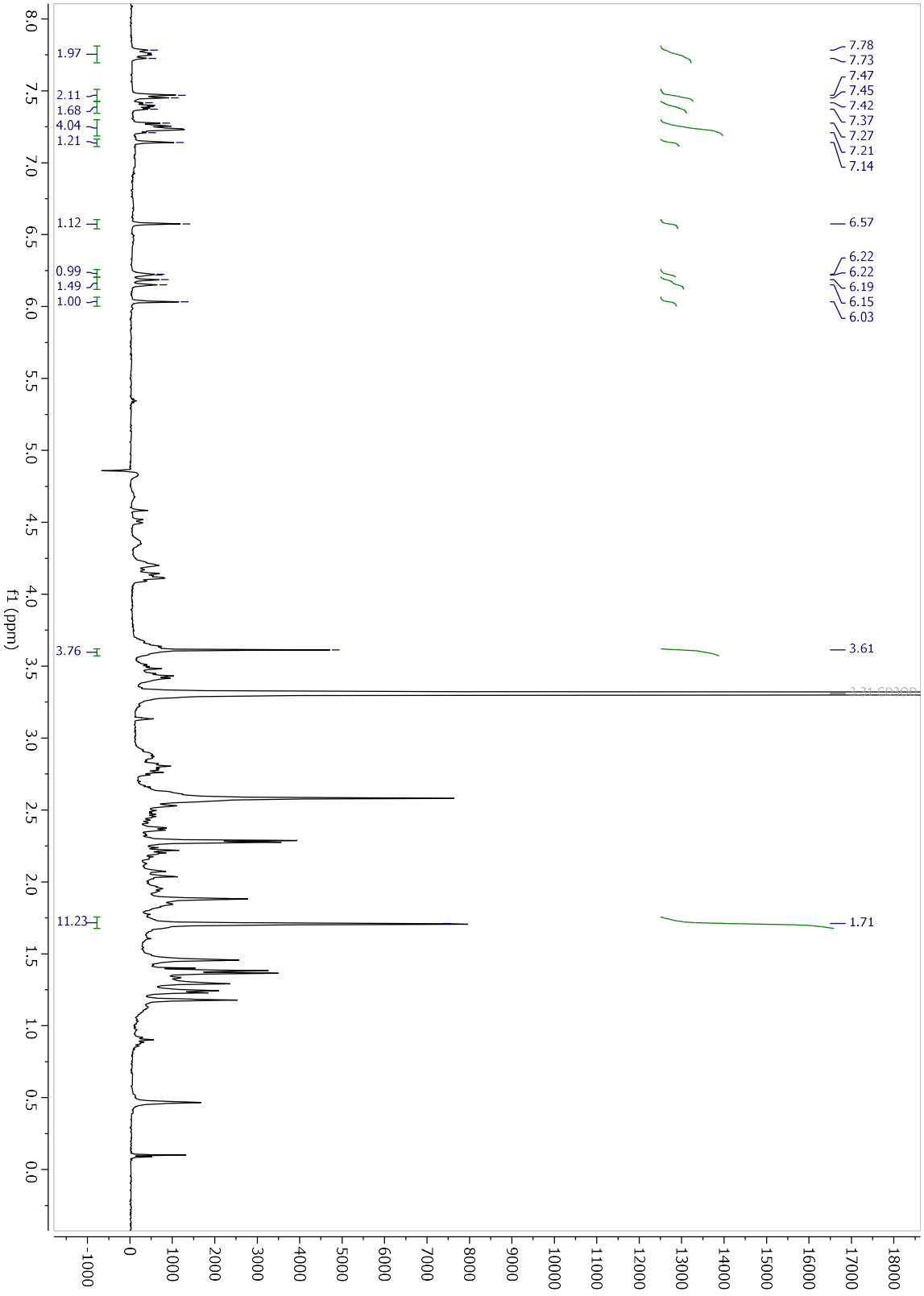

^{1}H NMR DMSO-d_6

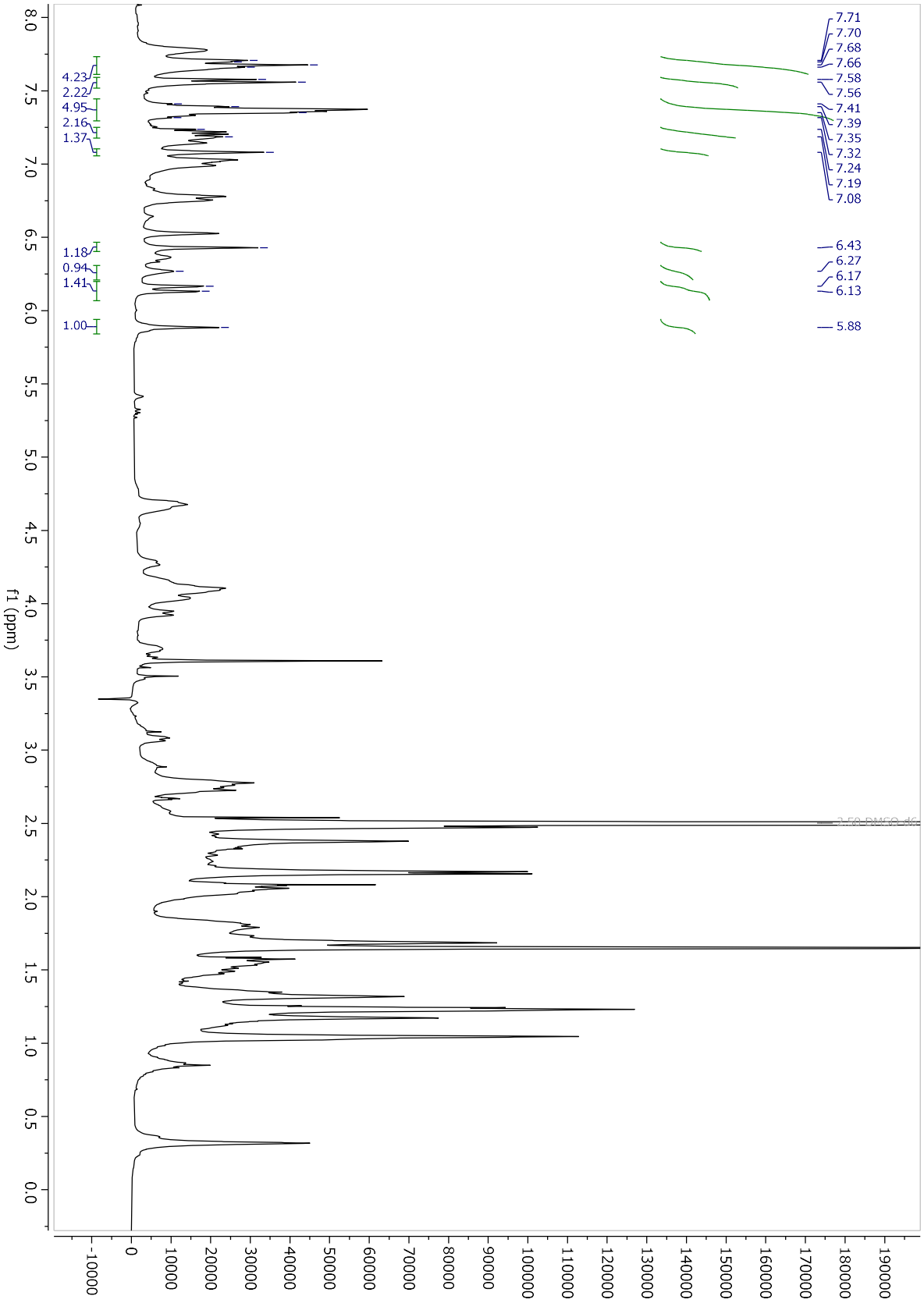

^{13}C NMR DMSO-d_6

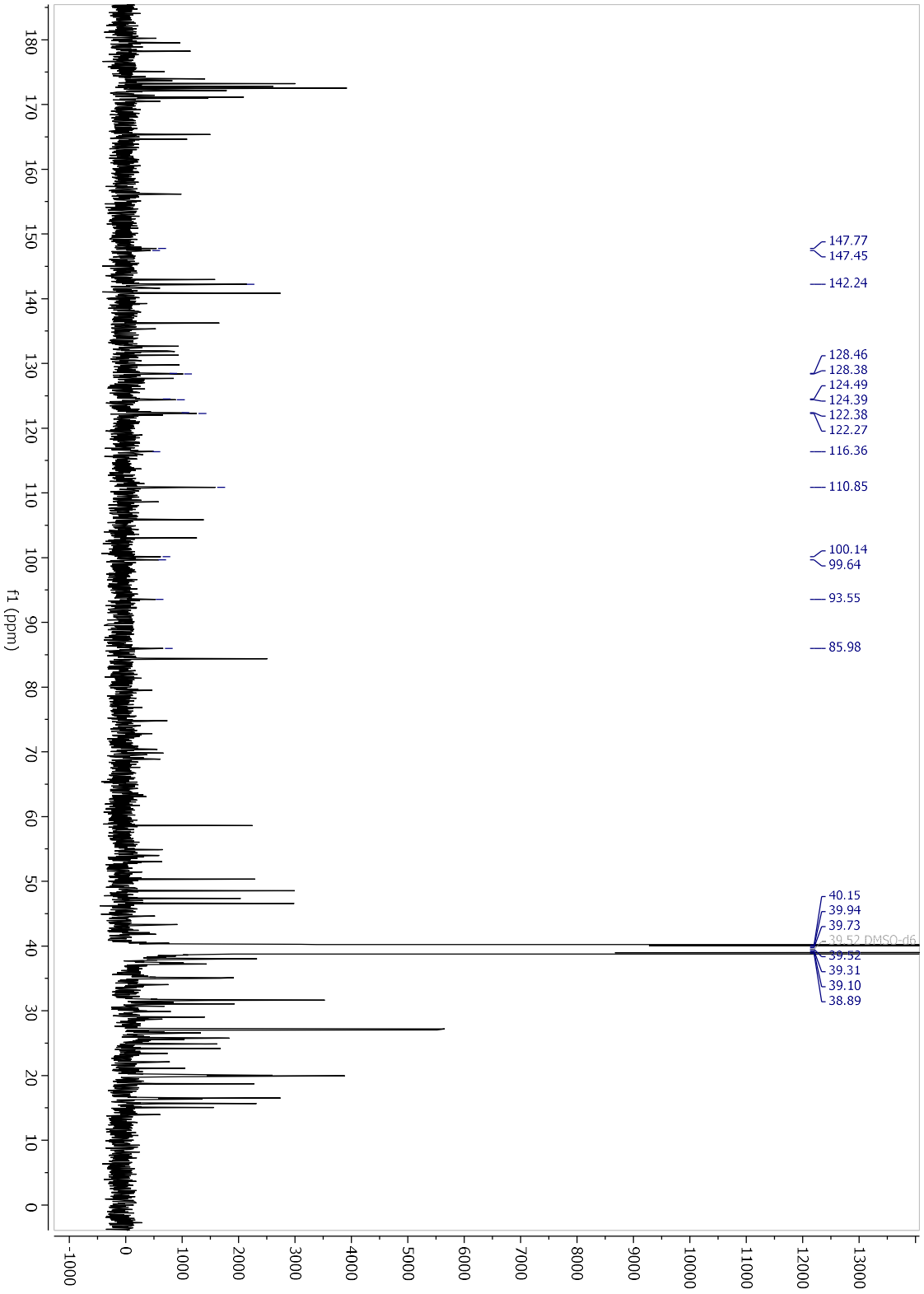

Compound 8

^{1}H NMR MeOD-d_4

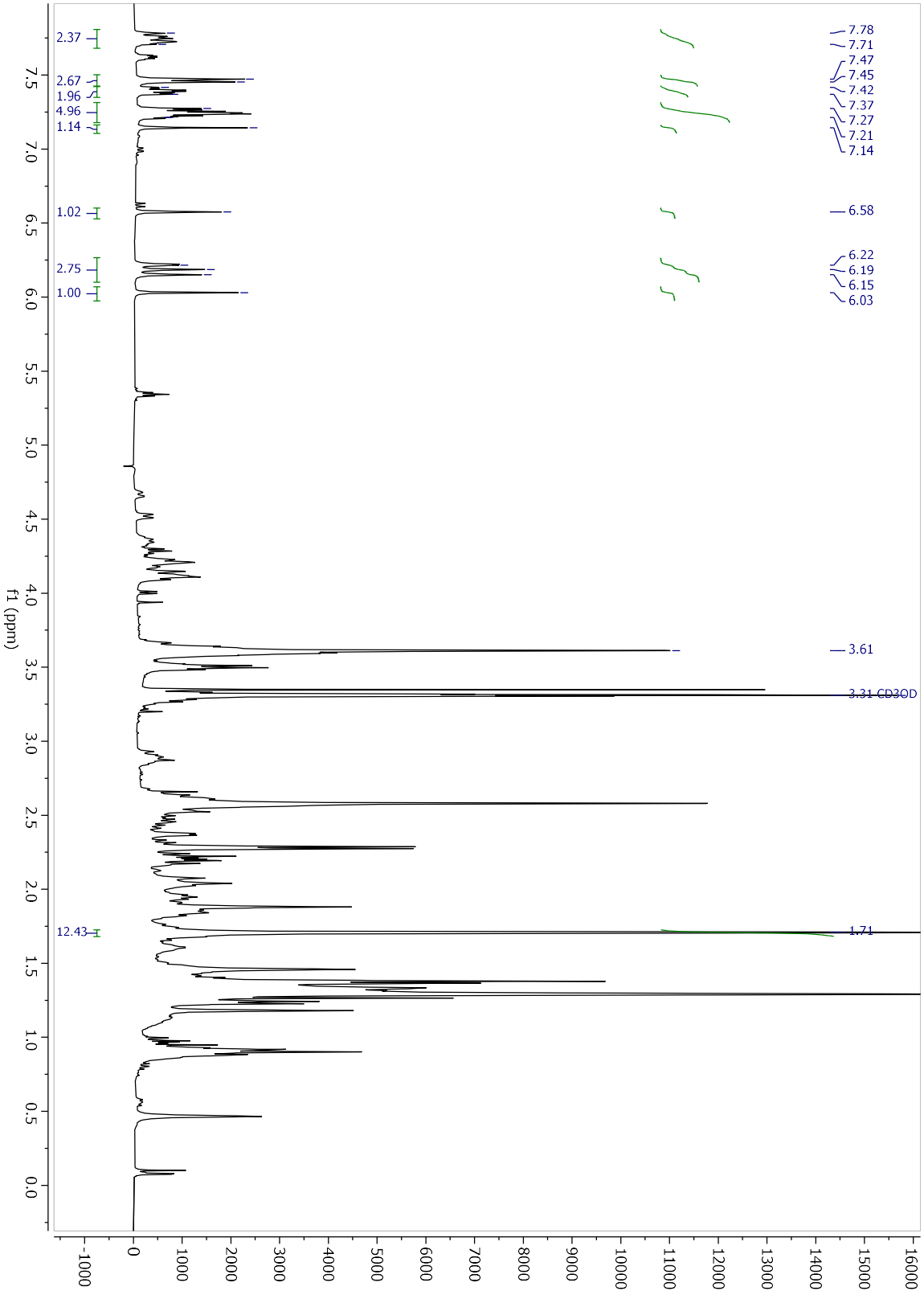

^{1}H NMR DMSO-*d*$_{6}$

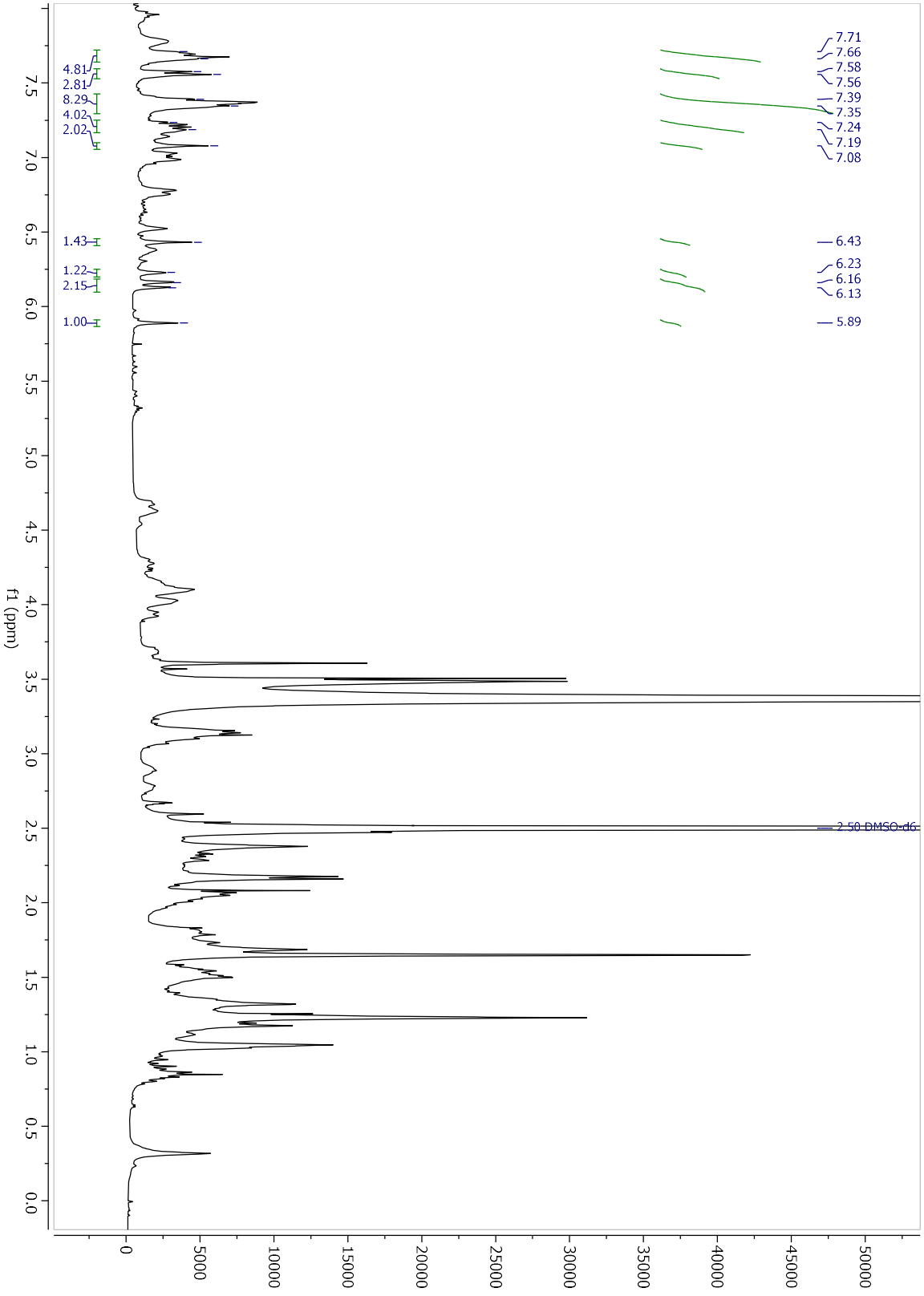

^{13}C NMR DMSO-d_6

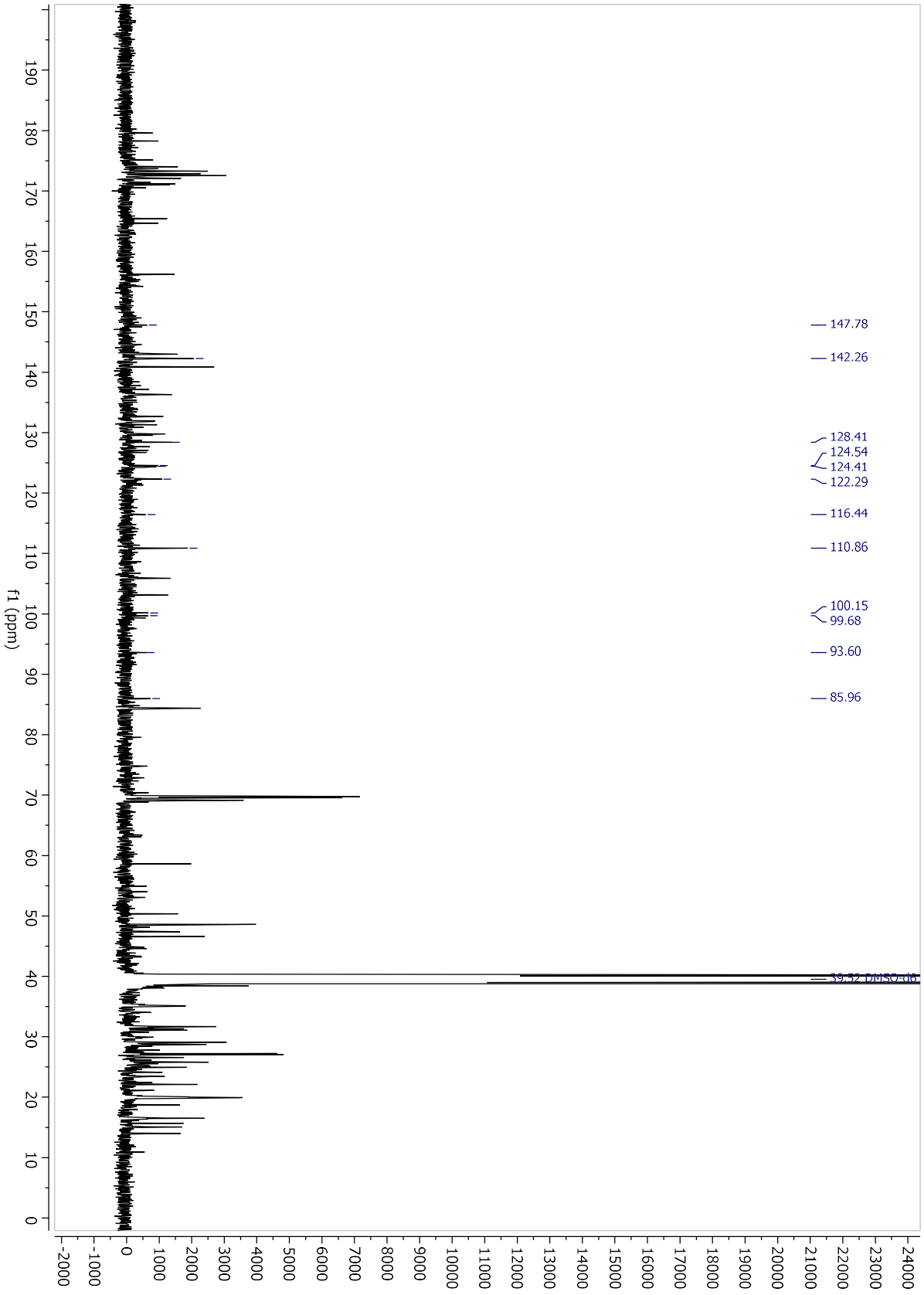

Compound 9

^{1}H NMR *D_2O*

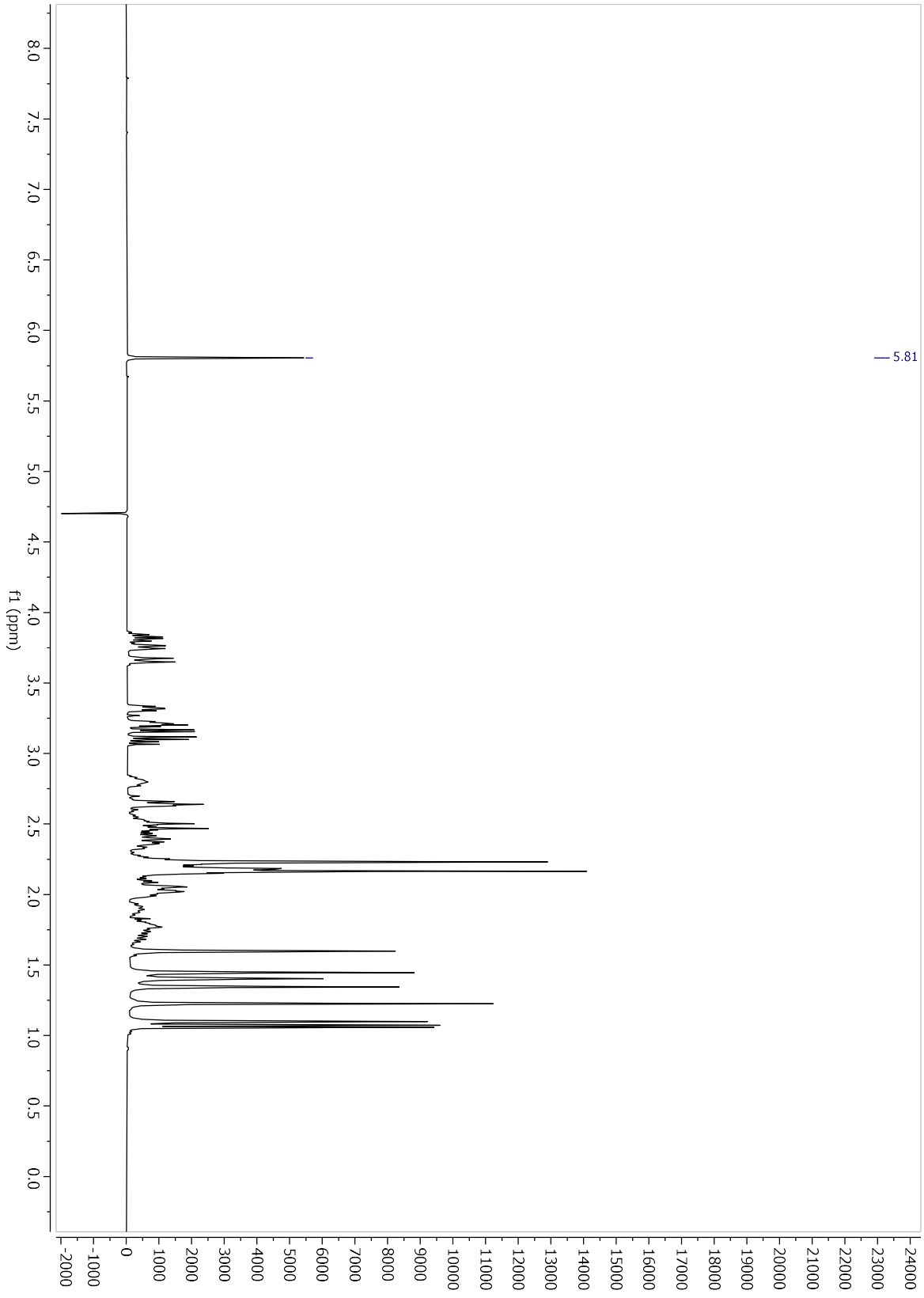

^{1}H NMR *DMSO-d$_6$*

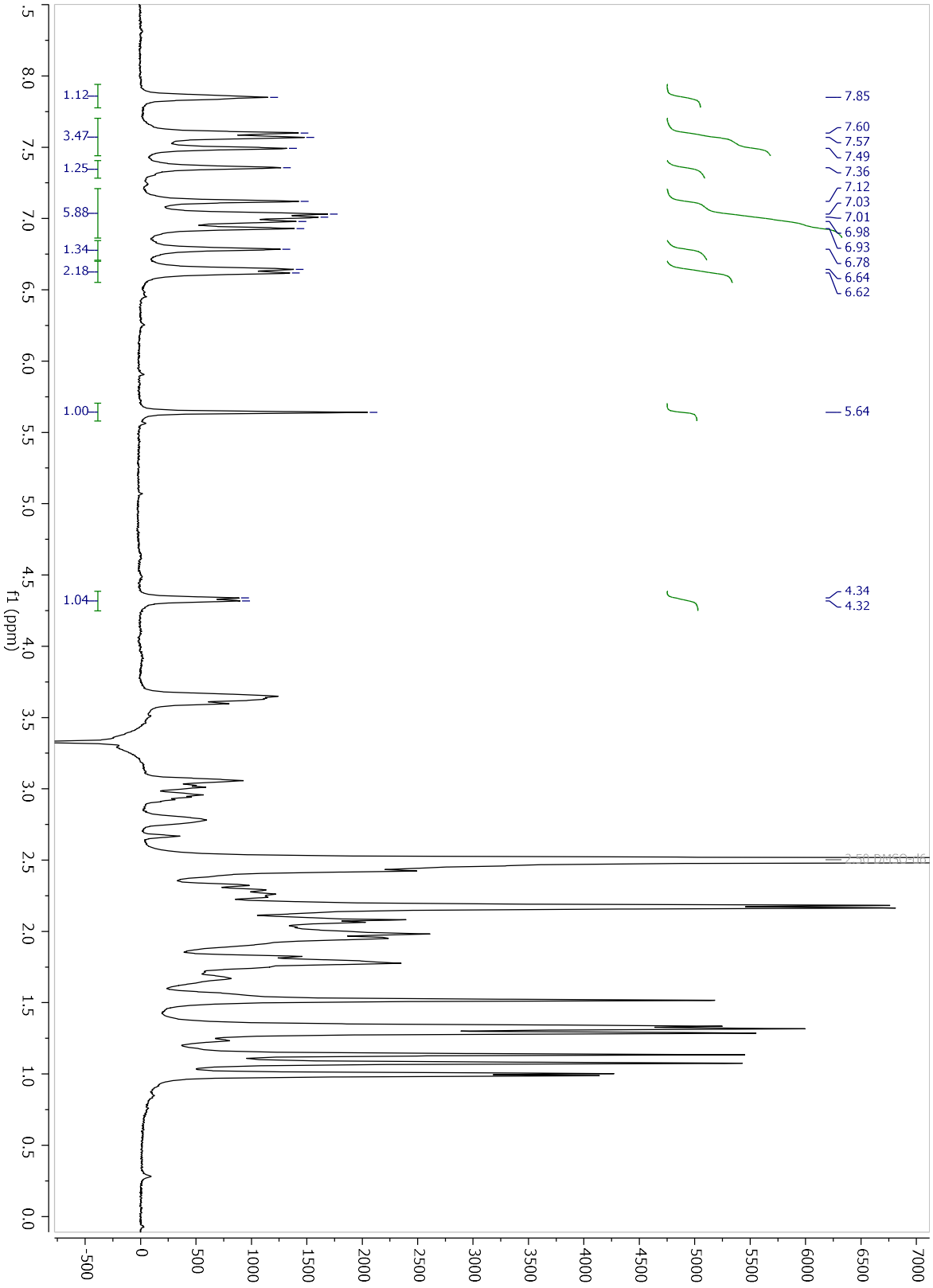

^{13}C NMR *DMSO-d_6*

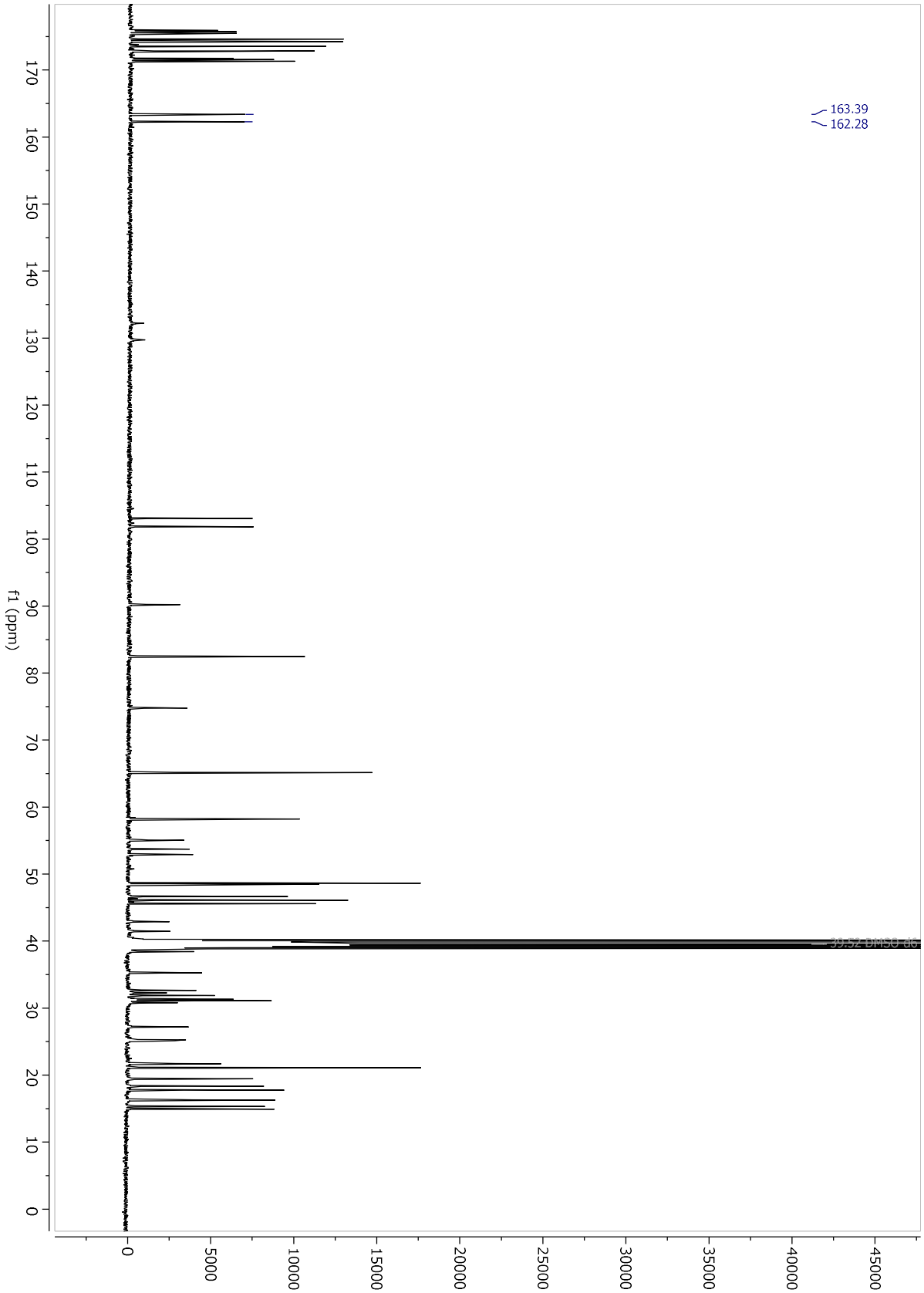

Compound 10

^{1}H NMR *D_2O*

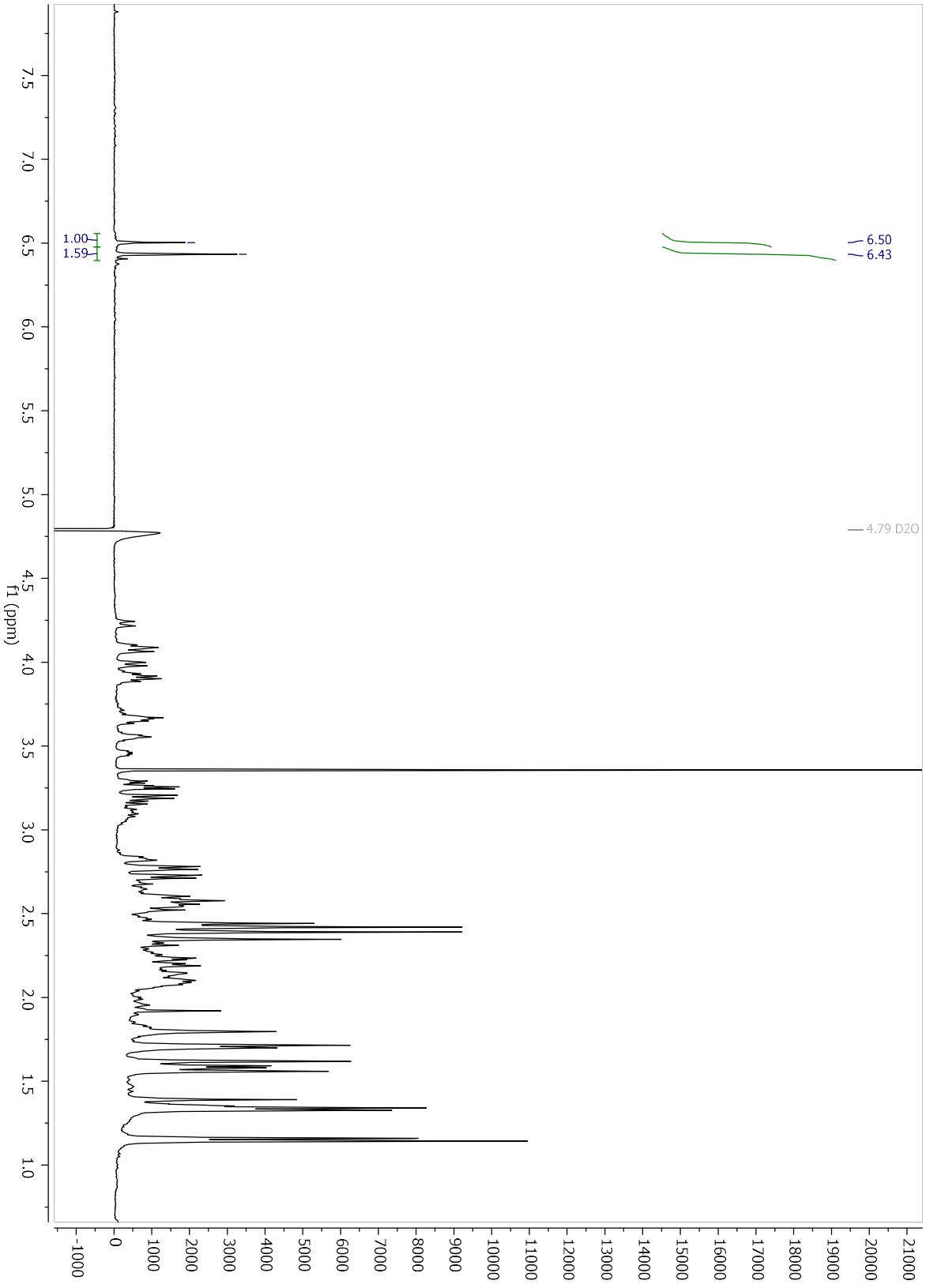

Compound 11

^{1}H NMR *MeOD-d$_4$*

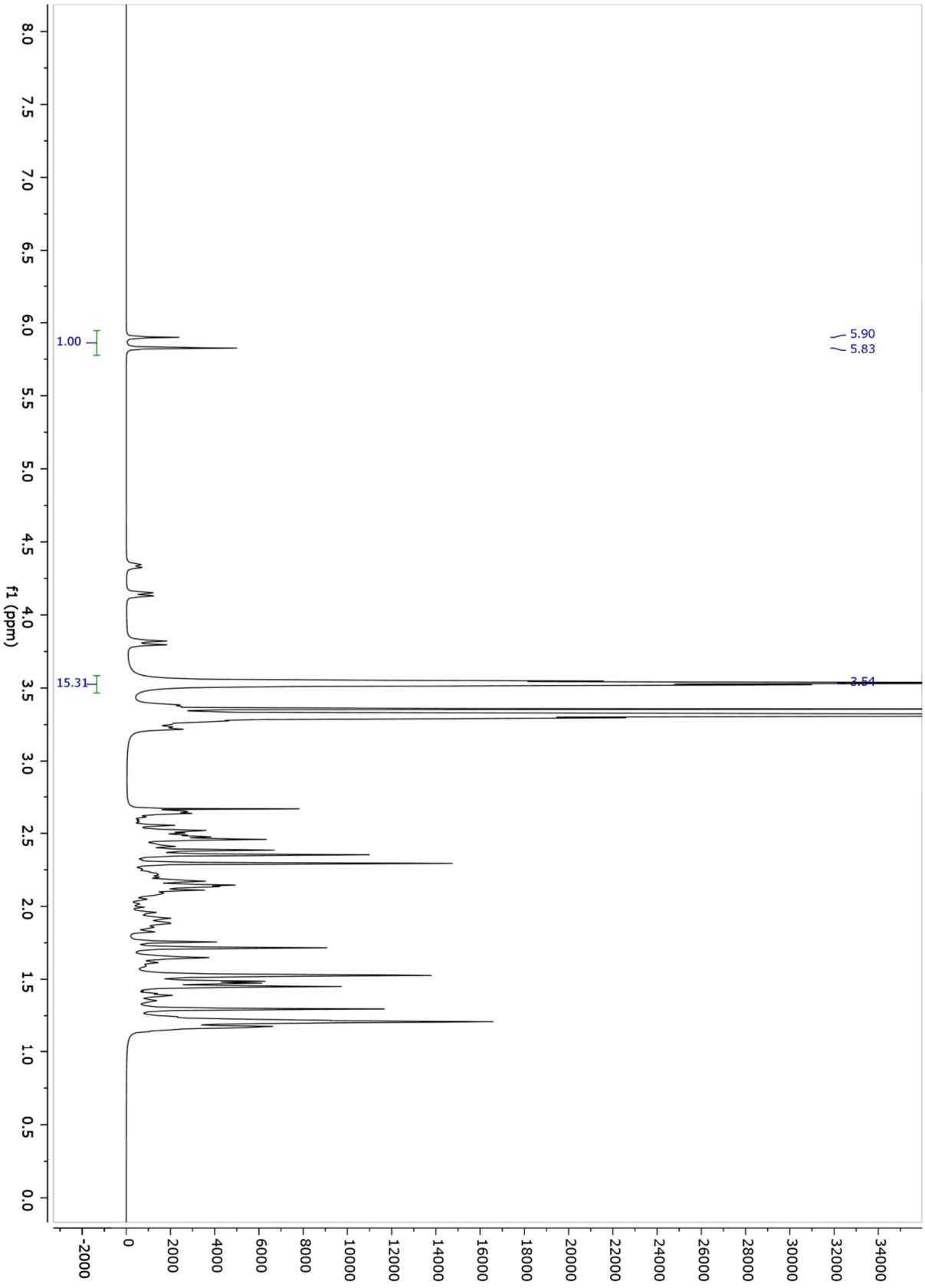

Compound 12

^{1}H NMR *D_2O*

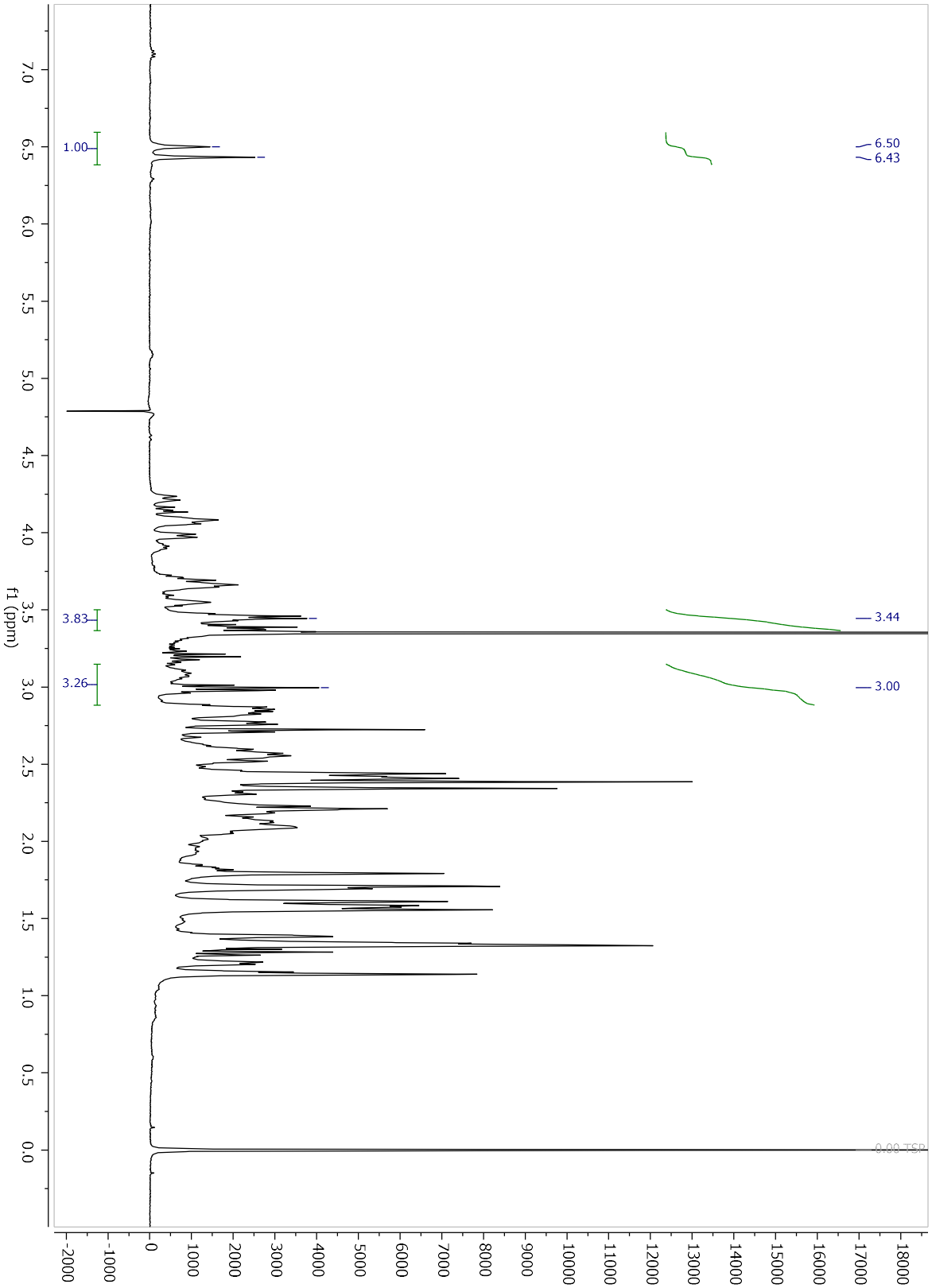

Compound 13

^{1}H NMR *MeOD-d$_4$*

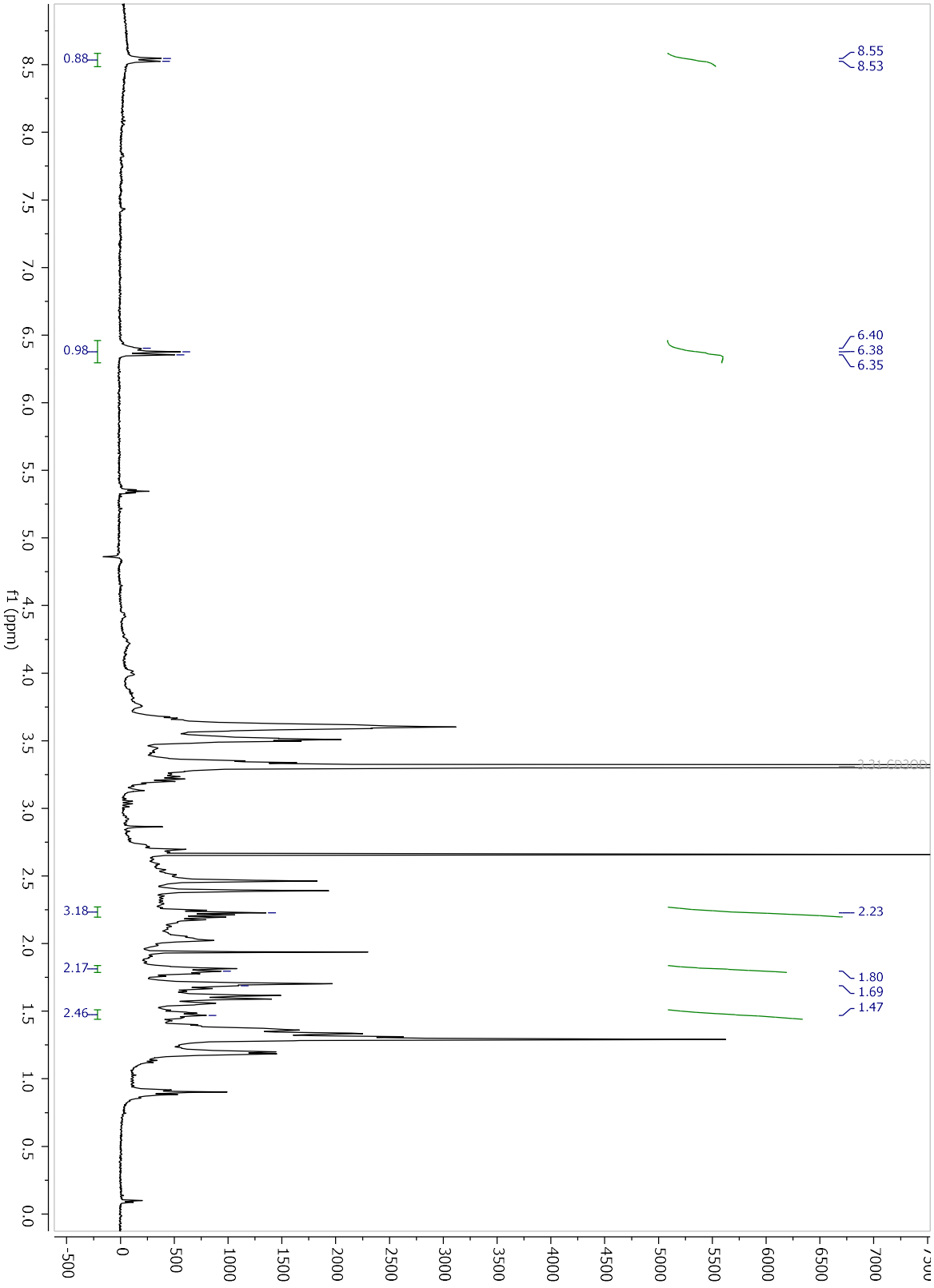

Compound 14

^{1}H NMR *MeOD-d$_4$*

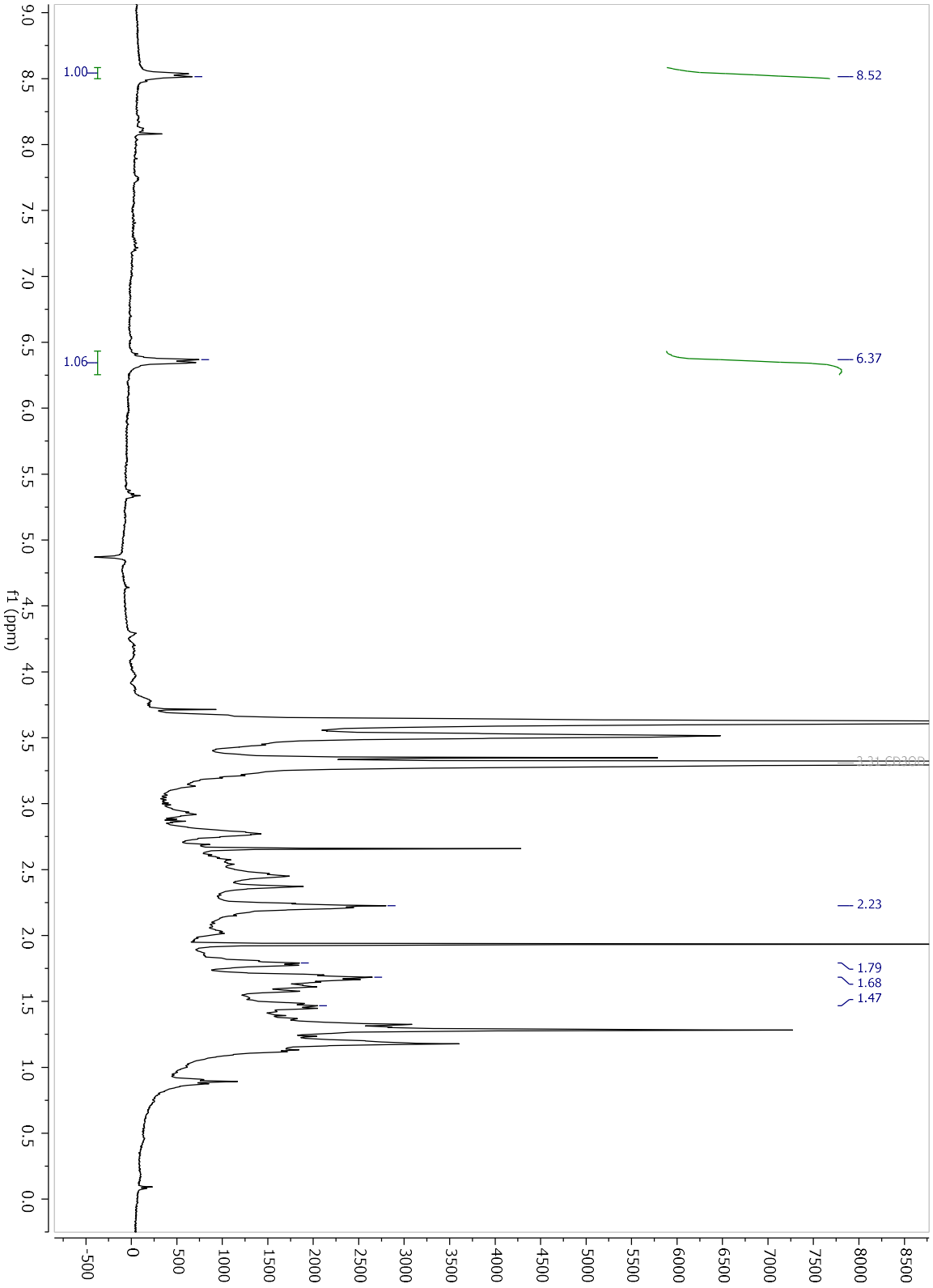

Compound 15

^{1}H NMR *D_2O*

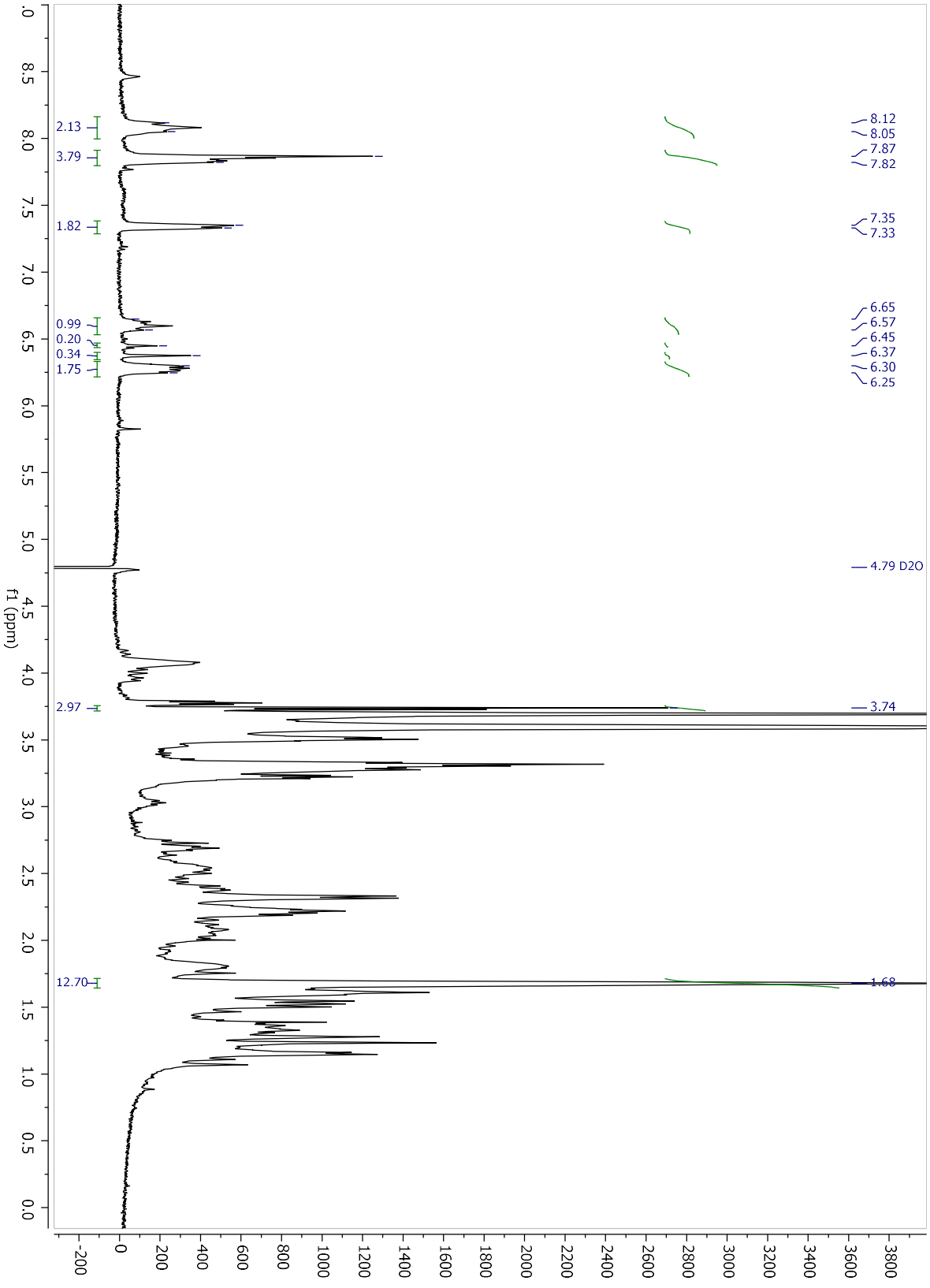

Compound 16

^{1}H NMR *MeOD-d$_4$*

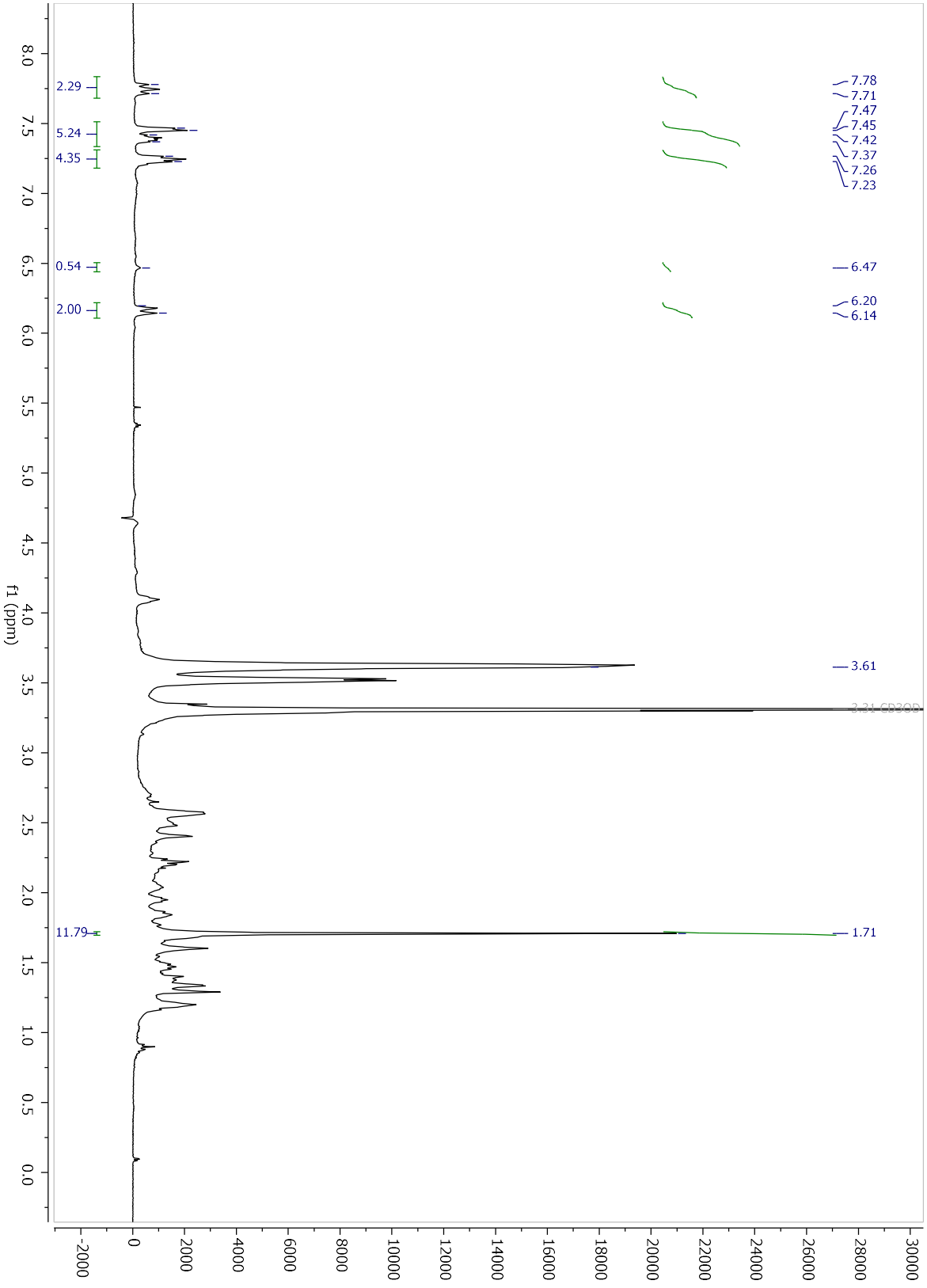

Compound 17

^{1}H NMR in MeOH-d_4

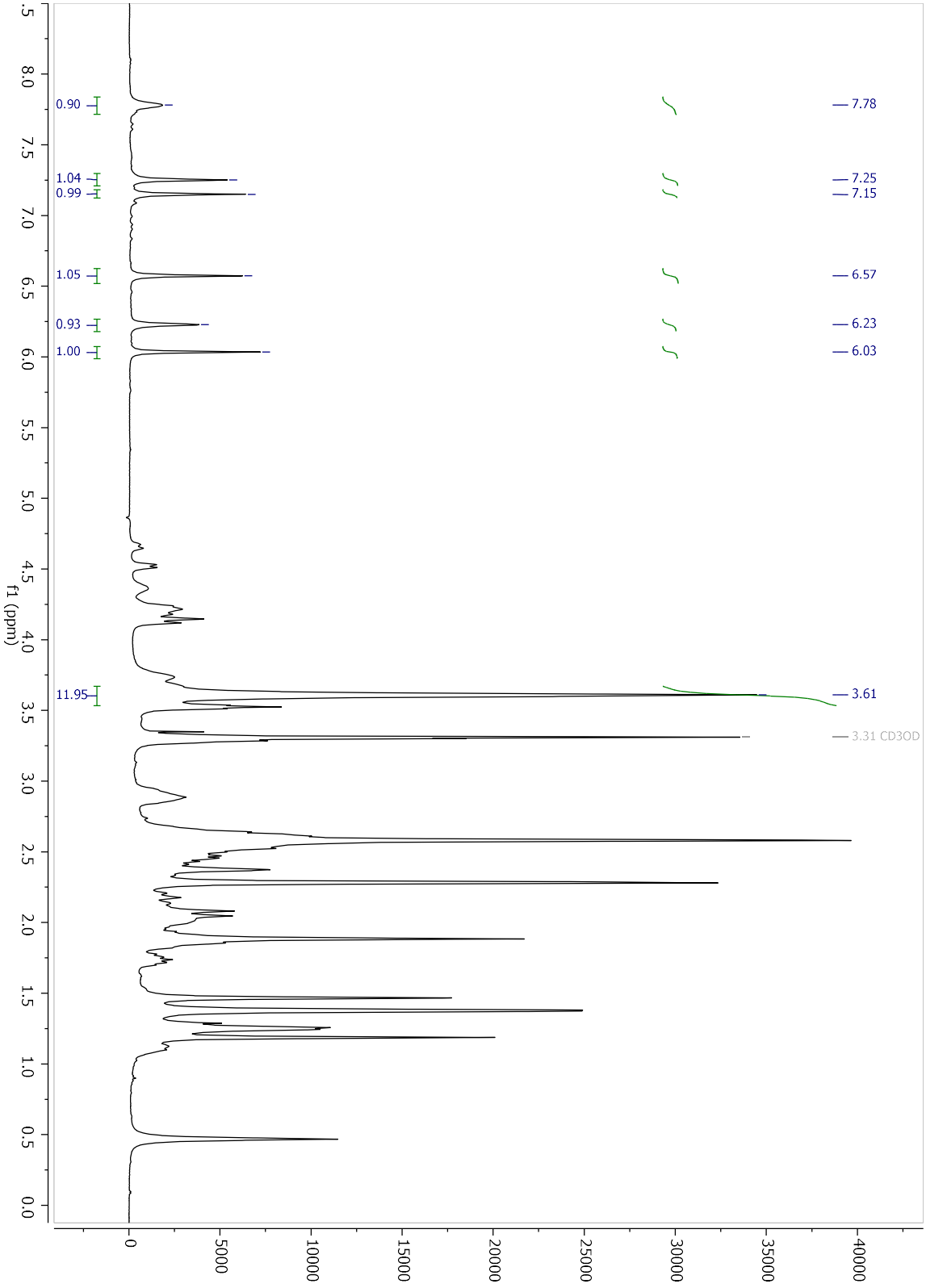

^{1}H NMR in DMSO-d_6

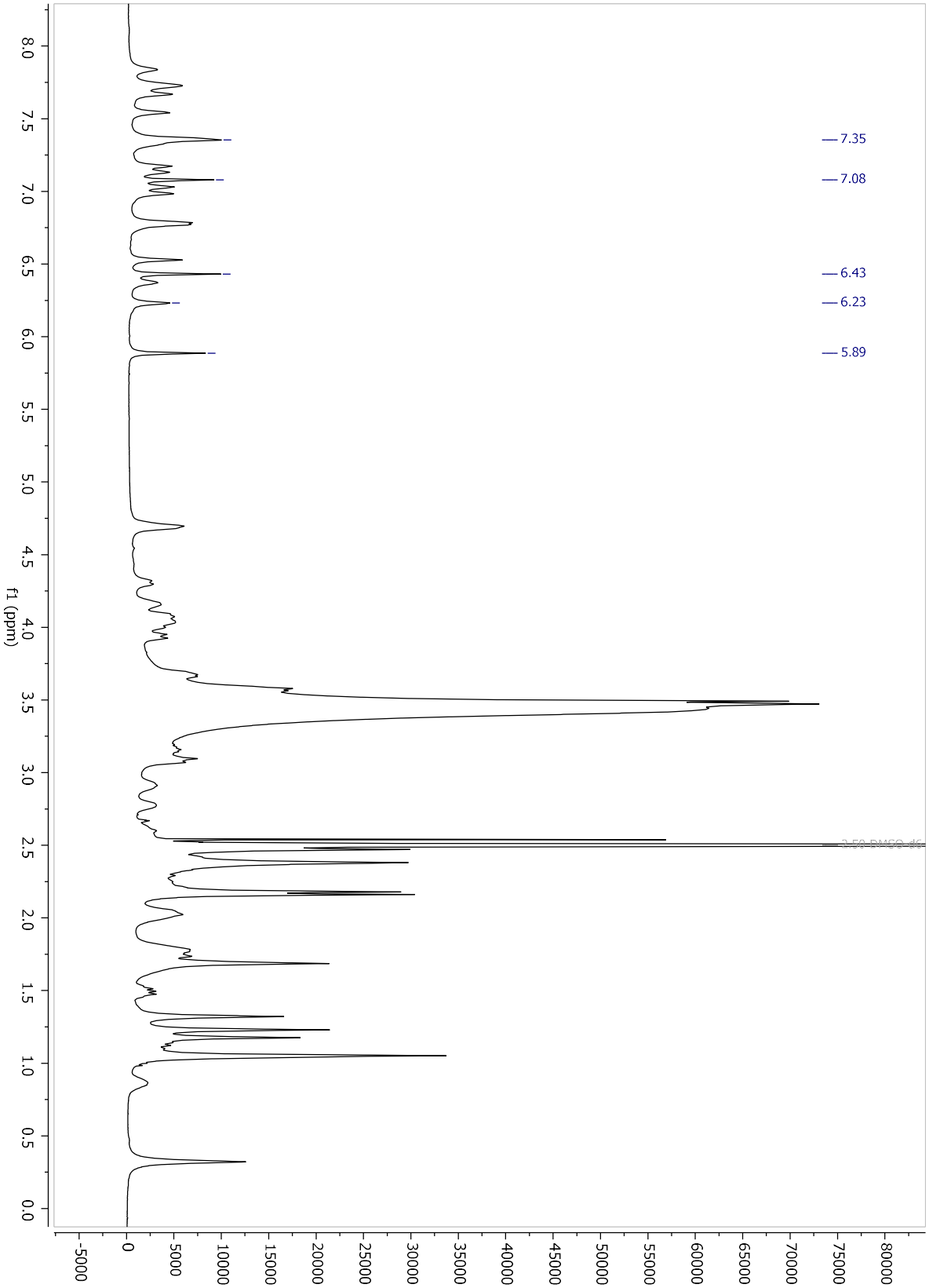

^{13}C NMR in DMSO-d_6

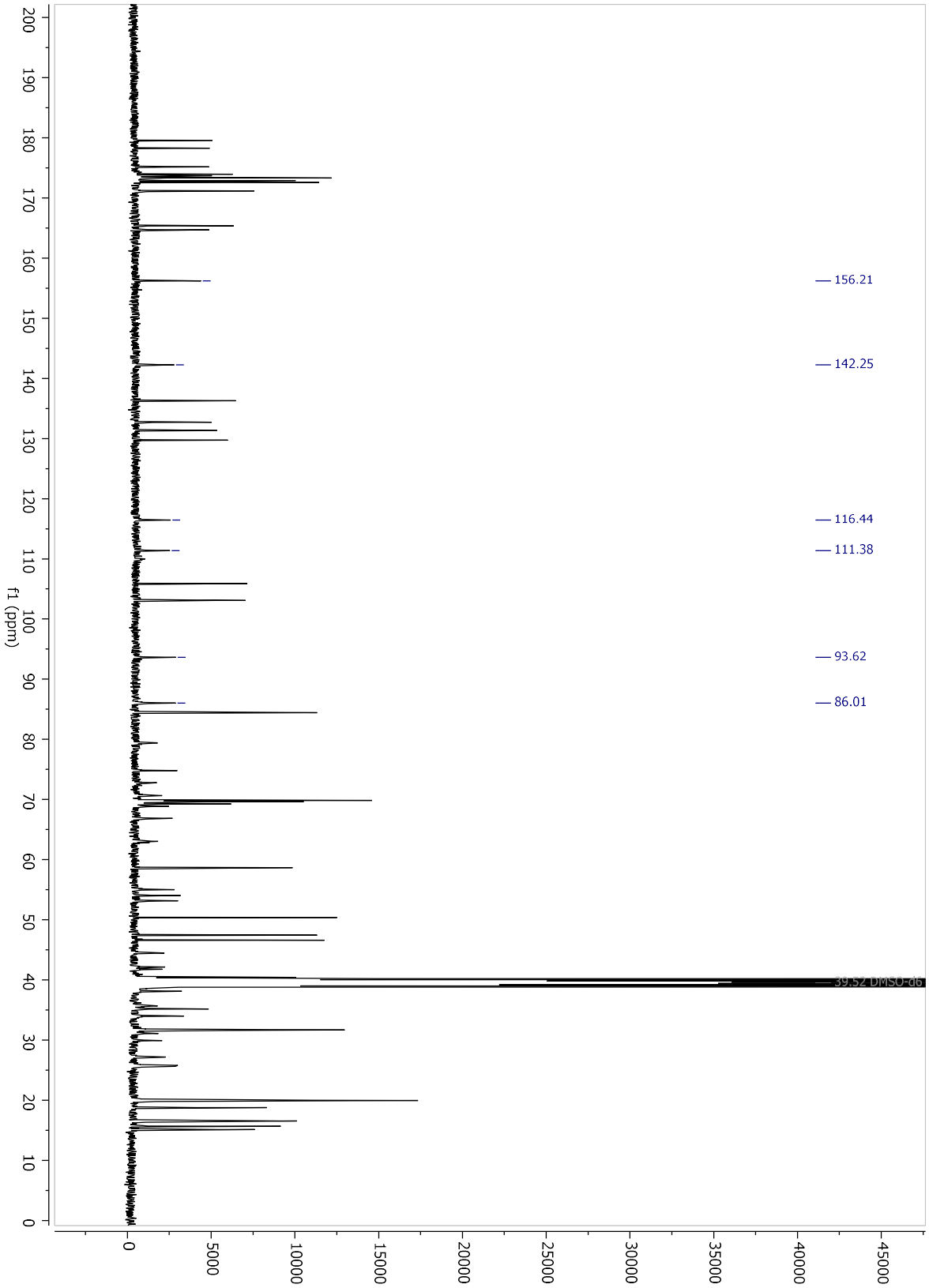

Compound 18

^{1}H NMR in MeOH-d_4

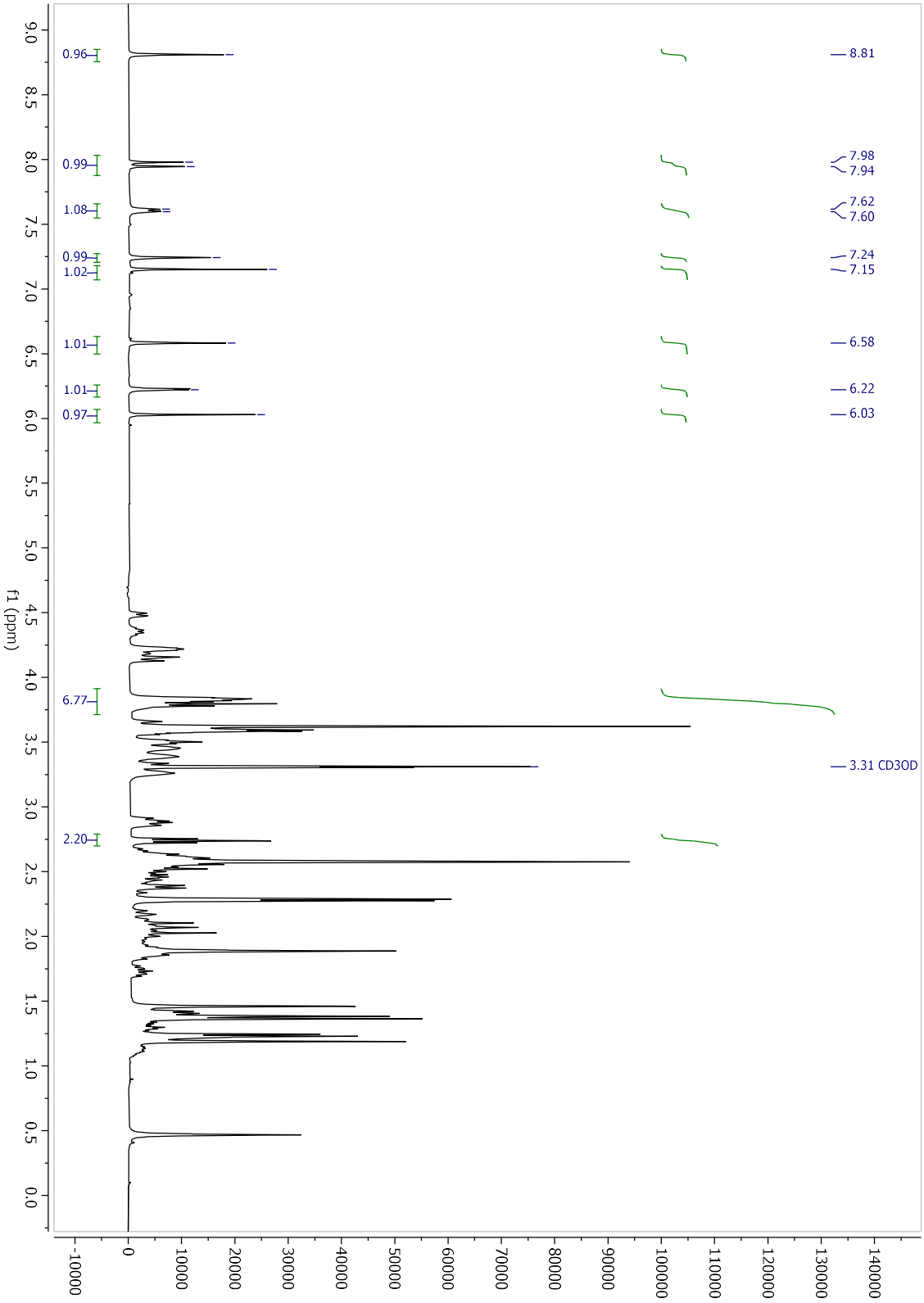

Compound 19

^{1}H NMR in MeOH-d_4

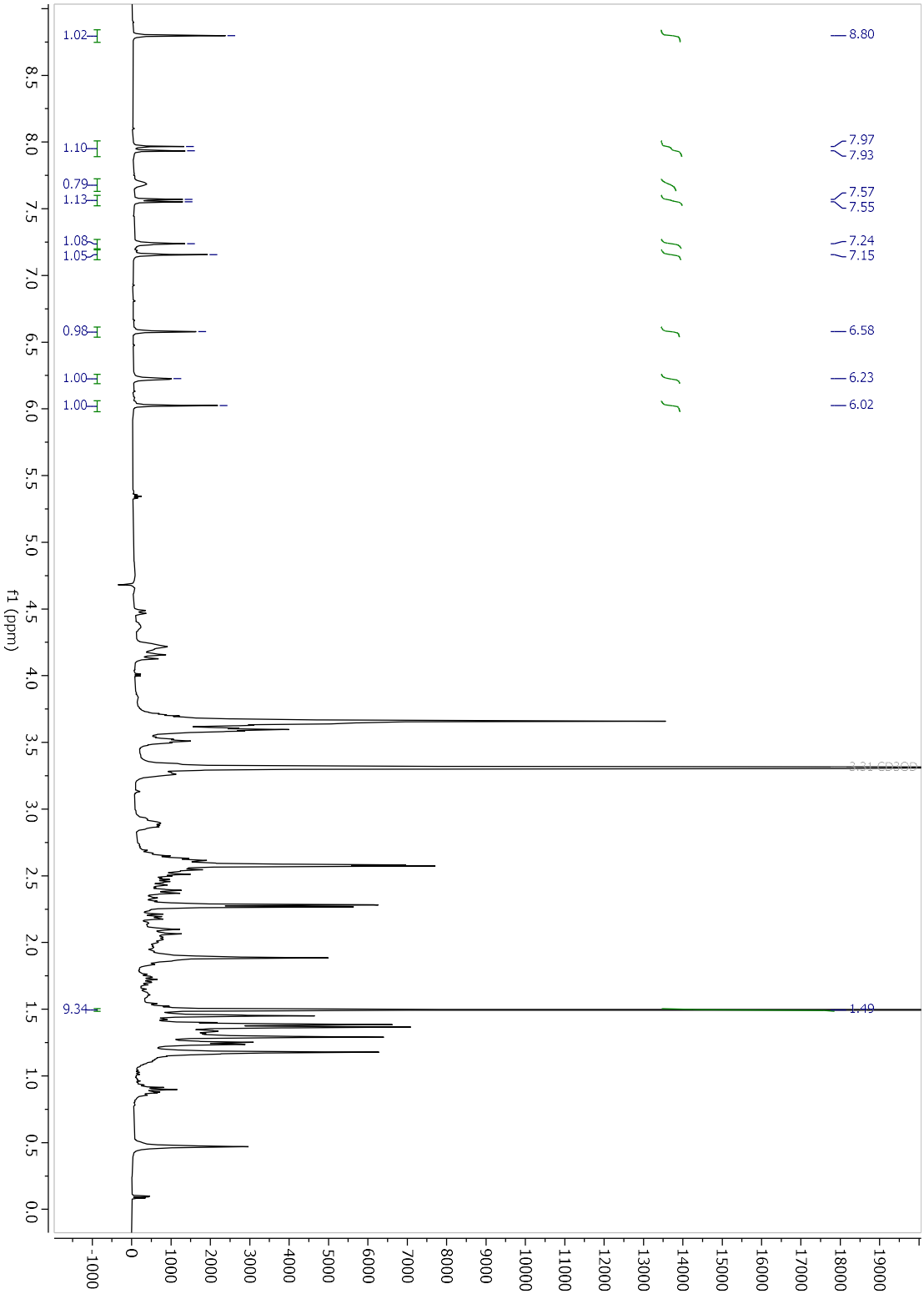

Compound 20

^{1}H NMR in MeOH-*d*$_4$

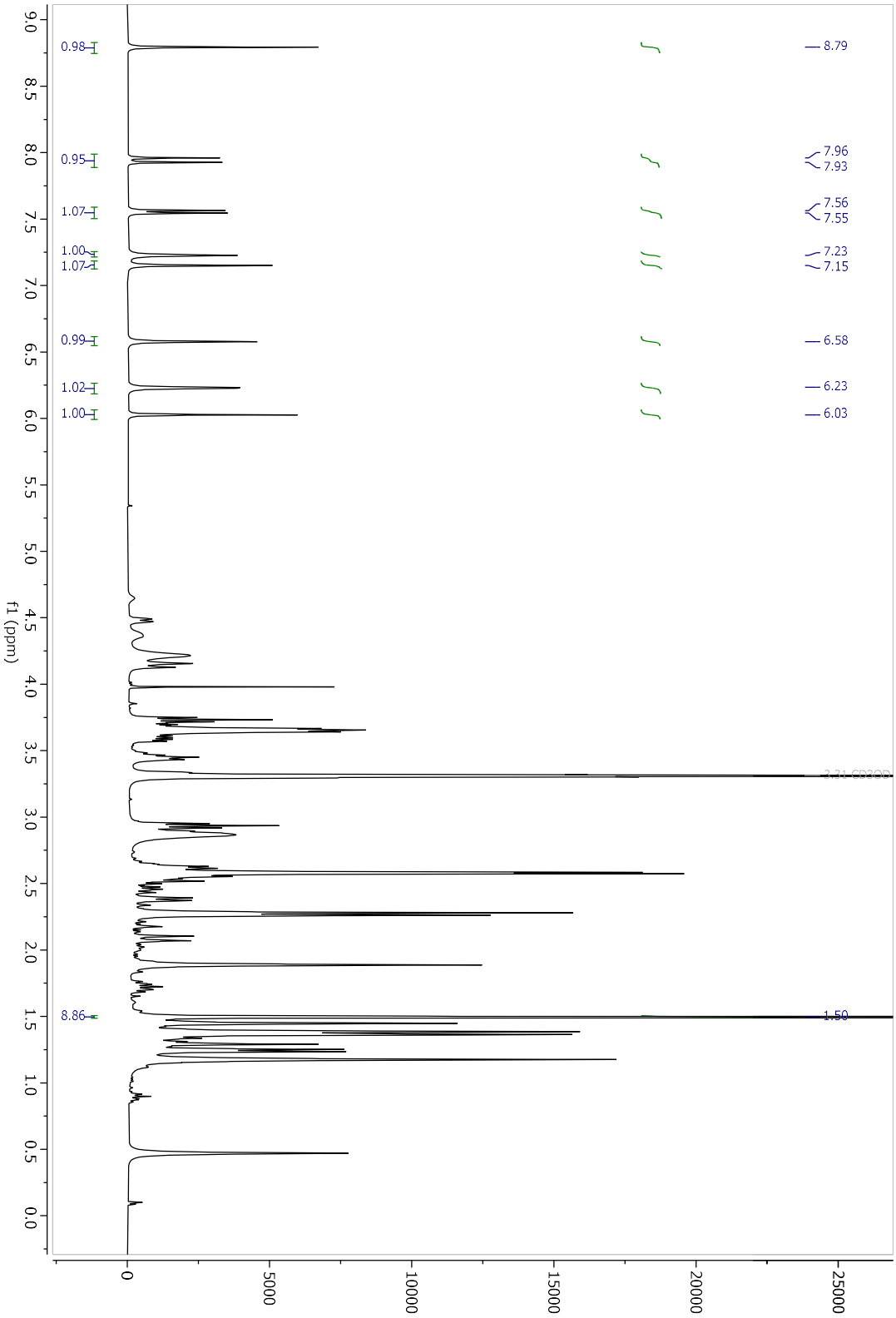

Compound 21

^{1}H NMR in MeOH-d_4

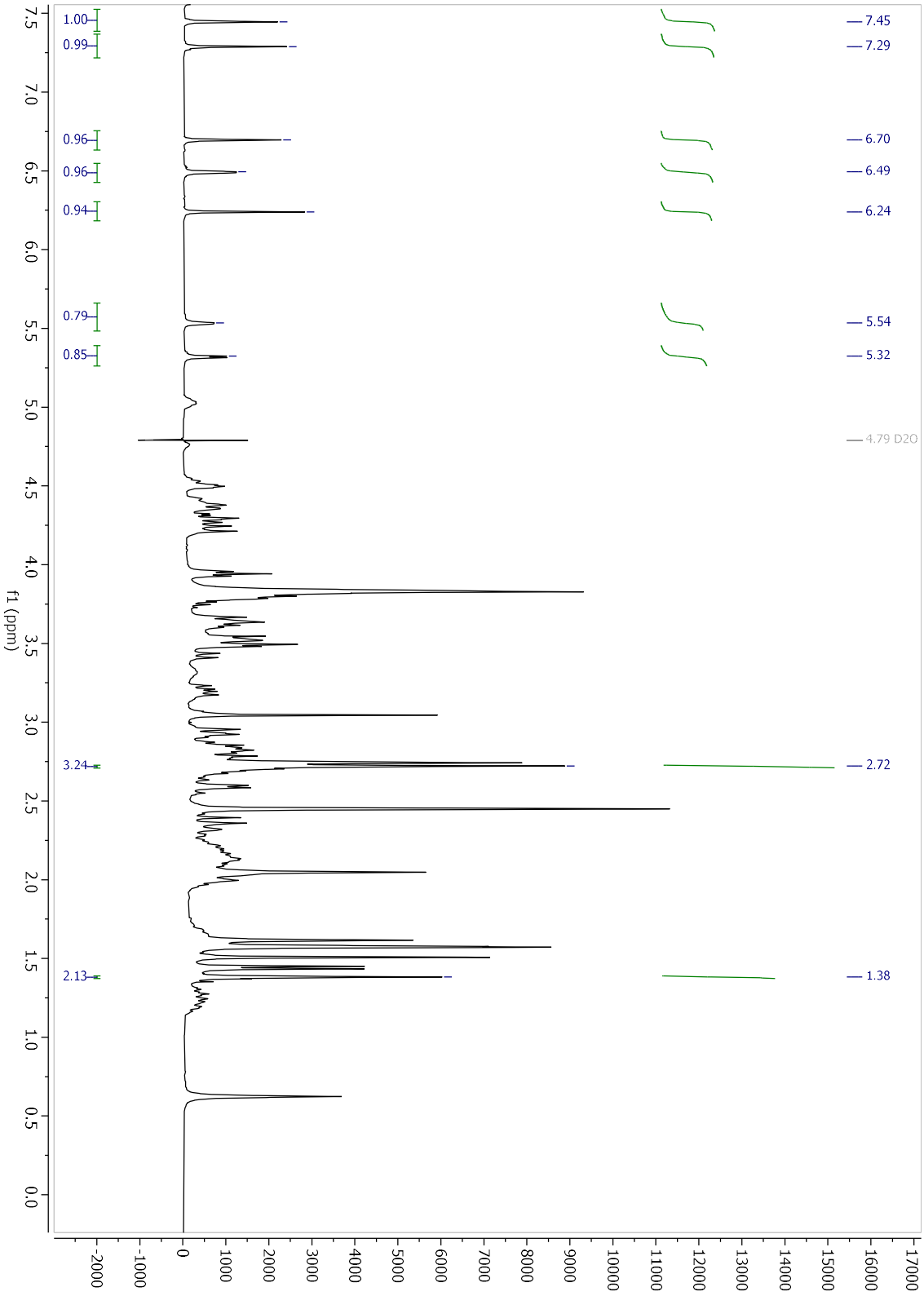

Compound 22

^{1}H NMR in MeOH-d_4

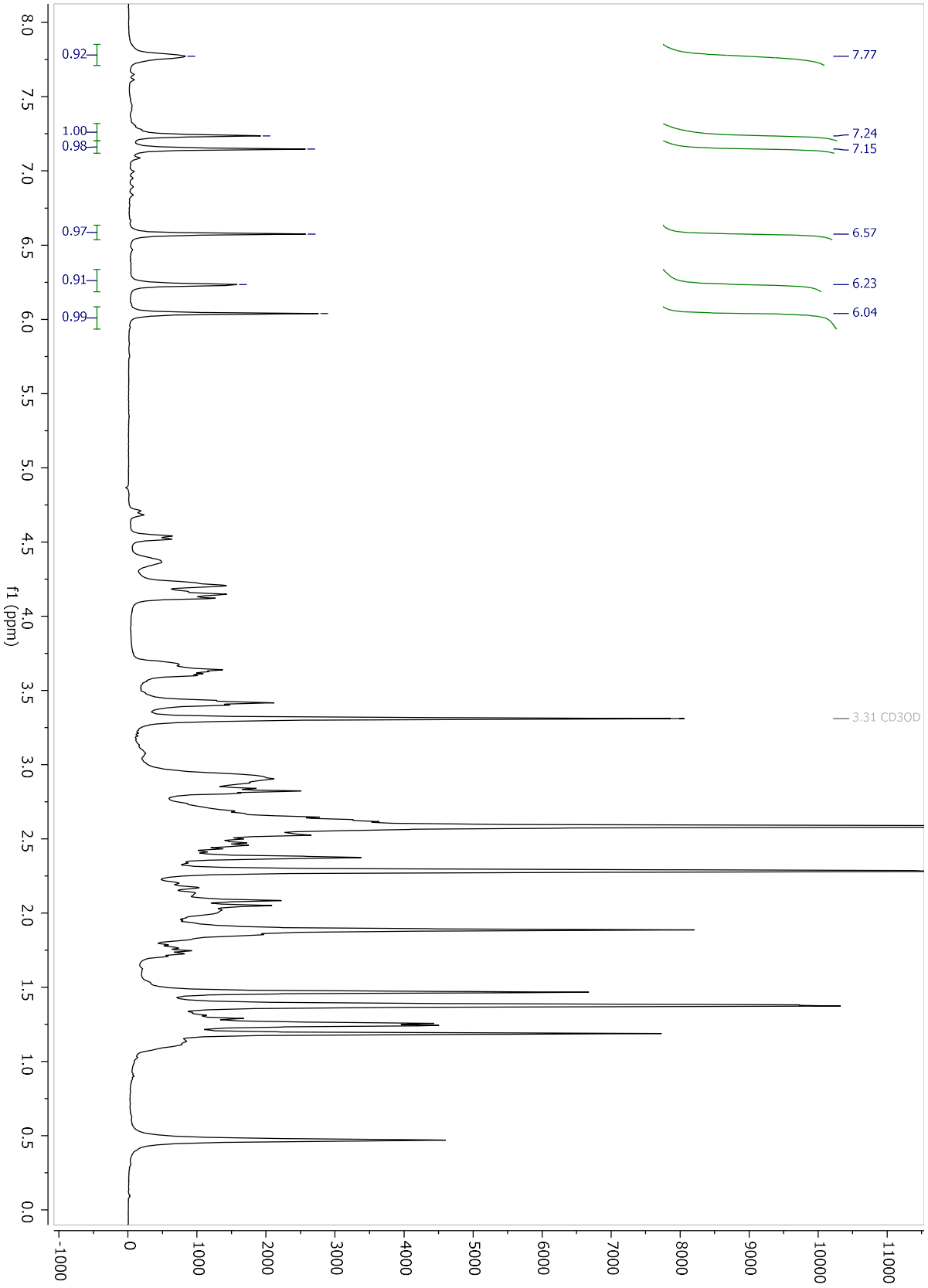

^{1}H NMR in DMSO-d_6

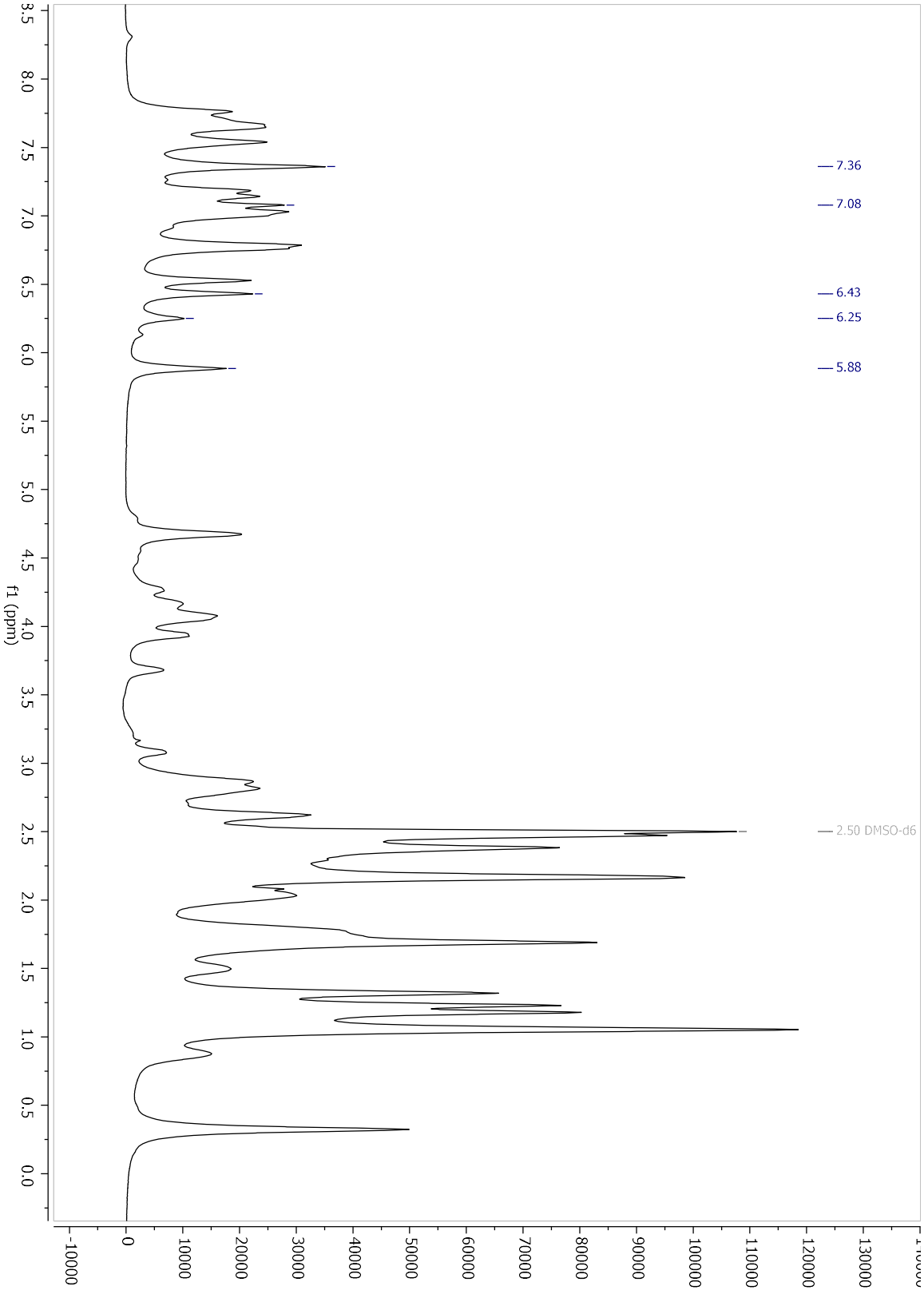

^{13}C NMR in DMSO-d_6

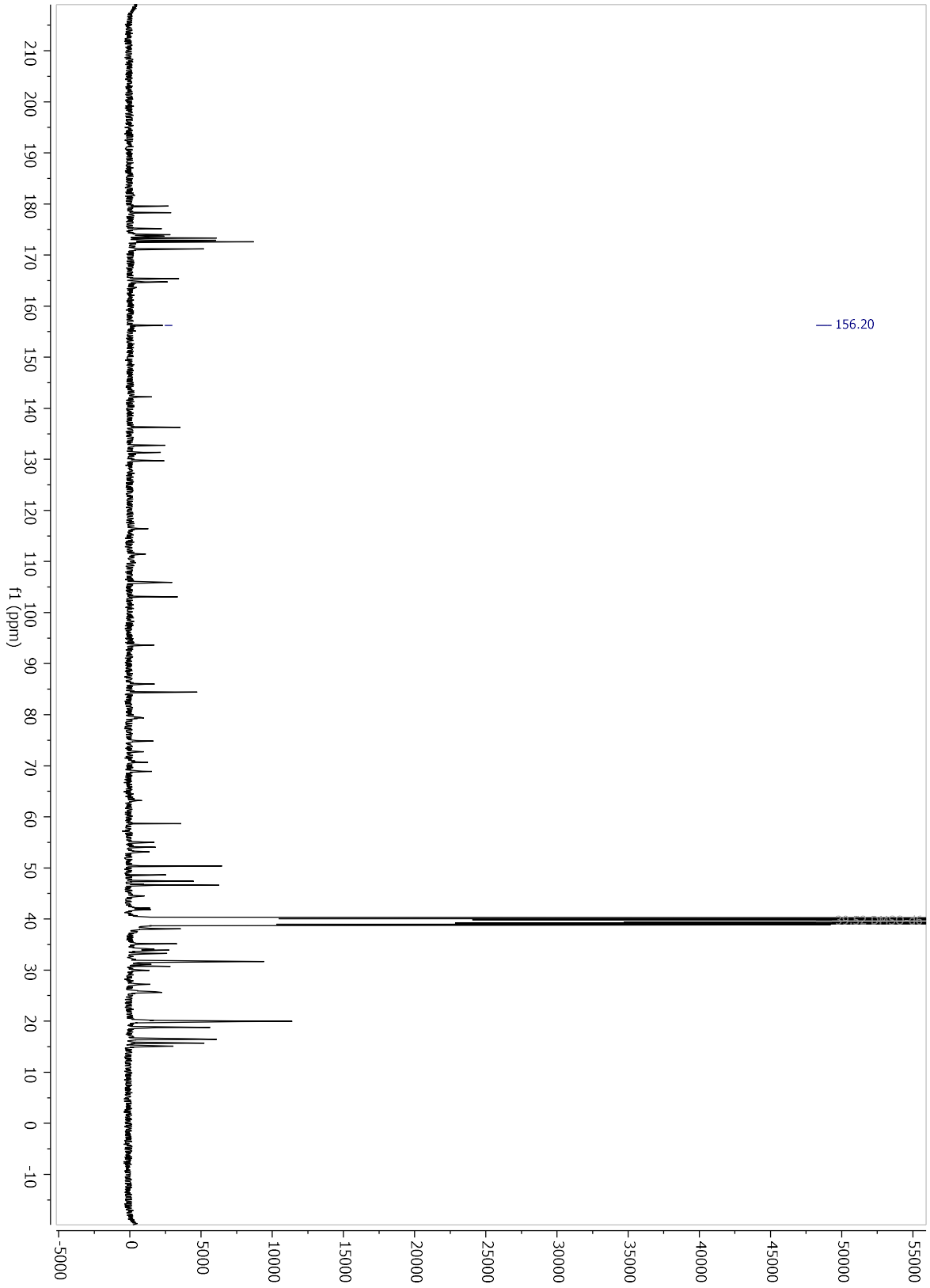

Compound 23

^{1}H NMR in MeOH-d_4

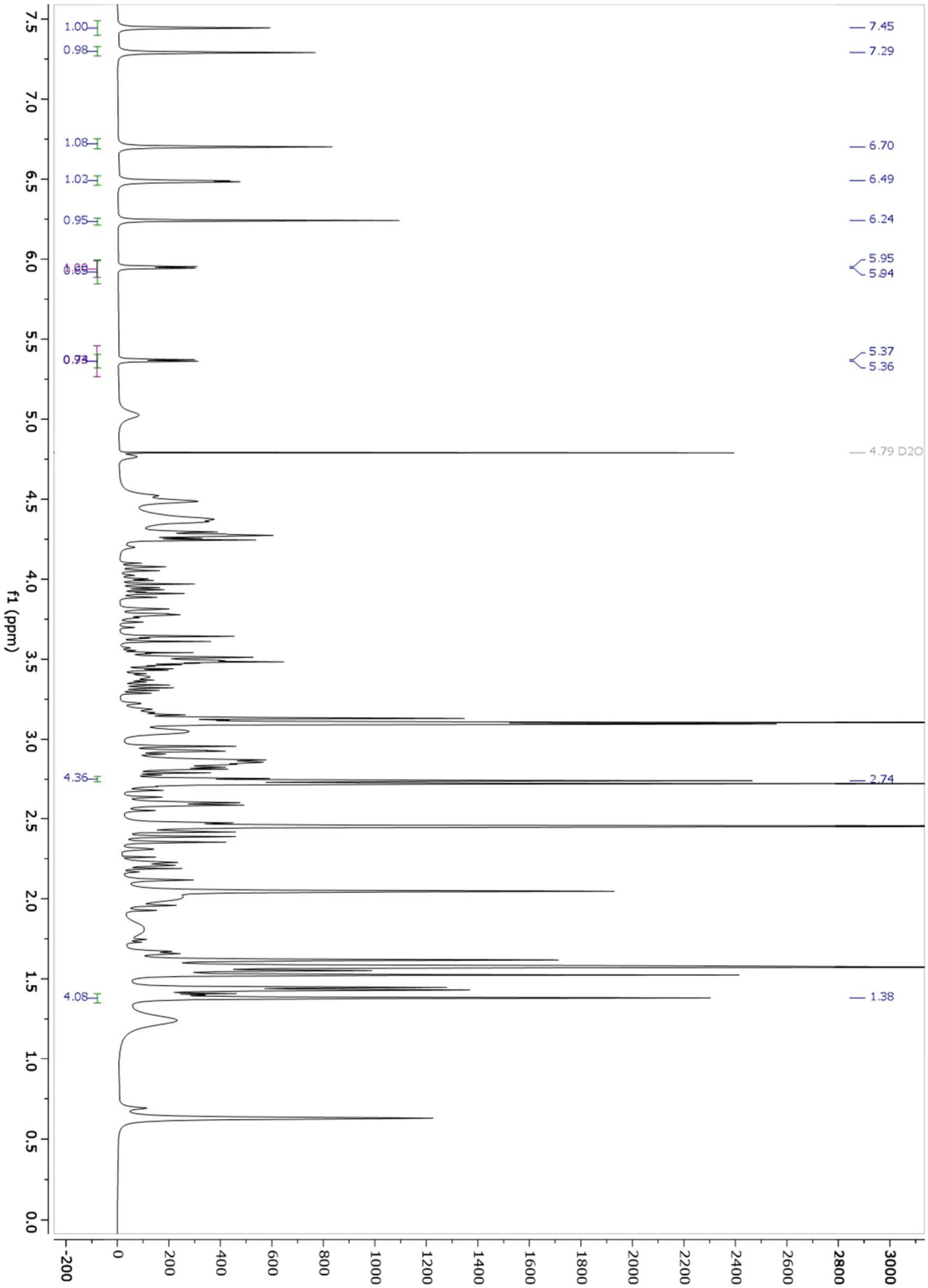

BOC-Ciprofloxacin (C1)

^{1}H NMR in $CDCl_3$

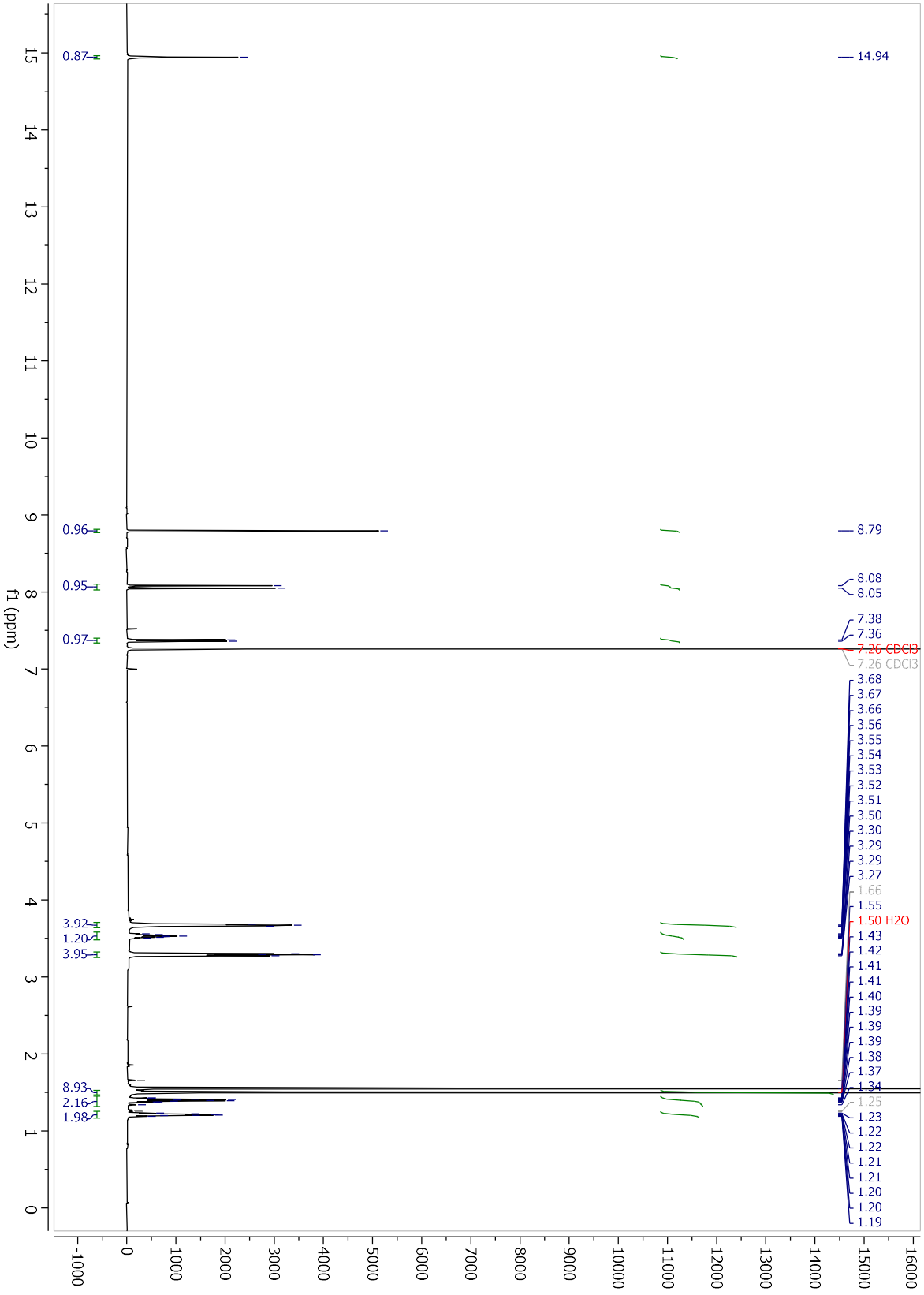

Boc-ciprofloxacin-proargyl ester (C2)

^{1}H NMR in $CDCl_3$

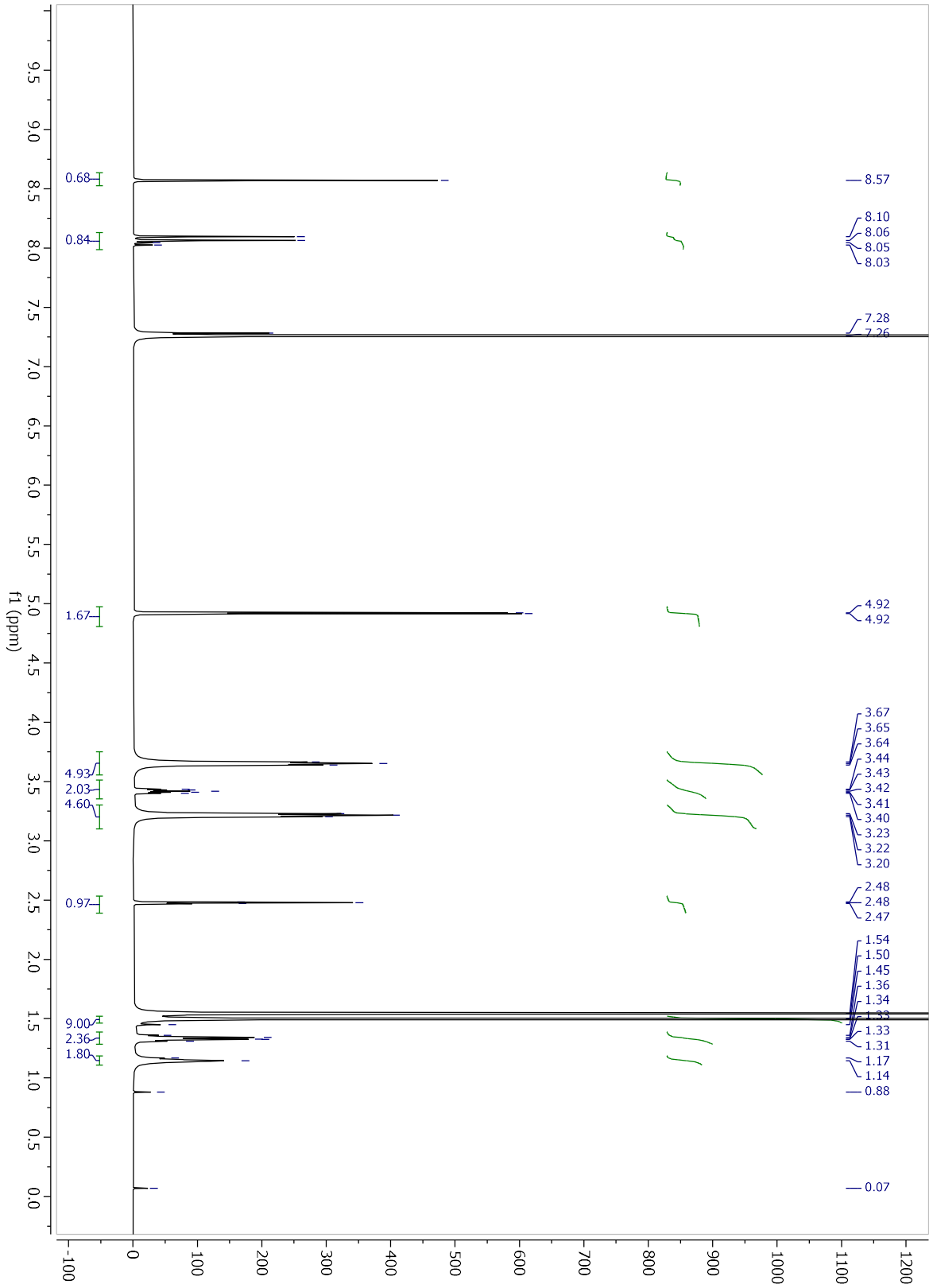

Ciprofloxacin-propargyl ester (C3)

^{1}H NMR in $CDCl_3$

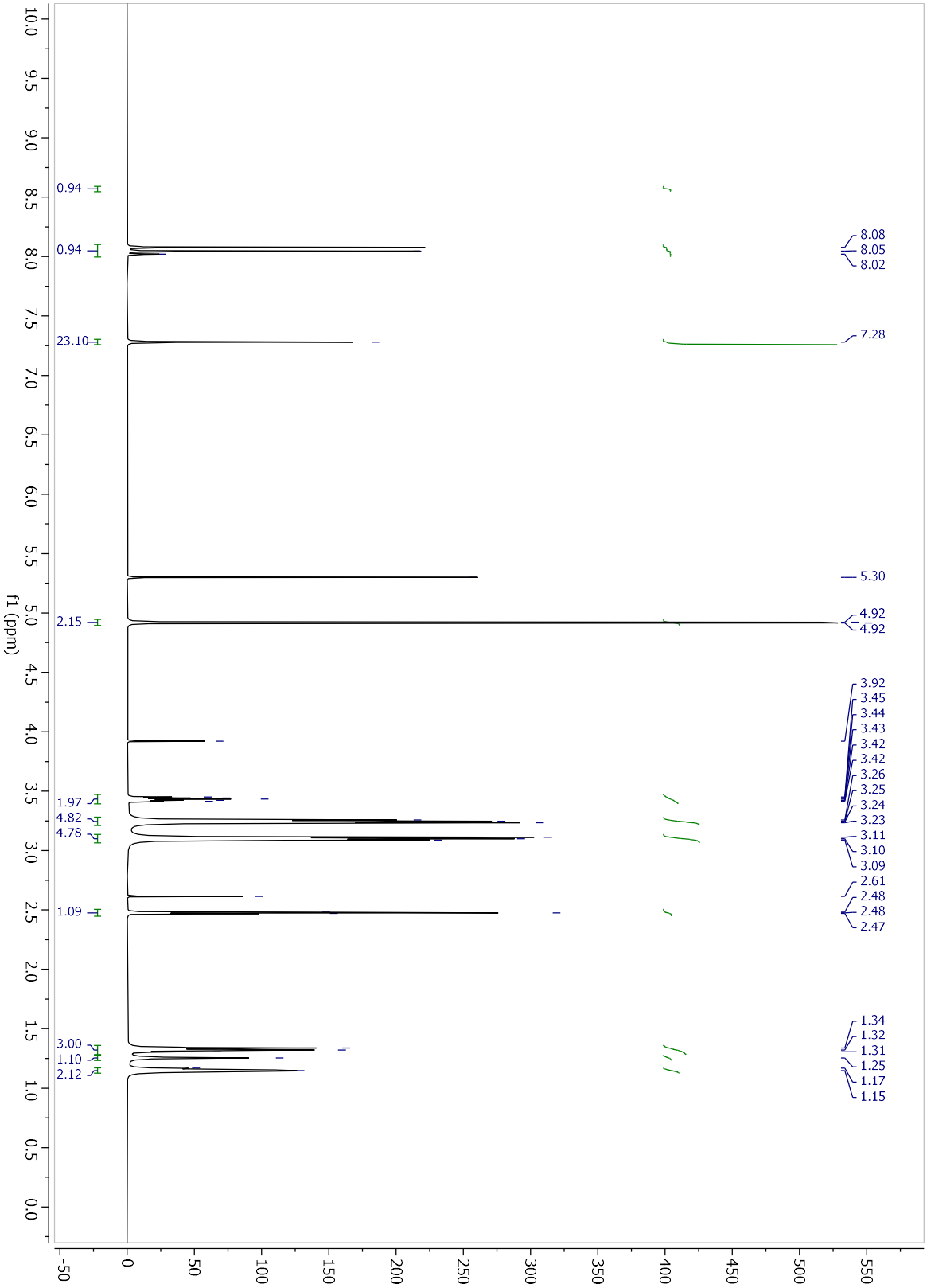

HRMS spectra

Compound 3

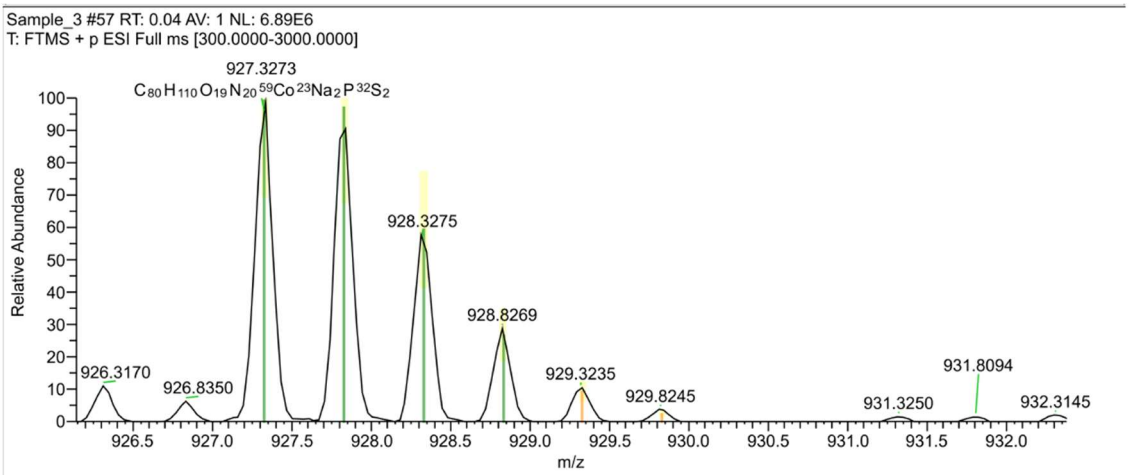

Peak Mass	Display F...	S Fit	RDB	Delta [pp...	Theo. ma...	Rank	Combine...	# Match...	# Missed...	MS Cov....	Pattern C...	MSMS M...
927.3273	$C_{80}H_{110}O_{19}N_{20}{}^{59}Co^{23}Na_2P^{32}S_2$	36.369764084359 7	35.50	-0.33	927.32758	1	92.01	6	0	95.1	95.82	(Collection)

Compound 4

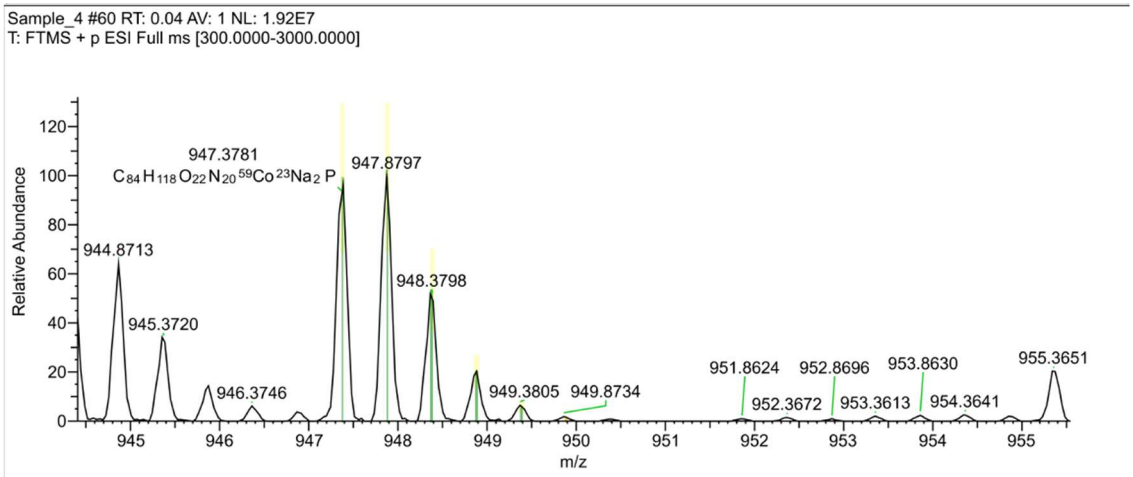

Peak Mass	Display F...	S Fit	RDB	Delta [pp...	Theo. ma...	Rank	Combine...	# Match...	# Missed...	MS Cov....	Pattern C...	MSMS M...
947.3781	$C_{84}H_{118}O_{22}N_{20}{}^{59}Co^{23}Na_2P$	35.322467122571 8	35.50	-1.19	947.37918	1	95.43	6	1	98.77	99.37	(Collection)

Compound 5

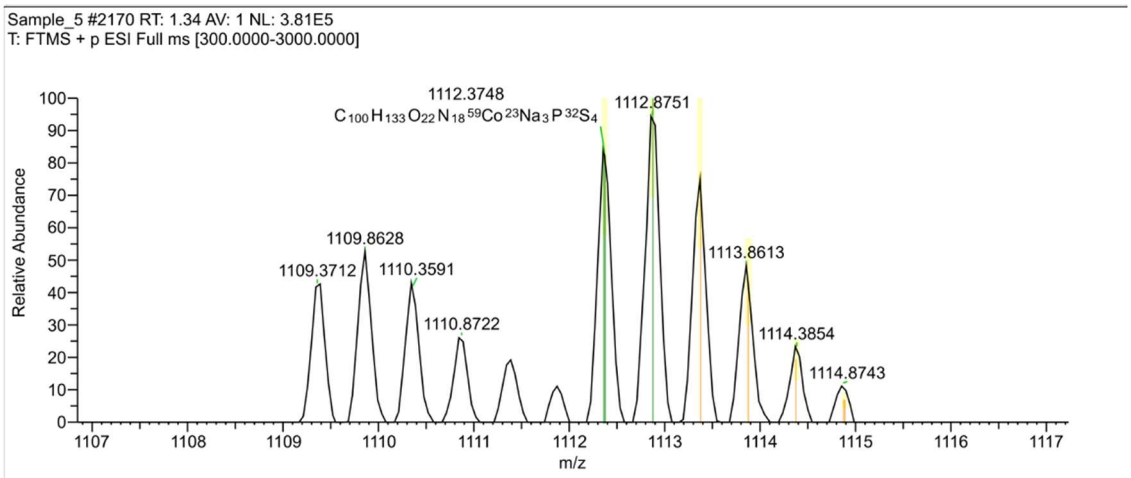

Peak Mass	Display F...	S Fit	RDB	Delta [pp...	Theo. ma...	Rank	Combine...	# Match...	# Missed...	MS Cov....	Pattern C...	MSMS M...
1112.3748	$C_{100}H_{133}O_{22}N_{18}{}^{59}Co^{23}Na_3P^{32}S_4$	18.080363001212 5	42.50	0.84	1112.37382	1	52.05	6	0	53.93	55.21	(Collection)

Compound 6

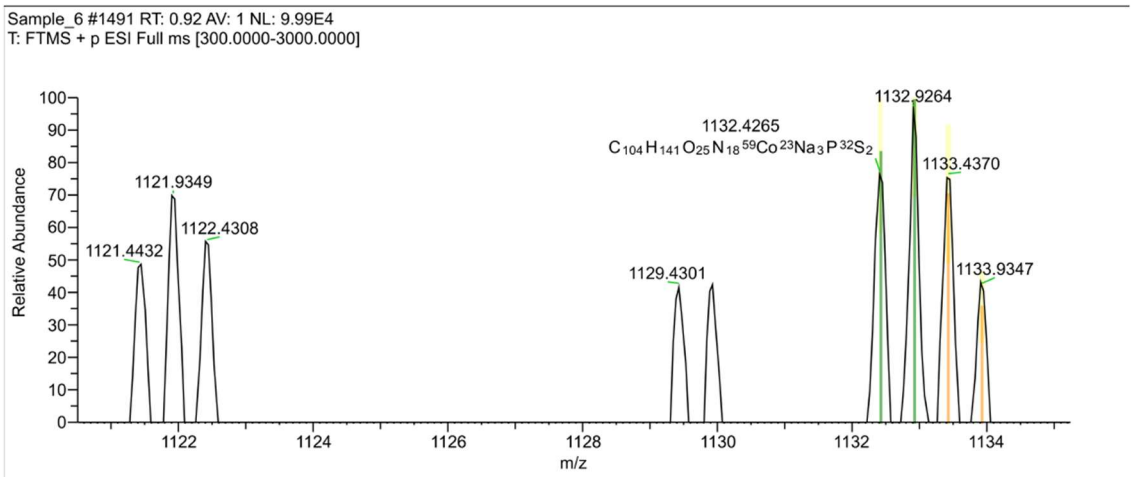

Peak Mass	Display F...	S Fit	RDB	Delta [pp...	Theo. ma...	Rank	Combine...	# Match...	# Missed...	MS Cov....	Pattern C...	MSMS M...
1132.4265	$C_{104}H_{141}O_{25}N_{18}{}^{59}Co^{23}Na_3P^{32}S_2$	28.575573672757 4	42.50	0.97	1132.42542	1	67.16	4	0	69.3	63.23	(Collection)

Compound 7

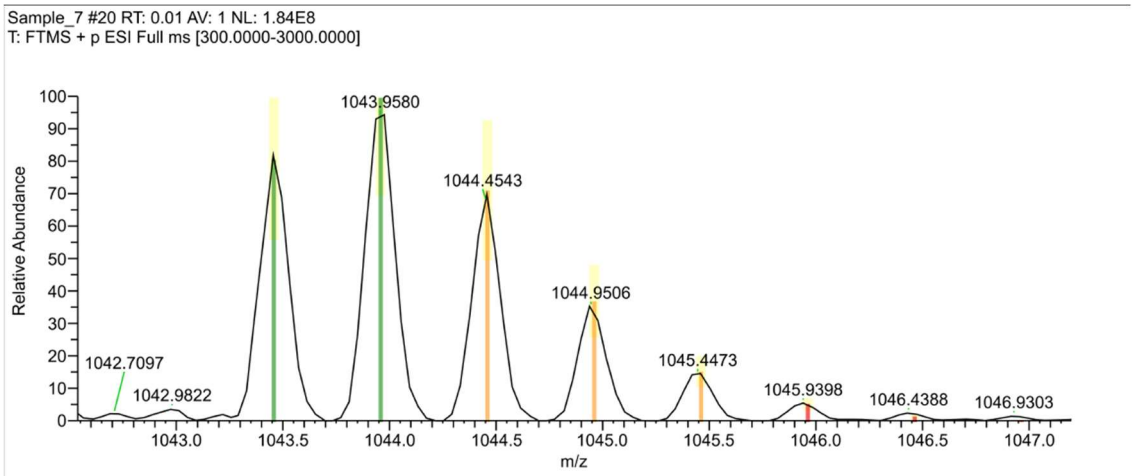

Peak Mass	Display F...	S Fit	RDB	Delta [pp...	Theo. ma...	Rank	Combine...	# Match...	# Missed...	MS Cov....	Pattern C...	MSMS M...
1043.4623	$C_{105}H_{141}O_{16}N_{18}{}^{59}Co^{23}NaP^{3}{}^{2}S_{2}$	10.990147944738	44.50	3.59	1043.45854	1	55.7	5	3	58.18	57.93	(Collection)

Compound 8

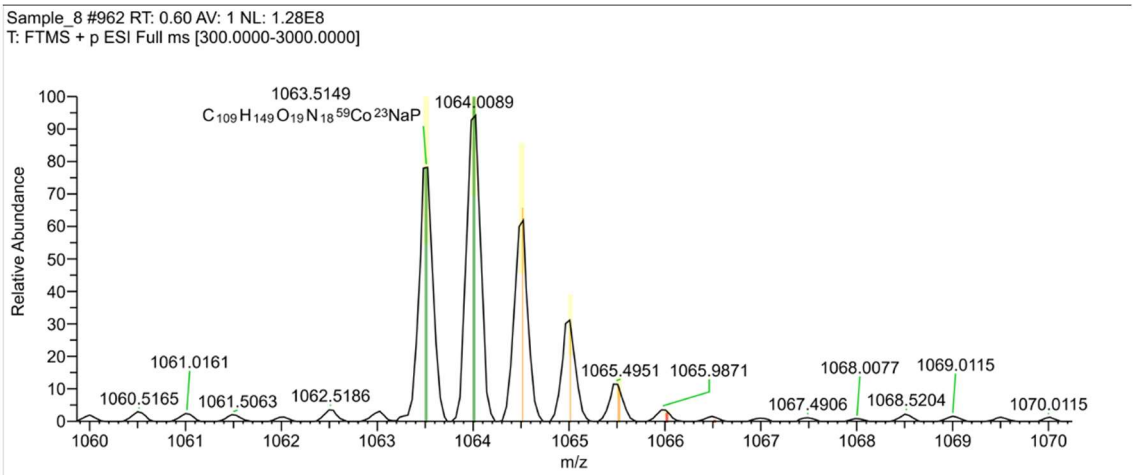

Peak Mass	Display F...	S Fit	RDB	Delta [pp...	Theo. ma...	Rank	Combine...	# Match...	# Missed...	MS Cov....	Pattern C...	MSMS M...
1063.5149	$C_{109}H_{149}O_{19}N_{18}{}^{59}Co^{23}NaP$	10.927883105753	44.50	4.47	1063.51014	1	58.75	5	2	61.4	61.87	(Collection)

Compound 13

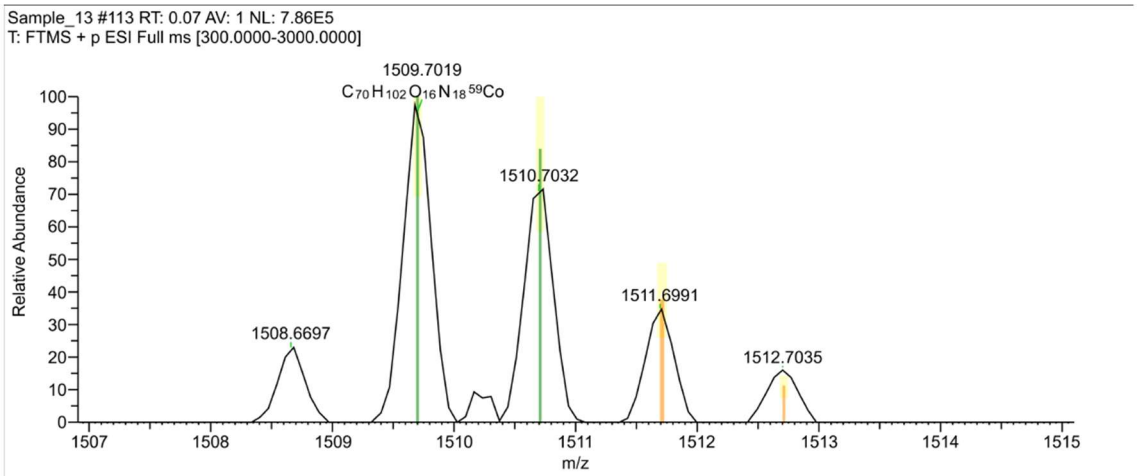

Peak Mass	Display F...	S Fit	RDB	Delta [pp...	Theo. ma...	Rank	Combine...	# Match...	# Missed...	MS Cov....	Pattern C...	MSMS M...
1509.7019	$C_{70}H_{102}O_{16}N_{18}{}^{59}Co$	24.27073 9040838	29.00	-1.90	1509.70477	1	68.8	4	0	71.28	78.92	(Collection)

Compound 14

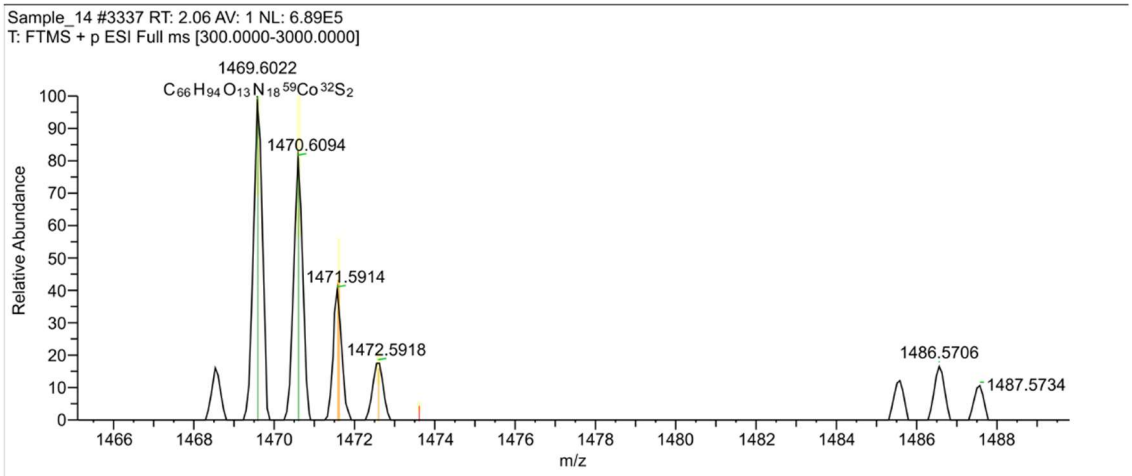

Peak Mass	Display F...	S Fit	RDB	Delta [pp...	Theo. ma...	Rank	Combine...	# Match...	# Missed...	MS Cov....	Pattern C...	MSMS M...
1469.6022	$C_{66}H_{94}O_{13}N_{18}{}^{59}Co{}^{32}S_2$	19.67663 6451032 2	29.00	0.41	1469.60157	1	72.55	4	1	75.49	73.85	(Collection)

Compound 15

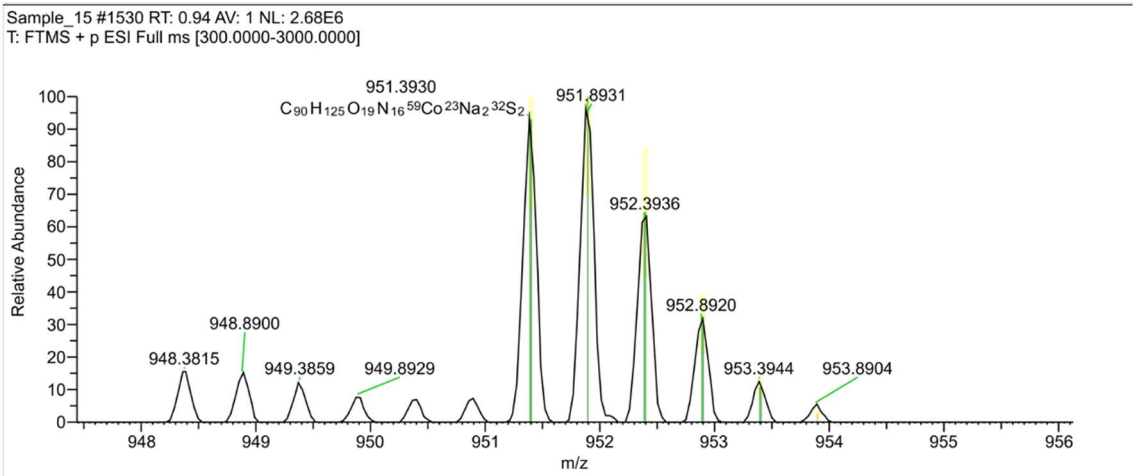

Peak Mass	Display F...	S Fit	RDB	Delta [pp...	Theo. ma...	Rank	Combine...	# Match...	# Missed...	MS Cov....	Pattern C...	MSMS M...
951.3930	$C_{90}H_{125}O_{19}N_{16}{}^{59}Co{}^{23}Na_2{}^{32}S_2$	45.17142692318 5	35.50	-0.24	951.39324	1	95.41	6	0	98.2	99.02	(Collection)

Compound 16

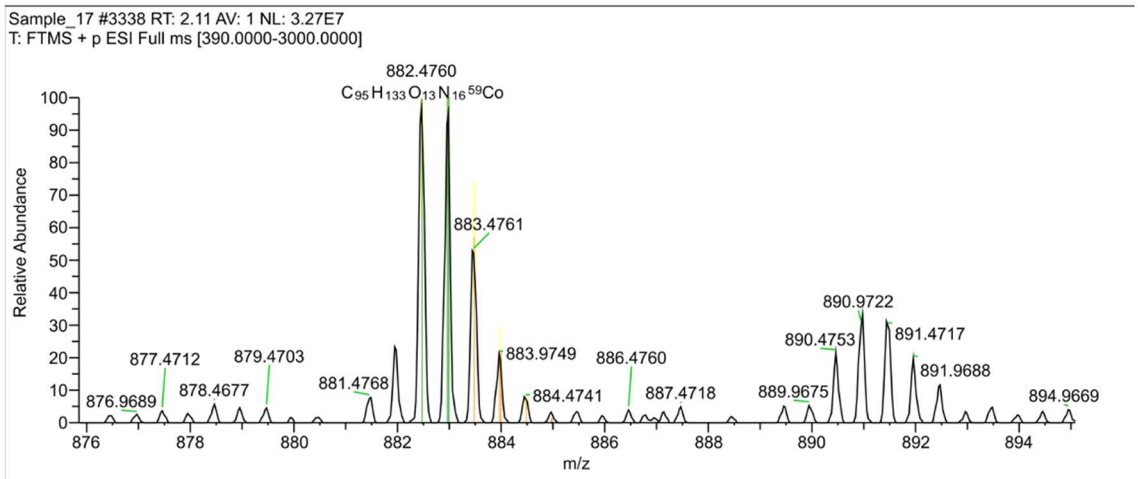

Peak Mass	Display F...	S Fit	RDB	Delta [pp...	Theo. ma...	Rank	Combine...	# Match...	# Missed...	MS Cov....	Pattern C...	MSMS M...
882.4760	$C_{95}H_{133}O_{13}N_{16}{}^{59}Co$	14.52049048190 42	37.50	-2.20	882.47795	1	66.42	5	1	69.3	68.44	(Collection)

Compound 18

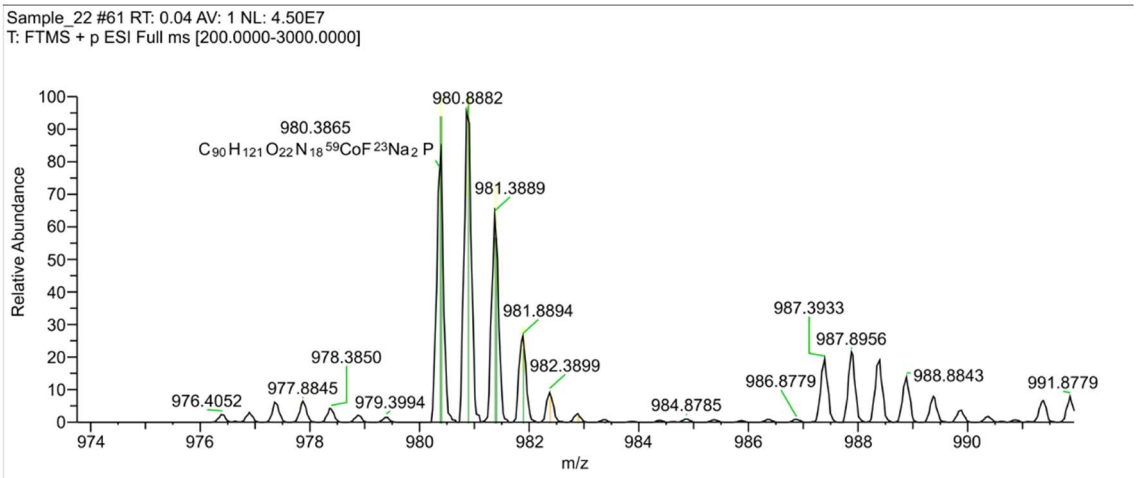

Peak Mass	Display F...	S Fit	RDB	Delta [pp...	Theo. ma...	Rank	Combine...	# Match...	# Missed...	MS Cov....	Pattern C...	MSMS M...
980.3865	$C_{90}H_{121}O_{22}N_{18}{}^{59}CoF^{23}Na_2P$	29.42383 0157992 1	38.50	-0.58	980.3870 4	1	92.13	6	1	95.61	96.7	(Collecti on)

Compound 19

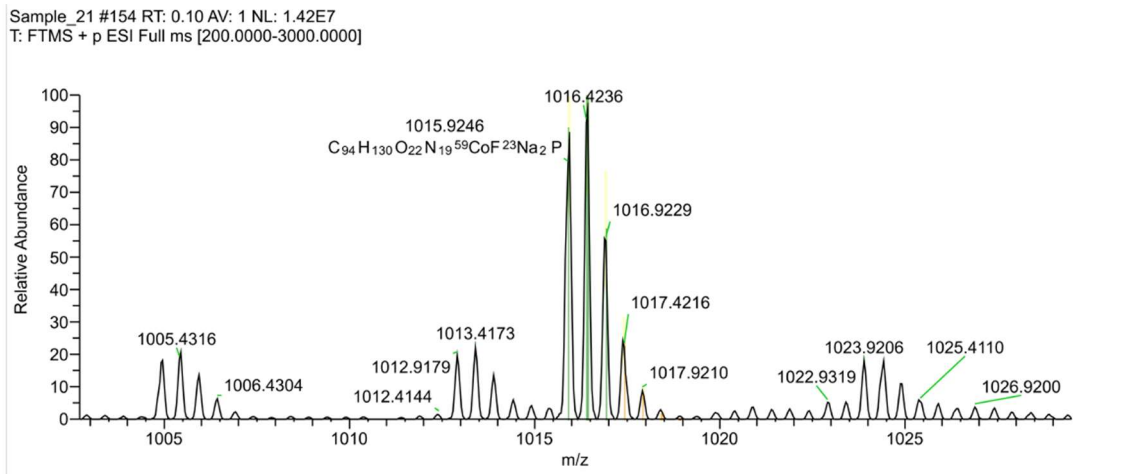

Peak Mass	Display F...	S Fit	RDB	Delta [pp...	Theo. ma...	Rank	Combine...	# Match...	# Missed...	MS Cov....	Pattern C...	MSMS M...
1015.924 6	$C_{94}H_{130}O_{22}N_{19}{}^{59}CoF^{23}Na_2P$	21.17134 4618017 8	38.50	0.75	1015.923 79	1	83.42	6	1	86.88	87.72	(Collecti on)

Compound 20

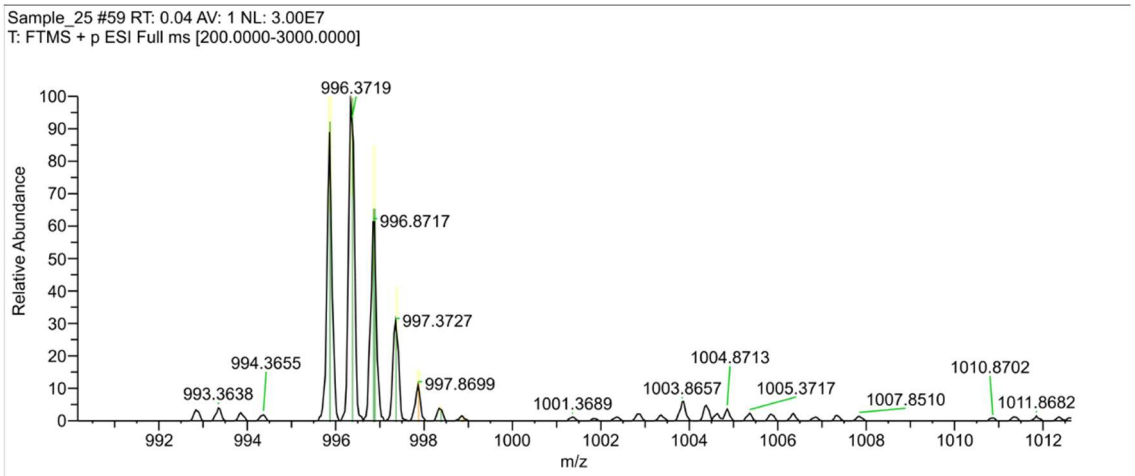

Peak Mass	Display F...	S Fit	RDB	Delta [pp...	Theo. ma...	Rank	Combine...	# Match...	# Missed...	MS Cov....	Pattern C...	MSMS M...
995.8717	$C_{90}H_{122}O_{19}N_{19}{}^{59}CoF^{23}Na_2P^3{}^2S_2$	38.700784874517 5	38.50	-0.49	995.8721 9	1	92.86	7	0	95.87	95.73	(Collecti on)

Compound 21

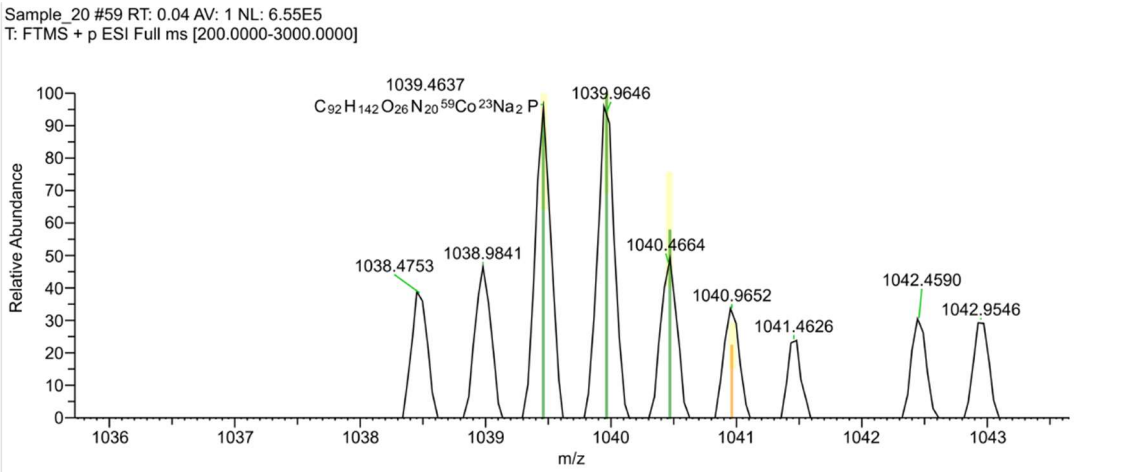

Peak Mass	Display F...	S Fit	RDB	Delta [pp...	Theo. ma...	Rank	Combine...	# Match...	# Missed...	MS Cov....	Pattern C...	MSMS M...
1039.4637	$C_{92}H_{142}O_{26}N_{20}{}^{59}Co^{23}Na_2P$	46.101187566773 2	31.50	0.80	1039.462 91	1	85.53	4	0	87.72	91.63	(Collecti on)

Compound 23

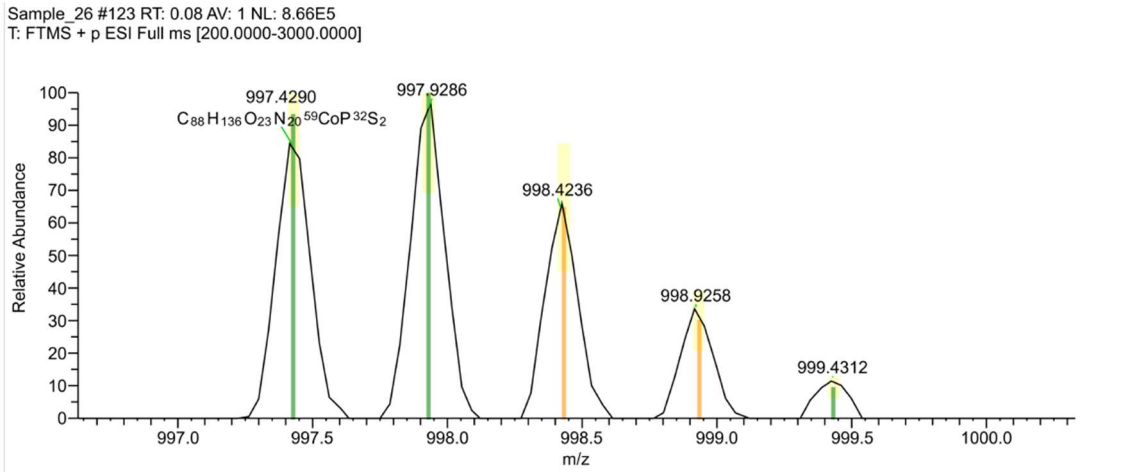

Peak Mass	Display F...	S Fit	RDB	Delta [pp...	Theo. ma...	Rank	Combine...	# Match...	# Missed...	MS Cov....	Pattern C...	MSMS M...
997.4290	$C_{88}H_{136}O_{23}N_{20}{}^{59}CoP^{32}S_2$	30.73433 7279247 7	31.50	-0.35	997.4293 6	1	64.7	5	0	66.59	68.08	(Collecti on)

UV/Vis spectra of CNCbl and NBD-X

Figure 1

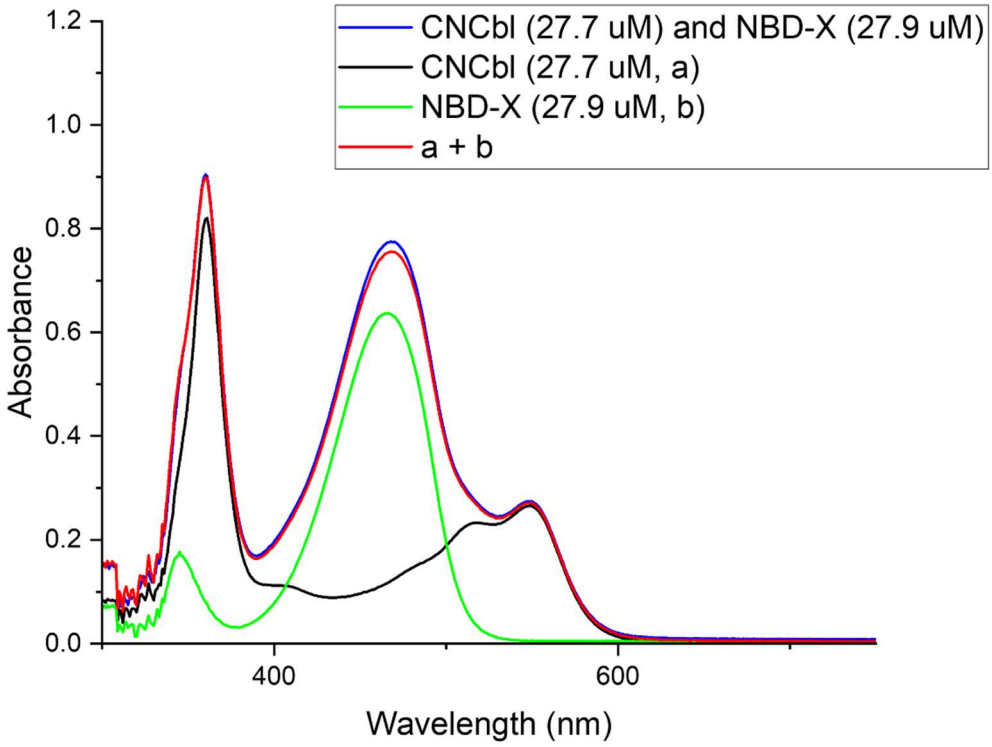

UV-Vis spectra of CNCbl (27.7 µM, black), NBD-X (27.9 µM, green) and CNCbl & NBD-X (1:1, blue) obtained in CH_3OH at 25 °C. The spectra of CNCbl and NBD-X have been combined in the Origin software (red).

Figure 2

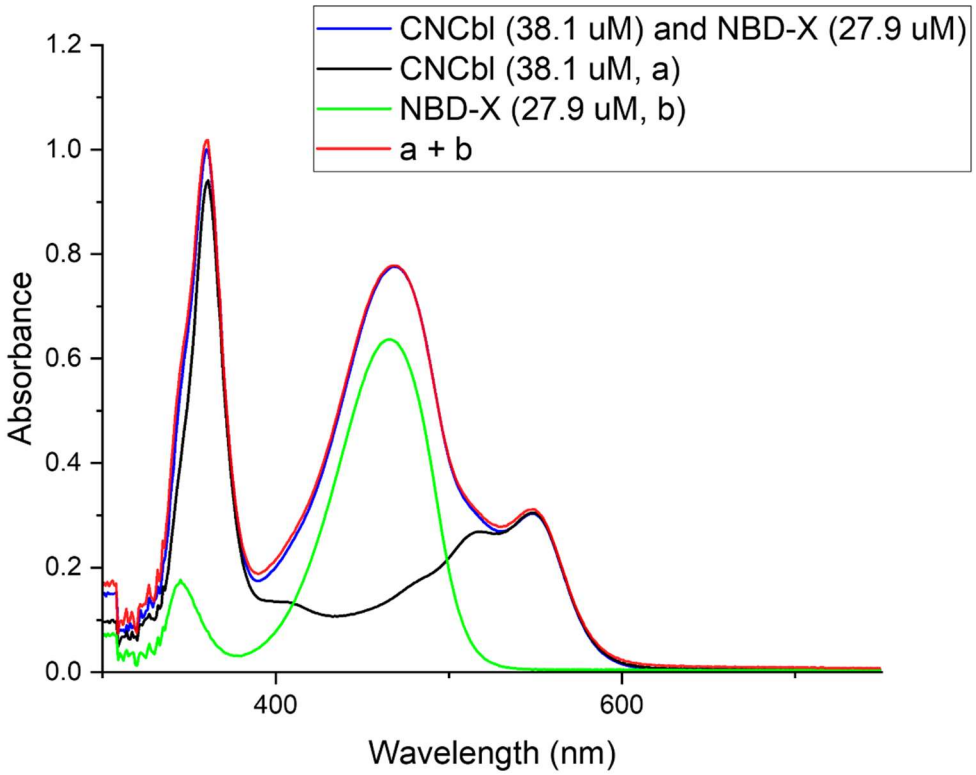

UV-Vis spectra of CNCbl (38.1 μM, black), NBD-X (27.9 μM, green) and CNCbl & NBD-X (1:1, blue) obtained in CH_3OH at 25 °C. The spectra of CNCbl and NBD-X have been combined in the Origin software (red).

Figure 3

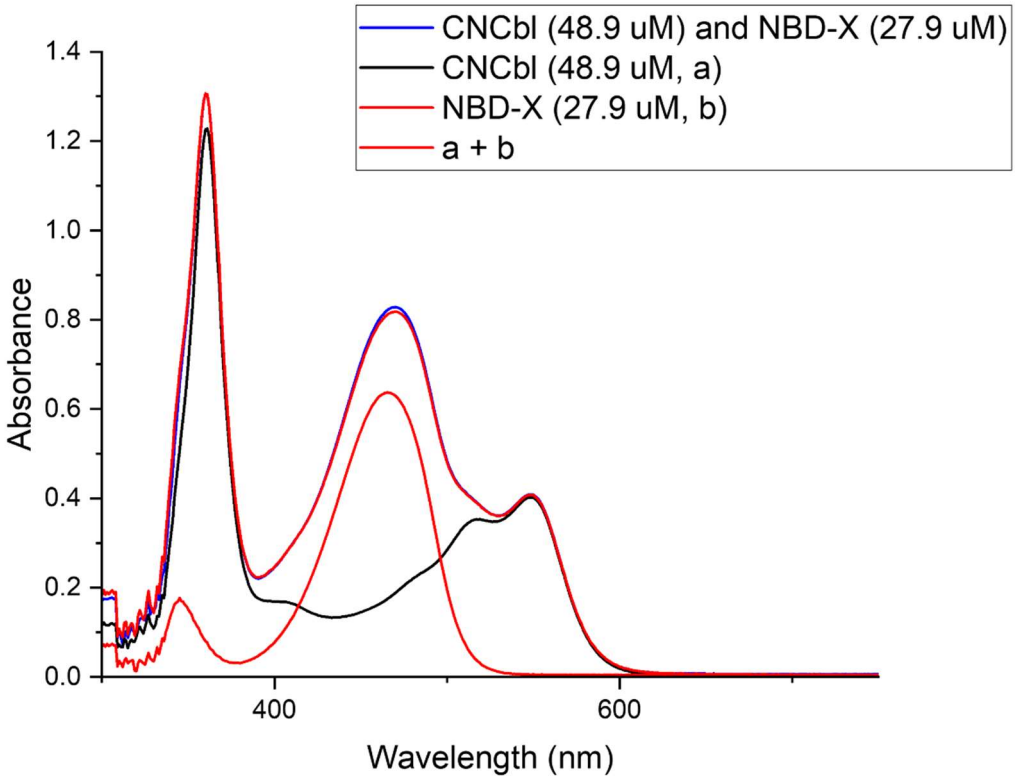

UV-Vis spectra of CNCbl (48.9 µM, black), NBD-X (27.9 µM, red) and CNCbl & NBD-X (1:1, blue) obtained in CH_3OH at 25 °C. The spectra of CNCbl and NBD-X have been combined in the Origin software (red).

Figure 4

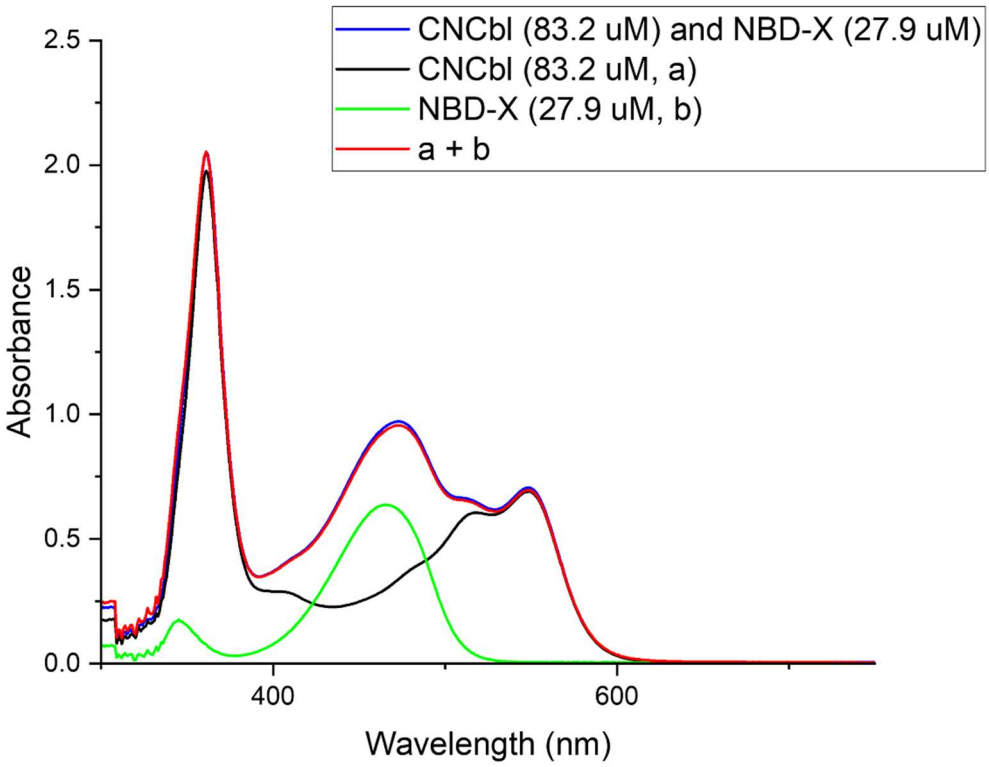

UV-Vis spectra of CNCbl (83.2 μM, black), NBD-X (27.9 μM, green) and CNCbl & NBD-X (1:1, blue) obtained in CH_3OH at 25 °C. The spectra of CNCbl and NBD-X have been combined in the Origin software (red).

Figure 5

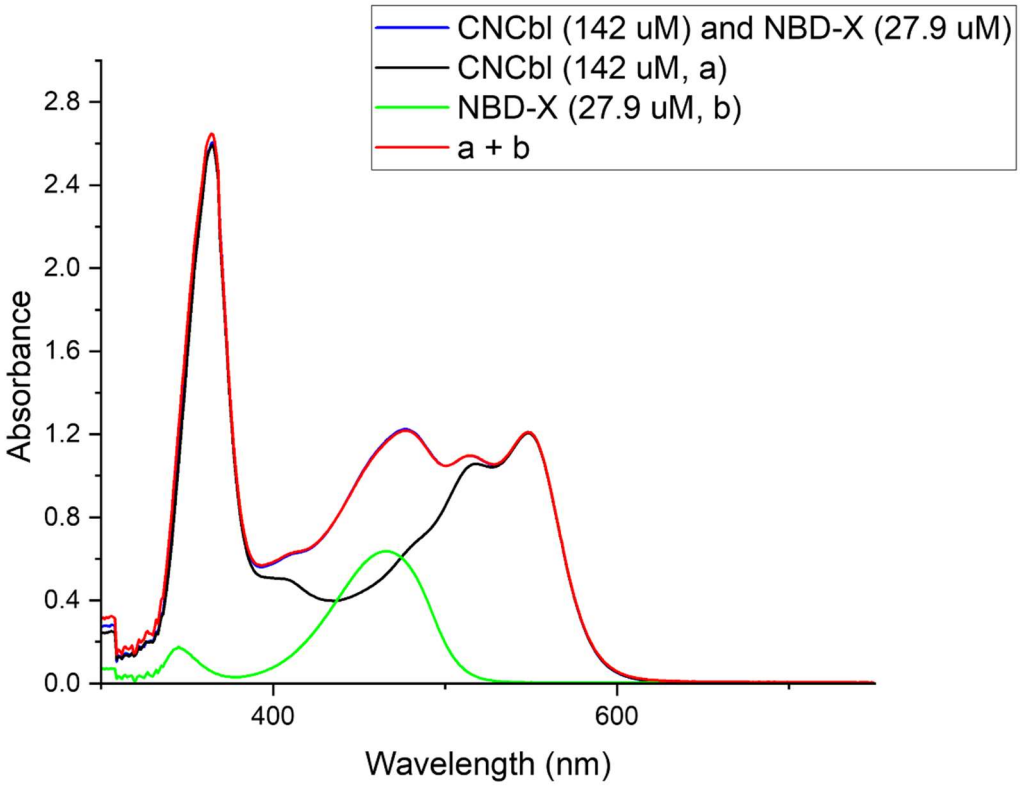

UV-Vis spectra of CNCbl (142 μM, black), NBD-X (27.9 μM, green) and CNCbl & NBD-X (1:1, blue) obtained in CH_3OH at 25 °C. The spectra of CNCbl and NBD-X have been combined in the Origin software (red).